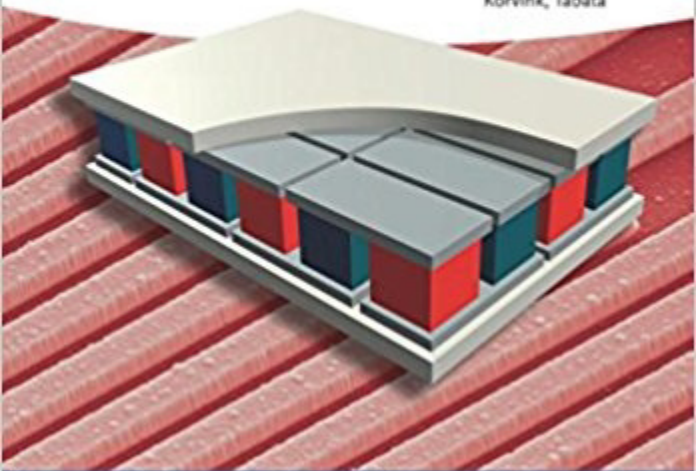


Diana Davila Pineda and Alireza Rezaniakolaei (Eds.)

# Thermoelectric Energy Conversion

Basic Concepts and Device Applications

Series Editors:  
Brand, Fedder, Hierold,  
Korvink, Tabata



ADVANCED MICRO & NANOSYSTEMS

AMN  
Advanced Micro & Nanosystems

**Thermoelectric Energy Conversion**  
**Basic Concepts and Device Applications**

**Related Titles**

- Briand, D., Yeatman, E., Roundy, S. (eds.)  
Micro Energy Harvesting  
2015  
Print ISBN: 978-3-527-31902-2  
eMobi ISBN: 978-3-527-67291-2  
ePub ISBN: 978-3-527-67292-9  
Adobe PDF ISBN: 978-3-527-67293-6  
ISBN: 978-3-527-67294-3
- Klauk, H. (ed.)  
**Organic Electronics II**  
More Materials and Applications  
2012  
Print ISBN: 978-3-527-32647-1  
ISBN: 978-3-527-64021-8  
ePub ISBN: 978-3-527-64022-5  
Adobe PDF ISBN: 978-3-527-64023-2  
eMobi ISBN: 978-3-527-64024-9
- Eibl, O., Nielsch, K., Peranio, N., Völklein, F. (eds.)  
**Thermoelectric Bi<sub>2</sub>Te<sub>3</sub> Nanomaterials**  
2015  
Print ISBN: 978-3-527-33489-6  
ISBN: 978-3-527-67260-8  
eMobi ISBN: 978-3-527-67261-5  
ePub ISBN: 978-3-527-67262-2  
Adobe PDF ISBN: 978-3-527-67263-9
- Brand, O., Dufour, I., Heinrich, S.M., Josse, F. (eds.)  
**Resonant MEMS**  
Fundamentals, Implementation, and Application  
2015  
Print ISBN: 978-3-527-33545-9  
ISBN: 978-3-527-67633-0  
eMobi ISBN: 978-3-527-67634-7  
ePub ISBN: 978-3-527-67635-4  
Adobe PDF ISBN: 978-3-527-67636-1
- Caironi, M., Noh, Y. (eds.)  
**Large Area and Flexible Electronics**  
2015  
Print ISBN: 978-3-527-33639-5  
ISBN: 978-3-527-67997-3  
eMobi ISBN: 978-3-527-67998-0  
ePub ISBN: 978-3-527-67999-7  
Adobe PDF ISBN: 978-3-527-68000-9
- Sun, Y., Liu, X. (eds.)  
**Micro- and Nanomanipulation Tools**  
2015

Print ISBN: 978-3-527-33784-2  
Adobe PDF ISBN: 978-3-527-69022-0  
WOL obook PDF ISBN: 978-3-527-69023-7  
eMobi ISBN: 978-3-527-69024-4  
ePub ISBN: 978-3-527-69025-1

Magdassi, S., Kamyshny, A., Shacham-Diamand, Y. (eds.)  
**Nanomaterials for 2D and 3D Printing**  
2017  
Print ISBN: 978-3-527-33819-1  
WOL obook PDF ISBN: 978-3-527-68579-0  
ePub ISBN: 978-3-527-68580-6  
Adobe PDF ISBN: 978-3-527-68582-0  
eMobi ISBN: 978-3-527-68584-4

Subramanian, V. (ed.)  
**2D and 3D Printing-based Fabrication**  
2016  
Print ISBN: 978-3-527-33826-9  
WOL obook PDF ISBN: 978-3-527-68602-5  
ePub ISBN: 978-3-527-68603-2  
eMobi ISBN: 978-3-527-68604-9  
Adobe PDF ISBN: 978-3-527-68605-6

Anders, J., Korvink, J.G. (eds.)  
**Micro and Nano Scale NMR**  
Technologies and Systems  
2018  
Print ISBN: 978-3-527-34056-9  
WOL obook PDF ISBN: 978-3-527-69728-1  
ePub ISBN: 978-3-527-69733-5  
Adobe PDF ISBN: 978-3-527-69734-2  
eMobi ISBN: 978-3-527-69735-9

Cicoira, F., Santato, C. (eds.)  
**Organic Electronics**  
Emerging Concepts and Technologies  
2013  
Print ISBN: 978-3-527-41131-3  
ISBN: 978-3-527-65096-5  
eMobi ISBN: 978-3-527-65097-2  
ePub ISBN: 978-3-527-65098-9  
Adobe PDF ISBN: 978-3-527-65099-6

Lin, Y., Lan, J., Liu, Y., Nan, C. (eds.)  
**Oxide Thermoelectric Materials**  
From Basic Principles to Applications  
2017  
Print ISBN: 978-3-527-34197-9  
Adobe PDF ISBN: 978-3-527-80752-9  
eMobi ISBN: 978-3-527-80753-6  
ePub ISBN: 978-3-527-80754-3  
WOL obook PDF ISBN: 978-3-527-80755-0

# **Thermoelectric Energy Conversion**

Basic Concepts and Device Applications

*Edited by*

*Diana Dávila Pineda*

*Alireza Rezania*

**WILEY-VCH**

**Editors****Dr. Diana Dávila Pineda**

IBM Research – Zurich Lab  
Science & Technology Department  
Säumerstrasse 4  
8803 Rüschlikon  
Switzerland

**Dr. Alireza Rezania**

Aalborg University  
Department of Energy Technology  
Pontoppidanstraede 101  
9220 Aalborg  
Denmark

All books published by **Wiley-VCH** are carefully produced. Nevertheless, authors, editors, and publisher do not warrant the information contained in these books, including this book, to be free of errors. Readers are advised to keep in mind that statements, data, illustrations, procedural details or other items may inadvertently be inaccurate.

**Library of Congress Card No.:**

applied for

**British Library Cataloguing-in-Publication Data**

A catalogue record for this book is available from the British Library.

**Bibliographic information published by the Deutsche Nationalbibliothek**

The Deutsche Nationalbibliothek lists this publication in the Deutsche Nationalbibliografie; detailed bibliographic data are available on the Internet at <<http://dnb.d-nb.de>>.

© 2017 Wiley-VCH Verlag GmbH & Co.  
KGaA, Boschstr. 12, 69469 Weinheim,  
Germany

All rights reserved (including those of translation into other languages). No part of this book may be reproduced in any form – by photoprinting, microfilm, or any other means – nor transmitted or translated into a machine language without written permission from the publishers. Registered names, trademarks, etc. used in this book, even when not specifically marked as such, are not to be considered unprotected by law.

**Print ISBN:** 978-3-527-34071-2

**ePDF ISBN:** 978-3-527-69814-1

**ePub ISBN:** 978-3-527-69813-4

**Mobi ISBN:** 978-3-527-69812-7

**oBook ISBN:** 978-3-527-69811-0

**Cover Design** Schulz Grafik-Design,  
Fußgönheim, Germany

**Typesetting** SPi Global, Chennai, India

**Printing and Binding**

Printed on acid-free paper

## Contents

**About the Editors** *xiii*

**Series Editors' Preface** *xv*

**List of Contributors** *xvii*

- 1 Utilizing Phase Separation Reactions for Enhancement of the Thermoelectric Efficiency in IV–VI Alloys 1**  
*Yaniv Gelstein*
- 1.1 Introduction 1
  - 1.2 IV–VI Alloys for Waste Heat Thermoelectric Applications 2
  - 1.3 Thermodynamically Driven Phase Separation Reactions 6
  - 1.4 Selected IV–VI Systems with Enhanced Thermoelectric Properties Following Phase Separation Reactions 9
  - 1.5 Concluding Remarks 11
  - References 11
- 2 Nanostructured Materials: Enhancing the Thermoelectric Performance 15**  
*Ngo Van Nong and Le Thanh Hung*
- 2.1 Introduction 15
  - 2.2 Approaches for Improving  $ZT$  16
  - 2.3 Recent Progress in Developing Bulk Thermoelectric Materials 18
  - 2.4 Bulk Nanostructured Thermoelectric Materials 20
    - 2.4.1  $\text{Bi}_2\text{Te}_3$ -Based Nanocomposites 20
    - 2.4.2 PbTe-Based Nanostructured Materials 21
    - 2.4.3 Half-Heusler Alloys 22
    - 2.4.4 Nanostructured Skutterudite Materials 24
    - 2.4.5 Nanostructured Oxide Materials 26
      - 2.4.5.1 p-Type Oxides 26
      - 2.4.5.2 n-Type Oxides 28
    - 2.5 Outlook and Challenges 28
    - Acknowledgement 29
    - References 29

<b>3</b>	<b>Organic Thermoelectric Materials</b>	<b>37</b>
	<i>Simone Fabiano, Ioannis Petsagkourakis, Guillaume Fleury, Georges Hadzioannou and Xavier Crispin</i>	
3.1	Introduction	37
3.2	Seebeck Coefficient and Electronic Structure	41
3.3	Seebeck Coefficient and Charge Carrier Mobility	44
3.4	Optimization of the Figure of Merit	45
3.5	N-Doping of Conjugated Polymers	46
3.6	Elastic Thermoelectric Polymers	48
3.7	Conclusions	48
	Acknowledgments	50
	References	50
<b>4</b>	<b>Silicon for Thermoelectric Energy Harvesting Applications</b>	<b>55</b>
	<i>Dario Narducci, Luca Belsito and Alex Morata</i>	
4.1	Introduction	55
4.1.1	Silicon as a Thermoelectric Material	55
4.1.2	Current Uses of Silicon in TEGs	56
4.2	Bulk and Thin-Film Silicon	57
4.2.1	Single-Crystalline and Polycrystalline Silicon	57
4.2.2	Degenerate and Phase-Segregated Silicon	60
4.3	Nanostructured Silicon: Physics of Nanowires and Nanolayers	63
4.3.1	Introduction	63
4.3.2	Electrical Transport in Nanostructured Thermoelectric Materials	63
4.3.3	Phonon Transport in Nanostructured Thermoelectric Materials	66
4.4	Bottom-Up Nanowires	66
4.4.1	Preparation Strategies	66
4.4.2	Chemical Vapor Deposition (CVD)	67
4.4.3	Molecular Beam Epitaxy (MBE)	68
4.4.4	Laser Ablation	68
4.4.5	Solution-Based Techniques	69
4.4.6	Catalyst Materials	69
4.4.7	Catalyst Deposition Methods	70
4.5	Material Properties and Thermoelectric Efficiency	71
4.6	Top-Down Nanowires	71
4.6.1	Preparation Strategies	71
4.6.2	Material Properties and Thermoelectric Efficiency	75
4.7	Applications of Bulk and Thin-Film Silicon and SiGe Alloys to Energy Harvesting	77
4.8	Applications of Nanostructured Silicon to Energy Harvesting	79
4.8.1	Bottom-Up Nanowires	79
4.8.2	Top-Down Nanowires	80
4.9	Summary and Outlook	83
	Acknowledgments	84
	References	84

<b>5</b>	<b>Techniques for Characterizing Thermoelectric Materials: Methods and the Challenge of Consistency</b>	<b>93</b>
	<i>Hans-Fridtjof Pernau</i>	
5.1	Introduction – Hitting the Target	93
5.2	Thermal Transport in Gases and Solid-State Materials	94
5.3	The Combined Parameter ZT-Value	97
5.3.1	Electrical Conductivity	98
5.3.2	Seebeck Coefficient	101
5.3.3	Thermal Conductivity	103
5.4	Summary	107
	Acknowledgments	107
	References	107
<b>6</b>	<b>Preparation and Characterization of TE Interfaces/Junctions</b>	<b>111</b>
	<i>Gao Min and Matthew Phillips</i>	
6.1	Introduction	111
6.2	Effects of Electrical and Thermal Contact Resistances	111
6.3	Preparation of Thermoelectric Interfaces	114
6.4	Characterization of Contact Resistance Using Scanning Probe	117
6.5	Characterization of Thermal Contact Using Infrared Microscope	121
6.6	Summary	123
	Acknowledgments	124
	References	124
<b>7</b>	<b>Thermoelectric Modules: Power Output, Efficiency, and Characterization</b>	<b>127</b>
	<i>Jorge García-Cañadas</i>	
7.1	Introduction	127
7.1.1	Moving from Materials to a Device	127
7.1.2	Differences in Characterization	128
7.1.3	Chapter Summary	130
7.2	The Governing Equations	130
7.2.1	Particle Fluxes and the Continuity Equation	130
7.2.2	Energy Fluxes and the Heat Equation	132
7.3	Power Output and Efficiency	136
7.3.1	Power Output	137
7.3.2	Efficiency	139
7.4	Characterization of Devices	142
7.4.1	Thermal Contacts	142
7.4.2	Additional Considerations	143
7.4.3	Constant Heat Input and Constant $\Delta T$	144
	References	145

<b>8</b>	<b>Integration of Heat Exchangers with Thermoelectric Modules</b>	<b>147</b>
	<i>Alireza Rezania</i>	
8.1	Introduction	147
8.2	Heat Exchanger Design – Consideration in TEG Systems	148
8.3	Cold Side Heat Exchanger for TEG Maximum Performance	150
8.4	Cooling Technologies and Design Challenges	154
8.5	Microchannel Heat Exchanger	156
8.6	Coupled and Comprehensive Simulation of TEG System	157
8.6.1	Governing Equations	157
8.6.2	Effect of Heat Exchanger Inlet/Outlet Plenums on TEG Temperature Distribution	158
8.6.3	Modified Channel Configuration	162
8.6.4	Flat-Plate Heat Exchanger versus Cross-Cut Heat Exchanger	164
8.6.5	Effect of Channel Hydraulic Diameter	167
8.7	Power–Efficiency Map	168
8.8	Section Design Optimization in TEG System	169
8.9	Conclusion	170
	Acknowledgment	170
	Nomenclature	170
	References	172
<b>9</b>	<b>Power Electronic Converters and Their Control in Thermoelectric Applications</b>	<b>177</b>
	<i>Erik Schatzl and Elena A. Man</i>	
9.1	Introduction	177
9.2	Building Blocks of Power Electronics	177
9.3	Power Electronic Topologies	179
9.3.1	Buck Converter	180
9.3.1.1	On-state	181
9.3.1.2	Off-state	181
9.3.1.3	Averaging	181
9.3.2	Boost Converter	182
9.3.3	Non-Inverting Buck Boost Converter	183
9.3.4	Flyback Converter	184
9.4	Electrical Equivalent Circuit Models for Thermoelectric Modules	185
9.5	Maximum Power Point Operation and Tracking	186
9.5.1	MPPT-Methods	187
9.5.1.1	Perturb and Observe	187
9.5.1.2	Incremental Conductance	189
9.5.1.3	Fractional Open Circuit Voltage	189
9.6	Case Study	191
9.6.1	Specifications	192
9.6.2	Requirements	193
9.6.3	Design of Passive Components	193
9.6.4	Transfer Functions	194

9.6.5	Design of Current Controller	196
9.6.6	MPPT Implementation	196
9.6.7	Design of Voltage Controller	198
9.7	Conclusion	201
	References	201
<b>10</b>	<b>Thermoelectric Energy Harvesting for Powering Wearable Electronics</b>	<b>205</b>
	<i>Luca Franciosi and Chiara De Pascali</i>	
10.1	Introduction	205
10.2	Human Body as Heat Source for Wearable TEGs	205
10.3	TEG Design for Wearable Applications: Thermal and Electrical Considerations	208
10.4	Flexible TEGs: Deposition Methods and Thermal Flow Design Approach	212
10.4.1	Deposition Methods	212
10.4.1.1	Screen Printing	213
10.4.1.2	Inkjet Printing	213
10.4.1.3	Molding	213
10.4.1.4	Lithography	214
10.4.1.5	Vacuum Deposition Techniques	214
10.4.1.6	Thermal Evaporation	214
10.4.1.7	Sputtering	215
10.4.1.8	Molecular Beam Epitaxy (MBE)	215
10.4.1.9	Metal Organic Chemical Vapor Deposition (MOCVD)	216
10.4.1.10	Electrochemical Deposition	216
10.4.1.11	Vapor–Liquid–Solid (VLS) Growth	216
10.4.2	Heat Flow Direction Design Approach in Wearable TEG	217
10.5	TEG Integration in Wearable Devices	218
10.6	Strategies for Performance Enhancements and Organic Materials	221
10.6.1	Organic Thermoelectric Materials	223
	References	225
<b>11</b>	<b>Thermoelectric Modules as Efficient Heat Flux Sensors</b>	<b>233</b>
	<i>Gennadi Gromov</i>	
11.1	Introduction	233
11.1.1	Applications of Heat Flux Sensors	233
11.1.2	Units of Heat Flux and Characteristics of Sensors	234
11.1.3	Modern Heat Flux Sensors	235
11.1.4	Thermoelectric Heat Flux Sensors	236
11.2	Applications of Thermoelectric Modules	238
11.3	Parameters of Thermoelectric Heat Flux Sensors	240
11.3.1	Integral Sensitivity $S_a$	240
11.3.2	Sensitivity $S_e$	241
11.3.3	Thermal Resistance $R_T$	241
11.3.4	Noise Level	241

11.3.5	Sensitivity Threshold	241
11.3.6	Noise-Equivalent Power <i>NEP</i>	242
11.3.7	Detectivity $D^*$	242
11.3.8	Time Constant $\tau$	243
11.4	Self-Calibration Method of Thermoelectric Heat Flux Sensors	243
11.4.1	Sensitivity	243
11.4.1.1	Method	243
11.4.1.2	Examples	245
11.4.2	Values of NEP and $D^*$	247
11.5	Sensor Performance and Thermoelectric Module Design	247
11.5.1	Dependence on Physical Properties	248
11.5.2	Design Parameters	248
11.6	Features of Thermoelectric Heat Flux Sensor Design	249
11.7	Optimization of Sensors Design	250
11.7.1	Properties of Thermoelectric Material	251
11.7.2	Parameters of Thermoelectric Module	251
11.7.2.1	Pellets Form-Factor	251
11.7.2.2	Thermoelement Height	252
11.7.2.3	Dimensions of Sensors	254
11.7.2.4	Pellets Number	254
11.7.3	Features of Real Design	255
11.8	Experimental Family of Heat Flux Sensors	257
11.8.1	HTX – Heat Flux and Temperature Sensors (HT – Heat Flux and Temperature)	257
11.8.2	HFX – Heat Flux Sensors without Temperature (HF – Heat Flux)	257
11.8.3	HRX-IR Radiation Heat Flux Sensors (HR – Heat Flux Radiation)	257
11.9	Investigation of Sensors Performance	259
11.9.1	General Provisions	259
11.9.2	Calibration of Sensor Sensitivity	259
11.9.3	Sensitivity Temperature Dependence	261
11.9.4	Thermal Resistance	263
11.9.5	Typical Temperature Dependence of the Seebeck Coefficient	264
11.9.6	Conclusions	264
11.10	Heat Flux Sensors at the Market	265
11.11	Examples of Applications	268
11.11.1	Microcalorimetry: Evaporation of Water Drop	268
11.11.2	Measurement of Heat Fluxes in Soil	269
11.11.3	Thermoelectric Ice Sensor	269
11.11.4	Laser Power Meters	274
	References	278
12	<b>Photovoltaic-Thermoelectric Hybrid Energy Conversion</b>	283
	<i>Ning Wang</i>	
12.1	Background and Theory	283

12.1.1	Introduction	283
12.1.2	PV Efficiency	285
12.1.3	TEG Efficiency	285
12.1.4	PVTE Module Generated Power and Efficiency	285
12.1.5	Energy Loss	285
12.1.6	Cost	286
12.1.7	Overall Feasibility	289
12.2	Different Forms of PVTE Hybrid Systems: The State of the Art	292
12.2.1	PVTE Hybrid Systems Based on Dye-Sensitized Solar Cell (DSSC)	292
12.2.2	Dye-Sensitized Solar Cell with Built-in Nanoscale $\text{Bi}_2\text{Te}_3$ TEG	294
12.2.3	PVTE Using Solar Concentrator	294
12.2.4	Solar-Thermoelectric Device Based on $\text{Bi}_2\text{Te}_3$ and Carbon Nanotube Composites	296
12.3	Optimizations of PVTE Hybrid Systems	297
12.3.1	Geometry Optimization of Thermoelectric Devices in a Hybrid PVTE System	297
12.3.2	Enhancing the Overall Heat Conduction and Light Absorption	298
12.3.3	Fishnet Meta-Structure for IR Band Trapping for Enhancement of PVTE Hybrid Systems	299
12.3.4	Full-Spectrum Photon Management of Solar Cell Structures for PVTE Hybrid Systems	300
12.3.5	An Automotive PVTE Hybrid Energy System Using Maximum Power Point Tracking	301
12.4	Application of PVTE Hybrid Systems	302
12.4.1	Novel Hybrid Solar System for Photovoltaic, Thermoelectric, and Heat Utilization	303
12.4.2	Development of an Energy-Saving Module via Combination of PV Cells and TE Coolers for Green Building Applications	303
12.4.3	Performance of Solar Cells Using TE Module in Hot Sites	303
12.5	Summary	306
	References	307

## About the Editors

**Diana Dávila Pineda** is currently an Advanced Senior Engineer at the IBM Research – Zurich Lab. She received her B.Sc. in Electronic Engineering, from the Tecnológico de Monterrey, Mexico in 2004 and her M.S. in Micro and Nanoelectronic Engineering in 2008 and Ph.D. in Electronic Engineering in 2011 from the Universitat Autònoma de Barcelona, Spain. She has conducted research on fuel cells, nanomaterials, thermoelectricity, spintronics and MEMS devices in multidisciplinary environments such as the Microelectronics Institute of Barcelona (IMB-CNM, CSIC), the Catalonia Institute for Energy Research (IREC), the International Iberian Nanotechnology Laboratory (INL) and ETH Zurich. Her current research interests focus on the development and integration of nanostructured thermoelectric materials for powering micro/nanodevices.

**Alireza Rezania** studied Mechanical Engineering at University of Mazandaran, Iran and, got his PhD in Energy Engineering from Aalborg University in 2012. He is an Assistant Professor in Department of Energy Technology at Aalborg University, Denmark, where he holds the position of Thermoelectric Research Programme Chair. His current research interests include low power energy harvesting, fluid mechanics, thermal engineering with focus on micro heat transfer surfaces applied to thermoelectric modules, and integration of thermoelctric technology with renewable systems and sensor applications.

## Series Editors' Preface

The emerging field of autonomous and ultra-low power sensor systems as an important domain in the Internet of Things and as providers of Big Data has triggered a new wave of research for energy harvesters and in particular of such harvesters based on thermoelectric principles. Competing with continuously improving batteries, which may allow the operation of ultra-low power sensor systems for several years, thermoelectric energy conversion systems are optimized with respect to material efficiency for applications around room temperature and thermal matching by enhanced system design of the thermal interfaces, maintaining high temperature differences at sufficient thermal heat flux. The latter aspect is in particular also important for thermoelectric systems for waste heat recovery, which operate at higher temperature differences, but still at (very) low Carnot efficiencies. Return of investment depends significantly on optimized system design, low cost, large area fabrication technologies, and low material costs.

We present the 14<sup>th</sup> volume of Advanced Micro & Nanosystems (AMN), entitled *Thermoelectric Energy Conversion*.

Professor Dr Alireza Rezania, Aalborg University, and Dr Diana Dávila Pineda, IBM Research – Zurich, are both renowned experts in this domain. They were very successful in coordinating a number of leading researchers and authors from research and industry to present a book on thermoelectric energy conversion. This book will be of great benefit for scientists and graduate students entering the field or looking for specific information, and also for industry researchers, technology strategists, and deciders in companies, who want to get a quick, but comprehensive access to the field of thermoelectric energy conversion.

Atlanta, Pittsburgh, Zurich,  
Freiburg, Kyoto, April 2017

*Oliver Brand  
Gary K. Fedder  
Christofer Hierold  
Jan G. Korvink  
Osamu Tabata*

## List of Contributors

***Luca Belsito***

CNR  
Institute for Microelectronics and  
Microsystems  
via P. Gobetti 101  
40129 Bologna  
Italy

***Xavier Crispin***

Linköping University  
Department of Science and  
Technology  
Campus Norrköping  
S-60174 Norrköping  
Sweden

***Simone Fabiano***

Linköping University  
Department of Science and  
Technology  
Campus Norrköping  
S-60174 Norrköping  
Sweden

***Guillaume Fleury***

CNRS-Université de Bordeaux-INP  
(UMR5629)  
Laboratoire de Chimie des Polymères  
Organiques (LCPO)  
33615 Pessac Cedex  
France

***Luca Franciosi***

CNR-IMM Institute for  
Microelectronics and Microsystems  
Via Monteroni  
University Campus  
73100 Lecce  
Italy

***Jorge García-Cañadas***

Universitat Jaume I  
Department of Industrial Systems  
Engineering and Design Campus del  
Riu Sec, 12071 Castellón  
Spain

***Yaniv Gelbstein***

Ben-Gurion University of the Negev  
Department of Materials Engineering  
Beer-Sheva 84105  
Israel

***Gennadi Gromov***

PromLegion Ltd.  
46 Warshavskoeshosse  
115230 Moscow  
Russia

**Georges Hadzioannou**

CNRS-Université de Bordeaux-INP  
(UMR5629)  
Laboratoire de Chimie des Polymères  
Organiques (LCPO)  
33615 Pessac Cedex  
France

**Le Thanh Hung**

Technical University of Denmark  
Department of Energy Conversion  
and Storage  
Frederiksborgvej 399  
4000 Roskilde  
Denmark

**Elena A. Man**

Aalborg University  
Department of Energy Technology  
Pontoppidanstraede 111  
9220 Aalborg  
Denmark

**Gao Min**

Cardiff University  
Institute of Energy and Environment  
School of Engineering  
The Parade  
Cardiff  
UK

**Alex Morata**

Catalonia Institute for Energy  
Research (IREC)  
Department of Advanced Materials  
for Energy Applications  
Jardins de les Dones de Negre 1  
E-08930 Sant Adrià de Besòs  
Barcelona  
Spain

**Dario Narducci**

University of Milano Bicocca  
Department of Materials Science  
via R. Cozzi 55  
20125 Milan  
Italy

**Ngo Van Nong**

Technical University of Denmark  
Department of Energy Conversion  
and Storage  
Frederiksborgvej 399  
4000 Roskilde  
Denmark

**Chiara De Pascali**

CNR-IMM Institute for  
Microelectronics and Microsystems  
Via Monteroni  
University Campus  
73100 Lecce  
Italy

**Hans-Fridtjof Pernau**

Fraunhofer Institute for Physical  
Measurement Techniques, IPM,  
Department GP/TMS  
Heidenhofstr. 8  
79110 Freiburg  
Germany

**Ioannis Petsagkourakis**

CNRS-Université de Bordeaux-INP  
(UMR5629)  
Laboratoire de Chimie des Polymères  
Organiques (LCPO)  
33615 Pessac Cedex  
France

**Matthew Phillips**

Cardiff University  
Institute of Energy and Environment  
School of Engineering  
The Parade  
Cardiff  
UK

***Alireza Rezania***

Aalborg University  
Department of Energy Technology  
Pontoppidanstraede 101  
9220 Aalborg  
Denmark

***Erik Schatz***

Aalborg University  
Department of Energy Technology  
Pontoppidanstraede 111  
9220 Aalborg  
Denmark

***Ning Wang***

University of Electronic Science and  
Technology of China  
Department of Microelectronics  
and Solid-state Electronics  
Chengdu 610054  
P.R. China

## 1

## Utilizing Phase Separation Reactions for Enhancement of the Thermoelectric Efficiency in IV–VI Alloys

*Yaniv Gelbstein*

*Ben-Gurion University of the Negev, Department of Materials Engineering, Beer-Sheva, 84105, Israel*

### 1.1 Introduction

In recent years, demands for energy efficiency have motivated many researchers worldwide to seek innovative methods capable of enhancing the efficiency of the thermoelectric energy conversion of heat to electricity. Since the dimensionless thermoelectric figure of merit  $ZT$  ( $=\alpha^2\sigma T/\kappa$ , where  $\alpha$  is the Seebeck coefficient,  $\sigma$  is the electrical conductivity,  $\kappa$  is the thermal conductivity, and  $T$  is the absolute temperature) can be regarded to be proportional to the thermoelectric efficiency for a given temperature difference, materials improvements in this direction include either electronic optimization methods for maximizing the  $\alpha^2\sigma$  product or phonons scattering methods for minimizing the thermal conductivity (the denominator of  $ZT$ ). These methods and approaches mainly involve interfaces and submicron generation methods, which are much more effective in phonon scattering (rather than electron scattering), and consequently reducing the lattice contribution to the thermal conductivity,  $\kappa_L$ , without adversely affecting the other involved electronic properties. The main challenge while dealing with submicron features and interfaces for phonon scattering lies in the ability to retain these features under the thermal conditions involved and the suppression of undesirable coarsening effects over time. One plausible method for overcoming this challenge is based on using thermodynamically driven phase separation (i.e., spinodal decomposition or nucleation and growth) reactions, resulting in submicron and multiinterface features, owing to the separation of the matrix into two distinct phases, upon controlled heat treatments. The resultant features from these reactions are considered as more thermodynamically stable than other conventional nanostructuring methods, based on rapid consolidation of nanopowders obtained by energetic ball milling or melt spinning, which are susceptible to grain growth upon prolonged high temperature operation conditions. The key in choosing appropriate thermoelectric compositions, which follow phase separation reactions, is the requirement for a miscibility gap between the involved phases. This condition is strongly dependent on the nature

of the chemical pair interaction between the involved substitution elements. They can either distribute randomly in the host materials or separate the system into different phase components. An attractive chemical interaction can lead to an inhomogeneous distribution of the substitution atoms, leading to phase separation. Otherwise, the atoms will be substituted in the host system with a high solubility, forming a single solid solution phase. For achieving phase separation, compositions with attractive chemical interactions are required.

## 1.2 IV–VI Alloys for Waste Heat Thermoelectric Applications

The binary IV–VI compounds, based on columns IV (Ge, Pb, and Sn) and VI (Te, Se, and S) of the periodic table, are narrow-band (~0.2–0.3 eV) mixed ionic–covalent compounds, which are known for several decades as the most efficient thermoelectric materials for intermediate temperature ranges of up to 500 °C. The possibility for operation under the temperature range of 100–500 °C is significant from a practical point of view for converting waste heat generated in automotive diesel engines, in which a maximal temperature of 500 °C is developed, into useful electricity, and thus reducing fuel consumption and CO<sub>2</sub> emission. In the automotive industry, the minimal cold side temperature of ~100 °C is mainly limited by the maximum available water flow rate through the radiator.

Lead chalcogenides (PbTe, PbSe, and PbS) crystallize in a NaCl cubic lattice, similarly to what happens in the high temperature phases of SnTe and GeTe. The latter follow a second-order lattice distortion to rhombohedral or orthorhombic structures upon decreasing the temperature, the significance of which on practical thermoelectric applications will be reviewed in detail in the following paragraphs. Another characteristic of the IV–VI compounds is the large deviation of stoichiometry, which in the case of PbTe is extended toward both Pb- and Te-rich compositions, enabling control of the electronic conduction toward n- and p-type conduction, respectively. In the case of GeTe, the deviation of stoichiometry is toward Te-rich compositions only, resulting in high carrier concentration ( $10^{20}$ – $10^{21}/\text{cm}^3$ ) p-type conduction, which is beyond the optimal required for thermoelectric applications ( $\sim 10^{19}/\text{cm}^3$ ). To reduce the holes concentration in order to obtain optimal thermoelectric properties, it is necessary to dope GeTe with donor-type electroactive impurities. Bi<sub>2</sub>Te<sub>3</sub> acts as a donor when it is dissolved in GeTe. In the case of PbTe, the most common dopants are PbI<sub>2</sub> and Bi for obtaining optimal thermoelectric n-type compositions and Na for the p-type. Yet, for many years, owing to opposite influences of the carrier concentration on the various properties involved in the thermoelectric figure of merit,  $ZT$ , all the attempts to maximize the  $ZT$  value of the binary IV–VI compounds beyond ~1 just by electronically doping optimization did not succeed. In the recent years, combined methods of electronic optimization and nanostructuring for reduction of the lattice thermal conductivity in IV–VI based alloys resulted in much higher  $ZT$  values of up to ~2.2, as can be seen in Figure 1.1a,b for various p- and n-type compositions, respectively [1–13].

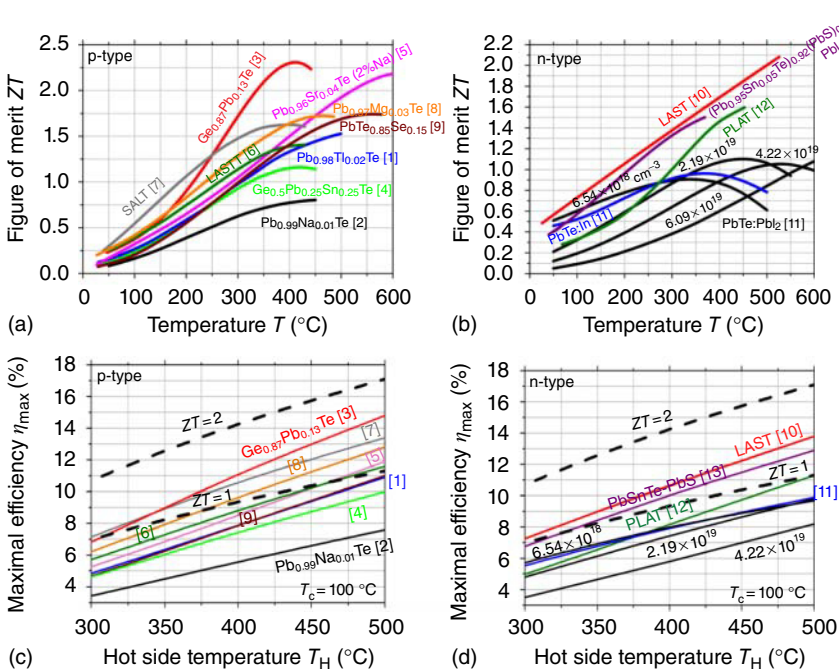


**Figure 1.1**  $ZT$  values of the most efficient IV-VI alloys recently published – the p-type:  $Pb_{0.98}Tl_{0.02}Te$  [1],  $Pb_{0.99}Na_{0.01}Te$  [2],  $Ge_{0.87}Pb_{0.13}Te$  [3],  $Ge_{0.5}Pb_{0.25}Sn_{0.25}Te$  [4],  $Pb_{0.96}Sr_{0.04}Te$  (2%Na) [5],  $Ag_{0.9}Pb_5Sn_3Sb_{0.7}Te_{10}$  – LASTT [6],  $Na_{0.95}Pb_{20}SbTe_{22}$  – SALT [7],  $Pb_{0.97}Mg_{0.03}Te:Na$  [8],  $PbTe_{0.85}Se_{0.15}$ :2%Na [9]; and n-type:  $AgPb_{18}Sb_{20}$  – LAST [10],  $PbTe$  (0.1 at%In) [11],  $Pbl_2$  doped  $PbTe$  with various carrier concentrations of  $6.54 \times 10^{18}$ ,  $2.19 \times 10^{19}$ ,  $4.22 \times 10^{19}$  and  $6.09 \times 10^{19}/cm^3$  [11],  $K_{0.95}Pb_{20}Sb_{1.2}Te_{22}$  – PLAT [12], and  $(Pb_{0.95}Sn_{0.05}Te)_{0.92}(PbS)_{0.08}$ :0.055 mol%  $Pbl_2$  [13]. (Pei et al. 2012 [8]. Reproduced with permission of Nature Publishing Group.)

It can be seen in the figure that early attempts to optimize the p-type Na-doped  $PbTe$  ( $Pb_{0.99}Na_{0.01}Te$  [2]) and the n-type  $Pbl_2$ -doped  $PbTe$  with various carrier concentrations of  $6.54 \times 10^{18}$ ,  $2.19 \times 10^{19}$ ,  $4.22 \times 10^{19}$ , and  $6.09 \times 10^{19}/cm^3$  [11] resulted in relatively low maximal  $ZT$ s of 0.8 and 1.1, respectively. An effect of reduction of the carrier concentration on reduction of the maximal temperature at which maximal  $ZT$  is obtained because of electronic doping optimization can be easily seen for the  $Pbl_2$ -doped  $PbTe$  [11] compositions in the figure. This finding had initiated the functionally graded materials (FGM) concept, in which thermoelectric legs composed of a singular matrix compound (e.g.,  $PbTe$ ) doped by a gradual dopant concentration, each optimal in its correspondent temperature along the leg, yield higher average  $ZT$  values than any singular doping concentration over the wide temperature gradients, usually apparent in practical operations. Yet, even this approach did not yield average  $ZT$ s higher than 1 for common operation conditions of 100–500 °C, and novel approaches for  $ZT$  enhancement had to be considered. One of such approaches, inspired by Kaidanov and Ravich [14], was based on advanced electronic doping based on generation of localized “deep” resonant states lying inside the energy gap, which are capable of pinning the Fermi energy of the compounds at a

favorable level, required for electronic thermoelectric optimization. Related to IV–VI based compounds, it was found that Group III dopants (Al, Ga, In, Tl) can be utilized for generation of such states. Application of this approach for thermoelectric optimization of n-type In-doped PbTe [11] resulted in higher average  $ZT$  for the temperature range of 100–500 than any of the  $\text{PbI}_2$ -doped materials, but without any success in increasing the average  $ZT$  beyond 1. On the other hand, a dramatic increase of the maximal  $ZT$  to a level of ~1.5 was recently demonstrated upon Tl doping of PbTe for the p-type  $\text{Pb}_{0.98}\text{Tl}_{0.02}\text{Te}$  [1] composition (Figure 1.1a). A second approach that was taken in the recent years for enhancement of the  $ZT$  values of IV–VI based alloys is based on nanostructuring for reduction of the lattice thermal conductivity. Several examples of nanostructured materials with maximal  $ZTs$  higher than 1 and in some cases even higher than 2 are illustrated in Figure 1.1a,b. These include the p-type  $\text{Ag}_x(\text{Pb},\text{Sn})_m\text{Sb}_y\text{Te}_{2+m}$  (LASTT) [6],  $\text{NaPb}_m\text{SbTe}_{2+m}$  (SALT) [7],  $\text{Ge}_x(\text{Sn}_y\text{Pb}_{1-y})_{1-x}\text{Te}$  [3, 4], and the n-type  $\text{AgPb}_m\text{SbTe}_{2+m}$  (LAST) [10],  $\text{KPb}_m\text{SbTe}_{m+2}$  (PLAT) [12], and  $(\text{Pb}_{0.95}\text{Sn}_{0.05}\text{Te})_x(\text{PbS})_{1-x}$  [13] families of materials; all exhibit nanostructures and very low lattice thermal conductivities. Different mechanisms for nanostructuring are involved in the above-listed examples. Yet, two of the most efficient materials listed in Figure 1.1a,b are the p-type  $\text{Ge}_{0.87}\text{Pb}_{0.13}\text{Te}$  [3] and the n-type  $(\text{Pb}_{0.95}\text{Sn}_{0.05}\text{Te})_{0.92}(\text{PbS})_{0.08}$  [13] compositions, both following thermodynamically driven phase separation reactions of the matrix into two distinct submicron phases. Since such reactions and the correspondent nanophases are considered as much more thermodynamically stable than many of the other methods listed above, as required for long-term thermoelectric applications, a detailed description of this effect and the conditions for achieving it will be given in the next paragraph.

It is noteworthy that the above-listed methods and compositions resulting in maximal  $ZTs$  higher than 1, as shown in Figure 1.1a,b, did not necessarily result in higher average  $ZTs$  than 1 over the entire operation temperature range (100–500 °C) required for automotive waste heat recovery. For such applications the maximal possible thermoelectric efficiency, defined as the ratio between the obtained electrical power on the load resistance and the absorbed heat, can be calculated using Eq. (1.1).

$$\eta = \frac{\Delta T}{T_H} \cdot \frac{\sqrt{1 + \overline{ZT}} - 1}{\sqrt{1 + \overline{ZT}} + \frac{T_C}{T_H}} \quad (1.1)$$

where  $\eta$  is the thermoelectric efficiency,  $\overline{ZT}$  is the average dimensionless thermoelectric figure of merit,  $T_C$  is the cold side temperature of the thermoelectric sample,  $T_H$  is the hot side temperature of the thermoelectric sample, and  $\Delta T$  is the temperature difference along the thermoelectric sample ( $\Delta T = T_H - T_C$ ).

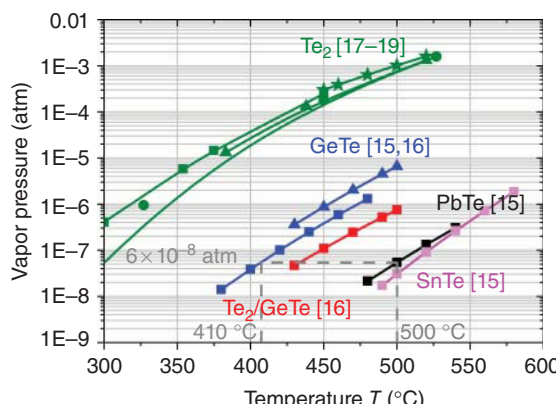
The maximal thermoelectric efficiency values for the samples shown in Figure 1.1a,b, calculated using Eq. (1.1) and the average  $ZTs$  for each composition, are illustrated in Figure 1.1c,d for a constant cold side temperature of 100 °C and varied hot side temperatures in the range of 300–500 °C. From these figures it can be easily seen that some of the recently published compositions

showing maximal  $ZT$ s higher than 1 and in some cases even higher than 1.6, do not necessarily show higher efficiency values than those calculated using Eq. (1.1) for an average  $ZT$  of 1 (dashed line in the figure). On the other hand, some of the compositions show very high efficiency values of up to 14–15% (the p-type  $\text{Ge}_{0.87}\text{Pb}_{0.13}\text{Te}$  [3] and the n-type  $\text{AgPb}_{18}\text{SbTe}_{20}$  – LAST [10] compositions) for the temperature range of 100–500 °C.

Besides high average  $ZT$ s, other important factors required for practical applications include high mechanical properties and improved structural and chemical stability at the operating temperatures. Mechanical properties are important in determining the performance of thermoelectric materials since they are subject in the course of their operation to various mechanical and thermal stresses. In this context, it was recently shown that the less thermoelectrically efficient p- $\text{Pb}_{1-x}\text{Sn}_x\text{Te}$  compound, compared to Na-doped PbTe, is more favorable for practical thermoelectric applications because of the highly mechanical brittle nature of the latter [2]. Regarding chemical and structural stability, PbTe-based compounds were associated for many years with improved structural and chemical stability at the operating temperatures than GeTe-based compounds. The improved chemical stability is due to a lower vapor pressure, namely, lower sublimation rates of PbTe, as can be seen in Figure 1.2.

In telluride-based thermoelectric materials (e.g., PbTe and GeTe), the main degradation mechanism during normal operation conditions (100–500 °C) is sublimation of GeTe, PbTe, or SnTe in a molecular form (Figure 1.2). For PbTe, the maximal allowed hot side temperature for long operation conditions is 500 °C, corresponding to a maximal vapor pressure of  $\sim 6 \times 10^{-8}$  atm (Figure 1.2). It can be seen from the figure that this vapor pressure corresponds to a temperature of  $\sim 410$  °C for the case of GeTe, which can be considered as the maximal allowed operation temperature for this class of materials. Beyond this temperature, high sublimation and corresponding degradation rates can be expected. An improved structural stability of PbTe compared to GeTe was considered for many years mainly because of the single-phase cubic NaCl structure of PbTe over the whole operating temperature range, in contrast to the rhombohedral to cubic NaCl phase transition at 427 °C in GeTe. Recently, the highly efficient

**Figure 1.2** Temperature dependence of the vapor pressures of various IV–VI alloys and the mostly volatile elements in these systems [15–19].



p-type  $\text{Ge}_x\text{Pb}_{1-x}\text{Te}$  alloys, including the  $\text{Ge}_{0.87}\text{Pb}_{0.13}\text{Te}$  composition shown in Figure 1.1a, were shown to follow a second-order phase transition from the high-temperature cubic phase to the low-temperature rhombohedral phase with a decreased phase transition temperature,  $T_c$ , by moving from  $\text{GeTe}$  toward  $\text{PbTe}$  richer compositions [20]. Second-order phase transitions occur when a new state of reduced symmetry develops continuously from the disordered (high temperature) phase and are characterized by the absence of discontinuities of the thermodynamic state functions (entropy, enthalpy, volume). The character of the phase transition (first- or second-order) is important to determine whether a certain material is suitable for serving in thermoelectric applications in which large temperature gradients are usually involved. In such instances, a singular intermediate temperature  $T_c$  at which one crystal structure is transformed into another with the corresponding sharp variation of the lattice parameters (as in first-order transitions) can result in mechanical weakness. A continuous variation of the lattice parameters from one phase to the other (as in second-order transitions) is more favorable from the mechanical stability standpoint. Therefore,  $\text{Ge}_x\text{Pb}_{1-x}\text{Te}$  alloys exhibit a very high potential, both from mechanical stability and thermoelectric performance considerations, for being involved as p-type legs in practical thermoelectric applications. Since the very high maximal  $ZTs$  of the p-type  $\text{Ge}_{0.87}\text{Pb}_{0.13}\text{Te}$  and the n-type  $(\text{Pb}_{0.95}\text{Sn}_{0.05}\text{Te})_{0.92}(\text{PbS})_{0.08}$  compositions in Figure 1.1a,b are mainly attributed to very low lattice thermal conductivity values resulting from nano- and submicron features originating from phase separation reactions, a detailed description of these reactions and their potential in enhancement of the thermoelectric figure of merit is given in the next paragraph.

### 1.3 Thermodynamically Driven Phase Separation Reactions

As mentioned earlier, retaining a submicron structure during a practical thermoelectric operation under a large temperature gradient is of great importance. One method for retaining such structures is based on the generation of thermodynamically driven phase separation reactions such as spinodal decomposition or nucleation and growth. For understanding the thermodynamic conditions required for generation of such reactions, a basic understanding of the thermodynamics of mixing is required and will be given referring to Figure 1.3.

The Gibbs energy of mixing,  $\Delta G_m$ , for a binary A–B mixture, can be described in terms of Eq. (1.2) [21].

$$\begin{aligned}\Delta G_m &= \Delta H_m - T\Delta S_m \\ &= \omega \cdot x \cdot (1-x) + T \cdot R \cdot [(1-x) \cdot \ln(1-x) + x \cdot \ln(x)]\end{aligned}\quad (1.2)$$

The left term of Eq. (1.2) represents the enthalpy of mixing,  $\Delta H_m$ , while the right term represents the entropy term of mixing ( $-T\Delta S_m$ ), where  $T$  is the absolute temperature,  $\Delta S_m$  is the entropy of mixing,  $x$  is the concentration of one of the mixture's components (the concentration of the other component is therefore

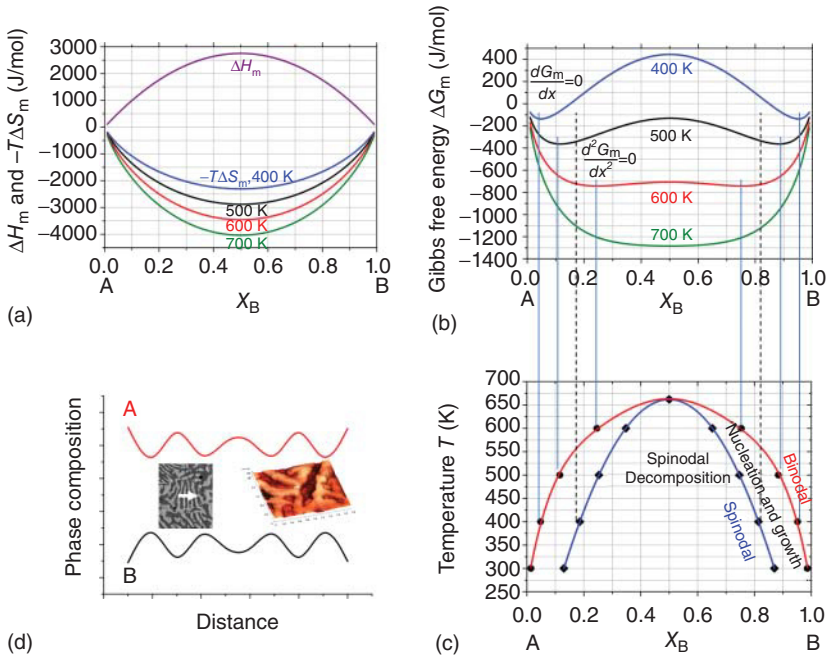


**Figure 1.3** Compositional dependencies of the enthalpy,  $\Delta H_m$ , entropy,  $-T\Delta S_m$ , terms of mixing (a), and Gibbs free energy of mixing,  $\Delta G_m$  (b) for various temperatures; a phase diagram, built from the thermodynamic terms mentioned above, showing a miscibility gap between two components A and B in a binary mixture (c) and a representative phase separation microstructure showing a continuous variation of the concentration of the components A and B in the A–B binary mixture described above (d).

$1 - x$ ),  $\omega$  is the interaction parameter between the mixture's components A and B, and  $R$  is the ideal gas constant ( $=8.314 \text{ J/mol/K}$ ). In ideal mixtures or ideal solutions, in which the enthalpies of mixing equal zero,  $\Delta G_m$  is solely determined by the entropy of mixing. The regular solution model, described by Eq. (1.2), is a simple example of a nonideal solution that can be referred to many of the binary mixtures available in practical thermoelectric systems.  $\Delta S_m$  is always positive, since there is always a positive entropy gain upon mixing, and therefore  $-T\Delta S_m$  is always negative, as described in Figure 1.3a for various temperatures. Therefore, it can be shown that entropy considerations will solely lead to a homogeneous solution with an always negative  $\Delta G_m$  function. Consequently, the miscibility characteristics of the two components A and B in a binary mixture are solely determined by the enthalpy of mixing and more specifically by the dimensionless interaction parameter  $\omega$  (Eq. (1.2)) between the mixture's components. A negative chemical interaction ( $\omega < 0$ ), which is the most common situation, will lead to a high solubility substitution of the matrix A and B atoms, forming a single solubility phase. In this case, both  $\Delta H_m$  and  $\Delta G_m$  will follow the same trend of the  $(-T\Delta S_m)$  function in Figure 1.3a, exhibiting one deep minimum. A more rare situation, in which an attractive chemical interaction

( $\omega > 0$ ) exists, can lead to an inhomogeneous distribution of the substitution atoms, leading to phase separation and a miscibility gap in the phase diagram as will be explained in the following few sentences. In this case,  $\Delta H_m$  will follow the trend observed in Figure 1.3a, exhibiting one maximum, and  $\Delta G_m$ , which is the sum of the positive  $\Delta H_m$  and the negative ( $-T\Delta S_m$ ) functions, and will follow the two local minima trend shown in Figure 1.3b. The  $\Delta G_m$  curves, obtained at various temperatures as shown in Figure 1.3b, can determine the phase diagram of the system (Figure 1.3c). Steady-state conditions, defined by the binodal curve, representing the limits of solid solubility, can be obtained by the intersection of each of the isothermal curves of Figure 1.3b with a common tangent. These are the local minima compositions, obtained for each temperature, satisfying the  $dG_m/dx = 0$  condition. The spinodal curve of the phase diagram (Figure 1.3c) is determined by the inflection points ( $d^2G_m/dx^2 = 0$ ) of the free energy isotherms of Figure 1.3b. Under the spinodal curve, namely, between the inflection points, where the curvature of the free energy function is negative ( $d^2G_m/dx^2 < 0$ ), the spinodal decomposition mechanism of phase separation can occur. Therefore, for compositions within the spinodal curve, a homogeneous solution is unstable against microscopic compositional fluctuations, and there is no thermodynamic barrier to the growth of a new phase. As a result, the phase transformation is spontaneous, does not require any external activation energy, and is solely diffusion controlled. The compositions between the spinodal and the binodal curves, in which the curvature of the free energy function is positive ( $d^2G_m/dx^2 > 0$ ), are considered as metastable, and in this region of the phase diagram the nucleation and growth mechanism for phase separation will dominate. In this region, a nucleus of a critical size has to form before it is energetically favorable for it to grow. Therefore, in contrast to the spinodal decomposition which can be treated purely as a diffusion problem, by an approximate analytical solution to the general diffusion equation, theories of nucleation and growth have to involve thermodynamic considerations, and the diffusion problem involved in the growth of the nucleus is far more difficult to solve. Furthermore, owing to the rapid phase separation mechanism involved in spinodal decomposition, this reaction is uniformly distributed throughout the materials by continuous low amplitude periodic modulations and not just at discrete nucleation sites as in the nucleation and growth regime. As a result, spinodal decomposition is characterized by a very finely dispersed microstructure, shown in Figure 1.3d, which can significantly reduce the lattice thermal conductivity and consequently maximize  $ZT$ . In this figure, the continuous compositional modulations of A and B atoms, obtained by crossing the two separated phases, can be easily seen. The first explanation of the fluctuation's periodicity was originally given by Hillert [22], upon derivation of a flux equation for one-dimensional diffusion on a discrete lattice based on a regular solution model. The equation takes into account the interfacial energy effects between adjacent separated phases. Subsequently, the effects of coherency strains on dictating the morphology were included by Cahn [23]. Therefore, both of the phase separation phenomena described above represent two mechanisms by which a solution of two or more components can be separated into distinct phases with different chemical compositions and physical properties. Owing to the rapid reactions involved,

usually the associated microstructure is finely dispersed and in many cases under defined stabilization conditions as in the submicron range, which is optimal for reduction of the lattice thermal conductivity and enhancement of  $ZT$ . In recent years, several thermoelectric material classes have shown  $ZT$  enhancement due to phase separation of one single matrix composition into two distinct phases. One example is the Heusler family of compounds. Phase separation of the quaternary Heusler compounds  $\text{Co}_2\text{Mn}_{1-x}\text{Ti}_x\text{Sn}$  into  $\text{Co}_2\text{MnSn}$  and  $\text{Co}_2\text{TiSn}$  [24], and of  $\text{Ti}_{(1-x)}\text{Mn}_x\text{CoSb}$  into  $\text{TiCoSb}$  and  $\text{MnCoSb}$  [25], resulting in submicron periodicity of the phase-separated material as well as a major reduction of the thermal conductivity was recently shown by Felser's group [24, 25]. Moreover, theoretical phase diagram calculations for the system  $\text{CoTi}_{1-x}\text{Fe}_x\text{Sb}$  clearly show a miscibility gap and a tendency for spinodal decomposition [26], highlighting the potential for enhancement of the  $ZT$  values due to phase separation in this system as well. In the next paragraph, several specific examples for IV–VI based compounds, exhibiting enhanced thermoelectric properties following phase separation reactions, will be given in more details.

## 1.4 Selected IV–VI Systems with Enhanced Thermoelectric Properties Following Phase Separation Reactions

As mentioned above in relation to Figure 1.1, two of the recently reported most efficient n- and p-type IV–IV based compounds are the  $(\text{Pb}_{0.95}\text{Sn}_{0.05}\text{Te})_{0.92}(\text{PbS})_{0.08}$  and  $\text{Ge}_{0.87}\text{Pb}_{0.13}\text{Te}$  compositions, respectively, both following a phase separation reaction into nanoscaled domains. Investigation of the quasi-binary  $\text{PbTe}$ – $\text{PbS}$  and  $\text{PbTe}$ – $\text{GeTe}$  phase diagrams (Figure 1.4a,b) reveals that both exhibit an extended miscibility gap and that both of the compositions mentioned above fall inside the nucleation and growth zone of the phase diagrams, namely, between the binodal and spinodal curves. It is noteworthy that for the former, the phase diagram of the  $\text{Pb}_{0.95}\text{Sn}_{0.05}\text{Te}$ – $\text{PbS}$  system is also shown as a blue curve in the same graph, based on calculation of  $\text{Pb}_{0.95}\text{Sn}_{0.05}\text{Te}$  using the  $\text{PbTe}$ – $\text{SnTe}$  phase diagram instead of pure  $\text{PbTe}$  for the 100% point, pure  $\text{PbS}$  for the 0% point, and intermediate reported points at 900, 1000, and 1200 K [27]. Indeed, for  $\text{Ge}_{0.87}\text{Pb}_{0.13}\text{Te}$ , following a solution annealing treatment for stabilizing the matrix high temperature single phase at a high temperature (873 K), a series of lower temperature (723 K) aging thermal treatments resulted in nucleation of Pb- and Ge-rich domains [3] and corresponding low thermal conductivity values. In this case, the phases' stability over time was relatively high.

Another example of interest, concerning the  $\text{Ge}_x(\text{Sn}_y\text{Pb}_{1-y})_{1-x}\text{Te}$  compositions [4], is described in the following related to Figure 1.5. These compositions based on the quasi-ternary  $\text{GeTe}$ – $\text{PbTe}$ – $\text{SnTe}$  system include the specific p-type  $\text{Ge}_{0.5}\text{Pb}_{0.25}\text{Sn}_{0.25}\text{Te}$  composition, exhibiting a maximal  $ZT$  of 1.2 as shown in Figure 1.1a and the widely investigated  $\text{Ge}_{0.6}\text{Sn}_{0.1}\text{Pb}_{0.3}\text{Te}$  composition [29–32], the microstructure of which is shown in Figure 1.3d.

The  $\text{GeTe}$ – $\text{PbTe}$ – $\text{SnTe}$  quasi-ternary phase diagram, showing an extended miscibility gap and a tendency to phase separation, is illustrated in Figure 1.5a,

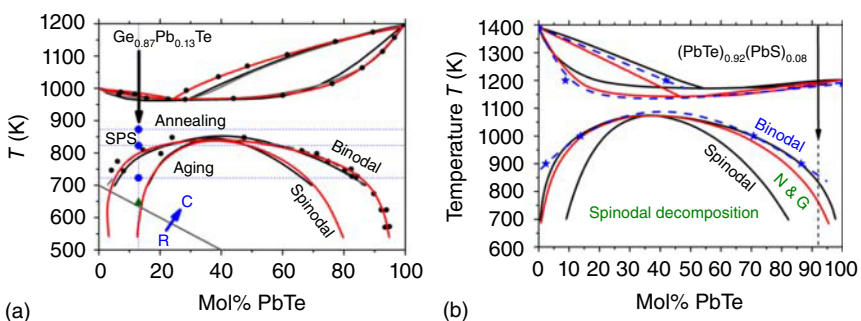


**Figure 1.4** Quasi-binary PbTe—GeTe (a) [3] and PbTe—PbS (black curve [27], red curve [28], and blue curve – calculated for 100% Pb0.95Sn0.05Te instead of PbTe based on the PbTe—SnTe phase diagram [27]) and (b) phase diagrams showing a miscibility gap and a tendency for phase separation. The highly efficient  $(\text{Pb}_{0.95}\text{Sn}_{0.05}\text{Te})_{0.92}(\text{PbS})_{0.08}$  and  $\text{Ge}_{0.87}\text{Pb}_{0.13}\text{Te}$  thermoelectric compositions are clearly indicated. For the PbTe—GeTe phase diagram the transition temperatures from rhombohedral (R) to cubic (C) structures are also indicated. (Volykhov *et al.* 2006 [27]. Reproduced with permission of Springer.)

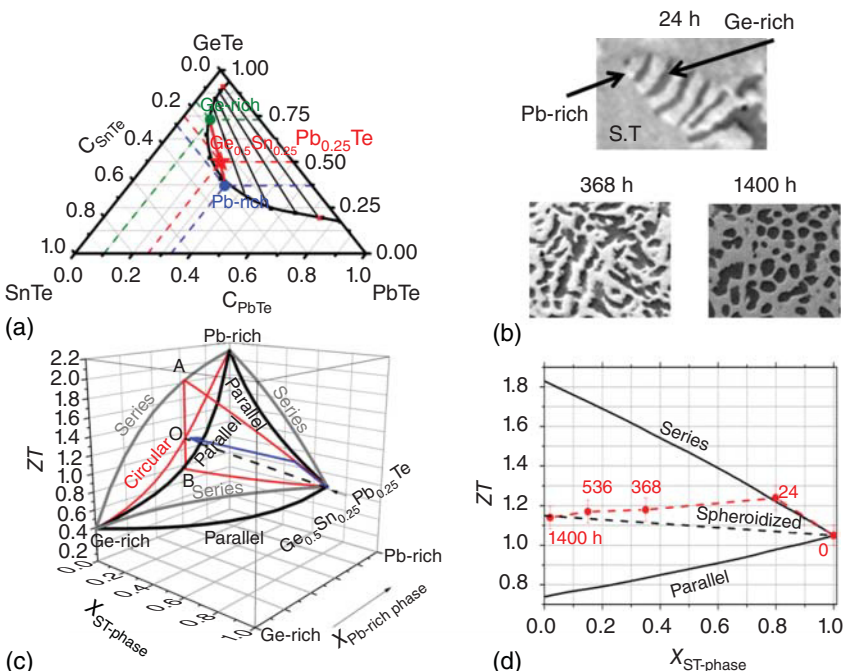


**Figure 1.5** Quasi-ternary GeTe—PbTe—SnTe phase diagram showing a well-defined miscibility gap (a), as well as morphological (b), 3-D ZT (c), and 2-D ZT (d) variations upon thermal treatment at 400 °C for different durations for the p-type Ge0.5Pb0.25Sn0.25Te composition. (Gelbstein 2012 [4]. Reproduced with permission of Elsevier.)

indicating the nominal  $\text{Ge}_{0.5}\text{Pb}_{0.25}\text{Sn}_{0.25}\text{Te}$  composition mentioned above, falling well inside the miscibility gap in the area corresponding to spinodal decomposition, which separates into Ge-rich (dark) and Pb-rich (bright) phases (Figure 1.5b). In this figure, it can be seen that the phase separation evolution follows various morphological stages from lamellar (at 24 h of 400 °C thermal treatment) to spheroidized (at 1400 h) geometries with some influence on the resultant  $ZT$  values as shown in Figure 1.5c,d. This figure shows results of the investigation of the influence of geometrical morphologies on  $ZT$  following various phase separation stages performed using the general effective media (GEM) theory [33], showing only slight variations of  $ZT$  during the phase separation reaction, highlighting the high thermoelectric stability of these reactions compared to other common nanogeneration methods.

## 1.5 Concluding Remarks

In the current chapter, the main advances in IV–VI based thermoelectric materials reported in recent years were reviewed. It was shown that during the recent years both due to nanostructuring methods for reduction of thermal conductivity and optimal electronic doping approaches, very high  $ZT$ 's of up to ~2.2 were achieved, rendering this class of thermoelectric materials as the most thermoelectrically efficient up to temperatures of ~500 °C, which is ideal for converting the waste heat generated in diesel automotive engines into useful electricity. The generation of phase separation reactions for retaining the nanostructuring during practical operation conditions was described in detail as one of the most advanced approaches for  $ZT$  enhancement in such materials. The conditions for phase separation reactions, including the necessity for miscibility gap between the various components of the system and the distinction between the specific characteristics of the spinodal decomposition and nucleation and growth regimes of this gap, were described. Advanced optimal doping approaches based on generation of localized “deep” resonant states lying inside the energy gap, which are capable of pinning the Fermi energy of the compounds at a favorable level required for electronic thermoelectric optimization, were also described as useful for enhancement of the  $ZT$  values. All of the described methods for enhancing and retaining the  $ZT$  values upon long-term thermoelectric applications can be extended to many other classes of thermoelectric materials.

## References

- 1 Heremans, J.P., Jovovic, V., Toberer, E.S., Saramat, A., Kurosaki, K., Charoenphakdee, A., Yamanaka, S., and Jeffrey Snyder, G. (2008) Enhancement of thermoelectric efficiency in PbTe by distortion of the electronic density of states. *Science*, **321**, 554–557.
- 2 Gelbstein, Y. (2011)  $\text{Pb}_{1-x}\text{Sn}_x\text{Te}$  alloys: application considerations. *J. Electron. Mater.*, **40** (5), 533–536.

- 3 Gelbstein, Y., Davidow, J., Girard, S.N., Chung, D.Y., and Kanatzidis, M. (2013) Controlling metallurgical phase separation reactions of the  $\text{Ge}_{0.87}\text{Pb}_{0.13}\text{Te}$  alloy for high thermoelectric performance. *Adv. Energy Mater.*, **3** (6), 815–820.
- 4 Gelbstein, Y. (2013) Phase morphology effects on the thermoelectric properties of  $\text{Pb}_{0.25}\text{Sn}_{0.25}\text{Ge}_{0.5}\text{Te}$ . *Acta Mater.*, **61**, 1499–1507.
- 5 Biswas, K., He, J., Blum, I.D., Wu, C.-I., Hogan, T.P., Seidman, D.N., Dravid, V.P., and Kanatzidis, M.G. (2012) High performance bulk thermoelectrics with all scale hierachial architectures. *Nature*, **489**, 414–418.
- 6 Androulakis, J., Hsu, K.F., Pcionek, R., Kong, H., Uher, C., D'Angelo, J.J., Downey, A., Hogan, T., and Kanatzidis, M.G. (2006) Nanostructuring and high thermoelectric efficiency in *p*-Type  $\text{Ag}(\text{Pb}_{1-y}\text{Sn}_y)_m\text{SbTe}_{2+m}$ . *Adv. Mater.*, **18**, 1170–1173(LASTT).
- 7 Poudeu, P.F.P., D'Angelo, J., Downey, A.D., Short, J.L., Hogan, T.P., and Kanatzidis, M.G. (2006) High thermoelectric figure of merit and nanosstructuring in bulk *p*-type  $\text{Na}_{1-x}\text{Pb}_m\text{Sb}_y\text{Te}_{m+2}$ . *Angew. Chem. Int. Ed.*, **45**, 3835–3839(SALT).
- 8 Pei, Y., Wang, H., Gibbs, Z.M., LaLonde, A.D., and Jeffrey Snyder, G. (2012) Thermopower enhancement in  $\text{Pb}_{1-x}\text{Mn}_x\text{Te}$  alloys and its effect on thermoelectric efficiency. *NPG Asia Mater.*, **4**, 1–6.
- 9 Pei, Y., Shi, X., LaLonde, A., Wang, H., Chen, L., and Jeffrey Snyder, G. (2011) Convergence of electronic bands for high performance bulk thermoelectrics. *Nature*, **473**, 66–69.
- 10 Hsu, K.F., Loo, S., Guo, F., Chen, W., Dyck, J.S., Uher, C., Hogan, T., Polychroniadis, E.K., and Kanatzidis, M.G. (2004) Cubic  $\text{AgPb}_m\text{SbTe}_{2+m}$ : bulk thermoelectric materials with high figure of merit. *Science*, **303**, 818.
- 11 Gelbstein, Y., Dashevsky, Z., and Dariel, M.P. (2005) High performance *n*-type PbTe-based materials for thermoelectric applications. *Phys. B*, **363**, 196–205.
- 12 Poudeu, P.F.P., Gueguen, A., Wu, C.-I., Hogan, T., and Kanatzidis, M.G. (2010) High figure of merit in nanostructured *n*-type  $\text{KPb}_m\text{SbTe}_{m+2}$  thermoelectric materials. *Chem. Mater.*, **22**, 1046–1053.
- 13 Androulakis, J., Lin, C.-H., Kong, H.-J., Uher, C., Wu, C.-I., Hogan, T., Cook, B.A., Caillat, T., Paraskevopoulos, K.M., and Kanatzidis, M.G. (2007) Spinodal decomposition and nucleation and growth as a means to bulk nanostructured thermoelectrics: enhanced performance in  $\text{Pb}_{1-x}\text{Sn}_x\text{Te}-\text{PbS}$ . *J. Am. Chem. Soc.*, **129**, 9780–9788.
- 14 Kaidanov, V.I. and Ravich, Y.I. (1985) Deep and resonance states in  $\text{A}^{\text{IV}}\text{B}^{\text{VI}}$  semiconductors. *Sov. Phys. Uspekhi*, **28** (1), 31–53.
- 15 Northrop, D.A. (1971) Thermogravimetric investigation of the vaporization of lead telluride, tin telluride, and germanium telluride. *J. Phys. Chem.*, **75** (1), 118.
- 16 Molchanov, M.V., Alikhanyan, A.S., Zlomanov, V.P., and Yashina, L.V. (2002) Mass spectrometric study of vapor composition over germanium telluride. *Inorg. Mater.*, **38** (6), 559.
- 17 Ubelis, A.P. (1982) Temperature dependence of the saturated vapor pressure of tellurium. *J. Eng. Phys. Thermophys.*, **42** (3), 309.
- 18 Dushman, S. (1962) *Scientific Foundations of Vacuum Technique*, 2nd edn, John Wiley & Sons, p. 669.

- 19 Madelung, O., Rössler, U., and Schulz, M. (eds) (1998) *Landolt-Bornstein-Group 3 Condensed Matter*, Non Tetrahedrally Based Elements and Binary Compounds I, vol. **41c**, Springer-Verlag, p. 1.
- 20 Gelbstein, Y., Ben-Yehuda, O., Dashevsky, Z., and Dariel, M.P. (2009) Phase transitions of p-type (Pb<sub>x</sub>Sn<sub>y</sub>Ge<sub>z</sub>)Te based alloys for thermoelectric applications. *J. Cryst. Growth*, **311**, 4289–4292.
- 21 Ho, I.-H. and Stringfellow, G.B. (1996) Solid phase immiscibility in GaInN. *Appl. Phys. Lett.*, **69** (18), 2701–2703.
- 22 Hillert, M. (1961) A solid solution model for inhomogeneous systems. *Acta Metall.*, **9**, 525.
- 23 Cahn, W. (1961) On spinodal decomposition. *Acta Metall.*, **9**, 795.
- 24 Graf, T., Barth, J., Blum, C.G.F., Balke, B., and Felser, C. (2010) Phase-separation-induced changes in the magnetic and transport properties of the quaternary Heusler alloy Co<sub>2</sub>Mn<sub>1-x</sub>Ti<sub>x</sub>Sn. *Phys. Rev. B*, **82**, 104420.
- 25 Graf, T., Felser, C., and Parkin, S.S.P. (2011) Simple rules for the understanding of Heusler compounds. *Prog. Solid State Chem.*, **39**, 1–50.
- 26 Dinh, V.A., Sato, K., and Katayama-Yoshida, H. (2010) First principle study of spinodal decomposition thermodynamics in half-Heusler alloy CoTi<sub>1-x</sub>Fe<sub>x</sub>Sb. *J. Superconduct. Novel Magnetis.*, **23**, 75–78.
- 27 Volykhov, A.A., Yashina, L.V., and Shtanov, V.I. (2006) Phase relations in pseudobinary systems of germanium, tin, and lead chalcogenides. *Inorg. Mater.*, **42** (6), 596–604.
- 28 Laugier, A. (1973) Thermodynamics and phase diagram calculations in II–IV and IV–VI ternary systems using an associated solution model. *Rev. Phys. Appl.*, **8**, 259–269.
- 29 Gelbstein, Y., Dado, B., Ben-Yehuda, O., Sadia, Y., Dashevsky, Z., and Dariel, M.P. (2010) High thermoelectric figure of merit and nanostructuring in bulk p-type Ge<sub>x</sub>(Sn<sub>y</sub>Pb<sub>1-y</sub>)<sub>1-x</sub>Te alloys following a spinodal decomposition reaction. *Chem. Mater.*, **22** (3), 1054–1058.
- 30 Dado, B., Gelbstein, Y., Mogilansky, D., Ezersky, V., and Dariel, M.P. (2010) The structural evolution following the spinodal decomposition of the pseudo-ternary (Pb<sub>0.3</sub>Sn<sub>0.1</sub>Ge<sub>0.6</sub>)Te compound. *J. Electron. Mater.*, **39** (9), 2165–2171.
- 31 Dado, B., Gelbstein, Y., and Dariel, M.P. (2009) Nucleation of nano-size particles following the spinodal decomposition in the pseudo-ternary Ge<sub>0.6</sub>Sn<sub>0.1</sub>Pb<sub>0.3</sub>Te compound. *Scr. Mater.*, **62** (2), 89–92.
- 32 Gelbstein, Y., Rosenberg, Y., Sadia, Y., and Dariel, M.P. (2010) Thermoelectric properties evolution of spark plasma sintered (Ge<sub>0.6</sub>Pb<sub>0.3</sub>Sn<sub>0.1</sub>)Te following a spinodal decomposition. *J. Phys. Chem. C*, **114**, 13126–13131.
- 33 Gelbstein, Y. (2012) Morphological effects on the electronic transport properties of three-phase thermoelectric materials. *J. Appl. Phys.*, **112**, 113721.

## 2

# Nanostructured Materials: Enhancing the Thermoelectric Performance

*Ngo Van Nong and Le Thanh Hung*

*Technical University of Denmark, Department of Energy Conversion and Storage, Frederiksborgvej 399, 4000 Roskilde, Denmark*

## 2.1 Introduction

By converting heat into electricity, thermoelectric (TE) materials offer a viable solution for waste heat harvesting to reduce our dependence on fossil fuels and to reduce greenhouse gas emissions. However, the application of TE materials to utilize waste heat is still limited due to the low efficiency of TE system, that is, about 5% for commercial devices. Therefore, developing high efficiency TE materials for waste heat recovery systems is urgent and will benefit for both economy and environment. The conversion efficiency of TE materials is evaluated by the dimensionless figure of merit,  $ZT$  defined as

$$ZT = T \frac{S^2 \sigma}{\lambda} = T \frac{S^2 \sigma}{\lambda_e + \lambda_L} \quad (2.1)$$

where  $T$  is the average temperature of the hot and cold sides,  $S$  is the Seebeck coefficient, and  $\sigma$  and  $\lambda$  are the electrical and thermal conductivity of the material. The total thermal conductivity ( $\lambda$ ) is the sum of the electronic thermal conductivity ( $\lambda_e$ ) and the lattice thermal conductivity ( $\lambda_L$ ). The challenge to develop TE materials with high performance is to tailor the interconnected TE physical parameters – electrical conductivity, Seebeck coefficient, and thermal conductivity for a crystalline system. Nanostructures provide a chance to disconnect the linkage between thermal and electrical transport by introducing some new scattering mechanisms. Recent improvements in TE efficiency appear to be crucial by the efforts to reduce the lattice thermal conductivity through nanostructure design. Reducing the size and dimensionality of TE materials in nanoscale and nanostructured materials has been demonstrated to effectively increase the TE performance due to the quantum confinement and nanostructure effects [1]. The development of nanostructured materials including super-lattice systems and nanowires has been well presented in recent reviews [2–9].

This chapter summarizes the progress that has been made in recent years in developing bulk nanostructured materials to enhance the TE performance.

Unlike many other nanostructured materials, bulk nanostructured materials have shown the most promise for practical applications since they can be fabricated in large quantities and suitable for TE device configurations. The materials focused in this chapter include Bi–Te alloys, PbSb-based materials, half-Heusler (HH) alloys, skutterudite compounds, and some novel nanostructured high-*ZT* oxides.

## 2.2 Approaches for Improving *ZT*

It is clear from Eq. (2.1) that a material with high *ZT* needs to have a large Seebeck coefficient, which is often the cases of semiconductors or insulators with low carrier concentration, and a high electrical conductivity like metals having high carrier concentration. The relationship between carrier concentration and the Seebeck coefficient (*S*) and the electrical conductivity ( $\sigma$ ) can be expressed as

$$S = \frac{8\pi^2 k_B^2}{3eh^2} m^* T \left( \frac{\pi}{3n} \right)^{\frac{2}{3}} \quad (2.2)$$

$$\sigma = ne\mu \quad (2.3)$$

where  $k_B$  is the Boltzmann constant,  $e$  is the carrier charge,  $h$  is Planck's constant,  $m^*$  is the effective mass of the charge carrier,  $n$  is the carrier concentration, and  $\mu$  is the carrier mobility. Typically, good TE materials are heavily doped semiconductors with carrier concentration of  $10^{19}$ – $10^{21}/\text{cm}^3$  [10]. The Seebeck coefficient is large when a single type of carriers, that is, electron (n-type) or hole (p-type) is remained, because mixed n-type/p-type charge carriers will lead to a low Seebeck coefficient due to the opposite Seebeck effect. To achieve single type of carrier, it is necessary to select materials with suitable energy bandgaps and appropriate doping, in which n-type and p-type can be well separated. Therefore, effective TE materials are often heavy doped semiconductors in order to have both a single carrier type and sufficiently high carrier mobility.

An effective TE material also needs to have a low thermal conductivity to maintain a temperature gradient. Aforementioned, thermal conductivity ( $\lambda$ ) of TE materials, consists of two parts:  $\lambda_L$ , which results from heat transporting phonons travelling through the crystal lattice, and  $\lambda_e$ , which comes from heat carrying charge carriers (electrons or holes) moving through the crystal lattice. According to the Wiedemann–Franz Law,

$$\lambda_e = L\sigma T \quad (2.4)$$

where  $L$  is the Lorenz number, the electronic thermal conductivity is proportional to the electrical conductivity. Therefore, it is not always the best choice for TE materials to reduce the electronic thermal conductivity since the electrical conductivity will be inversely affected and has little or no improvement in *ZT*. Lattice thermal conductivity  $\lambda_L$  can be defined by the following expression [11].

$$\lambda_L = \frac{1}{3} C_v v_s \Lambda \quad (2.5)$$

where  $C_v$  is heat capacity,  $v_s$  is the sound velocity, and  $\Lambda$  is the phonon mean free path. It can be seen from Eq. (2.5) that lattice thermal conductivity is not determined by the electronic structure. Therefore, enhancement of  $ZT$  could be achieved by minimizing the lattice thermal conductivity.

Main approaches for improving  $ZT$  of TE materials are mentioned below.

The first approach suggested by Slack is the “phonon glass electron crystal-PGEC,” which proposes for the compounds that conduct the electricity as a crystalline material and the heat as a glass [12]. The research of new TE systems based on the PGEC concept has led to an intensive effort to better understand the mechanisms that affect the phonons scattering without changing significantly the electrical charge propagation. This approach can be applied to search for the materials with complex crystal structures, where voids and rattlers (heavy element atoms weakly bounded to the structure) would act as effective phonon scattering centers and reduce the lattice thermal conductivity significantly. With this approach, high  $ZT$  materials such as skutterudites [13], clathrates [14, 15], and zintl compounds [16] have been found.

The second approach is through vacancies, interstitial atoms, and solid solutions, which increase mass fluctuations resulting in higher phonon scattering. This approach is the most achievable in materials such as  $Zn_4Sb_3$  [17, 18] and HH alloys [19].

The third approach is the nanostructuring of TE materials, which suggests that the  $ZT$  enhancement can be realized with nanoscale, nanostructured morphologies [20, 21]. Nanostructures can enhance the density of states (DOS) near Fermi level via quantum confinement and therefore increase the Seebeck coefficient, which provides a way to decouple thermopower and electrical conductivity.

The other approach is through the TE nanocomposites, which are constructed by incorporating TE nanostructures in a matrix of bulk TE material or compacting various TE nanostructures in a bulk form coupled with heavy doping as illustrated in Figure 2.1. Faleev and Léonard [22] have developed a model to predict the TE performance of a nanocomposite system with spherical metallic nanoinclusion using the band bending concept at the metal–semiconductor interface acting as energy filters. They have shown that the Seebeck coefficient of

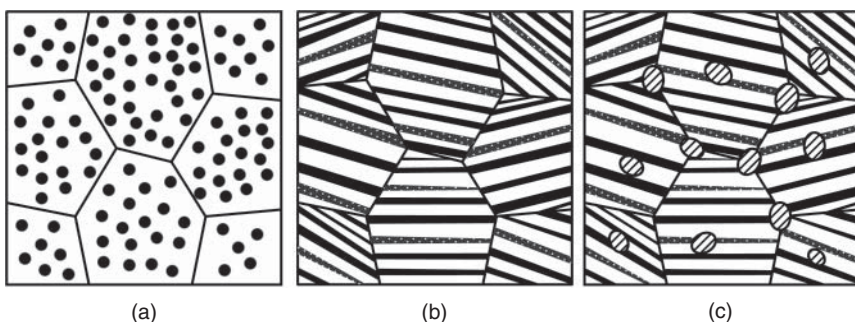


**Figure 2.1** Schematic illustration of nanocomposite approach by nano-precipitates within grains (a), nano-lamella within grains (b), and heavy doping with embedded nanoinclusions (c).

TE nanocomposite is always enhanced, as compared with a nanoinclusion-free system. The enhancement of  $ZT$  is dominant by the reduction in the lattice thermal conductivity for low doping, while the electronic contribution becomes more important for high doping.

Successful examples for this approach is PbS—Ag nanocomposite, in which Ag nanodomains not only contribute to block phonon propagation, but also provide electrons to the PbS host semiconductor and reduce the PbS intergrain energy barriers for charge transport. The outstanding electrical properties along with low thermal conductivities of PbS—Ag samples resulted in a TE figure of merit up to a  $ZT = 1.7$  at 850 K [23]. Another example has been also successfully demonstrated on the Lu-doped layered cobaltite system with Ag metal nanoinclusions, leading to a remarkable improvement of  $ZT$  [24].

### 2.3 Recent Progress in Developing Bulk Thermoelectric Materials

Over the past 10 years, the exploration of high performance TE materials has attracted great attention from an academic research perspective. The development of TE materials has made an impressive progress in improving  $ZT$ . Figure 2.2 shows  $ZT$  as a function of temperature for state-of-the-art p-type (a) and n-type (b) bulk TE materials.

For p-type materials, in low temperature range (RT – 550 K) besides Bi<sub>2</sub>Te<sub>3</sub> alloy [25] a new class of TE materials based on MgAgSb with comparable  $ZT$  of 1–1.4 has been recently developed [26]. It is worth to note that  $ZT$  of these new materials increase with increasing temperature, while the tendency of  $ZT$  is opposite for Bi<sub>2</sub>Te<sub>3</sub>-based materials. In the temperature region from 550 to 900 K, there exist different high-performance TE systems such as PbTe [27], PbTe—SrTe [28], Clathrate [14], skutterudite compound [13], and TAGS [29]. Notably in medium temperature range, a high  $ZT$  of 1.4 has been achieved for a textured oxide system of Bi<sub>0.875</sub>Ba<sub>0.125</sub>CuSeO [30, 31]. In high temperature region above 900 K, Cu<sub>2</sub>Se [32], Zint compounds [16], HH alloys [33, 34], and SiGe [35], and layered cobaltite oxides [24] are the potential TE materials.

As for n-type TE materials, in low temperature region below 550 K the dominant material is still Se-doped Bi<sub>2</sub>Te<sub>3</sub> alloy [36]. In the temperature range of 550–900 K, the best TE material so far are skutterudite compounds with a maximum  $ZT$  up to 1.7 at 850 K [37]. Some other TE systems such as HH alloys [38], PbTe [39], and Mg<sub>2</sub>Si [40] are also the high  $ZT$  materials. In the high temperature region, there exist only few potential TE materials; they are Si<sub>0.78</sub>Ge<sub>0.22</sub> [41], La<sub>3</sub>Te<sub>4</sub> [42], and doped ZnO [43, 44].

In order to evaluate how efficient these TE materials can bring up, the efficiency of each material was calculated as a single leg using the numerical modeling as presented in our previous works [44, 45].

$$\eta = 1 - \frac{S_c T_c + \frac{1}{u_c}}{S_h T_h + \frac{1}{u_h}} \quad (2.6)$$

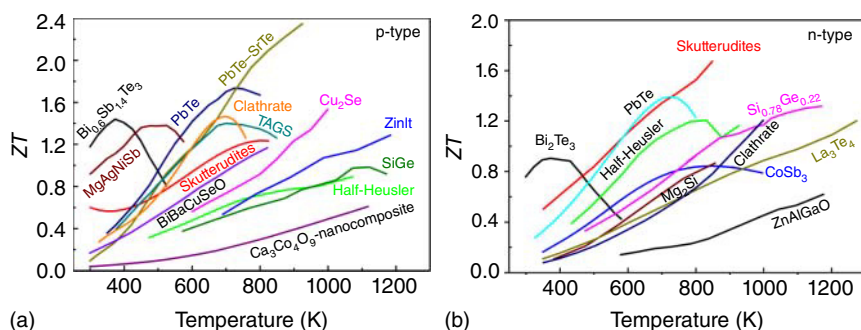


**Figure 2.2** The materials figure of merit,  $ZT$  as a function of temperature for state-of-the-art bulk thermoelectric materials: (a) for p-type materials and (b) for n-type materials.

**Table 2.1** Calculated efficiency of collected TE materials at the hot side temperatures of 700, 900, and 1100 K, while the cold side temperature is fixed at 300 K.

Materials	Maximum efficiency (%)			
	$T_h = 520\text{ K}$	$T_h = 700\text{ K}$	$T_h = 900\text{ K}$	$T_h = 1100\text{ K}$
p-Type	$\text{Bi}_{0.6}\text{Sb}_{1.4}\text{Te}_3$ [25]	5.6	—	—
	$\text{MgAgNiSb}$ [26]	10	—	—
	$\text{Hf}_{0.5}\text{Zr}_{0.5}\text{CoSb}_{0.8}\text{Sn}_{0.2}$ [33]	5.8	8.9	—
	$\text{Yb}_{14}\text{Mn}_{0.2}\text{Al}_{0.8}\text{Sb}_{11}$ (ZnIn) [16]	4.5	7.6	10.8
	$\text{Cu}_2\text{Se}$ [32]	6.2	9.8	—
	PbTe [27]	11.1	—	—
	PbTe-SrTe [28]	9.5	15.3	—
	Skutterudites [13]	10.3	14.5	—
	SiGe [46]	5	7.8	10.4
	$(\text{AgSbTe})_{0.15}(\text{GeTe})_{0.85}$ [29]	10.2	—	—
n-Type	$\text{Ba}_8\text{Au}_{5.3}\text{Ge}_{40.7}$ [14]	10	—	—
	$(\text{Ca},\text{Lu},\text{Ag})_3\text{Co}_4\text{O}_{9+}$ [24]	2.6	~4	5.3
	$\text{Bi}_2\text{Te}_3$ [36]	7.5	—	—
	$\text{Ba}_{0.08}\text{La}_{0.05}\text{Yb}_{0.04}\text{Co}_4\text{Sb}_{12}$ [37]	11.1	—	—
	$\text{Ti}_{0.5}(\text{Zr}_{0.5}\text{Hf}_{0.5})_{0.5}\text{NiSn}_{0.998}\text{Sb}_{0.002}$ [38]	7.7	13.8	—
	Skutterudites [13]	10.5	14	—
	$\text{PbTe}_{1-x}\text{I}_x$ ( $x = 0.0012$ ) [39]	10.1	—	—
	$\text{Si}_{0.78}\text{Ge}_{0.22}$ [41]	5.8	9.5	—
	$\text{Ba}_8\text{Ga}_{16}\text{Ge}_{30}$ [15]	3.6	6.7	—
	$\text{Mg}_2\text{SiSn}$ [40]	9.4	—	—
	$\text{La}_3\text{Te}_4$ [42]	4.3	7.2	10.0
	$\text{ZnAlGaO}$ [44]	2.6	~4	5.3

Missing (—) data corresponds to the temperature region, where the TE materials are out of the working temperature range.

where  $S_c$ ,  $S_h$ ,  $T_c$ ,  $T_h$  are the Seebeck coefficient and the temperature at the cold and the hot side temperature;  $u_c$  and  $u_h$  are the reduced current density at the cold and the hot side temperature, respectively.

Provided in Table 2.1 is the conversion efficiency ( $\eta$ ) of each single material under various the hot side temperatures, while the cold side temperature is fixed at 300 K. It can be seen from Table 2.1 that below 900 K PbTe-based materials, skutterudites and HH compounds are the most promising materials for making high performance TE power generation devices. In the high temperature region above 900 K, although oxides have low conversion efficiency, they are still promising due to their significant higher efficiency ratio (efficiency per material cost) than that for intermetallic compounds, that is, Zintl and  $\text{La}_3\text{Te}_4$  [45].

In the following sections, we will focus on recent developments of typical bulk nanostructures/nanocomposites materials with high potential for large scale applications.

## 2.4 Bulk Nanostructured Thermoelectric Materials

### 2.4.1 $\text{Bi}_2\text{Te}_3$ -Based Nanocomposites

Doped- $\text{Bi}_2\text{Te}_3$  and their related nanocomposites are extensively used for commercial TE devices. Shown in Figure 2.3 is  $ZT$  as a function of temperature for polycrystalline p-type  $\text{Bi}_{0.4}\text{Sb}_{1.6}\text{Te}_3$  (a) and n-type  $\text{Bi}_2(\text{Te},\text{Se})_3$  (b) bulk nanocomposites, fabricated by spark plasma sintering technique (SPS) from ball-milled nanopowders. Since the materials sintered by SPS often show anisotropic transport properties, it is important to characterize all TE parameters in the same direction. In-plane  $ZT$  reached a value of over 1.4 at 327 K [47] for p-type and 0.8 at 420 K for n-type. It is clear from Figure 2.3 that the TE properties of SPS-sintered samples are anisotropic and the effect is much more substantial for n-type than p-type. In addition, the samples sintered by SPS are highly textured leading to an enhanced in-plane TE properties.

An in-plane  $ZT$  of ~1.1 at 398 K was reported for n-type  $\text{Bi}_2\text{Te}_3$ -based nanocomposites [48]. The reports on the properties of p-type  $\text{Bi}_2\text{Te}_3$ -based nanocomposites show a wide variation in the  $ZT$  values, ranging from ~0.5 to 1.56 for similar compositions. For example, a high  $ZT$  of about 1.5 at 390 K was achieved in  $(\text{Bi},\text{Sb})_2\text{Te}_3$  nanocomposites by melt spinning single elements of Bi, Sb, and Te followed by the SPS process [49], while a  $ZT$  of 0.51 was reported for nanostructured bulk  $\text{Bi}_{0.5}\text{Sb}_{1.5}\text{Te}_3$  sample at 375 K [50]. The  $ZT$  values of 1.47 [51] and 1.56 [52, 53] were obtained in nanocomposites fabricated by hot pressing of  $\text{Bi}_2\text{Te}_3$  and  $\text{Sb}_2\text{Te}_3$  nanopowders with diameters below 20 nm and with 5–15 nm diameter precipitates produced by melt spinning and SPS. A similar  $ZT$  value of 1.47 was also observed for a 0.2 wt.% Mn-decorated  $\text{Bi}_{0.5}\text{Sb}_{1.5}\text{Te}_3$  nanocomposite [54]. Several attempts have been made on the nanocomposites of  $\text{Bi}_2\text{Te}_3$  with  $\text{B}_4\text{C}$  nanoparticles addition [55] and with  $\text{MoS}_2$  nanoinclusion [56] or mixed with  $\text{In}_2\text{Te}_3$  [57]. The thermal conductivity was observed to be significantly reduced. Very recently, we have achieved a  $ZT$  of 1.5 at 325 K for a nanocomposite of  $\text{Bi}_{0.4}\text{Sb}_{1.6}\text{Te}_3$  with 0.05% B-doped single wall carbon nanotubes (SWCNTS) and 10% Te addition, which is about 16% improvement as compared to the matrix sample [58] (Figure 2.4).

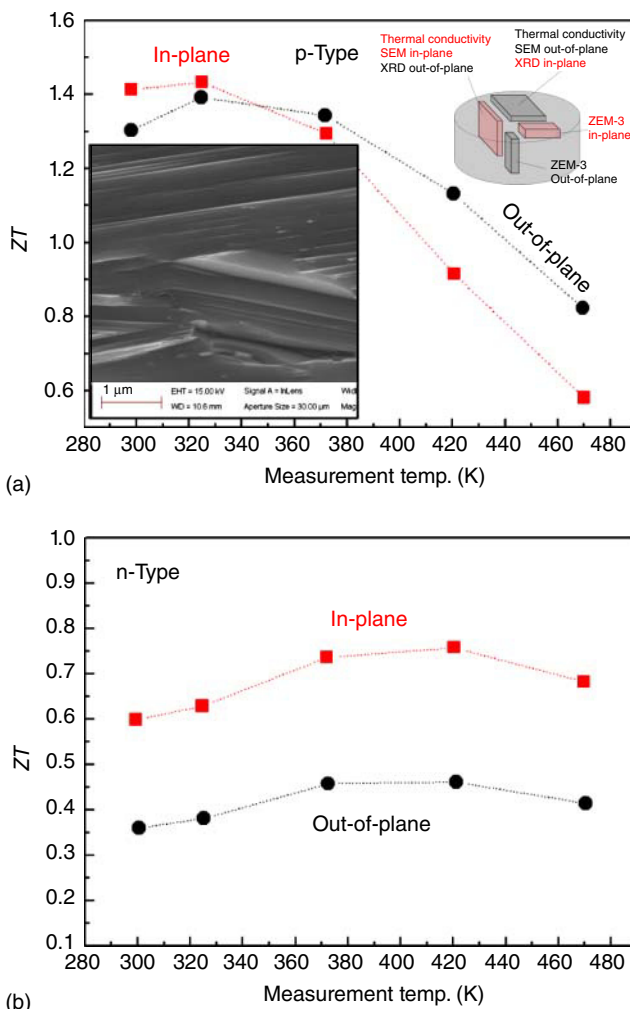


**Figure 2.3**  $ZT$  versus temperature of polycrystalline bulk nanostructured samples of p-type  $\text{Bi}_{0.4}\text{Sb}_{1.6}\text{Te}_3$  (a) and n-type  $\text{Bi}_2(\text{Te},\text{Se})_3$  (b) prepared by spark plasma sintering (SPS). The properties were characterized perpendicular (in-plane) and parallel (out-plane) to the applied pressure direction. Inset figure is a typical SEM image observed in-plane.

#### 2.4.2 PbTe-Based Nanostructured Materials

A very high  $ZT$  of about 2.2 at 915 K [28] was achieved for a p-type PbTe–SrTe (4 mol%) nanostructures doped with 2 mol% Na prepared by SPS, as shown in Figure 2.5. By controlling and fine-tuning the mesoscale architecture of nanostructured TE materials (Figure 2.5a), the lattice thermal conductivity was intensively reduced due to the increasing phonon scattering. This increase in  $ZT$  beyond the threshold of 2 (Figure 2.5b) highlights the role of, and need for, multiscale hierarchical architecture in controlling phonon scattering in bulk TE materials. A similar  $ZT$  value of 2 was also observed in complex nanostructured PbTe-based n-type compound  $\text{Ag}_{1-x}\text{Pb}_{18}\text{SbTe}_{20}$  fabricated by

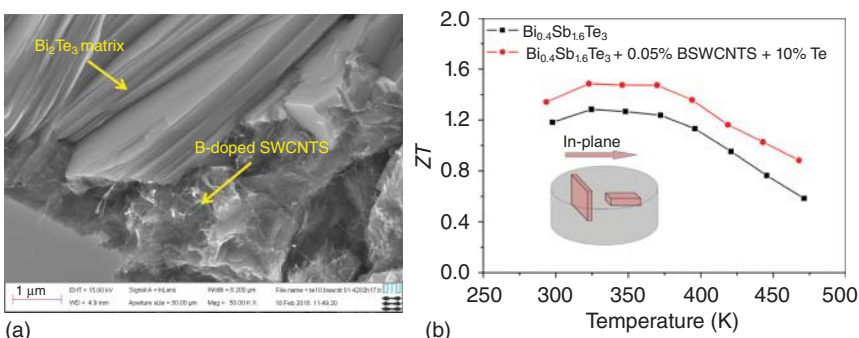


**Figure 2.4** (a) SEM image for a typical nanocomposite of p-type  $\text{Bi}_{0.4}\text{Sb}_{1.6}\text{Te}_3$  with 0.05% B-doped single wall carbon nanotube (SWCNTS) and 10% Te. (b)  $ZT$  as a function of temperature measured in-plane for nanocomposite as compared with a standard sample.

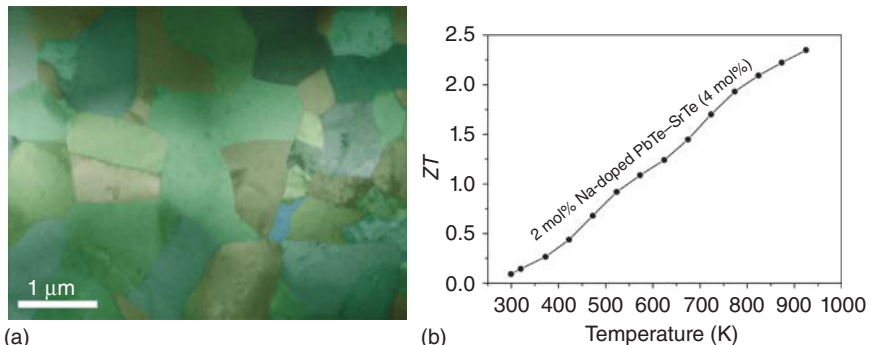


**Figure 2.5** (a) Low-magnification TEM image with mesoscale grains and (b)  $ZT$  as a function of temperature for nanocomposite of  $\text{PbTe}-\text{SrTe}$  (4 mol%) doped with 2 mol% Na prepared by SPS. (Biswas *et al.* 2012 [28]. Reproduced with permission of Nature Publishing Group.)

the melt-grown method [59]. A high  $ZT$  of 1.7 at 750 K has been obtained for Na-doped  $\text{Mg}_x\text{Pb}_{1-x}\text{Te}$  alloys [27]. A  $ZT$  value higher than 1 has also been achieved for a number of other PbTe-based nanostructured materials, including  $\text{AgPb}_m\text{SbTe}_{2+m}$ ,  $\text{AgPb}_m\text{Sn}_n\text{SbTe}_{2+m+n}$ ,  $\text{NaPb}_m\text{SbTe}_{2+m}$ ,  $\text{KPb}_m\text{SbTe}_{m+2}$ , and  $\text{PbTe}-\text{PbS}$  [56–66].

#### 2.4.3 Half-Heusler Alloys

HH alloys are very promising materials for waste heat recovery applications due to their high TE performance, environmental friendliness, high stability, moderate cost, and good mechanical properties [19, 34, 67–90]. Associated with their high Seebeck coefficient and electrical conductivity is the relatively high thermal conductivity of HH alloys, which is their main drawback. Much effort has

been put to find HH compositions and preparation methods that result in optimum TE properties [19, 34, 67–69, 71–77, 79–81, 83–86, 88–90]. The p-type HH alloy with stoichiometric composition  $\text{Hf}_{0.5}\text{Zr}_{0.5}\text{CoSb}_{0.8}\text{Sn}_{0.2}$  has become especially appealing after the finding of its record  $ZT = 0.8$  at 973 K by nanostructuring approach [19]. From a theoretical point of view, nanostructures help scattering phonons but not electrons, or even increase the electrical conductivity by other effect due to band engineering such as the modulation doping effect. The  $ZT$  values of 0.97 at 973 K and  $\geq 1$  at 1073 K were achieved in nanostructured  $\text{Hf}_{0.44}\text{Zr}_{0.44}\text{Ti}_{0.12}\text{CoSb}_{0.8}\text{Sn}_{0.2}$  prepared by hot-pressing (HP) [88]. Lately, it has been reported that in addition to nanostructures, the intrinsic phase separation of HH [68, 69, 75, 81, 90] is also a key feature to reduce its thermal conductivity without a negative effect on the electrical conductivity. In order to develop and preserve phase separation as well as nanostructures, appropriate preparation methods are necessary. Conventional hot pressing of material after ball milling has the major drawback of drastic grain growth. On the other hand, SPS is a novel method with the superior features to maintain the inhomogeneity necessary for selective phonon-scattering. The method has become inevitable for the synthesis of TE nanostructured materials. Shown in Figure 2.6 is typical microstructure and  $ZT$  as a function of temperature for our recently developed p-type bulk nanostructured  $\text{Hf}_{0.5}\text{Zr}_{0.5}\text{CoSn}_{0.2}\text{Sb}_{0.8}$  prepared by SPS. A maximum  $ZT$  value of 0.9 at 973 K was achieved [77]. The microstructure with nano arrays embedded in the matrix (Figure 2.6a) resulted in a significant reduction of the thermal conductivity, leading to better  $ZT$  values than an ingot sample over the whole investigated temperature region (Figure 2.6b).

Very recently, high quality HH alloys of  $\text{FeNb}_{1-x}\text{Hf}_x\text{Sb}$  and  $\text{FeNb}_{1-y}\text{Zr}_y\text{Sb}$  ( $x, y = 0 \div 0.16$ ) have been developed by levitation melting and SPS [34]. A peak  $ZT$  of 1.5 was reached at 1200 K for  $\text{FeNb}_{0.88}\text{Hf}_{0.12}\text{Sb}$  and  $\text{FeNb}_{0.86}\text{Hf}_{0.14}\text{Sb}$ . This research group has also demonstrated a prototype TE module made of n-type ZrNiSn-based alloys and p-type FeNbSb compounds with a conversion efficiency of 6.2% at a temperature difference of 655 K. Together with low cost, excellent mechanical properties and stability, these findings open up a great opportunity of using HH alloys for high-temperature TE power generation devices.

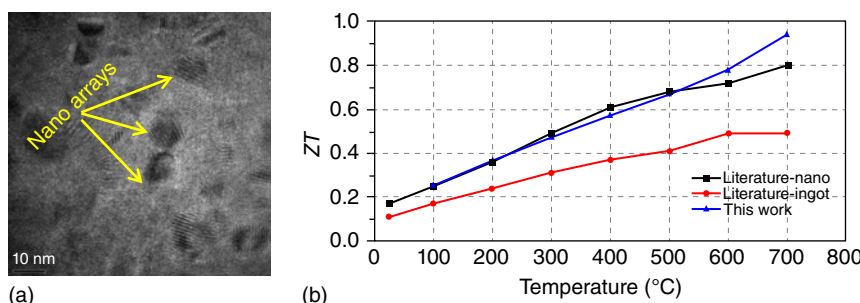


**Figure 2.6** (a) High resolution TEM image showing multi nano-arrays embedded in the matrix of HH. (b)  $ZT$  versus temperature of p-type  $\text{Hf}_{0.5}\text{Zr}_{0.5}\text{CoSn}_{0.2}\text{Sb}_{0.8}$  SPS sintered HH alloy as compared with a similar composition of ingot and hot-pressed samples reported in Ref. [33].

#### 2.4.4 Nanostructured Skutterudite Materials

Skutterudite materials with the general formula of  $BX_3$  where B is the transition metal of Fe, Co, Rh, or Ir, and X is a pnictogen such as P, As, or Sb. The crystalline structure of  $BX_3$  skutterudite consists of two  $B_4X_{12}$  units and two large empty cages per unit cell. The empty cages can be filled with alkali, alkaline-earth, rare-earth, actinide, or Tl elements forming the formula of  $A_yB_4X_{12}$  with maximum fill cages when  $y$  is equal to 1. Therefore, there are hundreds of families of skutterudite materials which can bring a great potential application in many different fields, one of this is TE energy conversion [91].

As for nanostructured skutterudites materials, different approaches have been proposed to achieve a figure of merit as high as possible. The combination of doping elements and control particles/grain sizes of bulk sample is the preferred methodology. Compacting nanopowders is the preferable method to fabricate bulk nanostructured skutterudites. The synthesis method of nanopowders can be roughly summarized into: (i) wet chemical synthesis such as solvothermal route [92], sol–gel [93], hydrothermal [94], coprecipitation process [95], and (ii) physical synthesizes, for example, ball milling [13, 96], melt spinning [97–104].

A wet chemically synthesized nanostructured inorganic material has low-cost, low-temperature reaction, and can be easily implemented for mass production. Therefore, this synthesis method has attracted considerable interest in the fabrication of skutterudites materials. The starting inorganic materials normally are grade analytical chlorides of metal such as  $SbCl_3$ ,  $CoCl_2$ ,  $NiCl_2$ , and so on, and agent tetra ethylene glycol,  $NaBH_4$  for solvothermal synthesis, or  $HCl$ ,  $NH_3$  for co-precipitation, and  $C_6H_8O_7$  for the sol–gel method. The synthesis temperature is kept at room temperature for co-precipitation, and 220–290 °C for the solvothermal process. The reaction duration is from 12 to 72 h. By using the wet chemical method, the obtained particle sizes of powder are in the range of 10–200 nm [92, 93, 95, 105–112]. Most of the studies were conducted on the  $CoSb_3$  based compound with partially filled cages of skutterudite structures [105], or partially substituted Co sites by other transition metal of Ni, or Fe [108, 109, 111].

The main purpose of controlling particle/grain size is to increase phonon scattering to reduce the lattice thermal conductivity of the TE sample. The thermal conductivity of the pure  $CoSb_3$  sample was reduced below 1 W/m/K in the temperature range of 300–600 K [95, 105, 111], which is lower about an order magnitude than that of single crystal sample [113]. In this case, the grain size of fabricated sample is less than 100 nm. Despite the low value of thermal conductivity the figure of merit of those samples is still small, that is, less than 0.2 at 700 K [95, 105, 111]. By introducing filling element into cage sites of  $A_yB_4X_{12}$ , the thermal conductivity values were also reduced by a factor of two for the case of  $Ba_{0.048}CoSb_3$  [105],  $LaFe_3CoSb_{12}$ ,  $CeFe_3CoSb_{12}$ , and  $La_{0.5}Ce_{0.5}Fe_3CoSb_{12}$  [106, 107]. Consequently, improvement in the figure of merit is obviously seen, the high-value  $ZT$  of 0.82 attained at 773 K for the  $La_{0.5}Ce_{0.5}Fe_3CoSb_{12}$  sample. In addition, the sintering technique also plays a crucial role. The study by Mi *et al.* [92, 109] shows that the SPS is dominated with shorter sintering duration and

higher density, as well as better maintain nanostructures of synthesis powder in the bulk sample. Despite the advantages of low-cost, easy to control the size of powder, the quality of powder of the wet chemical synthesis still needs to be further optimized [95, 112] to obtain a better value of  $ZT$ . It should be noticed here that the skutterudite powder synthesized by wet chemical methods has not been widening apply in the fabrication of TE module. The quality of chemical, the solution, water, and so on, and also many step of preheating or drying during the process could be the cause of introducing the contaminated elements.

In contrast to the wet chemical synthesis, the physical method uses high energy to produce the alloy with higher crystallize, and hence it would further improve the  $ZT$  value [114]. With the rapid solidification the melt spinning technique provides a useful tool for bulk nanostructuring skutterudite materials [97–104]. By using this method the stoichiometry of compounds was first produced by solid state reaction method either using fast melting in tube ampule or arc-melting, the ingots are then inductively melted under protection gas and spun on the cold copper wheel. The SPS technique is usually used to consolidate the ribbon. In general, the studies on skutterudites based on  $\text{CoSb}_3$  is mostly investigated with various of filling fraction in the cage sites by using rare earth element of Yb [97, 98, 102, 103], Ce [99, 100, 104], or Ca [101], Ba [102]. The typically obtained nanocrystal size is from 10 to 100 nm which can be controlled by adjusting the rotating speed of the cold copper wheel. The grain size of bulk nanostructured form is in the range of 100–300 nm, especially can be up to 50  $\mu\text{m}$  [102]. As the results of introducing the nanostructured size, the thermal conductivity reduces remarkably as compared to non-nanostructured samples, that is, the decreasing by a factor of two is reported on n-type  $\text{Yb}_{0.3}\text{Co}_4\text{Sb}_{12}$  materials [97]. Interestingly, the increment of Seebeck coefficient of about 10% was also observed in smaller nano-grains [97]. The high  $ZT$  values of 1.3 for n-type  $\text{Yb}_{0.3}\text{Co}_4\text{Sb}_{12.3}$  [98] and 1 for p-type  $\text{Ce}_{0.9}\text{Fe}_{3.4}\text{Co}_{0.6}\text{Sb}_{12}$  [99, 100] were obtained at 800 K. However, the small quantity by melt spinning for nanostructuring skutterudite materials has limited the usage of these materials for constructing TE device. It is, therefore, expected that the large quantity with high quality of materials would be taken into account.

With advantages of mass production, that is, can be produced tons of nanostructured powders the high energy ball milling offers a great possibility of realizing material research into application [13, 96, 114–122]. Recently, the high  $ZT$  values of 1.3 at 775 K for  $\text{DD}_{y}(\text{Fe}_{1-x}\text{Co}_x)_4\text{Sb}_{12}$  ( $\text{DD}$ : didymium) p-type and 1.6 at 800 K for  $(\text{Mm},\text{Sm})_y\text{Co}_4\text{Sb}_{12}$  ( $\text{Mm}$ : mischmetal) n-type skutterudite materials have been obtained [13], which will be expedited for building up a high conversion efficiency TE module. The high energy ball milling can reduce the crystallite size to nanoscale from 50 to 300 nm, resulting in improvement of  $ZT$  from 20% to 200% [116, 118, 119]. The hot press is used to consolidate the nanopowder with pressure around 60 MPa, the temperature of sintering 700 °C for holding 30 min [13]. Using SPS technique, we have optimized a sintering process, which is potential for mass production with TE performance similar to the best result reported so far on the same compositions (Figure 2.7a–c).

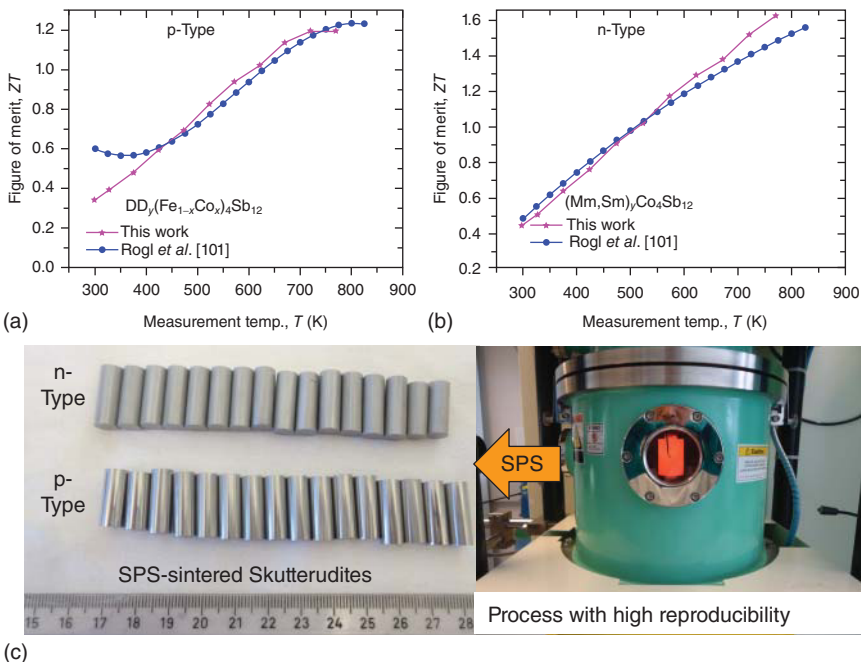


**Figure 2.7**  $ZT$  as a function of temperature for nanostructured p-type (a) and n-type (b) our skutterudite materials sintering by spark plasma sintering as compared with hot pressed sample reported in Ref. [13]. (c) Photos showing a possible mass production of high performance skutterudite materials by SPS.

## 2.4.5 Nanostructured Oxide Materials

### 2.4.5.1 p-Type Oxides

For p-type oxide TE materials, nanoscale layered cobaltite systems [24, 123–139] have been intensively investigated due to their good TE performance [128, 132] ( $ZT = 0.83$  at 973 K for the single crystal [128]). However, single crystals are less likely to be applied for fabricating practical TE devices. It is hence highly desirable to achieve sufficient TE properties in a polycrystalline form of these oxides. Among layered cobaltite systems, misfit-layered  $Ca_3Co_4O_{9+}$  oxides have attracted much attention due to their low cost, good TE performance as well as their highly durability at high temperatures [123–130, 133–139]. In fact, many attempts have been made over the years to enhance the TE performance of the polycrystalline  $Ca_3Co_4O_9$  by either ions doping [125–127, 129, 133, 134, 137] and improving the fabrication methods, for example, employing HP or SPS techniques [127, 135, 136, 139].

SPS technique, which is a pressure assisted pulsed current fast sintering process, offers an advantageous way to fabricate nanostructured bulk materials. With SPS technique, the microstructure of the material and crystal growth are well controlled while maintaining the original properties of the materials. Employing this fabrication method, we have synthesized some  $Ca_3Co_4O_{9+}$ -based nanocomposites with microstructural design consisting of

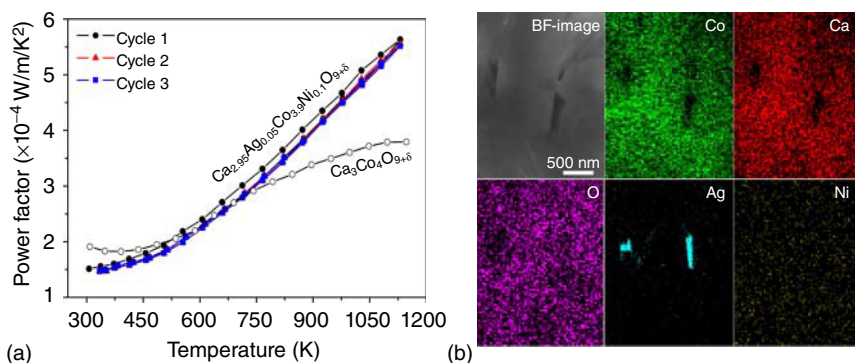


**Figure 2.8** (a) Power factor as a function of temperature for  $\text{Ca}_{2.95}\text{Ag}_{0.05}\text{Co}_{3.9}\text{Ni}_{0.1}\text{O}_{9+}$  nanocomposite. (b) STEM-EDX elements mapping of the nanocomposite sample.

oriented lamellar-like nanostructures doped with heavy ions together with embedded metallic nanoinclusions, for example, Ag. Shown in Figure 2.8 is an example of Ni and Ag co-doped  $\text{Ca}_3\text{Co}_4\text{O}_{9+}$  nanocomposite prepared by SPS. At 1100 K, the power factor was more than 40% improved comparing with a pure  $\text{Ca}_3\text{Co}_4\text{O}_{9+}$  sample (Figure 2.8a). It is worth to note that the TE performance is reproduced after various thermal cycles. It is evident from Figure 2.8b that Ni homogenously distributed, while Ag remains some nanosized crystals in the matrix. This suggests that Ni fully substituted for Co, while Ag only partly doped for Ca and the rest stays as nanoinclusions. A  $ZT$  value of 0.4 was achieved at 1100 K for this material. A higher  $ZT$  value of 0.5 at 1000 K was reported for a polycrystalline nanocomposite of  $\text{Ca}_3\text{Co}_4\text{O}_{9+}$  either doped or added with Ag [140]. Figure 2.9 shows  $ZT$  versus temperature and high-resolution transmission electron microscopy (HRTEM) image (a), and long-term stability test at high temperature (b) for a nanostructured bulk sample  $\text{Ca}_{2.8}\text{Lu}_{0.15}\text{Ag}_{0.05}\text{Co}_4\text{O}_9$  prepared by SPS. HRTEM image shows an evidence of Ag metallic nanoinclusions in the misfit-layered cobalt oxide matrix (Figure 2.9a, inset). This effective

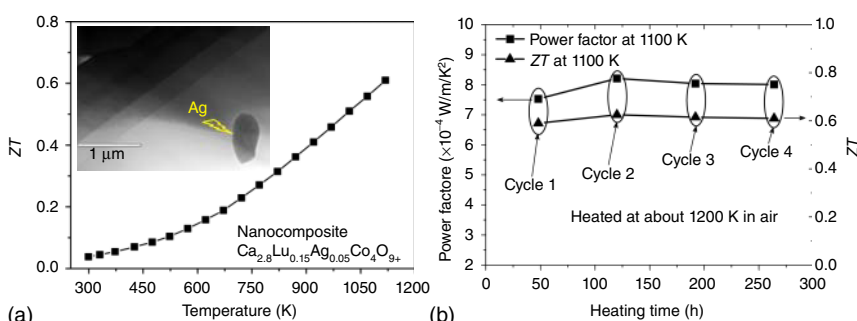


**Figure 2.9** (a)  $ZT$  as a function of temperature and HRTEM image showing a spherical metallic nanoinclusion for heavy doped layered cobaltite nanocomposite. (b) Power factor and  $ZT$  at 1100 K under various heat treatment cycles. (Van Nong *et al.* 2011 [24]. Reproduced with permission of Wiley.)

nanostructural approach has led to a remarkable improvement of  $ZT = 0.6$  at 1100 K resulted from a significantly reduction in the thermal conductivity and the enhanced power factor [24]. It is more interesting to note that  $ZT$  of this material is further improved by about 6% after a subsequent heat treatment and then this high  $ZT$  value maintained even after further extremely heating and cooling cycles (Figure 2.9b). The excellent chemical and thermal stability of this material as well as the rapid increase in  $ZT$  with increasing temperature strongly suggest this system as a very promising oxide TE material for high temperature power generation.

A segmented p-type material of doped misfit-layered cobaltite  $\text{Ca}_{2.8}\text{Lu}_{0.15}\text{Ag}_{0.05}\text{Co}_4\text{O}_{9+\delta}$  and HH  $\text{Ti}_{0.3}\text{Zr}_{0.35}\text{Hf}_{0.35}\text{CoSb}_{0.8}\text{Sn}_{0.2}$  alloy was demonstrated with a maximum conversion efficiency of 5% at  $\Delta T \approx 756$  K, which is the highest value reported for a oxide-based material [141].

#### 2.4.5.2 n-Type Oxides

Nanostructured ZnO-based oxides have gained much interest because they are low-cost along with their good TE properties [43, 44, 142–145]. A small amount of Al doping could result in a remarkable decrease in the electrical resistivity and change the conduction behavior from semiconducting to metallic. A long history of development through nanostructuring as well as heavily doping on this material for high temperature TE oxide has recently led to a successive progress in  $ZT = 0.47$  at 1000 K and 0.65 at 1247 K for a dual doping of Al and Ga using conventional pressing techniques [44]. Jood *et al.* [43] have reported a figure-of-merit,  $ZT$  of 0.44 at 1000 K for a nanostructured Al-doped ZnO. Very recently, a  $ZT$  value of 0.6 at 1273 K has been achieved [143], again confirming that the ZnO-based oxide is a good candidate n-type high temperature TE material.

CdO-based oxides and their nanocomposites have recently emerged as new n-type TE oxide materials [146–148]. A  $ZT$  value of 0.41 at 1000 K was achieved for nanocomposite of CdO with  $\text{SiO}_2$  nanoinclusion resulted from a 80% reduction of the thermal conductivity [146]. With Eu and Pr doping, the  $ZT$  values increase from 0.2 [147] to 0.38 [148] at 1000 K.

## 2.5 Outlook and Challenges

*Bulk nanostructured materials* have made an impressive progress with many high  $ZT$  systems such as PbTe-SrTe ( $ZT_{\max} = 1.7 \div 2.2$ ), Clathrates ( $ZT_{\max} = 1.2 \div 1.4$ ), Skutterudites ( $ZT_{\max} = 1.2 \div 1.7$ ), HH alloys ( $ZT_{\max} = 1.1 \div 1.5$ ), and TE oxides ( $0.6 \div 1.4$ ). However, so far most of them have not yet been realized in high efficiency practical devices. There exist a big gap between the efficiency of TE materials and the efficiency of their modules. To approach practical applications of TE energy conversion, some issues should be carefully considered:

- *Stability under large temperature gradients:* on operation, a TE device is subjected to high temperatures under large temperature differences. Under such conditions, nanostructures may suffer an intensive microstructure

evolution, which can deteriorate the TE performance. In addition, under large temperature difference with fast enough cooling at the cold side the intrinsic properties are also very much different when measuring the material under small temperature difference.  $\text{Zn}_4\text{Sb}_3$  with a max  $ZT \sim 1.4$  [18] is an typical example for this case. Under a large temperature at the hot side above 473 K and a fast enough cooling at the cold side, Zn whiskers were observed to come out of the materials at the cold part which eventually gets a mechanical failure [149]. Therefore, it strongly suggests that one should test the materials under large temperature gradients before building up their modules.

- *Mechanical properties under thermal cycling:* the long-term stability of TE materials and devices is equally important to their conversion efficiency. The mismatch in thermal expansion coefficient between difference crystal phases co-existing in the TE nanostructured or nanocomposite materials as well as between TE materials with contact materials is often the major reason leading to the device failure. Therefore, effort should be also put on improving the mechanical strength of high performance TE materials.
- *Interfacial contact resistances:* large interfacial thermal and electrical contact resistances are the main reason for the gap between the efficiencies of TE materials and modules. It is important to not only minimize the contact resistance but also to prevent it from diffusion/reaction. Developing advanced joining techniques and in-situ methods to understand the mechanism at interfaces under dynamic condition should play an important role in making future high efficiency TE devices.

## Acknowledgement

The authors gratefully acknowledges support by the European Commission for the NanoCaTe project under the contract No. 604647.

## References

- 1 Hicks, L.D. and Dresselhaus, M.S. (1993) *Phys. Rev. B*, **47**, 727.
- 2 Chen, Z.G., Hana, G., Yanga, L., Cheng, L., and Zou, J. (2012) *Progr. Nat. Sci. Mater. Int.*, **22**, 535.
- 3 Jiang, Q., Yang, J., Liu, Y., and He, H. (2016) *J. Adv. Dielectr.*, **6**, 1630002.
- 4 Kanatzidis, M.G. (2010) *Chem. Mater.*, **22**, 648.
- 5 Li, J.F., Liu, W.S., Zhao, L.D., and Zhou, M. (2010) *NPG Asia Mater.*, **2**, 152.
- 6 Liu, W., Yan, X., Chen, G., and Ren, Z. (2012) *Nano Energy*, **1**, 42.
- 7 Mohanraman, R., Lan, T.-W., Hsiung, T.-C., Amada, D., Lee, P.-C., Ou, M.-N., and Chen, Y.-Y. (2015) *Front. Chem.*, **3**, 1.
- 8 Pichanusakorn, P. and Bandaru, P. (2010) *Mater. Sci. Eng. R. Rep.*, **67**, 19.
- 9 Shakouri, A. (2011) *Annu. Rev. Mater. Res.*, **41**, 399.
- 10 Vaqueiro, P. and Powell, A.V. (2010) *J. Mater. Chem.*, **20**, 9577.
- 11 Stackhouse, S. and Stixrude, L. (2010) *Rev. Mineral. Geochem.*, **71**, 253.
- 12 Slack, G.A. and Tsoukala, V.G. (1994) *J. Appl. Phys.*, **76**, 1665.

- 13 Rogl, G., Grytsiv, A., Rogl, P., Bauer, E., Hochenhofer, M., Anbalagan, R., Mallik, R.C., and Schafler, E. (2014) *Acta Mater.*, **76**, 434.
- 14 Zhang, H., Borrman, H., Oeschler, N., Candolfi, C., Schnelle, W., Schmidt, M., Burkhardt, U., Baitinger, M., Zhao, J.T., and Grin, Y. (2011) *Inorg. Chem.*, **50**, 1250.
- 15 Shi, X., Yang, J., Bai, S., Yang, J., Wang, H., Chi, M., Salvador, J.R., Zhang, W., Chen, L., and Wong-Ng, W. (2010) *Adv. Funct. Mater.*, **20**, 755.
- 16 Toberer, E.S., Cox, C.A., Brown, S.R., Ikeda, T., May, A.F., Kauzlarich, S.M., and Jeffrey Snyder, G. (2008) *Adv. Funct. Mater.*, **18**, 2795.
- 17 Chitroub, M., Besse, F., and Scherrer, H. (2008) *J. Alloys Compd.*, **460**, 90.
- 18 Snyder, G.J., Christensen, M., Nishibori, E., Caillat, T., and Iversen, B.B. (2004) *Nat. Mater.*, **3**, 458.
- 19 Yan, X., Joshi, G., Liu, W., Lan, Y., Wang, H., Lee, S., Simonson, J.W., Poon, S.J., Tritt, T.M., Chen, G., and Ren, Z.F. (2010) *Nano Lett.*, **11**, 556.
- 20 Bux, S.K., Fleurial, J.-P., and Kaner, R.B. (2010) *Chem. Commun. (Cambridge)*, **46**, 8311.
- 21 Szczech, J.R., Higgins, J.M., and Jin, S. (2011) *J. Mater. Chem.*, **21**, 4037.
- 22 Faleev, S.V. and Léonard, F. (2008) *Phys. Rev. B: Cond. Mat. Mater. Phys.*, **77**, 1.
- 23 Ibáñez, M., Luo, Z., Genç, A., Piveteau, L., Ortega, S., Cadavid, D., Dobrozhana, O., Liu, Y., Nachtegaal, M., Zebarjadi, M., Arbiol, J., Kovalenko, M.V., and Cabot, A. (2016) *Nat. Commun.*, **7**, 10766.
- 24 Van Nong, N., Pryds, N., Linderoth, S., and Ohtaki, M. (2011) *Adv. Mater.*, **23**, 2484.
- 25 Ma, Y., Hao, Q., Poudel, B., Lan, Y., Yu, B., Wang, D., Chen, G., and Ren, Z. (2008) *Nano Lett.*, **8**, 2580.
- 26 Zhao, H., Sui, J., Tang, Z., Lan, Y., Jie, Q., Kraemer, D., McEnaney, K., Guloy, A., Chen, G., and Ren, Z. (2014) *Nano Energy*, **7**, 97.
- 27 Pei, Y., Lalonde, A.D., Heinz, N.A., Shi, X., Iwanaga, S., Wang, H., Chen, L., and Snyder, G.J. (2011) *Adv. Mater.*, **23**, 5674.
- 28 Biswas, K., He, J., Blum, I.D., Wu, C.-I., Hogan, T.P., Seidman, D.N., Dravid, V.P., and Kanatzidis, M.G. (2012) *Nature*, **489**, 414.
- 29 Hsu, K.F., Loo, S., Guo, F., Chen, W., Dyck, J.S., Uher, C., Hogan, T., Polychroniadis, E.K., and Kanatzidis, M.G. (2004) *Science*, **303**, 818.
- 30 Sui, J., Li, J., He, J., Pei, Y.-L., Berardan, D., Wu, H., Dragoe, N., Cai, W., and Zhao, L.-D. (2013) *Energy Environ. Sci.*, **6**, 2916.
- 31 Zhao, L.D., Berardan, D., Pei, Y.L., Byl, C., Pinsard-Gaudart, L., and Dragoe, N. (2010) *Appl. Phys. Lett.*, **97**, 2010.
- 32 Liu, H., Shi, X., Xu, F., Zhang, L., Zhang, W., Chen, L., Li, Q., Uher, C., Day, T., and Snyder, G.J. (2012) *Nat. Mater.*, **11**, 422.
- 33 Yan, X., Joshi, G., Liu, W., Lan, Y., Wang, H., Lee, S., Simonson, J.W., Poon, S.J., Tritt, T.M., Chen, G., and Ren, Z.F. (2011) *Nano Lett.*, **11**, 556.
- 34 Fu, C., Bai, S., Liu, Y., Tang, Y., Chen, L., Zhao, X., and Zhu, T. (2015) *Nat. Commun.*, **6**, 8144.
- 35 Joshi, G., Lee, H., Lan, Y., Wang, X., Zhu, G., Wang, D., Ryan, W., Cuff, D.C., Tang, M.Y., Dresselhaus, M.S., Chen, G., Ren, Z., Joshi, G., Lee, H.,

- Lan, Y., Wang, X., Zhu, G., Wang, D., Gould, R.W., Cuff, D.C., Tang, M.Y., Dresselhaus, M.S., Chen, G., Ren, Z. (2008) *Nano Lett.*, **2008**, 8, 4670.
- 36 Kim, C., Kim, D.H., Kim, H., and Chung, J.S. (2012) *ACS Appl. Mater. Interf.*, **4**, 2949.
- 37 Shi, X., Yang, J., Salvador, J.R., Chi, M.F., Cho, J.Y., Wang, H., Bai, S.Q., Yang, J.H., Zhang, W.Q., and Chen, L.D. (2012) *J. Am. Chem. Soc.*, **134**, 2842.
- 38 Schwall, M. and Balke, B. (2013) *Phys. Chem. Chem. Phys.*, **15**, 1868.
- 39 LaLonde, A.D., Pei, Y., and Snyder, G.J. (2011) *Energy Environ. Sci.*, **4**, 2090.
- 40 Zhang, Q., He, J., Zhu, T.J., Zhang, S.N., Zhao, X.B., and Tritt, T.M. (2008) *Appl. Phys. Lett.*, **93**, 4.
- 41 Wang, X.W., Lee, H., Lan, Y.C., Zhu, G.H., Joshi, G., Wang, D.Z., Yang, J., Muto, A.J., Tang, M.Y., Klatsky, J., Song, S., Dresselhaus, M.S., Chen, G., and Ren, Z.F. (2008) *Appl. Phys. Lett.*, **93**, 1.
- 42 May, A.F., Fleurial, J.P., and Snyder, G.J. (2010) *Chem. Mater.*, **22**, 2995.
- 43 Jood, P., Mehta, R.J., Zhang, Y., Peleckis, G., Wang, X., Siegel, R.W., Borca-Tasciuc, T., Dou, S.X., and Ramanath, G. (2011) *Nano Lett.*, **11**, 4337.
- 44 Ohtaki, M., Araki, K., and Yamamoto, K. (2009) *J. Electron. Mater.*, **38**, 1234.
- 45 Hung, L.T., Van Nong, N., Linderoth, S., and Pryds, N. (2015) *Phys. Stat. Sol. A-Appl. Mater. Sci.*, **212**, 767.
- 46 Seol, J.H., Jo, I., Moore, A.L., Lindsay, L., Aitken, Z.H., Pettes, M.T., Li, X., Yao, Z., Huang, R., Broido, D., Mingo, N., Ruoff, R.S., and Shi, L. (2010) *Science*, **328**, 213.
- 47 Han, N.P.L., Spangsdorf, S.H., Nong, N.V., Hung, L.T., Ngan, H.P., Chen, Y., Roch, A., and Stepien, L. (2016) *R S C Advances*, **6**, 59565.
- 48 Yan, X., Poudel, B., Ma, Y., Liu, W.S., Joshi, G., Wang, H., Lan, Y., Wang, D., Chen, G., and Ren, Z.F. (2010) *Nano Lett.*, **10**, 3373.
- 49 Xie, W., Wang, S., Zhu, S., He, J., Tang, X., Zhang, Q., and Tritt, T.M. (2013) *J. Mater. Sci.*, **48**, 2745.
- 50 Zhang, C., Peng, Z., Li, Z., Yu, L., Khor, K.A., and Xiong, Q. (2015) *Nano Energy*, **15**, 688.
- 51 Cao, Y.Q., Zhao, X.B., Zhu, T.J., Zhang, X.B., and Tu, J.P. (2008) *Appl. Phys. Lett.*, **92**, 2.
- 52 Xie, W., Tang, X., Yan, Y., Zhang, Q., and Tritt, T.M. (2009) *Appl. Phys. Lett.*, **94**, 102111.
- 53 Xie, W., Tang, X., Yan, Y., Zhang, Q., and Tritt, T.M. (2009) *J. Appl. Phys.*, **105**, 113713.
- 54 Hwang, S., Il Kim, S., Ahn, K., Roh, J.W., Yang, D.J., Lee, S.M., and Lee, K.H. (2013) *J. Electron. Mater.*, **42**, 1411.
- 55 Jung, S.J., Park, S.Y., Kim, B.K., Kwon, B., Kim, S.K., Park, H.H., Kim, D.I., Kim, J.Y., Bin Hyun, D., Kim, J.S., and Baek, S.H. (2015) *Acta Mater.*, **97**, 68.
- 56 Keshavarz, M.K., Vasilevskiy, D., Masut, R.A., and Turenne, S. (2014) *Mater. Charact.*, **95**, 44.
- 57 Zhai, Y., Zhang, T., Xiao, Y., Jiang, J., Yang, S., and Xu, G. (2013) *J. Alloys Compd.*, **563**, 285.
- 58 Han, N.P.L., Van Nong, N., Hung, L.T., Roch, A., and Stepien, L. (2017) *RSC Advances*, submitted.

- 59 Harman, T.C., Harman, T.C., Taylor, P.J., Walsh, M.P., and Laforge, B.E. (2002) *Science*, **297**, 2229.
- 60 Sootsman, J.R., Kong, H., Uher, C., D'Angelo, J.J., Wu, C.I., Hogan, T.P., Caillat, T., and Kanatzidis, M.G. (2008) *Angew. Chem. Int. Ed.*, **47**, 8618.
- 61 Girard, S.N., He, J., Li, C., Moses, S., Wang, G., Uher, C., Dravid, V.P., and Kanatzidis, M.G. (2010) *Nano Lett.*, **10**, 2825.
- 62 Biswas, K., He, J., Zhang, Q., Wang, G., Uher, C., Dravid, V.P., and Kanatzidis, M.G. (2011) *Nat. Chem.*, **3**, 160.
- 63 Zhou, M., Li, J.F., and Kita, T. (2008) *J. Am. Chem. Soc.*, **130**, 4527.
- 64 He, J., Sootsman, J.R., Girard, S.N., Zheng, J.C., Wen, J., Zhu, Y., Kanatzidis, M.G., and Dravid, V.P. (2010) *J. Am. Chem. Soc.*, **132**, 8669.
- 65 Quarez, E., Hsu, K., Pcionek, R., Frangis, N., Polychroniadis, E.K., and Kanatzidis, M.G. (2005) *J. Am. Chem. Soc.*, **127**, 9177.
- 66 He, J., Girard, S.N., Kanatzidis, M.G., and Dravid, V.P. (2010) *Adv. Funct. Mater.*, **20**, 764.
- 67 Deng, S., Tang, X., Yang, P., and Li, M. (2009) *J. Mater. Sci.*, **44**, 939.
- 68 Fecher, G.H., Rausch, E., Balke, B., Weidenkaff, A., and Felser, C. (2015) *Phys. Stat. Sol.*, **16**, 716.
- 69 Geng, H. and Zhang, H. (2014) *J. Appl. Phys.*, **116**, 033708.
- 70 Graf, T., Felser, C., and Parkin, S.S.P. (2011) *Prog. Solid State Chem.*, **39**, 1.
- 71 Gofryk, K., Kaczorowski, D., Plackowski, T., Mucha, J., Leithe-Jasper, A., Schnelle, W., and Grin, Y. (2007) *Phys. Rev. B*, **75**, 224426.
- 72 Katsuyama, S., Matsuo, R., and Ito, M. (2007) *J. Alloys Compd.*, **428**, 262.
- 73 Kawano, K., Kurosaki, K., Muta, H., and Yamanaka, S. (2008) *J. Appl. Phys.*, **104**, 1.
- 74 Kim, S.I., Lee, K.H., Mun, H.a., Kim, H.S., Hwang, S.W., Roh, J.W., Yang, D.J., Shin, W.H., Li, X.S., Lee, Y.H., Snyder, G.J., and Kim, S.W. (2015) *Science*, **348**, 109.
- 75 Kirievsky, K., Gelbstein, Y., and Fuks, D. (2013) *J. Solid State Chem.*, **203**, 247.
- 76 Kurosaki, K., Muta, H., and Yamanaka, S. (2004) *J. Alloys Compd.*, **384**, 51.
- 77 Van Nong, N., Ngan, H., Duc, N., Thanh, L., and Tai, L.T. (2017) *J. Mater. Sci.*, submitted.
- 78 Pierre, J., Skolozdra, R.V., Tobola, J., Kaprzyk, S., Hordequin, C., Kouacou, M.A., Karla, I., Currat, R., and Leliévre-Berna, E. (1997) *J. Alloys Compd.*, **262–263**, 101.
- 79 Ponnambalam, V., Alboni, P.N., Edwards, J., Tritt, T.M., Culp, S.R., and Poon, S.J. (2008) *J. Appl. Phys.*, **103**, 063716.
- 80 Ponnambalam, V., Zhang, B., Tritt, T.M., and Poon, S.J. (2007) *J. Electron. Mater.*, **36**, 732.
- 81 Rausch, E., Balke, B., Ouardi, S., and Felser, C. (2014) *Phys. Chem. Chem. Phys.*, **16**, 25258.
- 82 Rogl, G., Grytsiv, A., Gürth, M., Tavassoli, A., Ebner, C., Wünschek, A., Puchegger, S., Soprunyuk, V., Schranz, W., Bauer, E., Müller, H., Zehetbauer, M., and Rogl, P. (2016) *Acta Mater.*, **107**, 178.
- 83 Sekimoto, T., Kurosaki, K., Muta, H., and Yamanaka, S. (2006) *J. Alloys Compd.*, **407**, 326.

- 84 Shen, Q., Chen, L., Goto, T., Hirai, T., Yang, J., Meisner, G.P., and Uher, C. (2001) *Appl. Phys. Lett.*, **79**, 4165.
- 85 Skoug, E.J., Zhou, C., Pei, Y., and Morelli, D.T. (2009) *J. Electron. Mater.*, **38**, 1221.
- 86 Toboła, J. and Pierre, J. (2000) *J. Alloys Compd.*, **296**, 243.
- 87 Wunderlich, W. and Motoyama, Y. (2009) *Mater. Res. Soc. Symp. Proc.*, **1128**, 21.
- 88 Yan, X., Liu, W., Chen, S., Wang, H., Zhang, Q., Chen, G., and Ren, Z. (2013) *Adv. Energ. Mater.*, **3**, 1195.
- 89 Xie, W., Weidenkaff, A., Tang, X., Zhang, Q., Poon, J., and Tritt, T. (2012) *Nanomaterials*, **2**, 379.
- 90 Krez, J., Balke, B., Felser, C., Hermes, W., and Schwind, M. (2015) *Phys. Chem. Chem. Phys.*, **17**, 1.
- 91 Luo, H., Krizan, J.W., Muechler, L., Haldolaarachchige, N., Klimczuk, T., Xie, W., Fuccillo, M.K., Felser, C., and Cava, R.J. (2015) *Nat. Commun.*, **6**, 6489.
- 92 Mi, J.L., Zhu, T.J., Zhao, X.B., and Ma, J. (2007) *J. Appl. Phys.*, **101**, 054314.
- 93 Chu, Y., Tang, X., Zhao, W., and Zhang, Q. (2008) *Cryst. Growth Des.*, **8**, 208.
- 94 Liu, H., Wang, J., Hu, X., Li, L., Gu, F., Zhao, S., Gu, M., Boughton, R.I., and Jiang, M. (2002) *J. Alloys Compd.*, **334**, 313.
- 95 Toprak, M.S., Stiewe, C., Platzek, D., Williams, S., Bertini, L., Müller, E., Gatti, C., Zhang, Y., Rowe, M., and Muhammed, M. (2004) *Adv. Funct. Mater.*, **14**, 1189.
- 96 Rogl, G., Grytsiv, A., Rogl, P., Bauer, E., and Zehetbauer, M. (2011) *Intermetallics*, **19**, 546.
- 97 Li, H., Tang, X., Su, X., Zhang, Q., and Uher, C. (2009) *J. Phys. D: Appl. Phys.*, **42**, 145409.
- 98 Li, H., Tang, X., Zhang, Q., and Uher, C. (2008) *Appl. Phys. Lett.*, **93**, 252109.
- 99 Tan, G., Liu, W., Wang, S., Yan, Y., Li, H., Tang, X., and Uher, C. (2013) *J. Mater. Chem. A*, **1**, 12657.
- 100 Tan, G., Zheng, Y., and Tang, X. (2013) *Appl. Phys. Lett.*, **103**, 1.
- 101 Thompson, D.R., Liu, C., Yang, J., Salvador, J.R., Haddad, D.B., Ellison, N.D., Waldo, R.A., and Yang, J. (2015) *Acta Mater.*, **92**, 152.
- 102 Salvador, J.R., Waldo, R.A., Wong, C.A., Tessema, M., Brown, D.N., Miller, D.J., Wang, H., Wereszczak, A.A., and Cai, W. (2013) *Mater. Sci. Eng. B: Solid-State Mater. Adv. Technol.*, **178**, 1087.
- 103 Li, H., Tang, X., and Zhang, Q. (2009) *J. Electron. Mater.*, **38**, 1224.
- 104 Yan, Y.G., Wong-Ng, W., Kaduk, J.A., Tan, G.J., Xie, W.J., and Tang, X.F. (2011) *Appl. Phys. Lett.*, **98**, 142106.
- 105 Banik, A. and Biswas, K. (2014) *Mater. Sci. Semicond. Process.*, **27**, 593.
- 106 Lu, P.-X., Wu, F., Han, H.-L., Wang, Q., Shen, Z.-G., and Hu, X. (2010) *J. Alloys Compd.*, **505**, 255.
- 107 Lu, P., Shen, Z., and Hu, X. (2009) *J. Mater. Res.*, **24**, 2873.
- 108 Li, J.Q., Feng, X.W., Sun, W.A., Ao, W.Q., Liu, F.S., and Du, Y. (2008) *Mater. Chem. Phys.*, **112**, 57.

- 109 Mi, J.L., Zhao, X.B., and Zhu, T.J. (2007) *Int. Conf. Thermoelectr. ICT, Proc.*, **2**, 16.
- 110 Mi, J.L., Zhao, X.B., Zhu, T.J., Tu, J.P., and Cao, G.S. (2006) *J. Alloys Compd.*, **417**, 269.
- 111 Bertini, L., Stiewe, C., Toprak, M., Williams, S., Platzek, D., Mrotzek, A., Zhang, Y., Gatti, C., Müller, E., Muhammed, M., and Rowe, M. (2003) *J. Appl. Phys.*, **93**, 438.
- 112 Toprak, M., Zhang, Y., Muhammed, M., Zakhidov, A.A., Baughman, R.H., and Khayrullin, I. (1992) Eighteenth Int. Conf. Thermoelectr. Proceedings, ICT'99 (Cat. No.99TH8407), IEEE **1999**, 382.
- 113 Caillat, T., Borshchevsky, A., and Fleurial, J.-P. (1996) *J. Appl. Phys.*, **80**, 4442.
- 114 Sales, B.C., Mandrus, D., and Williams, R.K. (1996) *Science*, **272**, 1325.
- 115 Jie, Q., Wang, H., Liu, W., Wang, H., Chen, G., and Ren, Z. (2013) *Phys. Chem. Chem. Phys.*, **15**, 6809.
- 116 Rogl, G., Setman, D., Schafler, E., Horky, J., Kerber, M., Zehetbauer, M., Falmbigl, M., Rogl, P., Royanian, E., and Bauer, E. (2012) *Acta Mater.*, **60**, 2146.
- 117 Zhou, X., Wang, G., Zhang, L., Chi, H., Su, X., Sakamoto, J., and Uher, C. (2012) *J. Mater. Chem.*, **22**, 2958.
- 118 Zhang, L., Grytsiv, A., Kerber, M., Rogl, P., Bauer, E., and Zehetbauer, M. (2010) *J. Alloys Compd.*, **490**, 19.
- 119 Rogl, G., Grytsiv, A., Bauer, E., Rogl, P., and Zehetbauer, M. (2010) *Intermetallics*, **18**, 57.
- 120 Rogl, G., Grytsiv, A., Rogl, P., Bauer, E., Kerber, M.B., Zehetbauer, M., and Puchegger, S. (2010) *Intermetallics*, **18**, 2435.
- 121 Zhang, L., Grytsiv, A., Rogl, P., Bauer, E., and Zehetbauer, M. (2009) *J. Phys. D: Appl. Phys.*, **42**, 225405.
- 122 Alboni, P.N., Ji, X., He, J., Gothard, N., and Tritt, T.M. (2008) *J. Appl. Phys.*, **103**, 113707.
- 123 Lu, Y., Song, Y., Feng, J., and Wang, F.P. (2010) *Mater. Sci. Forum*, **650**, 132.
- 124 Mikami, M., Ando, N., and Funahashi, R. (2005) *J. Solid State Chem.*, **178**, 2186.
- 125 Nan, J., Wu, J., Deng, Y., and Nan, C.W. (2003) *J. Eur. Ceram. Soc.*, **23**, 859.
- 126 Nong, N.V., Liu, C.J., and Ohtaki, M. (2011) *J. Alloys Compd.*, **509**, 977.
- 127 Nong, N.V., Liu, C.J., and Ohtaki, M. (2010) *J. Alloys Compd.*, **491**, 53.
- 128 Shikano, M. and Funahashi, R. (2003) *Appl. Phys. Lett.*, **82**, 1851.
- 129 Song, Y., Sun, Q., Zhao, L., Wang, F., and Jiang, Z. (2009) *Mater. Chem. Phys.*, **113**, 645.
- 130 Tang, G., Yang, W., Wen, J., Wu, Z., Fan, C., and Wang, Z. (2015) *Ceram. Int.*, **41**, 961.
- 131 Terasaki, I., Ishii, Y., Tanaka, D., Takahata, K., Iguchi, Y. (2000) *Jpn. J. Appl. Phys.*, **2001**, 40, L65.
- 132 Terasaki, I., Sasago, Y., and Uchinokura, K. (1997) *Phys. Rev. B*, **56**, R12685.
- 133 Wang, Y., Sui, Y., Cheng, J., Wang, X., Miao, J., Liu, Z., Qian, Z., and Su, W. (2008) *J. Alloys Compd.*, **448**, 1.

- 134 Wang, Y., Sui, Y., Li, F., Xu, L., Wang, X., Su, W., and Liu, X. (2012) *Nano Energy*, **1**, 456.
- 135 Wu, N., Holgate, T.C., Van Nong, N., Pryds, N., and Linderoth, S. (2013) *J. Electron. Mater.*, **42**, 2134.
- 136 Wu, N., Holgate, T.C., Van Nong, N., Pryds, N., and Linderoth, S. (2014) *J. Eur. Ceram. Soc.*, **34**, 925.
- 137 Wu, N., Van Nong, N., Pryds, N., and Linderoth, S. (2015) *J. Alloys Compd.*, **638**, 127.
- 138 Xiang, P.H., Kinemuchi, Y., Kaga, H., and Watari, K. (2008) *J. Alloys Compd.*, **454**, 364.
- 139 Yin, T., Liu, D., Ou, Y., Ma, F., Xie, S., Li, J.F., and Li, J. (2010) *J. Phys. Chem. C*, **114**, 10061.
- 140 Wang, Y., Sui, Y., Cheng, J., Wang, X., and Su, W. (2009) *J. Alloys Compd.*, **477**, 817.
- 141 Hung, L.T., Van Nong, N., Snyder, G.J., Viet, M.H., Balke, B., Han, L., Stamate, E., Linderoth, S., and Pryds, N. (2015) *Energy Convers. Manage.*, **99**, 20.
- 142 Han, L., Hung, L.T., Van Nong, N., Pryds, N., and Linderoth, S. (2013) *J. Electron. Mater.*, **42**, 1573.
- 143 Brockway, L., Vasiraju, V., Sunkara, M.K., and Vaddiraju, S. (2014).
- 144 Jood, P., Mehta, R.J., Zhang, Y., Borca-Tasciuc, T., Dou, S.X., Singh, D., and Ramanath, G. (2013) *RSC Adv.*, **4**, 6363.
- 145 Han, L., Van Nong, N., Zhang, W., Hung, L.T., Holgate, T., Tashiro, K., Ohtaki, M., Pryds, N., and Linderoth, S. (2014) *RSC Adv.*, **4**, 12353.
- 146 Li, L., Liang, S., Li, S., Wang, J., Wang, S., Dong, G., and Fu, G. (2014) *Nanotechnology*, **25**, 425402.
- 147 Wang, S., Liu, F., Lü, Q., Dai, S., Wang, J., Yu, W., and Fu, G. (2013) *J. Eur. Ceram. Soc.*, **33**, 1763.
- 148 Wang, S., Lü, Q., Li, L., Fu, G., Liu, F., Dai, S., Yu, W., and Wang, J. (2013) *Scr. Mater.*, **69**, 533.
- 149 Hung, L.T., Van Nong, N., The, N.D., Han, L., Pryds, N., Iversen, B.B., and Yin, H. (2017) *Adv. Func. Mater.*, submitted.

## 3

### Organic Thermoelectric Materials

*Simone Fabiano<sup>1</sup>, Ioannis Petsagkourakis<sup>2</sup>, Guillaume Fleury<sup>2</sup>, Georges Hadzioannou<sup>2</sup>, and Xavier Crispin<sup>1</sup>*

<sup>1</sup>Linköping University, Department of Science and Technology, Campus Norrköping, Bredgatan 34, S-60174, Norrköping, Sweden

<sup>2</sup>CNRS-Université de Bordeaux-INP (UMR5629), Laboratoire de Chimie des Polymères Organiques (LCPO), Building B8 Allée Geoffroy Saint Hilaire, 33615, Pessac Cedex, France

#### 3.1 Introduction

Thermoelectric generators (TEGs) convert heat into electricity, and could contribute to the world's increasing energy demand by harvesting low-energy-density heat, such as waste heat produced during the conversion of fossil fuels to electricity or heat from solar radiation. The efficiency of the heat–electricity conversion is dictated by the material properties. One of the pressing challenges in thermoelectricity is to find a naturally abundant material with good thermoelectric properties that can enable the implementation of TEG on an industrial scale. We then present the key material properties that help define the heat-to-electricity conversion efficiency. The ability of a material to transport heat and electrical currents is dictated by the values of the thermal ( $\lambda$ ) and electrical ( $\sigma$ ) conductivities. The independent transport of electrons and phonons in a material is described by Ohm's law ( $\vec{i} = \sigma \vec{E}$ ) and Fourier's law ( $\vec{q} = -\lambda \vec{\nabla} T$ ), respectively. The thermoelectric phenomenon arises in the simultaneous presence of both electrical and thermal currents. The Seebeck effect refers to the possibility of creating an electrostatic potential and thus an electrical current from a temperature gradient (see second term in Eq. (3.1)). A TEG is an electronic device that uses the Seebeck effect to convert a heat flow into an electron flow.

$$\vec{i} = \sigma(\vec{E} - S\vec{\nabla}T) \quad (3.1)$$

Here  $E$  is the electric field,  $i$  is the electric current density,  $T$  is the temperature, and  $S$  is the Seebeck coefficient. The Seebeck coefficient is defined as the open circuit voltage obtained between the two ends of a material subjected to a temperature difference.

$$S = \left( \frac{dV}{dT} \right)_{I=0} \quad (3.2)$$

Seebeck coefficients can be as small as a few microvolts per kelvin for metals and as large as several millivolts per kelvin for electrical insulators [1, 2].

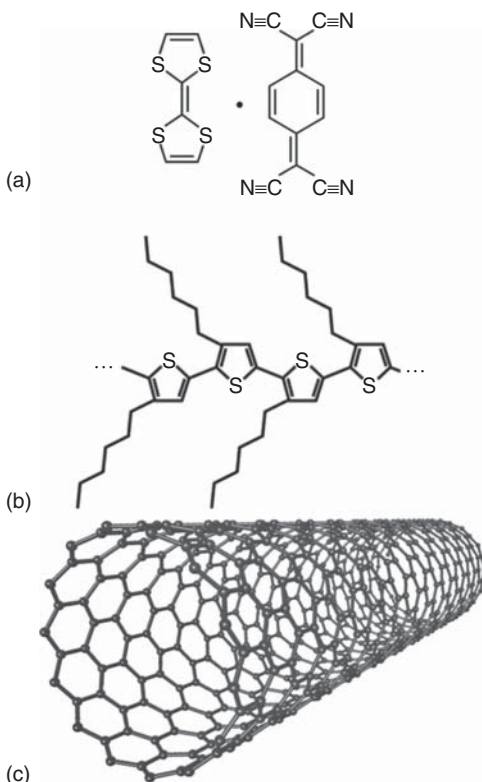
In order to generate an electrical power ( $P = VI$ ,  $V$  is the potential and  $I$  is the current), a thermoelectric material should have the following two properties: (i) it should transport the current efficiently, that is, possess a high electrical conductivity  $\sigma$ ; (ii) it should produce a significant thermo-induced voltage, that is, have a high Seebeck coefficient ( $V = S\Delta T$ ); and (iii) it should have a low thermal conductivity  $\lambda$ , to ensure that a large temperature difference ( $\Delta T$ ) is maintained. The maximum efficiency of a TEG is governed by material parameters ( $S$ ,  $\lambda$ ,  $\sigma$ ) regrouped in the thermoelectric figure of merit  $Z$  (see Eq. (3.3)). Hence,  $Z$  (units per Kelvin) can be seen as a measure of the thermoelectric efficiency of a given material.

$$Z = \frac{\sigma S^2}{\lambda} \quad (3.3)$$

$ZT$  quantifies the ratio between the thermal energy passing through the thermoelectric element and the electrical energy produced. The best thermoelectric materials possess  $ZT$  values around unity. One of the major challenges in thermoelectricity is that no efficient thermoelectric materials of high abundance have been found for low temperature applications (<500 K) [3], while 50% of the waste heat and the solar thermal energy lie in the range 300–500 K. The efficiency of the TEG is the ratio between the thermal power input and the electrical power output [3] and it is proportional to  $(1 + ZT)^{1/2}$ . A TEG composed of a material with  $ZT = 1$  is expected to reach 5% efficiency if the temperature difference between its hot and cold sides is set to 100 K.

Thermoelectric materials constitute a special class of materials with low thermal conductivity and high electrical conductivity, often described as “phonon-glass and electron-crystal” materials [4]. Organic conductors are known for their intrinsic low thermal conductivity (such as glasses or other amorphous systems), but they are electrically conducting. There are various classes of organic conductors, such as doped small conjugated molecules or organic charge transfer salt (e.g., tetrathiafulvalene-7,7,8,8-tetracyanoquinodimethane TTF-TCNQ; Figure 3.1a), doped conjugated polymers (e.g., poly(3-hexylthiophene; Figure 3.1b) or carbon-based nano-objects (e.g., carbon nanotubes CNT; Figure 3.1c). The key advantage of polymers is that they can form homogeneous, pin-holes-free films by solution processing, compared to small molecules that typically prefer to organize in crystals. Conducting polymers were discovered in the late 1970s when it was demonstrated for the first time that poly(acetylene) exposed to iodine vapors could become conductive through a redox reaction [5–7]. As a result, its electrical conductivity increased from  $10^{-9}$  to  $10^4$  S/cm followed by the formation of a metal-like low-weight and flexible material, which subsequently became known as a “synthetic metal” [7]. This phenomenon is sometimes called “doping” in analogy with inorganic semiconductors. There are however major differences between organic and inorganic semiconductors. For conducting polymers, a counterion not covalently bound to the polymer neutralizes the doping charge carried by the polymer chain. Also, dopant concentrations are in the parts per million range for inorganics, but range from a few

**Figure 3.1** Chemical structure of few classes of organic (semi)conductors:  
 (a) charge transfer salt TTF–TCNQ,  
 (b) conjugated polymer P3HT, and  
 (c) carbon nanotube, CNT.



percent up to 40% for conducting polymers. Neutral or undoped conjugated polymers have electrical conductivity values close to those of insulators, while oxidized or doped conjugated polymers are called conducting polymers because they show similarities with doped semiconductors and sometimes metals. Highly doped conducting polymers without side chains are typically insoluble. A common strategy for solubility enhancement lies in a dispersion formation via micelle-like particles either with a soluble polymeric counterion (polystyrene sulfonate for poly(3,4-ethylenedioxythiophene), PEDOT:PSS) [8] or using an ionic surfactant serving as a counterion (camphorsulfonic acid for polyaniline, Pani-CSA) [9]. The presence of specific high boiling point solvents favors better polymer chain organization, removes the excess of insulating materials, and can therefore increase the conductivity by several orders of magnitude [10, 11]. This effect is morphological in nature and is called “secondary” doping (to distinguish it from the “primary” effect related to oxidation/doping of the polymer). Highly conducting PEDOT:PSS thin films or patterns can be created on flexible surfaces via a low temperature water process, such as coating, spraying, and printing [8].

Today’s thermoelectric materials of choice for low temperature energy conversion are bismuth chalcogenides, such as bismuth antimony telluride alloys with  $ZT \sim 1$  (power factor  $PF = \sigma S^2 = 4500 \mu\text{W}/\text{m/K}^2$ ,  $\lambda = 1.2 \text{ W}/\text{m/K}$ ) at room temperature [12]. They are used in niche applications such as radioisotope TEGs to power satellites. Those alloys are of low natural abundance and manufactured

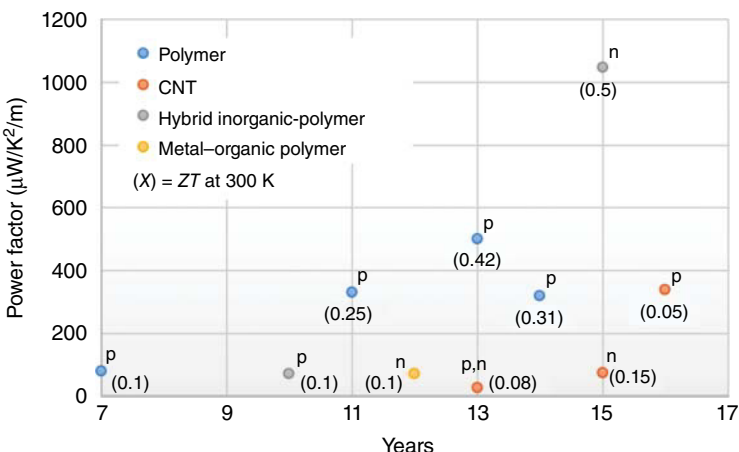


**Figure 3.2** Historical development of the thermoelectric power factor for various classes of emerging thermoelectric materials. Conducting polymers (blue), carbon nanotubes (red), hybrid inorganic–polymer composites (gray), and metal–organic polymers (yellow). p and n stand for positive and negative conduction. The text in parentheses is the value of  $ZT$  at 300 K and the reference from which the data are taken. Data sources: 2007 [13], 2010 [14]; 2011 [15], 2012 [16], 2013 blue point [17], 2013 red point [18], 2014 [19], 2015 red point [20], 2015 grey point [21], 2016 [22]. Figure inspired from [23].

using expensive processes, impeding the widespread use of thermoelectric installations for waste heat recovery. Thus, widely available organic thermoelectric materials have become of interest, despite their lower efficiencies. Figure 3.2 shows the evolution of PF over time for various potential classes of new abundant thermoelectric materials operating around room temperature. Owing to their intrinsic low thermal conductivity ( $\lambda < 1.5 \text{ W/m/K}$ ), semiconducting polymers constitute one such class (blue points). Up to now, only p-doped polymers showed decent thermoelectric properties, with PFs of  $78 \mu\text{W/m/K}^2$  [ $ZT = 0.1$ ] [13],  $330 \mu\text{Wm}^{-1}\text{K}^{-2}$  [ $ZT = 0.25$ ] [15],  $320 \mu\text{Wm}^{-1}\text{K}^{-2}$  [ $ZT = 0.31$ ] [19],  $500 \mu\text{Wm}^{-1}\text{K}^{-2}$  [ $ZT = 0.42$ ] [17]. The challenge with n-doped polymers is to increase the doping level to reach high conductivity while maintaining air stability. Note that metal–organic polymers offer an opportunity to get n-type polymers with  $ZT = 0.1$  [16] (yellow point).

Individual CNTs are a priori not promising as thermoelectrics because of their intrinsic high thermal conductivity ( $\lambda = 1000 \text{ W/m/K}$ ). However, thick layers of CNTs, composed of unaligned “bundles and mats,” have much lower thermal conductivities – about  $30 \text{ W/m/K}$ . When the material is made of separated individual bundles,  $\lambda$  can reach  $3 \text{ W/m/K}$  because of the thermal contact resistance between bundles. Previous works have reported the thermoelectric properties of both n- and p-doped CNT-based materials with a mix of semiconducting SWCNTs and metallic SWCNTs. Although there was a rise in PF values (red points in Figure 3.2) from  $25 \mu\text{W/m/K}^2$  [ $ZT = 0.08$ ] [18] to  $75 \mu\text{W/m/K}^2$  [ $ZT = 0.15$ ] [20], the high conductivity of the metallic CNTs limited the PF. To tackle this problem, researchers have exploited recent separation protocols

based on specific physicochemical interactions of CNTs with certain conjugated polymers, more especially polyfluorenes [24]. In doing so, they purified and obtained samples with less than 1% of metallic SWCNTs and reached  $\text{PF} = 340 \mu\text{W/m/K}^2$  [22]. CNTs display other desirable features for thermoelectric applications, besides the ease of both n- and p-doping. They are much more resistant to thermal degradation than polymers, and thus have a broader operating temperature range. For temperatures above 200 °C, degradation of molecular dopants might take place, but other atomic dopants could be more resilient. Like semiconducting polymers, CNTs can be functionalized to create stable dispersions and can be used as inks for printed electronics, which is seen as a low-cost manufacturing method to replicate the hundreds of thermocouples required in a TEG. Finally, SWCNTs could be combined with inorganic nanostructures or conducting polymers to design hybrid nanocomposites (gray points in Figure 3.2 from [14, 21]). The independent control of doping level of the conducting polymer matrix and of the s-SWCNT might open up new avenues for thermoelectric optimization. Recent results are promising, with PF claimed to reach 1000  $\mu\text{W/m/K}^2$  [21], but further investigation is needed.

## 3.2 Seebeck Coefficient and Electronic Structure

The Seebeck coefficient is intimately related to the electronic structure and mobility of the charge carrier. Mott's formula [25], which is valid for both hopping and band motion transport mechanisms, states that

$$S = C \left\{ \frac{d[\ln(\sigma(E))]}{dE} \right\}_{E=E_F} \propto \left\{ \frac{d \ln N(E)}{dE} \right\}_{E=E_F} \quad (3.4)$$

where  $C = \pi^3 k^2 T / 2|e|$ . From Einstein's equation,  $\sigma(E) \propto N(E)D(E)$ , where  $N(E)$  is the density of states (DoS) and  $D(E)$  is the diffusion coefficient. If we assume that the diffusion coefficient is constant with energy, the Seebeck coefficient is proportional to the derivative of  $\ln N(E)$  at the Fermi level energy  $E_F$ . Hence, controlling the shape of the density of state at the Fermi level in a material should enable tuning its Seebeck coefficient. Hence, it is crucial to understand the electronic structure of conducting polymers.

The removal of electrons from the top of the valence band (VB) in a single polymer chain can lead to two different localized positively charged quasi particles: positive polarons (radical cation) and bipolarons (dication) balanced by atomic or molecular counterions. Highly oxidized polythiophenes such as PEDOT are known to show a very small electron spin resonance (ESR) signal, suggesting the presence of polaron pairs or bipolarons [26]. While the structure of the neutral chain is typically characterized by an aromatic character, the bipolaron distortion has a quinoid character characterized by a change in bond length alternation (Figure 3.3a). This geometrical distortion around the excess of positive charge defines the extent of the wavefunction of the (bi)polaron [27], featured by two new empty in-gap states ( $i, i^*$ ) [29, 30]. In an amorphous phase, bipolaron levels are localized on a segment of the chains. At high oxidation levels, the wave function

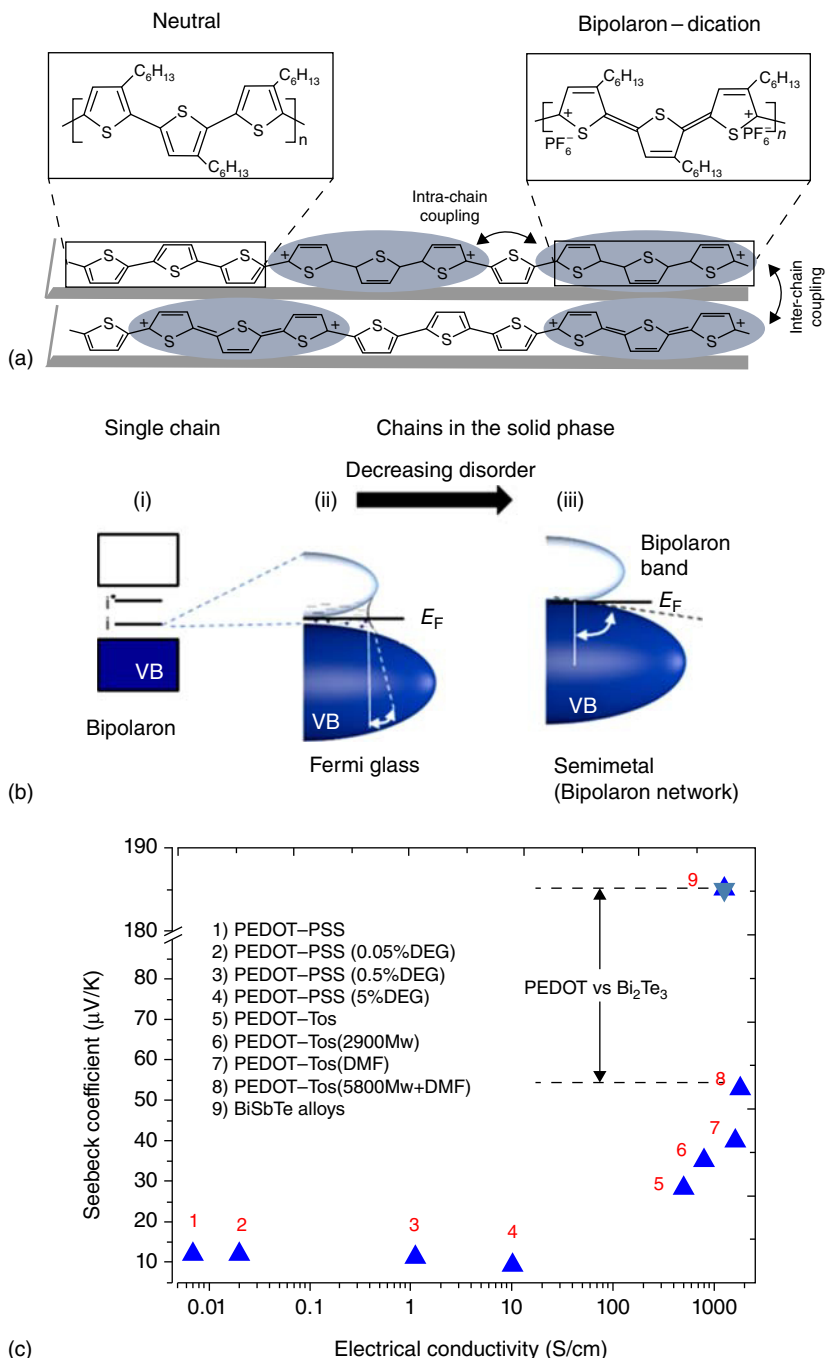


**Figure 3.3** (a) Chemical structure of a neutral polythiophene chain, and a chain that carries a bipolaron. At high doping level, the coupling between bipolaron wavefunctions can be either intra-chain or inter-chain, and this is at the origin of the creation a bipolaronic band. (b) Electronic structure of a polymer chain with (i) one bipolaron. Sketch of the logarithm of the density of state  $\ln N(E)$  for an amorphous (ii) bipolaronic polymer solid with localized states around the Fermi level  $E_F$ ; as well as for (iii) a semi-metallic network of bipolarons with the Fermi level lying in a delocalized band. The slope of  $\ln N(E)$  at  $E_F$  is proportional to the Seebeck coefficient. (c) Seebeck coefficient versus electrical conductivity of various PEDOT derivatives (triangle) compared to Sb-doped  $\text{Bi}_2\text{Te}_3$  (star) [27]. Further improvement in structural order (higher  $\sigma$ ) should in principle result in even larger  $\alpha$  and thus a higher thermoelectric power factor  $PF$ . For the sake of comparison, good thermoelectric material (nanostructured BiSbTe alloy) [28] display similar conductivity range as that of PEDOT, but a much higher Seebeck coefficient than PEDOT derivatives. Figure adapted from [27].



of the charged defects localized on the same chain overlap, and a one-dimensional “intra-chain” band is created [31]. This band does, however, not extend through the three dimensions of the solid, owing to disorder and the absence of the inter-chain electronic coupling [32]. For this reason, in-gap states are spatially localized with a spread in energy distribution. The Fermi level lies in a smooth region of the density of state and among localized states between the VB and the bipolaron band for a disordered bipolaronic polymer solid (Figure 3.3b) [33]. The slope of  $\ln N(E)$  at  $E_F$  is small, which explains the small Seebeck coefficient for amorphous bipolaronic systems. The solid can be considered as a Fermi glass, which means that the  $E_F$  is within localized states [34, 35]. In a Fermi glass, the carrier is localized and temperature-activated hopping is needed for the transport. In such a situation,  $\sigma \rightarrow 0$ , when  $T \rightarrow 0$ . This is the case for the PEDOT:PSS samples 1–4 in Figure 3.3c.

When disorder decreases, some crystalline domains are formed and short interchain distances result in an overlap of the  $\pi$ -electronic density of adjacent packed chains, which promotes the delocalization of electronic wave function [36], so bipolarons spread across several chains (Figure 3.3a) [37]. Highly oxidized PEDOT possesses up to one charge carrier per three monomer units [38]. For semicrystalline bipolaronic polymers, a network of bipolarons is formed such that the bipolaron wave functions overlap and create an extended empty bipolaron band, merging with the filled VB. This is the electronic structure of a semimetal with a large slope of  $\ln N(E)$  at  $E_F$ . Like metals, the conductivity diminishes when the sample is heated, because the delocalized carriers scatter with phonons. In Figure 3.3c, one observes an evolution from various PEDOT derivatives from low Seebeck coefficient at low conductivity to high Seebeck coefficient at high conductivity, which reflects the Fermi glass to semimetal transition [39].

Further improvement in structural order (higher  $\sigma$ ) should, in principle, result in even larger  $\alpha$  and thus a higher thermoelectric power factor  $PF$ . For the sake of comparison, a good thermoelectric material (nanostructured BiSbTe alloy) [30] displays a similar conductivity range as that of PEDOT, but a much higher Seebeck coefficient than PEDOT derivatives.

### 3.3 Seebeck Coefficient and Charge Carrier Mobility

The charge carrier mobility  $\mu$  of conducting polymers is linked to the electronic structure of the material and thus to the Seebeck coefficient. Except for specific samples found with appropriate morphology to exhibit semimetallic or metallic character, the main charge transport mechanism in conducting polymer samples is the thermally activated hopping transport between conducting sites existing in an intrachain and an interchain level (Figure 3.4a). One often refers to a non-homogeneous model with crystalline “metallic islands” dispersed in the amorphous “insulating” polymer matrix [41]. Therefore, a material with an increased number of these conducting domains would have a higher hopping rate and hence higher charge carrier mobility. From a structural point of view, a high degree of crystallinity benefits the hopping transport in the polymer material by decreasing the disorder and promoting interchain  $\pi-\pi$  interactions. However, electronically, these “metallic islands” are the extended  $\pi$ -systems formed in the doped conjugated chains, where the charge carriers are being delocalized. Consequently, the number of those sites in the polymer (and

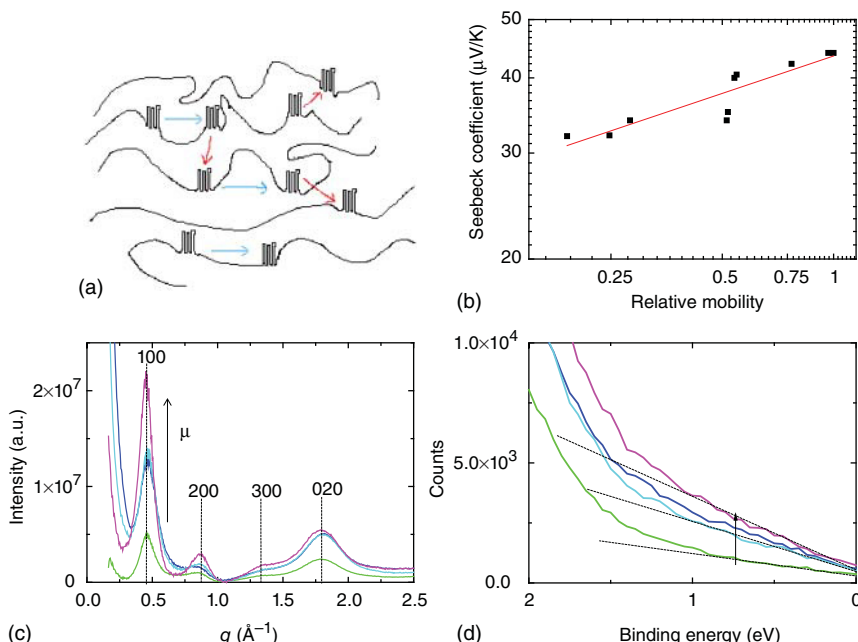


**Figure 3.4** (a) Hopping charge transport between the metallic islands of the chains in an interchain (red) and intrachain (blue) level. (b) The Seebeck coefficient versus the relative mobility for PEDOT:Tos samples with various charge carrier mobilities but constant carrier concentration. The charge carrier mobilities were normalized with respect to the highest value in this study. [40]. (c) The radially averaged intensity of 2D-GIWAXS patterns for PEDOT:Tos samples of varying charge carrier mobility and constant charge carrier concentration. The degree of crystallinity increases with the area under the (1 0 0) peak. (d) The UPS spectra at lower binding energies for the PEDOT:Tos samples presented in Figure 3.4b, where the broadening of the band edge is observed with the increase of  $\mu$  [41].

thus the charge carrier mobility) is related both to the polymer charge carrier concentration  $n$  and to the degree of crystallinity of the material. Considering that the Seebeck coefficient is strongly related both to the filling and the shape of the DoS, it is not trivial to decorrelate the charge carrier concentration with the charge carrier mobility and extract a relationship between  $\mu$  and  $S$ , which in fact would be translated in the effect of the DoS shape to the  $S$ .

Upon constant doping concentration though, any modifications on the charge carrier mobility should be related only to the structural properties of the material as indicated by the X-ray diffraction pattern in Figure 3.4c (high mobility is connected to high diffraction intensity). An increase in the degree of crystallinity of the polymer should extend the  $\pi$ -system of the doped conjugated chains because the p-orbitals of the units would overlap. This results in a broadening of the deep  $\pi$ -bands in the band edge as probed by ultraviolet photoelectron spectroscopy (UPS) (Figure 3.4d), which extends to the even deeper bands near the Fermi energy [36, 42]. Thus, the slope of the DoS at the Fermi level would become steeper and the Seebeck coefficient of the material should increase, following Eq. (3.4). This is clearly observed in Figure 3.4b, where the Seebeck coefficient is plotted against the relative charge carrier mobility, for various PEDOT:Tos materials of constant carrier concentration. As a result, a mild dependence of  $S = \mu^{0.2}$  can be extracted. This mild dependency actually highlights the effect of the shape of the DoS to the polymer thermoelectric properties. Ultimately, an increase of the charge carrier mobility would also benefit the electrical conductivity, since  $\sigma$  is analogous to  $\mu$  ( $\sigma = en\mu$ ), resulting in an enhanced thermoelectric power factor ( $PF \approx 236 \mu\text{W}/\text{m/K}^2$ ) [40].

### 3.4 Optimization of the Figure of Merit

If the charge carrier concentration in a material is high then its Seebeck coefficient is small (e.g., metals); reciprocally, electric insulators display high thermovoltages. The charge carrier concentration, or oxidation level, in the conducting polymer poly-3,4-ethylenedioxythiophene–tosylate (PEDOT:Tos) can be decreased by exposure to a chemical reducing agent tetrakis(dimethylamino)ethylene (TDAE) [14]. The conductivity diminishes dramatically from 300 S/cm at 36% oxidation level down to  $10^{-4}$  S/cm at 15 % oxidation level (Figure 3.5a). The Seebeck coefficient  $S$  is modified by a factor of 20 upon exposure of the polymer to the TDAE vapor, such that the power factor  $\sigma S^2$  reaches an optimum  $324 \mu\text{W}/\text{m/K}^2$  at the oxidation level of 22%. Another example is illustrated in Figure 3.5b for PEDOT:PSS introduced in an electrochemical transistor. Tuning the gate voltage controls the oxidation level and similarly an optimum is found for the power factor [43]. Note that these are not the highest reported values for PEDOT:PSS, but illustrate optimization through an electrochemical method. Note that the maximum in the power factor does not mean that the maximum thermoelectric efficiency is exactly at that oxidation level. Indeed, thermal conductivity varies with charge carrier concentration as well. In electrically conducting materials, heat is transported both through

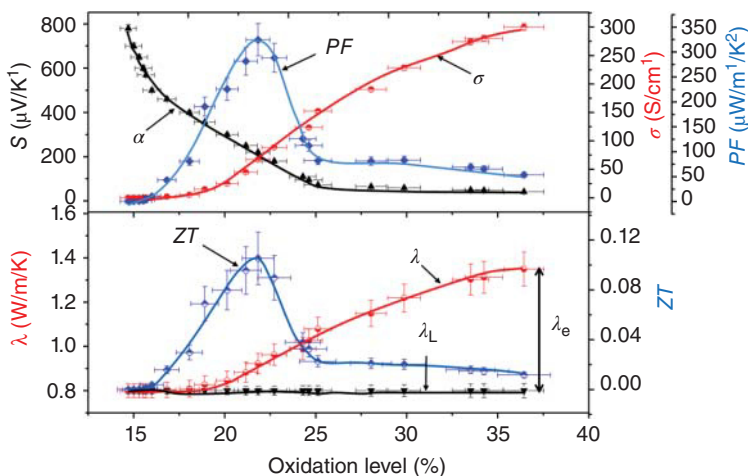


**Figure 3.5** Seebeck coefficient, electrical conductivity, power factor  $\sigma S^2$ , thermal conductivity, and figure of merit ( $ZT$ ) of PEDOT:Tos versus oxidation level at 300 K. (Khan *et al.* 2016 [27]. Reproduced with permission of Wiley.)

phonons (lattice contribution to the thermal conductivity  $\lambda_L$ ) and through electrons (electronic contribution  $\lambda_e$ ) such that

$$\lambda = \lambda_e + \lambda_L \quad (3.5)$$

$$\lambda_e = LT\sigma \quad (3.6)$$

Equation (3.6) is the Wiedemann–Franz’s law, which shows the relationship between the electrical conductivity and the electronic contribution to thermal conductivity.  $L$  is the Lorentz factor equal to  $L_0 = 2.4 \times 10^{-8} \text{ J}^2/\text{K}^2/\text{C}^2$  for a free electron gas. The obtained apparent  $L$  is roughly a factor of 2.5 as large as the Sommerfeld value  $L_0$  for PEDOT:Tos [44]. The value of the apparent  $L$  depends on the nature of the polymers, and is, for example, close to  $L_0$  for PEDOT:PSS [45]. The origin of the observed deviation between the as-obtained apparent  $L$  and the Sommerfeld value is still not clear. Conducting polymers have a non-negligible electronic contribution to the thermal conductivity (similar to metals and doped semiconductors). The bottom graph of Figure 3.5 displays the total thermal conductivity of thin films of PEDOT:Tos versus its oxidation level, assuming that  $L = 2.5L_0$  and that  $L$  is constant with the oxidation level. In the limit of low electrical conductivity, the thermal conductivity for PEDOT:Tos approaches about 0.8  $\text{W}/\text{mK}$ , which represents the lattice contribution  $\lambda_L$  [44]. We now summarize the evolution of the three material parameters ( $\lambda, S, \sigma$ ) versus oxidation level for a conducting polymer and accurately estimate the maximum  $ZT = 0.11$  for PEDOT:Tos for an oxidation level of  $\sim 22\%$  at room temperature [27].

### 3.5 N-Doping of Conjugated Polymers

TEGs are typically composed of many thermocouples connected electrically in series and thermally in parallel. A thermocouple is made of two materials with different temperature-dependent properties so that a temperature gradient

across the device generates an electrical voltage. Owing to the thermal gradient, electrons in the n-type leg of a thermocouple diffuse toward the cold side, while holes diffuse in the p-type leg, also to the cold side. Thus, they generate a voltage at the hot side. Hence, to create efficient organic TEGs, n-type organic conductors must be designed. With the exception of just a few polymers based on benzodifurandione–phenylenevinylene derivatives that show n-type conductivity as high as 14 S/cm [46], solution-processed n-doped conducting polymers typically suffer from a low conductivity ( $\sigma < 10^{-2}$  S/cm) [47]. The low  $\sigma$  translates into low PF and ultimately into a low  $ZT$ . Linear – “torsion-free” – ladder-type conducting polymers, such as the solution-processible n-type polybenzimidazobenzophenanthroline (BBL), can achieve n-type conductivity as high as 2.4 S/cm when doped with strong amino-based reducing agents. These values are three orders of magnitude higher than those measured in *distorted* n-type donor–acceptor polymers, such as the naphthalenediimide–bithiophene-based P(NDI2OD-T2) (Figure 3.6a). An adequate description of polarons in long BBL oligomers (approaching the polymer limit) suggests that the polaron wavefunction in low-band-gap  $\pi$ -conjugated ladder-type polymers has a multi-configurational character. The computed BBL polaron delocalization length is larger than that of P(NDI2OD-T2), suggesting also a high polaron mobility along the chain (Figure 3.6b). In this frame, the high BBL electron conductivity can be already rationalized at the single-chain scale. By carefully modulating the doping levels, the power factor  $\sigma S^2$  of BBL reaches an optimum of 0.43  $\mu\text{W}/\text{m}/\text{K}^2$ , which is one order of magnitude higher than that achieved in P(NDI2OD-T2) (Figure 3.6c,d) [48].

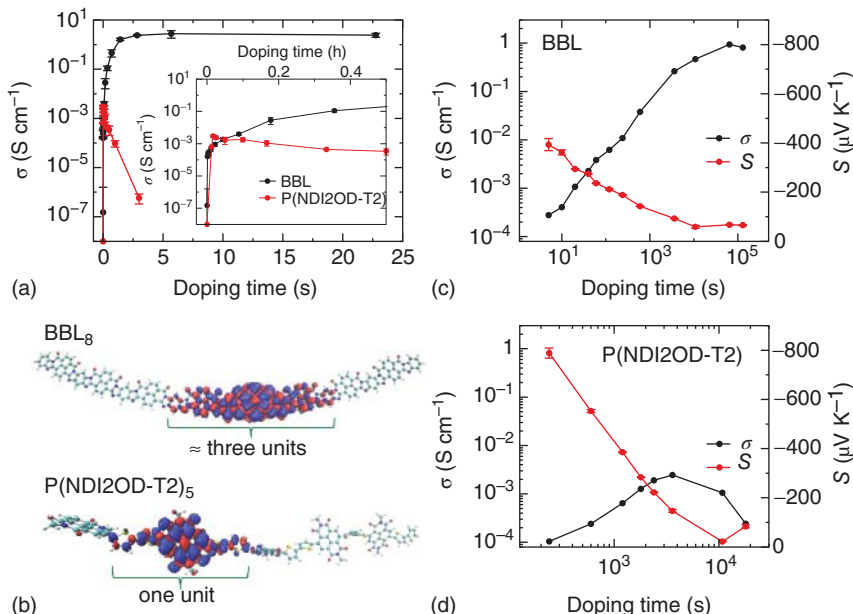


**Figure 3.6** (a) Electrical conductivity of BBL and P(NDI2OD-T2) films as a function of doping time. (b) Computed spin density distributions of the BBL and P(NDI2OD-T2) oligomers. (c, d) Electrical conductivity  $\sigma$  and Seebeck coefficient  $S$  versus doping time for BBL and P(NDI2OD-T2). Adapted from [48].

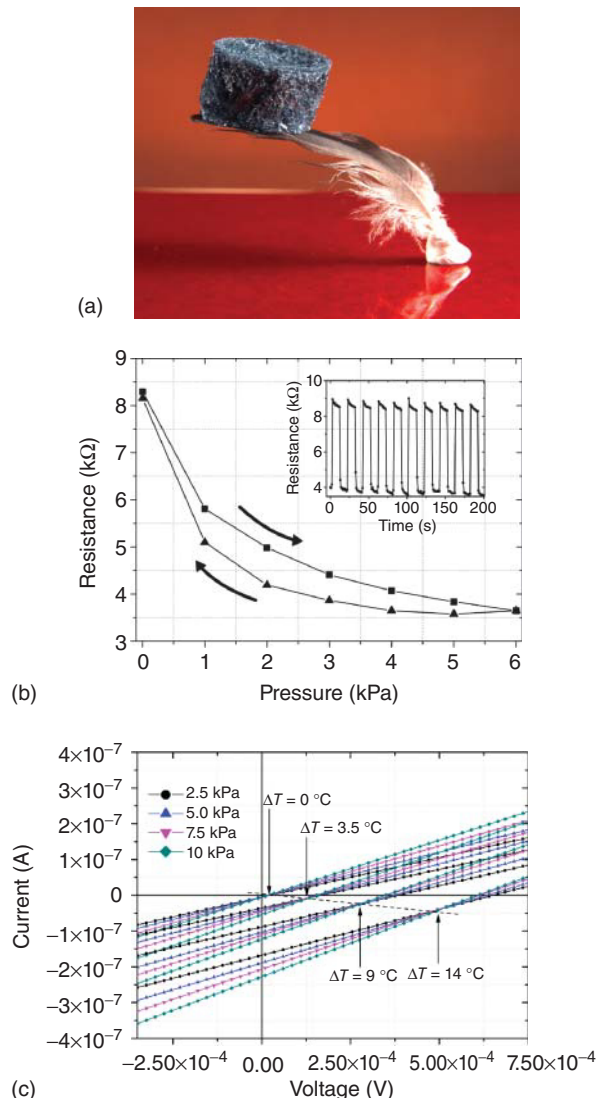
### 3.6 Elastic Thermoelectric Polymers

The combination of elastic and thermoelectric properties seems to be unique for conducting polymers and is likely difficult to achieve with inorganic thermoelectric materials. Very few studies demonstrate the possibility to create all-organic TEGs [49]. These devices can operate at modest temperature gradients and still exhibit power generation sufficient for applications in autonomous microsystems, wireless sensors, or wearable electronics. Hence, we can also foresee the possibility of creating elastic/flexible polymer-based micro-TEGs as power source for e-skin. Recently, yet another type of elastic thermoelectric device has been utilized as sensors for e-skin applications. Carbon aerogels have recently been suggested as material for resistive pressure sensors [50]. Polyurethane elastic porous scaffold coated with PEDOT:PSS resulted in the first dual parameter (pressure and temperature) sensors [51]. This approach combines the concept of thermoelectricity with a porous elastic system. A similar approach and application is demonstrated with polymer composite made of conducting polymer PEDOT:PSS aerogel and silane elastomeric cross-linking agent (Figure 3.7a) [27]. The electrical resistance versus pressure was measured for these aerogels (Figure 3.7b). For a very small pressure of <1 kPa, there was a large drop in the resistance, but for high pressure the resistance was saturated. Hence, this sensor can be used in applications such as measuring heart beats or for measuring the touch of a finger on a keyboard. Note that a hysteresis is observed upon releasing the pressure, but the resistance comes back to its original value. The inset of Figure 3.7b shows how the resistance varies upon several press–release cycles without degradation. Figure 3.7c displays the response of a sensor made of the Cellulose NanoFibrils-PEDOT:PSS aerogel sandwiched between two silver coated glass electrodes. When the aerogel was compressed, its resistance decreased, which is visible as an increase in the slope of the Ohmic current–voltage ( $I$ – $V$ ) linear curves as plotted for 2.5, 5, 7.5, and 10 kPa. When a temperature difference was applied between the electrodes (by approaching a warm object close to one electrode), a thermovoltage equal to  $S\Delta T$  was created, which shifted the  $I$ – $V$  curves ( $\Delta T = 0, 3.5, 9, 14$  °C), as in Figure 3.7c. Hence, such dual-parameter sensors allow decoupling the pressure and temperature readings in a simple way.

### 3.7 Conclusions

Despite exciting advances in material science, it is not yet clear how cheap TEGs must be fabricated to become economically viable. The electricity they generate should payback the investment made to fabricate and operate the device. A simple comparison with solar cells shows us the challenge. TEGs require 50 times more active material than solar cells, while possessing five times lower efficiency. At present, the first organic and carbon-based TEGs provide a power of about 10  $\mu$ W/cm<sup>2</sup>, which is three orders of magnitude lower than the power generated in solar cells. Hopefully, there is plenty of room for improvement for TEGs

**Figure 3.7** (a) Photograph by Eliot Gomez of the PEDOT:PSS-silane aerogel. (Reproduced with kind permission of Eliot Gomez.) (b) Press–release for one cycle in several steps while the inset shows cyclic pressing and releasing. (c)  $I$ – $V$  curves for the aerogel under various levels of pressures and temperature differences. The curves clearly show a change in slope with pressure and voltage shift with increased temperature difference. (Panels (b) and (c): Khan *et al.* 2016 [27]. Reproduced with permission of Wiley.)



through further optimization of materials and device architectures. The scientific and technological challenges of large-area TEGs will not be solved soon. Instead, one can foresee many niche applications for organic and carbon-based TEGs, certainly as power source for sensors and more sophisticated devices in the medical, security, and environmental sectors.

We have summarized how the electrical conductivity, the Seebeck coefficient, and the thermal conductivity of conducting polymers depend on their oxidation level. The optimum thermoelectric figure of merit,  $ZT$ , for the conducting polymers PEDOT:Tos reaches a maximum of  $ZT = 0.1$ . The world record value published is  $ZT = 0.4$  at room temperature. The modest heat-to-electricity conversion of conducting polymers compared to the best inorganic thermoelectric material ( $\text{Bi}_2\text{Te}_3$  with  $ZT = 1$ ) is only because of their low Seebeck coefficient (since the ratio of electronic to thermal conductivity is identical). Therefore, the main challenge for conducting polymer TEGs is to increase the Seebeck coefficient. In that prospect, we have pinpointed the importance of the morphology to increase the mobility, and at the same time, tune the density of state and enhance the Seebeck coefficient. Although n-type polymer thermoelectrics are still less efficient than p-type, there emerge some design rules at the molecular scale to enhance the doping level while keeping good electron conductivity.

Organic thermoelectrics is still a young field of research with exciting promises because those materials are solution processible at low temperatures, which is a prerequisite to use low-cost techniques such as printing in order to fabricate large-area thermoelectric devices. Also, polymers have unique properties compared to inorganic materials: they are light weight and flexible and can even be elastics. This again opens up new fields of research and potential applications for energy harvesting from the body with flexible TEGs, or dual temperature/pressure sensors for electronic skin.

## Acknowledgments

The authors acknowledge the European Research Council (ERC-starting-Grant 307596), the Swedish Foundation for Strategic Research, the Knut and Alice Wallenberg foundation, The Swedish Energy Agency, and the Advanced Functional Materials Center at Linköping University.

## References

- 1 Heremans, J.P. *et al.* (2002) Thermoelectric power of bismuth nanocomposites. *Phys. Rev. Lett.*, **88** (21), 216801.
- 2 Goupil, C. *et al.* (2011) Thermodynamics of thermoelectric phenomena and applications. *Entropy*, **13** (8), 1481.
- 3 Heikes, R.R. and Ure, R.W. (1961) *Thermoelectricity: Science and Engineering*, Interscience Publishers, New York.
- 4 Snyder, G.J. and Toberer, E.S. (2008) Complex thermoelectric materials. *Nat. Mater.*, **7** (2), 10.

- 5 Heeger, A.J. (2001) Semiconducting and metallic polymers: the fourth generation of polymeric materials. *J. Phys. Chem. B.*, **105** (36), 8475–8491.
- 6 Shirakawa, H. (2001) The discovery of polyacetylene film: the dawning of an era of conducting polymers (Nobel lecture). *Angew. Chem. Int. Ed.*, **40** (14), 2574–2580.
- 7 MacDiarmid, A.G. (2001) “Synthetic Metals”: a novel role for organic polymers (Nobel lecture). *Angew. Chem. Int. Ed.*, **40** (14), 2581–2590.
- 8 Groenendaal, L. *et al.* (2000) Poly(3,4-ethylenedioxothiophene) and its derivatives: past, present, and future. *Adv. Mater.*, **12** (7), 481–494.
- 9 Lee, K. *et al.* (2006) Metallic transport in polyaniline. *Nature*, **441** (7089), 65–68.
- 10 Crispin, X. *et al.* (2006) The origin of the high conductivity of poly (3,4-ethylenedioxothiophene)-poly (styrenesulfonate)(PEDOT-PSS) plastic electrodes. *Chem. Mater.*, **18** (18), 4354–4360.
- 11 Cao, Y., Qiu, J. and Smith, P. (1995) Effect of solvents and co-solvents on the processibility of polyaniline: I. solubility and conductivity studies. *Synth. Met.*, **69** (1–3), 187–190.
- 12 Yim, W. and Rosi, F. (1972) Compound tellurides and their alloys for peltier cooling—a review. *Solid-State Electron.*, **15** (10), 1121–1140.
- 13 Hiroshige, Y., Ookawa, M. and Toshima, N. (2007) Thermoelectric figure-of-merit of iodine-doped copolymer of phenylenevinylene with dialkoxyphenylenevinylene. *Synth. Met.*, **157** (10–12), 467–474.
- 14 See, K.C. *et al.* (2010) Water-processable polymer-nanocrystal hybrids for thermoelectrics. *Nano Lett.*, **10** (11), 4664–4667.
- 15 Bubnova, O. *et al.* (2011) Optimization of the thermoelectric figure of merit in the conducting polymer poly(3,4-ethylenedioxothiophene). *Nat. Mater.*, **10** (6), 429–433.
- 16 Sun, Y.M. *et al.* (2012) Organic Thermoelectric Materials and Devices Based on p- and n-Type Poly(metal 1,1,2,2-ethenetetrathiolate)s. *Adv. Mater.*, **24** (7), 6.
- 17 Kim, G.H. *et al.* (2013) Engineered doping of organic semiconductors for enhanced thermoelectric efficiency. *Nat. Mater.*, **12** (8), 719–723.
- 18 Nonoguchi, Y. *et al.* (2013) Systematic conversion of single walled carbon nanotubes into n-type thermoelectric materials by molecular dopants. *Sci. Rep.*, **3**, 3344.
- 19 Lee, S.H. *et al.* (2014) Transparent and flexible organic semiconductor nanofilms with enhanced thermoelectric efficiency. *J. Mater. Chem. A*, **2** (20), 7288–7294.
- 20 Fukumaru, T., Fujigaya, T. and Nakashima, N. (2015) Development of n-type cobaltocene-encapsulated carbon nanotubes with remarkable thermoelectric property. *Sci. Rep.*, **5**, 7951.
- 21 Wang, H. *et al.* (2015) Thermally driven large n-type voltage responses from hybrids of carbon nanotubes and poly(3,4-ethylenedioxothiophene) with tetrakis(dimethylamino)ethylene. *Adv. Mater.*, **27** (43), 6855–6861.
- 22 Avery, A.D. *et al.* (2016) Tailored semiconducting carbon nanotube networks with enhanced thermoelectric properties. *Nature Energy*, **1** (4), 16033.

- 23 Crispin, X. (2016) Thermoelectrics: carbon nanotubes get high. *Nature Energy*, **1**, 16037.
- 24 Nish, A. *et al.* (2007) Highly selective dispersion of single-walled carbon nanotubes using aromatic polymers. *Nat. Nanotechnol.*, **2** (10), 640–646.
- 25 Cutler, M. and Mott, N.F. (1969) Observation of Anderson Localization in an Electron Gas. *Phys. Rev.*, **181** (3), 1336–1340.
- 26 Zykwinska, A. *et al.* (2003) In situ EPR spectroelectrochemical studies of paramagnetic centres in poly(3,4-ethylenedioxythiophene) (PEDOT) and poly(3,4-butylenedioxythiophene) (PBuDOT) films. *Chem. Phys.*, **292** (1), 31–45.
- 27 Khan, Z.U. *et al.* (2016) Thermoelectric polymers and their elastic aerogels. *Adv. Mater.*, **28** (22), 4556–4562.
- 28 Poudel, B. *et al.* (2008) High-thermoelectric performance of nanostructured bismuth antimony telluride bulk alloys. *Science*, **320** (5876), 5.
- 29 Cornil, J., Beljonne, D. and Brédas, J.-L. (1995) Nature of optical transitions in conjugated oligomers. I. Theoretical characterization of neutral and doped oligo(phenylenevinylene)s. *J. Chem. Phys.*, **103** (2), 834–841.
- 30 Brédas, J., Wudl, F. and Heeger, A. (1987) Polarons and bipolarons in doped polythiophene: a theoretical investigation. *Solid State Commun.*, **63** (7), 577–580.
- 31 Stafström, S. and Brédas, J. (1988) Evolution of the electronic structure of polyacetylene and polythiophene as a function of doping level and lattice conformation. *Phys. Rev. B*, **38** (6), 4180.
- 32 Prigodin, V.N. and Efetov, K.B. (1993) Localization transition in a random network of metallic wires: a model for highly conducting polymers. *Phys. Rev. Lett.*, **70** (19), 2932–2935.
- 33 Lavarda, F.C. *et al.* (1994) Insulator-to-metal transition in polythiophene. *Phys. Rev. B*, **49** (2), 979–983.
- 34 Sariciftci, N., Heeger, A. and Cao, Y. (1994) Paramagnetic susceptibility of highly conducting polyaniline: disordered metal with weak electron–electron interactions (Fermi glass). *Phys. Rev. B*, **49** (9), 5988.
- 35 Heeger, A.J. (2001) Semiconducting and metallic polymers: the fourth generation of polymeric materials (Nobel lecture). *Angew. Chem. Int. Ed.*, **40** (14), 2591–2611.
- 36 Koller, G. *et al.* (2007) Intra- and intermolecular band dispersion in an organic crystal. *Science*, **317** (5836), 351–355.
- 37 Beljonne, D. *et al.* (2001) Optical signature of delocalized polarons in conjugated polymers. *Adv. Funct. Mater.*, **11** (3), 229–234.
- 38 Zotti, G. *et al.* (2003) Electrochemical and XPS studies toward the role of monomeric and polymeric sulfonate counterions in the synthesis, composition, and properties of poly(3,4-ethylenedioxythiophene). *Macromolecules*, **36** (9), 3337–3344.
- 39 Bubnova, O. *et al.* (2014) Semi-metallic polymers. *Nat. Mater.*, **13** (2), 190–194.
- 40 Petsagourakis, I. *et al.* (2017) Correlating the Seebeck coefficient of thermoelectric polymer thin films to their charge transport mechanism. Submitted.

- 41 Kaiser, A.B. and Skakalova, V. (2011) Electronic conduction in polymers, carbon nanotubes and graphene. *Chem. Soc. Rev.*, **40** (7), 3786–3801.
- 42 Crispin, X. *et al.* (2004) Electronic delocalization in discotic liquid crystals: a joint experimental and theoretical study. *J. Am. Chem. Soc.*, **126** (38), 11889–11899.
- 43 Bubnova, O., Berggren, M. and Crispin, X. (2012) Tuning the thermoelectric properties of conducting polymers in an electrochemical transistor. *J. Am. Chem. Soc.*, **134** (40), 16456–16459.
- 44 Weathers, A. *et al.* (2015) Significant electronic thermal transport in the conducting polymer poly(3,4-ethylenedioxythiophene). *Adv. Mater.*, **27** (12), 2101–2106.
- 45 Liu, J. *et al.* (2015) Thermal conductivity and elastic constants of PEDOT: PSS with high electrical conductivity. *Macromolecules*, **48** (3), 585–591.
- 46 Shi, K. *et al.* (2015) Toward high performance n-type thermoelectric materials by rational modification of BDPPV backbones. *J. Am. Chem. Soc.*, **137** (22), 6979–6982.
- 47 Schlitz, R.A. *et al.* (2014) Solubility-limited extrinsic n-type doping of a high electron mobility polymer for thermoelectric applications. *Adv. Mater.*, **26** (18), 2825–2830.
- 48 Wang, S. *et al.* (2016) Thermoelectric properties of solution-processed n-doped ladder-type conducting polymers. *Adv. Mater.*, **28** (48), 10764–10771.
- 49 Bubnova, O. and Crispin, X. (2012) Towards polymer-based organic thermoelectric generators. *Energ. Environ. Sci.*, **5** (11), 9345.
- 50 Yin, X., Vinod, T. and Jelinek, R. (2015) A flexible high-sensitivity piezoresistive sensor comprising a Au nanoribbon-coated polymer sponge. *J. Mater. Chem. C*, **3** (35), 9247–9252.
- 51 Zhang, F. *et al.* (2015) Flexible and self-powered temperature-pressure dual-parameter sensors using microstructure-frame-supported organic thermoelectric materials. *Nat. Commun.*, **6**, 8356.

## 4

# Silicon for Thermoelectric Energy Harvesting Applications

Dario Narducci<sup>1</sup>, Luca Belsito<sup>2</sup>, and Alex Morata<sup>3</sup>

<sup>1</sup>University of Milano Bicocca, Department of Materials Science, via R. Cozzi 55, 20125, Milan, Italy

<sup>2</sup>CNR, Institute for Microelectronics and Microsystems, via P. Gobetti 101, 40129, Bologna, Italy

<sup>3</sup>Catalonia Institute for Energy Research (IREC), Department of Advanced Materials for Energy Applications, Jardins de les Dones de Negre 1, E-08930 Sant Adrià de Besòs, Barcelona, Spain

## 4.1 Introduction

### 4.1.1 Silicon as a Thermoelectric Material

Last two decades have seen a remarkable return of interest toward thermoelectricity as a tool to recover and partially convert into electricity low-temperature waste heat. Specifically, microharvesting, namely thermal harvesting aimed at the local generation of high added-value, small electric powers, has raised a wide interest, also in connection with the development and deployment of distributed, intercommunicating wireless sensor networks. Nanotechnology has actually had a fantastic impact onto the conversion rate that can be achieved by thermoelectric generators (TEGs) [1], with thermoelectric figure of merit grown up by almost a factor three over less than 15 years. Such a tremendous result was due both to novel classes of thermoelectric materials but also to old materials that rejuvenated by nanostructuring. Nanowires and nanolayers, along with multi-layered structures, have actually improved the thermoelectric characteristics of many age-old materials [2–4] by either enabling the reduction of their thermal conductivity  $\kappa$  or by increasing their power factor (PF)  $\sigma S^2$  (where  $\sigma$  is the electrical conductivity and  $S$  is the Seebeck coefficient). Both approaches clearly lead to an increase of the thermoelectric figure of merit  $ZT = \sigma S^2 T / \kappa$  (where  $T$  is the absolute temperature), although their impact on device power output is not equivalent [5].

As thermoelectric performances have remarkably enhanced, bringing TEGs at the wedge of bulk production, attention has extended to selecting materials and technologies that could be effectively and economically scaled up. As a consequence, geo-abundance and low material costs have added up as major technological constraints to the development of thermoelectric materials and devices. Thus, the revamped interest toward silicon, silicon–germanium alloys, and silicides has come to no surprise, as the surge of scientific publications on this specific subject over the last five years has shown up.

In the history of nanostructured thermoelectric silicon a milestone was surely set at 2008, when *Nature* published back-to-back two seminal papers by Hochbaum *et al.* [6] and by Boukai *et al.* [7] on silicon nanowires (SiNWs). In both papers, the authors independently demonstrated that phonon scattering at the outer roughened walls of SiNWs causes the thermal conductance of single-crystalline silicon (scSi) to drop by almost a factor 100, with only a marginal impact onto scSi electrical conductivity. Since then the nanowire paradigm has been extended to a host of other materials, 1D nanostructures becoming a reference for thermoelectricity [8, 9]. At the same time a remarkable effort has been placed on devising novel approaches to manufacturing nanowires, especially for silicon, where microelectronic technology sets a natural standard to fulfill so as to enable easy upscale [10–12]. Also nanolayers have shown significant potentials for the reduction of silicon thermal conductivity. Exactly as in SiNWs, dimensional constraints by themselves are not sufficient to significantly reduce thermal conductivity in 2D, and an accurate control over surface roughness is required [13, 14].

Top-down approach is not unique, however. Nanocrystallinity and second-phase formation also provide an interesting toolbox to improve Si thermoelectric properties, with the additional advantage of lower production costs and of larger input heat currents. Use of  $\text{SiO}_x$  precipitates [15] and of nanovoids [16] has been explored. The aim is that of selectively reducing  $\kappa$  over  $\sigma$ .

Although most of the research till recent times has focused on strategies to decrease  $\kappa$ , dimensionally constrained nanostructures may also increase silicon PF. The effect of nanosizing on the PF has been explored both theoretically and experimentally by several authors [17, 18]. Although results are less final, they clearly show an alternate, possibly complementary way to increase Si thermoelectric efficiency.

In this chapter, all approaches will be critically reviewed. Special emphasis will be placed on the interplay between preparation methodology and thermoelectric performances, as the former rules critical characteristics of the nanostructure that are nowadays clearly known to be in control of the transport properties of the material. In the second part of the chapter usability and applications of Si nanostructures will be discussed, also providing an outlook to frontiers in research and development of dimensionally constrained silicon for thermoelectricity.

#### 4.1.2 Current Uses of Silicon in TEGs

The use of silicon as a thermoelectric material in TEGs has been already proposed in the early 2000, both in bulk and thin film form [19–28]. Despite the very low thermoelectric figure of merit of bulk silicon and silicon films, both in polysilicon and single-crystal silicon form, silicon-based TEG devices have been developed to fully exploit the potential of highly advanced silicon micromachining technology. Such advantage was particularly relevant in creating microTEGs for specific applications. In some cases, micromachining capabilities could even allow to integrate the TEG within an electronic application specific integrated circuit (ASIC), as proposed in [26], in which a complementary metal–oxide semiconductor (CMOS)-compatible TEG was used as an on-chip power supply

for a CMOS circuit. This is possible for the perfect compatibility of silicon as a thermoelectric material with microelectronic technology, which is not true for other thermoelectric materials like tellurides. In such micromachined TEGs, a planar structure is generally adopted, using essentially the same technology usually employed for thermoelectric sensors (thermopiles), where use is made of horizontal thermocouples fabricated over suspended thin dielectric membranes and therefore thermally isolated from the underlying silicon substrate. Such arrangement and the need to use thin films for processing requirements made these devices not optimized for thermoelectric conversion, compared to other structures based on bulk thermoelectric materials. Moreover, microTEGs often employed standard CMOS polysilicon films as thermoelectric material. This was mainly motivated by compatibility with assessed CMOS fabrication processes, although this choice was clearly not ideal for the performances of the thermoelectric conversion. In addition, in some cases only one doping type was available and plain n-type polysilicon/metal thermocouples were the only option for the device.

In order to overcome such limitations, some attempts to adapt silicon technology to a vertical thermocouple arrangement of bulk thermocouples have been proposed. In [19], for instance, a TEG based on vertically arranged single-crystal silicon thermoelements of alternate n and p-type doping was presented, in which the silicon thermocouples were obtained by high aspect ratio deep reactive ion etching of massive silicon wafers with an original technique. The fabrication process presented there ended up with the fabrication of bulk single-crystal silicon thermocouples that could be used to implement self-standing vertical arrays of thermoelements for power generation. In this way, the final device could have size comparable to those built with bulk thermoelectric materials, since a whole silicon wafer was etched through to make the silicon thermoelements of the TEG. However, due to the intrinsic limitations of silicon as a thermoelectric material when used in bulk or thin film form, all the micromachined TEGs based on silicon presented in the literature generally provided a generated power below  $1 \mu\text{W}$  for the typical temperature differences applied, independently of the technology adopted.

## 4.2 Bulk and Thin-Film Silicon

### 4.2.1 Single-Crystalline and Polycrystalline Silicon

It is well known that scSi is a relatively poor material for thermoelectric applications. Actually, in spite of its large PF, its  $ZT$  around room temperature falls below 0.01 due to its quite large thermal conductivity. Figure 4.1 displays the Seebeck coefficient versus temperature of p-type and n-type scSi as measured in the 1950s by Geballe and Hull [29] and more recently re-measured by Stranz *et al.* [30, 31]. It was actually shown [32] that the largest PFs are achieved at carrier densities close or beyond the degeneration threshold ( $\approx 10^{19}/\text{cm}^3$ ), where the PF may reach values larger than  $0.5 \text{ mW/m/K}^2$ . It is then very unfortunate that scSi lattice thermal conductivity displays in the same temperature region

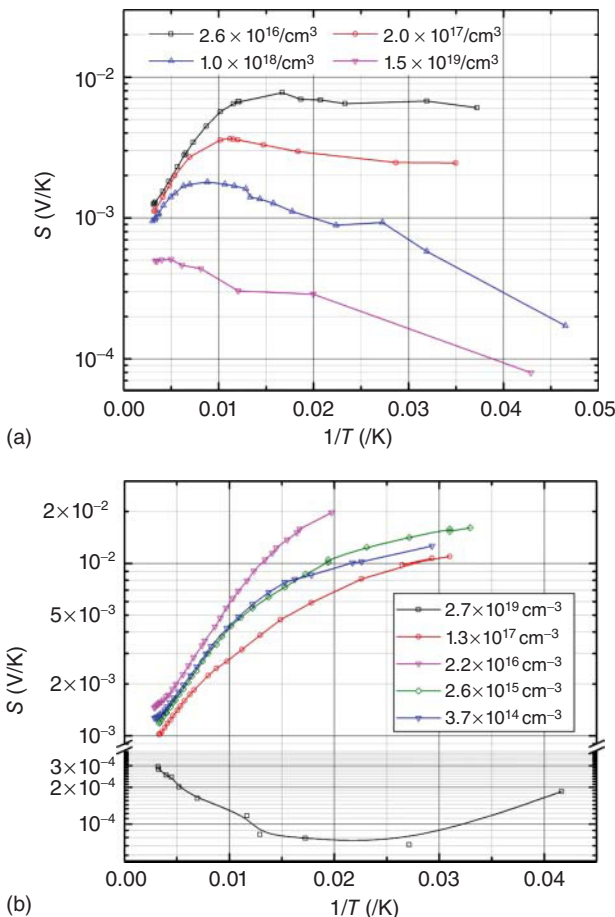
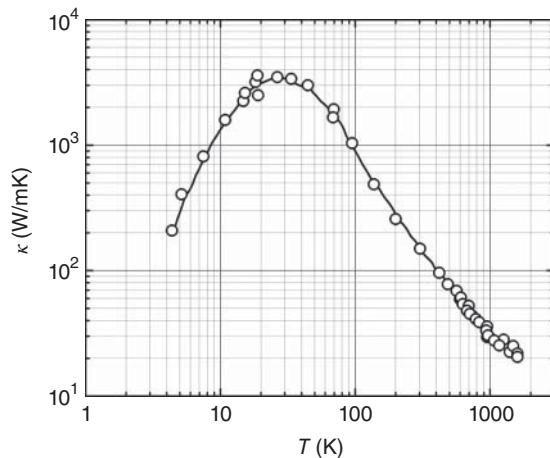


**Figure 4.1** Seebeck coefficients of (a) p-type and (b) n-type single-crystalline silicon at various doping levels. (Geballe and Hull 1955 [29]. Reproduced with permission of American Physical Society.)

very large values (Figure 4.2) therefore severely limiting its overall efficiency as a thermoelectric material.

A rather common way, quite largely explored in the past, to reduce Si  $\kappa$  was that of introducing both point and extended defects capable of scattering acoustic phonons. While lattice imperfections were also bound to lower the carrier mobility, it was found that polycrystallinity succeeded in decreasing  $\kappa$  more than  $\sigma$ , so to improve the material figure of merit that were reported to achieve values of 0.023 at 300 K in 42-nm grained polycrystalline silicon films [34]. Clearly enough, such values cannot compete in terms of overall efficiency with standard thermoelectric materials such as  $\text{Bi}_2\text{Te}_3$ . Nonetheless, silicon has maintained a non-marginal niche of application in microelectronics, where the advantages related to its immediate integrability has paved the way to its exploitation as the reference material for the first generation of thermal microharvesters.

**Figure 4.2** Thermal conductivity of single-crystalline silicon.  
 (Glassbrenner and Slack 1964 [33]. Reproduced with permission of American Physical Society.)



However, the unique capabilities of microfabrication enabled by the use of silicon in TEGs do not end up with their integrability with signal/power conditioning electronics. Especially when microharvesters are needed, Si micromachining and the large toolbox deployable to define Si structures on the micron and submicron scale discloses rather unique possibilities to compensate low conversion efficiencies with a wise temperature profiling and an effective thermal management.

In spite of its limited performances, still silicon has found applications in integrated microharvesters where its integrability has prevailed over its fair efficiency [27]. At the same time, strategies were explored to decrease its thermal conductivity without reducing the electrical conductivity. Among them, the use of SiGe alloys was found to be successful, improving thermoelectric efficiency up to  $\approx 7\%$  [35]. Germanium alloying favorably impacts on  $ZT$  by reducing the thermal conductivity while preserving  $\sigma$ .

Over more recent years the improved understanding of phonon dynamics, mostly coming from the analysis of heat conduction in nanostructures, has helped refine strategies to decrease Si thermal conductivity with marginal impact onto charge carrier mobility. *Defect engineering* has actually proved to enable truly low  $\kappa$  to be reachable by the use of selective scattering centers. Among the strategies to improve the thermoelectric properties of a material, a very promising and challenging one has been that of selecting structural defects capable of scattering phonons without reducing electron mobility. While this approach is actually bound to fail in standard materials, it has proven very effective at the nanoscale. The basic idea has been that of profiting of the different wavelengths  $\lambda$  of conduction electrons and of acoustic phonons. Centers with characteristic size intermediate between the wavelengths of electrons and phonons might incoherently scatter phonons (then reducing their lifetime) while reflecting electrons, thus preserving their mean free path (MFP). Typical sizes of selective scattering objects in silicon are expected to be in the range 10–100 nm, that is, the standard size of nanoprecipitates (NPs) and of grains in nanocrystalline materials [36]. Proper size is however only one ingredient of

the recipe. Two other factors actually rule the selectivity of scattering objects. On one side, the potential landscape experienced by electrons upon scattering must be conveniently shaped so that carriers may either tunnel through them or, less commonly, thermally overcome them (by thermionic emission). It may be shown that in nanocomposites barrier heights and widths are correlated to the Fermi energies of the two phases, while they depend upon the grain size and on the density of surface states at nanograin boundaries in single-phase nanocrystalline solids [37]. On the other side, a multi-scaled size distribution of nano-objects is desirable. Actually, the spectral thermal conductivity  $\kappa'(\omega)$  displays large contributions over a wide range of phonon frequencies. As an example, it has been quite recently demonstrated that heat transport above room temperature significantly involves phonon modes of very long wavelengths (of some micrometers and more) [38]. As a result, effective reduction of  $\kappa$  requires silencing phonons modes extending over an extended range of wavelengths. No single defect, no matter how engineered, may be effective enough. This implies the need of introducing collections of (multi-scaled) scattering centers aimed at hindering phonon diffusion over length scales from 10 nm to 10  $\mu\text{m}$  [39].

#### 4.2.2 Degenerate and Phase-Segregated Silicon

Non-dimensionally constrained silicon is not however bound to low  $ZT$  values, as long as silicon acts as an embedding matrix for nanocomposites. The effect of precipitates in silicon was recently reviewed by Narducci *et al.* [40]. Manifestly enough, the simple introduction of grain boundaries (GBs) may be expected to lead to a degradation of both the thermal and electrical conductivities, with little or no advantage as of the thermoelectric efficiency. This was widely confirmed in non-degenerate polycrystalline silicon, namely for doping levels up to  $10^{18}/\text{cm}^3$  [41]. However, already in 1988 Vining had shown that the thermoelectric properties of heavily boron-doped nanocrystalline silicon (ncSi) may display an unprecedented improvement of  $ZT$  upon precipitation of  $\text{SiB}_3$  [42], leading to an unexpected increase of hole mobility [32]. The electrical conductivity and the Seebeck coefficient measured in ncSi pellets obtained by hot-pressing at 1250 °C display anomalies, with the thermopower increasing with the boron concentration between 1.0% at. and 20% at. Vining speculated that a second phase with larger Seebeck coefficient could be held responsible for the enhanced  $S$ , although this was conflicting with the carrier density getting to a maximum for a boron density of 10% at. (Figure 4.3). Also, anomalously high hole mobility was measured, ranging around  $35 \text{ cm}^2/\text{V}\cdot\text{s}$  at 300 K. In principle high mobility is consistent with potential barriers at GB that, because of the high doping levels, may be tunneled through [43].

Concurrent increase of the electrical conductivity and of the Seebeck coefficient in highly boron-doped ncSi was discussed by Narducci *et al.* [44, 45]. In silicon thin films doped with a boron concentration of 0.9% mol. and with columnar nanograins with an in-plane size of  $\approx 50$  nm annealing up to 1000 °C resulted in the doubling of the electrical conductivity while the Seebeck coefficient was also unexpectedly found to increase from 0.10 to 0.45 mV/K. A PF of

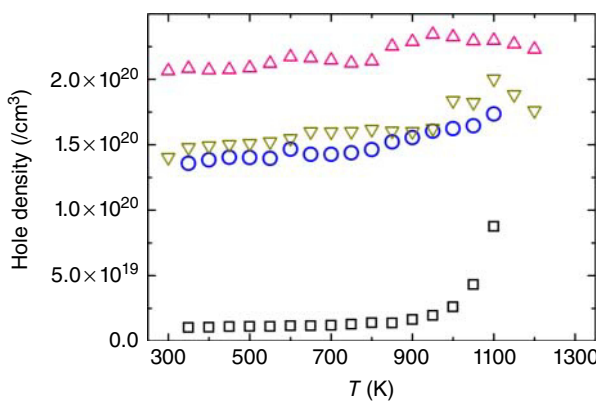


**Figure 4.3** Anomalous trends of the carrier density in heavily doped hot-pressed ncSi samples. Note the larger hole density at 10% at. nominal concentration. (Data from Vining 1991 [32].)

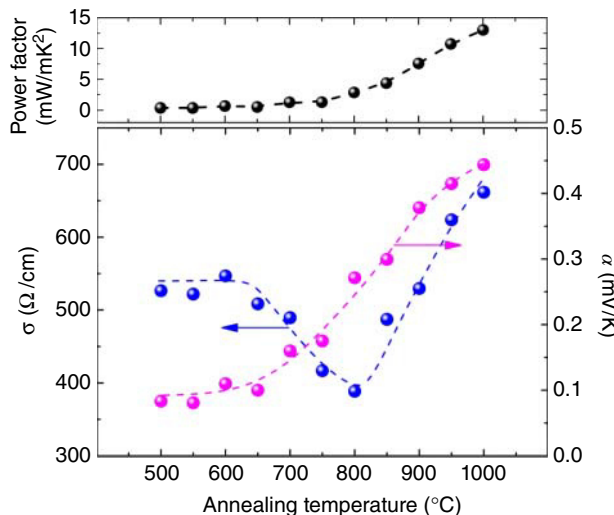


**Figure 4.4** Seebeck coefficient, electrical conductivity, and power factor at 300 K of heavily boron-doped nanocrystalline silicon thin films upon annealing. (Narducci *et al.* 2015b [40]. Reproduced with permission of Royal Society of Chemistry.)

13 mW/K<sup>2</sup>/m was attained, with hole mobility at 300 K of 79 cm<sup>2</sup>/V/s [44, 46] (Figure 4.4). PFs were then more than 6 times larger than those observed in comparably doped single-crystal silicon, and almost 25 times larger than in nanostructured silicon [47]. Further increase of the PF and of the hole mobility was observed for larger nominal boron concentrations [48]. The dependence of the carrier density upon the annealing temperature could be correlated to the precipitation of boron-enriched Si–B second phases at ncSi GBs [48, 49].

In a study on nanosilicon pellets obtained by spark plasma sintering (SPS) Schierning and coworkers [34] reported transmission electron microscopy

(TEM) evidence that sintering had led to the precipitation of an amorphous phase. Interestingly, annealing of n-type samples led to an initial decrease of the electrical conductivity, with a minimum at 700 °C, followed by a recovery for higher annealing temperatures. PFs reached  $\approx 4.5$  mW/K<sup>2</sup>/m at 1000 °C while electron Hall mobility at room temperature was found to account to 61 cm<sup>2</sup>/V/s. Further claims of high PFs ( $\approx 4.4$  mW/K<sup>2</sup>/m at 800 °C) were reported by Kurosaki and collaborators [50]. Nanometric precipitates of a SiP<sub>x</sub> second phases were observed in heavily phosphorus-doped Si pellets obtained by SPS. Structural (semi)coherence with the embedding microcrystalline silicon matrix led to a reduction of the thermal conductivity but also to an increase of the PF, both concurring to relatively large *ZT* values.

An analysis of the physics behind the anomalous increase of the PF is beyond the goals of this chapter. Suffice here to say that a simple picture where potential barriers at GBs may be invoked as responsible for an increase of the PF is not consistent with the complex experimental set of data available even only for ncSi. Also from a theoretical point of view it was shown that GBs alone cannot justify an enhancement of the PF [51]. A more sophisticated conceptual framework must be developed, instead. Actually, GBs and precipitates may filter low-energy (cold) carriers, thus decreasing the density of non-localized electrons (holes) that sets the Seebeck coefficient in n-type (p-type) silicon. However, electron (hole) mobility also depends on their lifetime or, equivalently, on their MFP. Actually, high-energy (hot) carriers are scattered by electron-electron and electron-phonon interactions more efficiently than low-energy carriers, so that their spectral mobility  $\mu(E)$  is not necessarily larger. Furthermore, a mechanism must be available to thermalize the carriers, which is not unescapably the case when carriers travel ballistically instead than diffusively through the medium. Overall, the coexistence of more processes must be considered, as reported in recent studies [40, 52, 53]. Conversely, it might be noteworthy to mention that an increase of the PF and of *ZT* in nanocomposite does not contrast with the so-called Bergman–Lévy limit [54, 55]. In a series of papers, Bergman and Lévy rigorously demonstrated that in a binary composite the figure of merit may never exceed that of the component with the largest *ZT*. Actually, while no limitation applies to the PF [56], even for *ZT* the Bergman–Lévy limit could be proved only neglecting all interface contributions. Thus, limits hold true only when dealing with strictly mechanical mixtures of two phases. Such a picture may be adequate for macroscopic composites (mixtures) but it is clearly not appropriate with nanocomposites. Specifically, in ncSi embedding nanometric second phases the role of interfaces (and of the associated potential barriers) is essential, so one has not to invoke a second phase with large *ZT* to explain unexpectedly large figures of merit.

As a general conclusion, while dimensional constrains, which will be analyzed in the forthcoming sections, have paved an effective and validated way to use silicon in thermoelectrics, research on bulk silicon as a thermoelectric material still retains a substantial interest. Single-crystalline silicon has found uses in TEGs mostly due to its immediate integrability. However it would be of little surprise that the intrinsically modest thermoelectric efficiencies of silicon and of related bottom-up nanocomposites could be enhanced by clever

physico-chemical manipulations, profiting of the profound knowledge of silicon chemistry developed in microelectronic manufacturing.

## 4.3 Nanostructured Silicon: Physics of Nanowires and Nanolayers

### 4.3.1 Introduction

Thermoelectric performance of a material depends mainly on three intrinsic parameters, that is, Seebeck coefficient, electrical conductivity, and thermal conductivity. As mentioned, these parameters are included in the figure of merit  $ZT$  that is directly related with the maximum conversion efficiency that can be achieved. In bulk materials  $S$ ,  $\sigma$ , and  $\kappa_e$  are linked, and thus they cannot be tailored independently. In this section, we will analyze the effects that nanostructuring can produce on the properties of silicon based materials. Two strategies can be adopted to increase the figure of merit. A first approach is to maximize the PF. Although some possibilities are presented in theory and despite the intensive research in the last decades, it was already noted how only few significant  $ZT$  improvements have been reported so far due to enhancements of the PF resulting from the formation of nanostructures. However, the definition of the influence of low dimensionality in the charge transport is important as it provides tools for the optimization of the thermoelectric devices and its matching to the most suitable working temperature. In contrast, big improvements have been obtained thanks to a drop of thermal conductivity in nanoscaled systems. In this second strategy, a reduction of the dimensions or the introduction of nanometric defects can lead to an important phonon scattering that causes a decrease of the thermal conductivity without any major detriment of the electrical conductivity.

### 4.3.2 Electrical Transport in Nanostructured Thermoelectric Materials

Among the quantities defining the PF, those involving electronic diffusion can be derived from the Boltzmann transport equation (BTE), which describes the evolution of particle distribution  $f$  in a system under a perturbation (in this case electric field and temperature):

$$\left( \frac{df}{dt} \right)_{\text{SC}} = \frac{df}{dt} + \frac{dk}{dt} \nabla_k f + \frac{dr}{dt} \nabla_r f \quad (4.1)$$

where  $k$  is the particle momentum and the subscript SC labels the scattering-equilibrated distribution. In order to solve Eq. (4.1) we assume that electrons equilibrate due to the effect of random scattering. Thus, we introduce a relaxation time ( $\tau$ ) defined as  $df/dt = (f - f_0)/\tau$  (where  $f_0$  is the equilibrium distribution).

A detailed analysis of the equation is out of the scope of this chapter and can be found elsewhere [57–59]. Provided that electron distribution at equilibrium follows Fermi Dirac statistics and using suitable approximations one obtains that

$$\sigma \equiv \left. \frac{J}{\varepsilon} \right|_{\frac{dT}{dx}=0} = q^2 X_0 \quad (4.2)$$

$$\kappa_e \equiv -\left. \frac{Q}{\frac{dT}{dx}} \right|_{J=0} = \frac{1}{T} \left[ X_2 - \frac{X_1^2}{X_0} \right] \quad (4.3)$$

$$S \equiv \left. \frac{\varepsilon}{\frac{dT}{dx}} \right|_{J=0} = \mp \frac{1}{qT} \left[ \frac{X_1}{X_0} - E_F \right] \quad (4.4)$$

where  $J$  is the current density,  $\varepsilon$  is the electric field,  $Q$  is the heat current,  $q$  is the carrier charge,  $E_F$  is the Fermi energy, and

$$X_i \equiv - \int_{E_0}^{\infty} g(E) \tau(E) v^2(E) E^i (df_0/dE) dE \quad (4.5)$$

(where  $g(E)$  is the density of states). Thus, all quantities depend on the fundamental properties of the material, namely on its band structure (Density of States – DOS). For materials where bands can be approximated with a parabolic function close to the Fermi level, the density and the carrier effective mass set the material electronic behavior. The energy dispersion function at the Brillouin zone center can be written as

$$E_{3D}(k) = \frac{\hbar^2}{2} \left( \frac{k_x^2}{m_x} + \frac{k_y^2}{m_y} + \frac{k_z^2}{m_z} \right) \quad (4.6)$$

where  $\hbar$  is the reduced Planck constant and  $m_i$  is the principal components of the effective mass tensor. For 2D (nanolayers) and 1D (nanowires) systems

$$E_{2D}(k) = \frac{\hbar^2}{2} \left( \frac{k_x^2}{m_x} + \frac{k_y^2}{m_y} \right) + E_n, \quad E_n = \frac{\hbar^2 \pi^2 n^2}{2a^2 m_z}, \quad n = 1, 2, 3, \dots \quad (4.7)$$

$$E_{1D}(k) = \frac{\hbar^2}{2} \left( \frac{k_x^2}{m_x} \right) + E_{n_x, n_y}, \\ E_{n_x, n_y} = \frac{\hbar^2 \pi^2}{2a^2} \left( \frac{n_y^2}{m_y} + \frac{n_z^2}{m_z} \right), \quad n_y, n_z = 1, 2, 3, \dots \quad (4.8)$$

where  $a$  is the thickness of the thin film or the diameter of a nanowire. From Eqs. (4.6)–(4.8) it is possible to obtain the DOS for 3D, 2D, and 1D systems, respectively. Considering that only the lowest sub-band ( $n=1$ ) affects the transport properties, the three equations may be summarized as

$$g(E) = \frac{N}{g_D a^{3-D}} \left( \frac{2m_{\text{eff}}}{\hbar^2} \right)^{\frac{D}{2}} (E - E_0)^{\frac{D}{2}-1}, \quad E \geq E_0, \\ g_D = \begin{cases} 2\pi^2 & \text{for } D = 3 \\ D\pi & \text{for } D = 1, 2 \end{cases}, \quad m_{\text{eff}} = \sqrt[D]{\prod_{i=1}^{3-D} m_i} \quad (4.9)$$

Assuming that carrier dynamics is limited by scattering, a suitable assumption for low electric fields, carrier velocity reads

$$v^2(E) = \frac{2(E - E_0)}{Dm_\sigma} \quad (4.10)$$

where  $m_\sigma$  is the so-called inertial effective mass, defined as the harmonic average, in the transport direction, of the effective masses of the degenerate conduction valleys. Further assuming that the relaxation time follows a power law equation,  $= \tau_0(E - E_0)^r$ , we can obtain an explicit expression for  $X_{i,D}$ :

$$X_{i,D} = \frac{N\tau_0}{m_\sigma g_D a^{3-D}} \left( \frac{2m_d}{\hbar^2} \right)^{\frac{D}{2}} (k_B T)^{r+\frac{D}{2}+i} \left( \frac{2(r+i)}{D} + 1 \right) F_{r+\frac{D}{2}+i-1}(\eta) \quad (4.11)$$

where  $F_j(\eta) = \int_0^\infty [x^j / (e^{(x-\eta)} + 1)] dx$  and  $\eta = (E_F - E_0)/k_B T$  is the reduced Fermi energy.

Now we can express the different quantities in  $ZT$  using the explicit form of Eq. (4.11). Let us first pay attention to the electrical conductivity (Eq. (4.2)). This quantity will increase when the charge carrier density or the carrier mobility increase, as  $\sigma = n e \mu$ . The analysis of the dependency of mobility upon the carrier density can be found elsewhere [60]. Regarding charge carrier density, it can be written as

$$n \equiv \int_{E_0}^\infty g(E)f_0(E)dE = \frac{N}{g_D a^{3-D}} \left( \frac{2k_B T m_d}{\hbar^2} \right)^{\frac{D}{2}} F_{\frac{D}{2}-1}(\eta) \quad (4.12)$$

Thus the carrier density increases as  $a$  is reduced, being this change more pronounced for low dimension systems. Another factor clearly influencing the number of charge carriers is  $\eta$ . This parameter is deeply dependent on the material band structure and in some cases on temperature.

The second factor that contributes to the figure of merit is the electronic thermal conductivity. This parameter is essentially related to the electrical conductivity, having likely dependence on  $n$  and  $\mu$ . Indeed,  $\sigma$  and  $\kappa_e$  are linked through the Lorentz number  $L$

$$\kappa_e = \sigma L T ; \\ L = \left( \frac{k_B}{e} \left[ \frac{\left( r + \frac{D}{2} + 2 \right) F_{r+\frac{D}{2}+1}(\eta)}{\left( r + \frac{D}{2} \right) F_{r+\frac{D}{2}-1}(\eta)} - \left( \frac{\left( r + \frac{D}{2} + 1 \right) F_{r+\frac{D}{2}+1}(\eta)}{\left( r + \frac{D}{2} \right) F_{r+\frac{D}{2}-1}(\eta)} \right)^2 \right] \right) \quad (4.13)$$

Concerning the Seebeck coefficient, we can write it using Eqs. (4.4) and (4.11):

$$S = \mp \frac{K_B}{e} \left( \frac{\left( r + \frac{D}{2} + 1 \right) F_{r+\frac{D}{2}}(\eta)}{\left( r + \frac{D}{2} \right) F_{r+\frac{D}{2}-1}(\eta)} - \eta \right) \quad (4.14)$$

Thus,  $|S|$  decreases by increasing  $\eta$ . As of the evolution of  $|S|$  with temperature, the variation in the Fermi energy has to be taken into consideration. In doped silicon, the carrier concentration is stable in a certain range of temperatures and is set by the doping. Nevertheless, in this case the Fermi energy decreases with  $T$  and then  $|S|$  is enhanced. In the case of intrinsic silicon (or in doped silicon

at sufficiently high temperatures)  $|S|$  will decrease as a result of the contribution to the Seebeck coefficient by carriers of opposed sign (compensation in the bipolar regime).

### 4.3.3 Phonon Transport in Nanostructured Thermoelectric Materials

The total thermal conductivity of a material is the sum of charge carriers ( $\kappa_e$ ) and lattice ( $\kappa_L$ ) thermal conductivity. The latter normally represents the major contribution and then the biggest impact in the figure of merit.

The so-called semi-classical theory is derived from the assumption that we consider the system as a gas of non-interacting particles. In this case we obtain that  $\kappa_L = C_L v l$ , where  $C_L$  is the thermal capacity,  $v = dr/dt$  is the average phonon velocity and  $l$  is the phonon mean free path. Then, the key to decrease thermal conductivity is to reduce any of the three factors, that is, the  $C_L$ ,  $v$ , and  $l$ .

We can use again Boltzmann transport equation (4.1) but considering the wave and position vector of phonons instead of electrons. In this case,  $f$  is the Bose–Einstein distribution function instead of the Fermi–Dirac distribution function. With these considerations, if  $g_p$  is the phonon DOS

$$C_L = \frac{dU}{dT} = \frac{d \int f_p E(k) g_p(E) dE}{dT} \quad (4.15)$$

The previous equations are valid under the assumption of non-interacting particles. One can include the harmonic interaction between nearest neighbors by introducing the phonon group velocity  $v = d\omega/dt$ , where  $\omega$  is the phonon frequency,  $\omega = \sqrt{(4K)/m} \sin(ka_0/2)$ , and  $K$  is a term accounting for the strength of the interaction and  $a_0$  is the distance between atoms. For silicon,  $v \approx 9 \times 10^3$  m/s. For every  $k$  value both low energy (acoustic) and high energy (optical) phonon modes are found. Acoustic phonons account for the inter-unit lattice cell response to external stimuli (e.g., temperature variations or electric fields). Instead, high energy phonons describe intra-cell interactions.

The most usual approach for the reduction of  $\kappa_L$  by nanostructuring is the reduction of the mean free path of phonons that is related to the phonon wavelengths. As will be shown in next sections, the generation of structures like SiNW with dimensions smaller than the wavelength of part of the phonons involved in the heat transport has proven to drastically reduce the heat conduction of bulk material.

## 4.4 Bottom-Up Nanowires

### 4.4.1 Preparation Strategies

The bottom-up approach for SiNWs fabrication consists in the addition of silicon atoms to form long one-dimensional crystalline structures with diameters going from a few nanometers to a few hundred nanometers. The arrangement of atoms needed to provide a crystalline growth requires a reversible path between the liquid or gas phase containing the precursor and the solid substrate. Usually,

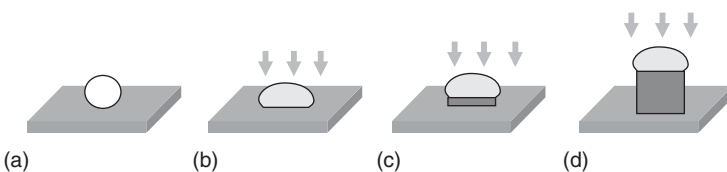


**Figure 4.5** Scheme of the vapor–liquid–solid (VLS) mechanism for growing nanowires. (a) Gas precursor introduction into the chamber, (b) precursor adsorption and dissociation at the catalyst surface, (c) material diffusion across the particle, and (d) precipitation of nanowire material and grow of the nanowire.

catalytic particles are distributed on the surface acting as seeds or growth nuclei. Most frequently, the nanowires grow through the so-called vapor–liquid–solid (VLS) mechanism (Figure 4.5). It was defined and reported for the first time by Wagner and Ellis in 1963 [61] and was intensively studied in the following years [62, 63]. The metal particle present on the surface alloys with silicon, becoming liquid at the process temperature. Then, a gas is introduced in the surrounding atmosphere that contains a silicon precursor (commonly  $\text{SiH}_4$  or  $\text{SiCl}_4$ ). This precursor is adsorbed and dissociated at the catalyst surface and Si is incorporated into the droplet. A supersaturation in the liquid alloy leads to the precipitation of silicon in the liquid droplet–solid silicon interface. This process continues, producing the growth of crystalline silicon below the droplet and the generation of a nanowire.

In a likely way, nanowires can be obtained by means of the so-called vapor–solid–solid (VSS) mechanism. In this case, the metal particle catalyzing the precursor decomposition on the substrate surface does not melt or form a liquid alloy. High enough surface or bulk mobilities are required that allow Si atoms to migrate to the precursor–substrate interface.

In the following, a short description of some of the most common techniques accessible for the growth of SiNW is presented.

#### 4.4.2 Chemical Vapor Deposition (CVD)

Chemical vapor deposition (CVD) technique is the most popular route to obtain bottom-up SiNWs due to its scalability, its capability to generate high aspect ratio structures with selectable dimensions and doping, and the possibility of selecting the regions where the growth takes place. This technique was initially developed for the fabrication of thin films. Its use for SiNWs requires the introduction of some mechanisms to block direct silicon growth on the sample and restrict the deposition to the metal regions. A large collection of CVD variants exist, that differentiate on parameters like pressure, temperature, and the mechanisms that can aid the decomposition of the precursor gas in the surface. Very frequently, low pressure is used, among other reasons, to prevent the oxidation of the silicon surface and the metal precursors. In this situation, the technique is denoted as low pressure chemical vapor deposition (LPCVD).

The temperature needed to trigger the precursor decomposition process strongly depends on the gas used and on the ability of the metal to catalyze the reaction. When using liquid  $\text{SiCl}_4$ , the required temperature is higher than

for gaseous precursors like  $\text{SiH}_4$  and  $\text{Si}_2\text{H}_6$ . Process temperatures typically of 800–1000 °C are needed for growing SiNWs with  $\text{SiCl}_4$  [64, 65], while a range from 350 to 700 °C is used for  $\text{SiH}_4$  or  $\text{Si}_2\text{H}_6$  [66–70].

Another variant of this technique is the so called plasma enhanced vapor deposition (PECVD). In conventional CVD growth processes, the dissociation of the precursor molecule is often considered as the rate limiting step. Temperature and the ability of the catalyst to dissociate the precursor are key factors for the NWs growth. With the assistance of plasma, the gaseous species are pre-dissociated in the atmosphere, so a broader range of catalysts can be used and the temperature can be reduced [71–73]. An inconvenience of this approach is the formation of parasitic deposition of amorphous silicon that can hinder some practical applications. Together with the versatility of CVD to produce SiNWs with selected lengths and diameters at different temperatures and pressures, the technique holds other convenient benefits. An essential advantage is the possibility to introduce a dopant gas precursor in a controlled way during the structure self-assembly.  $\text{PH}_3$  and  $\text{B}_2\text{H}_6$  are the gases most often used to produce n and p doped nanowires, respectively. As a counterpart, *in situ* doping can hinder the directional growth of the nanowires, mostly for the structures with diameters below 50 nm [74, 75]. Also, high doping levels are difficult to achieve due to unwanted gas phase decomposition of the dopant precursor gas during the growth process [76].

#### 4.4.3 Molecular Beam Epitaxy (MBE)

As in the case of CVD, also molecular beam epitaxy (MBE) is a classical technique used to deposit high quality layers. The extension to the fabrication of one-dimensional nanostructures was done after observing that metal impurities initiated the generation of nanowires. In this route, a silicon source is heated in high vacuum up to evaporation, providing a gaseous beam of Si atoms. The as-generated gas reaches the surface of the substrate where metal particles initiate the growth via the previously described VLS mechanism. In this case, however, the metal does not act as a dissociating agent for the precursor but promotes the growth by forming an alloy with the semiconductor. MBE offers excellent control over the synthetic conditions, allowing, for example, the fabrication of heterostructures with abrupt interfaces. MBE also presents a very good control on the generated nanowires in terms of crystallinity and doping [77–79]. As a counterpart, growth rates are very low and it is not possible to generate structures with a radius less than 40 nm.

#### 4.4.4 Laser Ablation

A different way to achieve the production of SiNW is by means of a laser irradiating a target consisting of a mixture of Si and the catalyst – that are therefore submitted to elevated temperatures. A flow of inert gas is introduced in the system during the process. The collision with the gas particles cools the ablated material, causing the growth of nanowires on a substrate that is not necessarily silicon, provided that metal particles remain liquid. The diameter and length of the resulting nanowires is not as easily tunable as in the case of CVD, since these factors

depend on the catalytic material and on the gas used. On the other side, the technique allows to grow long SiNWs in short times, with rates of some micrometers per minute. The high temperature involved can be a limitation for its use with some substrates, but it also allows to use materials with high eutectic temperatures [80, 81]. This method presents some capabilities that are inaccessible for a typical CVD, as the possibility of ablating chemicals that are to be incorporated in the NW. A clear disadvantage compared to other techniques is instead the requirement of complex and expensive equipment.

#### 4.4.5 Solution-Based Techniques

The growth in a liquid environment is the most cost-effective method among those existing for producing SiNWs. The techniques encompass the so-called solution–liquid–solid (SLS) and the supercritical-fluid–liquid–solid (SFLS) processes. In its former version, an organic solvent dissolving the silicon precursor is used. In the latter, a supercritical organic fluid containing the silicon precursor at high pressure is put in contact with a substrate containing the metal catalyst. As for the VLS, the substrate is submitted to a high enough temperature to produce the generation of a liquid metal–Si alloy. The solution of the precursor and subsequent saturation take place, leading to the growth of the SiNW [82–84].

#### 4.4.6 Catalyst Materials

One of the most important factors for the fabrication of SiNW is the metal catalyst. This metal has to be selected among those allowing for a stable SiNW growth, which mainly depends on the material surface tension and on the vapor pressure at the process conditions. On the other side, the process conditions have to fulfill the restrictions imposed by the substrate or the application. The chosen catalyst directly determines the minimum process temperature for VLS, which corresponds to the silicon–catalyst eutectic temperature. The phase diagram of a silicon–metal mixture provides further information concerning the temperature conditions that must be selected to make the growth feasible and also about the possibilities and limitations of the resulting nanowires. We can distinguish three kinds of phase diagrams (Figure 4.6). In the first two kinds, a single eutectic point occurs at low temperatures, but in kind A the Si concentration in the eutectic is above 10%, while in the case B the eutectic is at very low Si concentrations. Type C is characterized by the presence of one or more silicide phases, with elevated eutectic temperatures. The high solubility of Si implies that the energy needed to introduce a Si atom in the alloy is low. This facilitates a fast growth of the nanowires and enables the use of substrates that are sensitive to high temperatures. Conversely, this can be a disadvantage when trying to generate multi-material nanowires with sharp interfaces as the silicon already dissolved in the catalyst droplet precipitates slowly when submitted to a change in the atmosphere composition. This limitation can be overcome by using materials from type B phase diagrams, presenting a much smaller buffer of dissolved Si. Unfortunately, this also implies longer growth times.

Another key reason for choosing or discarding a catalyst is that the electric properties of the wires can be importantly affected by metal traces that remain in

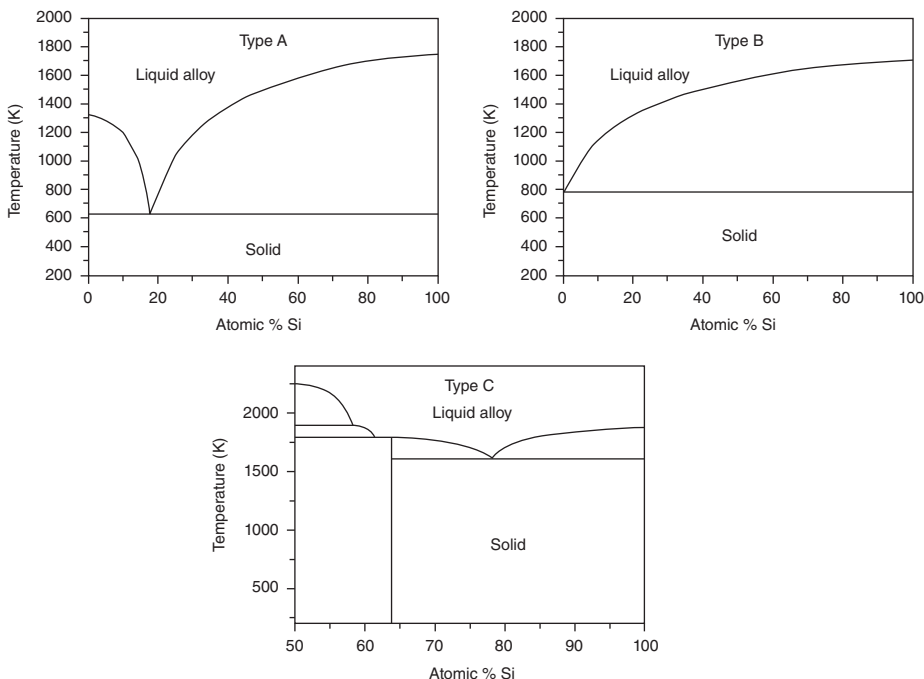


**Figure 4.6** Schemes of the three kind of silicon-metal phase diagrams.

silicon during the growth process. This interaction with silicon is also important because it can generate incompatibilities with CMOS processes, an important obstacle to the introduction of the SiNWs growth in industrial microelectronics facilities. The impact of the presence of impurities on the electric properties of a silicon crystal depends on how close their ionization energies are to the center of the Si band gap.

Gold is by far the most frequently used catalyst [85–92]. The main reasons for this common choice is its high chemical stability, its low eutectic temperature ( $363^{\circ}\text{C}$ ), and the possibility of depositing it as thin film or from commercial colloidal dispersions. Relatively high abundance and non-toxicity are also important factors. Conversely, Au poses important concerns for applications in Si fabrication technology. Traces of this metal along the nanowire can negatively affect the conductivity of the material by introducing charge carrier recombination centers. Other materials that have been used are copper [93], aluminum [94–96], silver [97], indium [62, 73, 98], gallium [99], zinc [100, 101], iron [102], platinum [103], or titanium [104].

#### 4.4.7 Catalyst Deposition Methods

The SiNWs position and diameters will be determined by the growth conditions and the size of the catalyst. For this reason, the particle deposition methodology becomes important, mostly when looking at practical applications. In this situation, the control of the NW features and the selection of the areas where they have to grow are essential.

A very popular way to generate a matrix of metal particles consists in the deposition of a thin film on the substrate that is submitted to high temperatures. The partial melting of the layer or the formation of a liquid alloy leads to a dewetting process producing nanometric droplets on the surface. Features like size and density of the particles are to some extent tunable by choosing parameters such as the layer thickness and the annealing temperature.

A second common approach consists in the use of a colloidal dispersion of nanoparticles. In this case the distribution of particle sizes can be very narrow and the concentration sets the number of particles per unit area in the surface.

Although simple and effective for some applications, both the aforementioned methods lack the capacity of selectively chose the area where the gold has to be present. In this respect, other techniques like the so called galvanic displacement enables the deposition to take place only in the areas where silicon is exposed [105–107].

## 4.5 Material Properties and Thermoelectric Efficiency

As mentioned, decisive experimental evidence of the improvement of thermoelectric figures using SiNWs were published in 2008 by Hochbaum *et al.* [6] and Boukai *et al.* [7]. The experimental demonstration of this decoupling between thermal and electrical conductivity in one-dimensional structures stirred research in the field. However, only few works have dealt with the study of nanowires grow with bottom-up techniques. Calaza *et al.* [108] measured the thermal properties of arrays formed by p-type Si nanowires with a mean diameter of 100 nm grown by LPCVD in a platform provided with integrated test elements (heaters and thermometers). The nanowires presented a very reduced thermal conductivity, ranging from 2 to 3 W/m/K in a temperature range from room temperature to 250 °C. The lower reduction compared with the top-down fabricated nanowires reported by Boukai *et al.* (1.2 W/m/K) could be attributed to a smaller surface roughness presented by the nanowires grown by VLS.

## 4.6 Top-Down Nanowires

### 4.6.1 Preparation Strategies

Top-down SiNWs are generally produced by lithography providing sufficient resolution to achieve the needed feature size for the wires, which is typically in the range 30–100 nm. Some suitable techniques to nanolithographically pattern SiNWs are illustrated in Figure 4.7.

Such nanopatterning techniques are necessary to fully exploit the potential of SiNWs in thermoelectric conversion, since thermal conductivity significantly decreases only for diameters smaller than 100 nm, particularly for single-crystal SiNWs in which phonon surface scattering is dominant.

In order to achieve such resolution with affordable costs, excluding the extremely costly deep-ultra violet (UV) stepper systems employed in nanoelectronics, three main techniques can be considered (Figure 4.7). The first one is

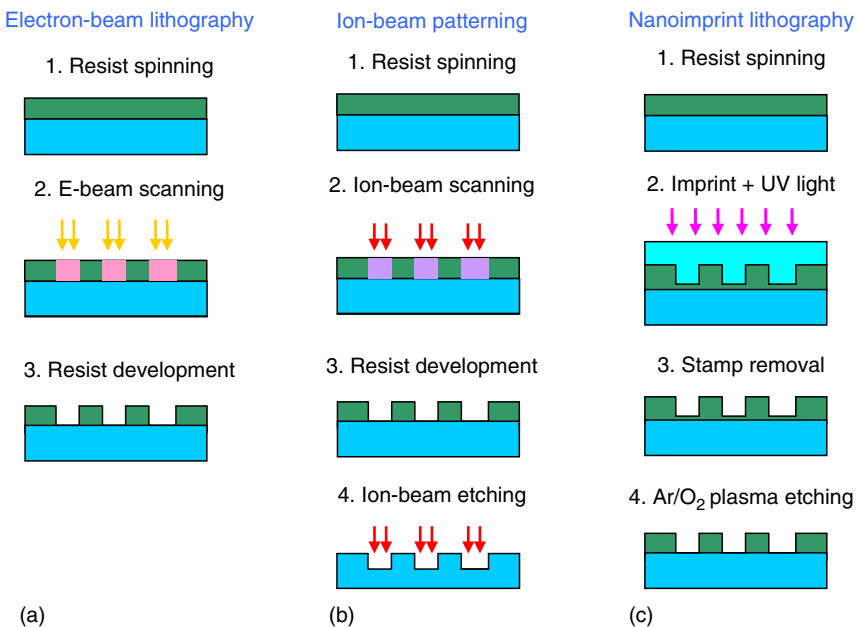


**Figure 4.7** Nanolithography techniques suitable for top-down fabrication of silicon nanowires: electron-beam lithography (a), ion-beam lithography or etching (b), nanoimprint lithography (c).

electron beam lithography (EBL), in which a focused electron beam is utilized to pattern an electron-sensitive resist such as poly-methyl methacrylate (PMMA). Thanks to the low wavelength associated to the high-energy electrons of the beam (with energy in the 10–100 keV range), such patterning can reach the resolution required for the top-down fabrication of the nanowires. An analogous technique can be implemented using an ion beam, with potentially even higher resolution due to the higher energy of ions compared to electrons owing to their larger mass. Such high energy also allows for direct etching of silicon using a focused high-energy ion beam (FIB).

Since both ion and electron beam lithography are scanning methods, they are basically slow. Depending on the patterned area, the required resolution and density of the pattern, the scanning time may range from a few hours to a few days. In the latter case the cost will be not affordable for most applications, including thermoelectric conversion.

A possible way to overcome the problem is using UV-assisted nanoimprint lithography. This technique is halfway between molding and lithography, since a stamp is utilized to imprint the desired geometry on a UV-sensitive polymer, which is then treated by UV exposure before removing the stamp. In the latest technological developments, such technique is implemented with soft stamps, made of polydimethylsiloxane (PDMS) or other soft polymers with a thin glass backplate. In this way, the flexible stamps adapt to the substrate, and possibly embed defects or particles without losing contact with the substrate on a too large area, thus limiting the yield decrease. Quite evidently, the stamp itself must

contain the nanometric geometry needed to fabricate the nanowires and is in most cases produced by EBL with subsequent plasma etching on silicon or glass substrates. However, in this case the high fabrication cost is only related to the master stamp, which can be replicated many times on different soft stamps that in turn can be used to pattern many substrates. Thus, the patterning cost hugely decreases compared to the cases of direct electron or ion beam lithography on the pattern of interest.

Following the nanolithographic step, all methods (except direct FIB etching) require a pattern transfer on the active material, namely silicon in our case, either single-crystalline or polycrystalline (Figure 4.8).

First, the nanowire geometry, created on some kind of photoresist or imprint polymer, needs to be transferred to the silicon layer utilized to obtain the nanowires. This is typically done by anisotropic etching such as reactive ion etching (RIE), which can be generally performed on the thin layers used for the nanowires by directly using photoresist as a RIE mask (step 1). In performing RIE, a plasma recipe with sufficient anisotropy must be adopted since even a small under-etching of the mask would be sufficient to destroy the nanowire, particularly if small diameters are designed on the pattern. To this purpose, traditional capacitively coupled (CC) etching systems are often preferred to high density plasma such as inductively coupled plasmas (ICPs) for their slower etching rate (in the range 10–100 nm/min), allowing for a better control of the etching process. Another important issue is the availability of an etch-stop material (such as  $\text{SiO}_2$ ) under the silicon layer used as a starting point to pattern the nanowires. Most of the CC RIE etching processes potentially usable to perform an etching based pattern transfer in top-down Si nanowire fabrication make use of chlorine or fluorine-based chemicals (such as  $\text{SiCl}_4$  or  $\text{CF}_4$ ) and are much slower on dielectrics such as  $\text{SiO}_2$  or  $\text{Si}_3\text{N}_4$  than on silicon. Thus, these materials can be effectively used as etch-stop layers underneath the nanowires.

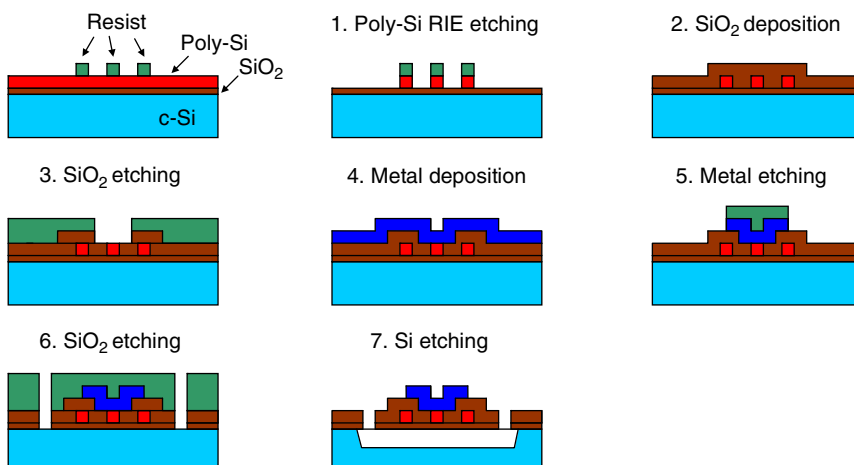


**Figure 4.8** Post-lithography steps in top-down fabrication of silicon nanowires.

Once the geometry of the nanowires in silicon is defined by RIE etching, the fabrication generally requires some additional step to integrate the nanowires in the TEG device in an effective way. The first thing that is always needed is some electrical passivation of the nanowires, which can be obtained by depositing a dielectric material over them (step 2 in Figure 4.8). To this purpose, a typically chosen material is  $\text{SiO}_2$  deposited by low-pressure chemical vapor deposition (LPCVD) from  $\text{SiH}_4$  and oxygen (at 400 °C) or from tetraethyl-orthosilicate (TEOS) at 800 °C. In both cases, a pinhole-free, conformal layer is obtained that electrically passivates the nanowires and protects them from the influence of the external environment.  $\text{SiO}_2$  has also a very low thermal conductivity (in the order of 1 W/m/K) and therefore does not affect the thermoelectric efficiency of the nanowire arrays in the TEG.

After passivation, metal contacts to the nanowire are also necessary to create the thermocouples in the TEG and to connect the device to the external readout circuitry through bonding pads. To do that, the passivation layer must be selectively removed from the contact region over the nanowires (step 3 in Figure 4.8) using a purposely designed pattern on photoresist by conventional lithography.  $\text{SiO}_2$  etching in this case can be performed either by wet or RIE processes to uncover the surface of the nanowires that have to be contacted. Afterwards (steps 4 and 5), a metal layer is deposited on the sample and subsequently patterned to create the metal connections. A good choice for the metal layer can be an alloy of aluminum and silicon (typically with silicon-to-aluminum ratios between 1% and 2%), that can be annealed to improve the contact resistance of the metal/Si nanowire interface at 400 °C without excessive silicon diffusion in the Al layer.

After metal etching, the thermocouples are defined and the TEG device is in principle ready to operate. It must be said, however, that some kind of micro-machining of the massive silicon substrate is often adopted in fabricating the TEG to improve the thermal isolation of the nanostructured thermocouples and consequently enhance the device performance. Such micromachining step can be straightforwardly executed once the nanowires are completely passivated by  $\text{SiO}_2$  using, for example, some  $\text{SiO}_2$ -selective anisotropic silicon etchant such as tetra-methyl-ammonium hydroxide (TMAH) after patterning a suitable geometry over the  $\text{SiO}_2$  passivation on the front side of the sample (step 7 of Figure 4.8). TMAH can also be made selective to aluminum by adding ammonium peroxydisulfate and silicon powder or silicic acid. Other possible options are isotropic silicon etching by  $\text{SF}_6$  plasma from the front side or backside pass-through micro-machining by TMAH or deep-reactive ion etching (DRIE) of silicon.

The basic technique described in Figures 4.7 and 4.8 has a severe limitation since it allows obtaining just one layer of nanowires. This is not ideal for the TEG application since the number of nanowires per unit length on the nanostructured thermoelement is a key point for efficiency and should be in principle larger than the one obtainable with one level of nanowires. A possible technique to improve the linear density of the nanowires in top-down technology has been proposed in [109] and is here schematically illustrated in Figure 4.9.

With this technique, the nanowires are fabricated starting from a mould obtained with a stack of  $\text{SiO}_2$  and  $\text{Si}_3\text{N}_4$  layers on which a nanolithographic

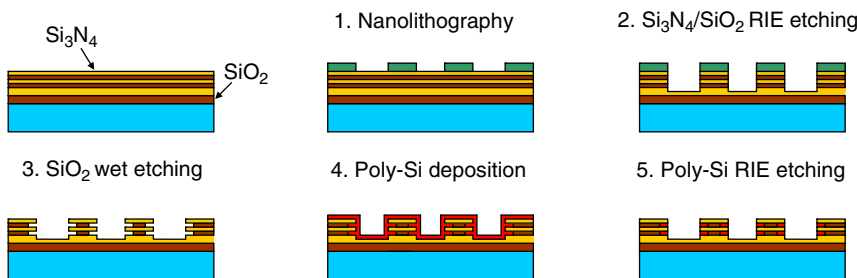


**Figure 4.9** Top-down fabrication of stacked polycrystalline silicon nanowires.

pattern is defined by RIE etching (steps 1 and 2 in Figure 4.9). Afterwards, an isotropic wet  $\text{SiO}_2$  etching is utilized to create recesses on the patterned stack (step 3) that are subsequently filled by a polysilicon deposition performed by LPCVD (step 4). RIE polysilicon etching is finally employed to eliminate the excess of deposited polysilicon and to obtain the nanowires within the  $\text{SiO}_2$  recesses (step 5). In this way, many nanowire layers can be potentially fabricated by increasing the height of the  $\text{SiO}_2/\text{Si}_3\text{N}_4$  stack, significantly increasing the linear density of nanowires within the nanostructured thermoelements beyond the intrinsic limitations of the one-level fabrication illustrated in Figure 4.8.

#### 4.6.2 Material Properties and Thermoelectric Efficiency

The thermoelectric properties of top-down fabricated SiNWs are in any respect similar to those obtained by bottom-up growth. However, some important differences may arise depending on the crystal texture of the nanowires. This is particularly relevant in top-down fabrication since in this case the nanowires can be either single-crystal or polycrystalline, depending on the preparation method. Bottom-up grown nanowires, on the contrary, are generally single-crystal.

Crystal texture affects both the electrical and thermal properties of the nanowires. Thermal conductivity in polycrystalline SiNWs is influenced by the presence of GBs, which give rise to additional phonon scattering with respect to lattice or impurity phonon scattering. As a consequence, polycrystalline SiNWs typically present a much lower thermal conductivity compared to single-crystal nanowires with similar size. Moreover, the type of doping used in the polycrystalline SiNWs is also influential because it can promote or inhibit the growth of grains within the nanowires during the thermal annealing steps required for doping activation. In particular, two of the most widely used dopant species for silicon, boron, and phosphorus, present opposite effects on grain growth during thermal annealing of the nanowires, since phosphorus enhances the growth of the grains while boron inhibits it. As a result, the crystal texture of boron-doped polycrystalline nanowires is typically much finer than that of phosphorus-doped ones, and their thermal conductivity is consequently lower.

In polycrystalline nanowires, actually, the effect of GBs acts in combination with phonon surface scattering on the wires, giving rise to very low thermal conductivity values even for nanowires with diameter in the range of 100 nm.

Typically, the values obtained on nanowires with cross-section in the order of  $100 \times 100 \text{ nm}^2$  on heavily doped polycrystalline SiNWs are around 2–3 W/m/K for boron-doped nanowires and 4–5 W/m/K for phosphorus-doped nanowires [14]. Single-crystal nanowires of comparable cross section and doping, differently than the polycrystalline ones, would present a thermal conductivity around 60–70 W/m/K. This is in principle an advantage that the use of polycrystalline SiNWs presents, and that is closely related to top-down fabrication, since bottom-up growth of polycrystalline SiNWs is not easily achievable. However, it must be said that the polycrystalline texture also presents some disadvantages when the electrical properties are considered.

In fact, the doping of the nanowires is normally chosen in order to maximize the PF  $\sigma S^2$ . Now, in both poly- and single-crystal silicon (either in nanowire or in film form), the doping level  $c$  affects  $S$  and  $\sigma$  in a very different way. Even though the absolute Seebeck coefficient  $S$  is not easy to model analytically, particularly in the high doping range, its variation is logarithmic with  $1/c$  [29], becoming proportional to  $c^{-2/3}$  only at very high doping levels. Electrical conductivity, on the contrary, is almost proportional to  $c$ , even though electrical mobility is very different for low and high doping ranges due to ionized impurity scattering in heavily doped silicon. This means that, generally speaking, by increasing the silicon doping level the PF can be improved since the decrease of  $S^2$  is generally much lower than that simultaneously induced on  $1/\sigma$ . As a result, in TEGs the doping of the nanowires is often pushed to the maximum possible level, which is actually bounded by physical limitations related to the activation of the doping species in silicon. Since, in fact, the dopant atoms must be substitutional in the crystal lattice to give rise to a free carrier, the first requirement to be fulfilled for doping activation is that the doping species has to be in solid solution within silicon at the annealing temperature, and not in a precipitate form. At the maximum allowed annealing temperature for silicon (1100 °C), the solid solubility of the most common dopant species for silicon (boron, phosphorus, and arsenic) is slightly above  $10^{20}/\text{cm}^3$ .

In polycrystalline SiNWs, doping activation is also influenced by the presence of GBs, which are amorphous and consequently prevent the activation of the dopant atoms that segregate there. This effect is particularly important in boron-doped polysilicon since boron segregates preferably within GBs, and this causes a doping depletion within the grain, which is responsible for a resistivity increase. That is the reason why electrical resistivity in boron-doped polycrystalline SiNWs cannot be typically decreased below  $6 \times 10^{-3} \Omega \text{ cm}$ . Phosphorus, on the contrary, preferably segregates on the inner side of the grains and consequently a much better doping activation can be reached, with electrical resistivity in the order of  $10^{-3} \Omega \text{ cm}$ . As a result, despite the very low thermal conductivity, the thermoelectric figure of merit of polycrystalline SiNWs at 300 K is lower than in single-crystal SiNWs with very small diameters (20–30 nm), mainly because of their worse electrical properties. However, this disadvantage in TEG devices can be partly compensated by the fact that high diameters can be adopted in polycrystalline nanowires without degrading too much their figure of merit. This is not the case for single-crystal SiNWs, instead.

## 4.7 Applications of Bulk and Thin-Film Silicon and SiGe Alloys to Energy Harvesting

Very few are the applications of silicon itself as a thermoelectric material as of its low  $ZT$ . However, its alloys with Ge (meant to decrease its thermal conductivity) have been (and still are, to a large extent) the reference material for many key applications of thermoelectricity. On one side, SiGe thin films provide ways of easy on-chip integration of a TEG. On the other hand, Si—Ge alloys have been extensively used as massive legs in radioisotope thermoelectric generators (RTGs) to power deep-space probes. In this case, SiGe alloys have been the natural choice as no mature materials able to sustain the high temperatures typical of this class of TEGs were available in the 1970s.

Focusing onto integrated applications, most of the reported research has been aimed at developing TEG designs that coped with the relatively high thermal conductivity of the material to compensate for the relatively low conversion efficiency. Achieving large heat currents and minimal thermal shunts could actually make output power densities competitive with those obtainable with high- $ZT$  standards. A good example of such an approach comes from a series of papers published by the Infineon Labs over the first years of 2000. The major problem with integrated TEGs is actually that of forcing the heat flow through planar elements that are oriented normal to the thermal gradient. Decoupling the thermal vias from the (bulk) substrate could be achieved by opening cavities under the TEG elements (Figure 4.10) [27]. In this way the wafer could be used as the thermal contact to the heat sink. This, coupled with a proper choice of the doping level of the substrate, allowed to minimize the otherwise large reduction of the temperature difference actually applied over the thermoelectric legs. For a front-to-back  $\Delta T$  of 3 K an actual temperature drop of 1.7 K was estimated to

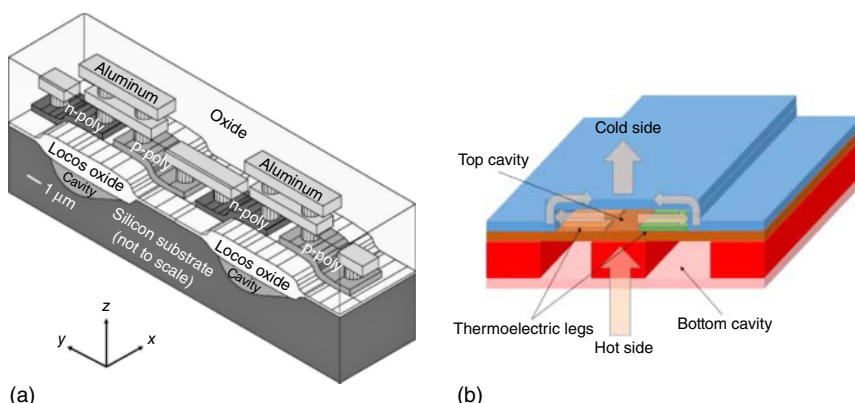


**Figure 4.10** Comparison of the layouts of the on-chip TEG developed by (a) Strasser *et al.* and (b) Xie *et al.* [110]. Note in both cases the cavity underneath the legs. In Xie's design additional cavities force the heat to flow out while preventing thermalization with the TEG. Drawing on the left reproduced with permission of Elsevier. ((a) Strasser *et al.* 2002 [27]. Reproduced with permission of Elsevier.)

occur over the thermoelectric leg. In addition, the reduced thermal shunt enabled a relatively large heat flow through the device legs that compensated for the low  $ZT$  and the small  $\Delta T$  (that further reduced the conversion efficiency), so that an output power density of  $\approx 5 \mu\text{W}/\text{cm}^2$  could be attained when applying a temperature difference over the chip as small as 10 K [26, 111].

A different design was developed by Xie *et al.* [110] using a fully CMOS-compliant fabrication process in a Ge-free thermoelectric device. A double set of cavities was generated to force heat to flow through p- and n-legs lying parallel to the substrate. Heat was then injected from the substrate, forced to flow parallel to it over a membrane sustaining the thermoelectric elements and then dissipated through a vacuum-insulated thermal collector. An output power density of  $1.5 \mu\text{W}/\text{cm}^2$  over a  $\Delta T$  of 5 K was reported, a value mostly limited by the relatively large electrical resistance associated to the micrometric size of the contact pads.

Use of suspended legs in microharvesters was proposed by Leonov and coworkers at IMEC [112]. Hole- and electron-doped SiGe films were deposited onto sacrificial trapezoidal  $\text{SiO}_2$  blocks that were shaped by using a photoresist mask with variable thickness along with a focus energy matrix [113]. Beveled walls helped deposit the active layers. At the process end,  $\text{SiO}_2$  blocks were wet-etched away leaving an Al-contacted p-n series the hot side of which was separated from the substrate by 6  $\mu\text{m}$ . Power density was measured to be  $\approx 1 \mu\text{W}/\text{cm}^2$  for  $\Delta T = 5$  K, mostly limited by local failures (short- and open-circuits) within the chip.

An even more radical approach to minimize thermal shunts was pursued by Yu and co-worker [114]. In their layout, thermoelectric legs were bridging fully separated blocks in a comb structure. After deposition of an interdigitated p-n Si series (lying flat onto the substrate) the comb was realized by deep RIE from the back, with the thermoelectric legs lying across the substrate fingers. The temperature difference could then be applied to the two blocks, ensuring heat to flow almost entirely through the thermoelectric legs. Since the only possible shunt was the radiative coupling between the hot and cold blocks, a large thermal current could be converted into electric power. Also, large temperature differences could be applied without losses from direct thermal coupling between the hot and cold sink. A very large power density of about  $100 \mu\text{W}/\text{cm}^2$  for a  $\Delta T$  of 30 K was measured, apparently a huge value compared to Leonov's results of  $6.4 \mu\text{W}/\text{cm}^2$  upon application of the same  $\Delta T$ .

Beyond the specific design, use of thermoelectric thin films and of planar technologies unavoidably incurs limitations originating from the large electrical resistance of the microharvester. Device resistances in excess to  $1 \text{ M}\Omega$  are common, as a result of the contact resistances at the microscale. Thus, electrical matching is usually impossible to be achieved when thermal harvesters operates as power sources for macroscopic sensors or actuators. This obviously implies a severe reduction of the actual conversion efficiency. This simple fact highlights two basic, interlaced issues. Firstly, integrated thermoelectric harvesters are naturally meant to be effectively used as power sources for microelectronics, not as general purpose heat converters. Also the opposite is actually true, namely that macroscopic (bulk) thermoelectric harvesters may not so conveniently used to generate electric powers to be delivered to microelectronic components unless

a less-than-optimal power density may be accepted in view of the low power consumption of the components themselves. This leads to the general conclusion that any direct comparison between the power density achievable with macroscopic and microscopic harvesters is misleading further than unfair. Planar thermoelectric converters have therefore a world on itself they qualify for, not competing with the surely much larger power densities provided by conventional, non-integrated TEGs. Secondly, in integrated harvesters (possibly more than in bulk TEGs) side technologies are qualifying parts of the device and module fabrication. Both thermal and electrical contacts make actually a major difference in terms of the TEG real efficiency, so that it is highly desirable that thermoelectric research for microharvesting further concentrates its effort onto collateral aspects of thermoelectric material science ranging from contact metallurgy to material mechanical properties, then not limiting to enhanced  $ZT$  materials.

## 4.8 Applications of Nanostructured Silicon to Energy Harvesting

### 4.8.1 Bottom-Up Nanowires

Although enhanced thermoelectric properties of SiNWs have been demonstrated, the introduction of these structures into a practical device is still challenging. To avoid power losses it is mandatory an optimal arrangement of the nanowires between hot and cold sinks, and a perfect electrical connection. Setting a bridge between nanostructures and macroscopic world requires precise manufacturing as the one that can be provided by silicon micromachining processes. Commonly, top-down platforms embedding bottom-up NWs are required. However, bottom-up NW growing methodology can be interesting in order to achieve a higher density of nanowires and increase the volumetric power. Two main obstacles have to be solved for the application of these approaches. First, it is important to restrict the area where the NW will grow to the active part of the device. Second, long distances between hot and cold parts have to be provided in order to avoid thermal shunts by convection or radiation.

A proof-of-concept of a thermoelectric micro-generator using VLS nanowire growth was proposed by Davila *et al.* [115]. Figure 4.11 shows a sketch of the device. Silicon p-doped nanowires were grown in a silicon micromachined device, contacting a suspended platform with the bulk of the chip. In a harvesting scenario, the device is put in contact with a hot surface. The low thermal mass of the platform allows for a rapid cooling compared to bulk, providing the necessary temperature difference for generating power. A series of heaters/thermometers and metal pads allowed to control and measure heat while extracting the generated current. In order to achieve a long separation between hot and cold parts, a series of microspacers were introduced that remained suspended in the final prototype, held by the NWs array. A distance of 90  $\mu\text{m}$  was achieved between the walls. The gold catalyst particles were deposited by means of galvanic displacement, a selective method that allowed introducing the seeds

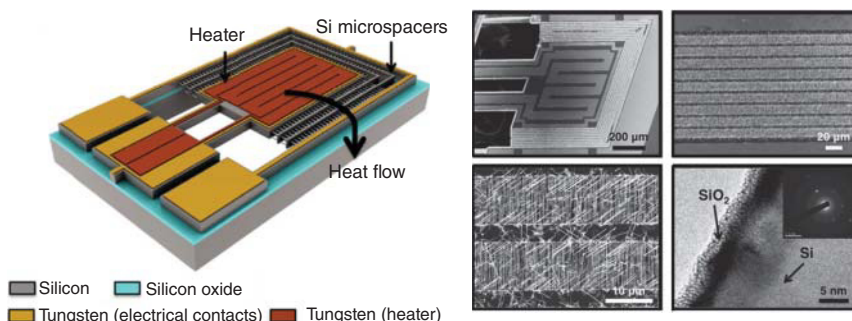


**Figure 4.11** (a) Sketch showing the design of a thermoelectric micro-generator. (b) Images of the resulting prototypes, showing details of the nanowire growing regions and nanowire structure. (Dávila *et al.* 2012 [115]. Reproduced with permission of Elsevier.)

only in the Si exposed surfaces. With this configuration, a power density close to  $1.5 \text{ mW/cm}^2$  was demonstrated by providing a temperature difference of  $300^\circ\text{C}$ .

#### 4.8.2 Top-Down Nanowires

Constraints acting on the conversion efficiency of top-down nanowire-based TEGs will be illustrated with reference to the typical structure of a lateral TEG as the one sketched in Figure 4.12.

The device is made of thermoelements with complementary doping (alternating n- and p-type) composed by a large number of stacked nanowires in parallel, that are connected in order to create a sufficient number of thermocouples in series. In the figure, the polycrystalline stacked nanowires described in the previous section have been utilized in the TEG by way of example – although the use of other types of nanowires within the same structure is also possible.

During operation, the thermal flow in the TEG is as represented in Figure 4.13.

The device is used in contact with a hot surface at a temperature  $T_h$  larger than the ambient temperature  $T_a$ . As a result, a thermal flow is built up across

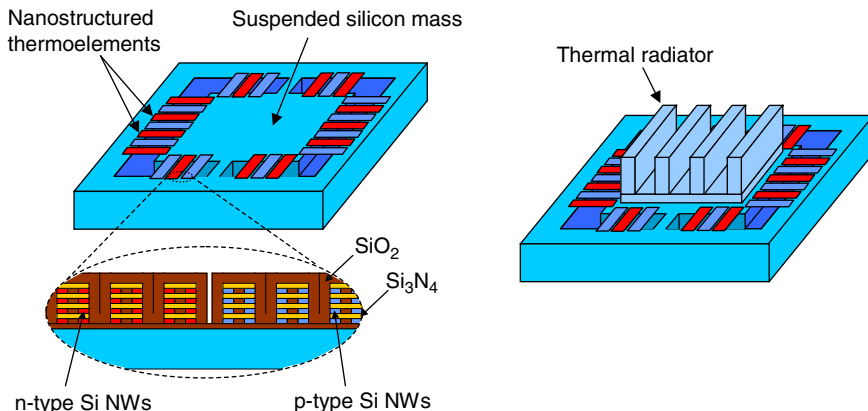


**Figure 4.12** Lateral TEG based on top-down fabricated stacked silicon nanowires.

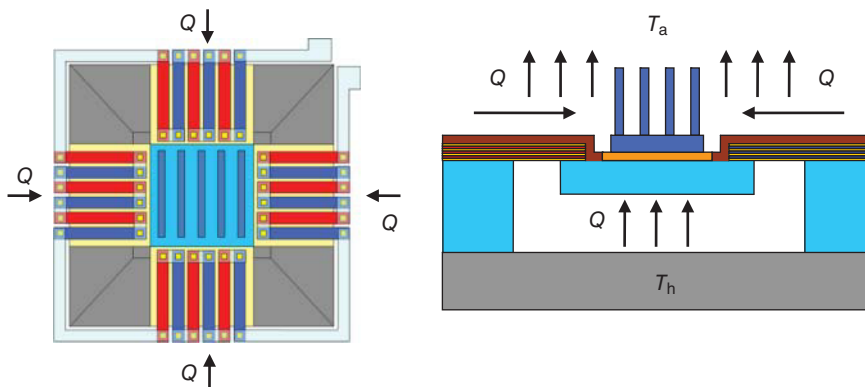


**Figure 4.13** Thermal flow in lateral TEG during harvesting.

the device that gives rise to a temperature difference across the nanostructured thermocouples. Being  $\Delta T$  the temperature difference, the power  $P$  transferred to an electrical load in matching conditions by the TEG can be written as

$$P = \frac{(n_{tp} S_{pn} \Delta T)^2}{4R_{tp}} \quad (4.16)$$

where  $S_{pn}$  is the overall Seebeck coefficient of the individual p–n nanostructured thermocouple composed by complementarily doped nanowires in the device,  $n_{tp}$  is the number of thermocouples connected in series in the device, and  $R_{tp}$  is the overall electrical resistance of such thermocouple chain.

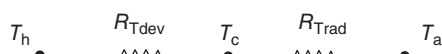
Equation (4.16) clearly shows that in order to obtain a high conversion power it would be desirable to increase as much as possible the temperature difference  $\Delta T$  in the device and to keep  $R_{tp}$  low. Both parameters actually depend on the design of the TEG, since the thermal behavior of the device can be schematically modeled by the series connection of two thermal resistances (Figure 4.14).

In the model,  $R_{Tdev}$  represents the overall thermal resistance of the device, whereas  $R_{Trad}$  is the thermal resistance between the device and the surrounding environment and  $T_c$  is the temperature of the cold contact of the thermocouples. In case a dissipater is utilized on the TEG, as shown in Figure 4.12, such resistance is actually the thermal resistance of the heat sink. From the model, the temperature difference  $\Delta T$  in the TEG computes to

$$\Delta T = T_h - T_c = (T_h - T_a) \frac{R_{Tdev}}{R_{Tdev} + R_{Trad}} \quad (4.17)$$

Thus, considering a given temperature difference between the hot surface and the environment,  $\Delta T$  is enhanced if the thermal resistance of the device is comparable or even larger than that of the heat sink. This is actually not possible for typical TEGs, since the thermal resistance of heat sinks (particularly in natural convection regime, which is almost always the case of interest for TEGs) is always

**Figure 4.14** Simplified thermal model of the



higher than that achievable with the device. Moreover, the thermal resistance of the device cannot be increased indefinitely, since its electrical resistance would increase as well because of physical and geometrical constraints. For instance, the thermal resistance of the device may be increased by designing longer thermoelements, but this will also increase their electrical resistance and therefore  $R_{tp}$  in Eq. (4.16), limiting their performance. Moreover, it must be kept in mind that  $R_{Tdev}$  is the overall thermal resistance of the device, and not that of the nanowires only, and therefore includes the effect of other materials in the TEG, such as the  $\text{Si}_3\text{N}_4/\text{SiO}_2$  dielectric membrane or the silicon anchors on the suspended mass (as shown in Figure 4.12) and, more importantly, the effect of thermal exchange through air toward the surrounding environment and the hot surface (Figure 4.13). Given such constraints and the properties of the materials employed in the TEG, an optimum design can be achieved starting from the characteristics of the chosen heat sink. In this optimization procedure, quite obviously, the availability of nanowires with low thermal conductivity and electrical resistivity will be of help to reach good conversion performances.

Another possible design of a top-down nanowire-based TEG is the one based on a vertical arrangement of SiNWs (Figure 4.15).

This kind of device is described by an analogous thermal model (reported in the figure), in which the thermal resistance of the heat sink is completely similar to the case of the lateral TEG but the device resistance  $R_{Tdev}$  has a very different dependence on the design parameter and is generally lower, as it is difficult to fabricate long vertical nanowires.

In the scientific literature, the vertical arrangement has been already proposed for TEGs based on top-down SiNWs [30, 31, 116–122], whereas the lateral device

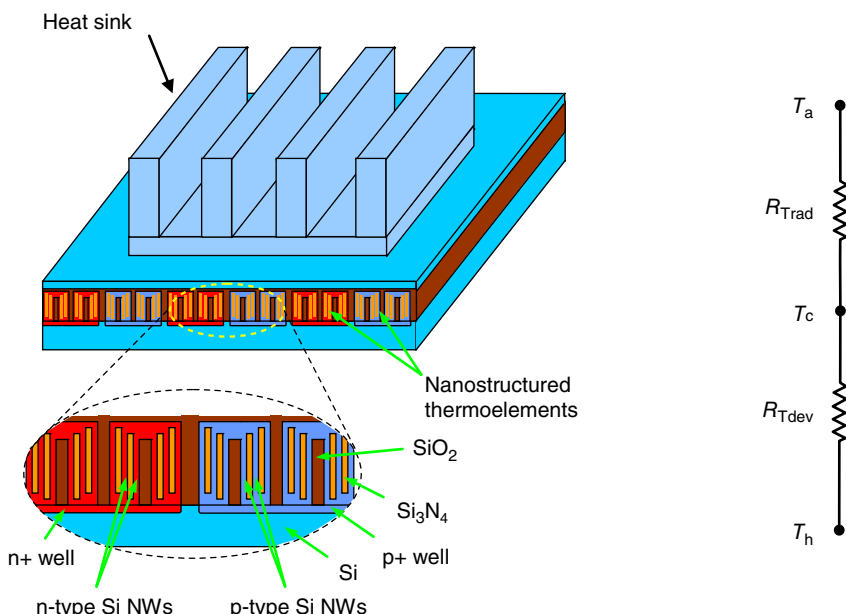


Figure 4.15 Vertical TEG based on top-down fabricated silicon nanowires.

has only been presented in TEGs based on bottom-up nanowires [115]. In vertical devices, one of the main problems is the limited aspect ratio that can be obtained in top-down nanowires manufactured by anisotropic etching, which generally results in a maximum length of the nanowires around a few microns. This results in a very low thermal resistance per device unit area, leading in turn to a marginal  $\Delta T$  across the device during operation, and then to a truly small generated power.

The other problem is the manufacturing of the thermocouples from the vertical nanowire array, since this operation requires the metal connection of different levels on the device, which may be misaligned by several microns, making lithography problematic. In the device represented in Figure 4.15, this difficulty is partially overcome by the use of complementarily doped p- and n-type nanowires in the thermoelements.

## 4.9 Summary and Outlook

In this chapter, we have reviewed the applications of silicon as a thermoelectric material. It has been shown that, apart for its use in SiGe alloys for RTEGs, silicon is possibly the only thermoelectric material that has seen no use as a bulk material. As discussed, many age-old and novel materials largely outperform it as of thermoelectric efficiency. Instead, silicon has found specific applications in integrated devices, where its immediate compatibility with microelectronic standards justified its deployment for thermal harvesting.

This state of affairs has quite changed over the last decade. On one side, the discovery that silicon nanostructures may be capable of  $ZT$  of order of 1 due to the reduction of its thermal conductivity has motivated a novel interest for this classic material. Both bottom-up and top-down techniques have rapidly developed to enable the fabrication of SiNWs (and nanolayers) with methods capable of rapid scale-up. Although applications in modules are still marginal if not lacking, it is appropriate to imagine that SiNW will find actual use in the short term, especially for microharvesting. The main hurdles to be overcome have been reviewed, and directions of research in the field have been outlined. Also for the standard thin film technology advancements have been reported. Silicon-based nanocomposites were shown to be able of unexpectedly large PFs, still retaining the relatively low thermal conductivity typical of ncSi.

Overall, thermoelectric silicon apparently deserves the renewed attention it has received over the last years. As for all thermoelectrics, also for silicon it is to be stressed that the way from material physics to real modules will be paved by the development of suitable side technologies. As an example, lowering thermal and electrical contact resistances are of paramount importance, especially for nanostructured silicon – thus calling for research on silicon contact metallurgy. In addition, innovative device layouts are also expected to play an important role as of the actual electric power density microharvesters may generate. One may then legitimately conclude that over the next years silicon will possibly attract the concurrent expertise of material scientists, physicists, chemists, and engineers – an almost perfect blend of competences that might address the further development of silicon as a thermoelectric material following a device-driven approach.

## Acknowledgments

This work was supported by FP7-NMP-2013-SMALL-7, SiENERGY (Silicon Friendly Materials and Device Solutions for Microenergy Applications), Contract No. 604169.

## References

- 1 Heremans, J.P. *et al.* (2013) When thermoelectrics reached the nanoscale. *Nat. Nanotechnol.*, **8** (July), 471–473.
- 2 Kanatzidis, M.G. (2010) Nanostructured thermoelectrics: the new paradigm? *Chem. Mater.*, **22** (3), 648–659.
- 3 Minnich, A.J. *et al.* (2009) Bulk nanostructured thermoelectric materials: current research and future prospects. *Energy Environ. Sci.*, **2** (5), 466.
- 4 Snyder, G.J. and Toberer, E.S. (2008) Complex thermoelectric materials. *Nat. Mater.*, **7** (2), 105–114.
- 5 Narducci, D. (2011) Do we really need high thermoelectric figures of merit? A critical appraisal to the power conversion efficiency of thermoelectric materials. *Appl. Phys. Lett.*, **99** (10), 102104.
- 6 Hochbaum, A.I. *et al.* (2008) Enhanced thermoelectric performance of rough silicon nanowires. *Nature*, **451** (7175), 163–167.
- 7 Boukai, A.I. *et al.* (2008) Silicon nanowires as efficient thermoelectric materials. *Nature*, **451** (7175), 168–171.
- 8 Amato, M. *et al.* (2014) Silicon–germanium nanowires: chemistry and physics in play, from basic principles to advanced applications. *Chem. Rev.*, **114**, 1371–1412.
- 9 Dasgupta, N.P. *et al.* (2014) 25th Anniversary article: semiconductor nanowires – synthesis, characterization, and applications. *Adv. Mater.*, **26**, 2137–2183.
- 10 Juhasz, R. *et al.* (2004) Controlled fabrication of silicon nanowires by electron beam lithography and electrochemical size reduction. *Nano Lett.*, **5** (2), 275–280.
- 11 Pennelli, G. (2009) Top down fabrication of long silicon nanowire devices by means of lateral oxidation. *Microelectron. Eng.*, **86** (11), 2139–2143.
- 12 Za’bah, N.F. *et al.* (2012) Top-down fabrication of single crystal silicon nanowire using optical lithography. *J. Appl. Phys.*, **112**, 024309.
- 13 Neogi, S. and Donadio, D. (2015) Thermal transport in free-standing silicon membranes: influence of dimensional reduction and surface nanostructures. *Eur. Phys. J. B*, **88** (3), 1–9.
- 14 Suriano, F. *et al.* (2015) Influence of grain size on the thermoelectric properties of polycrystalline silicon nanowires. *J. Electron. Mater.*, **44** (1), 371–376.
- 15 Petermann, N. *et al.* (2015) Thermoelectrics from silicon nanoparticles: the influence of native oxide. *Eur. Phys. J. B*, **88** (6), 163.

- 16 Lorenzi, B. *et al.* (2014) Paradoxical enhancement of the power factor of polycrystalline silicon as a result of the formation of nanovoids. *J. Electron. Mater.*, **43** (10), 3812–3816.
- 17 Neophytou, N. *et al.* (2013) Simultaneous increase in electrical conductivity and Seebeck coefficient in highly boron-doped nanocrystalline Si. *Nanotechnology*, **24** (20), 205402.
- 18 Tian, Y. *et al.* (2012) One-dimensional quantum confinement effect modulated thermoelectric properties in InAs nanowires. *Nano Lett.*, **12**, 6492–6497.
- 19 Allison, S.C. *et al.* (2003) A bulk micromachined silicon thermopile with high sensitivity. *Sens. Actuators, A*, **104** (1), 32–39.
- 20 Bottner, H. *et al.* (2004) New thermoelectric components using microsystem technologies. *J. Microelectromech. Syst.*, **13** (3), 414–420.
- 21 Hasebe, S. *et al.*, 2004 Polymer Based Smart Flexible Thermopile for Power Generation. 17th IEEE International Conference on Micro Electro Mechanical Systems. Maastricht MEMS 2004 Technical Digest. IEEE, pp. 689–692.
- 22 Huesgen, T., Woias, P., and Kockmann, N. (2008) Design and fabrication of MEMS thermoelectric generators with high temperature efficiency. *Sens. Actuators, A*, **145–146**, 423–429.
- 23 Jacquot, A. *et al.*, 2002. Fabrication and Modeling of an In-plane Thermoelectric Micro-generator. Twenty-First International Conference on Thermoelectrics, 2002. Proceedings ICT '02. IEEE, pp. 561–564.
- 24 Kishi, M. *et al.*, 1999. Micro Thermoelectric Modules and Their Application to Wristwatches as an Energy Source. Eighteenth International Conference on Thermoelectrics. Proceedings, ICT'99 (Cat. No.99TH8407). IEEE, pp. 301–307.
- 25 Leonov, V. *et al.* (2007) Thermoelectric converters of human warmth for self-powered wireless sensor nodes. *IEEE Sens. J.*, **7** (5), 650–657.
- 26 Strasser, M. *et al.* (2004) Micromachined CMOS thermoelectric generators as on-chip power supply. *Sens. Actuators, A*, **114** (2–3), 362–370.
- 27 Strasser, M. *et al.* (2002) Miniaturized thermoelectric generators based on poly-Si and poly-SiGe surface micromachining. *Sens. Actuators, A*, **97–98**, 535–542.
- 28 Toriyama, T., Yajima, M. & Sugiyama, S., 2001. Thermoelectric Micro Power Generator Utilizing Self-standing Polysilicon-metal Thermopile. Technical Digest. MEMS 2001. 14th IEEE International Conference on Micro Electro Mechanical Systems (Cat. No.01CH37090). IEEE, pp. 562–565.
- 29 Geballe, T. and Hull, G. (1955) Seebeck effect in silicon. *Phys. Rev.*, **98** (4), 940–947.
- 30 Stranz, A. *et al.* (2013) Thermoelectric properties of high-doped silicon from room temperature to 900 K. *J. Electron. Mater.*, **42** (7), 2381–2387.
- 31 Stranz, A., Waag, A., and Peiner, E. (2013) High-temperature performance of stacked silicon nanowires for thermoelectric power generation. *J. Electron. Mater.*, **42** (7), 2233–2238.
- 32 Vining, C.B. (1991) A model for the high-temperature transport properties of heavily doped n-type silicon–germanium alloys. *J. Appl. Phys.*, **69**, 331–341.

- 33** Glassbrenner, C.J. and Slack, G.A. (1964) Thermal conductivity of silicon and germanium from 3 K to the melting point. *Phys. Rev.*, **134**, A1058–A1069.
- 34** Claudio, T. *et al.* (2014) Nanocrystalline silicon: lattice dynamics and enhanced thermoelectric properties. *Phys. Chem. Chem. Phys.*, **16** (47), 25701–25709.
- 35** Yang, J. and Caillat, T. (2006) Thermoelectric materials for space and automotive power generation. *MRS Bull.*, **31** (03), 224–229.
- 36** Wang, Z. *et al.* (2011) Thermal conductivity of nanocrystalline silicon: Importance of grain size and frequency-dependent mean free paths. *Nano Lett.*, **11** (6), 2206–2213.
- 37** Pernot, G. *et al.* (2010) Precise control of thermal conductivity at the nanoscale through individual phonon-scattering barriers. *Nat. Mater.*, **9** (6), 491–495.
- 38** Henry, A.S. and Chen, G. (2008) Spectral phonon transport properties of silicon based on molecular dynamics simulations and lattice dynamics. *J. Comput. Theor. Nanosci.*, **5** (2), 141–152.
- 39** Zhao, L.-D., Dravid, V.P., and Kanatzidis, M.G. (2014) The panoscopic approach to high performance thermoelectrics. *Energy Environ. Sci.*, **7**, 251.
- 40** Narducci, D., Frabboni, S., and Zianni, X. (2015a) Silicon de novo: energy filtering and enhanced thermoelectric performances of nanocrystalline silicon and silicon alloys. *J. Mater. Chem. C*, **3**, 12176–12185.
- 41** Xie, J. *et al.* (2009) Characterization of heavily doped polysilicon films for CMOS-MEMS thermoelectric power generators. *J. Micromech. Microeng.*, **19**, 125029.
- 42** Vining, C.B., 1988. The Thermoelectric Properties of Boron-doped Silicon and Silicon-Germanium in the As-hot Pressed Conditions, JPL/Calif. Inst. of Tech. Technical Report.
- 43** Seto, J.Y.W. (1975) The electrical properties of polycrystalline silicon films. *J. Appl. Phys.*, **46** (12), 5247–5254 Available at: <http://link.aip.org/link/?JAP/46/5247/1>.
- 44** Narducci, D. *et al.* (2012b) Impact of energy filtering and carrier localization on the thermoelectric properties of granular semiconductors. *J. Solid State Chem.*, **193**, 19–25.
- 45** Narducci, D. *et al.*, 2010. Opportunities and Challenges in the Use of Heavily Doped Polycrystalline Silicon as a Thermoelectric Material. Proc. 8th European Conf. on Thermoelectrics. Como (Italy): CNR, pp. 141–146.
- 46** Narducci, D. *et al.* (2012a) High figures of merit in degenerate semiconductors. Energy filtering by grain boundaries in heavily doped polycrystalline silicon. *AIP Conf. Proc.*, **1449** (1), 311–314.
- 47** Bux, S.K. *et al.* (2009) Nanostructured bulk silicon as an effective thermoelectric material. *Adv. Funct. Mater.*, **19** (15), 2445–2452.
- 48** Narducci, D. *et al.* (2014) Enhancement of the power factor in two-phase silicon-boron nanocrystalline alloys. *Phys. Stat. Sol. (a)*, **1258** (6), 1255–1258.

- 49 Narducci, D. *et al.* (2011) Enhanced thermoelectric properties of strongly degenerate polycrystalline silicon upon second phase segregation. *Mater. Res. Soc. Symp. Proc.*, 1–6, volume 1314.
- 50 Yusufu, A. *et al.* (2014) Bottom-up nanostructured bulk silicon: a practical high-efficiency thermoelectric material. *Nanoscale*, **6** (22), 13921–13927.
- 51 Bachmann, M., Czerner, M., and Heiliger, C. (2012) Ineffectiveness of energy filtering at grain boundaries for thermoelectric materials. *Phys. Rev. B*, **86** (11), 115320.
- 52 Zianni, X. and Narducci, D. (2015) Parametric modeling of energy filtering by energy barriers in thermoelectric nanocomposites. *J. Appl. Phys.*, **117**, 035102.
- 53 Zianni, X., Neophytou, N., and Narducci, D. (2015) Compact model for thermoelectric power factor enhancement by energy barriers in a two-phase composite semiconductor. *Mater. Today: Proc.*, **2** (2), 497–503.
- 54 Bergman, D.J. and Levy, O. (1991) Thermoelectric properties of a composite medium. *J. Appl. Phys.*, **70** (1991), 6821–6833.
- 55 Levy, O. and Bergman, D.J. (1999) Scaling behaviour of the thermopower in a two-component composite near a percolation threshold. *J. Phys. A: Math. Gen.*, **25**, 1875–1884.
- 56 Bergman, D.J. and Fel, L.G. (1999) Enhancement of thermoelectric power factor in composite thermoelectrics. *J. Appl. Phys.*, **85** (May), 8205–8216.
- 57 Neophytou, N. (2015) Prospects of low-dimensional and nanostructured silicon-based thermoelectric materials: findings from theory and simulation. *Eur. Phys. J. B*, **88** (4), 86.
- 58 Pichanusakorn, P. and Bandaru, P. (2010) Nanostructured thermoelectrics. *Mater. Sc. Eng.: R Rep.*, **67** (2–4), 19–63.
- 59 Rowe, D.M. and Bhandari, C.M. (1983) Modern thermoelectrics. London: Holt, Rinehart and Winston. ISBN: 0039104338.
- 60 Huang, M.-J., Weng, C.-C., and Chang, T.-M. (2010) An investigation of the phonon properties of silicon nanowires. *Int. J. Therm. Sci.*, **49** (7), 1095–1102.
- 61 Wagner, R.S. and Ellis, W.C. (1964) Vapor–liquid–solid mechanism of single crystal growth. *Appl. Phys. Lett.*, **4** (5), 89.
- 62 Givargizov, E.I. and Sheftal', N.N. (1971) Morphology of silicon whiskers grown by the VLS-technique. *J. Cryst. Growth*, **9**, 326–329.
- 63 Wagner, R.S. (1970) VLS mechanism of crystal growth, in *Whisker Technology* (ed. A.P. Levitt), Wiley-Interscience, New York, NY, USA, pp. 47–119.
- 64 Hochbaum, A.I. *et al.* (2005) Controlled growth of Si nanowire arrays for device integration. *Nano Lett.*, **5** (3), 457–460.
- 65 Inasawa, S. (2015) In-situ observation of the growth of individual silicon wires in the zinc reduction reaction of  $\text{SiCl}_4$ . *J. Cryst. Growth*, **412**, 109–115.
- 66 Cui, Y. *et al.* (2001) Diameter-controlled synthesis of single-crystal silicon nanowires. *Appl. Phys. Lett.*, **78** (15), 2214.
- 67 Gadea, G. *et al.* (2015) Towards a full integration of vertically aligned silicon nanowires in MEMS using silane as a precursor. *Nanotechnology*, **26** (19), 195302.

- 68** Hofmann, S. *et al.* (2008) Ledge-flow-controlled catalyst interface dynamics during Si nanowire growth. *Nat. Mater.*, **7** (5), 372–375.
- 69** Westwater, J. (1997) Growth of silicon nanowires via gold/silane vapor–liquid–solid reaction. *J. Vacuum Sci. Technol. B: Microelectr. Nanometer Struct.*, **15** (3), 554.
- 70** Wu, Y. *et al.* (2004) Controlled growth and structures of molecular-scale silicon nanowires. *Nano Lett.*, **4** (3), 433–436.
- 71** Hamidinezhad, H., Akbar Ashkarran, A., and Abdul-Malek, Z. (2014) Vertically-tapered silicon nanowire arrays prepared by plasma enhanced chemical vapor deposition: synthesis, structural characterization and photoluminescence. *Mater. Sci. Semicond. Process.*, **27**, 26–32.
- 72** Hofmann, S. *et al.* (2003) Gold catalyzed growth of silicon nanowires by plasma enhanced chemical vapor deposition. *J. Appl. Phys.*, **94** (9), 6005.
- 73** Iacopi, F. *et al.* (2007) Plasma-enhanced chemical vapour deposition growth of Si nanowires with low melting point metal catalysts: an effective alternative to Au-mediated growth. *Nanotechnology*, **18** (50), 505307.
- 74** Fasoli, A. and Milne, W.I. (2012) Overview and status of bottom-up silicon nanowire electronics. *Mater. Sci. Semicond. Process.*, **15** (6), 601–614.
- 75** Wallentin, J. and Borgström, M.T. (2011) Doping of semiconductor nanowires. *J. Mater. Res.*, **26** (17), 2142–2156.
- 76** Schmid, H. *et al.* (2009) Doping limits of grown *in situ* doped silicon nanowires using phosphine. *Nano Lett.*, **9** (1), 173–177.
- 77** Das Kanungo, P. *et al.* (2008) Controlled *in situ* boron doping of short silicon nanowires grown by molecular beam epitaxy. *Appl. Phys. Lett.*, **92** (26), 263107.
- 78** Schubert, L. *et al.* (2004) Silicon nanowiskers grown on  $\langle 111 \rangle$ Si substrates by molecular-beam epitaxy. *Appl. Phys. Lett.*, **84** (24), 4968.
- 79** Werner, P. *et al.* (2006) On the formation of Si nanowires by molecular beam epitaxy. *Int. J. Mater. Res.*, **97** (7), 1008–1015.
- 80** Eisenhawer, B. *et al.* (2011) Growth of doped silicon nanowires by pulsed laser deposition and their analysis by electron beam induced current imaging. *Nanotechnology*, **22** (7), 075706.
- 81** Morales, A. and Lieber, C. (1998) A laser ablation method for the synthesis of crystalline semiconductor nanowires. *Science (New York, N.Y.)*, **279** (5348), 208–211.
- 82** Dong, A., Tang, R., and Buhro, W.E. (2007) Solution-based growth and structural characterization of homo- and heterobranched semiconductor nanowires. *J. Am. Chem. Soc.*, **129** (40), 12254–62.
- 83** Heitsch, A.T. *et al.* (2008) Solution-liquid–solid (SLS) growth of silicon nanowires. *J. Am. Chem. Soc.*, **130**, 5436–5437.
- 84** Holmes, J. *et al.* (2000) Control of thickness and orientation of solution-grown silicon nanowires. *Science (New York, N.Y.)*, **287** (5457), 1471–1473.

- 85 Ho, T.-W. and Hong, F.C.-N. (2012) A novel method to grow vertically aligned silicon nanowires on Si (1 1 1) and their optical absorption. *J. Nanomater.*, **2012**, 1–9.
- 86 Latu-Romain, L. *et al.* (2008) Growth parameters and shape specific synthesis of silicon nanowires by the VLS method. *J. Nanopart. Res.*, **10** (8), 1287–1291.
- 87 Lew, K.-K. and Redwing, J.M. (2003) Growth characteristics of silicon nanowires synthesized by vapor–liquid–solid growth in nanoporous alumina templates. *J. Cryst. Growth*, **254** (1–2), 14–22.
- 88 Morin, C. *et al.* (2011) Patterned growth of high aspect ratio silicon wire arrays at moderate temperature. *J. Cryst. Growth*, **321** (1), 151–156.
- 89 Salhi, B., Grandidier, B., and Boukherroub, R. (2006) Controlled growth of silicon nanowires on silicon surfaces. *J. Electroceram.*, **16** (1), 15–21.
- 90 Stelzner, T. *et al.* (2007) Silicon nanowire synthesis on metal implanted silicon substrates. *Nucl. Instrum. Meth. Phys. Res. Sect. B: Beam Interact. Mater. Atoms*, **257** (1–2), 172–176.
- 91 Thissandier, F. *et al.* (2014) Tuning silicon nanowires doping level and morphology for highly efficient micro-supercapacitors. *Nano Energy*, **5**, 20–27.
- 92 Yuan, G. *et al.* (2009) Synthesis and photoelectrochemical study of vertically aligned silicon nanowire arrays. *Angew. Chem.*, **121** (51), 9860–9864.
- 93 Yao, Y. and Fan, S. (2007) Si nanowires synthesized with Cu catalyst. *Mater. Lett.*, **61** (1), 177–181.
- 94 Osada, Y. (1979) Growth and structure of silicon fibers. *J. Electrochem. Soc.*, **126** (1), 31.
- 95 Wang, Y. *et al.* (2006) Epitaxial growth of silicon nanowires using an aluminium catalyst. *Nat. Nanotechnol.*, **1** (3), 186–189.
- 96 Whang, S.-J. *et al.* (2007) B-doping of vapour–liquid–solid grown Au-catalysed and Al-catalysed Si nanowires: effects of B 2 H 6 gas during Si nanowire growth and B-doping by a post-synthesis in situ plasma process. *Nanotechnology*, **18** (27), 275302.
- 97 Weber, L. (2002) Equilibrium solid solubility of silicon in silver. *Metall. Mater. Trans. A*, **33** (4), 1145–1150.
- 98 Wang, Z.W. and Li, Z.Y. (2009) Structures and energetics of indium-catalyzed silicon nanowires. *Nano Lett.*, **9** (4), 1467–1471.
- 99 Sharma, S. and Sunkara, M.K. (2004) Direct synthesis of single-crystalline silicon nanowires using molten gallium and silane plasma. *Nanotechnology*, **15** (1), 130–134.
- 100 Chung, S.-W., Yu, J.-Y., and Heath, J.R. (2000) Silicon nanowire devices. *Appl. Phys. Lett.*, **76** (15), 2068.
- 101 Yu, J.-Y., Chung, S.-W., and Heath, J.R. (2000) Silicon nanowires: preparation, device fabrication, and transport properties. *J. Phys. Chem. B*, **104** (50), 11864–11870.

- 102 Morales, A.M. (1998) A laser ablation method for the synthesis of crystalline semiconductor nanowires. *Science*, **279** (5348), 208–211.
- 103 Weyher, J. (1978) Some notes on the growth kinetics and morphology of VLS silicon crystals grown with platinum and gold as liquid-forming agents. *J. Cryst. Growth*, **43** (2), 235–244.
- 104 Kamins, T.I. *et al.* (2000) Chemical vapor deposition of Si nanowires nucleated by TiSi<sub>2</sub> islands on Si. *Appl. Phys. Lett.*, **76** (5), 562.
- 105 Doerk, G.S. *et al.* (2011) Micellar block copolymer templated galvanic displacement for epitaxial nanowire device integration. *J. Mater. Chem.*, **21** (24), 8807.
- 106 Gao, D. *et al.* (2005) Selective growth of Si nanowire arrays via galvanic displacement processes in water-in-oil microemulsions. *J. Am. Chem. Soc.*, **127** (13), 4574–4575.
- 107 Magagnin, L. *et al.* (2002) Selective deposition of gold nanoclusters on silicon by a galvanic displacement process. *Microelectron. Eng.*, **64** (1–4), 479–485.
- 108 Calaza, C. *et al.* (2015) Bottom-up silicon nanowire arrays for thermoelectric harvesting. *Mater. Today: Proc.*, **2** (2), 675–679.
- 109 Ferri, M. *et al.* (2011) Ultradense silicon nanowire arrays produced via top-down planar technology. *Microelectron. Eng.*, **88** (6), 877–881.
- 110 Xie, J., Lee, C., and Feng, H. (2010) Design, fabrication, and characterization of CMOS MEMS-Based thermoelectric power generators. *J. Microelectromech. Syst.*, **19** (2), 317–324.
- 111 Strasser, M. *et al.*, 2003. Micromachined CMOS Thermoelectric Generators as On-chip Power Supply. TRANSDUCERS 2003 - 12th International Conference on Solid-State Sensors, Actuators and Microsystems, Digest of Technical Papers. pp. 45–48.
- 112 Su, J. *et al.* (2010) A batch process micromachined thermoelectric energy harvester: fabrication and characterization. *J. Micromech. Microeng.*, **20**, 104005.
- 113 Su, J. *et al.* (2008) Process development on large-topography microstructures for thermoelectric energy harvesters. *Proc. Power MEMS*, **2008**, 365.
- 114 Yu, X. *et al.* (2012) CMOS MEMS-based thermoelectric generator with an efficient heat dissipation path. *J. Micromech. Microeng.*, **22** (10), 105011.
- 115 Dávila, D. *et al.* (2012) Monolithically integrated thermoelectric energy harvester based on silicon nanowire arrays for powering micro/nanodevices. *Nano Energy*, **1** (6), 812–819.
- 116 Kwong, D.-L. *et al.* (2012) Vertical silicon nanowire platform for low power electronics and clean energy applications. *J. Nanotechnol.*, **2012**, 1–21.
- 117 Li, Y. *et al.* (2011) Chip-level thermoelectric power generators based on high-density silicon nanowire array prepared with top-down CMOS technology. *IEEE Electron Device Lett.*, **32** (5), 674–676.
- 118 Li, Y. *et al.* (2012) Improved vertical silicon nanowire based thermoelectric power generator with polyimide filling. *IEEE Electron Device Lett.*, **33** (5), 715–717.

- 119 Li, Y. *et al.* (2012) Top-down silicon nanowire-based thermoelectric generator: design and characterization. *J. Electron. Mater.*, **41** (6), 989–992.
- 120 Stranz, A. *et al.* (2011) Measurements of thermoelectric properties of silicon pillars. *Sens. Actuators, A*, **171** (1), 48–53.
- 121 Stranz, A. *et al.* (2011) Nanowire silicon as a material for thermoelectric energy conversion. *Microsyst. Technol.*, **18** (7–8), 857–862.
- 122 Stranz, A., Waag, A., and Peiner, E. (2011) Thermal characterization of vertical silicon nanowires. *J. Mater. Res.*, **26** (15), 1958–1962.

## 5

# Techniques for Characterizing Thermoelectric Materials: Methods and the Challenge of Consistency

Hans-Fridtjof Pernau

Fraunhofer Institute for Physical Measurement Techniques, IPM, Department GP/TMS, Heidenhofstr. 8, 79110 Freiburg, Germany

## 5.1 Introduction – Hitting the Target

This chapter will focus on the characterization of thermoelectric materials, especially the correct determination of the  $ZT$ -value.

And here the story starts: “What’s correct?”

In technical terms, it has to be called *accurate*. Accuracy and its technical and scientific meaning are defined by ISO norm 5725 [1]. It consists of two parts: the precision and the trueness. Both have to be within specified limits to obtain an accurate result. Two examples for poor accuracy can be seen in Figure 5.1. In our case, achieving reasonable accuracy is extremely difficult as the parameters that determine the  $ZT$ -value and thereby the quality of a thermoelectric material are linked by the Onsager–Callen relation:

$$\begin{bmatrix} \vec{J} \\ \vec{\dot{Q}} \end{bmatrix} = \begin{bmatrix} \sigma & S\sigma \\ TS\sigma & \lambda \end{bmatrix} \begin{bmatrix} \vec{E} \\ -\vec{\nabla} T \end{bmatrix}$$

The Onsager–Callen relation combines the electrical flux  $\vec{J}$  and the thermal flux  $\vec{\dot{Q}}$ , which are driven by the electrical field  $\vec{E}$  and the thermal gradient  $-\vec{\nabla} T$ . Beside this, the Seebeck coefficient  $S$ , the electrical conductivity  $\sigma$ , and the thermal conductivity  $\lambda$  are determined by the number and mobility of the carriers. Good metals with a high number of free electrons have a low Seebeck coefficient but a high thermal conductivity. We will have a closer look at this in the next section.

Because of this relationship between the important material parameters a small change in the external condition, for example, the temperature gradient, will lead to changed current flux conditions and thereby a change in all parameters to be determined. In general, this would make it necessary to determine all parameters within the same measurement under the exact same conditions to obtain the best results. In the case of separate measurements each parameter has to be fitted carefully over temperature to evaluate the  $ZT$ -value at a certain point.

The next section will go back to basics to explain the difficulties that arise from the experimental point of view during the determination of the  $ZT$ -value.

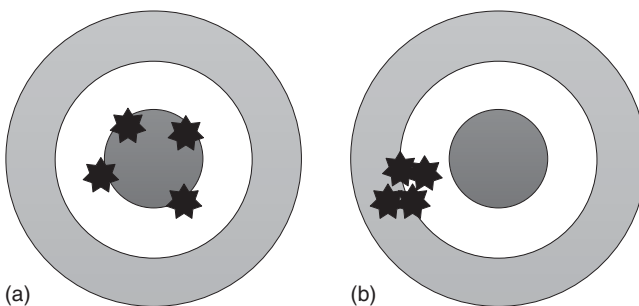


**Figure 5.1** (a) The trueness is good but the precision is poor. (b) The precision is good but not the trueness. In both cases the accuracy is low.

## 5.2 Thermal Transport in Gases and Solid-State Materials

Thermal transport in matter is realized by three different processes: radiation, convection, and conductive heat transport. Depending on the system, a combination of these will cause the total heat transport.

*Heat transport via radiation* depends on the temperature of a body and its surrounding. The thermal flux emitted by a body is described by the Stefan–Boltzmann law:

$$\dot{Q} = \epsilon \sigma A T^4$$

$\epsilon$  is the emissivity of the surface of the body and is, in general, wavelength, surface texture, and structure dependent. A perfect mirror has an emissivity of 0 and an ideal black body radiator, 1, at all wavelengths. Real surfaces, however, are somewhere in between, typical ceramics and thermoelectric materials are in the range of 0.8–0.9, while blank metal surfaces are rather closer to 0. Radiation can transport heat in a vacuum as well as in media such as gases or liquids. Thus, preventing radiation losses becomes rather crucial at high temperatures or more generally where there is a high temperature gradient between the object and its surrounding. The emissivity at a given wavelength is equal to the absorption, for example, when you are on the beach with a cold glass of beer it radiates heat to the surrounding but also receives radiation, for example, from the shining sun and the hot sand. In sum, the cold beer will heat up even if it is in weak direct conductive contact to warm objects.

$$\dot{Q} = \epsilon_b \sigma A_b (T_b^4 - T_s^4)$$

$\sigma$  is the Stefan–Boltzmann constant ( $5.67 \times 10^{-8} \text{ W/m}^2/\text{K}^4$ ). If the surrounding is more confined (e.g., a small box) this equation will change according to the exact geometry of the body as well as the surrounding.

Radiative heat transport does not involve matter; thus, no matter is exchanged with the surrounding.

*Heat transport via convection* uses mass and thereby matter transport, for example, of heated gas to transport heat away from a hot solid object,

for example, an open chimney. Convective transport therefore needs an intermediation media such as a gas or liquid to transport heat from one object to another. Therefore, mechanical confinement of free spaces (e.g., filling up with wool) or the use of vacuum can hinder convective losses rather efficiently. Calculation of these losses strongly depends on the geometry and surface structure, and even the microstructure of the involved objects and is therefore rather difficult to evaluate. In general, the conducted heat is given by:

$$\dot{Q} = h \cdot A \cdot \Delta T$$

It is dependent on the surface area  $A$ , the temperature gradient  $\Delta T$ , and the transfer coefficient  $h$ . This coefficient depends, as mentioned before, on the structure and geometry of the surface as well as the properties of the heat transporting medium. These are its speed  $u$ , the viscosity  $\nu$ , the heat capacity  $c$ , and the thermal conductivity  $\lambda$ . These properties together form the important parameters, the Nusselt, Prandl, Grashof, and the Reynolds numbers. These numbers will differ in the case of laminar or turbulent fluxes. In the following, these parameters are given for laminar natural convection on a flat wall using the medium air at standard ambient conditions. The Nusselt number determines how well the heat is transferred from the surface with length  $L$  to its surrounding:

$$Nu(T) = \frac{h \cdot L}{\lambda} = \left\{ 0.825 + \frac{0.387 Re^{\frac{1}{6}}}{\left( 1 + \left( \frac{0.492}{Pr} \right)^{\frac{9}{16}} \right)^{\frac{8}{27}}} \right\}$$

The exchange of heat between the surface and the medium takes place only within a small layer close to the surface. The Prandl number is an indicator of the layer thickness:

$$Pr = \frac{\nu}{\alpha} \approx 0.71$$

with  $\alpha$  the thermal diffusivity. Around room temperature, the Prandl number can be seen as constant.

The Grashof number compares the gravity, the viscous forces, and the flotation force in the medium. This number is rather critical for the total calculation:

$$Gr(T) = \frac{g \cdot \beta \cdot (T_K - T_u) \cdot L^3}{\nu^2} \quad \text{with } \beta = \frac{2}{(T_K + T_u)}$$

The last important number is the Reynolds number, the product of Grashof and Prandl numbers. If it is larger than  $10^9$ , then the flow is no longer laminar but turbulent; in the case of free convection around room temperature it is about a factor of 10 smaller than this limit.

$$Re = Gr \cdot Pr$$

These formulas give a first feeling about the strength of convective heat transport. It may be necessary to use an effective surface area to get more precise results. The equation will change dramatically in the case of forced convection.

A realistic determination of convective losses can be calculated using finite element simulations.

When a new measurement setup is constructed, one should plan tests to measure convective losses and if necessary compare them with simulations as they will form a large part within the uncertainty budget of the experiment [2].

*Conductive heat transport* is also a matter free way to transfer heat from one point to another but it needs the matter itself.

In a gas or a liquid the motion of the molecules is determined by the absolute temperature. An increased temperature at one point in the gas will lead to faster vibrating molecules in the surrounding. By collisions the gas molecules transfer this higher velocity to other molecules and so the heat is spread in the gas from the original heat source point. But in median no matter is transferred.

In a solid bulk material the position of the atoms/molecules is much more confined; thus, they will only vibrate around their fixed position (as long as the solid does not melt). The movement of the atoms is comparable to the oscillation of a guitar string. These oscillations are called *phonons* and will be important to reach a high  $ZT$ .

If we assume that a bulk material can be seen as a perfect crystal with a size  $L^3$  and a distance between the atoms of  $d$ , there is the largest wavelength of  $2L$  for very low temperatures and a shorter wavelength of  $2d$  for very high temperatures. Within these limits, the oscillation modes are thermally activated and thereby the heat capacity ( $C_v$ ) increases proportional to  $T^3$ . The maximum heat capacity is given by the Dulong–Petit law as

$$\lim_{T \rightarrow \infty} C_v = 6 \cdot \frac{1}{2} \cdot N_A \cdot k_b \cdot T = 3R$$

In general, the conducted heat through a surface area  $A$  and within a length of  $L$  in a gas, liquid, or solid bulk material can be written as

$$\dot{Q} = \overleftrightarrow{\lambda} \cdot \frac{A}{L} \cdot \vec{\Delta T}$$

Within a solid the thermal conductivity may be a tensor and thereby anisotropic for the different directions.

A very important difference arises as the solid becomes electrically conductive; thus free carriers are present inside the solid material, which can be described as a carrier gas. Therefore, the thermal conductivity will be a combination of two parts, first of the phonons and second of the carrier gas:

$$\lambda = \lambda_{ph} + \lambda_c.$$

As has been shown in chapter 2, one way to enhance the  $ZT$ -value is to reduce the phonon part without influencing the carrier part. This is due to the fact that the carrier part is directly linked to the electrical properties of the material:

$$\lambda_c = L \cdot T \cdot nq\mu = L \cdot T \cdot \sigma$$

The linking elements are the Lorentz number, which is a material parameter and not a constant, and the temperature. This leads directly to the next section, the combined parameter  $ZT$ -value and how to measure it.

### 5.3 The Combined Parameter ZT-Value

$$ZT = \frac{S^2 \sigma}{\lambda} T$$

The  $ZT$ -value consists of the Seebeck coefficient  $S$  squared, the electrical conductivity  $\sigma$ , and the thermal conductivity  $\lambda$ , and  $T$  the absolute temperature.  $ZT$  is a unit free parameter that combines all important parameters for a good thermoelectric material as described by Altenkirch [3] in 1909.

The Seebeck coefficient should be as high as in a semiconductor:

$$S = \frac{8\pi^2 k_b^2}{3q h^2} m^* T \left( \frac{\pi}{3n} \right)^{\frac{2}{3}}$$

Here,  $q$  is the carrier charge,  $h$  the Planck constant,  $m^*$  the effective mass of the carriers, and  $n$  the charge carrier density. The electrical conductivity should be as high as in a metal:

$$\sigma = n q \mu = \frac{n q^2 \pi}{m^*}$$

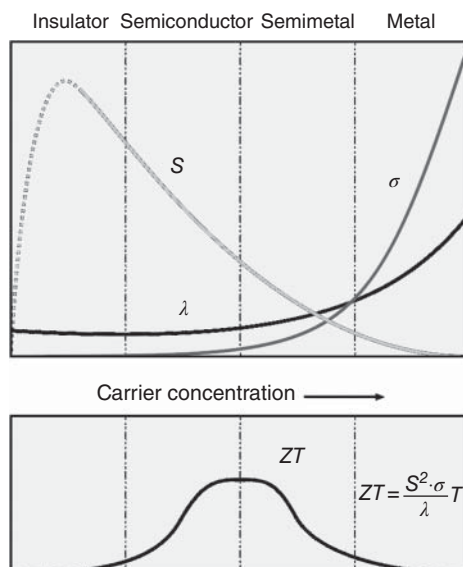
and the thermal conductivity should be as low as in a glass:

$$\lambda = \lambda_{ph} + \lambda_c = \lambda_{ph} + L \cdot T \cdot n q \mu = \lambda_{ph} + L \cdot T \cdot \sigma$$

As can be seen, all parts of the  $ZT$ -value directly depend on the carrier properties, the carrier concentration  $n$  and the mobility  $\mu$ . This dependency is illustrated within Figure 5.2. For a certain temperature there will be an optimum point to reach maximum  $ZT$ -value.

Beside this optimization the introduction of nanostructures inside a bulk material is used to reduce the phonon part of the thermal conductivity

**Figure 5.2** All parts of the  $ZT$ -value depend on the carrier properties, especially the carrier concentration. Therefore, one will find an optimum carrier concentration level for a certain temperature where the  $ZT$ -value is at its maximum. Please keep in mind that this point is strongly temperature dependent; thus a material has to be optimized at its desired operation temperature.



[4–6] without hindering the electronic parameters as suggested by Hicks and Dresselhaus [7] in 1993.

Theoretically, this will lead to a higher  $ZT$ -value, which has to be determined in different experiments. But this enhancement of the  $ZT$ -value is often connected with an introduction of anisotropy into the material [8, 9] so the determination may become rather challenging. Within the next section this challenge to determine the parameters of the  $ZT$ -value will be discussed. The starting point will be, on first consideration, the easiest parameter, the electrical conductivity.

### 5.3.1 Electrical Conductivity

Electrical conductivity seems to be the easiest parameter as theoretically only Ohms law has to be taken into account.

$$U = R \cdot I; \rho = R \cdot \frac{A}{l}; \sigma = \frac{1}{\rho}$$

By applying a current  $I$  to a conducting strip with length  $l$  and cross section  $A$  one will measure a voltage difference  $U$  and thereby a resistance  $R$ . The specific resistivity  $\rho$  and the specific conductivity  $\sigma$  can be easily calculated in this case.

Unfortunately, real measurement equipments have test wires that have a resistance; so the so-called four-wire technique has to be used to compensate in order to measure the real numbers (see Figure 5.3a). To measure the sheet resistance  $R_{sq}$  of a thin quasi infinite sample the contact arrangement shown in Figure 5.3b is used. The specific resistance can be calculated using the current  $I$  and the measured voltage  $V$  as

$$R_{sq} = \frac{\pi}{\ln 2} \cdot \frac{U}{I}; \rho = d \cdot R_{sq}$$

Here,  $d$  is the thickness of the measured sheet, which should be much smaller than the distance  $s$  between the contact tips. The contact tips have to be equidistant; otherwise, the formula for the sheet resistance changes. Analytic formulas for various geometrical arrangements have been calculated by Smits [10] and Valdes [11].

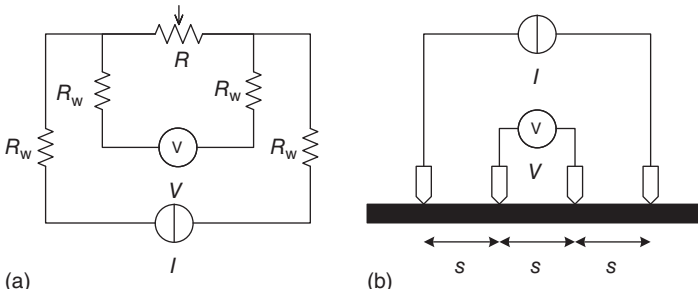


**Figure 5.3** (a) Four-wire-technique to measure the real resistance of a resistive element avoiding the resistance of the test wires  $R_{tw}$ . (b) To measure the resistivity of a thin sheet one can use the four-point method. The sheet has to be thin and compared to the distance  $s$  between the contact points quasi infinite. Valdes and Smits calculated analytical formulas to measure the sheet resistance in other geometrical situations [10, 11].

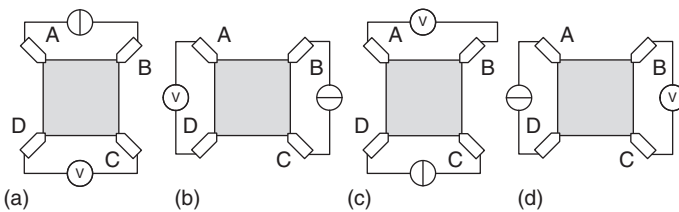


**Figure 5.4** Arrangement of the contact for the van der Pauw measurement of the specific resistance. For a complete measurement all four contact configurations have to be measured. If a direct current (DC) is used, all configurations have to be measured in both polarities.

Another common arrangement to measure the specific electrical resistance of a sample is the so-called van der Pauw geometry. In most cases it is used as the original experiment in Hall measurement experiments [12, 13]. The contact arrangement for a thin square-shaped sample can be seen in Figure 5.4.

In general, the shape of the sample can be arbitrary but the contacts have to be arranged at its edges. To obtain the specific resistance at least two measurements have to be done. First, one has to apply the current between contacts A and B and measure the voltage between contacts C and D. Second, the current is applied between B and C and the voltage measured between D and A. This will lead to two resistances, which can be used to calculate the specific resistance as follows:

$$R_{AB,CD} = \frac{U_{CD}}{I_{AB}};$$

$$R_{BC,DA} = \frac{U_{DA}}{I_{BC}} \Rightarrow \exp\left(-\frac{\pi d}{\rho} \cdot R_{AB,CD}\right) + \exp\left(-\frac{\pi d}{\rho} \cdot R_{BC,DA}\right) = 1$$

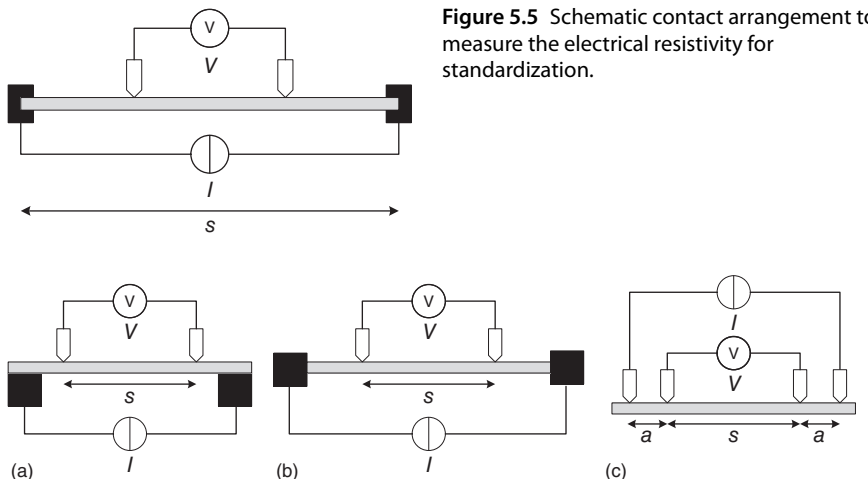
This equation can only be evaluated iteratively; an estimation formula for the specific resistance is the following:

$$\rho = \frac{\pi d}{\ln 2} \cdot \frac{R_{AB,CD} + R_{BC,DA}}{2} \cdot f$$

The factor  $f$ , which can be found in the original publications by van der Pauw [12, 13], is itself dependent on the measured resistances. The thickness of the sample has to be small compared to the distance between the contact tips as in the four-point geometry. For a complete measurement all four contact configurations have to be measured. If a direct current (DC) is used, all configurations have to be measured in both polarities. All four evaluated specific resistances should be equal; the measurement result is the average value of all four.

Unfortunately, none of the previously shown methods is really used in the standardized measurements at the national metrological institutes such as the NPL, NIST, or PTB. Between 2000 and 2003, NPL and PTB had an FP5 project (grant number G6RD-CT-2000-00210) where the van der Pauw method was compared to the used eddy current and bar measurement methods.

Most national metrological institutes use the bar measurement method (see Figure 5.5) [14]. A long bar (10–30 cm length) is clamped on both ends to the current leads. Two razor blade electrodes arranged in a fixed distance are put on the surface and the voltage between both is measured. To stabilize the



temperature during the measurement the whole setup can be submerged in an oil bath. Using such big samples reduces the influence of geometry uncertainties as well as inhomogeneities within the reference material.

For most thermoelectric materials, however, the maximum sample size is limited to a few tens of millimeters in each direction; therefore, beside the van der Pauw method there are three typical measurement arrangements used as can be seen in Figure 5.6.

The highest uncertainties in all cases arise from the error in the determination of the sample geometry as well as the position of sample clamps, supports, and the measurement tips. Typically, the size of a sample can be determined with an uncertainty of  $\pm 10 \mu\text{m}$ , and the position of the current inputs with an uncertainty between  $\pm 50$  and  $\pm 100 \mu\text{m}$ . The highest uncertainty arises typically from the voltage probes as these are not needles (to form a point contact) but thermoelements with a ball-shaped head with up to  $0.5 \text{ mm}$  radius. Some setups use shielded thermoelements; also in this case typical heads have a radius of about  $0.5 \text{ mm}$ . As will be shown in the next section, the heads may be flattened at the contact point to the sample to enhance the thermal contact between the sample and the thermoelements. Therefore, the geometrical uncertainty budget can rise up to  $\pm 5\%$  [15, 16]. Using optimized mechanical guidance of the current and voltage probes will improve the repeatability [17]. In all cases, calibration functions similar to those of Smits and Valdes have to be used to evaluate the resistance from the measured voltage and current data. Using the van der Pauw method reduces the uncertainty with respect to the determination of the thickness of the sample. Recent round robin tests have shown that these rather larger uncertainties are typical numbers [18, 19]. Fortunately, even for

thin films and semiconductors there are measurement standards available to validate measurement setups at room temperature [20–22]. Some alloys such as constantan or pure metals such as nickel [23] offer the possibility to validate measurement setups also at high temperatures.

It should be mentioned that a thermoelectric material cannot be measured within a classic DC measurement. Owing to the large Peltier effect, compared to a normal metal, applying a DC voltage will lead to an additional temperature shift and thereby voltage shift. This shift can be utilized to measure  $ZT$  directly as will be discussed later [24, 25]. To avoid this shift a so-called DC delta mode measurement can be done [26]. DC current is not applied constantly to the sample but only in short pulses, and the polarity is also changed. Using different currents a quasi-current–voltage-slope (I–V curve) can be obtained. The other possibility is to use a real AC (alternating current) measurement and measure an I–V curve. The inverse slope of the I–V-curve represents the differential ohmic resistance at 0 V.

### 5.3.2 Seebeck Coefficient

As shown in the last section even the “easy” parameter electrical resistivity may have some critical points; the Seebeck coefficient will be even more challenging as small voltages of a few hundred microvolts and small temperature differences of a few Kelvins have to be measured accurately. In general, the Seebeck coefficient is given by

$$S = \frac{\partial U}{\partial T} \approx \frac{\Delta U}{\Delta T}$$

Most commercially available high temperature Seebeck measurement setups use one of the three basic arrangements shown in Figure 5.7 [17, 27–30]. The sample to be investigated is placed between or on-top of two separate sample supports where it is held in place by an applied force (clamped or by installing a weight).

In configuration (a), the sample is clamped between the two current inputs. Within one of the inputs a heater ( $H$ ) is installed, which will introduce a

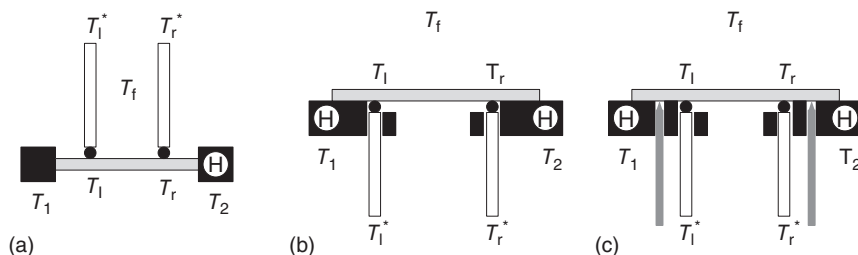


**Figure 5.7** In configuration (a) the sample is clamped between the two current inputs. Within one of the inputs a heater ( $H$ ) is installed, which will introduce a temperature gradient on the sample for measuring the Seebeck coefficient. Configurations (b) and (c) use the same general arrangement for the thermocouples but different ways to introduce the current into the sample for a parallel measurement of the resistivity. In configuration (b) the current is introduced via the sample supports. Configuration (c) uses needles to introduce the current into the sample.

temperature gradient on the sample for measuring the Seebeck coefficient. Long thermocouples are used as voltage probes for the resistivity measurement as well to measure the temperature gradient and the arising voltage difference.

Configurations (b) and (c) use the same general arrangement for the thermoelements but different ways to introduce the current into the sample for a parallel measurement of the resistivity. In configuration (b), the current is introduced via the sample supports. Configuration (c) uses needles to introduce the current into the sample. In both cases, the two sample supports have an installed heater so that a temperature gradient can be applied in two directions. The thermocouples are guided through the sample supports so that they are in thermal contact not only to the sample but also to the supports.

Let us take a closer look at all arrangements during the measurement of the Seebeck coefficient. In all cases the setups are placed within a furnace to thermalize the sample to a set temperature  $T_f$ . If the right heater is switched on the temperatures will rise and in general we will reach the situation of

$$T_f < T_1 < T_2$$

In the sample, we will find the situation

$$T_f < T_1 < T_l < T_r < T_2$$

From the difference  $|T_l - T_r| = \Delta T_s$  will arise the thermovoltage  $\Delta U$ . The main problem is the measured temperature, which will be different from the temperature inside the sample. One may ask “why that?”

In the case of configuration (a) the thermocouples are in contact with the sample but via radiation and convection, also with the lower furnace temperature. The larger the difference between the real sample temperature and the furnace is, the more the measured temperature is lowered. Thus the measured temperature in the left thermocouple is lowered by  $\delta$  and that in the right by  $\delta' > \delta$ . Therefore, the measured temperature difference will be smaller than the real:

$$\Delta T_m = |T_l^* - T_r^*| < \Delta T_s$$

This effect is sometimes called *cold finger effect* [16]. If the thermal contact between the sample and the thermocouples is good this effect will be small but it will result in a slightly bigger measured Seebeck coefficient than the real one [15]. To reduce this effect the contact area, which is theoretically a point, can be enlarged by flattening the thermocouple ball, but this will lead to a higher uncertainty in the resistance measurement as mentioned in the previous section.

In configurations (b) and (c), the thermocouples are also in thermal contact with the sample supports and thereby with the heater. The measured temperature of the two thermocouples will therefore be closer to the temperature within the sample. Because of the contact to the heater the measured temperature difference will be slightly larger than the real one and therefore the measured Seebeck coefficient will be smaller than the real one. In all cases, the effect will be stronger for thinner samples than for big bulky ones. Also in the case of a weak thermal contact between the sample and thermocouples this effects will be larger, but in case (b)/(c) it is smaller than in case (a) and the Seebeck coefficient will not be overestimated [18, 19, 27, 31]. Nevertheless, one has to consider an uncertainty between

5% and 8% for the measurement of the Seebeck coefficient [17, 27–29]. All measurement setups allow the simultaneous measurement of both the Seebeck coefficient and the electrical conductivity in the same direction within the sample.

In a close collaboration between Fraunhofer IPM and the PTB (German equivalent to NIST or NPL) in Berlin a Seebeck measurement system was developed that showed reduced absolute errors below 2  $\mu\text{V}$ . It utilizes the Seebeck measurement procedure published by Boffoue *et al.* [31] (arrangement according to Figure 5.7c) using a transient determination of the Seebeck coefficient. By using this procedure it is possible to assess the measured data, for example, due to loss of thermal contact during the measurement [17, 27, 28, 32]. This system is now used by the PTB to develop reference samples for the Seebeck coefficient [28, 32].

Within the last few years, reference samples have been developed by NIST and PTB, which can be obtained in various geometries fitting to most commercial measurement setups [28, 32, 33]. In addition, pure nickel or thermoelement materials such as chromel or alumel can be used to validate measurement systems [23, 31] but the Seebeck coefficient is much smaller than within real thermoelectric samples. For more information, please check Mackey *et al.* who published a detailed review on uncertainties that arise during the power factor measurement [15, 16].

In case of thin films no reference samples are available at present. This may be due to the fact that thin film samples are much more delicate in their reaction to air and at high temperatures. Experiences from the laboratory show that this is a real problem. At the moment, an internal round robin test on thin film samples is running in the European FP7-Projekt NanoCaTe (Grant Number: 604647).

### 5.3.3 Thermal Conductivity

For the determination of thermal conductivity there are several methods available. The most commonly used is the LFA (laser flash analyze or laser flash method). Also very common, especially for thin film samples, is the so-called 3 Omega method, and last the TDTR (time domain thermoreflectance method). In the following, all three will be presented briefly.

The *LFA method* measures the passage time of a heat pulse through a flat disc sample. A schematic drawing can be seen in Figure 5.8. The complete setup is placed in a controlled thermal surrounding such as a furnace or a thermostat. An infrared laser shoots a flash on the lower face of the sample. On the upper face of the sample an infrared detector measures the time ( $t$ ) and the amount of heat coming out of the sample. So the first parameter detected by the LFA method is not the thermal conductivity but the temperature conductivity [34–36]

$$\alpha = 0.1388 \cdot \frac{d^2}{t_{\frac{1}{2}}} = \frac{\lambda}{\rho \cdot C_p}$$

To obtain the thermal conductivity from this measurement the density  $\rho$  as well as the heat capacity  $C_p$  is required. They have to be measured separately via a differential calorimetry and a dilatometry measurement or a reference sample with known properties can be measured in comparison within the same experiment. Therefore, the reference sample as well as the sample to be measured should

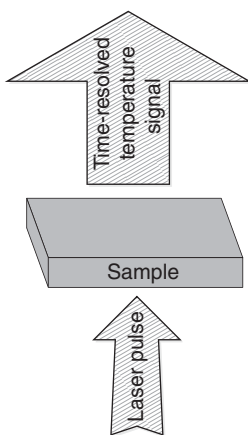


**Figure 5.8** Schematic diagram of the LFA method. A disc sample is placed within a controlled thermal surrounding. An infrared laser pulse is irradiated onto the lower face of the sample. The time the heat pulse needs to propagate to the upper face of the sample is measured with an infrared detector.

have the same size and thickness ( $d$ ). To ensure equal optical behaviors both have to be coated in the same way, for example, using graphite spray coating. By comparing the time-dependent heat flux curves measured on both samples the thermal conductivity can be calculated.

For the accuracy of this measurement the coating as also the sample shape are critical parameters as they will directly affect the result. Samples have to be cut and polished with parallel surfaces. A typical error for this comparative measurement is 5–8%. Experience from the laboratory shows that this is equal to or sometimes even better than the separate measurement of all required parameters with differential scanning calorimetry and dilatometry.

The LFA method is well established for bulk and thick film samples; for samples in the nanometer range other methods may be more suitable.

One of these methods is the *TDTR measurement*. A basic scheme can be seen in Figure 5.9. It can be used for thin films as well as for bulk samples. The sample has to be covered with a thin film (<100 nm) of aluminum [37]. The surface of the coated sample has to be reflective so the roughness has to be small. The measurement is again an optical method. A high-power heating pulse locally heats up the sample; the heat then propagates into the sample and the underlying substrate. A second laser pulse with much lower energy measures the reflectance

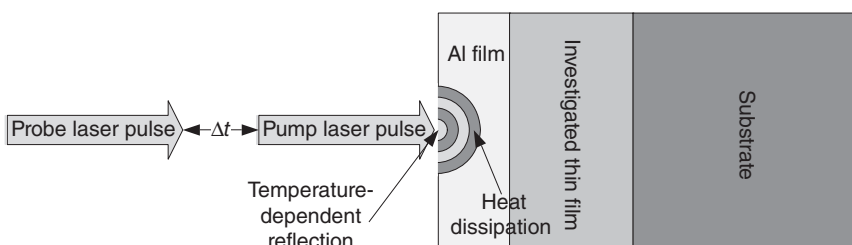


**Figure 5.9** Schematic view on the TDTR method. A laser pulse heats up the surface and a second probe pulse measures the reflectance of the surface, which is a direct indicator of the temperature of the surface. By measuring at different times after the pump pulse, the thermal conductivity can be derived.

of the aluminum surface, which depends on its temperature. Measuring the temperature at different times after the heating pulse allows the thermal conductivity to be calculated. For details please see the publication of Cahill [37]. Typical uncertainties are around 5% but strongly depend on the individual sample.

The last method is the *3 Omega* method [38–40]. A bolometer structure connected to the sample (see Figure 5.10) is used in this measurement setup. An AC current is applied to this structure and the voltage drop is measured via two separate terminals. The signals arising in this system are shown in Figure 5.11.

Applying a heating current with frequency  $\omega$  to the structure will introduce a heating power and thereby a heat flux into the sample with frequency  $2\omega$ . Therefore, the temperature of the sample will oscillate with the same frequency  $2\omega$  as will the resistance of the bolometer. As the voltage is the product of current and resistance one will obtain a complex term

$$U(t) = R(t) \cdot I(t) = R_0(1 + \alpha_R \Delta T \cos(2\omega t + \phi)) \cdot I_0 \cos(\omega t)$$

**Figure 5.10** Basic 3 Omega setup: An AC current is applied to a simple linear bolometer structure and the voltage drop is measured at two separate terminals. The lengths between the voltage terminal and the width and thickness of the strip heater have to be determined precisely.

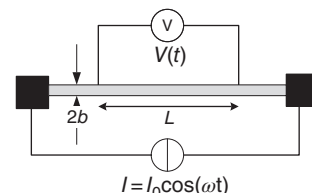
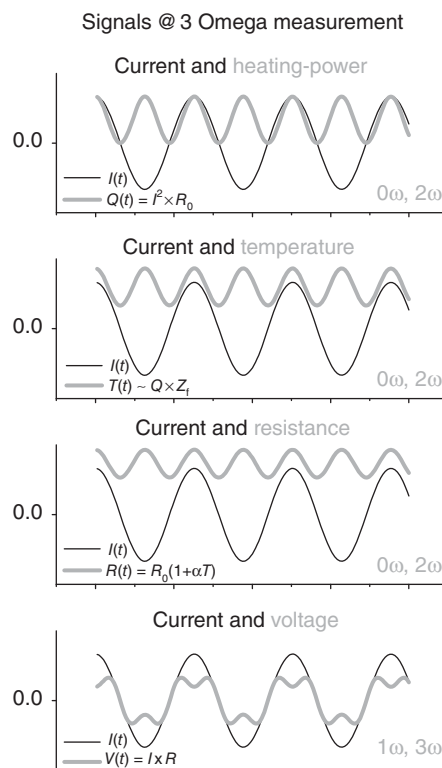


**Figure 5.11** Signals and their frequency components are important with the 3 Omega experiment.  $Z_f$  is the thermal transfer function, which includes the thermal conductivity of the sample under the bolometer.



with

$$\alpha_R = \frac{1}{R} \cdot \frac{dR}{dT}$$

where  $\alpha_R$  is the temperature coefficient of the bolometer and  $R_0$  is the DC resistance of the sample at  $T_0$ . Rearranging, we obtain

$$U(t) = R_0 I_0 \cos(\omega t) + \frac{\alpha_R R_0 I_0 \Delta T}{2} [\cos(3\omega t + \phi) + \cos(\omega t + \phi)]$$

The 3 Omega voltage is thereby directly proportional to the temperature change:

$$U_{3\omega} = \frac{1}{2} U_0 \alpha_R \Delta T$$

Assuming the heater width ( $2b$ ) is small, Cahill calculated this temperature difference to be

$$\Delta T = \frac{P}{L\pi\lambda} \left( \frac{1}{2} \ln \left( \frac{1}{2} \ln \left( \frac{\kappa}{b^2} - \frac{1}{2} \ln(2\omega) \right) + \ln 2 - \gamma - i\frac{\pi}{4} \right) \right)$$

With  $\gamma$  the Euler number and  $P$  the power applied to the heater

$$P(t) = I(t)^2 \cdot R(t) = \frac{I_0^2 R(t)}{2} (1 + \cos(2\omega t))$$

Using these expressions the thermal conductivity can be defined by

$$\lambda = \frac{U_0^3 \alpha_R}{4\pi L R_0} \frac{\ln f_2 / \ln f_1}{(U_{3\omega,1} - U_{3\omega,2})}$$

This formula uses only the difference between two points; in a real experiment one may plot the 3 Omega amplitude over the logarithmic frequency, and the steepness of the curve is then proportional to the thermal conductivity.

A well written review about various geometries for the bolometers and the typical uncertainties to be achieved was published by Dames and Chen [39]. Typical uncertainties for the simple bolometer structure are in the range of 5–10%. Most effects on the accuracy are the exact geometrical parameters of the bolometer as well as the precise temperature coefficient, which has to be measured separately.

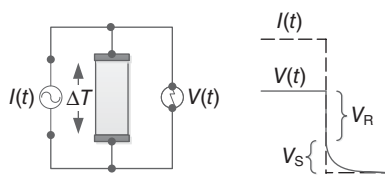
It has to be mentioned that there should be a large number of reference bulk samples available in order to verify one's own system. In most cases such reference samples will be directly shipped along while purchasing a measuring instrument. So the complex property of thermal conductivity seems to be the “easiest.”

One may ask “Isn't there one measurement for  $ZT$  in one shot?” Yes there is! Birkholz built a  $ZT$ -measurement setup in the 1960s and Jacquot *et al.* [41] in 2011; a more commonly known method is that by Harman and coworkers [24, 25].

By applying a block current to a thermoelectric material Harman used the Peltier effect to introduce a temperature difference between the two current terminals (see Figure 5.12). When the current is switched to 0, the voltage first drops fast and then, because of the thermal properties of the sample and the thermoelectric parameters, slowly. By measuring both parts of this voltage drop and comparing them Harman showed that the  $ZT$ -value can be calculated according to

$$ZT = \frac{V_s}{V_r}$$

**Figure 5.12** Schematic of the Harman method. A block current is applied to a sample, which will introduce a temperature gradient due to the Peltier effect. By measuring the voltage one may obtain  $ZT$  directly.



Theoretically, the uncertainty of the Harman method should be very low <5% [2, 42, 43]. The main point is that temperature losses due to radiation have to be minimized or measured separately. A second point is that the contact resistance should be very small compared to the sample resistance because otherwise Joule heating in the contact will interfere with the Harman measurement. The Harman method also works for thin film samples and is often used to measure the properties of assembled thermoelectric modules.

## 5.4 Summary

There are many methods to determine the parameters leading to the figure of merit  $ZT$  for bulk materials, but fewer for thin film samples. When measuring Seebeck coefficient, electrical conductivity, and thermal conductivity in different experiments one has to be sure to determine all parameters in the same direction as anisotropy introduced by nanostructuring or, as in case of bismuth-telluride, crystal growth may lead to different results [44, 45]. Nevertheless, the total uncertainty budget that has to be assumed for the  $ZT$ -value is between 20% and 30%. Fortunately, for most of the parameters there are reference materials now available or in development to reduce this value within the next years.

## Acknowledgments

The authors thank the European Union's Seventh Programme for research, technological development and demonstration (Grant No. 604647) for sponsoring the current work which is part of the NanoCaTe research project.

## References

- 1 ISO (1994) ISO 5725:1–5. Accuracy (Trueness and Precision) of Measurement Methods and Results, International Organization for Standardization, Vernier, Geneva, Switzerland.
- 2 Vasilevskiy, D., Simard, J.M., Masut, R.A., and Turenne, S. (2015) System for simultaneous harman-based measurement of all thermoelectric properties, from 240 to 720 K, by use of a novel calibration procedure. *J. Electron. Mater.*, **44**, 1733–1742.
- 3 Altenkirch, E. (1909) Thermopiles. *Phys. Z.*, **10**, 560–568.

- 4 Ebling, D.G., Jacquot, A., Jagle, M., Bottner, H., Kuhn, U., and Kirste, L. (2007) Structure and thermoelectric properties of nanocomposite bismuth telluride prepared by melt spinning or by partially alloying with IV–VI compounds. *Phys. Status Solidi RRL*, **1**, 238–240.
- 5 Rogl, G. and Rogl, P. (2011) Mechanical properties of skutterudites. *Sci. Adv. Mater.*, **3**, 517–538.
- 6 Yan, X., Joshi, G., Liu, W., Lan, Y., Wang, H., Lee, S., Simonson, J.W., Poon, S.J., Tritt, T.M., Chen, G., and Ren, Z.F. (2010) Enhanced thermoelectric figure of merit of p-type half-heuslers. *Nano Lett.*, **11**, 556–560.
- 7 Hicks, L.D. and Dresselhaus, M.S. (1993) Effect of quantum-well structures on the thermoelectric figure of merit. *Phys. Rev. B*, **47**, 12727–12731.
- 8 Venkatasubramanian, R., Siivola, E., Colpitts, T., and O’quinn, B. (2001) Thin-film thermoelectric devices with high room-temperature figures of merit. *Nature*, **413**, 597–602.
- 9 Winkler, M., Liu, X., König, J., Kirste, L., Böttner, H., Bensch, W., and Kienle, L. (2012) Sputtered p-Type  $Sb_2Te_3/(Bi,Sb)_2Te_3$  Soft Superlattices Created by Nanoalloying. *J. Electron. Mater.*, **41**, 1322–1331.
- 10 Smits, F.M. (1958) Measurement of sheet resistivities with the four-point probe. *Bell Syst. Tech. J.*, **37**, 711–718.
- 11 Valdes, L.B. (1954) Resistivity measurements on germanium for transistors. *Proc. Inst. Radio Eng.*, **42**, 420–427.
- 12 Pauw, L.J.V.D. (1958) A method of measuring specific resistivity and Hall effect of discs of arbitrary shape. *Philips Res. Rep.*, **13**, 1–9.
- 13 Pauw, L.J.V.D. (1959) A method of measuring the resistivity and hall coefficient on Lamellae of arbitrary shape. *Philips Tech. Rev.*, **20**, 220–224.
- 14 Henderson, L., Hall, M., Harmon, S., Ashcroft, G., Warnecke, P., Schumacher, B., Rietveld, G., Brigodiot, G., Hocking, C., White, A. and Bodenberger, R. (2004) Final report (open version) on activities within the RTD Project G6RD-CT-2000-00210. *CETM*. NLP.
- 15 Mackey, J., Dynys, F., and Sehirlioglu, A. (2014) Uncertainty analysis for common Seebeck and electrical resistivity measurement systems. *Rev. Sci. Instrum.*, **85**, 085119.
- 16 Mackey, J., Sehirlioglu, A. and Dynys, F. (2014) Detailed Uncertainty Analysis of the ZEM-3 Measurement System. NASA Technical Report Series ed.: NASA.
- 17 NETZSCH (2016) *Simultaneous Determination of the Seebeck Coefficient and Electrical Conductivity – SBA 458 Nemesis*, GMBH.
- 18 Wang, H., Porter, W.D., Böttner, H., König, J., Chen, L., Bai, S., Tritt, T.M., Mayolet, A., Senawiratne, J., Smith, C., Harris, F., Gilbert, P., Sharp, J., Lo, J., Kleinke, H., and Kiss, L. (2013a) Transport properties of bulk thermoelectrics: an international round-robin study, Part II: thermal diffusivity, specific heat, and thermal conductivity. *J. Electron. Mater.*, **42**, 1073–1084.
- 19 Wang, H., Porter, W.D., Böttner, H., König, J., Chen, L., Bai, S., Tritt, T.M., Mayolet, A., Senawiratne, J., Smith, C., Harris, F., Gilbert, P., Sharp, J.W., Lo, J., Kleinke, H., and Kiss, L. (2013b) Transport properties of bulk thermoelectrics—an international round-robin study, Part I: Seebeck coefficient and electrical resistivity. *J. Electron. Mater.*, **42**, 654–664.

- 20** NIST and N. I. O. S. A. T (2004a) Standard Reference Material 2541; Silicon Resistivity Standard – 0.01 ohm cm Level, NIST, Gaithersburg, MD, USA.
- 21** NIST and N. I. O. S. A. T (2004b) Standard Reference Material 2543; Silicon Resistivity Standard - 1 ohm·cm Level, NIST, GAithersburg, MD, USA.
- 22** VLSIStandards (2012) *ITO Sheet Resistance Standard*, VLSIStandards.
- 23** Burkov, A.T., Heinrich, A., Konstantinov, P.P., Nakama, T., and Yagasaki, K. (2001) Experimental set-up for thermopower and resistivity measurements at 100–1300 K. *Meas. Sci. Technol.*, **12**, 264.
- 24** Harman, T.C. (1958) Special techniques for measurement of thermoelectric properties. *J. Appl. Phys.*, **29**, 1373–1374.
- 25** Harman, T.C., Cahn, J.H., and Logan, M.J. (1959) Measurement of thermal conductivity by utilization of the peltier effect. *J. Appl. Phys.*, **30**, 1351–1359.
- 26** Tektronix (2016) Low Level Measurements Handbook—Precision DC Current, Voltage, and Resistance Measurements, Tektronix.
- 27** Boor, J.D., Stiewe, C., Ziolkowski, P., Dasgupta, T., Karpinski, G., Lenz, E., Edler, F., and Mueller, E. (2013) High-temperature measurement of Seebeck coefficient and electrical conductivity. *J. Electron. Mater.*, **42**, 1711–1718.
- 28** Lenz, E., Haupt, S., Edler, F., Ziolkowski, P., and Pernau, H.F. (2012) Traceable measurements of electrical conductivity and Seebeck coefficient of  $\beta$ -Fe0.95Co0.05Si2 and Ge in the temperature range from 300 K to 850 K. *Phys. Status Solidi C*, **9**, 2432–2435.
- 29** LINDSEIS (2016) LSR –3 Linseis – Seebeck Coefficient & Electric Resistivity Unit, LINDSEIS.
- 30** Ulvac (2016) *Ulvac ZEM 5 Seebeck-coefficient electrical resistance measuring system* [Online]. <http://www.ulvac.eu/en/products/components/thermal-analysis/zem-5.html>, May 4th 2017.
- 31** Boffoue, O., Jacquot, A., Dauscher, A., Lenoir, B., and Stolzer, M. (2005) Experimental setup for the measurement of the electrical resistivity and thermopower of thin films and bulk materials. *Rev. Sci. Instrum.*, **76**, DOI: 10.1063/1.1912820.
- 32** Lenz, E., Edler, F., and Ziolkowski, P. (2013) Traceable thermoelectric measurements of seebeck coefficients in the temperature range from 300 K to 900 K. *Int. J. Thermophys.*, **34**, 1975–1981.
- 33** NIST and N. I. O. S. A. T (2011) Standard Reference Material 3451; Low-Temperature Seebeck Coefficient Standard (10 K to 390 K), NIST, Gaithersburg, MD, USA.
- 34** Cape, J.A. and Lehman, G.W. (1963) Temperature and finite pulse-time effects in the flash method for measuring thermal diffusivity. *J. Appl. Phys.*, **34**, 1909–1913.
- 35** Cowan, R.D. (1963) Pulse method of measuring thermal diffusivity at high temperatures. *J. Appl. Phys.*, **34**, 926–927.
- 36** Parker, W.J., Jenkins, R.J., Butler, C.P., and Abbott, G.L. (1961) Flash method of determining thermal diffusivity, heat capacity, and thermal conductivity. *J. Appl. Phys.*, **32**, 1679–1684.
- 37** Cahill, D.G. (2004) Analysis of heat flow in layered structures for time-domain thermoreflectance. *Rev. Sci. Instrum.*, **75**, 5119–5122.

- 38** Cahill, D.G. (1990) Thermal-conductivity measurement from 30-K to 750-K: the 3-Omega method. *Rev. Sci. Instrum.*, **61**, 802–808.
- 39** Dames, C. and Chen, G. (2005)  $1\omega$ ,  $2\omega$ , and  $3\omega$  methods for measurements of thermal properties. *Rev. Sci. Instrum.*, **76**, 124902.
- 40** Jacquot, A., Vollmer, F., Bayer, B., Jaegle, M., Ebling, D.G., and Böttner, H. (2010) Thermal conductivity measurements on challenging samples by the 3 Omega method. *J. Electron. Mater.*, **39**, 1621–1626.
- 41** Jacquot, A., Jaegle, M., Pernau, H.-F., König, J. D., Tarantik, T., Bartholomé, K. and Böttner, H. (2011) Simultaneous Measurement of Thermoelectric Properties with the new IPM ZT-Meter. *Conference on Thermoelectrics*. Thessaloniki.
- 42** Ao, X., de Boor, J., and Schmidt, V. (2011) Radiation-corrected harman method for characterization of thermoelectric materials. *Adv. Energy Mater.*, **1**, 1007–1011.
- 43** Iwasaki, H., Koyano, M., and Hidenobu, H. (2002) Evaluation of the figure of merit on thermoelectric materials by harman method. *Jpn. J. Appl. Phys.*, **41**, 6606.
- 44** Han, L., Spangsdorf, S.H., Nong, N.V., Hung, L.T., Zhang, Y.B., Pham, H.N., Chen, Y.Z., Roch, A., Stepien, L., and Pryds, N. (2016) Effects of spark plasma sintering conditions on the anisotropic thermoelectric properties of bismuth antimony telluride. *RSC Adv.*, **6**, 59565–59573.
- 45** Joraide, A.A. (1993) The effect of anisotropy on the electrical properties of compacted semiconductor  $(\text{Bi}_2\text{Te}_3)25-(\text{Sb}_2\text{Te}_3)75$  powders. *J. Appl. Phys.*, **73**, 7478–7481.

## 6

# Preparation and Characterization of TE Interfaces/Junctions

*Gao Min and Matthew Phillips*

*Cardiff University, Institute of Energy and Environment, School of Engineering, The Parade, Cardiff, UK*

## 6.1 Introduction

Thermoelectric devices (also known as *modules*) are solid-state energy converters that can convert heat into electricity for power generation or pump heat from one junction to another for refrigeration [1–5]. Figure 6.1 shows a schematic diagram of the structure and main components of a conventional thermoelectric module [6]. A key step in the fabrication of thermoelectric devices is to join an n-type thermoelement with a p-type thermoelement through a metallic contact layer. The existence of various contact layers and interfaces between the layers will inevitably introduce both electrical and thermal contact resistances into a practical thermoelectric device. As a result, this will lead to the consumption of energy at these interfaces and a reduction in the device performance (as compared with that predicted by an ideal model where the contact resistances are neglected). In order to minimize the performance reduction due to the contact resistances of the interfaces, preparation and characterization of thermoelectric junction/interfaces become an important prerequisite for thermoelectric module fabrication. In this chapter, a theoretical outline of the effects of contact resistances on the performance of thermoelectric device will be given, followed by a discussion of key factors and challenges that are crucial to the design and fabrication of thermoelectric interfaces/junctions, with a focus on evaluation and minimization of the thermoelectric contact resistances. The purpose of this chapter is to provide a brief overview on the basic principles and the state-of-the-art technologies that are crucial to achieving low-contact resistances for the fabrication of high-performance thermoelectric devices.

## 6.2 Effects of Electrical and Thermal Contact Resistances

The performance of a thermoelectric module will deteriorate owing to the existence of electrical and thermal contact resistances. Electrical contact resistance

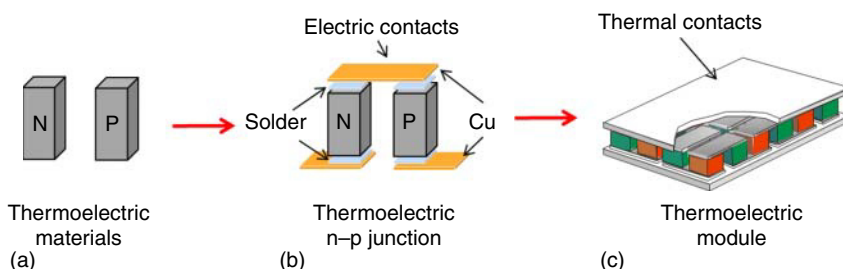


**Figure 6.1** Schematic diagram of (a) an n-type and p-type thermoelement; (b) a thermocouple formed by soldering n-type and p-type thermoelements with copper layers; and (c) a thermoelectric module consisting of a number of thermocouples connected electrically in series and thermally in parallel. The contact interfaces formed in fabrication processes have a significant effect on the performances of thermoelectric devices.

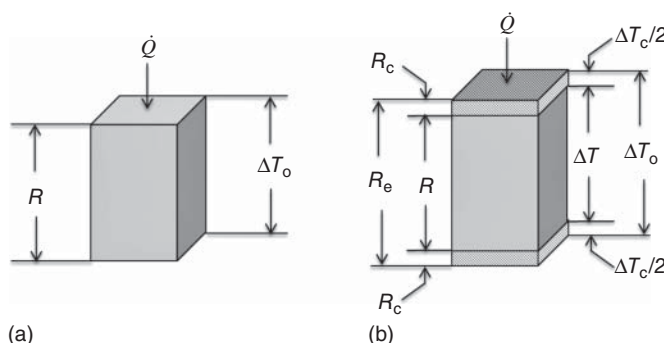


**Figure 6.2** Schematic diagram of (a) a thermoelement without contact layer; (b) a thermoelement with contact layers at the top and bottom ends.

will result in additional Joule heat at junctions, while thermal contact resistance will decrease the temperature difference across the thermoelectric materials because of the temperature drop on contact layers. The effect of both electrical and thermal contact resistance on the performance of thermoelectric modules can be evaluated by the change of the dimensionless figure of merit,  $ZT$ . In this section, a simplified model is developed to describe the influence of electrical and thermal contact resistances on the performance of thermoelectric devices and provide a quantitative evaluation of the contact resistance required for satisfactory manufacturing of thermoelectric modules.

Considering a single thermoelement without contact resistance as shown in Figure 6.2a, its dimensionless thermoelectric figure of merit is given by [6]

$$ZT = \frac{\alpha^2 T}{RK} \quad (6.1)$$

where  $\alpha = V/\Delta T_o$  is the Seebeck coefficient of the thermoelement ( $\Delta T_o$  is the temperature difference across the thermoelement,  $V$  is the Seebeck voltage generated under  $\Delta T_o$ );  $R = \rho(l/A)$  and  $K = k(A/l)$  are the electrical resistance and

thermal conductance of the thermoelement, respectively ( $\rho$  and  $k$  are the electrical resistivity and thermal conductivity of thermoelectric material, and  $A$  and  $l$  are the cross-sectional area and length of thermoelement). Without the influence of the contact resistances, it can be shown that the  $ZT$  of the thermoelement (Eq. (6.1)) is the same as the  $ZT$  ( $= \alpha^2 T / \rho k$ ) of the thermoelectric material.

If electrical contact resistance exists due to the existence of the contact layers as shown in Figure 6.2b, the effective electrical resistance of the thermoelement becomes [7]

$$R_e = R \left( 1 + \frac{2R_c}{R} \right) \quad (6.2)$$

where  $R_c$  is the electrical contact resistance. The interface layers also cause a reduction in the temperature difference across the thermoelement due to temperature drops across the contact layers. In this case,  $\Delta T_o = \Delta T + \Delta T_c$  (where  $\Delta T$  is the temperature difference across the actual thermoelement and  $\Delta T_c$  is the temperature drop across the interface layers). The thermal contact conductance of the interface layer can be defined as  $K_c = Q/(\Delta T_c/2)$  (where  $Q$  is the heat flow through the thermoelement), and the effective thermal conductance of the thermoelement can be expressed as [7]

$$K_e = \frac{K}{1 + 2K/K_c} \quad (6.3)$$

The Seebeck voltage will also decrease owing to a smaller temperature difference across the thermoelement. The effective Seebeck coefficient in this case is given by

$$\alpha_e = \frac{\alpha}{1 + 2K/K_c} \quad (6.4)$$

As a result, the effective  $ZT$  of the thermoelement can be expressed as

$$ZT_e = \frac{ZT}{(1 + 2R_c/R)(1 + 2K/K_c)} \quad (6.5)$$

Defining the electrical contact resistivity (also known as *specific contact resistance*) as  $\rho_c = R_c A$  and the thermal contact conductivity as  $k_c = K_c/A$ , the relative reduction of the  $ZT$  is given by

$$\frac{ZT_e}{ZT} = \frac{1}{(1 + 2\rho_c/\rho l)(1 + 2k/k_c l)} \quad (6.6)$$

It can be seen that the relative reduction in the  $ZT$  of a thermoelectric device depends on the ratios of  $\rho_c/\rho$  and  $k/k_c$  and the length of the thermoelement. Equation (6.6) provides a quantitative measure of the contact resistances to ensure that the reduction in the  $ZT$  of the thermoelectric device is limited to an acceptable level. For example, in order to meet the requirement of  $ZT$  reduction being limited to 10%, with 5% each due to electrical and thermal contact respectively, the required contact resistivity for a given length is shown in Table 6.1. It can be seen that shorter lengths require smaller contact resistivities to obtain performance.

**Table 6.1** The required contact resistivities and thermoelement length for ensuring the reduction in  $ZT$  being limited to 10% using  $\text{Bi}_2\text{Te}_3$ , which possesses an electrical resistivity of  $1 \times 10^{-5} \Omega \text{ m}$  and thermal conductivity of  $1.5 \text{ W/m K}$ .

$l (\text{mm})$	$\rho_c (\Omega \text{ cm}^2)$	$k_c (\text{W/m}^2 \text{ K})$
0.1	$2.6 \times 10^{-7}$	$5.7 \times 10^5$
0.5	$1.3 \times 10^{-6}$	$1.1 \times 10^5$
1.0	$2.6 \times 10^{-6}$	$5.7 \times 10^4$
1.5	$4.0 \times 10^{-6}$	$3.8 \times 10^4$
2.0	$5.3 \times 10^{-6}$	$2.9 \times 10^4$
2.5	$6.6 \times 10^{-6}$	$2.3 \times 10^4$
3	$7.9 \times 10^{-6}$	$1.9 \times 10^4$
5	$1.3 \times 10^{-5}$	$1.1 \times 10^4$

The contact resistances have a similar effect on the power output and conversion efficiency of thermoelectric devices. The maximum power output at the match load is given by [5, 6]

$$P_{\max} = \frac{(\alpha \Delta T)^2}{4\rho} \cdot \frac{A}{(l + \rho_c/\rho)(1 + 2kl_c/k_c l)^2} \alpha \quad (6.7)$$

Similarly, it is important to minimize both the electrical and thermal contact resistances in order to limit the reduction in the maximum power output. Clearly, making thermoelectric interfaces with small contact resistances is an important requirement in thermoelectric module fabrication processes.

### 6.3 Preparation of Thermoelectric Interfaces

In order to meet the requirements of output voltage and facilitate convenient heat transfer, a thermoelectric module usually consists of many thermoelectric junctions connected electrically in series and thermally in parallel as shown in Figure 6.1c. Manufacturing of such modules involves the simultaneous assembly of thermoelectric junctions all at once. However, in order to ensure satisfactory contact resistances at all interfaces, suitable contact layers and assembly conditions need to be thoroughly investigated and determined using a simple unijunction prior to module assembly involving multiple junctions. This section focuses on the research efforts required in preparation of a unijunction for the determination of satisfactory thermoelectric interfaces/junctions.

The basic requirement for the contact layers used in thermoelectric modules is to join thermoelements with good electrical and thermal conductivities, and satisfactory mechanical strength. These requirements can usually be met by employing soldering or brazing techniques with appropriate selection of solders or brazing materials. However, owing to the elevated temperatures required for

soldering or brazing processes, interdiffusion could occur among thermoelectric materials, brazing materials, and contact layers (usually copper). Copper is well known to have a high diffusion coefficient in semiconductors and can usually act as a dopant, resulting in degradation of thermoelectric properties if diffused into thermoelectric materials. Consequently, a barrier layer between thermoelectric materials and solders is required to prevent solders and/or contact layer materials from being diffused into thermoelectric materials.

A variety of techniques for the joining of thermoelements to electrodes have been employed, with the introduction of a barrier layer at various stages of the fabrication process. For bismuth telluride-based systems, barrier layers are typically electroplated or metal sprayed onto preformed pellets. Specific contact resistances on the order of  $10^{-6}$ – $10^{-5} \Omega \text{ cm}^2$  have been reported [8]. Early research conducted on skutterudites by the Jet Propulsion Laboratory in the late 1990s focused on the hot-side interface between the skutterudite and the electrode. Both foil [9] and powdered [10, 11] barrier layers were added to the presintered skutterudite powder and were hot-pressed together to improve the contact bond. Mixed results were observed with the powdered barrier layer, with densities close to 80–90% being observed. Thermal-stress-induced cracks were observed when the skutterudite and nickel powder were pressed together and this was attributed to a mismatch in the thermal expansion coefficients of the two materials. When the nickel was replaced with niobium, which has a closer matched expansion coefficient with the skutterudite, the specific contact resistance was found to be less than  $5 \times 10^{-6} \Omega \text{ cm}^2$  and mechanically stable. Low resistance values were also obtained when the powdered barrier layer was replaced with foils such as palladium but for both powder and foils contacts, no long-term stability data was presented. Other groups have reported the formation of good electrical and mechanical contacts using spark plasma sintering (SPS). In this technique the electrode, barrier layer, and presintered skutterudite are all placed in a graphite die and sintered in a one-step process [12–17]. One particularly interesting advantage of this method is that it allows different material combinations to be examined, enabling the physical properties to be tuned to those of the skutterudite. Zhao *et al.* have tested both titanium [12, 13, 15] and molybdenum [16] barrier layers and obtained specific contact resistances of around  $20 \times 10^{-6} \Omega \text{ cm}^2$  for the former, although a mechanical and electrical degradation in the contact joint was observed with the sample held at elevated temperatures for extended time periods. Fan *et al.* report excellent specific contact resistances while bonding ytterbium-filled skutterudites to nickel electrodes in a one-step sintering process [14], using a combination of molybdenum and titanium as a barrier layer. An addition buffer layer of molybdenum–copper was also placed between the barrier layer and the electrode to ensure that any thermal expansion mismatch with the nickel was minimized. A resistance of  $3 \times 10^{-6} \Omega \text{ cm}^2$  was observed with a slight increase to  $9 \times 10^{-6} \Omega \text{ cm}^2$  following several days of elevated temperature testing, with no cracks observed at the interface. Wojciechowski *et al.* [18] hot-pressed  $\text{CoSb}_3$  and then applied a  $1 \mu\text{m}$  nickel or  $2.5 \mu\text{m}$  molybdenum layer using magnetic sputtering. The elements were then resistance brazed to copper electrodes with the electrical resistance of the contact measured around  $(5\text{--}15) \times 10^{-6} \Omega \text{ cm}^2$ .

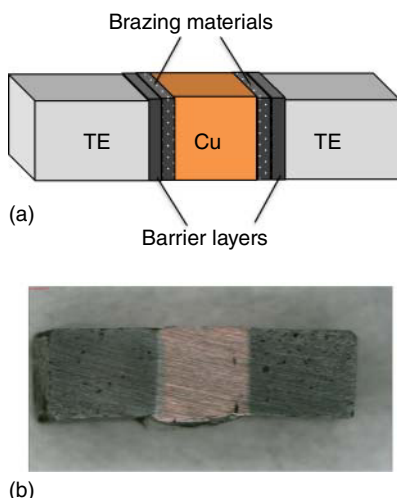


**Figure 6.3** A thermoelectric unijunction for investigation of electrical and thermal contact resistance, consisting of two thermoelements, a copper contact layer, barrier layer, and brazing materials. (a) A schematic diagram; (b) a photograph of skutterudite/copper junction.

However, this was accompanied by the interdiffusion of braze material into the thermoelement of up to 1.5 mm. The results presented in this section are of skutterudite thermoelements with a barrier layer electroplated post sintering.

In principle, the thermoelectric junctions employed for study of the contact resistances should be structured as close to a practical thermoelectric junction as possible. However, owing to the practicality of preparation and characterization, simple constructions of thermoelectric junctions should also be considered. Figure 6.3a shows a typical configuration frequently used for the study of the influence of contact layers. The junction consists of a copper contact layer sandwiched between two thermoelements of the same type, joined together by soldering or brazing. The barrier layers (usually nickel or palladium) were coated on the joining surfaces of thermoelements by electroplating. Figure 6.3b shows a photograph of a prepared thermoelectric junction using skutterudite materials at Cardiff Thermoelectric Laboratory.

The prebrazed junction is assembled in a sample holder shown in Figure 6.4a, held in place by a spring loaded grub screw. The sample holder is loaded into a quartz tube that sits inside a tube furnace (Figure 6.4b). The air from the quartz tube can be evacuated or purged with inert gases such as argon to remove oxygen prior to brazing at elevated temperatures. The furnace is set to the required temperature for brazing and the sample is then inserted in the hottest central part of the tube using external magnets to move the sample holder. Once the temperature has been reached and the joint is formed, the sample is removed to cool down in an oxygen-free environment. There is typically a large difference in the furnace temperature and the temperature at the sample holder and to measure this temperature difference a wireless thermocouple setup from Omega is used to accurately determine the temperature at the sample holder during the process. Once cooled, the sample is removed from the quartz tube and cleaned to remove any flux or dirt and then polished to provide a smooth surface for analysis.



(a)



(b)

**Figure 6.4** Sample holder (a) and furnace (b) for the assembly of thermoelectric unijunctions.

## 6.4 Characterization of Contact Resistance Using Scanning Probe

Determination of the electrical contact resistance at the junction interfaces provides important information that has crucial influence on the manufacturing quality of a thermoelectric module. There are a number of different ways of measuring the contact resistance [19], although many of the traditional techniques were designed for DC measurements of semiconductor–metal interfaces where thermoelectric effects are minimized. These include the twin contact, differential, Van der Pauw, and TLM methods among others. Although it is possible to adapt many of these techniques for thermoelectric-specific contact resistance and resistivity measurements, a well-established technique for this purpose is the extrapolation method or resistance scanning probe [7, 8, 20] as it is also known. The principle of this technique is shown in Figure 6.5. It is a three-probe setup, which consists of two fixed probes and one that can move across the sample surface. The sample is sandwiched between the two fixed

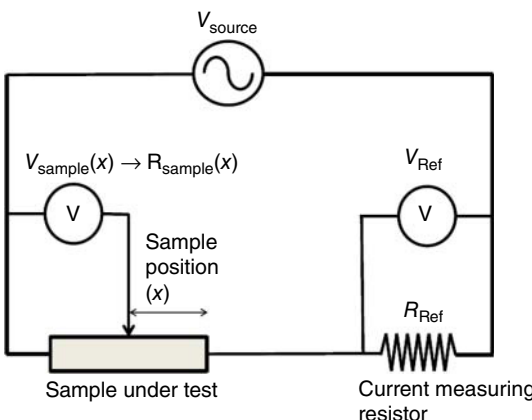


**Figure 6.5** Circuit diagram of an apparatus for contact resistance measurement based on scanning probe.

probes and connected to an AC voltage source through a reference resistance. The third probe is positioned on a surface of the sample that is perpendicular to the junction interfaces and is able to travel across the sample while maintaining good electrical contact by pressure to record voltage change as a function of position. A high accuracy and thermally stable resistor is connected in series in the circuit to determine the current. As a result, the resistance profile along the surface can be determined by

$$R(x) = \frac{V(x)}{V_{\text{ref}}} \cdot R_{\text{ref}} \quad (6.8)$$

where  $V(x)$  is the voltage measured at position  $x$ .  $R_{\text{ref}}$  is a reference resistor for current measurement and  $V_{\text{ref}}$  is the voltage across the reference resistor.

Figure 6.6 shows a schematic of typical resistance profiles that can be obtained by swiping the scanning probe along the surface of the thermoelectric unijunction. When the probe moves away from the reference contact (i.e., the one connected to the ground), the resistance between the reference contact and the scanning probe increases with increasing distance ( $x$ ) until it reaches the copper interface layer. Since the resistivity of the copper interface layer is approximately three orders of magnitude lower than that of the thermoelectric material, the resistance will remain almost constant over the region corresponding to the thickness of the copper interface layer. The resistance will again increase with increasing distance after the scanning probe enters into the second piece of the thermoelectric materials. If there is no contact resistance between the thermoelectric material and the copper interface layer, there is no abrupt change at interfaces as shown by the bottom curve of the resistance profiles in Figure 6.6. However, if a contact resistance exists at the interfaces between the thermoelectric materials and the copper layer, significant change at the interfaces will occur as shown by the middle and top curves of Figure 6.6. The middle curve indicates that noticeable contact resistance exists but no interdiffusion takes place at the interface. The top curve implies that both contact resistance and interdiffusion occur in the vicinity of the interfaces. Measuring the contact resistance,  $\Delta R$ , on the resistance profile (Figure 6.6), the contact resistivity can be determined by  $\Delta R/A$  (where  $A$  is the cross-sectional area of the interfaces). The diffusion

**Figure 6.6** Schematic of typical resistance profiles of thermoelectric unijunction: the bottom curve shows a perfect contact at interfaces; the middle curve shows the interfaces with noticeable contact resistance but no interdiffusion; and the top curve shows the interfaces with significant contact resistance and interdiffusion.

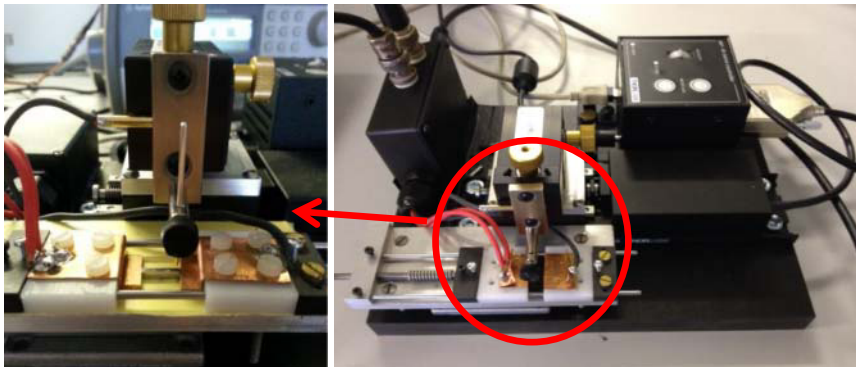
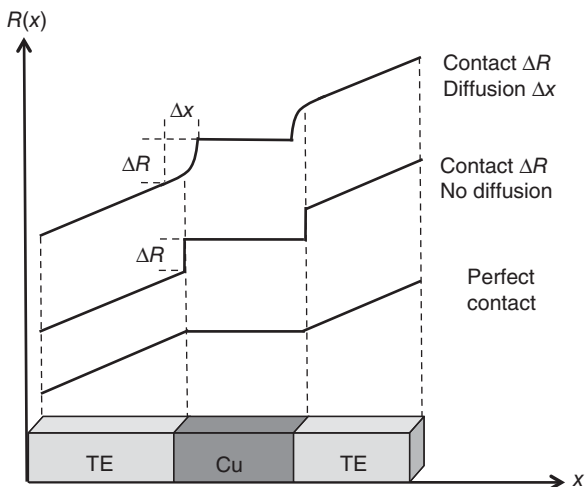


**Figure 6.7** Photograph of the apparatus for contact resistance measurement based on scanning probe.

length,  $\Delta x$ , can also be obtained from the resistance profile, providing useful information on materials interaction at interfaces. In addition, the resistivity of thermoelectric materials can be estimated from the slope of the resistance profile,  $dR/dx$ .

Figure 6.7 shows the photograph of a resistance scanning apparatus developed at Cardiff, which enables determination of the resistance profile with spatial resolution of 2  $\mu\text{m}$ . The scanning probe is a HD-PA4BS spring-loaded spear point purchased from Coda-Systems with the holding barrel screwed into a Quatar Research XYZ 300 ML platform and mounted on a Thorlabs MTS25/M-Z8E automated translation stage. The stage position and voltage reading are both controlled by a computer using a LabVIEW program, which enables automated scanning and data acquisition. An AC voltage source with a frequency of 40 Hz is used to minimize the errors due to thermoelectric effects. In order to ensure measurement accuracy, the system was calibrated by measuring the bulk resistance of a standard reference sample (SRM 1461 – stainless steel) from

NIST. The calibration was carried out at the temperature of 24 °C using both DC and AC voltage sources because the data provided by NIST was obtained using DC, while AC is necessary for measurements of thermoelectric materials. The results are shown in Table 6.2. The repeatability of the scanning resistance probe is 1.9% and 1.3% for DC and AC power sources, respectively. The systematic error of the system is about 1.7% for DC power source while it is 4.1% for AC power source.

The use of a fine resolution translation stage (MTS25/M-Z8E) offers a spatial resolution of less than 2 μm. This provides the capability of detecting the interdiffusion between thermoelectric materials and brazing materials on a microscale. Figure 6.8 shows a photograph of a skutterudite thermoelectric unijunction prepared using procedures described in Section 6.3. The corresponding resistance profile obtained using the scanning resistance probe is also shown in the figure. A region with a significantly low resistance can be seen to extend into the thermoelectric materials, although this region cannot be seen in the photograph. SEM examination confirms that the region is diffused with a noticeable amount of copper atoms. Figure 6.9 shows the resistance profiles obtained from three skutterudite junctions prepared under the same conditions except for using

**Table 6.2** Systematic error and repeatability of the resistance scanning probe determined using the standard reference sample (SRM 1461) from NIST.

Material	NIST value (nΩ m)	Scanning probe (nΩ m)	Repeatability (%)	Systematic error (%)
SRM 1461	807 (DC)	821 ± 15.8 (DC)	±1.9	±1.7
		774 ± 10.0 (AC)	±1.3	±4.1

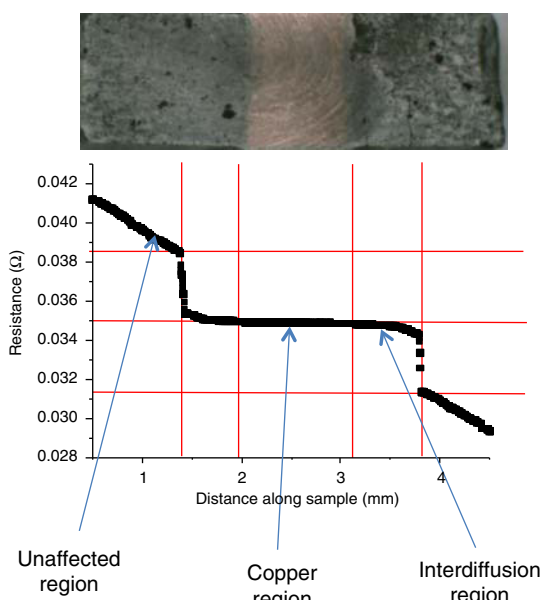


**Figure 6.8** Skutterudite thermoelectric unijunction and its corresponding resistance profile obtained using the scanning resistance probe, showing a significant interdiffusion region extended into the thermoelectric materials, although the region cannot be seen on the photograph.

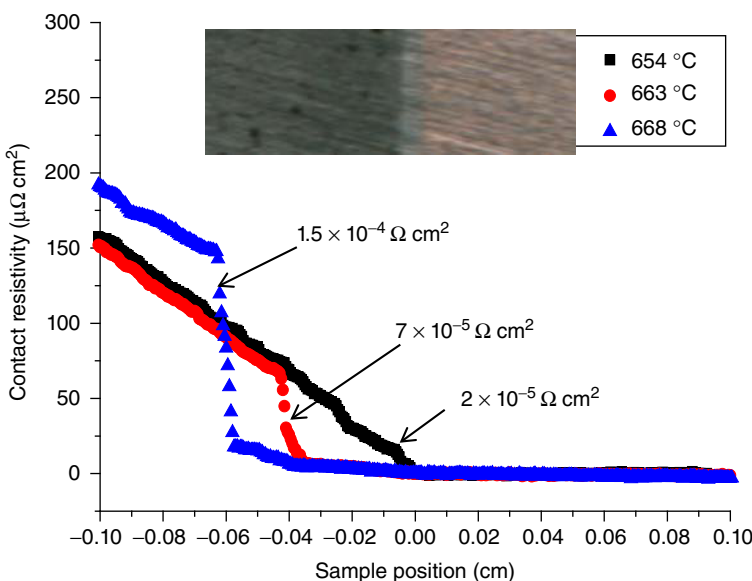


**Figure 6.9** The resistance profiles of three skutterudite thermoelectric junctions, which were prepared at 654, 663, and 668 °C, respectively. No interdiffusion takes place for the junction prepared at 654 °C, which also exhibits a low contact resistivity. The junction prepared at 663 °C shows a slightly larger contact resistivity but with some degree of interdiffusion. The junction prepared at 668 °C shows significant interdiffusion and larger contact resistivity.

different brazing temperatures (654, 663, and 668 °C, respectively). It can be seen that no interdiffusion takes place for the junction prepared at 654 °C, which also exhibits the lowest electrical contact resistivity. The junction prepared at 663 °C shows a slightly larger contact resistivity with some degree of interdiffusion. The junction prepared at 668 °C shows significant interdiffusion and larger contact resistivity. These results demonstrate that the resistance profiles obtained using a high-resolution scanning resistance probe can provide crucial information on contact resistance and interdiffusion at interfaces.

## 6.5 Characterization of Thermal Contact Using Infrared Microscope

As shown in Section 6.2, minimizing the thermal contact resistance at thermoelectric interfaces is equally important. Thermal contact resistance may be determined by examining the temperature profile at interfaces using an infrared microscope. When applying a temperature difference across a thermoelectric junction (Figure 6.3), a temperature profile will be established as shown schematically in Figure 6.10. Based on Fourier's law and neglecting the heat losses from the surfaces of the thermoelectric junction, the heat flux through the thermoelectric material is equal to the heat flux across the interfaces; we have

$$\kappa \cdot A \frac{\Delta T}{\Delta x} = \kappa_c \cdot A \cdot \Delta T_c \quad (6.9)$$

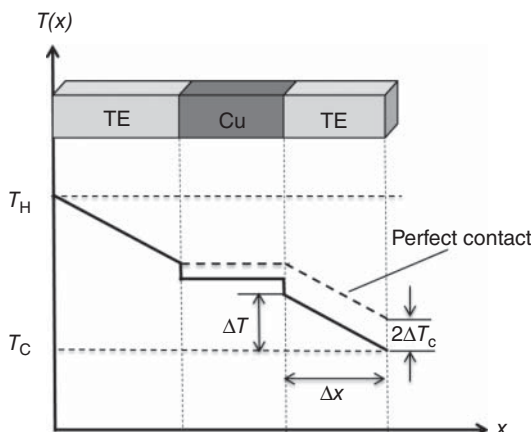


**Figure 6.10** Schematic temperature profile across a thermoelectric unijunction with no contact influence (dashed line) and with contact resistance (solid line).

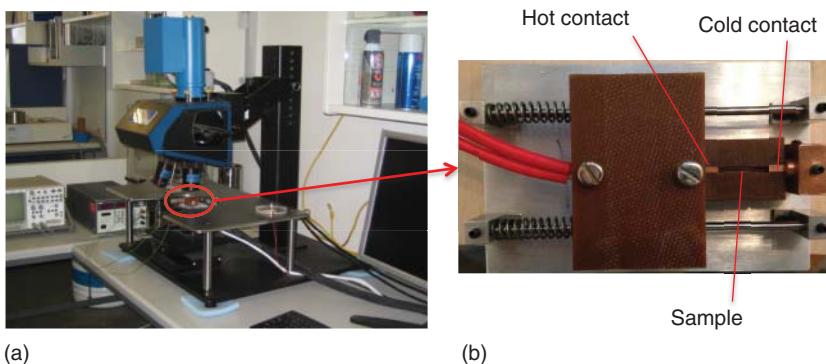


**Figure 6.11** Thermal contact resistance measurement system (a) infrared microscope; (b) sample holder.

where  $\kappa$  is the thermal conductivity of thermoelectric materials and  $\kappa_c$  is the contact thermal conductivity, which has a unit of  $\text{W}/\text{m}^2 \text{K}$ . For a given thermoelectric material with a known  $\kappa$ , the contact thermal conductivity  $\kappa_c$  can be determined using

$$\kappa_c = \frac{k}{\Delta T_c} \cdot \frac{\Delta T}{\Delta x} \quad (6.10)$$

where  $\Delta T$ ,  $\Delta T_c$ , and  $\Delta x$  can be determined from the measured temperature profile. An infrared microscope can be employed to measure the temperature profile with the required resolution to observe interface temperature drop. Figure 6.11a shows a thermal contact resistance measurement system developed at Cardiff based on an infrared microscope platform (Infrascope III, Quantum Focus). Figure 6.11b shows a sample holder with a heated tip on one end. The sample is sandwiched between the heated tip and a cold rod. This enables a temperature difference (5–10 K) established across the sample. Using the infrared

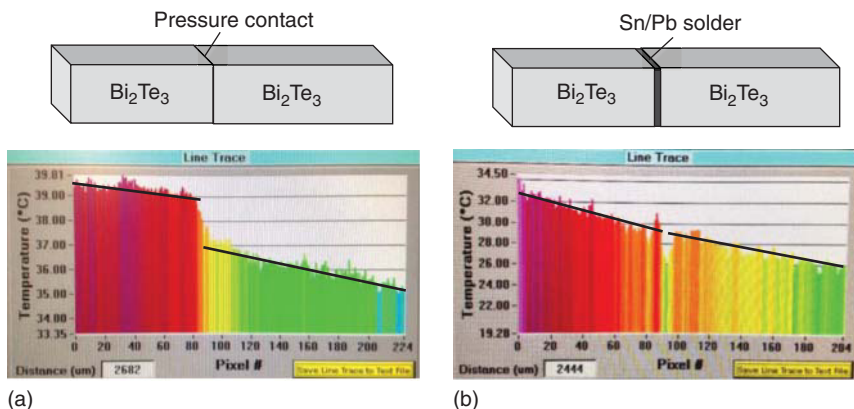


**Figure 6.12** Temperature profiles obtained by infrared microscope of thermoelectric interfaces: (a) interface formed by pressure contact; (b) interface formed by soldering using Sn/Pb solders.

microscope, the temperature profile on the surface of the junction can be observed. Figure 6.12 shows temperature profiles of an interface formed by two pieces of  $\text{Bi}_2\text{Te}_3$  jointed by pressure contact and by conventional Sn/Pb solder, respectively. A clear gap can be seen at the interface for the pressure contact (Figure 6.12a) while it is almost insignificant for soldering contact (Figure 6.12b). Determining  $\Delta T$ ,  $\Delta T_c$ , and  $\Delta x$  from Figure 6.12a,b with  $k = 1.5 \text{ W/m K}$ , the thermal contact conductivity,  $k_c$ , can be calculated using Eq. (6.10). The value is  $2.4 \times 10^3 \text{ W/m}^2 \text{ K}$  for the pressure contact and  $4.2 \times 10^4 \text{ W/m}^2 \text{ K}$  for the soldered contact. Compared with the data shown in Table 6.1, it is clear that a satisfactory thermal contact can be achieved using soldered interface.

## 6.6 Summary

The contact theory described in this chapter provides a quantitative measure of the effects of contact resistances (both electrical and thermal) on the performances of thermoelectric devices. For a given acceptable percentage reduction (from material performance to device performance), the required contact properties can be determined, which provide crucial benchmarks for module fabrication processes. In order to produce high-quality thermoelectric devices, an initial step is to develop low contact resistance interfaces. This is usually carried out experimentally by preparing a thermoelectric junction and through subsequent characterization of the contact resistances. The method and facilities employed for preparation of thermoelectric junction are discussed. The technique for characterization of electrical contact resistance based on a scanning resistance probe is described, together with experimental results to demonstrate the usefulness and capability of the equipment.

## Acknowledgments

We acknowledge EPSRC for financial support of the work associated with the funded project (EP/K029142/1). Dr J. Garcia-Canadas is acknowledged for initial setup of the furnace system shown in Figure 6.4. Dr J. J. Bomphrey is acknowledged for initial development of the resistance scanning probe shown in Figure 6.7. Mr Musab Othman is acknowledged for developing the sample holder and measuring temperature profiles of thermoelectric interfaces using Infrared Microscope (Figures 6.11 and 6.12).

## References

- 1 Ioffe, A.F. (1957) *Semiconductor Thermoelements and Thermoelectric Cooling*, Infosearch, London.
- 2 Rowe, D.M. and Bhandari, C.M. (1983) *Modern Thermoelectrics*, Holt, Rinehart and Winston, London.
- 3 Goldsmid, J.H. (1986) *Electronic Refrigeration*, London, U.K, Pion Limited.
- 4 Rowe, D.M. (1995) *CRC Handbook of Thermoelectric*, CRC Press, Boca Raton, FL.
- 5 Rowe, D.M. (2005) *CRC Handbook of Thermoelectrics: Micro to Nano*, CRC Press, Boca Raton, FL.
- 6 Gao, M. (2010) Thermoelectric energy harvesting, Chapter 5, in *Energy Harvesting for Autonomous Systems* (eds S. Beeby and N. White), Artech House Inc., pp. 135–157.
- 7 Gao Min, D., Rowe, M., Assis, O. and Williams, S.G.K. (1992) Determining the Electrical and Thermal Contact Resistance of a Thermoelectric Module, Proceeding of 11th International Conference on Thermoelectrics (Arlington, USA), pp. 210–212.
- 8 Mengali, O.J. and Seiler M.R. (1962) Contact Resistance Studies on Thermoelectric Materials, Symposium on Thermoelectric Energy Conversion, Advanced Energy Conversion, pp. 59–68.
- 9 Caillat, T., Fleurial, J.P., Snyder, G.J., Zoltan, A., Zoltan, D. and Borshchevsky, A. (1999) A New High Efficiency Segmented Thermoelectric Unicouple, 34th Intersociety Energy Conversion Engineering Conference, pp. 2567–2570.
- 10 Caillat, T., Fleurial, J.P., Snyder, G.J., and Borshchevsky, A. (2011) *Progress in the development of segmented thermoelectric unicouples at the Jet Propulsion Laboratory. MRS Proc.*, Cambridge University Press, **626**, pp. Z11.6
- 11 Caillat, T., Fleurial, J.-P., Snyder, G.J. and Borshchevsky, A. (2001) “Development of High Efficiency Segmented Thermoelectric Unicouples,” 20th IEEE International Conference on Thermoelectrics, pp. 282–285.
- 12 Zhao, D., Li, X., He, L., Jiang, W., and Chen, L. (2009) High temperature reliability evaluation of CoSb<sub>3</sub>/electrode thermoelectric joints. *Intermetallics*, **17**, 136–141.
- 13 Zhao, D., Geng, H., and Teng, X. (2012) Fabrication and reliability evaluation of CoSb<sub>3</sub>/W–Cu thermoelectric element. *J. Alloys Compd.*, **517**, 198–203.

- 14 Fan, X.C., Gu, M., Shi, X., Chen, L.D., Bai, S.Q., and Nunna, R. (2015) Fabrication and reliability evaluation of  $\text{Yb}_{0.3}\text{Co}_4\text{Sb}_{12}$ /Mo–Ti/Mo–Cu/Ni thermoelectric joints. *Ceram. Int.*, **41**, 7590–7595.
- 15 Zhao, D., Geng, H. & Chen, L. (2012) Microstructure contact studies for skutterudite thermoelectric devices. *Int. J. Appl. Ceram. Technol.*, **9**(4), 733–741.
- 16 Zhao, D., Tian, C., Tang, S., Liu, Y., Jiang, L., and Chen, L. (2010) Fabrication of a  $\text{CoSb}_3$ -based thermoelectric module. *Mater. Sci. Semicond. Process.*, **13**, 221–224.
- 17 Zhang Q. H., Huang X. Y., Bai S. Q., Shi X., Uher C., & Chen L. D. (2016) Thermoelectric devices for power generation: recent progress and future challenges. *Adv. Eng. Mater.*, **18**, 194–213.
- 18 Wojciechowski, K.T., Zybalia, R., and Mania, R. (2011) High temperature  $\text{CoSb}_3$ –Cu junctions. *Microelectron. Reliab.*, **51**, 1198–1202.
- 19 Berger, H.H. (1972) Contact resistance and contact resistivity. *J. Electrochem. Soc.*, **119** (4), 507–514.
- 20 Thimont, Y. (2014) Design of apparatus for Ni/Mg<sub>2</sub>Si and Ni/MSi1.75 contact resistance determination for thermoelectric legs. *J. Electron. Mater.*, **43**(6), 2023–2028.

# 7

## Thermoelectric Modules: Power Output, Efficiency, and Characterization

Jorge García-Cañadas

*Universitat Jaume I, Department of Industrial Systems Engineering and Design, Campus del Riu Sec, Castellón 12071, Spain*

### 7.1 Introduction

#### 7.1.1 Moving from Materials to a Device

The efficiency of a thermoelectric device is always lower than that predicted from the materials efficiency. This is due to different parasitic resistances that are introduced when forming a device, which consists of additional elements apart from thermoelectric legs. In a typical thermoelectric device (also known as *thermoelectric module*), a large number of n- and p-type semiconductor legs are alternatively connected electrically in series by metallic strips, also known as *electrodes* (see Figure 7.1). The intrinsic resistance of these strips and, more significantly, the contact resistance formed at the leg/electrode junction contribute to the total ohmic resistance of the device, which is no longer just the addition of the electrical resistances of the legs. A schematic variation of the resistance profile due to the different contributions mentioned (leg, contact, and electrode) can be observed in the resistance plot of Figure 7.1.

Apart from the electrodes, electrical insulator plates (usually ceramics) are required (see Figure 7.1). The outer surface of these plates form the final contact with the heat sink and the heat source. Since the device performance depends on the temperature difference reached at the sides of the thermoelectric legs (positions 0 and  $L_{TE}$  in Figure 7.1, with  $L_{TE}$  being the length of the thermoelectric leg) rather than the temperatures at the edges of the ceramic plates; a temperature drop (thermal resistance) is always present due to the ceramics, electrodes, and the contacts. A schematic variation of the temperature profile across the ceramics, electrodes, contacts, and thermoelectric leg can be observed in the temperature plot of Figure 7.1.

It is a challenge to study these parasitic losses and to minimize them as much as possible. The most crucial part of a thermoelectric module is the electrode/leg

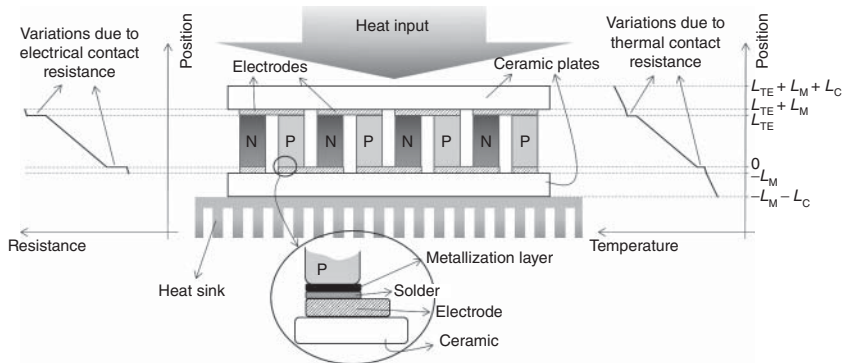


**Figure 7.1** Scheme of the structure and elements that form a thermoelectric module operating in power generation mode. N and P indicate the n- and p-type semiconductor material legs, respectively. Details of a junction are given in the circle. The plots at the sides represent the resistance and temperature profiles across the ceramic plates, electrodes, and thermoelectric material, whose lengths are  $L_C$ ,  $L_{TE}$ , and  $L_M$ , respectively.

junction. A typical structure of this junction is shown in the circle of Figure 7.1. A solder is commonly employed to provide the electrical contact between the legs and the electrodes. For most thermoelectric materials the soldering process is difficult and/or the solders react with the legs along the device operation [1]. For these reasons, a metallization layer is required between the solder and the legs (see circle in Figure 7.1). Its role is to improve solder wettability and block the interdiffusion of atoms across the junction, which eventually could produce the poisoning or degradation of the thermoelectric materials and thus worsen their performance.

As remarked above, it is very important to obtain low electrical and thermal contact resistance at the junctions, so the contact materials should possess high electrical and thermal conductivities and the capability to be made very thin. However, these are not the only requirements needed. In addition, contact materials should be stable at the high operating temperatures, provide mechanically strong bonds and match the thermal coefficient expansion of the thermoelectric legs. The latter is a crucial requirement, since a significant thermal expansion mismatch is going to produce high interfacial mechanical stresses that will produce fracture or cracks at the junctions, causing the increase of both electrical and thermal contact resistances. This requirement is especially relevant for intermediate and high temperature modules where thermal stress is more acute. This and the degradation of the legs due to interdiffusion at the junctions are usually the main reasons for the degradation of device performance after continuous thermal cycling (see Figure 7.2).

### 7.1.2 Differences in Characterization

Apart from the challenges in the device fabrication, characterization of thermoelectric devices is also a tedious and challenging task. One of the main difficulties when calculating device efficiency, given by the electrical power output divided by the heat power input, is the accurate determination of the latter [3]. For this

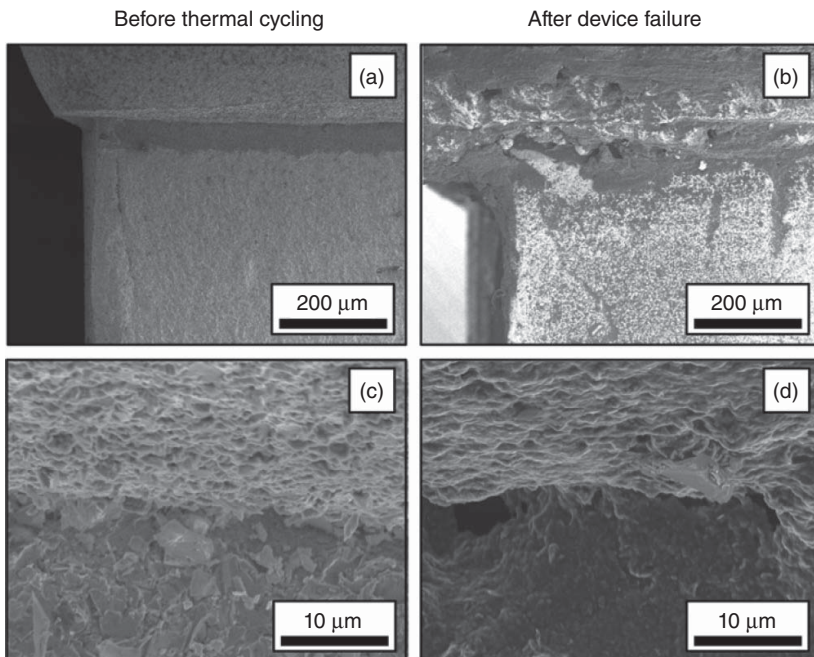


**Figure 7.2** Scanning electron microscopy images of the junction between a thermoelectric leg and a copper electrode (a, c) before and (b, d) after thermal cycling. Cracks, voids, pores, and interdiffusion can be identified after device failure. (Barako 2012 [2]. Reproduced with permission of Springer).

reason, electrical power is typically provided rather than efficiency values, in the literature and by module manufacturers.

Apart from electrical power output determination from current–voltage curves at various temperature differences ( $\Delta T$ ), plots of the variation of the open-circuit voltage and the total device electrical resistance with  $\Delta T$  frequently appear as well. Another important property of thermoelectric modules to be characterized is their behavior under thermal cycling, since cracks and material degradation can occur as previously mentioned, producing a performance decline. For this purpose, the evolution of the parameters previously mentioned (power output, open-circuit voltage, and total electrical resistance) with the number of cycles can be found in the literature [4, 5].

Another relevant consideration when moving from materials to modules is the significance of the figure of merit  $Z$ , which is typically calculated under small temperature gradients ( $\Delta T < 10$  K). Most of materials research is focused on achieving high *peak ZT*, whereas thermoelectric devices operate under large temperature gradients and a large *average ZT* in the temperature range of operation is more important [6]. On the other hand, the module figure of merit  $z$  differs from the material's  $Z$ . The former takes into account not only the electrical resistance of the materials but also the parasitic electrical resistances (electrodes, contact, and wires) that appear in the device.

### 7.1.3 Chapter Summary

Once the main concerns, problems, and challenges when moving from materials to modules have been introduced above, the fundamentals and basic theory describing the performance of thermoelectric modules operating in power generation mode is presented in the rest of the chapter. The governing equations concerning the particle and energy fluxes are introduced first in the next section. Then the power output and efficiency of the device are derived. Finally, different experimental considerations, important to provide reliable characterization results, are introduced.

## 7.2 The Governing Equations

### 7.2.1 Particle Fluxes and the Continuity Equation

In order to understand the physics behind thermoelectric phenomena, it is important to know the particle and energy fluxes in the materials (constitutive equations) and how these fluxes can be altered (continuity equations). Let us start with the electronic (particle) flux equations, which involve the flow or carriers (electrons and/or holes). In a thermoelectric material, the electrical current density  $J(x,t)$  can be expressed by the drift and diffusion contributions [7]. The drift current  $J_{\text{drift}}$  is due to the gradient of potential  $V(x,t)$ , and the diffusion current is induced by a gradient in the carrier concentration  $n(T,t)$  and/or a gradient in the carrier's velocity, governed by the diffusion coefficient  $D(T,t)$ ,

$$J = -\sigma \frac{\partial V}{\partial x} + q \frac{\partial(Dn)}{\partial x} = -\sigma \frac{\partial V}{\partial x} + qn \frac{\partial D}{\partial x} + qD \frac{\partial n}{\partial x}, \quad (7.1)$$

where  $x$  is the position in the material,  $t$  the time,  $\sigma$  the electrical conductivity, and  $q$  the elementary charge. It should be noticed that  $V$  is the potential at a position  $x$  in the material and not a potential difference. The term  $\Delta V$  will be used in this chapter when referring to a potential difference for clarity.

Both  $D$  and  $n$  can vary with position when temperature is not uniform in the material; hence Eq. (7.1) can be written as a function of their temperature derivatives,

$$J = -\sigma \frac{\partial V}{\partial x} + q \left( n \frac{\partial D}{\partial T} + D \frac{\partial n}{\partial T} \right) \frac{\partial T}{\partial x} = -\sigma \frac{\partial V}{\partial x} - \sigma S \frac{\partial T}{\partial x}, \quad (7.2)$$

reaching the generally adopted equation for the electrical current density (right part of Eq. (7.2)) when  $-\sigma S$  is equal to the factor multiplying the  $T$  gradient in Eq. (7.2), with  $S$  being the Seebeck coefficient.

Equation (7.2) finally includes the drift flux and a thermal-diffusion flux  $J_{\text{thermal}}$  with the temperature gradient as driving force. It should be noticed that these fluxes have opposite directions, and when  $J=0$  (open-circuit condition), they cancel each other at any position (see Figure 7.3a). In other words, the carriers being pushed by the temperature gradient induce an opposing electrostatic force when they cannot flow out through the external circuit, producing the open-circuit voltage  $\Delta V_{\text{oc}}$ . When a load is connected at the external circuit

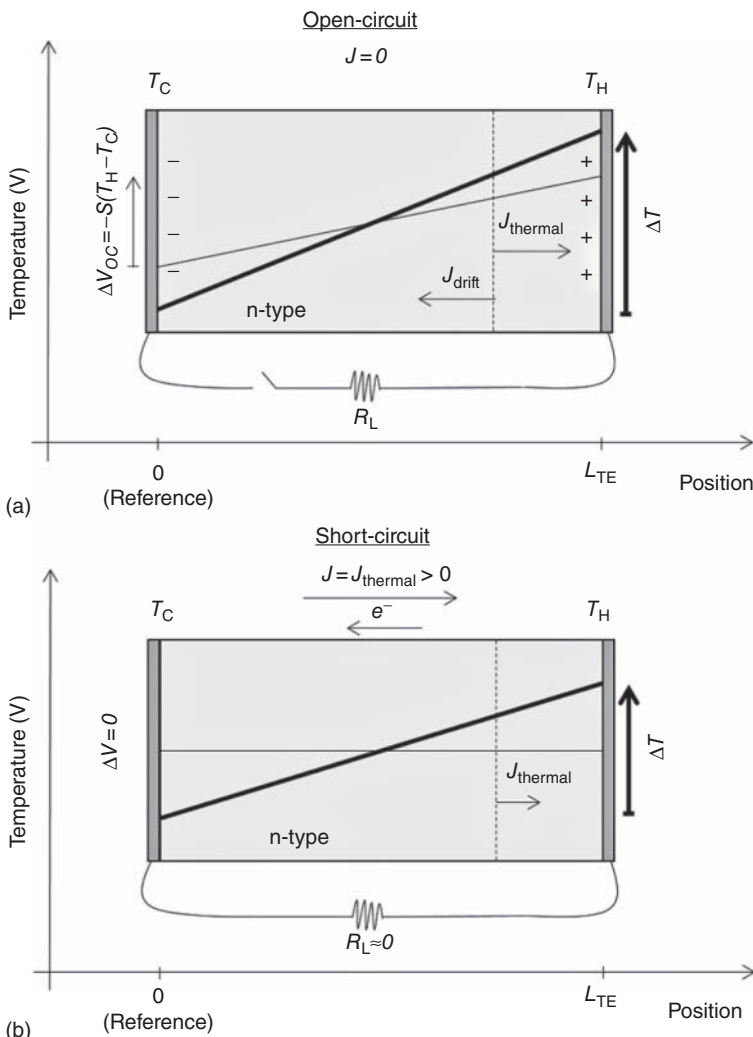


**Figure 7.3** Scheme of steady-state temperature (thick line) and voltage (thin line) profiles in an n-type thermoelectric material of length  $L_{TE}$  under power generation operation contacted by two metallic contacts (dark gray) to an external load resistance  $R_L$ . The dashed line represents a chosen position where the drift and thermal-diffusion fluxes are indicated. Open-circuit and short-circuit conditions are presented in (a) and (b), respectively. The thin and thick vertical arrows indicate the potential and temperature difference across the material, respectively.

and the circuit is closed, the carriers are allowed to flow out and the potential gradient is then reduced, with the thermal current being extracted. The current extracted increases as the load resistance  $R_L$  is decreased, reaching a maximum under short-circuit condition ( $R_L \approx 0$ ,  $\Delta V = 0$ ), when the drift flux goes to zero (see Figure 7.3b).

It should be noted in Figure 7.3 that the  $\Delta T$  is reduced at the short-circuit condition with respect to the open-circuit. This is due to the existence of the

Peltier effect when current flows, which cools down the hot side and heats up the cold side, decreasing to some extent the initial  $\Delta T$ , and consequently reducing the  $J_{\text{thermal}}$ . Also note that by convention  $J$  represents the flow direction of the positive charges and the electrons flow in the opposite direction as indicated in Figure 7.3b. Also note that following the convention adopted in electronics, the reference position for potential difference calculations is always located at the position negatively charged. Consequently, the origin for the position ( $x=0$ ) should also be placed at the negatively charged location. Otherwise, the directions of the fluxes would be wrong.

The continuity equation for the electrical flux is given by a conservation law, which states that the total amount of charge carriers in the material has to be conserved. Hence, the only way of varying the carrier concentration at a given volume  $A\Delta x$  of the material,  $A$  being the cross-sectional area, after a  $\Delta t$  is by the modification of the charge carrier flux,

$$q \frac{dn}{dt} = -\frac{\partial J}{\partial x}. \quad (7.3)$$

In Figure 7.4, it can be observed that the carrier density increases by one carrier after  $t + \Delta t$  as a consequence of the decrease in the carrier flux at position  $x$ . The carrier accumulated plus the two carriers flowing out equal the three carriers that initially entered the  $A\Delta x$  volume. By adding Eq. (7.2) into Eq. (7.3) and considering the materials properties independent of temperature, a new equation is obtained,

$$q \frac{\partial n}{\partial t} = -\sigma \frac{\partial^2 V}{\partial x^2} - \sigma S \frac{\partial^2 T}{\partial x^2}. \quad (7.4)$$

This equation indicates that variations of carrier density can only be achieved by a variation of the voltage or thermal gradient with position.

### 7.2.2 Energy Fluxes and the Heat Equation

Once the constitutive and continuity equations have been defined for charge carriers, let us now identify the corresponding equations for the energy fluxes in a thermoelectric material and how they can vary with position producing energy absorption or release. In the description, the notation  $J_Q$  will be used for heat fluxes, that is, the amount of energy crossing a cross-sectional area per unit time,

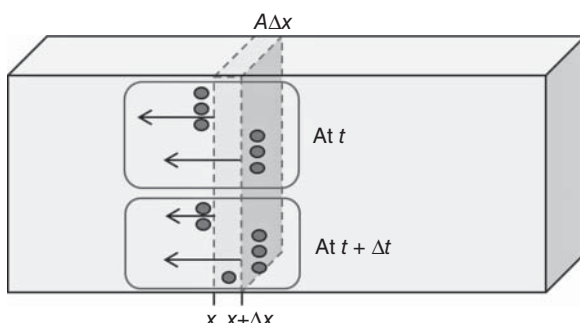


**Figure 7.4** Illustration of the variation of the electrical current density at positions  $x$  and  $x + \Delta x$  at two different times ( $t$  and  $t + \Delta t$ ), achieved by the accumulation of one carrier in the  $A\Delta x$  volume of the material. Carriers are represented by circles and fluxes by arrows.

given in  $\text{W/m}^2$ . Heat generation or absorption produced in a unit volume of the material per unit time, in  $\text{W/m}^3$ , will be represented by  $Q$ .

Two contributions to the total energy flux are typically identified in thermo-electric materials,

$$J_Q = -\lambda_{\text{TE}} \frac{\partial T}{\partial x} + STJ. \quad (7.5)$$

The first term is the conductive heat flux (Fourier law) and represents the conduction of heat from hot to cold parts within a material, which relates to the thermal conductivity of the thermoelectric material  $\lambda_{\text{TE}}$  and the temperature gradient. The second term,  $STJ$ , collects all the thermoelectric phenomena.

Deriving Eq. (7.5) versus position, the energy absorption/release processes in the material can be identified. As in the continuity equation for electronic current, the amount of energy in the material should be conserved. If a change in the energy flux is produced, it should be due to an absorption or release of energy, in other words, an increase or decrease in temperature. To illustrate this, Figure 7.4, employed for carriers, can be used. Just consider each circle as a certain amount of energy instead of a carrier.

Derivation of Eq. (7.5) results in

$$\begin{aligned} \frac{\partial J_Q}{\partial x} &= -\frac{\partial}{\partial x} \left( \lambda_{\text{TE}} \frac{\partial T}{\partial x} \right) + \frac{\partial}{\partial x} (STJ) \\ &= -\frac{\partial}{\partial x} \left( \lambda_{\text{TE}} \frac{\partial T}{\partial x} \right) + TJ \frac{\partial S}{\partial x} + SJ \frac{\partial T}{\partial x} + ST \frac{\partial J}{\partial x}. \end{aligned} \quad (7.6)$$

The last three terms of this equation indicate the different ways in which the energy flux given by  $STJ$  can be varied. They will be analyzed now in detail.

Let us start by the analysis of the term where  $S$  varies with position (second term at the right hand side of Eq. (7.6)). From this term the Peltier and Thomson effects can be deduced, as illustrated in Figure 7.5. When  $T$  is homogeneous in the system and a current flow exists, which could be the case right after the very first moment of applying a current to the system initially in equilibrium, only  $S$  variations occur at the junctions (positions 0 and  $L_{\text{TE}}$ ), owing to the different Seebeck coefficients of the metal and the thermoelectric material. In this case, the flux very close to the left side of the junction  $x=0$  increases significantly at the right side very close to the junction, which due to energy conservation produces an absorption of energy (cooling) equal to the difference between fluxes  $(S_M - S)TJ$ , with  $S_M$  being the Seebeck coefficient of the metallic contact (see Figure 7.5a). The physics behind this effect, in a simplistic view, relates to the gain of energy by each electron passing from an energy level in the metal to another level of higher energy in the thermoelectric material [8].

On the other hand, at position  $x=L_{\text{TE}}$  in Figure 7.5a the flux significantly decreases from the left hand side close to the junction to the right hand side, releasing heat (heating). This can be seen as the release of energy by the electrons when crossing the junction and moving from an energy level in the thermoelectric material to a lower energy level in the metal.

It should be noted that the heat fluxes in Figure 7.5 are indicated by the horizontal arrows, its length being given by the absolute value  $|STJ|$  and the direction

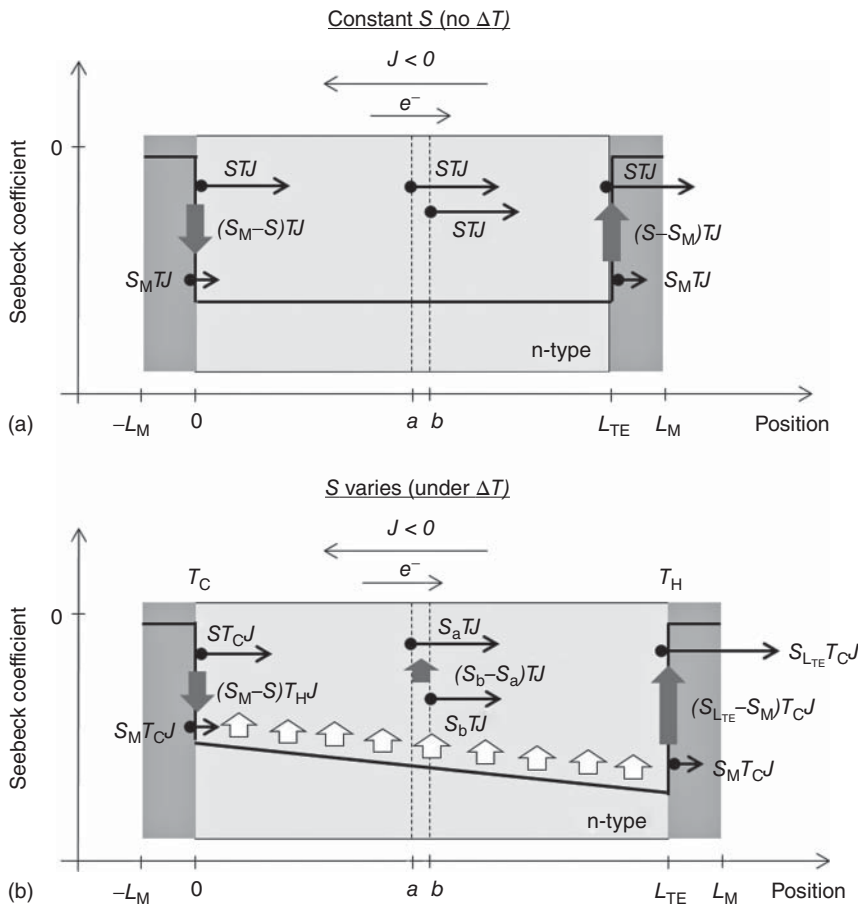


**Figure 7.5** Scheme of the different heat fluxes (thin horizontal arrows) and heat absorption/generation (vertical thick arrows) processes occurring because of variations of the Seebeck coefficient  $S$  at different positions of an n-type thermoelectric material connected to metallic contacts under the flow of a positive electrical current density  $J$ . (a) Only Peltier effect takes place at the junctions ( $0$  and  $L_{TE}$ ) when the  $S$  is constant in the materials (no temperature difference). (b) Under a  $T$  gradient  $S$  varies inside the thermoelectric material, which produces heat generation in the bulk (Thomson effect), as occurs between points  $a$  and  $b$  and also indicated by the extended white thick arrows. Peltier effect also takes place at the junctions.

adopted from the final sign obtained in the product of the parameters  $S$  and  $J$  ( $T$  is the absolute temperature and always positive). For a negative current and  $n$ -type material ( $S < 0$ ) a positive sign results and the flux points toward the right, indicating that the heat is pumped from left to right.

Let us now move to the case where the Seebeck coefficient varies within the material owing to the existence of a  $T$  difference (Figure 7.5b). This can take place for example at steady-state condition after applying a constant current to the system initially in equilibrium. Apart from the Peltier effect at the junctions, now the heat flux  $STJ$  varies inside the material. For example, at position  $a$ , the heat flux

is higher than at position  $b$ ; thus, a release of an amount of heat  $(S_b - S_a)TJ$  has to be produced. This release of heat occurs all along the extension of the material (indicated by the white arrows in Figure 7.5b), and is known as the *Thomson effect*,

$$Q_T = -TJ \frac{\partial S}{\partial x}. \quad (7.7)$$

If the  $S$  of the material only depends on  $T$ , which is usually the case, then Eq. (7.7) can be expressed as,

$$Q_T = -T \frac{dS}{dT} J \frac{\partial T}{\partial x}, \quad (7.8)$$

which is the most widely used equation for the Thomson effect. It should be noted that if the sign of the electric current is changed to positive and the temperature gradient does not change its sign, the Thomson heat is not released but absorbed in the bulk of the material.

After this analysis, somehow the Thomson effect can be seen as an extension of the Peltier effect in the bulk of the material (distributed Peltier effect), and for this reason some authors consider that the Peltier effect also takes place in the bulk, apart from occurring at the junctions. It should be noted that the heat released/absorbed at the junctions is much more significant than the heat absorbed/released in the bulk, since the variation of  $S$  is much smaller in the bulk compared to that at the junctions. For this reason, Thomson effect is typically neglected and becomes only relevant at large  $\Delta T$ .

Let us now pay attention to the term  $SJ\partial T/\partial x$  from Eq. (7.6). Using Eq. (7.2) for the electrical current where the product  $S\partial T/\partial x$  appears,

$$SJ \frac{\partial T}{\partial x} = -J \frac{\partial V}{\partial x} - \frac{J^2}{\sigma}. \quad (7.9)$$

Now two terms appear. The first one is the electrical work, also expressed usually as,

$$-J \frac{\partial V}{\partial x} = JE, \quad (7.10)$$

where  $E = -\partial V/\partial x$  is the electric field. The Joule heat generated in the material by the electrical conduction of carriers (heat dissipation) is the other term.

Finally, the last term in Eq. (7.6),  $ST\partial J/\partial x$ , relates by means of Eq. (7.3) to energy variations induced by changes in the carrier concentration (charge reorganization). This term becomes zero and current becomes uniform at steady-state condition, as a result of Eq. (7.3).

Hence, the variation of the energy flux in the material can occur by variations of heat conduction, the Peltier effect, the Thomson effect, the Joule heating, the electrical work, and the reorganization of carriers,

$$\frac{\partial J_Q}{\partial x} = -\frac{\partial}{\partial x} \left( \lambda_{TE} \frac{\partial T}{\partial x} \right) + T \frac{dS}{dT} J \frac{\partial T}{\partial x} - \frac{J^2}{\sigma} + JE + ST \frac{\partial J}{\partial x}. \quad (7.11)$$

In order to identify the continuity equation (energy conservation law) in a thermoelectric material, also known as the heat diffusion equation or simply the heat equation, the variations of energy flux in a material volume  $A dx$ , produced after

a time  $dt$ , are necessarily related to a gain or decrease in the temperature of the material,

$$dC_p \frac{\partial T}{\partial t} = -\frac{\partial J_Q}{\partial x}. \quad (7.12)$$

In this equation,  $d$  is the mass density and  $C_p$  is the specific heat, defined as the amount of energy required to increase the temperature of a unit mass of material by 1 K. It should be mentioned that heat transfer processes by convection or radiation can also occur at the boundaries of the material, but they are not considered in our analysis.

It can be noticed from Eqs. (7.11) and (7.12) that for a material initially at thermal equilibrium (homogeneous temperature), it is not possible to change its temperature unless an electrical current or heat input/removal is applied to it, in other words, an external source of energy is required, which thus needs to be added to the total energy balance. If an external electric field is applied to the system, then Eq. (7.12) becomes,

$$dC_p \frac{\partial T}{\partial t} = -\frac{\partial J_Q}{\partial x} + JE. \quad (7.13)$$

By combining Eqs. (7.11) and (7.13) the continuity equation becomes,

$$dC_p \frac{\partial T}{\partial t} = \frac{\partial}{\partial x} \left( \lambda_{TE} \frac{\partial T}{\partial x} \right) - T \frac{dS}{dT} J \frac{\partial T}{\partial x} + \frac{J^2}{\sigma} - ST \frac{\partial J}{\partial x}. \quad (7.14)$$

Under steady-state conditions and assuming that the thermal conductivity is independent of position ( $T$  independent), Eq. (7.14) takes the form,

$$\lambda_{TE} \frac{\partial^2 T}{\partial x^2} - T \frac{dS}{dT} J \frac{\partial T}{\partial x} + \frac{J^2}{\sigma} = 0, \quad (7.15)$$

which is the main equation that will be used for the efficiency evaluation in the next section. It should be noted that Eq. (7.15) is a second-order differential equation; hence, it requires two additional boundary conditions to provide a complete physical description of the system, as will be seen below.

### 7.3 Power Output and Efficiency

Characterizing thermoelectric devices in power generation mode typically involves the use of a heater block attached to the top side of the module acting as the heat source. Two different ways of supplying energy to the heater can be employed. On the one hand, the heater can be powered using a *constant power*, provided by a power source or a variable transformer able to regulate the power supply from the mains. In this mode, assuming that the conditions of the environment do not change, a *constant input heat flux* is applied on the thermoelectric device, which does not change when a current flow exists in the system. However, changes in the hot and cold side temperatures can be produced when electrical current is flowing due to the Peltier effect, which cools down the hot side and heats up the cold side, leading to a decrease in  $\Delta T$  with respect to its open-circuit value.

On the other hand, the heater can be powered by a power source with a *temperature controller*, which adapts the power supplied to the heater in order to maintain constant a set temperature. In this mode, when a decrease in the hot side temperature is produced by the Peltier effect under electric current flow, the controller increases the power supplied to the heater to maintain the hot side temperature at the set value, so the heat input changes depending on the electric current flow. This is known as *constant  $\Delta T$*  mode. Regarding efficiency measurements the constant  $\Delta T$  mode is less appropriate, since the heat input changes for the different levels of electric current and the losses produced by the Peltier effect become masked.

### 7.3.1 Power Output

Let us consider a thermoelectric device as that shown in Figure 7.1 formed by  $2N$  legs, with  $N$  being the number of n- and p-type semiconductor couples, under steady-state conditions. The heat power input  $Q_{in}$  reaching the module hot side is considered to flow without heat losses through the module. The amount of  $Q_{in}$  not converted into electrical power,  $Q_{out}$ , leaves the device at the cold side (see scheme of Figure 7.6a for a single couple). The material's properties are considered independent of temperature (constant properties model) and have an *average value* for the operating temperature range. They are also considered identical for both n- and p-type legs. The effect of the ceramic and electrodes will not be considered in the heat treatment.

Under these assumptions, the system delivers a certain amount of electric power  $P$  when connected to a load. The power delivered to the load is given by the product,

$$P = I\Delta V_L, \quad (7.16)$$

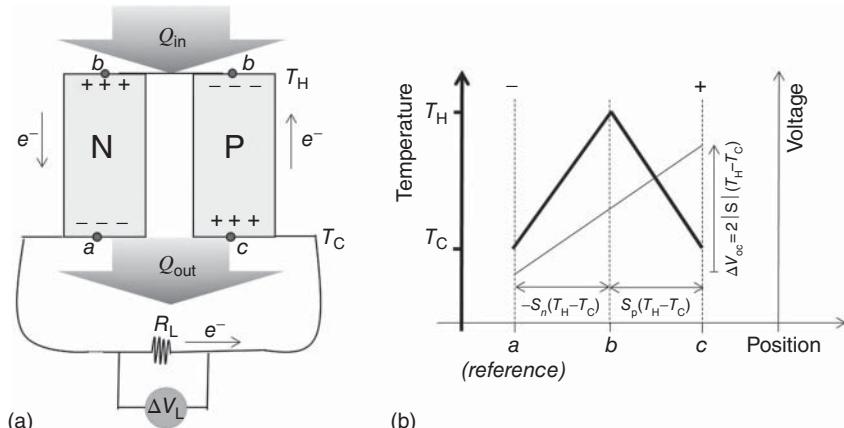


**Figure 7.6** (a) Scheme of an n- and p-type semiconductor couple under power generation mode delivering electric power to a load ( $R_L$ ). A scheme of the temperature (thick line) and voltage (thin line) profiles at open-circuit condition is given in (b) for positions  $a$ ,  $b$ , and  $c$ .  $S_n$  and  $S_p$  are the average Seebeck coefficient values for the given temperature range for the n- and p-type materials, respectively.

where  $I$  is the electric current and  $\Delta V_L$  the potential difference across the load,

$$\Delta V_L = IR_L. \quad (7.17)$$

It can be seen from Eq. (7.17) that  $\Delta V_L$  and  $I$ , and hence  $P$ , vary when changing the load resistance, which is a parameter that can be conveniently adjusted. In order to identify the value of  $R_L$ , which provides the maximum power for a given device,  $I-\Delta V_L$  curves are typically recorded. They are performed from the open-circuit voltage  $\Delta V_{oc}$  ( $R_L \rightarrow \infty$ ) to the short-circuit condition  $\Delta V_L = 0$  ( $R_L \approx 0$ ).

The open-circuit potential difference in the module is given by the addition of the  $\Delta V$  provided by each leg, as seen in Figure 7.6b for a couple. Note in this figure that in the calculation the sign of the product  $S(T_H - T_C)$  has to be changed when the reference position is not at the hot side (as a convention, the Seebeck potential difference is measured with respect to the hot side), as occurs for the n-type leg (see Figure 7.6b).

When the circuit is closed the open-circuit voltage of the module is dissipated in the load resistance and in the total ohmic resistance of the thermoelectric module, which includes contributions from materials, contacts, electrodes, and wires,

$$2N|S|(T_H - T_C) = IR_\Omega + IR_L. \quad (7.18)$$

The absolute average Seebeck coefficient  $|S|$  is adopted instead of independently considering the  $S$  values for the n- and p-type materials for simplicity. It is worth mentioning that  $R_\Omega$  is usually known as the *internal resistance of the device*, although some authors consider the internal resistance as just the addition of the intrinsic resistance of the thermoelectric materials, without including the parasitic resistances (contact, electrodes, and wires contribution). To avoid confusion,  $R_\Omega$ , which includes materials and parasitic contributions, is used in this chapter.

From Eq. (7.18) the current can be determined as,

$$I = \frac{2N|S|(T_H - T_C)}{R_\Omega + R_L}. \quad (7.19)$$

Introducing  $I$  from Eq. (7.19) and  $\Delta V_L$  from Eq. (7.17) in Eq. (7.16), the electrical power as a function of  $R_L$  results:

$$P = \frac{[2N|S|(T_H - T_C)]^2}{(R_\Omega + R_L)^2} R_L. \quad (7.20)$$

If we introduce now the parameter  $m = R_L/R_\Omega$ , then Eq. (7.20) becomes,

$$P = \frac{[2N|S|(T_H - T_C)]^2}{R_\Omega} \frac{m}{(1+m)^2}. \quad (7.21)$$

In order to identify the value of  $R_L$ , which provides the maximum power, keeping the rest of parameters fixed, the maximum power  $P_{max}$  is achieved when  $m = 1$ , that is, when  $R_L = R_\Omega$ ,

$$P_{max} = \frac{[2N|S|(T_H - T_C)]^2}{4R_\Omega}. \quad (7.22)$$

This equation predicts a parabolic relationship between  $P_{\max}$  and  $\Delta T$ , which experimentally is frequently found. However, it should be taken into account that Eq. (7.22) is a quite ideal result which involves a significant number of assumptions, so deviations can be found. They can result for example from the effect of ceramics, the variation of the material's parameters with temperature and changes in the  $\Delta T$  when  $R_L$  is varied (constant heat input characterization mode).

### 7.3.2 Efficiency

Employing the same assumptions as in the derivation of the power output for a thermoelectric module, let us now focus on the calculation of the efficiency  $\eta$  of the device, which is determined by the ratio between the electrical power output and the incident heat power at the hot side (see Figure 7.6a),

$$\eta = \frac{P}{Q_{\text{in}}}. \quad (7.23)$$

Since the equation for the power was already derived above (Eq. (7.21)), we only need the incident heat power to complete the efficiency calculation, which can be obtained from the energy balances at the sides of the thermoelectric legs (see Figure 7.7),

$$\frac{Q_{\text{in}}}{A} - 2N \frac{ST_H I}{A} + 2N \lambda_{\text{TE}} \left( \frac{\partial T}{\partial x} \right)_0 = 0, \quad \text{at } x = 0, \quad (7.24)$$

$$-\frac{Q_{\text{out}}}{A} + 2N \frac{ST_C I}{A} - 2N \lambda_{\text{TE}} \left( \frac{\partial T}{\partial x} \right)_{L_{\text{TE}}} = 0 \quad \text{at } x = L_{\text{TE}}. \quad (7.25)$$

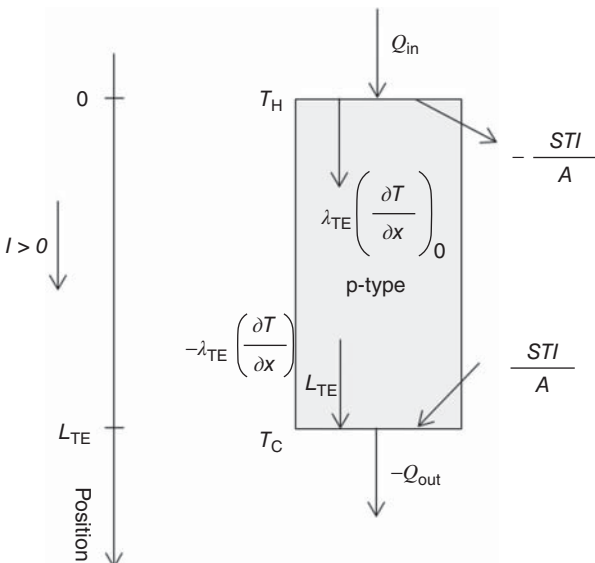


**Figure 7.7** Energy balances at the boundaries (positions 0 and  $L_{\text{TE}}$ ) of a p-type leg under power generation mode without contacts consideration. The arrows pointing in and out of the boundaries indicate heat addition and heat removal, respectively.

$Q_{\text{in}}$  can be added to Eq. (7.25) using  $Q_{\text{in}} = Q_{\text{out}} + P$ . However, it is easier to use Eq. (7.24). Note that the factor  $2N$  is needed since  $Q_{\text{in}}$  is applied to the whole device and each leg participates in its balance. In addition, to ensure the right sign of each term, heat inputs at the boundary are considered positive and outputs as negative. For this purpose the Peltier term was made negative at  $x=0$  (since  $S$  and  $I$  are positive), in addition to the heat conduction term at  $x=L_{\text{TE}}$  (since the  $T$  gradient is negative) and  $Q_{\text{out}}$ . Once all terms have the appropriate sign, their addition should be zero.

In order to obtain the  $T$  derivatives in the energy balances at the junctions (Eqs. (7.24) and (7.25)) the heat equation (Eq. (7.15)) for one leg should be solved. For simplicity the heat equation without Thomson heat will be considered,

$$\lambda_{\text{TE}} \frac{\partial^2 T}{\partial x^2} + \frac{I^2}{A\sigma} = 0. \quad (7.26)$$

The boundary conditions adopted are,

$$T(0) = T_{\text{H}} \quad \text{and} \quad (7.27)$$

$$T(L_{\text{TE}}) = T_{\text{C}}. \quad (7.28)$$

Performing a double integration in Eq. (7.26), we obtain,

$$T(x) = -\frac{I^2 x^2}{2\lambda_{\text{TE}} A\sigma} + C_1 x + C_2, \quad (7.29)$$

where  $C_1$  and  $C_2$  are integration constants that can be deduced from the boundary conditions (Eqs. (7.27) and (7.28)),

$$C_2 = T_{\text{H}} \quad \text{and} \quad (7.30)$$

$$C_1 = \frac{I^2 L_{\text{TE}}}{2\lambda_{\text{TE}} A\sigma} - \frac{(T_{\text{H}} - T_{\text{C}})}{L_{\text{TE}}}. \quad (7.31)$$

Then,  $T(x)$  and its derivative are given by,

$$T(x) = -\frac{I^2}{2\lambda_{\text{TE}} A\sigma} x^2 + \left[ \frac{I^2 L_{\text{TE}}}{2\lambda_{\text{TE}} A\sigma} - \frac{(T_{\text{H}} - T_{\text{C}})}{L_{\text{TE}}} \right] x + T_{\text{H}}. \quad (7.32)$$

$$\frac{dT}{dx} = -\frac{I^2}{\lambda_{\text{TE}} A\sigma} x + \frac{I^2 L_{\text{TE}}}{2\lambda_{\text{TE}} A\sigma} - \frac{(T_{\text{H}} - T_{\text{C}})}{L_{\text{TE}}}. \quad (7.33)$$

At  $x=0$ , Eq. (7.33) becomes,

$$\left( \frac{dT}{dx} \right)_0 = \frac{I^2 L_{\text{TE}}}{2\lambda_{\text{TE}} A\sigma} - \frac{(T_{\text{H}} - T_{\text{C}})}{L_{\text{TE}}}, \quad (7.34)$$

which can now be inserted into Eq. (7.24) to obtain  $Q_{\text{in}}$ ,

$$Q_{\text{in}} = 2N|S|T_{\text{H}}I + 2N\frac{1}{2}I^2R_{\text{leg}} - 2N\lambda_{\text{TE}}A\frac{(T_{\text{H}} - T_{\text{C}})}{L_{\text{TE}}}, \quad (7.35)$$

where  $R_{\text{leg}}$  is the intrinsic resistance of one leg,

$$R_{\text{leg}} = \frac{L_{\text{TE}}}{A\sigma}. \quad (7.36)$$

Note that the temperature gradient (Eq. (7.34)) differs from the situation at open circuit ( $I = 0$ ) owing to the Joule effect ( $0.5 I^2 R_{\text{leg}}$ ). Consequently, the heat removed by conduction from the junction ( $x = 0$ ) is reduced by  $0.5 I^2 R_{\text{leg}}$  with respect to the open-circuit condition (no Joule effect).

By dividing the power in Eq. (7.21) by the result of introducing Eq. (7.19) in Eq. (7.35) and after a few algebra steps, the efficiency results as,

$$\eta = \frac{(T_H - T_C)}{T_H} \frac{m}{\left[ 1 + m + 0.5 \frac{2NR_{\text{leg}}}{R_\Omega} \frac{(T_H - T_C)}{T_H} - \frac{(1+m)^2}{zT_H} \right]}, \quad (7.37)$$

where

$$z = \frac{2NS^2}{\lambda_{\text{TE}} R_\Omega} \frac{L}{A} \quad (7.38)$$

is the thermoelectric *module figure of merit*. It should be remembered that  $R_\Omega$  has been defined as the total ohmic resistance of the device, which can be expressed as,

$$R_\Omega = R_p + 2NR_{\text{leg}}, \quad (7.39)$$

where  $R_p$  is the total parasitic resistance. If the parasitic resistance is neglected ( $R_p = 0$ ) then  $z$  becomes the material's figure of merit  $Z$ ,

$$Z = \frac{S^2 \sigma}{\lambda_{\text{TE}}}. \quad (7.40)$$

In order to identify the value of  $R_L$ , which provides the maximum efficiency, Eq. (7.37) is derived with respect to  $m$  assuming the rest of parameters to be constant. When the derivative is equal to zero, the optimum value of  $m$  is identified as,

$$m_\eta = \sqrt{1 + zT_M}, \quad (7.41)$$

where  $T_M = 0.5(T_H + T_C)$  is the mean operating temperature. By introducing this result in Eq. (7.37), the maximized efficiency is obtained,

$$\eta_{\max} = \frac{(T_H - T_C)}{T_H} \frac{\sqrt{1 + zT_M} - 1}{\sqrt{1 + zT_M} + \frac{T_C}{T_H}}. \quad (7.42)$$

As a consequence of this equation, most research efforts are focused on materials development (increase  $z$ ) to improve the heat to electricity conversion efficiency. It is important to also take into account in Eq. (7.42) the Carnot efficiency term ( $\Delta T/T_H$ ), which highlights the importance of achieving a large  $\Delta T$  in the device, so the role of heat exchangers (heat management) to address a maximum  $\Delta T$  is also of significant importance.

As remarked above for the maximum power derivation, Eq. (7.42) involves a significant number of assumptions that should be carefully considered when accurate calculations are required. For example, if the peak  $Z$  of materials is introduced instead of using in  $z$  the average material's properties, much larger efficiencies could be predicted that are not accurate.

It should be noticed that different optimum values of  $R_L$  were obtained when pursuing for the maximum power ( $R_L = R_\Omega$ ) and efficiency ( $R_L = R_\Omega(zT_M + 1)^{0.5}$ ). This means that given a fabricated thermoelectric device, where  $N$ ,  $L_{TE}$ , and  $A$  are already fixed, more power will be produced for the case when heat power higher than  $Q_{in}$  can be supplied. However, for a fixed  $Q_{in}$ , more power will be produced in the maximum efficiency condition. It is worth mentioning that when designing the device,  $N$ ,  $L_{TE}$ , and  $A$  are design parameters and not fixed. If this is taken into account for the identification of the load resistance value that provides the maximum power, the result agrees with the efficiency optimization,  $R_L = R_\Omega(zT_M + 1)^{0.5}$  [9].

## 7.4 Characterization of Devices

When facing the task of characterizing a thermoelectric device, it is important to pay attention to multiple factors that can significantly influence your results, most of them related with thermal aspects (especially thermal contacts). A summary of good practices to mitigate these issues as much as possible is provided in this section.

### 7.4.1 Thermal Contacts

Only a small percentage of the total surface area of two solids brought into contact is actually in contact, as seen in Figure 7.8. This is due to the roughness of the materials that form peaks and valleys at a microscopic level. Consequently, most of the contact zone comprises a large number of air gaps, which considerably reduces the thermal conduction from one solid to the other. In order to improve this situation, different solutions can be implemented at the junction. One of the most frequent approaches is to employ a thin layer of thermal grease or a heat sink compound that will fill in the air gaps. Although these compounds do not usually present extraordinarily high thermal conductivities, they are able to transfer heat much better than air. When using thermal grease it is very important to just apply a very thin layer (only air gaps need to be filled). A thick layer could worsen the heat transfer and be detrimental. Soldering or the use of liquid metals that exhibit higher thermal conductivity than heat sink compounds can be also

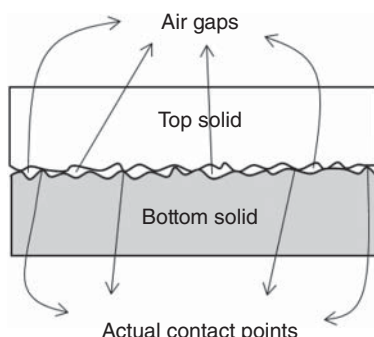


**Figure 7.8** Microscopic scheme of a thermal contact between two solids. Air gaps are predominant in the contacted area, which limits the heat transfer by conduction between the solids. Only a small fraction of the surfaces are actually contacted.

adopted, although the latter are usually more expensive. The soldering process is only possible in modules that present metallized ceramics.

Another common solution is to use a thin graphite sheet or thermal pads. However, although these materials are quite ductile, they do not usually fill in the air gaps as efficiently as the thermal grease or the liquid metals and require significant pressure to achieve suitable thermal contact. In contrast, they can perform better than thermal grease at high temperatures or vacuum conditions, where evaporation of chemicals contained in the thermal grease could more easily occur, producing dryness in the heat sink compound and hence worsening the thermal conduction. If thermal grease is used under these conditions, it is highly recommendable to clean and apply a fresh layer after each measurement.

If a copper block with inserted heater cartridges is used as the heat source, it is recommendable to apply a tolerance in the diameter of the holes in the block according to the expected thermal expansion of the heaters, especially at operation under large temperature differences. Spreading a very thin layer of thermal grease on the cartridges is also beneficial, especially when working in vacuum conditions, in order to improve the contact between the surface of the heaters and the copper block.

The clamping pressure in the characterization setup, which should be applied uniformly, is also of considerable importance, since pressure improves the thermal contacts and can significantly increase the power output. However, pressure should be carefully applied. A large pressure could produce cracks in the thermoelectric materials or at the junctions or even break the device. Module suppliers usually provide recommended pressure values (typically around 1 MPa) that should be checked to avoid damaging the device.

The flatness of the surface of the ceramic layers is also key to the issue of thermal contact. Some module manufacturers advise a tolerance of  $\pm 25 \mu\text{m}$  along the whole surface area (e.g., [www.customthermoelectric.com](http://www.customthermoelectric.com)). In addition, the surfaces should be clean and free from dirt and scratches.

#### 7.4.2 Additional Considerations

The efficiency of thermoelectric modules from the electrical power supplied to the heater is frequently estimated, assuming that heat losses do not take place and that all the heat dissipated in the heater block is completely transferred to the device. However, it is difficult to achieve these conditions mainly because of convective and radiative heat losses, which makes it difficult to accurately measure the incident heat power  $Q_{\text{in}}$  and hence the efficiency. Measurements under vacuum can considerably minimize heat convection; however, radiation losses are more difficult to suppress. In this respect it is recommended to use heater blocks of the same cross-sectional area as the thermoelectric device, which will reduce radiation heat transfer toward the cold side area. In addition, providing some kind of shielding around the heater block could be advantageous.

On the other hand, thermoelectric devices usually provide large currents; for this reason, relatively thick wires are typically soldered to modules, which can remove a significant amount of heat especially in small modules. If thin wires are soldered instead, they could not withstand the high current levels and, in

addition, they could increase the total ohmic resistance (internal resistance) of the device and hence reduce the power output. A similar situation can occur if thin long wires are used to contact the device with the measuring equipment that records the current and voltage signals. The length and cross-sectional area of the wire are proportional and inversely proportional, respectively, to its resistance.

In the case of tiny modules of a few couples, the total ohmic resistance could be quite low and thus approach the order of magnitude of electrical contact resistances. In this case, it is very important to perform a suitable soldering of the wires to the module. If the device is tested without soldered wires it is preferable to measure in a four-probe configuration. On the other hand, it is important to set the part of the module with the wires soldered at the cold side. Wires are usually soldered with a solder different from that employed for the legs, which do not necessarily present a high melting point. Moreover, it should be taken into account that usually the melting point of the solder is the parameter limiting the maximum hot side temperature operation, so it is important to know its value.

Regarding the thermocouples that are generally employed to measure the different temperatures of the system, it is important to place them as close as possible to the ceramics. If they are inserted into holes or just physically touching the ceramics, their tip should be surrounded with thermal grease to thermalize them. Otherwise, only the part of the tip in contact with the object is at the actual temperature. Thermocouples fabricated with very thin wires that can be inserted directly at the interfaces of the ceramics with the heat source or heat sink are ideal; however, they are quite difficult to handle and easily break.

#### 7.4.3 Constant Heat Input and Constant $\Delta T$

At the beginning of Section 7.3, the two most frequently used methods to obtain the  $I-\Delta V$  curves from which the power output is extracted were explained. When recording the  $I-\Delta V$  curve it is important to wait until reaching the steady state once the load resistance is varied. Changes in  $R_L$  modify the current and hence the Peltier effect at the junctions, consequently varying the temperature difference across the module. When measuring under the constant heat mode, establishing the new  $\Delta T$  will take time. On the other hand, in the constant  $\Delta T$  mode the temperature controller also needs some time to detect the temperature change (usually the thermocouple controlling the  $T$  is placed on the ceramic or at a certain distance from it) and regulate the heat input to return to the set temperature. If the  $I$  and  $\Delta V$  values are recorded without waiting for these processes to be completed, the results obtained will be misleading.

It is important to note that the slope of the  $I-\Delta V$  curves recorded by these two methods when both are starting from the same open-circuit voltage value will differ [10], as shown schematically in Figure 7.9a. In the case of the constant  $\Delta T$  method the slope provides the total ohmic resistance  $R_\Omega$  of the module at the operating temperature range (see Figure 7.9a). For the constant heat input mode, a larger resistance will be obtained and hence a lower power output. The decrease of the temperature difference, ( $\Delta T_{oc} - \Delta T_{cc}$ ), where  $\Delta T_{oc}$  and  $\Delta T_{cc}$  are the open-circuit and closed-circuit steady-state  $T$  differences respectively, reduces the initial open-circuit voltage  $\Delta V_{oc}$  and introduces an additional

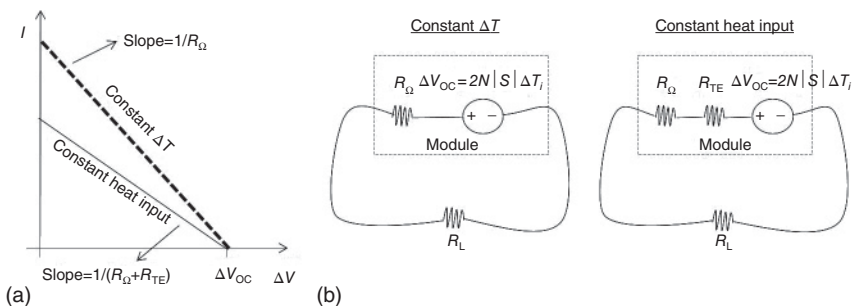


**Figure 7.9** (a) Scheme of  $I$ - $\Delta V$  curves under constant  $\Delta T$  (dashed line) and constant heat input (solid line) modes. (b) Steady-state equivalent circuits for both modes. A thermoelectric resistance  $R_{TE}$  in addition to the total ohmic resistance of the device  $R_\Omega$  is included in the constant heat input mode, which accounts for the variations in  $\Delta T$  that occur owing to the Peltier effect. A dashed square encloses the elements that define the thermoelectric module.

contribution to the total ohmic resistance of the device, which can be seen as a thermoelectric resistance  $R_{TE}$  (see equivalent circuits of Figure 7.9b) and modifies the slope of the  $I$ - $\Delta V$  curve (Figure 7.9a).

This analysis demonstrates the importance of indicating the method employed in the characterization of the device. It should be noted that the constant  $\Delta T$  method suppresses the thermoelectric resistance (intrinsic losses due to the Peltier effect) by introducing additional energy input in the system. Establishing a comparison to the field of photovoltaics, it would be similar to eliminate recombination events in a solar cell by increasing the amount of incident light during the evaluation of its power output, which discards one of the main losses of the system.

## References

- 1 Liu, W. *et al.* (2015) Current progress and future challenges in thermoelectric power generation: from materials to devices. *Acta Mater.*, **87**, 357–376.
- 2 Barako, M.T. *et al.* (2012) Thermal cycling, mechanical degradation, and the effective figure of merit of a thermoelectric module. *J. Electron. Mater.*, **42** (3), 372–381.
- 3 Wang, H. *et al.* (2014) Determination of thermoelectric module efficiency: a survey. *J. Electron. Mater.*, **43** (6), 2274–2286.
- 4 Garcia-Canadas, J. *et al.* (2013) Fabrication and evaluation of a skutterudite-based thermoelectric module for high-temperature applications. *J. Electron. Mater.*, **42** (7), 1369–1374.
- 5 Hatzikraniotis, E. *et al.* (2010) Efficiency study of a commercial thermoelectric power generator (TEG) under thermal cycling. *J. Electron. Mater.*, **39** (9), 2112–2116.
- 6 Wu, H.J. *et al.* (2014) Broad temperature plateau for thermoelectric figure of merit  $ZT > 2$  in phase-separated PbTe0.7S0.3. *Nature communications*, **5**, 4515.

- 7 Bakan, G. *et al.* (2013) High-temperature thermoelectric transport at small scales: thermal generation, transport and recombination of minority carriers. *Sci. Rep.*, **3**, 2724.
- 8 Lundstrom, M. (2011) Lecture 4: Thermoelectric Effects – Physical Approach, <https://nanohub.org/resources/11747>.
- 9 Baranowski, L.L., Jeffrey Snyder, G., and Toberer, E.S. (2014) Response to “Comment on ‘Effective thermal conductivity in thermoelectric materials’” [J. Appl. Phys. 113, 204904 (2013)]. *J. Appl. Phys.*, **115** (12), 126102.
- 10 Min, G. *et al.* (2015) Evaluation of thermoelectric generators by I–V curves. *J. Electron. Mater.*, **45** (3), 1700–1704.

**8**

## **Integration of Heat Exchangers with Thermoelectric Modules**

*Alireza Rezania*

*Aalborg University, Department of Energy Technology, Pontoppidanstraede 111, DK 9220, Aalborg, Denmark*

### **8.1 Introduction**

About 50–70% of potential thermal energy input to transportation and industrial processes is dissipated to the environment. The wasted, but available, thermal energy in both heavy and light duty vehicles and industrial processes opens up an opportunity for efficient energy recovery. The global energy efficiency could be enhanced by recovering energy from the exhaust and coolant systems of the vehicles and industrial processing plants.

Thermoelectric generation is one interesting and fast developing technology that is able to directly convert a fraction of the available thermal energy into electricity by means of semiconductor materials. This technology promises low-maintenance and silent devices, the use of environmentally friendly materials, and the capability of high reliability recovery systems with potential energy conversion efficiency near or greater than 10% with recent developments in thermoelectric materials. In order to take advantage of newly developed materials, a robust, high-performance, flexible, and well-designed recovery system that is able to tackle structural and thermal challenges is necessary.

Fundamentally, it is essential to have four basic components in a thermoelectric generator (TEG) system to be able to harvest energy. Apart from the TEG module, an electrical load, a heat source, and a heat sink are required to complete the TEG system. Performance of the TEG system is highly dependent on the interaction of these components. To achieve a high-performance system with overall efficiency close to conversion efficiency of thermoelectric materials, the components need to be considered thermally interdependent in the system designs. This chapter studies the effect of the heat exchangers design on system performance, and discusses the challenges through accurate analyses techniques while introducing proper cooling technologies.

## 8.2 Heat Exchanger Design – Consideration in TEG Systems

An analysis of waste thermal energy indicates that there is a significant opportunity to partially recover the waste heat from industrial processing such as steel and cement industries, glass processing, and paper processing [1]. Owing to recent developments in advanced micro- and nanothermoelectric materials, there is a massive amount of the industrial thermal energy that can be recovered at a matched temperature with many thermoelectric materials.

Optimization of conversion efficiency of TEGs for a given set of thermoelectric materials is widely discussed in detail, and is introduced as the following well-known equation [2, 3]:

$$\eta_{\max} = \left( \frac{P}{Q_h} \right)_{\max} = \left[ \frac{T_h - T_c}{T_h} \right] \cdot \left[ \frac{\left( \sqrt{1 + Z\bar{T}} - 1 \right)}{\sqrt{1 + Z\bar{T}} + \frac{T_c}{T_h}} \right] \quad (8.1)$$

where  $\bar{T} = (T_h + T_c/2)$  and  $Z\bar{T} = \sigma\alpha^2 T/k$  represent the ability of a thermoelectric material to efficiently produce electrical power, called *figure of merit*. In real applications of heat recovery and thermoelectric power system design, the temperature reservoirs of the heat source and heat sink are usually known rather than the temperature of the hot and cold junctions of the thermoelements. Therefore, it is problematic to estimate the best combination of the cold and hot junction temperature of the thermoelements to evaluate the potential of the heat recovery systems or to optimize the system efficiency or power density. Consequently, the well-known basic relationships describing TEG performance based on the temperature of the junctions, such as Eq. (8.1), needs to be developed according to more sophisticated optimization processes and analysis in order to offer a most efficient TEG in its system level. In order to create high-performance thermoelectric power generation systems, optimization of the TEG module requires coupling with the heat exchangers optimal design.

Thermoelectric power generation systems have some advantages over other types of waste heat recovery systems. TEG systems are silent, vibration free, reliable and compact with few or no moving parts. The purpose of heat exchangers exclusively designed for the TEG systems could not only have significant impact on the system performance but can also play a critical role in relation to the advantages of application of the TEGs in the recovery systems.

In order to reach predictable circumstances to maximize the system performance, the heat exchangers should provide isothermal boundary conditions on the hot and cold junctions of the TEG module. However, designing a heat exchanger configuration capable of providing isothermal interfaces and moreover assisting in minimizing the overall system weight and volume is challenging.

Multiplying the overall heat transfer conductance by the heat transfer surface area,  $UA$ , introduces an effective heat exchanger design parameter, which in general is a complex function of the structure of the heat exchanger, the type of the fluid exchanged, and the flow condition in the heat exchanger.

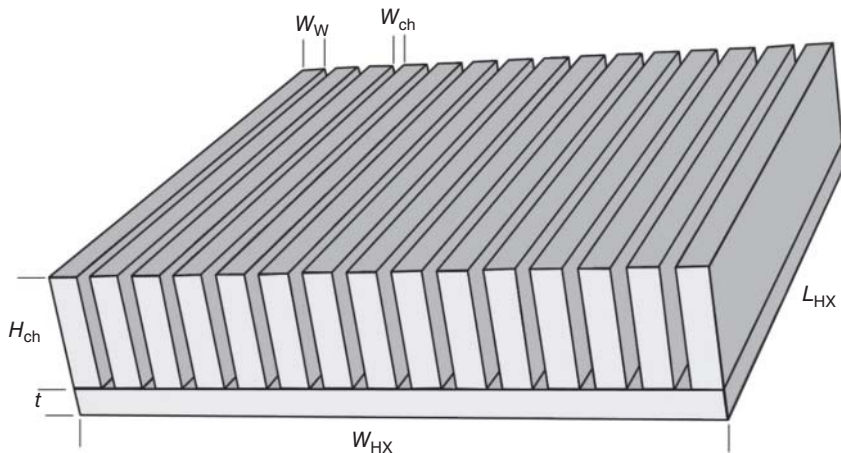


**Figure 8.1** Typical design of flat plate heat exchanger with parallel fins.

Kays and London [4] showed techniques to evaluate the UA for a typical heat exchanger based on its thermal resistance:

$$UA = \left( \frac{1}{\sum_i R_{th,i}} \right) \quad (8.2)$$

where  $R_{th,i}$  includes all the convective thermal resistance of the flow and all conductive thermal resistance of the heat exchanger. For a typical design with a flat plate heat exchanger and parallel fins, as shown in Figure 8.1, the UA value is

$$UA = \frac{1}{\left[ \left( \frac{1}{\eta_o A_f h} \right) + \left( \frac{t}{k_{HX} WL} \right) \right]} \quad (8.3)$$

In Eq. (8.3),  $h$  is the heat transfer coefficient in the channels,  $A_f$  is the total heat transfer area of the heat exchanger, and  $\eta_o$  is the overall surface efficiency of the heat exchanger. For a surface without a fin  $\eta_o = 1$ . As the fin is employed, the temperature gradient along the fin reduces the temperature efficiency of the extended surface. A correction factor called fin efficiency can help in taking into account the thermal resistance of the fins. The fin efficiency for a straight, rectangular, and low-thickness fin with an adiabatic tip is [5]

$$\eta_{fin} = \frac{\tanh \left( \sqrt{2h/k_f w_{ch}} H_{ch} \right)}{\sqrt{2h/k_f w_{ch}} H_{ch}} \quad (8.4)$$

Accordingly, the overall surface efficiency of the heat exchanger is

$$\eta_o = 1 - \frac{A_f}{A_b} (1 - \eta_{fin}) \quad (8.5)$$

Although evaluation of the overall fin efficiency is straightforward, the heat transfer coefficient is a function of the channel dimension, Reynolds number,  $Re$ , and the thermal properties of the fluid in the heat exchanger.

A trade-off between the maximum thermoelectric power generation and the mass flow rate in the heat sink represented by UA [6] shows that the maximum power point increases with higher UA in the hot side heat exchanger. However, power generation by TEG is limited to enhancement of the heat exchanger performance for a given mass flow rate in the hot heat exchanger. Improvement in the heat exchanger performance is only useful when the mass flow rate in the hot heat exchanger is high. This condition could become a critical design factor as cost constraints are considered in the system design.

The heat transfer coefficient can be defined as

$$h = Nu \frac{k_f}{D_h} \quad (8.6)$$

where  $Nu$  is the Nusselt number, and  $D_h$  is hydraulic diameter of the channel by

$$D_h = \frac{4A}{P} \quad (8.7)$$

In Eq. (8.7),  $A$  is the cross-sectional area of the channel and  $P$  is the wetted perimeter in the channel.

Kays and London [4] categorized the Nusselt number for fully developed velocity and temperature profiles in a laminar flow regime based on the cross-section shape of the channel. Incropera and Dewitt [5] presented the Nusselt number for turbulent pipe flow as follows:

$$Nu \propto Re^m \cdot Pr^n \quad (8.8)$$

where  $m = 0.5 - 0.8$  and  $n = 0.33 - 0.4$ . The Prandtl number,  $Pr$ , is defined as the ratio of the momentum diffusivity of the flow to its thermal diffusivity [7] and is given as

$$Pr = \frac{\vartheta}{\alpha} \quad (8.9)$$

where  $\vartheta$  and  $\alpha$  correspond to the kinematic viscosity and thermal diffusivity of the flow, respectively. The Reynolds number in a channel is generally given as

$$Re = \frac{\text{inertial forces}}{\text{viscous forces}} = \frac{\rho D_h v}{\mu} \quad (8.10)$$

In Eq. (8.10),  $v$  is the fluid velocity in the channel,  $\rho$  is the fluid density, and  $\mu$  is the fluid dynamic viscosity.

### 8.3 Cold Side Heat Exchanger for TEG Maximum Performance

Co-designing the thermoelements together with the thermal boundary conditions for the specific applications and available heat transfer coefficients can also play an important role in improving the TEG module performance. For a given heat transfer coefficient and UA, dissimilar thermal conductivity of the n- and p-type materials results in different temperature distribution in the thermoelements. The electrical resistance and the Seebeck coefficient of the

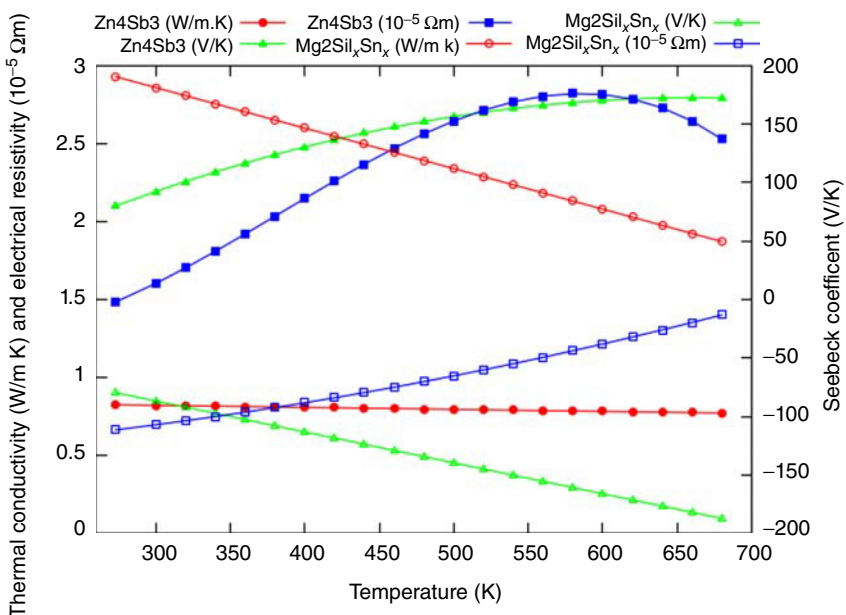


**Figure 8.2** Variation of thermoelectrical properties of dissimilar thermoelectric materials [9, 10].

materials, essential parameters in the power factor, are likewise coupled with the temperature distribution in the thermoelectric materials affected by the imposed thermal boundary conditions.

For a uni-couple, the footprint area ratio of the n- and p-type thermoelements is an important factor to maximize the power density. Geometry modification of the thermoelements associated with the UA may enhance the power generation in the module considerably. Jang *et al.* [8] found that a reduction of the thermoelement's foot print area may decrease the power generation while the conversion efficiency could improve.

For each stream in the heat exchanger, the convection heat transfer coefficient depends on the flow properties, the temperature properties, and the type of the coolant fluid. Figure 8.2 shows n-type Mg<sub>2</sub>Si<sub>1-x</sub>Sn<sub>x</sub> [9] and p-type Zn<sub>4</sub>Sb<sub>3</sub> [10] as two temperature-dependent thermoelectric materials considered in a study by Rezania *et al.* [11]. The study includes the parametric optimization of the TEG n/p footprint area ratios in conjunction with a practical range of the heat transfer coefficient to enhance the volumetric power generation in a TEG.

In contrast with the common studies about TEG optimization, which apply constant temperature on the cold junction, the use of heat transfer coefficient values offers more realistic thermal boundary conditions. In this case, the temperature difference between the hot and cold junctions of the thermoelements is different for dissimilar materials. For instance, the smaller temperature difference belongs to the n-type thermoelements, because of its higher thermal conductivity. Hence, as shown in Figure 8.3, increasing the footprint area ratio ( $A_n/A_p$ ) enhances the heat flux across the uni-couple. A higher heat flux leads to

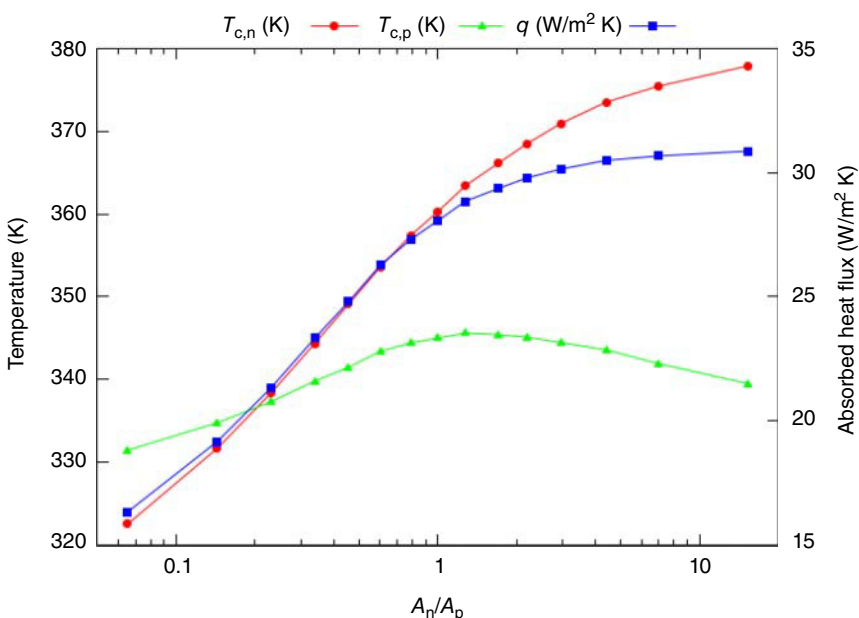


**Figure 8.3** Cold junction temperature of the thermoelements and hot junction heat absorbed,  $h = 2000 \text{ W}/\text{m}^2\text{K}$ ,  $T_h = 650 \text{ K}$ .

a higher cold side temperature of the n-type thermoelement at a constant heat transfer coefficient that corresponds to a lower temperature difference of the junctions in the thermoelement.

According to Figure 8.2, the Seebeck coefficient of the uni-couple slightly increases with the footprint area ratio; however, the temperature difference is the dominant factor of the voltage generation in the uni-couple. Furthermore, the total electrical resistance of the uni-couple shows a minimum value for a specific ratio of the footprint area. Overall, power generation by a uni-couple can be maximized by varying the footprint area ratio. At high values of  $A_n/A_p$ , the temperature difference in the thermoelements and, consequently, the voltage generation, reduce with a sharper slope at lower heat transfer coefficients. Thus the maximum power generation shifts to a larger footprint area ratio under high heat transfer coefficient conditions. Figure 8.4 shows that the maximum power generation occurs at  $A_n/A_p = 0.23, 0.33, 0.45, 0.6$ , for  $h = 50, 200, 500, 2000 \text{ W}/\text{K m}^2$ , respectively. The results indicate that the optimal footprint ratio not only strongly depends on the electrical resistance of the uni-couple but is also furthermore strongly coupled with thermal boundary conditions, specifically at low values of the heat transfer coefficient in the heat exchanger. The optimal footprint area ratio needs to be similarly considered in order to provide maximum conversion efficiency at the matched load condition. The results show that an increase in the heat transfer coefficient, and

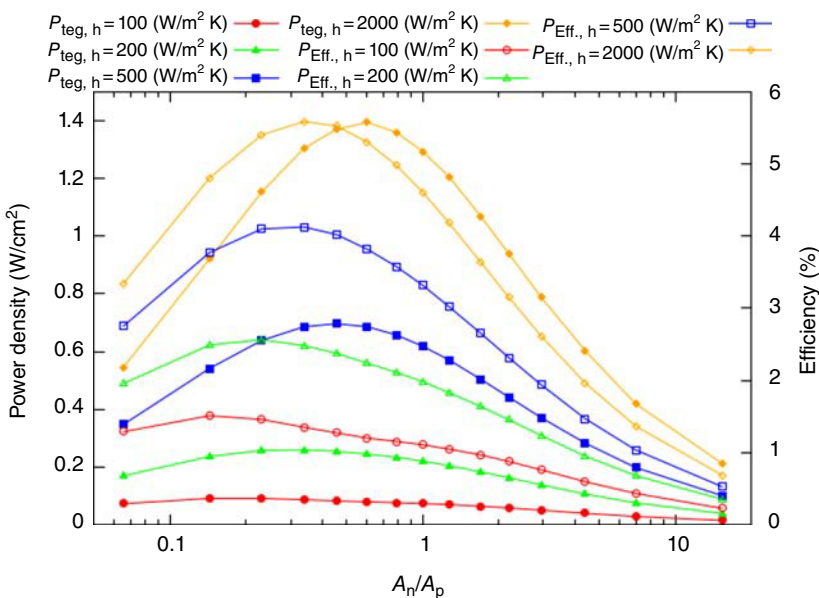


**Figure 8.4** Maximum power generation and efficiency by a uni-couple with variation of the footprint ratio,  $T_h = 650$  K.

consequently the heat flow across the uni-couple, shift the maximum efficiency to a smaller footprint area ratio.

Owing to the development of thermal boundary layers in channels of the heat exchanger, the heat transfer coefficient, which is high at the channel entrance, decreases along the channel. Moreover, the mean temperature of the fluid decreases in the hot side heat exchanger or increases in the cold side heat exchanger; thus the fluid's properties can change significantly. Consequently, evaluation of the UA in the flow direction can be difficult. The fluid's properties can vary significantly and have a critical impact on the UA evaluation and heat exchanger performance as discussed above.

Figure 8.5 compares the variation of the cold junction temperature of thermoelements along two heat exchangers as the channels in the heat exchangers have different hydraulic diameters ( $D_{h,\text{ch}\#1} = 0.53$  mm and  $D_{h,\text{ch}\#2} = 2.13$  mm). The heat exchangers provide the same average temperature difference between the hot and cold junctions of the thermoelements that yield the same voltage generation. In order to provide the same power generation, the mass flow rate in the larger channel needs to be more than the one in the smaller channel to provide the same average temperature profile ( $\dot{m}_{\text{ch}\#1} = 0.002$  (kg/s) vs.  $\dot{m}_{\text{ch}\#2} = 0.005$  (kg/s)). On the other hand, as the hydraulic diameter of the channel increases, the temperature profile of the fluid in the channels, and consequently the cold junction temperature of the thermoelements, become more homogeneous in both the flow direction and the width direction of the channel [12].

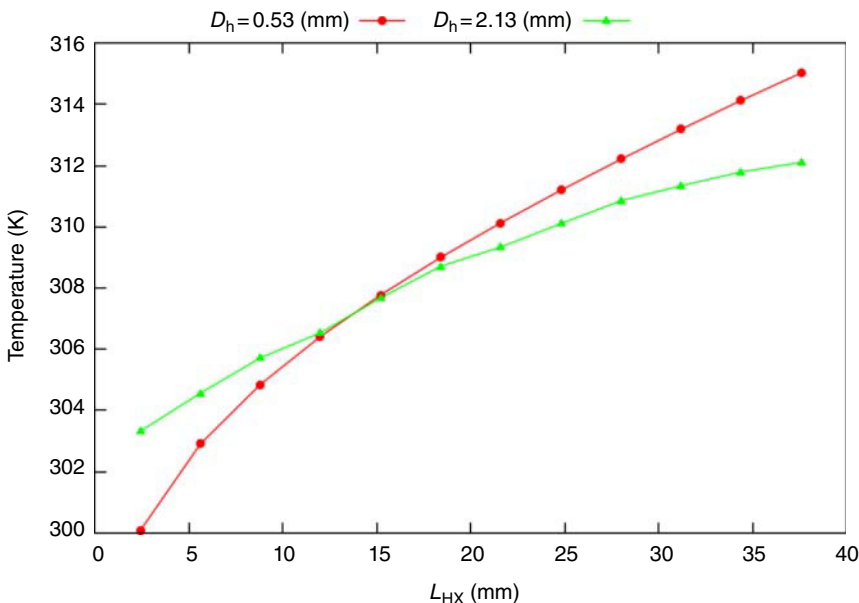


**Figure 8.5** Temperature variation of the cold junction of the TEG thermoelements as a function of the flow direction,  $\Delta T_{\text{teg,av}} = 252 \text{ K}$ .  $T_{h,\text{teg}} = 550 \text{ K}$ .

## 8.4 Cooling Technologies and Design Challenges

There are several types of fluids, cooling modes, and designs of heat exchangers that provide a vast range of heat transfer coefficients and need complex methods and models to predict the UA value along the heat exchanger. Depending on the TEG application and the design of a proper heat exchanger, various types of gas and fluid with different value for heat transfer coefficient could be used in a heat exchanger. Natural convection by air and water can yield a heat transfer coefficient up to 5 and  $100 \text{ W/m}^2 \text{ K}$  in a heat exchanger, respectively. Maximum heat transfer coefficient by air forced convection flow is  $40 \text{ W/m}^2 \text{ K}$ , while water could offer up to  $h = 6000 \text{ W/m}^2 \text{ K}$  [13].

It is worthy to note that gas-based heat exchangers have low heat transfer coefficient and, therefore, low UA because of the low thermal conductivity and Prandtl number of the gas. On the other hand, the UA value in a fluid-based heat exchanger is high owing to the high Prandtl number and thermal conductivity of the fluid. Generally, in heat exchangers with gas flow, the conductive term dominates the UA value while the convection term is the dominant factor in Eq. (8.3) when using a fluid.

Although it is quite important to design an efficient heat exchanger with a high UA among different types of heat exchangers, it is furthermore critical to estimate the pressure drop in the heat exchanger due to the interaction of the flow with the channel walls through friction. The pressure drop in a channel can be characterized by the Darcy–Weisbach equation as follows:

$$\Delta p_{\text{ch}} = f(Re) \cdot \frac{L}{D_h} \cdot \frac{\rho}{2} \cdot v^2 \quad (8.11)$$

where  $f(Re)$  is the friction factor in the channel. According to Eq. (8.11), there is a proportional relationship between the pressure drop and the hydraulic diameter of the channel. For a given mass flow rate, if the channel dimension is reduced in order to enhance the effective area of the heat exchanger and UA, the pressure drop increases dramatically due to an increment in the fluid velocity and a smaller hydraulic diameter. Since the pressure drop has a proportional relationship with the cooling energy required in the heat exchanger, the UA cooling energy must be properly coupled for optimizing the TEG system.

In order to follow the developments in the field of thermoelectric materials, the heat exchangers, especially in advanced TEG systems, should be able to provide a relatively high heat flux (i.e., 10–100 W/cm<sup>2</sup>) through the TEG module, while the design analysis and process must still focus on providing light-weight, low-cost, and compact heat exchangers.

There are various cooling technologies that could be considered for thermal management of thermoelectric applications. One way to transfer heat from the heat source is through heat spreaders that offer a reliable and cost-effective method to dissipate the heat with their high thermal conductivity. In this method, an intermediate conductive plate spreads the heat of hot spots from a small surface to a larger surface. Hence, the heat spreaders are typically used for heat sources with high heat flux density where a secondary heat exchanger delivers the heat to the ambient. This method offers solutions when the secondary heat exchanger is not efficient, there is space restriction, less expensive material is desired for the heat exchanger, or an air-cooling based heat exchanger is preferred to be used instead of a liquid-cooled heat exchanger.

Traditional air-cooling techniques are not an efficient and promising method for high power density cooling applications. With acceptable noise levels, this technology may transfer 1 W/cm<sup>2</sup> for a 60 °C temperature difference.

Piezoelectric fans are small solid-state devices that can operate with low power, low noise, and can be used for thermal management in many thermal portable devices. Acikalin *et al.* [14] reported that a piezoelectric fan could enhance heat transfer coefficient for 100%.

Heat pipes, which are a passive and indirect device, transport heat from a heat source to a heat sink where the removed heat is rejected to the cooling environment by forced or natural convection. Since a heat pipe acts as a passive capillary pump owing to its porous medium, it could provide thermal conductance up to 200 000 W/m K; however, the heat transfer coefficient of heat pipes is generally in the range of 10–300 W/m<sup>2</sup> K. When using heat pipes in compact energy recovery devices, it is worthy to note that the effectiveness of a heat pipe decreases with the reduction of its length. For instance, the performance of a heat pipe with length of about 1 cm is comparable with a solid piece of copper. Loop heat pipes separate the vapor and liquid paths and provide a much higher heat transfer coefficient compared to conventional heat pipes, 625 W/m<sup>2</sup> [15].

Liquid metal cooling offers high heat transfer over 200 W/m<sup>2</sup> using a magneto-fluid dynamics pump, while, for instance, a 15 kPa pressure drop is required to circulate 0.3 l/min of working fluid [16, 17]. Liquid metal has a much lower coefficient of thermal expansion compared to water and faces fewer problems in low temperature. For example, Ga–Sn–In eutectics can remain in liquid phase at even –19 °C.

FC-72-based immersion cooling, a direct cooling technology with a two-phase flow, can transfer 5–20 W/cm<sup>2</sup> of heat by natural convection. The heat flux by this technology could be enhanced up to 100 W/cm<sup>2</sup>. Since this technology works on the basis of natural convection, it would be limited to specific cooling applications. Furthermore, water is an incompatible working fluid in this technology because of its electrical and chemical characteristics.

Cooling capacity close to 100 W/cm<sup>2</sup> has been achieved by liquid jet impingement technology with a 0.3 l/min water flow at 300 kPa. This flow condition requires 7 W of cooling energy [18]. Microjet technology could provide more uniformity in the temperate profile over the hot surface compared to microchannel technology. However, this technology requires more fabrication steps and relatively high cooling energy.

Spray cooling is an interesting candidate for thermal management of reduced weight and dense system packaging [19], and could provide 160 W/cm<sup>2</sup> of heat flux [20]. In this technology, the liquid is broken up into fine droplets imposed on the hot surface. Therefore, the heated surface is cooled down by a combination of thermal conductance between the liquid and the surface and by evaporation at the liquid–vapor interface.

## 8.5 Microchannel Heat Exchanger

In order to provide a light-weight, low-cost and compact system, microchannel heat exchangers are an interesting candidate for TEG application. A microchannel heat exchanger contains several channels with typically 10–1000 μm hydraulic diameter. In practice, miniaturization of the channel is limited to creating a pressure drop that increases with the inverse of the second power of the channel width.

According to Eq. (8.6), the very small channel dimension provides a significantly high heat transfer coefficient. Furthermore, in a given heat exchanger substrate area as in Figure 8.1, the small dimension of the channel allows to increase the number of channels in the heat sink. The increment in the heat transfer area and the heat transfer coefficient enhances the UA of the heat exchanger. Heat transfer coefficient in an air-cooled microchannel can reach up to 1000 W/m<sup>2</sup> K, while a well-designed water-based microchannel heat exchanger is able to yield a 4000–10 000 W/m<sup>2</sup> K heat transfer coefficient. A heat transfer coefficient of 2500–5000 W/m<sup>2</sup> K has been measured in carbon-dioxide-flowing microchannels by Liao and Zhao [21]. Owing to the very small channel hydraulic diameter, a high heat transfer coefficient can be created with a relatively low Reynolds number in most of the microchannels compared to conventional large channels where the flow regime stays laminar.

Owing to increasing demands for minimizing the weight and volume of TEG systems with dissipation and accommodation of higher heat flux on the heat transfer junction, TEG systems require high-performance heat exchangers with high heat flow capability to reach their full performance potential. Microchannel heat exchangers are capable of providing high UA and managing heat transfer from TEG devices in a compact form (typically 10–20% of weight and volume

of comparable macrochannel heat exchangers). This technology is implemented in TEG technology application. The effectiveness of microscale heat exchangers in TEG applications has been reviewed by Rezania and Rosendahl [22–24] and Hendricks [25–27].

Since the pressure drop in a channel increases with the inverse of the second power of the channel width, there is a mutual misunderstanding that a microchannel heat exchanger requires high cooling energy due to the creation of a high pressure drop in the heat exchanger. In fact, a study by Wang and Holladay's [28] showed that the created pressure drop in a microchannel heat exchanger may not be higher than the one in a macrochannel heat exchanger for a given heat transfer performance if the microchannel heat exchanger is properly designed. Kandilkar and Upadhye [29] claimed to reach a  $300 \text{ W/cm}^2$  power density for a flow rate of  $1.5 \text{ l/min}$  at a  $24 \text{ kPa}$  pressure drop. Furthermore, Colgan *et al.* [30] reported the implementation of silicon microchannel coolers for a heat transfer density of  $400 \text{ W/cm}^2$  at  $24 \text{ kPa}$  for  $1.2 \text{ l/min}$ . A comparison between the jet impingement and microchannel technologies [31] indicates that the microchannel heat exchanger is more efficient for a heat exchange area smaller than  $7 \times 7 \text{ cm}^2$ .

## 8.6 Coupled and Comprehensive Simulation of TEG System

A coupled optimization analysis with detailed information of the TEG system behavior can aid the effectual selection of the design parameters and objective functions. The ANSYS Workbench analysis software package has the capability to solve the TEG differential equations while coupling them with hot and cold side heat exchangers. By using the finite volume technique to nodalize the TEG elements for given details of the heat exchanger interfaces and structure, and by entering mass flow rate and boundary conditions, a set of simultaneous equations for heat and current flows and temperatures can be solved.

### 8.6.1 Governing Equations

Thermoelectric modules, heat exchangers, and coolant flow elements can be integrated by applying the finite volume technique to couple the energy conservation, the continuity, and the heat flow equations:

$$\rho c \frac{\partial T}{\partial t} + \nabla \cdot \vec{q} = \dot{q}, \quad (8.12)$$

and the electric charge in the thermoelements

$$\nabla \cdot \left( \vec{j} + \frac{\partial \vec{D}}{\partial t} \right) = 0 \quad (8.13)$$

The coupled heat flow and the continuity of electric charge equations that include Joule heating and Seebeck and Thomson effects are [32]

$$\vec{q} = T \cdot [\alpha] \cdot \vec{j} - [k] \cdot \nabla T \quad (8.14)$$

$$\vec{j} = [\sigma] \cdot (\vec{E} - [\alpha]) \cdot \nabla T \quad (8.15)$$

$$\vec{D} = [\epsilon] \cdot \vec{E} \quad (8.16)$$

where Eq. (8.16) is a constitutive equation for a dielectric medium. Under steady-state condition, the electric field is irrotational and the system-coupled equations can be expressed as follows [33]:

$$\nabla \cdot (T \cdot [\alpha] \vec{J}) - \nabla \cdot ([k] \cdot \nabla T) = \dot{q} \quad (8.17)$$

$$\nabla \cdot ([\sigma] \cdot [\alpha] \cdot \nabla T) - \nabla \cdot ([\sigma] \cdot \vec{E}) = 0 \quad (8.18)$$

The electric power spent on work against the Seebeck field and on the Joule heating is included in the heat generation rate per unit volume ( $\dot{q}$ ) in Eq. (8.17).

A thermal boundary layer develops over a surface when the fluid free stream and surface temperatures differ. Near the wall, the velocity of the cooling fluid is principally zero and the local heat transfer between the wall and the fluid can be calculated as pure conduction:

$$q''_s = -k_s \left( \frac{\partial T}{\partial n} \right)_{\text{wall}} \quad (8.19)$$

where  $n$  is the local coordinate normal to the wall. On the other hand, by Newton's law of cooling, the convective heat transfer between the heat exchanger plate and the fluid can be expressed as:

$$q'' = h_f (T_s - T_f) \quad (8.20)$$

In the fluid, by considering the motion of single-phase fluids, that is, either liquid or gas, conservation of mass for constant density is simplified to

$$\nabla \cdot \vec{V} = 0 \quad (8.21)$$

To calculate the velocity and temperature distribution for a laminar regime, the following momentum and energy equations need to be solved [34]:

$$\rho \left[ \frac{\partial \vec{V}}{\partial t} + (\vec{V} \cdot \nabla) \vec{V} \right] = -\nabla p + \mu \nabla^2 \vec{V} + \rho \vec{f} \quad (8.22)$$

$$\rho c_p \left[ \frac{\partial T}{\partial t} + (\vec{V} \cdot \nabla) T \right] = k \nabla^2 T + \varnothing \quad (8.23)$$

where  $\vec{f}$  is the body force per unit of the fluid mass and  $c_p$  represents the specific heat of the fluid at constant pressure. The last term in Eq. (8.23) is the work done against viscous forces that is irreversibly converted into internal energy called *dissipation function*.

Figure 8.6 shows the geometric configuration of a TEG module with a cold side heat exchanger. The image shows a cross-sectional view of the device along the flow direction. By coupling the thermoelectric governing equations and the heat transfer equations in the heat exchanger, interactions among the entire system elements can be predicted and calculated.

### 8.6.2 Effect of Heat Exchanger Inlet/Outlet Plenums on TEG Temperature Distribution

TEG modules consist of ceramic substrates on both hot and cold sides that sandwich the thermoelectric elements for higher mechanical stability and

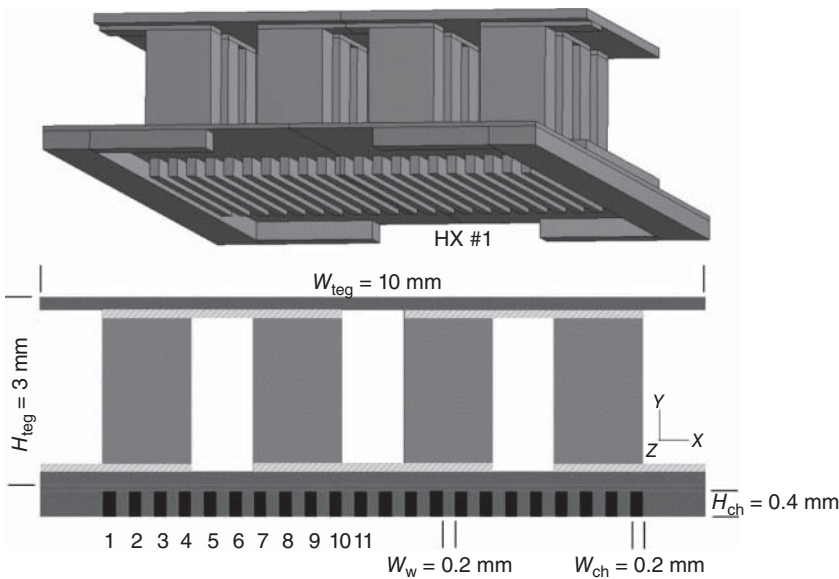


**Figure 8.6** TEG module with a cold side heat exchanger (cross-sectional view of the device).

electrically insulate the system components from each other and from the environment. Variations of the fluid temperature in the channel can have a strong effect on the temperature distribution in the thermoelements including the ceramic substrates. Figure 8.7 illustrates the contour of a local temperature comparison in the thermoelements of Figure 8.6 for pressure drops of  $\Delta p = 0.05 \text{ kPa}$  and  $\Delta p = 50 \text{ kPa}$  in a heat exchanger designed for the cold side ceramic substrate of the TEG module. There can be significant temperature differences at different locations of the thermoelements when the flow condition changes in the heat exchanger. For a constant heat flux on the hot side ceramic

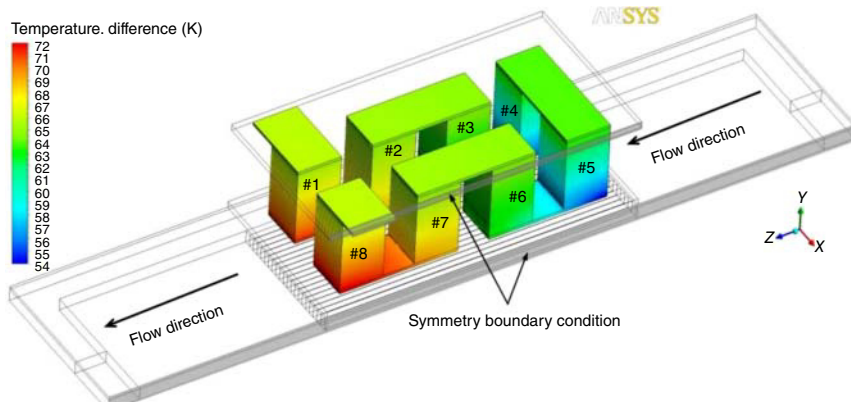


**Figure 8.7** Temperature difference contour of thermoelements and copper interfaces for two sample pressure drops,  $\Delta p = 0.05 \text{ kPa}$  and  $\Delta p = 50 \text{ kPa}$ .

substrate, the average temperature of the thermoelements at lower mass flow rate is higher than the case when higher mass flow rate cools the TEG. As the flow rate increases in the heat exchanger, the heat resistance of the flow reduces and transfers higher rates of heat. Therefore, for the mentioned pressure drops in the heat exchanger, the coolant fluid temperature at the channels inlet is closer to each other than the one in the channel outlet. Consequently, the local temperature difference is smaller for the thermoelements at the beginning of the heat exchanger compared to the thermoelements located at the end of the heat exchanger.

As shown in Figure 8.8, due to the high heat transfer coefficient and the effect of the channels' entrance geometry, the  $\Delta T_{\text{teg}}$  is higher for the first legs (legs #4 and #5) in the coolant flow direction. The temperature of the coolant fluid increases along the channel because of the heat absorption. Depending on the design of the thermoelements' location,  $\Delta T_{\text{teg}}$  can be also different in the cross-direction of the flow. In the configuration shown in Figure 8.8, the cooling effect is more efficient than at the middle of the heat exchanger, and the  $\Delta T_{\text{teg}}$  is higher for the thermoelements located at the edge compared to the elements at the middle of the module. Moreover, the applied heat flux at the end of the substrate along the flow direction causes a higher heat flow rate to cross through the legs and enhances  $\Delta T_{\text{teg}}$  in the thermoelements.

At a high mass flow rate, most of the heat that crosses through the TEG is absorbed where the legs are located. Therefore, there is a fluctuation in the channel surface temperature along the heat exchanger. A lower cooling energy causes a higher thermal resistance in the microchannel heat exchanger [35].

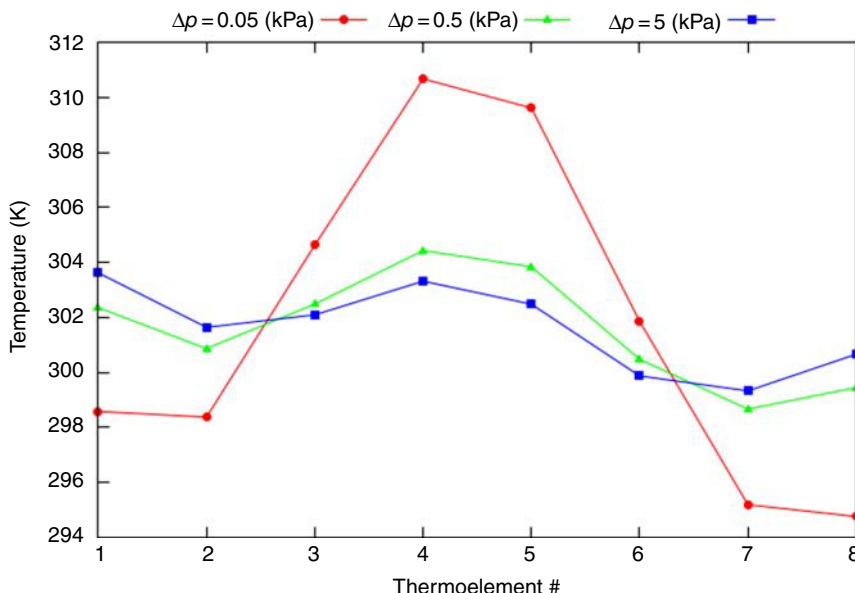


**Figure 8.8** Effect of the pressure drop in the microchannel heat exchanger on the created temperature difference of the cold and hot junctions of thermoelements.

When the mass flow rate decreases, the heat absorbing capacity of the coolant flow reduces, and the heat crosses through the thermoelements and diffuses in the heat exchanger substrate. Consequently, the heat removal ability of the heat exchanger decreases at the area under the thermoelements. The remaining region of the heat exchanger also plays a significant role in removing the heat. Thus, the increment in the temperature profile in the heat exchanger becomes more uniform. The temperature of the coolant fluid in the channels with lower mass flow rate raises sharper than the one in the higher mass flow rate case owing to the absorption of a higher amount of the heat per mass flow rate ( $Q/\dot{m}$ ) along the channel.

The rate of exchanged heat between the heat exchanger and TEG can furthermore be measured via calculation of the added thermal energy to the flow in the heat exchanger by taking the energy balance in the heat exchanger:

$$Q_{HX} = \dot{m}c_f(T_o - T_i) \quad (8.24)$$

Figure 8.9 shows the mass flow rate distribution and heat removed by the microchannels for three sample pressure drops in the heat exchanger. The mass flow rate distribution in the channels is affected by the inlet/outlet plenums of the heat exchanger. The heat removed by any channel in the heat exchanger, which not only depends on the design of the inlet/outlet plenum, is mostly affected by the arrangement of the thermoelements placed in the heat exchanger [22]. At low pressure drops, the inlet plenum design creates a uniform distribution of the mass flow rate in the channels. The minimum mass flow rate takes place at the channels at edge of the heat exchanger (channel #1 in

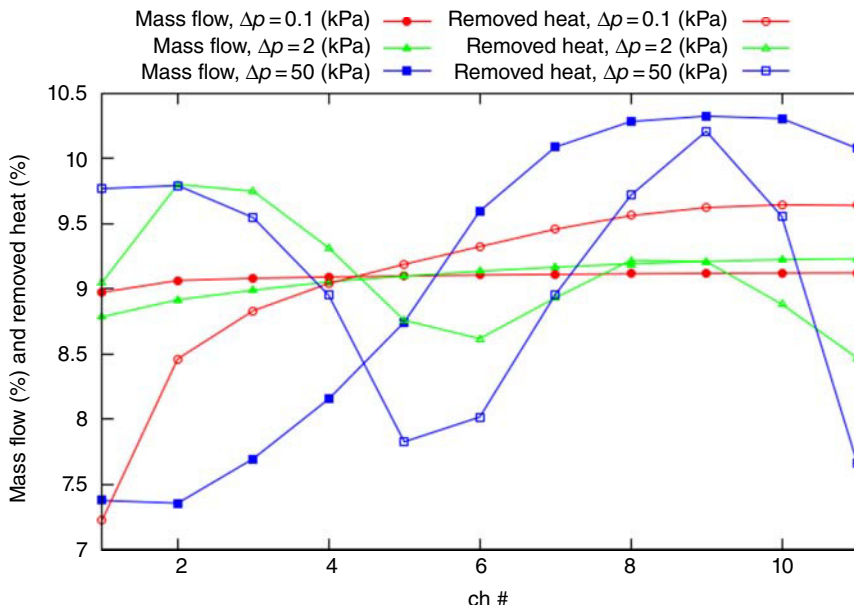


**Figure 8.9** Percentage of mass flow rate in channels and thermal energy removed by each channel for three sample pressure drops.

Figure 8.6), and the maximum flow rate at the middle channels. As mentioned, the heat diffusion in the substrate plate of the heat exchanger causes a uniform temperature distribution through the channels. Therefore, the arrangement of the thermoelements does not affect the heat transfer performance of the heat exchanger at low mass flow rates. Thus, the channels containing higher mass flow rate remove a higher rate of heat. Figure 8.9 indicates that the effect of the arrangement of the thermoelements and the inlet plenum design are both significant for the heat transfer performance of the heat exchanger at high pressure drop flows.

The profiles of mass flow rate distribution in the channels change as pressure drops vary. At middle range of pressure drops,  $\Delta p = 2 \text{ kPa}$  for an instance, the channels at the heat exchanger edge carry higher thermal energy ratio, because there is still thermal diffusion in the heat exchanger substrate. At higher pressure drop cases,  $\Delta p = 50 \text{ kPa}$  for an instance, higher rate of the thermal energy is removed by the channels underneath the thermoelements (channels #1, #2, and #3) than by the channels located between the thermoelements (channels #5 and #6), even though these channels have a higher mass flow rate compared to the channels closer to the heat exchanger edge.

### 8.6.3 Modified Channel Configuration

According to Figure 8.9, the channels located between the thermoelements have minor cooling effect in the heat exchanger, especially at high mass flow rate conditions, and remove less heat than the channels that are underneath the thermoelements. Therefore, removing the channels that are not as effective might help reduce the coolant fluid mass flow rate and the cooling energy in the heat exchanger. Figure 8.10 shows the modified heat exchanger configurations studied by Rezania and Rosendahl [23] in order to reduce the required cooling energy. In the design of HX#1 in Figure 8.6, the thickness of the channel wall is equal to channel width, while in HX#2 and HX#3, the number of channels is reduced by an increment in the channel wall thickness. HX#1, HX#2, and HX#3 contain 22, 16, and 8 active channels, respectively [23].

The lowest thermal resistance among the considered heat exchangers belongs to HX#1 since it has more active channels. On the other hand, because the mass flow rate in the HX#1 is the highest among the heat exchangers, this configuration needs the highest cooling energy. In HX#2 and HX#3, as the number of the channels decreases, while maintaining a constant pressure drop, the mass flow rate and cooling energy are reduced, but the thermal resistance is higher. Figure 8.11 illustrates that in configuration HX#2, the thermal resistance did not differ much from configuration HX#1, especially at high pressure drops. Nevertheless, the cooling energy in configuration HX#2 is lower than in configuration HX#1. Thus, this configuration can be an efficient replacement to be used in TEG systems. This advantage is due to the tailored distance between the thermoelements. Clearly, an optimal design of the heat exchanger configuration can be further optimized as the design of the TEG changes. In comparison with configuration HX#1, the HX#2 and HX#3 configurations reduce the cooling energy by 19% and 51%, respectively.

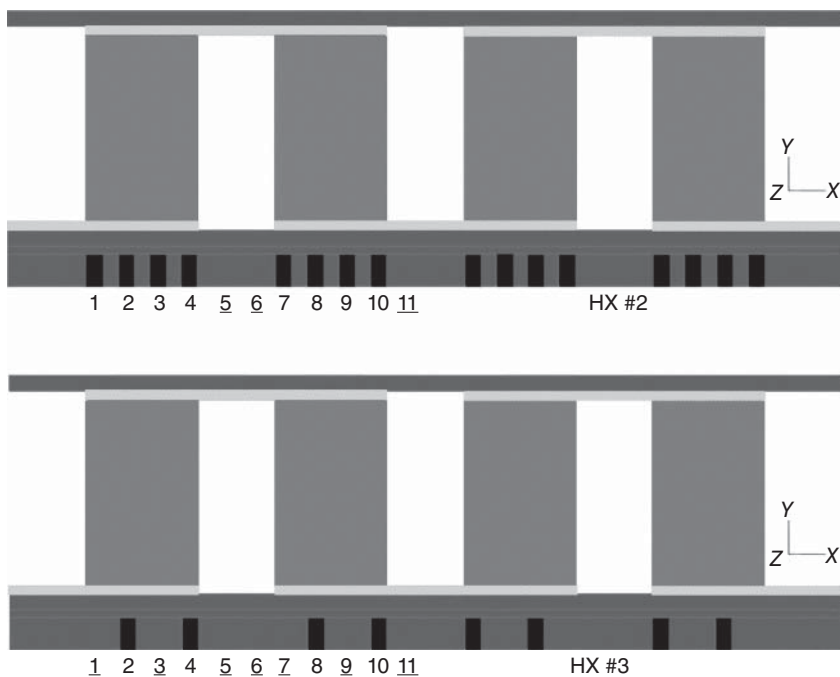


**Figure 8.10** Modified channel configuration based on original heat exchanger design in Figure 8.6.

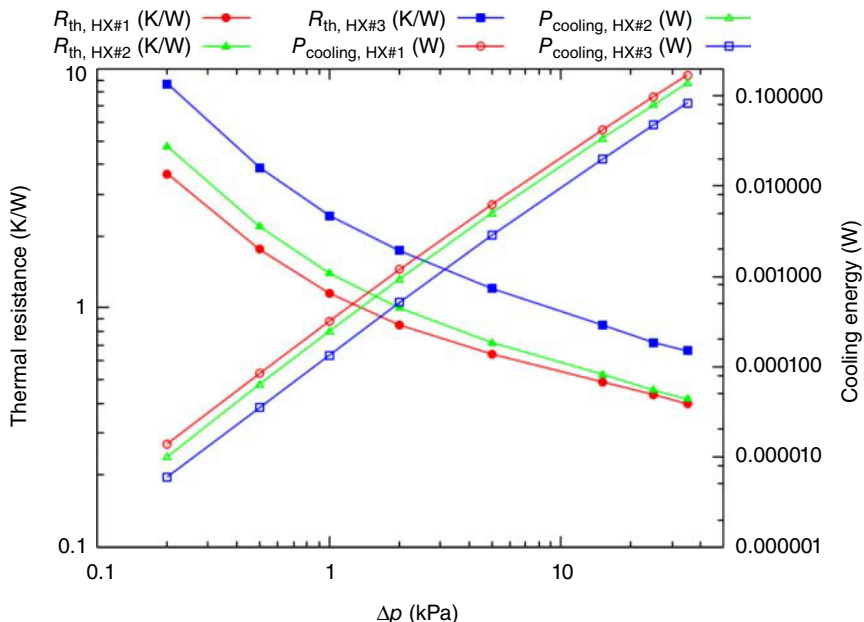


**Figure 8.11** Thermal resistances of the heat exchangers versus cooling energy in the heat exchangers.

### 8.6.4 Flat-Plate Heat Exchanger versus Cross-Cut Heat Exchanger

The design of the heat exchanger significantly affects the temperature distribution in the thermoelements and, therefore, the power generated by the TEG. The open-circuit voltage in a TEG uni-couple is defined as

$$v_{oc} = n\bar{\alpha}(T_h - T_c) \quad (8.25)$$

and the current in the TEG circuit can be expressed as

$$I = \frac{n\bar{\alpha}(T_h - T_c)}{R + R_l} \quad (8.26)$$

where the parameter  $R_l$  is the input resistance of the load circuit. The average Seebeck coefficient of the uni-couple in Eqs. (8.25, 8.26) is given by Decher [36]:

$$\bar{\alpha} = \frac{1}{T_h - T_c} \int_{T_c}^{T_h} (\alpha_p - \alpha_n) dT. \quad (8.27)$$

The TEG power generation at the load is defined as

$$P_{teg} = I^2 R_l \quad (8.28)$$

The required cooling power in the heat exchanger is related to the pressure drop and the volumetric flow rate and can be calculated as follows:

$$P_{cooling} = \Delta p \dot{V} \quad (8.29)$$

The pressure drop in the heat exchanger is an important factor that influences the net power of the TEGs. The net power supplied by the TEGs is therefore

$$P_{net} = P_{teg} - P_{cooling} \quad (8.30)$$

Different types and designs of heat exchanger have different advantages and disadvantages. For example, in a comparison between plate-fin and cross-cut heat exchangers, plate-fin heat exchangers are easily fabricated and produce small pressure drops [37], while the pin-fin heat exchanger can provide high heat transfer rates [38] due to the advantage of redeveloping the flow region. Kim *et al.* [39] showed that to determine the effectiveness of these heat exchangers, both the required cooling energy and the length of the heat exchangers need to be considered.

In general, pin-fin heat exchangers are recommended for applications requiring high cooling energy in a small length of the heat exchanger, while plate-fin heat exchangers have better performance when the heat exchanger has a larger length and needs to provide small range of cooling energy. Cross-cut heat exchangers are superior for operations in the relatively middle range of cooling energy and heat exchanger length [40]. Figure 8.12 shows the configuration of a plate-fin heat exchanger and a cross-cut heat exchanger with  $D_h = 75 \mu m$  applied on a TEG module, indicating the symmetric calculation domain that is a quarter of the device [24]. In contrast to the HX#2 design in Figure 8.10, a modified design of the fins under the thermoelements is studied in order to make a comparison between the heat exchangers for reducing the required cooling energy and for maximizing the net power output from the TEGs.

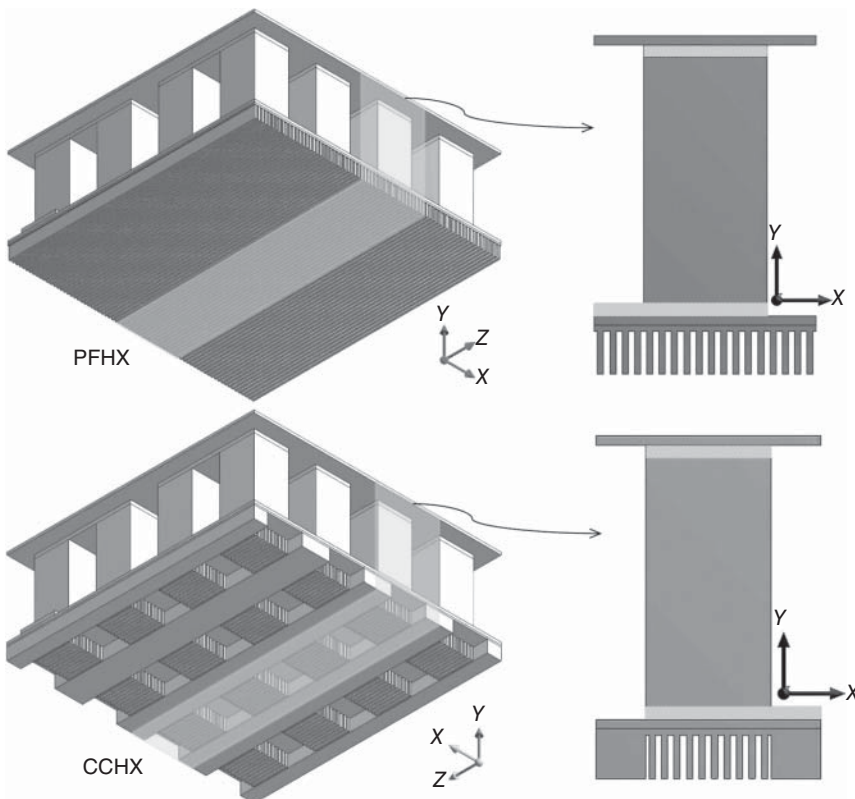


**Figure 8.12** Configuration of an applied plate-fin heat exchanger (PFHX) and a cross-cut heat exchanger (CCHX) with front view of symmetric calculation domain.

Microchannel heat exchangers contain several channels in contrast to typical heat exchangers with larger scale channels that make it difficult to achieve a constant temperature or a constant heat flux on the channel walls. Conductive heat transfer in the axial direction of the fluid flow on the substrate of heat exchangers with microscale dimensions may have a strong influence on the heat patterns in the heat exchanger, especially at low Reynolds number conditions [41]. Therefore, conjugate heat transfer effect should be accounted for in the microchannel heat exchangers. At low Reynolds number condition, the heat diffuses into the substrate of the cross-cut heat exchanger where no fin is designed. Therefore, the thermal performance of the cross-cut heat exchanger and, consequently, the power generated by the TEG reduce with the low flow inlet velocity conditions. However, the voltage generation does not drop significantly since the used coolant fluid is water, which has a relatively high specific heat capacity.

As Figure 8.13 shows, the cooling energy in the heat exchanger can be comparable with the power generated by the TEG if the cooling design parameters are not carefully considered. A mismatched cooling energy in a heat exchanger for low temperature difference conditions in the TEG can be higher than the power

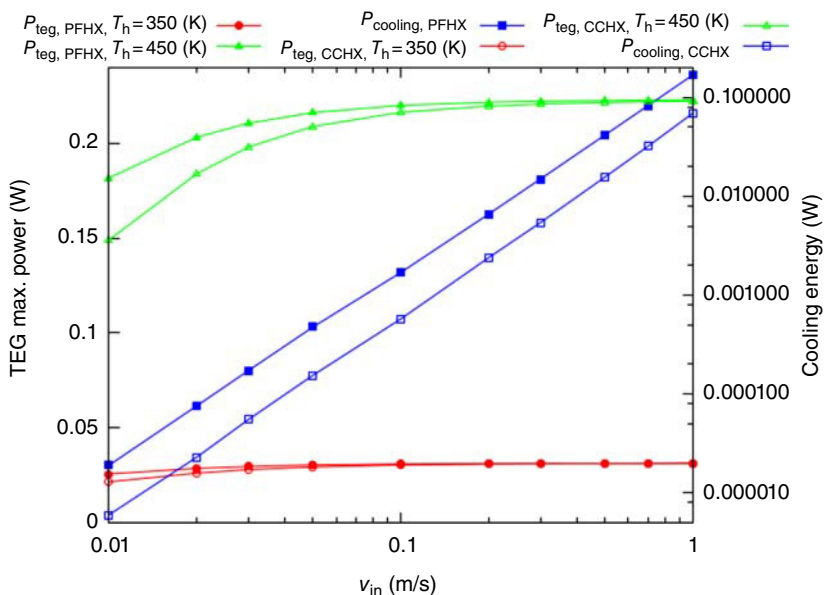


**Figure 8.13** Variation of the electric voltage generation and the required cooling energy with flow inlet velocity,  $A_{\text{teg}} = 1 \text{ cm}^2$ .

generated by the TEG, resulting in a negative net power. The negative impact of high coolant mass flow rate on the heat exchanger that results from this is furthermore shown experimentally by Rezania *et al.* [42].

Therefore, the range of applied mass flow rate or flow velocity needs to be carefully considered to avoid a negative net power. As the inlet velocity decreases, the power generation reduces and a lower cooling energy due to the lower pressure drop in the heat exchanger is generated. There is an optimal flow inlet velocity that offers the maximum net power. A critical parameter to define power generation in the TEG is the temperature difference between the hot and cold junctions. One way to control the cold junction temperature in higher hot junction temperature applications is to enhance the flow velocity in the heat exchanger. Although higher flow inlet velocity raises the cooling energy, it allows to create a higher temperature difference between the junctions.

Kim *et al.* [40] showed that for a heat exchanger with large dimensionless length,  $\log(L_{\text{HX}}/D_h)$ , and small dimensionless required cooling energy,  $\log\{P_{\text{cooling}}/[\mu^3/(\rho^2 D_h)]\}$ , the plate-fin design has a better performance than the cross-cut heat exchanger design. According to the heat exchanger design parameters shown in Figure 8.12,  $\log\{P_{\text{cooling}}/[\mu^3/(\rho^2 D_h)]\} < 11.35$  for  $\log(L_{\text{HX}}/D_h) = 1.03$ , which reassures that using a plate-fin heat exchanger will yield an enhanced performance. The plate-fin heat exchanger offers better thermal performance and higher net power at low flow rates, although it requires higher cooling energy for a given flow rate compared to the cross-cut heat exchanger. At high flow rate conditions, where the effect of cooling energy is significant, although the thermal performance of the plate-fin heat exchanger

is slightly superior, the required cooling energy is relatively high. Therefore, a TEG with a cross-cut heat exchanger offers higher net power at high flow inlet velocity. The variation of the power generation in the TEGs and of the required cooling energy in the heat exchangers with the flow inlet velocity indicates that the overall maximum net power is equal for both TEGs using a with cross-cut heat exchanger and a plate-fin heat exchanger.

### 8.6.5 Effect of Channel Hydraulic Diameter

The thermal resistance of the heat exchanger and the pressure drop through the heat exchanger are important factors to take into account for the optimization of the heat exchanger design. The heat transfer in the heat exchanger can be enhanced as the channel hydraulic diameter decreases and, consequently, the number of channels and the efficiency of the surface heat transfer increases. A smaller hydraulic diameter, however, causes a higher pressure drop in the channels and raises the cooling energy required in the heat exchanger. Channels with rectangular cross section have a higher heat transfer coefficient compared with trapezoidal and triangular shaped microchannels [43]. Channels with rectangular cross section give minimum thermal resistance when the channel width and the fin thickness are equal [44]. The channel hydraulic diameter can be optimized over the practical range of Reynolds number to yield a maximum net power output in the TEG device.

Rezania *et al.* [45] made a parametric study on the channels to evaluate the effect of the hydraulic diameter on the system performance (shown in Figure 8.6). Four different channel sizes with  $D_h = 900, 450, 150, 50 \mu\text{m}$  are considered. The channel dimensions (width and height) and the fin thickness are equal. Therefore, the number of channels in the applied heat exchangers for the fixed substrate area according to the hydraulic diameters is 4, 8, 24, and 72 channels, respectively, and the heat exchangers are called N4, N8, N24, and N72, correspondingly. The hot side temperature of the TEG module was fixed at 400 K.

For a given Reynolds number, the thermal resistance of the heat exchanger decreases with the channel hydraulic diameter. A smaller thermal resistance increases the temperature difference between the hot and cold junctions of the thermoelements and enhances the voltage generation. In case of using a low heat resistance coolant fluid ( $R_{\text{heat}} = 1/\dot{m}C_p$ ) such as water, the TEG cold junction temperature remains close to the flow inlet temperature after a specific value of applied Reynolds number. Therefore, the power generation in the TEG increases slightly with the Reynolds number at high Reynolds number conditions. In contrast, an increment of the pressure drop in the channel yields a higher cooling energy. As Eq. (8.10) expresses, a higher Reynolds number means a higher flow velocity and, consequently, a higher mass flow rate in the channels. Since the cooling energy is dependent on both of these parameters, the cooling energy can be significantly increased at greater Reynolds number conditions, and even generate a negative net power output as shown in Figure 8.14. Therefore, the limits of the Reynolds number for channels with different hydraulic diameters need to be carefully defined to avoid a negative net power output in the system.

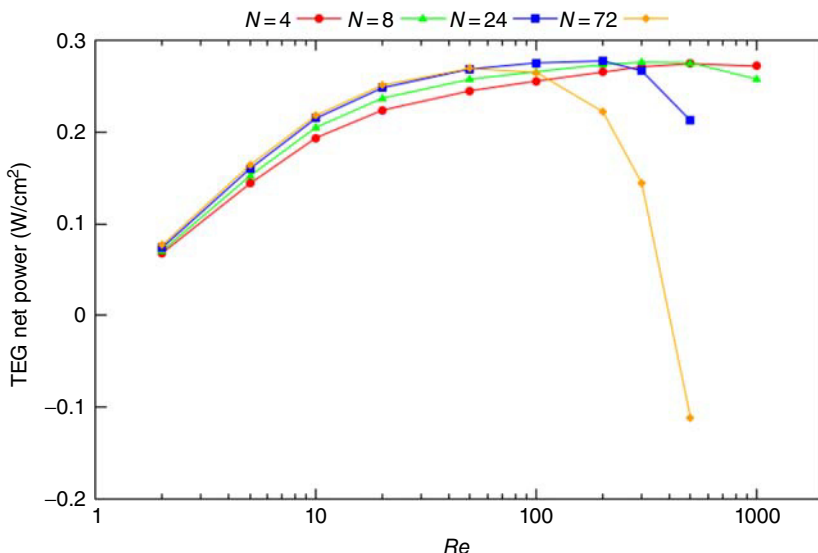


**Figure 8.14** Variation of the TEG net power output with variation of the Reynolds number in the channels.

For each design of heat exchanger, there is an optimal Reynolds number that maximizes the net power. Figure 8.14 shows that the optimal Reynolds number decreases as the hydraulic diameter of the channels reduces. The optimal Reynolds number for the studied heat exchangers N72, N24, N8, and N4 are  $Re = 50$ ,  $Re = 200$ ,  $Re = 500$ , and  $Re = 1000$ , respectively.

According to Eq. (8.1), the power generation in a TEG depends on both the module's efficiency and the heat flux across the TEG. As the Reynolds number increases in the heat exchanger, both these parameters increase.

## 8.7 Power-Efficiency Map

The optimization techniques of the TEG systems coupled with the heat transfer through the system using a maximum efficiency–power map for waste heat recovery applications offer maximum efficiency with only a small power penalty for a high specific power performance of the TEG system. Numerical optimization of the TEG design at the system level was demonstrated by Rezania *et al.* [46]. The coupled optimization functions were defined to solve the multiparameter design problems in the applied microchannel heat exchanger to maximize the output power and the cost performance of generic TEG systems. This multiparameter optimization model can contribute to better understanding of the relations between critical system design parameters. Critical design variables such as channel width, channel height, and fin thickness of the heat exchanger along with the fill factor of TEG were theoretically optimized over a wide range of cooling energy in the heat exchanger. The results illustrate that, for any cooling energy, there are particular channel widths and fin thicknesses that offer a maximum

output power in the TEG. The model is able to predict the effect of substrate thickness variation on an optimal design of the heat exchanger parameters and fill factor of the TEG. Furthermore, a relationship between the optimal cooling energy and the maximum performance cost of the system is achieved.

Hendricks *et al.* [47] performed a system-level design performance analysis of a TEG system subjected to appropriate thermal boundary conditions based on the characterization of the UA of the hot side heat exchanger. The results were presented as efficiency–power maps over a range of created temperature differences across the TEG and external load resistances. This analysis of the results provides a quick evaluation to track the system maximum power points and maximum efficiency depending on various critical design parameters and operating conditions. Furthermore, because in this analysis the exhaust temperature and ambient cooling temperature are fixed instead of the TEG hot and cold junction temperatures, both the maximum power and maximum efficiency occur at an external resistance ratio greater than 1. The internal resistance of the TEG module is conducted as a function of the variation of the TEG hot and cold junction temperatures with variation of the external resistance, and proposed Eq. (8.31) as the system optimal resistance, leading to a maximum power generation point:

$$R_{l,opt} = n \cdot R_i + \frac{2 \cdot R_{l,opt} \cdot (n \cdot R_i + R_{l,opt})}{\Delta T} \cdot \frac{\partial(\Delta T)}{\partial R_l} \quad (8.31)$$

Equation (8.31) generates a quadratic relationship for  $R_{l,opt}$ , and can be explicitly solved for the given design parameters and thermal boundary conditions affecting  $\Delta T$ . This equation confirms that the external resistance that gives a maximum power point in heat recovery application is greater than the internal resistance of the TEG module.

## 8.8 Section Design Optimization in TEG System

The temperature of the exhaust streams in waste heat recovery applications could be high. If applied, heat exchangers would be able to keep the cold side temperature of the TEG modules low, so the exhaust hot flow through the heat exchangers can experience a relatively large temperature drop along the heat exchanger. Temperature drops of the hot gas in the heat exchanger due to transfer of thermal energy from the hot gas to the TEG modules could reduce the heat transfer rate from the hot gas to the next TEG module along the heat exchanger. Consequently, the temperature differences between the hot and cold junctions of the TEG modules decreases along the heat exchanger so that each module has a higher temperature difference than the next TEG module along the flow in the system. In this case, an optimal TEG module designed for a specific operating temperature of the heat source and ambient does not have a maximum performance for all the modules placed along the heat exchanger.

Therefore, an advanced design technique of the TEG system should be utilized, which is referred to as “section design.” This technique provides an optimum TEG system design depending on the temperature variation of the hot gas in the heat exchanger.

The number of sections depends on the magnitude of the available overall temperature difference between the hot gas flow and the ambient. Crane *et al.* [48] indicated that the maximum number of sections is limited to about three considering the cost and system complexity issues. Optimization of the sections number based on a particular temperature and heat flux range in the hot gas flow direction helps avoid a mismatch in the TEG design [49]. There are complex design trade-offs associated with the power generation. The efficiency and the heat transferred in each section must be fully and carefully evaluated to achieve an optimum overall performance in a given energy recovery application.

## 8.9 Conclusion

Thermoelectric heat recovery systems have significant potential to enhance the efficiency of industrial and automotive thermal systems, by conversion of the waste heat into useful electrical energy through optimal design of high-performance and advanced TEG recovery systems. Proper design of a TEG system involves design optimization processes wherein the critical system components such as the TEG module and the heat exchangers are thermally coupled. This chapter provides a multidisciplinary optimization guide for maximizing the power generation and efficiency of the TEG system. The optimization techniques discussed in this chapter draw a map for future studies seeking a solution to achieve a high-performance TEG system by addressing the critical design parameters and their impact on the system overall performance.

## Acknowledgment

The author would like to acknowledge CTEC within the framework of Danish Council for Strategic Research, and NanoCaTe project granted by FP7 Programme. My sincere gratitude goes to Dr. Diana Dávila Pineda for her valuable contribution regarding the improvement of quality and unity of this chapter.

## Nomenclature

### Variables

$A$	area, $\text{m}^2$
$D$	electric flux density, $\text{C}/\text{m}^2$
$D_h$	hydraulic diameter, $\text{m}$
$\vec{E}$	electric field intensity vector, $\text{V}/\text{m}$
$c$	specific heat capacity, $\text{J}/\text{kg K}$
$H$	height, $\text{m}$
$h$	heat transfer coefficient, $\text{W}/\text{m}^2 \text{K}$
$I$	current, $\text{A}$
$J$	electric current density, $\text{A}/\text{m}^2$

$k$	thermal conductivity, W/m K
$L$	length, m
$\dot{m}$	mass flow rate, kg/s
$n$	number of uni-couples
$Nu$	Nusselt number
$P$	power, W, and wetted perimeter, m
$p$	pressure, Pa
$\Delta p$	pressure drop, Pa
$Pr$	Prandtl number
$Q$	absorbed heat, W
$q$	heat flux, W/m <sup>2</sup>
$\dot{q}$	heat generation rate per unit volume, W/m <sup>3</sup>
$R$	thermal resistance, K/W and electrical resistance, Ω m
$Re$	Reynolds number
$T$	temperature, K
$\Delta T$	temperature difference, K
$t$	thickness, m, and time, s
$U$	overall heat transfer coefficient, W/m <sup>2</sup> K
$\vec{V}$	velocity vector, m/s
$\dot{V}$	volumetric flow rate, m <sup>3</sup> /s
$W$	width, m
$v$	velocity, m/s and voltage, V
$w$	width, m

### Greek symbols

$\alpha$	thermal diffusivity, m <sup>2</sup> /s
$\epsilon$	dielectric permittivity matrix, F/m
$\eta$	efficiency
$\mu$	dynamic viscosity, N s/m <sup>2</sup>
$\vartheta$	kinematic viscosity, m <sup>2</sup> /s
$\rho$	density, kg/m <sup>3</sup>
$\sigma$	electrical conductivity, S/m

### Subscripts

amb	ambient
b	base
c	cold junction
cc	cross-cut
ch	channel
cooling	cooling energy
exh	exhaust
f	fluid
fin	fin
h	hot junction
HX	heat exchanger

i	inlet
l	load
max	maximum
n	n-type thermoelement
net	net
o	overall, outlet, optimum
opt	optimum
p	p-type thermoelement
s	surface
teg	thermoelectric generator
th	thermal
w	wall

## References

- 1 Energy Use, Loss and Opportunities Analysis: U.S. Manufacturing and Mining (2004) *U.S. Department of Energy, Industrial Technologies Program, Energetics, Inc. & E3M, Inc.*
- 2 Angrist, S.W. (1982) *Direct Energy Conversion*, 4th edn, Allyn and Bacon, Boston, MA.
- 3 Rowe, D.M. (ed.) (1995) *CRC Handbook of Thermoelectrics*, CRC Press, Boca Raton, FL.
- 4 Kays, W.M. and London, A.L. (1984) *Compact Heat Exchangers*, 3rd edn, McGraw-Hill, New York.
- 5 Incropera, F.P. and DeWitt, D.P. (1996) *Fundamentals of Heat and Mass Transfer*, John Wiley and Sons, New York.
- 6 Hendricks, T.J. (2007) Thermal system interactions in optimizing advanced thermoelectric energy recovery systems. *J. Energy Resour. Technol.*, **129**, 223–231.
- 7 White, F.M. (2006) *Viscous Fluid Flow*, 3rd edn, McGraw-Hill, New York ISBN 0-07-240231-8.
- 8 Jang, B., Han, S., and Kim, J.Y. (2011) Optimal design for micro-thermoelectric generators using finite element analysis. *Microelectron. Eng.*, **88**, 775–778.
- 9 Sondergaard, M., Christensen, M., Borup, K.A., Yin, H., and Iversen, B.B. (2012) Gravity-induced gradients in thermoelectric  $Mg_2Si_{0.9925-x}Sn_xSb_{0.0075}$ . *Acta Mater.*, **60**, 5745–5751.
- 10 Yin, H., Johnsen, S., Borup, K.A., Kato, K., Takatac, M., and Iversen, B.B. (2013) Highly enhanced thermal stability of  $Zn_4Sb_3$  nanocomposites. *Chem. Commun.*, **49**, 6540–6542.
- 11 Rezania, A., Rosendahl, L.A., and Yin, H. (2014) Parametric optimization of thermoelectric elements footprint for maximum power generation. *J. Power Sources*, **255**, 151–156.
- 12 Rezania, A. and Rosendahl, L.A. (2011) Evaluating thermoelectric power generation device performance using a rectangular microchannel heat sink. *J. Electron. Mater.*, **40** (5), 481–488.

- 13 Mayer, P.M. and Ram, R.J. (2006) Optimization of heat sink-limited thermoelectric generators. *Nanoscale Microscale Thermophys. Eng.*, **10**, 143–155.
- 14 Acikalin, T., Wait, S., Garimella, S., and Raman, A. (2004) Experimental investigation of the thermal performance of piezoelectric fans. *Heat Transfer Eng.*, **25**, 4–14.
- 15 Kim, J. and Golliher, E. (2002) Steady State Model of a Micro Loop Heat Pipe. Proceedings of 18th SemiTherm Symposium, San Jose, CA, pp. 137–144.
- 16 Miner, A. and Ghoshal, U. (2004) Cooling of high-power density microdevices using liquid metal coolants. *Appl. Phys. Lett.*, **85**, 506–508.
- 17 Ghoshal, U., Grimm, D., Ibrani, S., Johnston, C. and Miner, A. (2005) High-Performance Liquid Metal Cooling Loops. Proceedings of 21st SemiTherm Symposium, San Jose, CA, pp. 16–19.
- 18 Wang, E. et al. (2004) Micromachined jets for liquid impingement cooling of VLSI chips. *J. Microelectromech. Syst.*, **13**, 833–842.
- 19 Cader, T. and Tilton, D. (2004) Implementing Spray Cooling Thermal Management in High Heat Flux Applications. Proceedings of 2004 InterSociety Conference on Thermal Phenomena, pp. 699–701.
- 20 Cotler, A. et al. (2004) Chip-Level spray cooling of an LD-MOSFET RF power amplifier. *IEEE CPT Trans.*, **27**, 411–416.
- 21 Liao, S.M. and Zhao, T.S. (2002) Measurements of heat transfer coefficients from supercritical carbon dioxide flowing in horizontal mini/micro channels. *J. Heat Transfer*, **124**, 413–420.
- 22 Rezania, A. and Rosendahl, L.A. (2012) Thermal effect of a thermoelectric generator on parallel microchannel heat sink. *Energy*, **37**, 220–227.
- 23 Rezania, A. and Rosendahl, L.A. (2012) New configurations of micro plate-fin heat sink to reduce coolant pumping power. *J. Electron. Mater.*, **41** (6), 1343–1347.
- 24 Rezania, A. and Rosendahl, L.A. (2015) A comparison of micro-structured flat-plate and cross-cut heat sinks for thermoelectric generation application. *Energy Convers. Manage.*, **101**, 730–737.
- 25 Hendricks, T.J. and Karri, N.K. (2009) Micro- and nano-technology: a critical design key in advanced thermoelectric cooling systems. *J. Electron. Mater.*, **38** (7), 1257–1267.
- 26 Hendricks, T.J. (2008) Microtechnology: A Key to System Miniaturization in Advanced Energy Recovery and Conversion Systems. Proceedings of American Society of Mechanical Engineers 2nd International Conference on Energy Sustainability, Jacksonville, FL, Paper # ES2008-54244.
- 27 Hendricks, T.J. (2006) Microchannel & Minichannel Heat Exchangers in Advanced Energy Recovery & Conversion Systems. Proceedings of the ASME 2006 International Mechanical Engineering Congress and Exposition, IMECE2006 – Advanced Energy System Division, American Society of Mechanical Engineers, New York. Paper # IMECE2006-14594.
- 28 Wang, Y. and Holladay, J.D. (2005) *Microreactor Technology and Process Intensification, ACS Symposium Series 914*, American Chemical Society, Oxford University Press.

- 29** Kandilikar, S. and Upadhye, H. (2005) Extending the Heat Flux Limit with Enhanced Microchannels in Direct Single-Phase Cooling of Computer Chips. Proceedings of 21st SemiTherm Symposium, San Jose, CA, pp. 8–15.
- 30** Colgan, E. *et al.*, (2005) A Practical Implementation of Silicon Microchannel Coolers for High Power Chips. Proceedings of 21st SemiTherm Symposium, San Jose, CA, pp. 1–7.
- 31** Lee, D.Y. and Vafai, K. (1999) Comparative analysis of jet impingement and microchannel cooling for high heat flux applications. *Int. J. Heat Mass Transfer*, **42**, 1555–1568.
- 32** Landau, L.D. and Lifshitz, E.M. (1984) *Electrodynamics of Continuous Media*, 2nd edn, Butterworth-Heinemann, Oxford.
- 33** Antonova, E.E. and Looman, D.C. (2005) Finite Elements for Thermoelectric Device Analysis in ANSYS. 24th International Conference on Thermo-electrics, pp. 215–218.
- 34** Hasan, M.I. (2014) Investigation of flow and heat transfer characteristics in micro pin fin heat sink with nanofluid. *Appl. Therm. Eng.*, **63**, 598–607.
- 35** Husain, A. and Kim, K.Y. (2009) Analysis and optimization of electrokinetic microchannel heat sink. *Int. J. Heat Mass Transfer*, **52**, 5271–5275.
- 36** Decher, R. (1997) *Direct Energy Conversion – Fundamentals of Electric Power Production*, Oxford University Press, Inc., New York.
- 37** Kim, S.Y. and Webb R.L. (2003) Thermal Performance Analysis of Fan-Heat Sinks for CPU Cooling. Proceedings of the IMECE'03, IMECE2003, 42172, pp. 235–243.
- 38** Kim, D., Kim, S.J. and Ortega, A. (2003) Thermal Optimization of Microchannel Heat Sink with Pin Fin Structures. Proceedings of the IMECE'03, IMECE2003, 42180, pp. 593–602.
- 39** Kim, S.J., Kim, D.K., and Oh, H.H. (2008) Comparison of fluid flow and thermal characteristics of plate-fin and pin-fin heat sinks subject to a parallel flow. *Heat Transfer Eng.*, **29**, 169–177.
- 40** Kim, T.Y. and Kim, S.J. (2009) Fluid flow and heat transfer characteristics of cross-cut heat sinks. *Int. J. Heat Mass Transfer*, **52**, 5358–5370.
- 41** Morini, G.L. (2006) Scaling effects for liquid flows in microchannels. *Heat Transfer Eng.*, **27**, 64–73.
- 42** Rezania, A., Rosendahl, L.A., and Andreasen, S.J. (2012) Experimental investigation of thermoelectric power generation versus coolant pumping power in a microchannel heat sink. *Int. Commun. Heat Mass Transfer*, **39**, 1054–1058.
- 43** Gunnasegaran, P., Mohammed, H.A., Shuaib, N.H., and Saidur, R. (2010) The effect of geometrical parameters on heat transfer characteristics of microchannels heat sink with different shapes. *Int. J. Heat Mass Transfer*, **37**, 1078–1086.
- 44** Tuckerman, D.B. and Pease, R.F.W. (1981) High-performance heat sinking for VLSI. *IEEE Electron Device Lett.*, **2**, 126–129.
- 45** Rezania, A., Rosendahl, L.A. and Sørensen, K. (2014) Effects of Channel Geometry and Coolant Fluid on Thermoelectric Net Power. Proceedings from the 55th Conference on Simulation and Modelling (SIMS 55), Aalborg, Denmark, 21–22 October 2014, pp. 211–217.

- 46 Rezania, A., Yazawa, K., Rosendahl, L.A., and Shakouri, A. (2013) Co-optimized design of microchannel heat exchangers and thermoelectric generators. *Int. J. Therm. Sci.*, **72**, 73–81.
- 47 Hendricks, T.J., Karri, N.K., Hogan, T.P. and Cauchy, C.J. (2010) New Thermoelectric Materials and New System-Level Perspectives Using Battlefield Heat Sources for Battery Recharging. Proceedings of the 44th Power Sources Conference, Institute of Electrical and Electronic Engineers Power Sources Publication, Technical Paper #28.2, pp. 609–612.
- 48 Crane, D.T., LaGrandeur, J.W., and Bell, L.E. (2010) Progress report on BSST Led, J.S.DOE automotive waste heat recovery program. *J. Electron. Mater.*, **39** (9), 2142–2148.
- 49 Crane, D.T. and Bell, L.E. (2006) Progress Towards Maximizing the Performance of a Thermoelectric Power Generator. Proceedings of the 25th International Conference on Thermoelectrics, Vienna, Austria: IEEE, pp. 11–16.

**9**

## **Power Electronic Converters and Their Control in Thermoelectric Applications**

*Erik Schatz and Elena A. Man*

*Aalborg University, Department of Energy Technology, Pontoppidanstraede 111, 9220 Aalborg, Denmark*

### **9.1 Introduction**

In textbooks and scientific publications the load of thermoelectric modules is often presented by a resistance in order to simplify. However, in real applications the load is very seldom a pure resistance, but has its own specific voltage–current relationship depending on the specific case. A power electronic converter makes it possible to connect thermoelectric modules to a load with other voltage and current ratings than the thermoelectric modules [1–8]. This means that the thermoelectric module can charge a battery, power an electric machine, light a bulb, and so on. In Figure 9.1, it is seen how the power electronic converter is inserted between the thermoelectric modules and the load. Another important property of a power electronic converter is controllability. In order to protect either the thermoelectric modules or the load, the module current can be adjusted very quickly to the preferred value. Moreover, even though the input heat power changes or the load varies, the power electronic converter ensures that the module operates at its maximum power point. In this chapter, the main principles of power electronic converters and their control in thermoelectric applications will be given. At the end of the chapter, a case study will be presented where the theory and methods presented will be applied.

### **9.2 Building Blocks of Power Electronics**

Many power electronic converters exist with different advantages and disadvantages. However, the converters consist of the same fundamental components, which will be presented in this section.

The three basic passive components are the resistor, inductor, and capacitor. Their main properties are shown in Figure 9.2. In power electronic converters resistances should be minimized as they generate loss. The two other passive components, that is, the inductor and capacitor, both have the feature of being able to store energy. Owing to the integral part it plays in the voltage–current

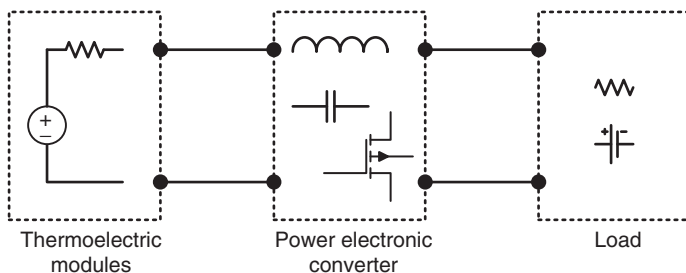


**Figure 9.1** System diagram of thermoelectric generator system.

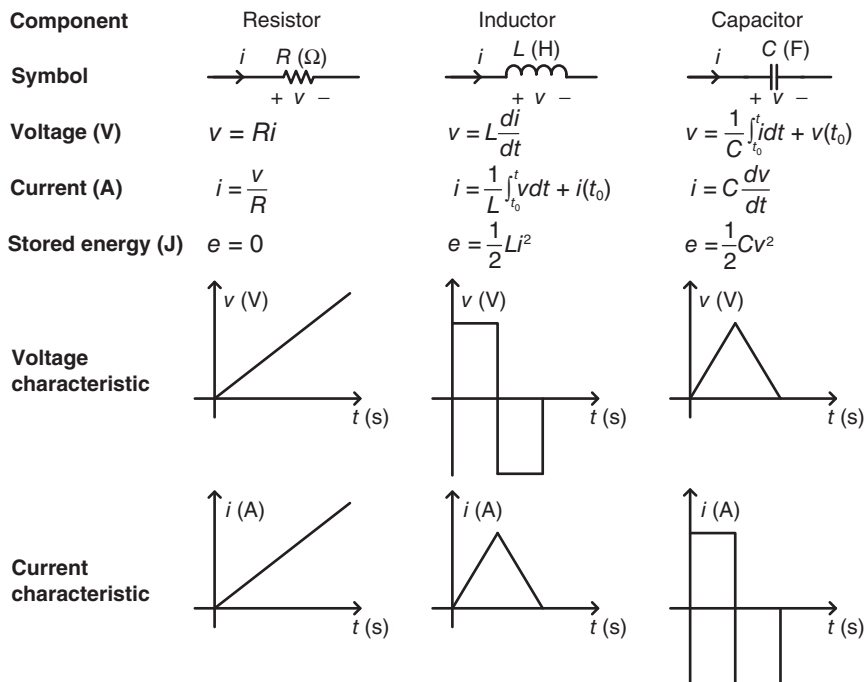


**Figure 9.2** Characteristics of passive electric components: resistor, inductor, and capacitor.

relationship, the inductor has a smoothing effect on the current and the capacitor has a smoothing effect on the voltage.

Another inductive component is the transformer. A transformer basically consists of two or several inductors magnetically connected to the same magnetic core. Several electric circuit models of the transformer exist, but the most well known is that of the ideal transformer shown in Figure 9.3. The ratio of the input and output voltage and current are determined by the ratio of the number of turns between the input and output sides of the transformer. This means that it is possible to connect a low-voltage input to a load with a very high voltage or the opposite. Owing to the magnetic coupling between the input and output sides of the transformer, the output and input are electrically isolated from each other, which, from a safety point of view in many applications, is a valuable feature.

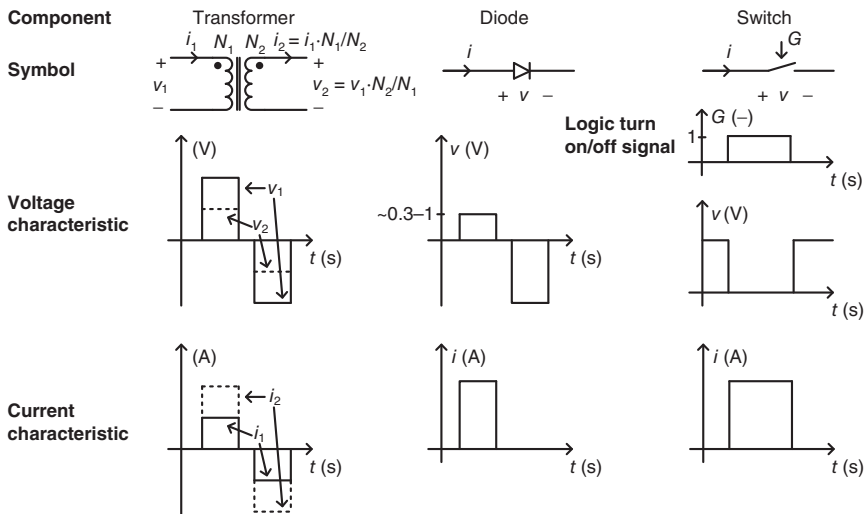


Figure 9.3 Characteristics of the transformer, diode, and switch.

It should be mentioned that the transformer only is able to transfer power of alternating current (AC) type between the input and output sides. If direct current (DC) is applied to the transformer the magnetic flux  $\phi$  of the magnetic core is constant. As the induced voltage is proportional to the derivative of the flux, that is,  $V_2 = N_2 \frac{d\phi}{dt}$ , the induced voltage will be zero. Therefore, the transformer blocks the DC. Ideally the transformer is lossless, that is, the power levels of the primary and secondary sides are almost equal:

$$p_1 = v_1 i_1 \approx v_2 i_2 = p_2 \quad (9.1)$$

This means that if the secondary voltage is higher than the primary voltage, the secondary current is lower than the primary current.

In the middle of Figure 9.3 a diode is seen. A diode is a semiconductor and has the important property of being able to conduct the current if it is forward biased (with voltage approx. 0.3–1 V). If the voltage on the other hand is negative, no current passes through the diode.

The last component in Figure 9.3 is the switch. The switch is basically a transistor, but in the field of power electronics the transistor is never operated in its linear region in order to avoid loss. It is therefore operated as a switch by a logic turn on/off signal, that is, either it is completely closed or fully open. The switch (or transistor) is the main reason for the wide use of power electronics in various applications: it makes it possible to convert a big amount of power with very low loss and together with modern computation circuits as microcontrollers or digital signal processors it makes the converter intelligent.

### 9.3 Power Electronic Topologies

Many different power electronic converter topologies can be found in the literature and several choices have to be made in order to select a proper

converter. One of the first parameters to be assessed is the input to output voltage ratio. If the output is lower than the thermoelectric input step-down converters are required. In contrast, if the output voltage is higher than the input a step-up converter is needed. However, for some applications the input can be both higher and lower than the output and in such situations converters with both step-down and step-up capabilities are necessary. The best converter is, as in many other design situations, a compromise between several considerations, for example, efficiency, cost, size, weight, reliability, and complexity. In some applications electric isolations between the input and output might also be a requirement. As mentioned before there are many possibilities for power electronic converters. Therefore, in this section only the most widely used converters suitable for thermoelectrics will be described.

### 9.3.1 Buck Converter

Even though thermoelectric modules often produce voltages lower than the load voltage some thermoelectric generator (TEG) applications require a step-down converter [9]. One of the most well-known step-down converters is the buck converter shown in Figure 9.4. The most essential principle of modern power electronic converters is the capability of the converter to switch between different states because of the semiconductors. In Figure 9.4 the switch  $S$  is either turned on (logic 1) or off (logic 0) by the logic gate signal  $G$ . In one switching period  $T_s$  the switch  $S$  is turned on for  $D T_s$  seconds and off for  $(1 - D) T_s$  seconds. The duty cycle  $D$  is the control variable that makes it possible to control the voltage and current of the converter.

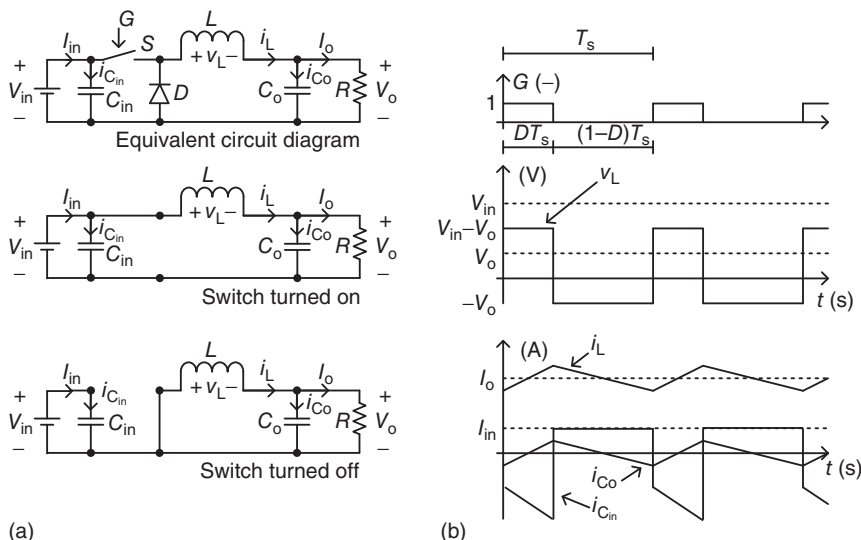


**Figure 9.4** (a) Circuit diagram of buck converter (top) during on-state (mid), and off-state (bottom) of the switch. (b) Logic gate signal (top), voltages (mid), and currents (bottom) during on and off states.

### 9.3.1.1 On-state

In this interval the inductor is the only component between the input and the output. In this mode, the inductor voltage and capacitor currents are given by

$$v_L = V_{in} - V_o \quad (9.2)$$

$$i_{C_o} = i_L - I_o \quad (9.3)$$

$$i_{C_{in}} = I_{in} - i_L \quad (9.4)$$

Because the input voltage is higher than the output, the inductor voltage in this interval is positive. Therefore, the current through it increases and energy is stored in it.

### 9.3.1.2 Off-state

When the switch is non-conducting the input and output are separated. In this situation the inductor voltage and capacitor currents are given by

$$v_L = -V_o \quad (9.5)$$

$$i_{C_o} = i_L - I_o \quad (9.6)$$

$$i_{C_{in}} = I_{in} \quad (9.7)$$

Because the inductor voltage is negative the current decreases and energy is therefore transferred to the load side.

### 9.3.1.3 Averaging

In steady state, that is, when the inductor current at time  $t$  is equal to the value at time  $t + T_s$ , the average voltage across the inductor in one switching period is zero [10, 11]. This knowledge is used to determine the relation between the input and output voltages; that is,

$$\begin{aligned} 0 &= \frac{1}{T_s} \int_t^{t+T_s} v_L dt \\ &= \frac{1}{T_s} \left( \int_t^{t+DT_s} (V_{in} - V_o) dt + \int_{t+DT_s}^{t+T_s} (-V_o) dt \right) \\ &\Downarrow \\ V_o &= DV_{in} \end{aligned} \quad (9.8)$$

The capacitors are used to smoothen the input and output currents. In steady state the average current through them is also zero as in the case of the inductor voltage. Therefore,

$$\begin{aligned} 0 &= \frac{1}{T_s} \int_t^{t+T_s} i_{C_o} dt \\ &= \frac{1}{T_s} \left( \int_t^{t+DT_s} (i_L - I_o) dt + \int_{t+DT_s}^{t+T_s} (i_L - I_o) dt \right) \\ &\Downarrow \\ I_o &= \frac{1}{T_s} \int_t^{t+T_s} i_L dt \end{aligned} \quad (9.9)$$

Not surprisingly, the output current is equal to the average inductor current. If it is assumed that the input power  $P_{\text{in}}$  is equal to the output power  $P_o$ , the input current is given by

$$P_{\text{in}} = P_o \quad (9.10)$$

⇓

$$V_{\text{in}} I_{\text{in}} = V_o I_o = D V_{\text{in}} I_o \quad (9.11)$$

⇓

$$I_{\text{in}} = D I_o \quad (9.12)$$

### 9.3.2 Boost Converter

The boost converter is one of the most used step-up converters both in general and for TEG systems [12, 13]. From the equivalent circuit diagram in Figure 9.5 it is seen that it has the same components as the buck converter, but arranged in another way. The output voltage and current can be controlled by the switch  $S$ . In the figure the voltages and currents of the converter can be seen during on and off states of the converter. By applying the same analysis used for the buck converter it can be shown that

$$V_o = \frac{V_{\text{in}}}{1 - D} \quad (9.13)$$

$$I_{\text{in}} = \frac{1}{T_s} \int_t^{t+T_s} i_L dt \quad (9.14)$$

$$I_o = (1 - D) I_{\text{in}} \quad (9.15)$$

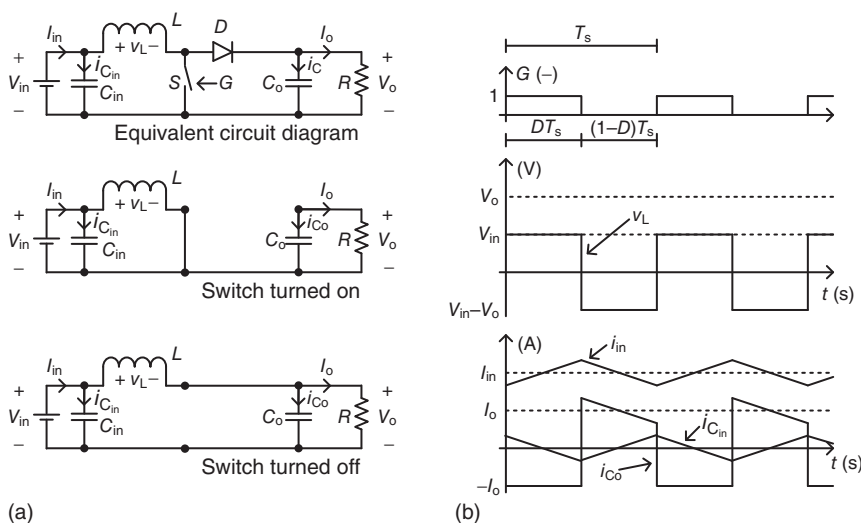


**Figure 9.5** (a) Circuit diagram of boost converter (top) during on-state (mid), and off-state (bottom) of the switch. (b) Logic gate signal (top), voltages (mid), and currents (bottom) during on and off states.

### 9.3.3 Non-Inverting Buck Boost Converter

If the output voltage is within the upper and lower limits of the input voltage it is possible to both step up and step down the voltage. The non-inverting buck-boost converter shown in Figure 9.6 has such capabilities. It is seen that this type of converter actually is a series connection of the buck and boost converters when they share the same inductor. The non-inverting buck-boost converter is often used in TEG-applications with fluctuating temperatures as it can handle a wide input voltage range [14–19]. The converter can be operated in three different modes:

**Buck mode:** In this mode switch  $S_2$  is in off-state all the time, and the output voltage and current are controlled by switch  $S_1$  as shown in Figure 9.4.

**Boost mode:** In this mode switch  $S_1$  is in on-state all the time, and the output voltage and current are controlled by switch  $S_2$  as shown in Figure 9.5.

**Buck-boost mode:** In this mode the two switches  $S_1$  and  $S_2$  are controlled synchronously, that is, they are in on and off states at the same time. Thereby, the output voltage can either be reduced or increased depending on the duration of the on-state. From a control point of view, the buck-boost mode is simple as only one control signal has to be applied.

The input and output voltage relations are given by

$$V_o = \begin{cases} DV_{in}, & \text{Buck mode} \\ \frac{1}{1-D} V_{in}, & \text{Boost mode} \\ \frac{D}{1-D} V_{in}, & \text{Buck-boost mode} \end{cases} \quad (9.16)$$

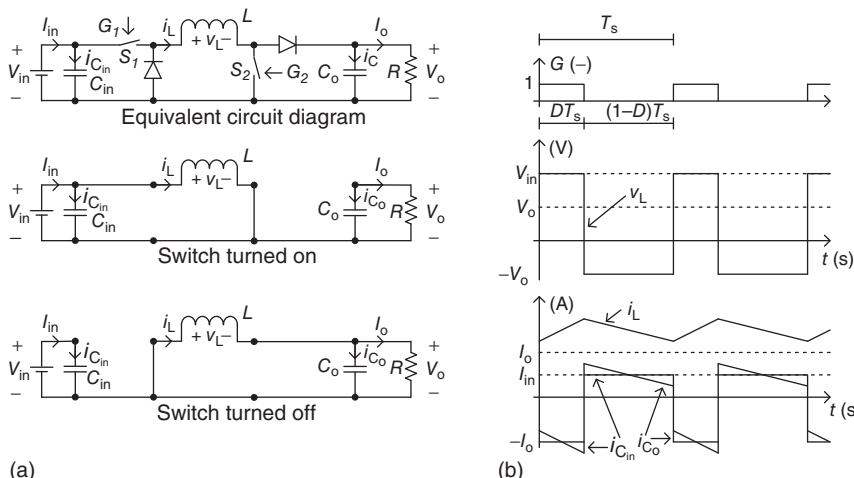


**Figure 9.6** (a) Circuit diagram of non-inverting buck-boost converter (top) during on-state in buck-boost mode (mid), and off-state in buck-boost mode (bottom) of the switch. (b) Logic gate signal (top), voltages (mid), and currents (bottom) during on and off states in buck-boost mode.

From the equations, it can be understood that in buck-boost mode the output voltage is higher than the input voltage for  $D > 0.5$  and lower for  $D < 0.5$ .

The average inductor current  $I_L$  for the three modes is given by:

$$I_L = \frac{1}{T_s} \int_t^{t+T_s} i_L dt = \begin{cases} I_o = \frac{1}{D} I_{in}, & \text{Buck mode} \\ I_{in} = \frac{1}{1-D} I_o, & \text{Boost mode} \\ \frac{1}{D} I_{in} = \frac{1}{1-D} I_o, & \text{buck-boost mode} \end{cases} \quad (9.17)$$

From the equations it is understood that the inductor current in buck-boost mode is higher than it would have been in buck mode or boost mode. For example, if the voltage gain is  $\frac{V_o}{V_{in}} = 2$ , the duty cycle would be  $\frac{1}{2}$  in boost mode and  $\frac{2}{3}$  in buck-boost mode. The inductor current would therefore be 50% higher in buck-boost mode than in boost mode for the same power transfer. Thereby, the loss of the inductor would be 125% higher in buck-boost mode than if the converter was operated in boost mode.

### 9.3.4 Flyback Converter

When electric isolation between the input and output sides is required or if there is a huge ratio between the input and output voltages a transformer can be utilized. The flyback converter shown in Figure 9.7 is one of the simplest transformer-based converters. It can be derived that the output voltage is given by

$$V_o = \frac{N_2}{N_1} \frac{D}{1-D} V_{in} \quad (9.18)$$

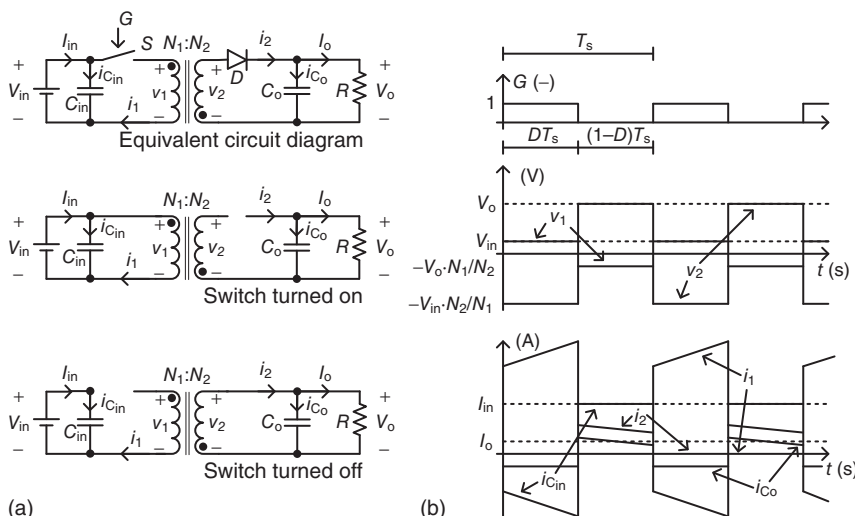


**Figure 9.7** (a) Circuit diagram of flyback converter (top) during on-state (mid), and off-state (bottom) of the switch. (b) Logic gate signal (top), voltages (mid), and currents (bottom) during on and off states.

It is understood that by properly selecting the turn ratio  $\frac{N_2}{N_1}$ , the flyback converter is able to provide a huge voltage gain. Therefore, this converter is often used in TEG applications and in particular in distributed TEG applications [20–22].

## 9.4 Electrical Equivalent Circuit Models for Thermoelectric Modules

It is well known that the open-circuit voltage of a thermoelectric module is proportional to the temperature gradient between the hot and cold plates of the module. When connected to a load the output voltage is however limited by the inner resistance of the device. The inner resistance depends on the average temperature between the plates, but is constant in many cases considered. In Figure 9.8, the inner voltage source and resistance of a thermoelectric module for different temperatures are shown. Both parameters can be described as first-order polynomials.

Thermoelectric modules can be modeled in a very simple way seen from an electric engineer's point of view. In Figure 9.9 two electric equivalent circuit models can be seen. The Thévenin model to the left in the figure is by far the most widely used as thermoelectric modules in most cases are series connected. However, when thermoelectric modules are connected in parallel the Norton equivalent model to the right is more beneficial.

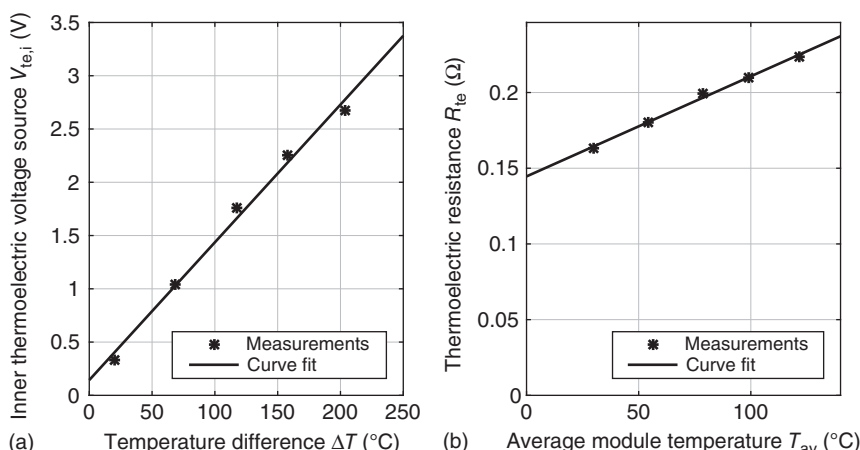
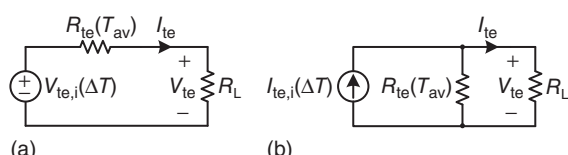


**Figure 9.8** Measurements and curve fits of a thermoelectric module. (a) Inner voltage source. (b) Inner resistance.

**Figure 9.9** Electrical equivalent circuit diagrams of thermoelectric module. (a) Thévenin equivalent. (b) Norton equivalent.



The Thévenin model includes an inner voltage source  $V_{te,i}$  whereas the Norton model includes an inner current source  $I_{te,i}$ . It is however easy to convert from one model to the other as the relationship between the two input sources is given by the thermoelectric resistance  $R_{te}$ ; that is,

$$V_{te,i} = R_{te} I_{te,i} \quad (9.19)$$

For both circuit models, the thermoelectric voltage and current are given by

$$V_{te} = V_{te,i} - R_{te} I_{te} \quad (9.20)$$

$$I_{te} = \frac{V_{te,i} - V_{te}}{R_{te}} \quad (9.21)$$

The thermoelectric power produced is given by the product of the thermoelectric voltage and current. However, the power can also be expressed by the inner voltage source; that is,

$$P_{te} = V_{te} I_{te} = V_{te,i} I_{te} - R_{te} I_{te}^2 \quad (9.22)$$

The thermoelectric power thereby follows the behavior of a second-order polynomial with the thermoelectric current as variable. In order to maximize the power produced the thermoelectric current therefore needs to be controlled at its maximum power point (MPP)  $I_{te,MPP}$ .

## 9.5 Maximum Power Point Operation and Tracking

The MPP current can be derived by utilizing the principle of a global maximum, where the slope with respect to the current is zero. Therefore,

$$\frac{dP_{te}}{dI_{te}} = V_{te,i} - 2R_{te} I_{te} = 0 \quad (9.23)$$

↓

$$I_{te,MPP} = \frac{V_{te,i}}{2R_{te}} \quad (9.24)$$

At MPP the thermoelectric voltage is

$$V_{te,MPP} = V_{te,i} - R_{te} I_{te,MPP} = V_{te,i} - R_{te} \frac{V_{te,i}}{2R_{te}} = \frac{V_{te,i}}{2} \quad (9.25)$$

It is seen that at MPP the thermoelectric voltage is half of the inner voltage source. The MPP load resistance can now be derived:

$$R_{L,MPP} = \frac{V_{te,MPP}}{I_{te,MPP}} = \frac{\frac{V_{te,i}}{2}}{\frac{V_{te,i}}{2R_{te}}} = R_{te} \quad (9.26)$$

At MPP the load resistor therefore needs to be the same as the thermoelectric resistance.

Finally, the maximum power can be derived:

$$P_{te,MPP} = V_{te,MPP} I_{te,MPP} = \frac{V_{te,i}}{2} \frac{V_{te,i}}{2R_{te}} = \frac{V_{te,i}^2}{4R_{te}} \quad (9.27)$$

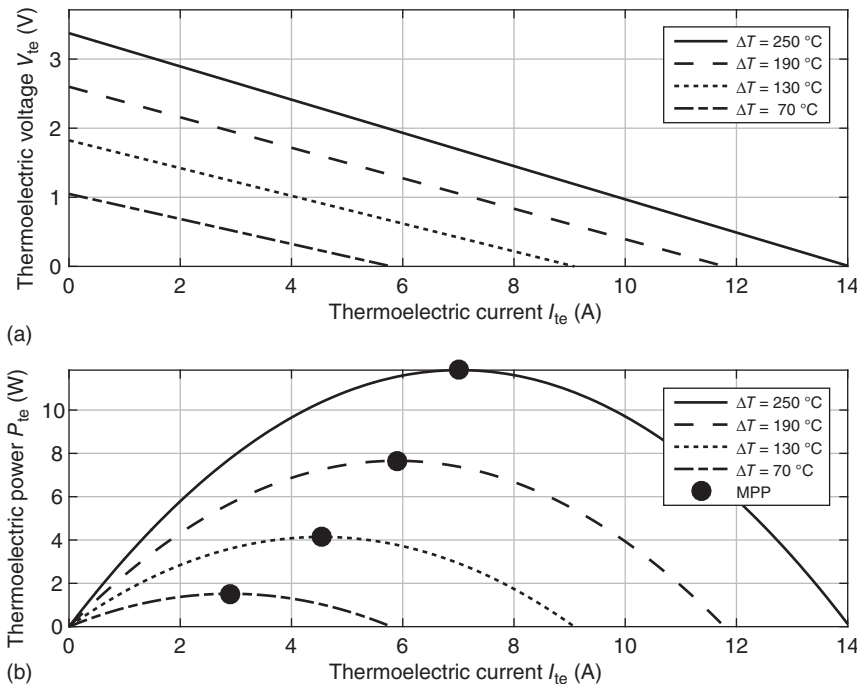


**Figure 9.10** Thermoelectric voltage (a) and power (b) dependency on the current for different temperature gradients.

In Figure 9.10, the produced output voltage and power can be seen as a function of the output current for different temperature gradients. The higher the temperature, the higher the voltage and power. However, it is also seen that the MPP current also depends on the temperature difference.

It can be understood that only a certain load resistor or current will make the thermoelectric module produce its maximum power. A maximum power point tracker (MPPT) is therefore necessary.

### 9.5.1 MPPT-Methods

The MPPT is basically the software of the power electronic converter that ensures that the thermoelectric modules are being operated at their MPP. Several algorithms for MPPT have been proposed for power electronic converters used in the field of photovoltaics (PV) [23]. These strategies can often also be applied for TEG systems. The most used strategies will be described here.

#### 9.5.1.1 Perturb and Observe

The perturb and observe (P&O) method is one of the most popular MPPTs for TEG and PV systems [2, 12, 13, 15, 18]. As the name indicates, it involves making a perturbation, observing the result, and then, based on the outcome, making a new perturbation. It is popularly called a hill-climbing method, which can be understood from the  $(I_{te}, P_{te})$ -curve in Figure 9.10. First, the current is zero, which means that the power also is zero. If a current is applied, the TEG produces a

certain power. Again, by applying a new current that is a little higher than the previous one, the power production also increases by a little.

The differences between the actual power at sample  $k$  and the previous power at sample  $k - 1$  are given by

$$\Delta P_{\text{te}}(k) = P_{\text{te}}(k) - P_{\text{te}}(k - 1) \quad (9.28)$$

Therefore, by increasing or decreasing the current with a step  $\Delta I$  and by evaluating the sign of the power difference  $\Delta P_{\text{te}}(k)$ , it is possible to reach the MPP. For example, if the actual current  $I_{\text{te}}(k)$  is higher than the previous current  $I_{\text{te}}(k - 1)$  and the power difference is positive, the controller knows that the power production increases when the current increases, and the controller will then continue to increase the current until the power difference becomes negative. If the current is higher than the MPP current the controller in the next step will decrease the current, which will result in a higher power, that is, a positive  $\Delta P_{\text{te}}(k)$ . Again, the controller will decrease the current until the power does not become higher. The flowchart of the P&O-method is illustrated in Figure 9.11. The current  $I_{\text{te}}^*$  is the reference current of the current controller. The MPPT needs to operate with a frequency significantly lower than the bandwidth of the current controller. However, the frequency should not be too low as the MPPT then will be too slow and therefore might not be able to track temperature variations. Also, in order to avoid big oscillations around the MPP the current step  $\Delta I$  can be decreased when the power is close to its maximum.

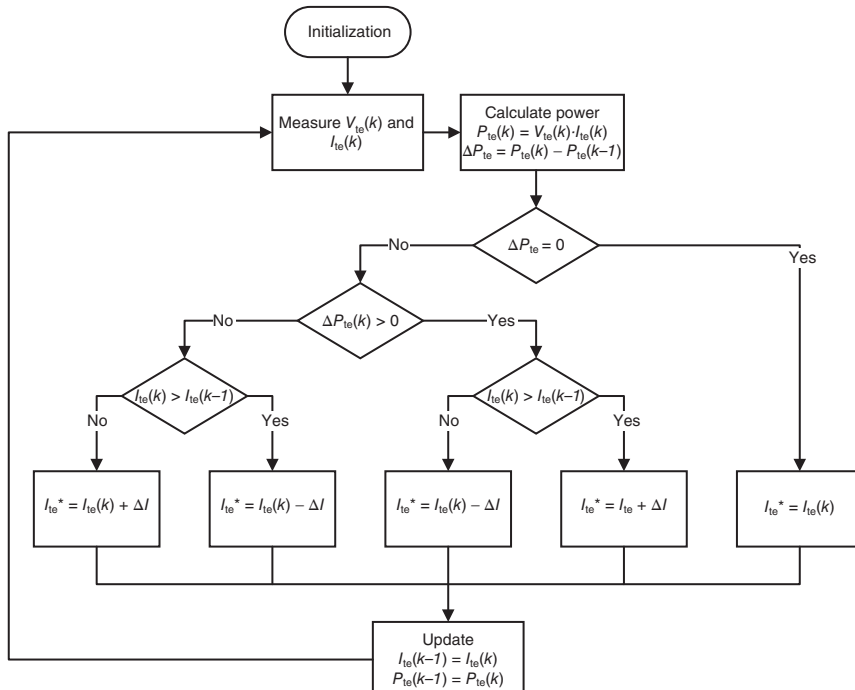


Figure 9.11 Flowchart of the perturb and observe method.

### 9.5.1.2 Incremental Conductance

The incremental conductance (IC) method utilizes the fact that at MPP the load resistance  $R_L$  is equal to the thermoelectric resistance  $R_{te}$ , that is, their conductances are equal [2, 24]. Therefore, the load conductance at MPP is equal to the negative slope of the  $(V_{te}, I_{te})$ -curve, that is, when

$$G_{L,MPP} = \frac{1}{R_{L,MPP}} = \frac{I_{te,MPP}}{V_{te,MPP}} = -\frac{dI_{te}}{dV_{te}} \quad (9.29)$$

the MPP is reached.

The IC-method is developed for PV systems in order to increase the dynamic performance just as for the P&O-method the current is either increased or decreased by a step  $\Delta I$ . In Figure 9.12, the output conductance and power are shown as a function of the output current for different temperature gradients. The conductance and power at MPP are also shown. When a step  $\Delta I$  is applied the corresponding voltage difference is measured.

The flowchart of the IC-method can be seen in Figure 9.13.

### 9.5.1.3 Fractional Open Circuit Voltage

The P&O and IC methods are classified as hill climbing methods. However, the fractional open circuit voltage method [16, 25] takes advantage of the knowledge regarding the output voltage at maximum power. It was previously shown that at

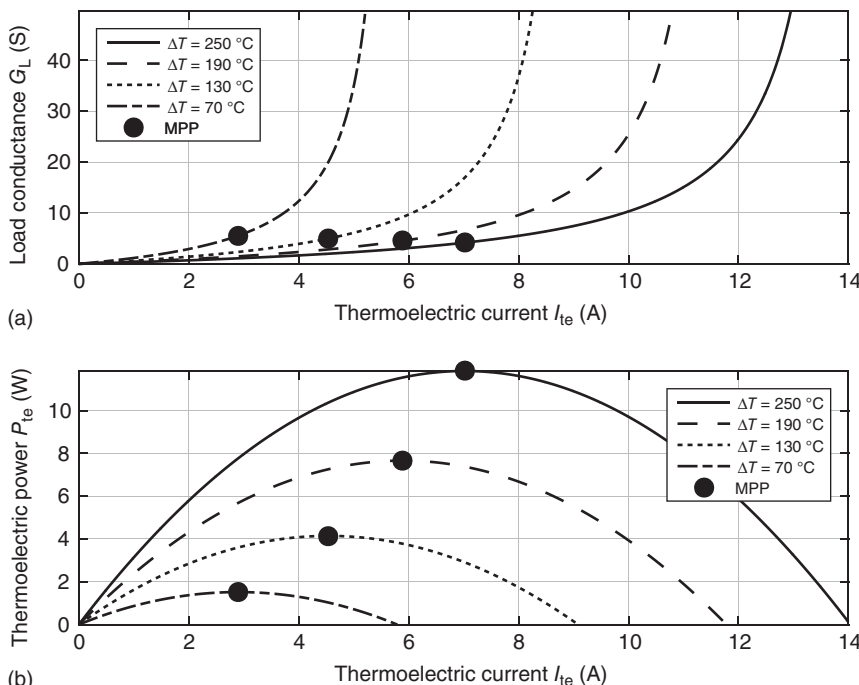


**Figure 9.12** Output conductance (a) and power (b) dependency on the output current for different temperature gradients.

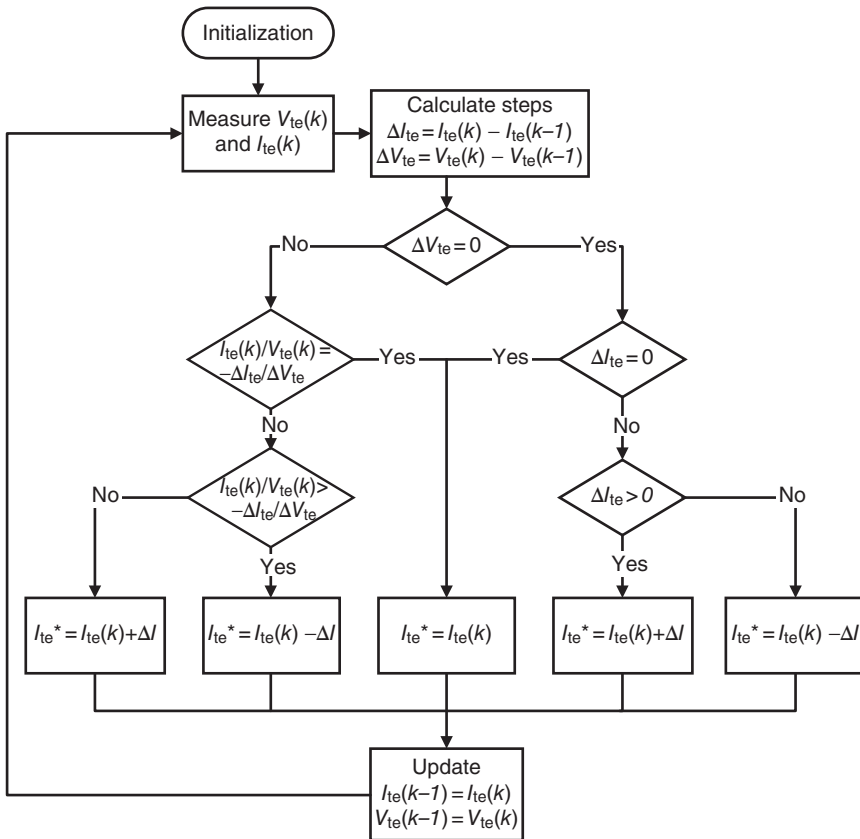


**Figure 9.13** Flowchart of the incremental conductance method.

maximum power the thermoelectric voltage is half of the inner voltage source; that is,

$$V_{te,MPP} = \frac{V_{te,i}}{2} \quad (9.30)$$

When no current is drawn of the TEG system the measured open circuit voltage is simply given by the inner voltage source. Therefore, by measuring the open circuit voltage  $V_{te,OC}$  during current interruptions the thermoelectric voltage reference can easily be determined:

$$V_{te}^* = \frac{V_{te,OC}}{2} \quad (9.31)$$

A voltage controller will then ensure that the thermoelectric voltage is settled to the reference  $V_{te}^*$ . Even though this method is very simple, it is seldom used owing to the fact that the power production is interrupted during the open circuit voltage measurement. This is contradictory as the whole purpose of a MPPT is to maximize the energy production. In order to disable the TEG the power electronic converter also needs to be able to disconnect the TEG. The buck converter has a built-in switch, but it is for example not possible to

disconnect the TEG system with the switch of the boost converter. Therefore, an extra switch is necessary, which will increase the total cost.

## 9.6 Case Study

In order to demonstrate how power electronic converters for TEG applications are designed and controlled a case study will be presented here. For the given application, thermoelectric modules will provide charging power for a battery through a boost converter.

In Figure 9.14, a system diagram is seen. In the MPPT block the thermoelectric voltage  $v_{te}$  and current  $i_{te}$  are measured. The output of the MPPT block is a reference output current  $i_{L,MP}^*$ . The charging voltage of the battery is not allowed to exceed a predefined maximum value specified by its data sheet. Therefore, when the battery voltage reaches the maximum allowed voltage, the boost converter needs to operate in voltage mode rather than in maximum power mode. When operating in voltage mode a voltage controller is necessary. The maximum allowed voltage  $V_{b,max}$  is the input reference of the voltage controller. The voltage controller will also provide an inductor current reference current  $i_{L,V}^*$ . A mode selector will decide which of the two inductor current references actually will be applied to the current controller; that is,

$$i_L^* = \begin{cases} i_{L,MP}^*, & i_{L,MP}^* < i_{L,V}^* \\ i_{L,V}^*, & i_{L,MP}^* \geq i_{L,V}^* \end{cases} \quad (9.32)$$

As can be understood, the smallest reference current will be selected. The current controller forces the error between the reference and the actual measured current  $E_i$  to be zero by adjusting the duty cycle  $d$  of the converter.

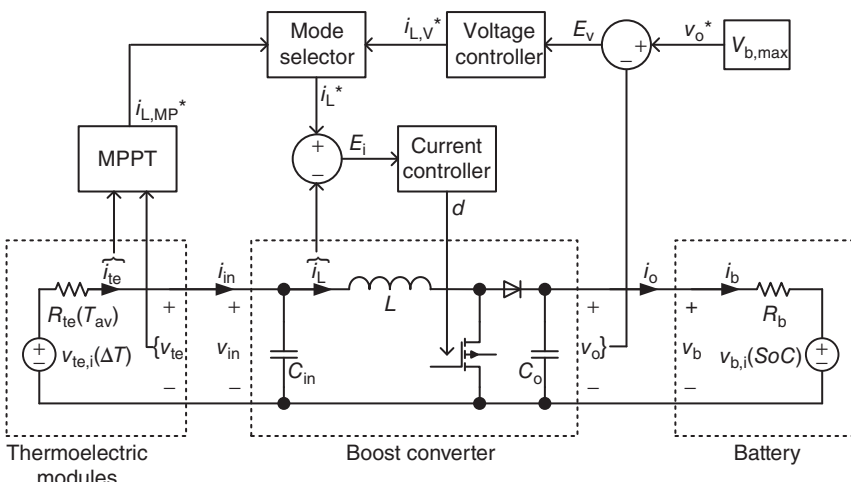


**Figure 9.14** System diagram of thermoelectric generator system used as case study.

### 9.6.1 Specifications

The thermoelectric module has a Seebeck coefficient of  $S = 0.05 \text{ V/K}$ . The inner resistance is given by

$$R_{\text{te}} = 0.5 + 0.002T_{\text{av}} \quad (9.33)$$

where the average temperature is

$$T_{\text{av}} = \frac{T_c + T_h}{2} \quad (9.34)$$

The cold side of the thermoelectric module is  $T_c = 20^\circ\text{C}$  and the maximum hot side temperature is  $T_{h,\text{max}} = 220^\circ\text{C}$ . The maximum temperature is considered as nominal. Therefore

$$V_{\text{te,i,nom}} = S(T_{h,\text{max}} - T_c) = 0.05(220 - 20) = 10 \text{ V} \quad (9.35)$$

$$T_{\text{av,nom}} = \frac{T_c + T_{h,\text{max}}}{2} = \frac{20 + 220}{2} = 120^\circ\text{C} \quad (9.36)$$

$$R_{\text{te,nom}} = 0.5 + 0.002T_{\text{av,nom}} = 0.5 + 0.002 \cdot 120 = 0.74 \Omega \quad (9.37)$$

The nominal current, power, and voltage of the thermoelectric modules and input of the power converter are therefore

$$I_{\text{in,nom}} = I_{\text{te,nom}} = \frac{V_{\text{te,i,nom}}}{2R_{\text{te,nom}}} = \frac{10}{2 \times 0.74} = 6.76 \text{ A} \quad (9.38)$$

$$P_{\text{in,nom}} = P_{\text{te,nom}} = \frac{V_{\text{te,i,nom}}^2}{4R_{\text{te,nom}}} = \frac{10^2}{4 \times 0.74} = 33.78 \text{ W} \quad (9.39)$$

$$V_{\text{in,nom}} = V_{\text{te,nom}} = \frac{P_{\text{in,nom}}}{I_{\text{in,nom}}} = \frac{33.78}{6.76} = 5 \text{ V} \quad (9.40)$$

The battery consists of four cells connected in series and has a nominal capacity of  $Q_{b,\text{nom}} = 10 \text{ Ah}$ . The nominal output voltage of the converter is equal to the nominal battery voltage, that is,  $V_{o,\text{nom}} = V_{b,\text{nom}} = 14.8 \text{ V}$ .

If it is assumed that the converter is lossless all the power of the thermoelectric modules is transferred to the battery terminals. The nominal duty cycle and output current are therefore

$$D_{\text{nom}} = \frac{V_{o,\text{nom}} - V_{\text{in,nom}}}{V_{o,\text{nom}}} = \frac{14.8 - 5}{14.8} = 0.66 \quad (9.41)$$

$$I_{o,\text{nom}} = \frac{P_{\text{in,nom}}}{V_{o,\text{nom}}} = \frac{33.78}{14.8} = 2.28 \text{ A} \quad (9.42)$$

In Figure 9.14 it is seen that similarly to the thermoelectric modules, the battery is modeled as a series connection of an inner voltage source  $v_{b,i}$  and resistance  $R_b$ . The resistance of the selected battery is  $R_b = 100 \text{ m}\Omega$ . The level of the inner voltage source depends on the state-of-charge (SoC) of the battery as shown in Figure 9.15. The SoC is calculated as follows:

$$\text{SoC} = \text{SoC}(t_0) + \frac{100}{Q_{b,\text{nom}}} \int_{t_0}^t \frac{i_b}{3600} dt \quad (9.43)$$

where  $\text{SoC}(t_0)$  is the initial state-of-charge level.

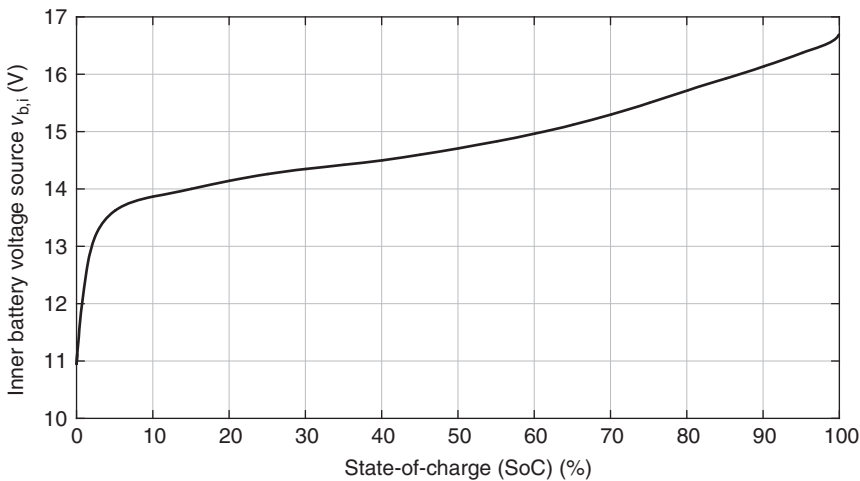


Figure 9.15 Inner battery voltage dependency on state-of-charge level.

### 9.6.2 Requirements

An important design parameter of the passive components is the allowed voltage and current ripple. The inductor current peak-to-peak ripple is allowed to be 10% of the average. In Eq. (9.14) it was shown that the average inductor current is equal to the average input current. Therefore,

$$\Delta I_L = 0.10 \cdot I_{in,nom} = 0.10 \cdot 6.76 = 0.68A \quad (9.44)$$

In order to consider the input and output currents as constant the current of these are maximum allowed to have a peak-to-peak ripple of 1% of the nominal; that is,

$$\Delta I_{in} = 0.01 \cdot I_{in,nom} = 0.01 \cdot 6.76 = 67.57 \text{ mA} \quad (9.45)$$

$$\Delta I_o = 0.01 \cdot I_{o,nom} = 0.01 \cdot 2.28 = 22.83 \text{ mA} \quad (9.46)$$

The peak-to-peak voltage ripple of the input and output are therefore

$$\Delta V_{in} = R_{te,nom} \Delta I_{in} = 0.74 \cdot 0.068 = 50 \text{ mV} \quad (9.47)$$

$$\Delta V_o = R_b \Delta I_o = 0.1 \cdot 0.023 = 2.3 \text{ mV} \quad (9.48)$$

Selection of the switching frequency is a trade-off among several parameters, for example, physical size of the passive components and switching loss. However, in this case study a frequency of  $f_s = 25 \text{ kHz}$  is chosen.

### 9.6.3 Design of Passive Components

During the turn-on period the voltage across the inductor is given by the input voltage. Therefore, the required inductance is

$$L = \frac{V_{in,nom}}{\Delta I_L} \frac{D_{nom}}{f_s} = \frac{5}{0.68} \frac{0.66}{25000} = 196 \mu\text{H} \quad (9.49)$$

The maximum current of the input capacitor is half of the inductor current ripple, which also can be seen from Figure 9.5. From geometrical considerations it can be shown that in one switching period the charge transfer of the input capacitor is given by

$$\Delta Q_{in} = 2 \int_{DT_s/2}^{DT_s} i_{C_{in}} dt = \frac{\Delta I_L}{2} \frac{D_{nom}}{2f_s} = \frac{0.68}{2} \frac{0.6622}{2 \cdot 25000} = 4.47 \mu C \quad (9.50)$$

The required input capacitance is therefore

$$C_{in} = \frac{\Delta Q_{in}}{\Delta V_{in}} = \frac{4.47 \times 10^{-6}}{50 \times 10^{-3}} = 89.48 \mu F \quad (9.51)$$

During the turn-on period the charge transfer of the output capacitor is

$$\Delta Q_o = \frac{I_{o,nom} \cdot D_{nom}}{f_s} = \frac{2.28 \cdot 0.6622}{25000} = 60.46 \mu C \quad (9.52)$$

The required input capacitance is therefore

$$C_o = \frac{\Delta Q_o}{\Delta V_o} = \frac{60.46 \times 10^{-6}}{2.3 \times 10^{-3}} = 26.49 mF \quad (9.53)$$

#### 9.6.4 Transfer Functions

In order to design the required current and voltage controllers of the converter, transfer functions of the converter are necessary. In order to derive the transfer functions, the converter is first analyzed; that is,

$$C_{in} \frac{dv_{in}}{dt} = i_{C_{in}} = \frac{V_{te,i} - v_{in}}{R_{te}} - i_L, T_s\text{-period} \quad (9.54)$$

$$L \frac{di_L}{dt} = v_L = \begin{cases} v_{in}, & dT_s\text{-period} \\ v_{in} - v_o, & (1-d)T_s\text{-period} \end{cases} \quad (9.55)$$

$$C_o \frac{dv_o}{dt} = i_{Co} = \begin{cases} -\frac{v_o - V_{bi}}{R_b}, & dT_s\text{-period} \\ i_L - \frac{v_o - V_{bi}}{R_b}, & (1-d)T_s\text{-period} \end{cases} \quad (9.56)$$

When averaging over one switching period one obtains

$$\left\langle C_{in} \frac{dv_{in}}{dt} \right\rangle_{T_s} = \frac{V_{te,i}}{R_{te}} - \frac{v_{in}}{R_{te}} - i_L \quad (9.57)$$

$$\left\langle L \frac{di_L}{dt} \right\rangle_{T_s} = v_{in} - v_o(1-d) \quad (9.58)$$

$$\left\langle C_o \frac{dv_o}{dt} \right\rangle_{T_s} = -\frac{v_o}{R_b} + \frac{V_{bi}}{R_b} + i_L(1-d) \quad (9.59)$$

It is assumed that each variable  $x$  is given by a DC part  $X$  and a small AC part  $\tilde{x}$ , that is,  $x = X + \tilde{x}$ . This is therefore inserted in the previous equations; that is,

$$\left\langle C_{in} \frac{d(V_{in} + \tilde{v}_{in})}{dt} \right\rangle_{T_s} = \frac{V_{te,i}}{R_{te}} - \frac{(V_{in} + \tilde{v}_{in})}{R_{te}} - (I_L + \tilde{I}_L) \quad (9.60)$$

$$\left\langle L \frac{d(I_L + \tilde{I}_L)}{dt} \right\rangle_{T_s} = (V_{in} + \tilde{v}_{in}) - (V_o + \tilde{v}_o) (1 - (D + \tilde{d})) \quad (9.61)$$

$$\begin{aligned} \left\langle C_o \frac{d(V_o + \tilde{v}_o)}{dt} \right\rangle_{T_s} &= -\frac{(V_o + \tilde{v}_o)}{R_b} + \frac{V_{b,i}}{R_b} \\ &\quad + (I_L + \tilde{I}_L) (1 - (D + \tilde{d})) \end{aligned} \quad (9.62)$$

The small AC parts are now separated from the DC parts. It is assumed that the product of two small AC-parts is insignificant; for example,  $\tilde{d} \cdot \tilde{I}_L \approx 0$ . Therefore,

$$\left\langle C_{in} \frac{d\tilde{v}_{in}}{dt} \right\rangle_{T_s} = -\frac{\tilde{v}_{in}}{R_{te}} - \tilde{I}_L \quad (9.63)$$

$$\left\langle L \frac{d\tilde{I}_L}{dt} \right\rangle_{T_s} = \tilde{v}_{in} - (1 - D)\tilde{v}_o + V_o\tilde{d} \quad (9.64)$$

$$\left\langle C_o \frac{d\tilde{v}_o}{dt} \right\rangle_{T_s} = -\frac{\tilde{v}_o}{R_b} + (1 - D)\tilde{I}_L - I_L\tilde{d} \quad (9.65)$$

The AC parts are now transformed into the Laplace domain; that is,

$$C_{in}sV_{in}(s) = -\frac{V_{in}(s)}{R_{te}} - I_L(s) \quad (9.66)$$

$$LsI_L(s) = V_{in}(s) - (1 - D)V_o(s) + V_oD(s) \quad (9.67)$$

$$C_o s V_o(s) = -\frac{V_o(s)}{R_b} + (1 - D)I_L(s) - I_L D(s) \quad (9.68)$$

The transfer functions are then given by

$$V_{in}(s) = -\frac{R_{te}}{R_{te}C_{in}s + 1}I_L(s) \quad (9.69)$$

$$V_o(s) = \frac{R_b(1 - D)}{R_bC_0s + 1}I_L(s) - \frac{R_bI_L}{R_bC_0s + 1}D(s) \quad (9.70)$$

$$\begin{aligned} LsI_L(s) &= -\frac{R_{te}}{R_{te}C_{in}s + 1}I_L(s) - \frac{R_b(1 - D)^2}{R_bC_0s + 1}I_L(s) \\ &\quad + \frac{R_bI_L(1 - D)}{R_bC_0s + 1}D(s) + V_oD(s) \end{aligned} \quad (9.71)$$

By manipulating the transfer functions, the duty cycle to inductor current transfer function can be derived:

$$\frac{I_L(s)}{D(s)} = \frac{V_o(R_{te}C_{in}s + 1)(R_bC_0s + 1) + R_bI_L(1 - D)(R_{te}C_{in}s + 1)}{Ls(R_{te}C_{in}s + 1)(R_bC_0s + 1) + R_{te}(R_bC_0s + 1) + R_b(1 - D)^2(R_{te}C_{in}s + 1)} \quad (9.72)$$

If both a current controller and a voltage controller are applied a cascaded control structure is often used, which also is the case in this study as shown in Figure 9.14. In such configuration the inner current loop needs to have sufficient higher bandwidth than the outer voltage loop, for example, by a factor of 10. Thereby, the inductor current can be seen as the only control input of the voltage controller. The inductor current to output voltage transfer function is therefore

$$\frac{V_o(s)}{I_L(s)} = \frac{R_b(1 - D)}{R_b C_o s + 1} \quad (9.73)$$

### 9.6.5 Design of Current Controller

When inserting the nominal values of the parameters of the duty cycle to inductor current transfer function one obtains

$$\frac{I_L(s)}{D(s)} = \frac{2.596 \times 10^{-6}s^2 + 0.0402s + 15.03}{3.438 \times 10^{-11}s^3 + 5.321 \times 10^{-7}s^2 + 0.002157s + 0.7514} \quad (9.74)$$

It is desirable to have a bandwidth of the controller sufficiently lower than the switching frequency. A bandwidth 100 times lower than the switching frequency is therefore chosen; that is,  $BW_i = 0.01 \cdot 2\pi f_s = 1571$  rad/s. A proportional–integral (PI) controller can therefore be designed:

$$\frac{D(s)}{E_i(s)} = 79.5 \frac{13 \times 10^{-5}s + 1}{s} \quad (9.75)$$

In Figure 9.16, the open loop bode plot of the current controller and plant can be seen. The poles and zeros of the system are also seen. The zero of the PI controller is placed at the highest pole of the plant. A phase margin of 84° is obtained, which is sufficient and the bandwidth is  $1.57 \times 10^3$  rad/s as desired.

In order to evaluate the performance of the current controller, different current reference steps are applied to a simulation model of the converter. The circuit and controller have been implemented in the circuit simulator PLECS. In Figure 9.17, it is seen that the current controller is able to track the inductor reference currents.

### 9.6.6 MPPT Implementation

It is chosen to apply the P&O-method as it is widely used. In Figure 9.11, it was shown that a value of  $\Delta I$  was either added to or subtracted from the thermoelectric output current depending on the internal states of the MPPT flowchart. In this case study it is actually the inductor current that is controlled, but as previously mentioned the average thermoelectric current is equal to the average inductor current. Therefore,

$$I_{L,MP}^* = I_{te}^* \quad (9.76)$$

It is decided to divide the current reference into steps of  $\Delta I = 0.1$  A, that is, approximately 1.5% of the nominal input current. The size of the step is a trade-off between the speed of the MPPT and the efficiency of the algorithm.

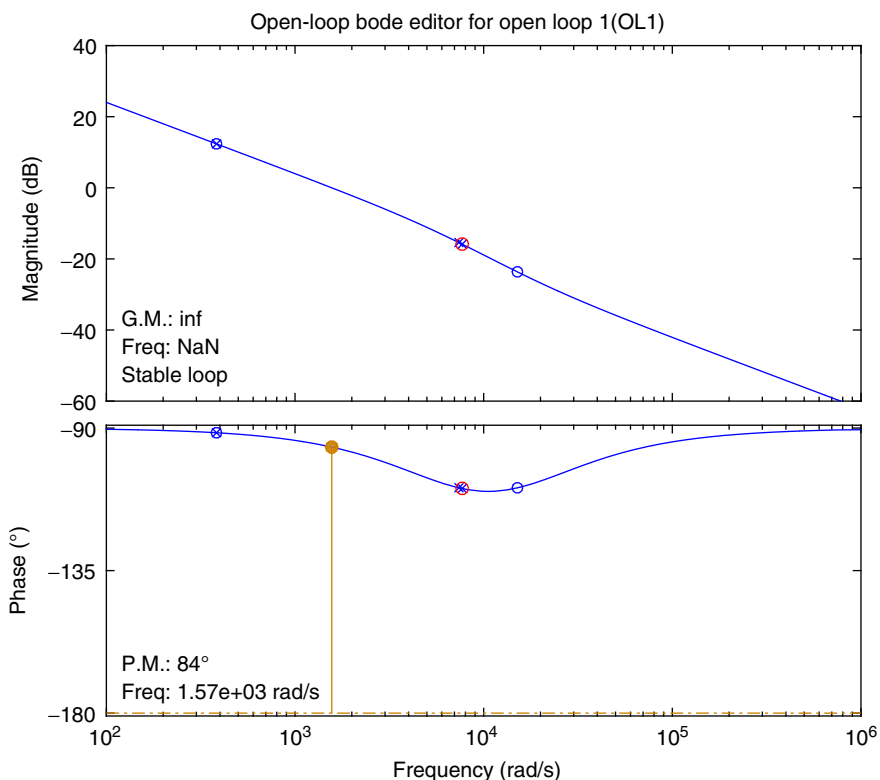


**Figure 9.16** Open loop bode plot of current controller and plant. Crosses: poles. Circles: zeros.

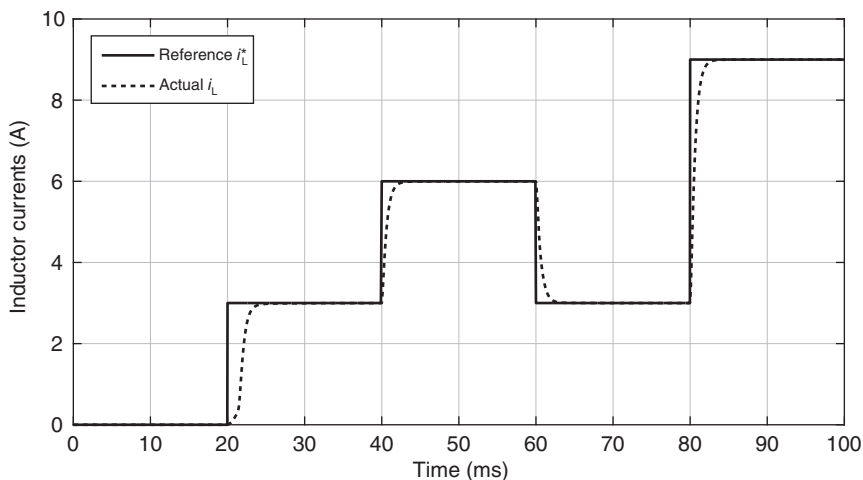


**Figure 9.17** Current controller performance evaluation. Actual and reference inductor currents.

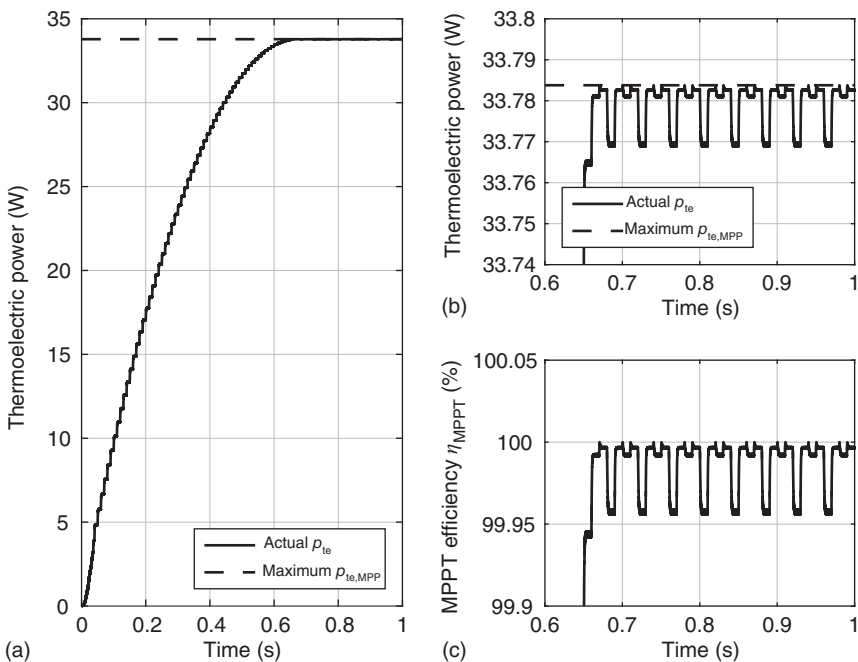


**Figure 9.18** Performance evaluation of the MPPT algorithm. (a) Actual and maximum thermoelectric power. (b) Zoom of power. (c) MPPT efficiency.

In order to demonstrate the operation of the MPPT a start scenario is shown in Figure 9.18. A constant temperature is applied to the hot side. In the figure, it is seen how the actual thermoelectric power produced reaches the maximum possible power. It is also seen that the power produced oscillates around the maximum possible. These oscillations cause the MPPT efficiency to be less than 100%. The oscillations however can be decreased by decreasing the current steps when the power produced approaches the maximum possible. The MPPT efficiency is defined as the ratio of the produced power relative to the maximum possible; that is,

$$\eta_{MPPT} = \frac{P_{te}}{p_{te,MPP}} 100\% = \frac{V_{te} i_{te}}{\frac{V_{te,i}^2}{4R_{te}}} 100\% \quad (9.77)$$

### 9.6.7 Design of Voltage Controller

When inserting the parameters in Eq. (9.73) the inductor current to output voltage transfer function is given by

$$\frac{V_o(s)}{I_L(s)} = \frac{0.03378}{0.002649s + 1} \quad (9.78)$$

It is chosen also to use a PI controller for the voltage controller; that is,

$$\frac{I_{LV}^*(s)}{E_v(s)} = 4650 \frac{2.6 \cdot 10^{-3}s + 1}{s} \quad (9.79)$$

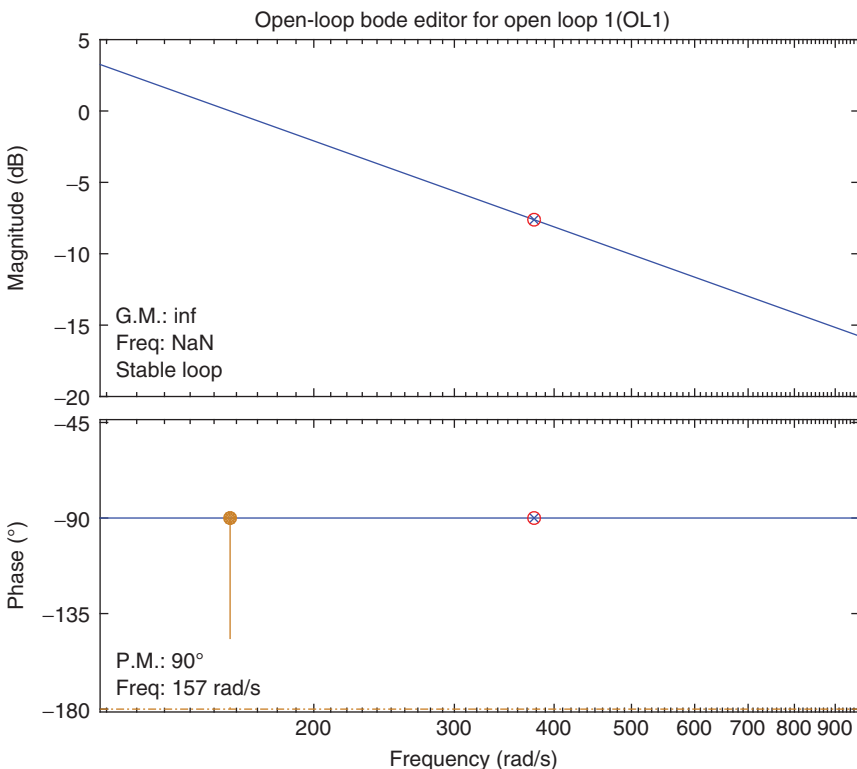


**Figure 9.19** Open loop bode plot of voltage controller and plant. Cross: pole, Circle: zero.

In Figure 9.19, the open loop bode plot of the voltage controller and plant is seen. The zero of the PI controller cancels out the pole of the plant. A phase margin of  $90^\circ$  is obtained and the bandwidth is  $157 \text{ rad/s}$  as desired, that is, 10 times lower than the bandwidth of the current controller.

In order to assess the performance of the voltage controller, several reference voltages have been applied to the controller in a simulation. In Figure 9.20 it is seen that the voltage controller is able to track the output voltage reference.

The main reason for having a voltage controller was to ensure that the maximum allowed voltage of the battery was not exceeded. In Figure 9.21 the thermoelectric power and battery voltage is seen during charging. The thermoelectric module produces maximum power until the battery voltage reaches its upper limit at 16.8 V. When this happens the converter switches to voltage mode and ramps down the produced power in order to have a constant voltage. A small overshoot during the transition from maximum power mode to voltage mode is seen. However, it is assumed that such a small peak for such a relatively short time will not affect the health of the battery. It should be noticed that the simulation actually has been done with a battery capacity 3600 times smaller than the 10 Ah nominal capacity in order to avoid too long a simulation time. In reality the battery of course cannot be charged in a few seconds. It will rather take a few hours depending on the level of the charging current.

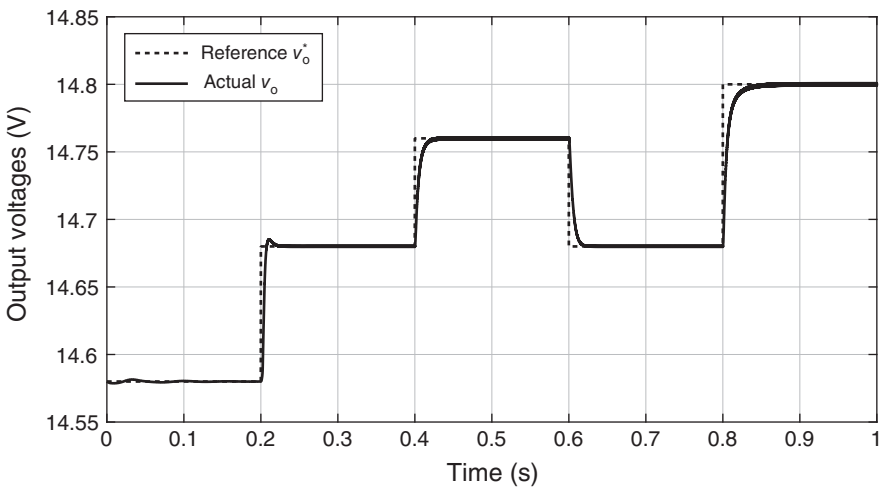


**Figure 9.20** Voltage controller performance evaluation. Actual and reference output voltage.

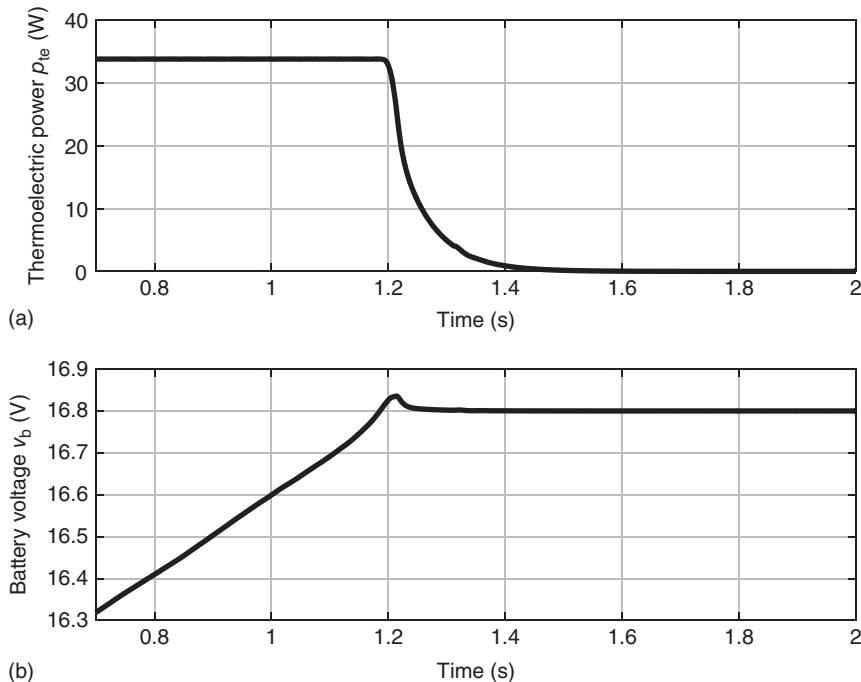


**Figure 9.21** Simulation of thermoelectric power production (a) and battery voltage (b) during charging first in maximum power mode and after approximately 1.2 s in voltage mode. The battery capacity has been reduced by 3600 in order to decrease the simulation time.

## 9.7 Conclusion

In this chapter, the basics of power electronic building blocks have been given. The fundamental components are the resistor, inductor, capacitor, transformer, switch, and diode. Suitable power electronic DC/DC converters for thermoelectric applications have also been presented. The converters have either step-down or step-up capabilities or both at the same time. For high voltage gain factors a transformer is utilized, which also provides galvanic isolation.

Two electrical equivalent circuit diagrams (Thévenin and Norton) of thermoelectric modules have been presented and the theory behind maximum power point operation and tracking has been explained.

In order to demonstrate the utilization of a power electronic converter and MPPT for thermoelectric applications a case study has been presented. For the case study a boost converter was charging a battery from a series connection of thermoelectric modules. The case study included the design procedure of the passive components and controllers of the converter. For MPPT the P&O method was applied. When the battery reached its maximum allowed voltage the boost converter was operating in voltage mode instead of maximum power mode.

## References

- 1 Kim, R.Y. and Lai, J.S. (2008) A seamless mode transfer maximum power point tracking controller for thermoelectric generator applications. *IEEE Trans. Power Electron.*, **23** (5), 2310–2318.
- 2 Laird, I., Lovatt, H., Savvides, N., Lu, D., and Agelidis, V.G. (2008) Comparative Study of Maximum Power Point Tracking Algorithms for Thermoelectric Generators. Power Engineering Conference. in *Proceedings of the Australasian Universities Power Engineering Conference (AUPEC)*.
- 3 Kim, S., Cho, S., Kim, N., and Park, J. (2010) A maximum power point tracking circuit of thermoelectric generators without digital controllers. *IEICE Electron. Express*, **7** (20), 1539–1545.
- 4 Ni, L.-X., Sun, K., Zhang, L., Xing, Y., Chen, M., and Rosendahl, L. (2011) Power Conditioning System for Thermoelectric Generator Based on Interleaved Boost Converter with MPPT Control. in *Proceedings of the International Conference on Electrical Machines and Systems (ICEMS)*.
- 5 Win, K.K., Dasgupta, S., and Panda, S.K. (2011) An Optimized MPPT Circuit for Thermoelectric Energy Harvester for Low Power Applications. in *Proceedings of the 8th International Conference on Power Electronics (ECCE)*.
- 6 Laird, I. and Lu, D.D.-C. (2013) High step-up DC/DC topology and MPPT algorithm for use with a thermoelectric generator. *IEEE Trans. Power Electron.*, **28** (7), 3147–3157.
- 7 Yamada, H., Kimura, K., Hanamoto, T., Ishiyama, T., Sakaguchi, T., and Takahashi, T. (2013) A novel MPPT control method of thermoelectric power generation with single sensor. *Appl. Sci.*, **3** (2), 545–558.

- 8 Cao, D. and Peng, F.Z. (2010) Multiphase Multilevel Modular DC-DC Converter for High Current High Gain TEG Application. in *Proceedings of the IEEE Energy Conversion Congress and Exposition*, pp. 4230–4237.
- 9 Montecucco, A., Siviter, J., and Knox, A.R. (2012) Simple, Fast and Accurate Maximum Power Point Tracking Converter for Thermoelectric Generators. in *Proceedings of the IEEE Energy Conversion Congress and Exposition*.
- 10 Erikson, R.W. and Maksimovic, D. (2000) *Fundamentals of Power Electronics*, 2nd edn, Kluwer Academic Publishers, Secaucus, NJ.
- 11 Mohan, N., Underland, T.M., and Robbins, W.P. (2003) *Power Electronics*, 3rd edn, John Wiley & Sons, Inc., New York.
- 12 Champier, D., Favarel, C., Bédécarrats, J.P., Kousksou, T., and Rozis, J.F. (2013) Prototype combined heater/thermoelectric power generator for remote applications. *J. Electron. Mater.*, **42** (7), 1888–1899.
- 13 Bunthern, K., Long, B., Christophe, G., Bruno, D., and Pascal, M. (2014) Modeling and Tuning of MPPT Controllers for a Thermoelectric Generator. in *Proceedings of the First International Conference on Green Energy (ICGE)*.
- 14 Vadstrup, C., Schatzl, E., and Chen, M. (2013) Individual module maximum power point tracking for thermoelectric generator systems. *J. Electron. Mater.*, **42** (7), 2203–2208.
- 15 Man, E., Sera, D., Mathe, L., Schatzl, E., and Rosendahl, L. (2016) Dynamic performance of maximum power point trackers in TEG systems under rapidly changing temperature conditions. *J. Electron. Mater.*, **45** (3), 1309–1315.
- 16 Montecucco, A. and Knox, A.R. (2015) Maximum power point tracking converter based on the open-circuit voltage method for thermoelectric generators. *IEEE Trans. Power Electron.*, **30** (2), 828–839.
- 17 Nagayoshi, H., Maiwa, H., and Kajikawa, T. (2013) Power conditioner with variable switching control for thermoelectric generator systems. *J. Electron. Mater.*, **42** (7), 2282–2286.
- 18 Phillip, N., Maganga, O., Burnham, K.J., Ellis, M.A., Robinson, S., Dunn, J., and Rouaud, C. (2013) Investigation of maximum power point tracking for thermoelectric generators. *J. Electron. Mater.*, **42** (7), 1900–1906.
- 19 Maganga, O., Phillip, N., Burnham, K.J., Montecucco, A., Siviter, J., Knox, A., and Simpson, K. (2014) Hardware implementation of maximum power point tracking for thermoelectric generators. *J. Electron. Mater.*, **43** (6), 2293–2300.
- 20 Wu, H., Sun, K., Chen, M., Chen, Z., and Xing, Y. (2013) Hybrid Centralized-Distributed Power Conditioning System for Thermoelectric Generator with High Energy Efficiency. in *Proceedings of the Energy Conversion Congress and Exposition (ECCE)*.
- 21 Desai, N.V., Ramadass, Y.K., and Chandrakasan, A.P. (2014) A Bipolar  $\pm 40$  MV Self-Starting Boost Converter with Transformer Reuse for Thermoelectric Energy Harvesting. in *Proceedings of the IEEE/ACM International Symposium on Low Power Electronics and Design (ISLPED)*.
- 22 Meli, M. and Dillersberger, H. (2014) Efficiently Harvesting Energy from Temperature Differences in Order to Power Wireless Systems. in *Proceedings of the Wireless Congress*.

- 23 Singh, G. (2013) Solar power generation by PV (photovoltaic) technology: a review. *J. Electron. Mater.*, **53**, 1–13.
- 24 Jeevitha, S., Rajan, S.E., and Rakesh, T. (2014) Performance Analysis of High Gain DC-DC Boost Converter for Thermoelectric Power Generation System. in *Proceedings of the International Conference on Green Computing Communication and Electrical Engineering (ICGCCEE)*.
- 25 Laird, I. and Lu, D.D.C. (2013) Steady State Reliability of Maximum Power Point Tracking Algorithms Used with a Thermoelectric Generator. in *Proceedings of the IEEE International Symposium on Circuits and Systems (ISCAS)*.

# 10

## Thermoelectric Energy Harvesting for Powering Wearable Electronics

*Luca Franciosi and Chiara De Pascali*

CNR-IMM Institute for Microelectronics and Microsystems, Via Monteroni, University Campus, Bld. A/3, 73100 Lecce, Italy

### 10.1 Introduction

The present chapter reports a comprehensive review of thermoelectric generator (TEG) devices modeling, human body heat source physics principles, fabrication methods, and recent research advances with a final overview of the performance enhancement efforts, integration, and exploitation of these power sources in wearable electronics.

### 10.2 Human Body as Heat Source for Wearable TEGs

In humans, the thermoregulatory system reacts to changing intensity of heat production in response to metabolic and muscular activities, as well as to varying temperature conditions of the environment, to maintain the core temperature within a narrow range around 37 °C (homeothermy). It essentially represents the temperature of the blood in circulation in the cranial, thoracic, and abdominal cavities [1]. The metabolic heat of a subject is traditionally measured in Met (1 Met = 58.15 W/m<sup>2</sup>) for body surface: the latter is of the order of 1.7 m<sup>2</sup> for an adult subject. A sleeping person has a metabolism of 0.8 Met (46 W/m<sup>2</sup>); the latter increases to 1.2 Met (70 W/m<sup>2</sup>) for a sitting person working in the office, and up to 9.5 Met (550 W/m<sup>2</sup>) during vigorous efforts [2].

The body heat is transferred, through tissues and blood vessels, to the skin and removed from it into the ambient by conduction, convection, radiation, and evaporation. Conduction heat transfer occurs when part of the body is in contact with solid surfaces in the environment. In the steady state, the heat transfer by conduction is described by the following equation:

$$q_{\text{cond}} = h_k(T_{\text{skin}} - T_{\text{surf}}) \text{ in (W/m}^2\text{)} \quad (10.1)$$

where  $h_k$  represents the conductive heat transfer coefficient, which depends on the surface area of contact and thermal properties of both the skin and the object. In a transient state, the amount of heat transferred to and from the solid in contact with the skin depends on the thermal inertia of the material, given by the product of its thermal conductivity, density, and specific heat. The greater the thermal inertia, the greater the heat transmitted to or removed from the skin is. When the surface area of contact is little (e.g., subject standing) or the thermal inertia of the material is very low, the heat transfer due to conduction represents a small proportion of the total heat balance of the human body. When both the thermal inertia and surface area of contact are large, the heat lost by conduction becomes considerable (e.g., subject lying on cold floor) [3].

The loss of convective heat from the human body is directly proportional to the difference between the mean temperature of the skin and that of the surrounding air:

$$q_{\text{conv}} = h_c(T_{\text{skin}} - T_{\text{air}}) \text{ in } (\text{W/m}^2) \quad (10.2)$$

with  $h_c$  being the convective heat transfer coefficient. Different works were aimed at finding the natural and forced convection heat transfer coefficients of human body, with the purpose of determining the amount of body heat exchanged with the environment by using theoretical and experimental methods applied to heated thermal manikins of different body shapes, size, and complexity of posture, in different microclimatic conditions, velocities, and directions of the surrounding air, typical of indoor and outdoor situations [4–10].

The radiative flux to and from the human body can be expressed as [11]

$$R = f_{\text{cl}}h_r(T_{\text{cl}} - T_r) \text{ in W/m}^2 \quad (10.3)$$

where  $h_r$  is the linear radiative heat transfer coefficient,  $f_{\text{cl}}$  is the ratio of clothed-to-nude body surface area,  $T_{\text{cl}}$  is the mean surface temperature of the clothed body, and  $T_r$  is the mean radiant temperature perceived by the body. The linearized radiative heat transfer coefficient can be calculated by

$$h_r = 4\epsilon k \frac{A_r}{A_D} \left[ 273.2 + \frac{T_{\text{cl}} - T_r}{2} \right]^3 \text{ in W/m}^2/\text{K} \quad (10.4)$$

where  $k = 5.67 \times 10^{-8} \text{ W/m}^2/\text{K}^4$  is the Stefan–Boltzmann constant,  $\epsilon = 0.95$  is the average body surface emissivity,  $A_r$  is the effective radiation area of the human body, and  $A_D$  is the DuBois body surface area. The ratio  $A_r/A_D$  was estimated to be 0.70 for a sitting person and 0.73 for a standing person [12];  $h_r = 4.7 \text{ W/m}^2/\text{K}$  for general purposes in typical indoor temperatures [11]. Interesting results about the estimation of  $h_r$  values for individual body segments were presented in [4, 6].

A wearable TEG is designed to harvest waste body heat through contact with human body skin, which represents the contact surface with the hot junctions of a thermopile. The thermal gradient between the body skin and the surrounding environment is exploited to generate power by Seebeck effect. Under a neutral environmental condition, in which no thermoregulatory action is required to maintain thermal balance, skin temperature typically ranges between about 30 and 34 °C. Numerous factors, including such environmental conditions as temperature, air-flow rate, air pressure and humidity, insulation by clothing,

**Table 10.1** Skin temperature (°C) in neutral, warm, and cold stable conditions.

Body location	Neutral environment	Warm environment	Cold environment
Forehead	35.8	36.5	30.7
Cheek	35.2	36.3	27.7
Front neck	35.8	36.8	33.5
Back neck	35.4	36.1	34.5
Chest	35.1	36.1	31
Back	35.3	36.3	32.5
Abdomen	35.3	36.2	28.7
Upper arm	34.2	36.4	24.7
Lower arm	34.6	36.1	27.3
Hand	34.4	36	23.0
Finger	35.3	36.7	21.0
Thigh	34.3	35.6	27.0
Shin	32.9	34.4	26.5
Calf	32.7	34.1	24.3
Foot	33.3	36.4	21.4
Mean temperature	34.8	35.6	27

Source: Huizenga 2004 [13]. Reproduced with permission of Elsevier.

influence the skin temperature and its spatial distribution on human body. In [13] the authors collected skin temperature distribution by using thermocouples attached on different body locations under neutral, warm, and cold environments (Table 10.1). Human subjects wearing a leotard and cotton socks were exposed to partial and whole-body cooling and heating in a controlled environmental chamber. Under neutral conditions, the mean skin temperature was very stable, with fluctuations within 0.1 °C during the observation period of 2 h. A maximum skin temperature variation of 3 °C was measured between the forehead and the front of the neck (the warmest sites) and the calf (the coolest site). When exposed at warm environment (31.5 °C), an increase of 0.6 °C of mean skin temperature was measured within 80 min of exposure, as a result of the vasodilatation, with a difference of 2.7 °C between the front of the neck and the calf. After cold exposure for 2 h at 15.6 °C, a mean skin temperature reduction of 1 °C was measured, with a wide variation recorded across the body, as result of the vasoconstriction. The neck retains the highest temperature, representing an important source of heat loss under cold exposure conditions.

Interesting results were also obtained by analyzing the skin temperature response to physical activity [14]. Infrared thermography was used to precisely map the cutaneous temperature distribution and its evolution during running exercise under controlled environmental conditions of temperature and humidity. The thermographic investigation revealed a not uniform reduction of the mean skin temperature during the early phase of exercise, probably due to

the cutaneous vasoconstrictor response to exercise. Such reduction is observed for the entire duration of the performance, for athletes subjected to a running exercise of increasing load intensity. Instead, during a constant load exercise, after a relative minimum, a slight increase of the mean skin temperature appeared and such result was correlated to the net result of the competition between the vasoconstrictor response, which is present for the entire duration of the exercise, and the vasodilator response, opposite to the former and induced by the increasing body temperature. However, the skin temperature during the exercise varies in different ways on different body sites, being more pronounced for peripheral zones less involved in running, such as upper limbs, and more moderate in the proximity of working muscles, such as calves. Experiments demonstrated that the skin temperature of upper limbs decreases by 2.5 and 3.75 °C after 30 min of running exercise, at constant and graded load intensity, respectively. Instead, skin temperature over calves decreases by about 1.5 °C, for both types of exercises.

### 10.3 TEG Design for Wearable Applications: Thermal and Electrical Considerations

Depending on the direction of the heat flow through the thermocouples and the orientation of the substrate surface, two main design approaches can be used to build a thermopile: a transversal (cross-plane) or a lateral (in-plane) configuration. The cross-plane configuration is typical of macro bulk thermoelectric module (TEM) or micro-TEM constituted of vertical pillar-type thermocouples connected electrically in series and thermally in parallel [15, 16]; the heat flows perpendicularly to the substrate and the hot and cold thermocouple junctions are placed on separate planes. In the in-plane configuration, the heat flows parallel to the substrate, which contains both the hot and cold junctions of thermocouples. To maximize the temperature drop on the thermocouple junctions, from which the thermoelectric power generation is also dependent, starting from small thermal gradients that are typically achievable for wearable applications, wearable TEMs are mostly based on a vertical configuration. However, the literature reports numerous examples of wearable planar TEMs, in which an optimized package was designed to maximize the thermal gradient between junctions [17–20].

Francioso *et al.* fabricated a flexible planar TEM with wavy-shaped poly-dimethylsiloxane (PDMS)/Kapton assembled package, with sputtering-deposited thin films as active p-type and n-type thermocouples (Figure 10.1) [22–24]. Thermal and electrical matching are required to extract the maximum power from the thermoelectric device. In the electrical domain, the maximum power across the load can be obtained, in matched load condition, by optimizing both the thermoelectric properties of materials and the design of the thermopile. Materials optimization is aimed at obtaining a high figure of merit,  $ZT$ , which depends on the Seebeck coefficient,  $S$ , electrical conductivity,  $\sigma$ , and thermal conductivity,  $\lambda$ , and is given by

$$ZT = \frac{S^2\sigma}{\lambda} T \quad (10.5)$$

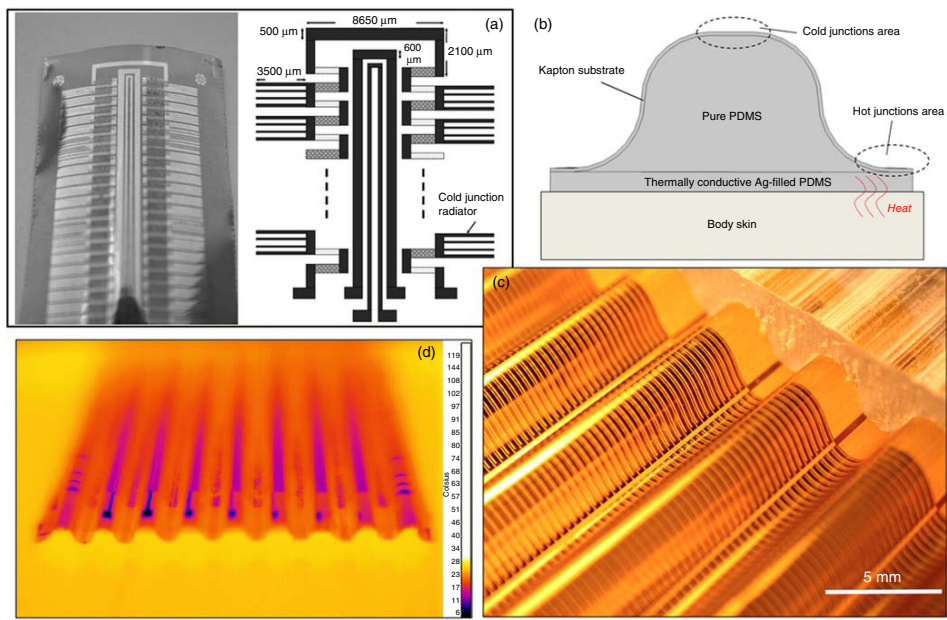


**Figure 10.1** (a) Digital photo and schematic of flexible planar TEM reported in [21]. (b) Schematic, (c) digital photo, and (d) thermal image of 3D-flexible planar TEM with wavy-shaped PDMS/Kapton assembled package, discussed in [22–24].

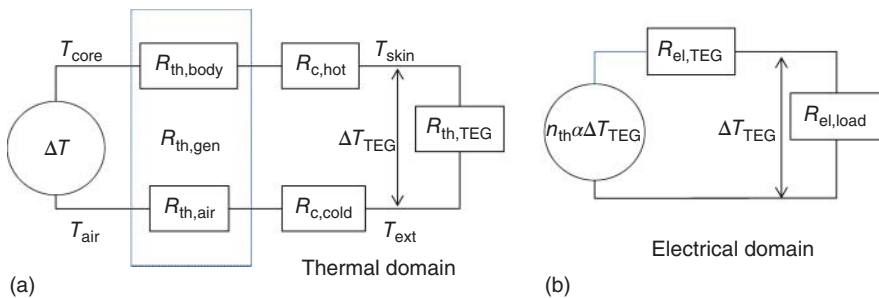


**Figure 10.2** Thermal (a) and electrical equivalent circuits (b) of a thermoelectric module in contact with the human skin.

In addition to the materials optimization, the design of the thermopile, with the dimensioning of the legs and of the number of thermocouples forming the module,  $n_{\text{th}}$ , directly contributes to determining the output voltage on the load ( $V_{\text{load}}$ ) by the generated open circuit voltage division between the internal electrical resistance of the TEG,  $R_{\text{el},\text{TEG}}$ , and the load resistance,  $R_{\text{el},\text{load}}$ :

$$V_{\text{load}} = \frac{R_{\text{el},\text{load}}}{R_{\text{el},\text{load}} + R_{\text{el},\text{TEG}}} n_{\text{th}} S \Delta T_{\text{TEG}} \quad (10.6)$$

The coupling to the thermal domain occurs through the temperature difference  $\Delta T_{\text{TEG}}$  between the hot and cold thermocouple junctions. The thermal and electrical equivalent circuits of a TEM in contact with the human skin are shown in Figure 10.2.

The thermal resistances included into the thermal circuit are representative of the human body ( $R_{\text{th},\text{body}}$ ), body/TEG contact interface ( $R_{\text{c},\text{hot}}$ ), TEG ( $R_{\text{th},\text{TEG}}$ ), TEG/air contact interface ( $R_{\text{c},\text{cold}}$ ), and surrounding air ( $R_{\text{th},\text{air}}$ ). The heat flow from the human body to the environment is a function of the temperature difference  $\Delta T$  between the body core  $T_{\text{core}}$  and environment  $T_{\text{air}}$  and the equivalent series thermal resistance of the circuit. Two different and more interesting design approaches for a micro-thermoelectric device were proposed in [15, 25].

Leonov exhaustively discussed the thermal design of a wearable TEG by defining the conditions that enable reaching maximum power, starting from the heat generated by the human body. Owing to the high thermal resistance of the ambient air and human body, the heat flow that can be transferred to the TEG is quite limited. Although depending on the body location and surrounding conditions, the average heat flow observed on human open skin under typical indoor conditions is in the range 1–10 m W/cm<sup>2</sup>, but it decreases to 4–5 m W/cm<sup>2</sup> in the case of skin areas covered by clothes [25]. To maximize the generated power, the TEG thermal resistance has to be of the order of those of the body and air. Assuming that the thermal resistance of interfaces is negligible, the gradient  $\Delta T_{\text{TEG}}$  between the junctions of the TEG as a function of  $\Delta T$  is given by

$$\Delta T_{\text{TEG}} = \frac{R_{\text{th},\text{TEG}}}{R_{\text{th},\text{TEG}} + R_{\text{th},\text{body}} + R_{\text{th},\text{air}}} \Delta T \quad (10.7)$$

The interesting aspect that emerged from Leonov's discussion is related to the separation of  $R_{\text{th,TEG}}$  into two components, which takes into account the thermal resistance of the thermopile,  $R_{\text{tp}}$ , and that of the encapsulation structure containing the thermopile,  $R_{\text{par}}$ , on which a certain amount of heat is inevitably dissipated. As shown in [25], the optimal temperature drop on the TEG depends on the thermal design of the "empty" TEG (without thermoelectric materials, and with the approximation  $R_{\text{empty-TEG}} \approx R_{\text{par}}$ ) and its interfaces on the cold and hot sides, but not on the thermoelectric properties of the p- and n-materials. Then, the maximum power generated by an optimized TEG is [25]

$$P_{\max} = \frac{Z \Delta T_{\text{tp,opt}}^2}{16(R_{\text{th,body}} + R_{\text{th,air}}) \left( 1 + \frac{R_{\text{th,body}} + R_{\text{th,air}}}{R_{\text{par}}} \right)} \quad (10.8)$$

where  $Z$  is the thermoelectric figure of merit and the optimal thermal gradient on the thermopile,  $\Delta T_{\text{tp,opt}}$ , is a function of the thermal resistance of the body, air, and encapsulation structure:

$$\Delta T_{\text{tp,opt}} = \frac{\Delta T}{2 \left( 1 + \frac{R_{\text{th,body}} + R_{\text{th,air}}}{R_{\text{par}}} \right)} \quad (10.9)$$

As opposed to Leonov's work, that of Glatz *et al.* [15] is not strictly oriented to a wearable application, but it discusses the optimal design of a micro-TEG focusing the attention on the importance of increasing the internal resistance of the TEG and minimizing the contact resistance of interfaces. The proposed design was performed by assuming that the TEG is connected to a hot and a cold reservoir via thermal contact resistances  $R_{c,\text{hot}}$  and  $R_{c,\text{cold}}$ . The thermal gradient  $\Delta T_{\text{TEG}}$  was expressed as a function of the temperature difference  $\Delta T$  between the hot and cold reservoir,  $K_C$ ,  $K_H$ , and  $K_G$ , which is the internal thermal resistance of the TEG:

$$\Delta T_{\text{TEG}} = \frac{K_G}{K_G + K_H + K_C} \Delta T \quad (10.10)$$

Assuming that both thermolegs do not vary in length,  $l$ , and cross-sectional area,  $A_o$ , the above equation can be rewritten as:

$$\Delta T_{\text{TEG}} = \frac{l(1 + A_V)}{l(1 + A_V) + \lambda_m(k_C + k_H)} \Delta T \quad (10.11)$$

where  $A_V = A_i/A_o$  is the ratio of the insulating to the active area. As shown in [15] the power per area is given by:

$$\frac{P}{A_G \Delta T^2} = \frac{S^2 \sigma}{16} \frac{l(1 + A_V)}{[l(1 + A_V) + \lambda_m(k_C + k_H)]^2} \quad (10.12)$$

It depends on the material properties ( $S, \lambda, \sigma$ ), the geometric design parameters ( $l$  and  $A_V$ ), and the thermal contact resistances per area of interface with the cold and hot sides of the TEG. Two interesting conclusions emerged through the discussion of Glatz: the first one is that the number of thermocouples and the cross-sectional area of the thermolegs determine the generated voltage and

current at the output of the TEG, but they do not influence the generated power per area; the second one is that the generated power is initially increasing with the length of the legs, and then it reaches a maximum, after which the negative effect of the internal electrical resistance of the TEG becomes dominant and causes the power reduction. However, the optimal leg length is independent of the thermoelectric properties of the materials,  $S$  and  $\sigma$ .

## 10.4 Flexible TEGs: Deposition Methods and Thermal Flow Design Approach

The increasing number of wearable sensors and devices rouses the need for miniaturized power sources characterized by lightness, high power density, and cheapness; during the last years the renewed interest in environmentally available power harvesting has led to an extensive research on the TEGs devices. Key mandatory requirements for wearable generator are reduced physical dimensions and flexibility of the substrate for comfortable clothes integration, which implies also the possibility for the deposited active materials to be able to withstand mechanical bending and to conform to nonplanar surfaces. The wearable TEG typically exploits the heat flow based on the temperature gradient between the human body and the environment air mass to generate a small voltage dominated by the so-called *Seebeck effect*. State-of-the-art TEGs exploit a cross-plane temperature gradient coupling, which requires a vertical thermocouples assembly approach during the fabrication process. About the bending properties of devices, the preferred kinds of active thermoelectric junctions are screen-printable pastes or slurries printed onto a flexible sheet or dispensed into predefined molds (PDMS, polyethylene naphthalate (PEN), polyethylene terephthalate (PET) polyimide).

In the near room temperature range typical of wearable applications, the bismuth/tellurium-based inorganic materials remain the state-of-the-art thermoelectrics with highest  $ZT$  values. The highest  $ZT$  values were reported for epitaxial,  $Sb_2Te_3/Bi_2Te_3$  based multilayers [26] and PbTeSe quantum dot superlattices [27], with  $ZT = 2.4$  at 300 K and  $ZT = 3.4$  at 575 K, respectively.

Recently, in order to allow the production of application-ready devices with high thermolegs aspect ratio, research activity has been oriented toward the production of nanocomposites with an enhanced interface-to-volume ratio and lower thermal conductivity by means of high pressure/high temperature techniques, such as ball milling, hot pressing, mechanical alloying, melt spinning nanoparticle, synthesis from gas phase, and spark plasma sintering. These methods allowed an efficiency increase by 40–75% compared to bulk thermoelectric materials [28].

### 10.4.1 Deposition Methods

The choice of the best deposition techniques for wearable TEGs must fulfill the requirement of thermoelectric junction fabrication able to produce a low generator internal resistance, high power density (e.g., vertical/vertical approach, see Section 10.4.2), and heat sink-less operation when possible. Reported below are the most used deposition techniques for wearable TEGs.

#### 10.4.1.1 Screen Printing

The screen-printing technique is characterized by a large variety of compatible substrates (plastics and textiles) and pastes suitable for large area production; it is relatively cheap, simple to implement, and allows also multilayer patterns alignment. The main advantages are related to good resolution (down to 20–50 µm for thicker film), high production rate, and complete devices fabrication without photolithographic steps. A key aspect of this technique is the preparation of pastes or powder suspensions; about Bi/Te/Sb based materials, the low melting point of these materials allows the milling of powders with single pure elements, while alloy formation is performed during the thermal treatment after deposition (typically in the presence of additional tellurium to optimize the stoichiometry) [29–32]. Suemori *et al.* [33] realized a flexible TEG on a polyethylene naphthalate film substrate using a printing process. The adopted material was a composite made by carbon nanotubes and polystyrene, containing approximately 35 vol.% of voids.

#### 10.4.1.2 Inkjet Printing

Inkjet printing is a direct-writing technique, which has the advantages of being maskless and being able to perform high precision localized deposition, thanks to precise computerized control of stage and nozzle parameters. Limitations of such technique are related to well-defined viscosity ranges for materials dispensing and thinner structures obtained with single step deposition.

Typical examples of application of inkjet to thermoelectric devices were reported in [30, 34, 35], in which 120 µm thick thermoelectric legs made by n-type Bi<sub>2</sub>Te<sub>3</sub> particles with epoxy resin addition were printed onto flexible substrates to fabricate a 62 single leg device with maximum output power of 25 µW at 20 K of thermal gradient. Owing to the limited thickness of deposited films, this technique is preferred when an in-plane temperature difference is available, or when vertical/lateral assembly approach is adopted (see Section 10.4.2). Otego [36], a German company, developed a proprietary roll-to-roll printing with organic semiconductors active materials, folded with a proprietary process to produce a cheap box-like thermoelectric generator.

#### 10.4.1.3 Molding

The molding technique makes use of a pre-fabricated mold of SU-8, micromilled ceramics or PDMS filled with thermoelectric active materials; recently, this technique has been largely investigated because of its capability to match well with wearable applications where the vertical temperature gradient approach is mandatory. The fabrication of mold can be performed by optical lithography or pouring template precursors in a microdrilled or CNC micromilled fabricated stamp. Bubnova *et al.* realized cavities in an SU-8 50 photoresist by photolithography technique, and then thermoelectric materials were dispensed into the mold openings by inkjet printing technique [37]. With a similar approach Kouma *et al.* fabricated a high-output-voltage micro-TEG made by thermocouples with an aspect ratio of 3.5 using a novel and simple fabrication method, in which thermoelectric nanopowders were filled in a photosensitive glass mold by using

aerosol deposition. Subsequent hot isostatic pressing was applied to improve the thermoelectric property [38].

#### 10.4.1.4 Lithography

The main advantages of lithography-based techniques for TEGs are the highest resolution for thermocouples integration, definition, and compatibility with most fabrication tools used for MEMS and CMOS processes. Huesgen *et al.* fabricated a multipurpose thermoelectric generator in a combined surface and bulk micromachining process, with n-doped poly-Si and Al as active materials. The thermocouples were deposited by thin-film processes with high integration density on the wafer surface; the heat flow path was perpendicular to the chip surface and guided by thermal connectors [39]. One side of the thermocouple junction was thermally connected to the heat source and thermally insulated to the heat sink by a cavity fabricated in the wafer substrate. Wang *et al.* realized a wearable miniaturized TEG specifically engineered for human body applications based on a surface micromachined poly-SiGe thermopile. Being worn on human body, the wearable TEG delivers an open-circuit output voltage of about 0.15 V and an output power of about 0.3 nW on a matched external load [40]. A more recent device from the same author was fabricated with a membraneless approach and KOH bulk micromachined in-plane thermopile made of poly-Si or poly-SiGe. The declared open-circuit output voltage was about 95.0 mV/K, with corresponding output power on a matched load of 2.34 nW/K<sup>2</sup> [41]. Sevilla *et al.* fabricated a flexible and semi-transparent thermoelectric energy harvester on bulk monocrystalline silicon (1 0 0) wafers; the upper silicon layer is then released with final thickness of 18  $\mu\text{m}$ , reducing the thermal loss significantly and generating nearly 30% more output power [42].

#### 10.4.1.5 Vacuum Deposition Techniques

The vacuum deposition techniques used for TEGs are different and the desirable features are strict film growth control and doping, high production yield, and high purity of precursors/sources. Reported below are the main characteristics of most used vacuum deposition-based techniques.

#### 10.4.1.6 Thermal Evaporation

Thermal evaporation is a physical vapor deposition (PVD) technique using joule-effect-heated material sources [43]; the source materials are vaporized and reach the target substrate with rare collisions with the gas molecules inside the evaporation chamber. Vacuum deposition with a pressure range between  $10^{-6}$  and  $10^{-8}$  mbar or lower limits the inclusion of impurities into the growing film. The composition of the deposited film is proportional to the relative vapor pressure of the solid or liquid material in the source. About thermal evaporation of Bi, Sb, and Te melting points are 544.7, 903.8, and 722.7 K respectively [44]. It also summarizes the temperatures for a given vapor pressure of these elements. Antimony has a vapor pressure of  $10^{-2}$  torr at temperatures below its melting point and is thus transformed to vapor by sublimation. The advantage of Sb sublimation is that the material will not melt and overflow out

of the crucible while heating the source, although control of the evaporation rate is difficult owing to its atom-cluster vaporization. Also, vaporizing the alloy produces a gradient in the deposited thin film owing to vapor pressure differences of Bi, Sb, and Te elements [45]. The effect of thermal annealing is crucial in thermally evaporated materials; Lin *et al.* investigated the influence of thermal annealing on the microstructures and thermoelectric properties of  $\text{Bi}_2\text{Te}_3$  thin films in the temperature range 100–250 °C. Experimental results showed that both the Seebeck coefficient and power factor were enhanced as the annealing temperature increased. Annealing at 250 °C for 30 min brought the Seebeck coefficient and power factor of n-type  $\text{Bi}_2\text{Te}_3$ -based thin films to about  $-132.02 \mu\text{V/K}$  and  $6.05 \mu\text{W/cm/K}^2$ , respectively [46].

#### 10.4.1.7 Sputtering

The sputtering deposition tool is widely used for wearable thermoelectric devices, and together with screen printing process, it is among the industry-preferred methods for fabrication of devices ready to go or already present on the market to the best of our knowledge [47]. The deposition of sputtered thin films is well documented in the scientific community and represents a very powerful method to precisely control the material stoichiometry and subsequent affected power factor [48]. Franciosi *et al.* realized through RF sputtering tool a complete thermoelectric generator with a Kapton/PDMS assembly able to incorporate a thin film fabricated TEG with a 3D PDMS package for wearable applications [24, 49].

#### 10.4.1.8 Molecular Beam Epitaxy (MBE)

Molecular beam epitaxy (MBE) is an ultra-high vacuum deposition method to deposit single crystals films and multilayers by means of one or several molecular or atomic beams interactions on the surface of a heated crystalline substrate. The MBE technique is characterized by a slow deposition rate (typically less than 1  $\mu\text{m/h}$ ) to allow the films to grow as an epitaxial layer. MBE systems are carefully designed to guarantee very high purity during the deposition, by means of high-vacuum chambers with pressure levels down to  $10^{-10}$  torr. Sources of pure constituent elements are evaporated or sublimated from effusion cells isolated from the substrate by molybdenum and tantalum shutters.  $\text{Bi}_2\text{Te}_3$  has been deposited by molecular beam epitaxy with a Seebeck coefficient of  $180 \mu\text{V/K}$  [50], and  $(\text{BiSb})_2\text{Te}_3$  has been reported with a Seebeck coefficient of  $184 \mu\text{V/K}$  and a power factor of  $1.6 \text{ mW/m/K}^2$  [51]. About thermoelectric V–VI based materials, Zhang *et al.* demonstrated that bismuth telluride is a 3D topological insulator, characterized by bulk material bandgap and gapless electronic surface states that are protected by time-reversal symmetry [52–54]. These surface states show a linear energy dispersion such as the relativistic particles; therefore surface carriers of topological insulators have special properties, such as extremely high mobilities or dissipationless spin-locked transport [55, 56]. Krumrain *et al.* investigated the growth of the topological insulator  $\text{Bi}_2\text{Te}_3$  on Si(1 1 1) substrates by means of MBE. Angular-resolved photoelectron spectroscopy revealed a linear energy dispersion of charge carriers at the surface, confirming the topologically insulating properties of the  $\text{Bi}_2\text{Te}_3$  epilayers [57].

#### 10.4.1.9 Metal Organic Chemical Vapor Deposition (MOCVD)

Metal–organic chemical vapor deposition (MOCVD) is a CVD method of materials epitaxial growth dominated by the surface chemical reaction of organic compounds or metalorganics and metal hydrides containing the elements of interest. The growth of the epitaxial layer is driven by pyrolysis of the chemicals precursors at the substrate surface and takes place at pressure between  $10^{-2}$  torr and 1 atm. MOCVD of thermoelectric materials and alloys has been investigated using precursors of trimethylbismuth, triethylantimony, diethyltellurium, and diethylselenium. High-quality n-type and p-type materials have been grown using the MOCVD tool. An important published result on  $\text{Bi}_2\text{Te}_3/\text{Sb}_2\text{Te}_3$  superlattice research used MOCVD to growth p-type material with a  $ZT$  of 2.4, and n-type material with a  $ZT$  of 1.4 [26], even if confirmation through independent measurements is still missing. State-of-the-art thermoelectric properties were achieved in the direction perpendicular to the layers of the superlattice.

#### 10.4.1.10 Electrochemical Deposition

Electrochemical deposition (ECD) of thin/thick thermoelectric films is a cheap alternative to previously listed methods because of its simplicity, low cost, and room temperature operation. Deposited materials may be different in terms of composition, deposition rates, alloys composition, and materials morphology.

From the point of view of thermoelectric-active materials growth, the main desirable features are the cheap setup and the possibility to deposit at rates of several tens of microns per hour. Different papers reported the ECD growth of n-type  $\text{Bi}_2\text{Te}_3$ , p-type  $\text{Bi}_{2-x}\text{Sb}_x\text{Te}_3$  and  $\text{Sb}_x\text{Te}_y$  compounds deposited at room temperature at a constant potential in a standard three-electrode configuration [58, 59].

Glatz *et al.* fabricated a low-cost generator prototype by the ECD technique; the thermoelectric materials were grown into a polymer mold. The fabricated devices generated up to  $2.6 \text{ nW/cm}^2/\text{K}^2$  for devices with NiCu thermocouples and up to  $0.29 \mu\text{W/cm}^2/\text{K}^2$  for  $\text{Bi}_2\text{Te}_3$ -based generators in planar state [60].

Recently Pelz *et al.* developed a fabrication process for an electrochemically deposited thermoelectric generator with two selectively dissolvable photoresists and galvanostatic electrodeposition. The novelties of the process are the usage of a multilamination technique to create legs and contacts structures and an industrial pick and placer, which allows dispensing of a selectively dissolvable photoresist to selectively define the deposition area of second-level materials [61].

#### 10.4.1.11 Vapor–Liquid–Solid (VLS) Growth

The interest in quantum confinement effects in V–VI nanowires (NWs) compounds, mainly related to the enhancement of thermoelectric properties and power factor, brought the scientific community to investigate different methods for synthesizing bismuth telluride NWs. Different papers reported the template-assisted electrodeposition, the synthesis by chemical routes, and also the metal-catalyst-assisted vapor–liquid–solid (VLS) growth technique [62–66].

The VLS mechanism is a well-known crystal growth mechanism that is assisted by a metal catalyst. The technique allows the 1D growth of NMs, whiskers, and

nano/microrods. The 1D crystal growth was developed about 50 years ago in the silicon industry and the mechanism was suggested for wider use by Wagner in 1964 [67]. In this mechanism, the metal catalyst deposited on the substrate forms liquid alloy droplets at a high temperature by incorporation of element vapors. Owing to temperature or vapor pressure fluctuation, the alloy becomes supersaturated, so the concentration of the components on the metal droplet is higher than the equilibrium concentration. At this point, the precipitation of the component at the liquid–solid interface happens in order to achieve minimum free energy of the system. The growth of bismuth telluride nanorods and nanobelts by VLS has been reported by Wang *et al.* [68] and by Wei *et al.* [69].

#### 10.4.2 Heat Flow Direction Design Approach in Wearable TEG

The design of a thermoelectric generator requires in general electrical and thermal optimization to enhance its generation properties when the working environment is related to the human body or other thermal sources close to room temperature. Hence, with regard to the choice of the deposition techniques reported above and the design of the generators, the identification of better thermocouples packaging and heat flow distribution is of crucial importance. About the microfabricated TEGs, they are classified according to the heat flow direction through the device and the approach related to the layout of the thermocouples during fabrication.

The following types of configurations may be found in the published literature, with reference to the design approach of a thermoelectric generator:

- 1) Devices with a lateral temperature gradient and planar fabricated junctions (lateral/planar approach).

These kind of devices are characterized by a limited contact area to available thermal flow surface and a limited thermal insulation of suspended region over the heated surfaces.

- 2) Devices with a vertical temperature gradient and planar fabricated junctions (vertical/planar approach).

These generators require an additional packaging step to assemble the planar fabricated junctions array in a vertical thermal flow adapted geometry. A typical example of vertical/planar approach is reported in [70, 71].

- 3) Devices with a diagonal temperature gradient and planar fabricated junctions (diagonal/planar approach).

Present approach makes use of a combination of high and low thermal conductivity material for the substrate, in order to generate a diagonal substrate temperature difference, reflected as a linear gradient in the embedded thermoelectric material couples [72].

- 4) Devices with a vertical temperature gradient and vertical planar fabricated junctions (vertical/vertical approach).

The vertical/vertical approach is the most common design method, largely adopted by the industry for Peltier coolers and bulk/thick film TEGs.

## 10.5 TEG Integration in Wearable Devices

In the last years, the growing interest in wearable electronic devices motivated the development of new materials and microfabrication technologies for the realization of smart functional clothing, with the integration of ultra-low power consumption sensors, actuators, and circuits into the textile. The main challenges are represented by the difficulty in realizing flexible and performing devices that can be rolled, bent, or folded without losing functionality. To this end, efforts are also devoted to the development of low-cost flexible encapsulation for enhancing the lifetime of these wearable devices, protecting them accordingly to ensure reliable performance during use.

To obtain full exploitation in practical implementations, wearable electronics also requires the adoption of new solutions for harvesting and storing energy for the devices power supply. Energy harvesting of thermal, mechanical, and solar energy sources available to a garment is an emerging technology that is able to potentially become a good alternative to batteries, because it is a flexible, light weight and self-renewing technology.

In the following, the discussion will be focused on thermal energy harvesting. In literature, numerous works discussed the optimal design and fabrication of TEGs for wearable applications, but few results were published about truly ready-to-use wearable solutions. In [73] promising results on thermoelectric polymer-coated commercial fabric were discussed, which represent a starting point for the development of flexible, air-permeable, wearable, fabric-based TEGs. A thermopile was realized on a substrate of commercial fabric by connecting in series thin strips of poly(3,4-ethylenedioxythiophene):poly(styrenesulfonate) (PEDOT:PSS) coated polyester fabric.

Silver wires were used as conductive connections, and silver paint was applied to the contact regions between the wire and the strip to reduce the contact resistance (Figure 10.3). Electrical measurements of electrical conductivity and Seebeck coefficient versus temperature confirmed the p-type nature of the semiconductor. A fabric TEG consisting of 5 PEDOT:PSS coated strips generated an output voltage of 4.30 mV at a thermal gradient of 75.2 K, with a maximum power of 12.29 nW, in matched load conditions. These results are interesting, but the proposed solution is still far from being ready for direct application in wearable context, in which the available temperature difference for the Seebeck generation is limited to a few degrees.

In [74] a wireless two-channel electroencephalography (EEG) system fully powered by a TEG was presented. The TEG, composed of 10 sections having a total hot plates area of  $64 \text{ cm}^2$  in contact with the skin surface, was designed to operate in typical indoor conditions, with room temperature ranging between 21 and 26 °C. The generator placed on the head of the patient, produced about  $30 \mu\text{W/cm}^2$ , at room temperature of 23 °C. In [75] the above system was improved and integrated in an office-style shirt (Figure 10.4). By spreading 17 small TEG modules having a thickness of 6.5 mm over the T-shirt, a power within the 0.8–1 mW range was harvested during sedentary activities in the office, increasing up to about 3 mW during walking activity in indoor environment, owing to the forced convection.

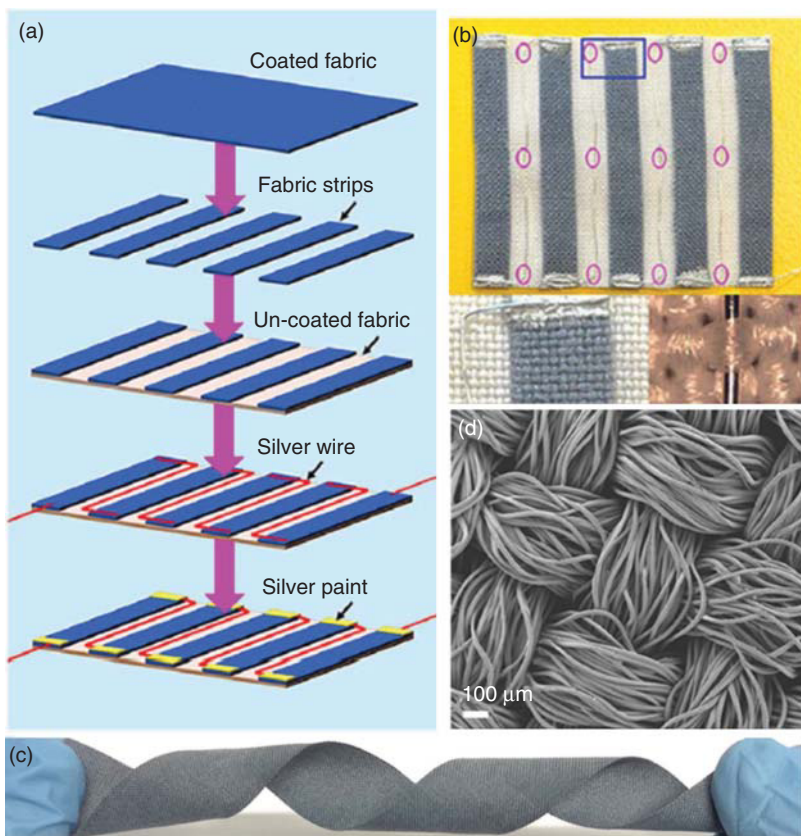


**Figure 10.3** (a) Procedure used in [73] for preparing an air-permeable, fabric-based TEG. (b) Photo of the positive face of the TEG device. (c) Digital photo and (d) SEM image of polyester fabric after PEDOT:PSS coating treatment. (Du *et al.* 2015 [73]. Reproduced with permission of Nature Publishing Group.)

In [76] the same authors evaluated the impact of the textile on the harvested power by a TEG, for different ways of integration in a T-shirt: the TEG realized by sandwiching a thermopile between two aluminum heat spreading plates was placed under the shirt in contact with the body skin. Experiments showed that the textile in contact with the cold plate of the device improves the heat spreading around the radiator, increasing the effective area of thermal exchange, as the heat conduction is greater along the cotton fibers yarn than across the textile. A more comfortable TEG integration in garments was obtained by using flexible carbon fabric-based spreading layers glued on the inner T-shirt side, with an improvement of the power generation of 30% compared with rigid aluminum plates. Results showed that textile can be used as an effective fabric radiator. In the final version proposed for integration in clothing, the device was hidden between two cotton layers, in order to be completely invisible, comfortable for users and easily handled during washing and ironing. Franciosio *et al.* realized also a prototype integrating an array of 100 thin films thermocouples of  $\text{Sb}_2\text{Te}_3$  and  $\text{Bi}_2\text{Te}_3$ ,

with an open circuit output voltage of 430 mV at 40 °C and an electrical output power up to 32 nW with matched load [77, 78]. Veri *et al.* also designed and realized a fully electrical DC–DC ASIC converter designed for TEG for energy harvesting applications coupled with a thick screen-printed generator with very high efficiency [79–82].

Kim *et al.* [83] optimized the fabrication process of screen-printed  $\text{Bi}_2\text{Te}_3$  and  $\text{Sb}_2\text{Te}_3$  thick films on a glass fabric. As a result, an array of 196 thermoelectric p–n dots were printed and well arranged on a glass fabric (Figure 10.5b). A band-type flexible glass fabric TEG with 11 couples of  $\text{Bi}_2\text{Te}_3$  and  $\text{Sb}_2\text{Te}_3$  500 µm thick-films was also fabricated (Figure 10.5a) and applied to human skin, generating an open-circuit output voltage of 2.9 mV, with a harvested output power of 3 µW on matched load at an air temperature of 15 °C.

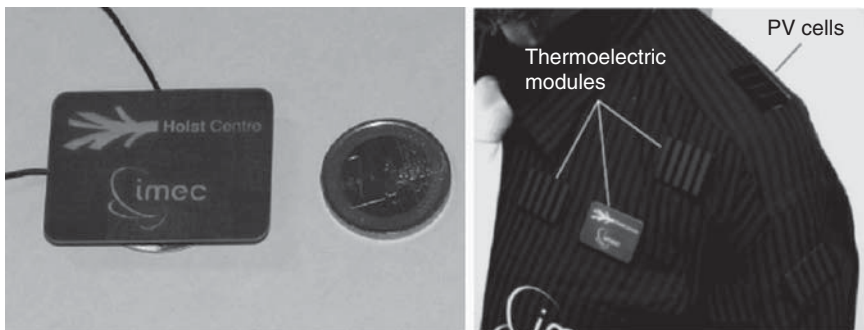


**Figure 10.4** TEG developed by [75] and its integration in an electrocardiography shirt. Different TEGs are painted like chameleon for invisibility; only one has a different color to give an idea about its size. (Reproduced with kind permission of Dr Vladimir Leonov/IMEC/Holst Center.)

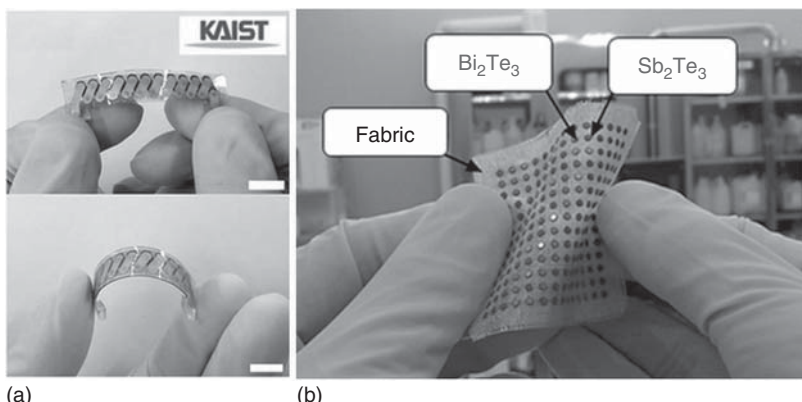


**Figure 10.5** (a) Band-type flexible TEG for harvesting thermal energy from human skin. (b) Photo of 196  $\text{Bi}_2\text{Te}_3$  and  $\text{Sb}_2\text{Te}_3$  dots on a glass fabric of 40 mm × 40 mm [83]. (Kim *et al.* 2014 [83]. Reproduced with permission of Royal Society of Chemistry.)

## 10.6 Strategies for Performance Enhancements and Organic Materials

The present section will review the emerging technologies and methods aimed at advancing to new state-of-the-art thermoelectric knowledge and new materials applications and reports the power factor enhancement trends devoted to or compatible with low temperature applications, such as the wearable generators. With regard to the materials optimization methods, the electrical conductivity, the Seebeck coefficient, and thermal conductivity are not independent, so it is difficult to optimize a single parameter without making the other ones worse. In order to overcome these limitations, the newest efforts are oriented toward: (i) power factor ( $P = S^2\sigma$ ) enhancement of both organic and inorganic materials by quantum size transport effects and (ii) new materials development (mainly on n-type polymers) about the organic semiconductor.

The pioneering work of Hicks and Dresselhaus [84] opened the discussion and research about quantum size effects and nanoscale advantages in thermoelectric materials, while the current strategies about the inorganic materials are dealing with different methods to improve the performance of well-known thermoelectric semiconductors, by means of exploitation of quantum size transport effects, nanoscale/microscale composite matrices, and band engineering.

It is widely accepted that the optimization of thermoelectrics materials presenting the following physical properties are highly desirable:

- High mobility
- High density of state effective mass
- Enhanced phonon scattering
- Low lattice thermal conductivity
- Low carrier inertial mass at given carrier concentration
- Large number of degenerate conducting bands.

With respect to the band engineering methods and technologies to increase the Seebeck coefficient, a review of the three most promising techniques are reported, in particular the *Electronic Resonance States* by distortions of the electronic density of states (DOS), the *Modulation Doping*, and the *Energy Filtering*. Published results of the scientific community about the thermal conductivity reduction and phonon scattering approach strategies are intentionally not reported here, even if their importance is undeniable.

The *Electronic Resonance States* approach exploits the effect of a dopant element inducing energy levels in excess of DOS near the Fermi level and contributes to an enhanced thermopower; this effect is a band structure property independent of the temperature. Friedel [85] introduced the concept of an impurity-induced resonant state described as a bound state with a positive energy with respect to the band edge, with similar energy as an extended state.

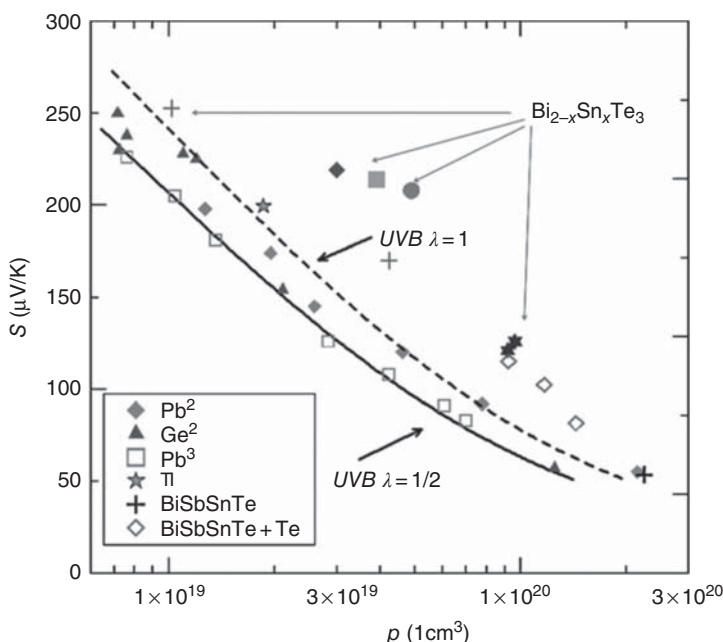
In order to better understand the effect of the distortion of the electronic DOS, the equation of the figure of merit for thermoelectrics can be written as [86]

$$ZT = \frac{S^2\sigma}{\lambda} T = (S^2n) \left( \frac{\mu}{\lambda} \right) qT$$

where  $S$  is the Seebeck coefficient,  $\sigma$  and  $\lambda$  are the electrical and thermal conductivities, and  $\mu$  is the carrier mobility. Big efforts have been devoted to increase the  $\mu/\lambda$  ratio, but this approach has a theoretical limitation because of the fact that the thermal conductivity has a lower limit, the so-called *amorphous limit*, where the phonon mean free path equals the atomic distance [87, 88]. A second way to increase the figure of merit is to modulate the term ( $S^2n$ ) directly related to the power factor  $P=S^2\sigma$  by engineering distortions of the electronic DOS near the Fermi level, as described earlier.

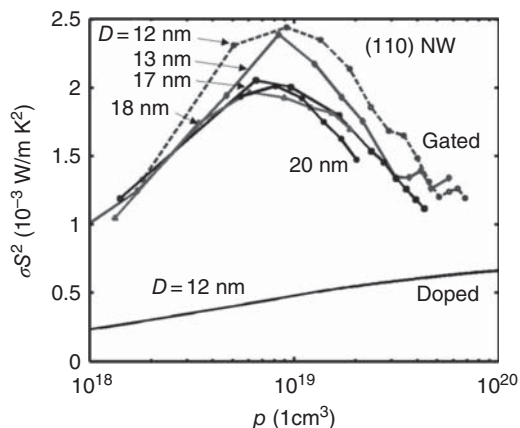
Jaworski *et al.* demonstrated that in  $\text{Bi}_2\text{Te}_3$  semiconductor the Sn doping element provides an excess DOS about 15 meV below the valence band edge; this modification of DOS enhances the Seebeck factor at room temperature [89]. However, the resonant state effect decreases at high temperatures, so it is a good candidate for low temperature applications.

Figure 10.6 shows the thermopower data for Pb- and Ge-doped  $\text{Bi}_{2-x}\text{Sn}_x\text{Te}_3$  samples at 300 K; the measured data showed an enhanced thermopower above the standard Pisarenko relation, confirming the effect of a resonant level [86]. The sample with  $x=0.015$  has double the Seebeck coefficient of similarly doped samples without Sn. The power factor of such samples is also enhanced above the values (solid and dashed lines) calculated using a classical parabolic band with the effective mass for the upper valence bands (UVB). The data points are obtained for the different acceptor impurities as marked in the figure.



**Figure 10.6** Pisarenko relation at 300 K for p-type  $\text{Bi}_2\text{Te}_3$  doped with different acceptor impurities; tin-doped samples showed enhanced Seebeck factor. (Heremans *et al.* 2012 [86]. Reproduced with permission of Royal Society of Chemistry.)

**Figure 10.7** Thermoelectric power factor of doped and gated [110] NWs with different diameters versus carrier density.



The *Modulation Doping*, realized by field effect electrostatic modulation, represents a convenient tool to control the carrier concentration in nanostructures such as silicon NMs because of its capability to decrease ionized impurity scattering. The methodology related to field effect transistor (FET) principle and regimes was extensively investigated and modeled in silicon industry in the past and it helps obtain high carrier densities and mobilities enhancing the power factor [90–92]. Neophytou and Kosina showed that electrostatic gating of p-type Si NWs investigated up to 20 nm in diameter enhances the power factors up to five times versus standard doped channels [93]. A main limitation is related to small areas of material that can be affected by remote doping or fabrication of gate/multigate electrodes. Figure 10.7 shows the thermoelectric power factor of gated NWs with different diameters versus carrier density together with the doped case power factor as solid-black line [110].

The *energy filtering* technique allows an improvement of the Seebeck coefficient and the power factor in structures with embedded nanometric precipitates or potential barriers. The technique is based on low energy carriers filtering/blocking by the energy barrier at polycrystalline grain boundaries, while highest energy electrons continue to give strong contribution to the conduction mechanism. Nevertheless, the energy filtering effect is not able to change the well-known dependency of  $\sigma$  and  $S$  on the carrier density  $n$  [94]. About the *energy filtering* approach applied to quantum wells structures, Neophytou *et al.* reported that energy filtering allows improvement of the Seebeck coefficient and the power factor in superlattices up to 27% [95]. Boron-doped nanocrystalline silicon including modulation doping and energy filtering strategies has been shown to exhibit an impressive power factor of about 15 mW/m/K [96].

### 10.6.1 Organic Thermoelectric Materials

In the domain of the wearable applications and whatever applications where the generated power cost is a very sensible issue, organic materials are good candidates for power generation with their clear advantages in terms of easy processibility, flexibility, lightweight, raw material abundance, and low-cost manufacturing. Moreover, organic semiconductors show thermal conductivity around

0.5 W/m/K, which is very close to the lower limit of inorganic materials [97]. Thermal conduction in conjugated polymers is generally controlled by phonons.

Different polymers such as polyaniline (PANI), poly(3,4-ethylenedioxythiophene):poly(styrenesulfonate) (PEDOT:PSS), poly(3,4-ethylenedioxythiophene):tosylate (PEDOT-Tos), polythiophene (PTH), polyacetylene (PA), polycarbazoles (PC), polyphenylenevinylene (PPV), and polypyrrole (PPY) have been investigated for many years, and some of them present very good figure of merit values, as described below. Best organic thermoelectric materials demonstrated  $ZT$  values of about 0.42 for the p-type PEDOT: PSS [98] and 0.20 for (n-type) coordination polymers poly[K<sub>x</sub>(Ni-ett)]; as example of complete thermoelectric generator based on organic materials, Sun *et al.* fabricated a 35-thermocouples-based device of 5 mm height and about 900  $\mu\text{m}$  thickness

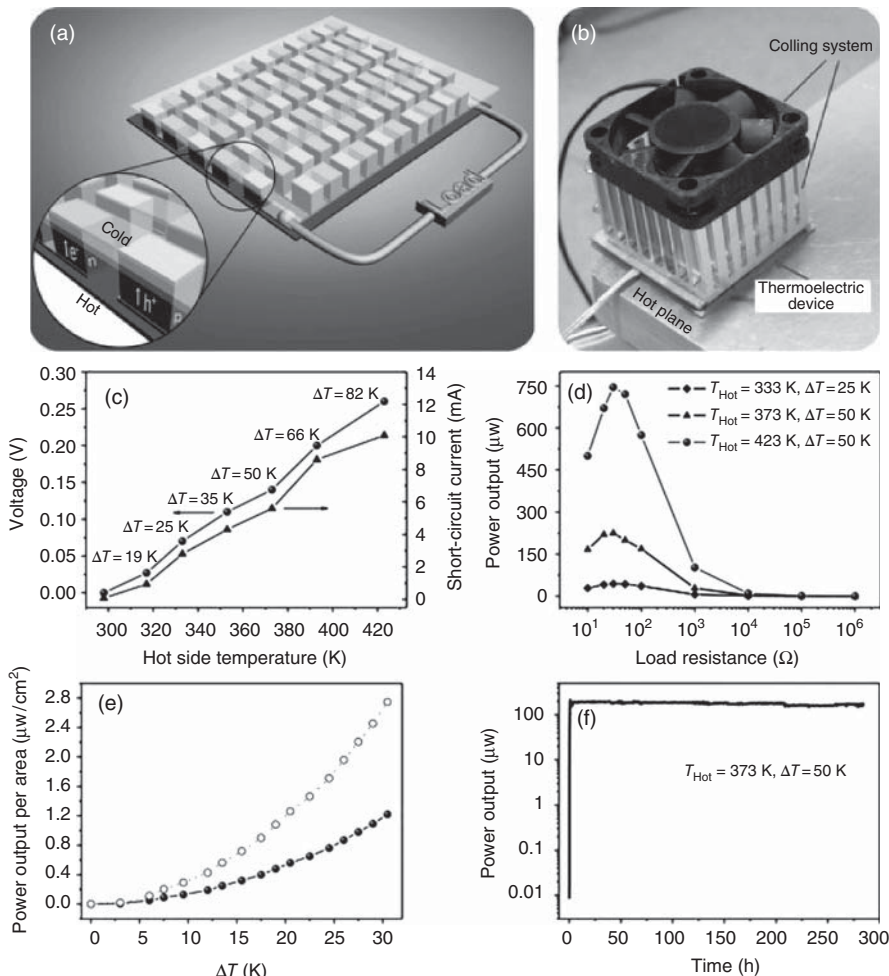


**Figure 10.8** Properties and long-term stability of the developed thermoelectric module with a packing density of 0.40. (Sun *et al.* 2012 [99]. Reproduced with permission of Wiley.)

[99]. The device produced an open-circuit voltage of 0.26 V with 80 K of temperature gradient, and a short-circuit current of about 10 mA. These values are among the highest power densities reported for organic TEMs. Figure 10.8 shows the properties and long-term stability of the fabricated TEM with a packing density of 0.40.

About current trends for optimization and power factor enhancement, we can identify different routes for materials optimization; for conducting polymers, a suggested method is to synthesize crystalline conductive polymers in order to discriminate effects of counterions, polymer chains, and assemblies. In addition, the alignment of polymer chains, interfaces, and crystallinity showed a huge impact on thermal conductivity of polymer films and charge transport [100].

Another tool for fine tuning of this family of materials is related to doping procedures, which introduce long-range electrostatic interactions affecting the interaction potential between adjacent polymer chains, the vibrational modes, and the cohesion energy. The optimization of the oxidation level in order to preserve thermoelectric properties and modulate the DOS at Fermi level is an additional enhancement method, similarly for the inorganic semiconductor [101].

Finally, the expected evolution of the applications scenarios is in good agreement with the latest market needs, and oriented toward the Internet of Things (IOT) and Internet of Everything (IOE) sensors network demand. A very attractive topic is represented by the thermoelectric textiles based on organic polymers that may effectively solve the integration issues, the low cost requirements, and safety (nontoxic) materials wished for wearable generators.

## References

- 1 Lim, C.L., Byrne, C., and Lee, J.K. (2008) Human thermoregulation and measurement of body temperature in exercise and clinical settings. *Ann. Acad. Med., Singapore*, **37** (4), 347–353.
- 2 Lai, D.T.H., Palaniswami, M., and Begg, R. (2016) *Healthcare Sensor Networks: Challenges Toward Practical Implementation*, CRC Press, Taylor & Francis Group 462 pp.
- 3 Houdas, Y. and Ring, E.F.J. (2013) *Human Body Temperature: Its Measurement and Regulation*, Springer Science & Business Media 238 pp.
- 4 de Dear, R.J., Arens, E., Hui, Z., and Oguro, M. (1997) Convective and radiative heat transfer coefficients for individual human body segments. *Int. J. Biometeorol.*, **40**, 141–156.
- 5 Kuwabara, K., Mochida, T., Nagano, K., and Shimakura, K. (2005) Experiments to determine the convective heat transfer coefficient of a thermal manikin. *Elsevier Ergonom. Book Ser.*, **3**, 423–429.
- 6 Kurazumi, Y., Tsuchikawab, T., Ishiiia, J., Fukagawa, K., Yamatoc, Y., and Matsubarad, N. (2008) Radiative and convective heat transfer coefficients of the human body in natural convection. *Build. Environ.*, **43** (12), 2142–2153.
- 7 Ono, T., Murakami, S., Ooka, R., and Omori, T. (2008) Numerical and experimental study on convective heat transfer of the human body in the outdoor environment. *J. Wind Eng. Ind. Aerodyn.*, **96** (10–11), 1719–1732.

- 8 Najjaran, A. (2012) Determining natural convection heat transfer coefficient of human body. *Trans. Control Mech. Syst.*, **1** (8), 362–369.
- 9 Kurazumi, Y., Rezgals, L., and Melikov, A.K. (2014) Convective heat transfer coefficients of the human body under forced convection from ceiling. *J. Ergonom.*, **4** (1) PAPER 1000126.
- 10 Fukazawa, T. and Tochihara, Y. (2015) The thermal manikin: a useful and effective device for evaluating human thermal environments. *J. Human-Environ. Syst.*, **18** (1), 21–28.
- 11 ASHRAE (1993) Physiological principles and thermal comfort, in *ASHRAE Handbook of Fundamentals*, ASHRAE Inc., Atlanta, pp. 8.1–8.29.
- 12 Fanger, P.O. (1967) Calculation of thermal comfort: introduction of a basic comfort equation. *ASHRAE Trans.*, **73** (2), III 4.1–III 4.20.
- 13 Huizenga, C., Zhang, H., Arens, E., and Wang, D. (2004) Skin and core temperature response to partial- and whole-body heating and cooling. *J. Therm. Biol.*, **29** (7–8), 549–558.
- 14 Tanda, G. (2015) The Use of Infrared Thermography to Detect the Skin Temperature Response to Physical Activity. 33rd UIT (Italian Union of Thermo-fluid-dynamics) Heat Transfer Conference, Journal of Physics: Conference Series 655, p. 012062.
- 15 Glatz, W., Muntwyler, S., and Hierold, C. (2006) Optimization and fabrication of thick flexible polymer based micro thermoelectric generator. *Sens. Actuators, A*, **132**, 337–345.
- 16 Schwyter, E., Glatz, W., Durrer, L., and Hierold, C. (2008) Flexible Micro Thermoelectric Generator based on Electroplated  $\text{Bi}_{2+x}\text{Te}_{3-x}$ . DTIP of MEMS and MOEMS – Symposium on Design, Test, Integration and Packaging of MEMS/MOEMS, 4752949.
- 17 Carmo, J.P., Goncalves, L.M., Wolffebuttel, R.F., and Correia, J.H. (2010) A planar thermoelectric power generator for integration in wearable microsystems. *Sens. Actuators, A*, **161** (1–2), 199–204.
- 18 Kao, P.H., Shih, P.J., Dai, C.L., and Liu, M.C. (2010) Fabrication and characterization of CMOS-MEMS thermoelectric micro generators. *Sensors*, **2010** (10), 1315–1325.
- 19 Yuan, Z., Ziouche, K., Bougrioua, Z., Lejeune, P., Lasri, T., and Leclercq, D. (2015) A planar micro thermoelectric generator with high thermal resistance. *Sens. Actuators, A*, **221**, 67–76.
- 20 Jin Bae, E., Hun Kang, Y., Jang, K.S., and Yun Cho, S. (2016) Enhancement of Thermoelectric Properties of PEDOT:PSS and Tellurium-PEDOT:PSS Hybrid Composites by Simple Chemical Treatment. *Scientific Reports* 6, Article number: 18805.
- 21 Franciosi, L., De Pascali, C., Farella, I., Martucci, C., Cretì, P., Siciliano, P., and Perrone, A. (2011a) Flexible thermoelectric generator for ambient assisted living wearable biometric sensors. *J. Power Sources*, **196** (6), 3239–3243.
- 22 Franciosi, L., De Pascali, C., Bartali, R., Morganti, E., Lorenzelli, L., Siciliano, P., and Laidani, N. (2013a) PDMS/Kapton interface plasma treatment effects on the polymeric package for a wearable thermoelectric generator. *ACS Appl. Mater. Interf.*, **5** (14), 6586–6590.

- 23 Franciosi, L., De Pascali, C., Siciliano, P., De Risi, A., D'Amico, S., Veri, C., and Pasca, M. (2013b) Thin Film Technology Flexible Thermoelectric Generator and Dedicated ASIC for Energy Harvesting Applications. Proceedings of the 2013 5th IEEE International Workshop on Advances in Sensors and Interfaces, IWASI 2013, 6576100, pp. 104–107.
- 24 Franciosi, L., De Pascali, C., and Siciliano, P. (2015) Experimental assessment of thermoelectric generator package properties: simulated results validation and real gradient capabilities. *Energy*, **86**, 300–310.
- 25 Leonov, V. (2011) Human machine and thermoelectric energy scavenging for wearable devices. *ISRN Renew. Energy*, **2011** (2011Article ID 78538, pp. 1–11).
- 26 Venkatasubramanian, R., Siivola, E., Colpitts, T., and O'Quinn, B. (2001) Thin-film thermoelectric devices with high room-temperature figures of merit. *Nature*, **413**, 597.
- 27 Harman, T.C., Taylor, P.J., Walsh, M.P., and LaForge, B.E. (2002) Quantum dot superlattice thermoelectric materials and devices. *Science*, **297**, 2229.
- 28 Nielsch, K., Bachmann, J., Kimling, J., and Bottner, H. (2011) Thermoelectric nanostructures: from physical model systems towards nanograinined composites. *Adv. Energy Mater.*, **1**, 713–731.
- 29 Kim, S.J., We, J.H., Kim, G.S., and Cho, B.J. (2012) Simultaneous measurement of the Seebeck coefficient and thermal conductivity in the cross-sectional direction of thermoelectric thick film. *J. Appl. Phys.*, **112** (10), 104511-1–104511-5.
- 30 Madan, D., Wang, Z., Chen, A., Juang, R.-c., Keist, J., Wright, P.K., and Evans, J.W. (2012) Enhanced performance of dispenser printed MA n-type  $\text{Bi}_2\text{Te}_3$  composite thermoelectric generators. *ACS Appl. Mater. Interfaces*, **4** (11), 6117–6124.
- 31 Nakamura, Y., Matsufuji, Y., and Inoue, M. (2012) Fabrication and properties of thermoelectric oxide thick films deposited with aerosol deposition method. *J. Phys. Conf. Ser.*, **352** (1), 0120262184 *IEEE Sensors Journal*, 14(7).
- 32 Navone, C., Soulier, M., Plissonnier, M., and Seiler, A.L. (2010) Development of  $(\text{Bi},\text{Sb})_2(\text{Te},\text{Se})_3$ -based thermoelectric modules by a screen-printing process. *J. Electron. Mater.*, **39** (9), 1755–1759.
- 33 Suemori, K., Hoshino, S., and Kamata, T. (2013) Flexible and lightweight thermoelectric generators composed of carbon nanotube–polystyrene composites printed on film substrate. *Appl. Phys. Lett.*, **103**, 153902.
- 34 Madan, D., Wang, Z., Chen, A., Wright, P.K., and Evans, J.W. (2013) High-performance dispenser printed MA p-Type  $\text{Bi}_{0.5}\text{Sb}_{1.5}\text{Te}_3$  flexible thermoelectric generators for powering wireless sensor networks. *ACS Appl. Mater. Interfaces*, **5**, 11872–11876.
- 35 Madan, D., Wang, Z., Chen, A., Winslow, R., Wright, P.K., and Evans, J.W. (2014) Dispenser printed circular thermoelectric devices using Bi and  $\text{Bi}_{0.5}\text{Sb}_{1.5}\text{Te}_3$ . *Appl. Phys. Lett.*, **104**, 013902.
- 36 Otego (2016) [www.otego.de](http://www.otego.de) (accessed May 3, 2016).
- 37 Bubnova, O., Khan, Z.U., Malti, A., Braun, S., Fahlman, M., Berggren, M., and Crispin, X. (2011) Optimization of the thermoelectric figure of merit in the conducting polymer poly(3,4-ethylenedioxythiophene). *Nat. Mater.*, **10**, 429–433.

- 38** Kouma, N., Nishino, T., and Tsuboi, O. (2013) A high-output-voltage micro-thermoelectric generator having high-aspect-ratio structure. *J. Micromech. Microeng.*, **23** (11), 114005.
- 39** Huesgen, T., Woias, P., and Kockman, N. (2008) Design and fabrication of MEMS thermoelectric generators with high temperature efficiency. *Sens. Actuators, A*, **145–146**, 423–429.
- 40** Wang, Z., Leonov, V., Fiorini, P., and Van Hoof, C. (2009) Realization of a wearable miniaturized thermoelectric generator for human body applications. *Sens. Actuators, A*, **156** (1), 95–102.
- 41** Wang, Z., van Andel, Y., Jambunathan, M., Leonov, V., Elfrink, R., and Vullers, R.J.M. (2011) Characterization of a bulk-micromachined membraneless in-plane thermopile. *J. Electron. Mater.*, **40** (5), 499–503.
- 42** Sevilla, G.A.T., Inayat, S.B., Rojas, J.P., Hussain, A.M., and Hussain, M. (2013) Flexible and semi-transparent thermoelectric energy harvesters from low cost bulk silicon (100). *Small*, **9**, 3916–3921.
- 43** Mattox, D.M. (2010) *Handbook of Physical Vapor Deposition (PVD) Processing*, 2nd edn, vol. 2010, William Andrew.
- 44** Rowe, D.M. (ed.) (2009) *Thermoelectrics Handbook – Macro to Nano*, CRC Taylor & Francis Group, Boca Raton, Florida, pp. 47-1–47–16 ISBN 0-8493-2264-2.
- 45** SreeHarsha, K.S. (2006) *Principles of Physical Vapor Deposition of Thin Films*, Elsevier.
- 46** Lin, J.M., Chen, Y.-C., and Lin, C.P. (2013) Annealing effect on the thermoelectric properties of  $\text{Bi}_2\text{Te}_3$  thin films prepared by thermal evaporation method. *J. Nanomater.*, 2013 Article ID 201017, pp. 1–6.
- 47** Micropelt (2016) Available from [www.micropelt.com](http://www.micropelt.com).
- 48** Fan, P., Zheng, Z.H., Li, Y.Z., Lin, Q.Y., Luo, J.T., Liang, G.X., Cai, X.M., Zhang, D.P., and Ye, F. (2015) Low-cost flexible thin film thermoelectric generator on zinc based thermoelectric materials. *Appl. Phys. Lett.*, **106** (7), 073901.
- 49** Francioso, L., De Pascali, C., Taurino, A., Siciliano, P., and De Risi, A. (2013c) Wearable and Flexible Thermoelectric Generator with Enhanced Package. Proceedings of SPIE – The International Society for Optical Engineering, Conference Smart Sensors, Actuators, and MEMS VI 8763, 876306.
- 50** Charles, E., Groubert, E., and Boyer, A. (1988) Structural and electrical properties of bismuth telluride films grown by the molecular beam technique. *J. Mater. Sci. Lett.*, **7**, 575–577.
- 51** Cho, S., Kim, Y., and Kettersson, J.B. (2004) Structural and thermoelectric properties in  $(\text{Sb}_{1-x}\text{Bi}_x)_2\text{Te}_3$  thin films. *Appl. Phys. A: Mater. Sci. Process.*, **79** (7), 1729–1731.
- 52** Zhang, H., Liu, C.X., Qi, X.L., Dai, X., Fang, Z., and Zhang, S.C. (2009) Topological insulators in  $\text{Bi}_2\text{Se}_3$ ,  $\text{Bi}_2\text{Te}_3$  and  $\text{Sb}_2\text{Te}_3$  with a single Dirac cone on the surface. *Nat. Phys.*, **5**, 438–442.
- 53** Chen, Y.L., Analytis, J.G., Chu, J.H., Liu, Z.K., Mo, S.K., Qi, X.L., Zhang, H.J., Lu, D.H., Dai, X., Fang, Z., Zhang, S.C., Fisher, I.R., Hussain, Z., and Shen, Z.X. (2009) Experimental realization of a three-dimensional topological insulator,  $\text{Bi}_2\text{Te}_3$ . *Science*, **325** (5937), 178–181.

- 54** Hasan, M.Z. and Kane, L. (2010) Colloquium: topological insulators. *Rev. Mod. Phys.*, **82**, 3045.
- 55** Moore, J.E. (2010) The birth of topological insulators. *Nature*, **464**, 194–198.
- 56** Xia, Y., Qian, D., Hsieh, D., Wray, L., Pal, A., Lin, H., Bansil, A., Grauer, D., Hor, Y.S., Cava, R.J., and Hasan, M.Z. (2009) Observation of a large-gap topological-insulator class with a single Dirac cone on the surface. *Nat. Phys.*, **5**, 398–402.
- 57** Krumrain, J., Mussler, G., Borisova, S., Stoica, T., Plucinski, L., Schneider, C.M., and Grützmacher, D. (2011) MBE growth optimization of topological insulator  $\text{Bi}_2\text{Te}_3$  films. *J. Cryst. Growth*, **324** (1), 115–118.
- 58** Boulanger, C. (2010) Thermoelectric material electroplating: a historical review. *J. Electron. Mater.*, **39** (9), 1818–1827.
- 59** Lim, J.R., Snyder, G.J., Huang, C.K., Herman, J.A., Ryan, M.A., and Fleurial, I.P. (2002) Thermoelectric Microdevice Fabrication Process and Evaluation at the Jet Propulsion Laboratory (JPL). Proceedings of ICT'02. 21st International Conference on Thermoelectrics, Long Beach, CA, USA, 25–29 August 2002 (IEEE) pp. 535–539.
- 60** Glatz, W., Schwyter, E., Durrer, L., and Hierold, C. (2009)  $\text{Bi}_2\text{Te}_3$ -based flexible micro thermoelectric generator with optimized design. *J. Microelectromech. Syst.*, **18** (3), 763–772.
- 61** Pelz, U., Jaklin, J., Rostek, R., Kröner, M., and Woias, P. (2015) Novel Fabrication Process for Micro Thermoelectric Generators ( $\mu$ TEGs). *J. Phys. Conf. Ser.*, **660**, 012084.
- 62** Lee, J., Farhangfar, S., Lee, J., Cagnon, L., Scholz, R., Gösele, U., and Nielsch, K. (2008) Tuning the crystallinity of thermoelectric  $\text{Bi}_2\text{Te}_3$  nanowire arrays grown by pulsed electrodeposition. *Nanotechnology*, **2008** (19), 365701.
- 63** Mannam, R., Agarwa, M., Roy, A., Singh, V., Varahramyan, K., and Davis, D. (2009) Electrodeposition and thermoelectric characterization of bismuth telluride nanowires. *J. Electrochem. Soc.*, **156** (8), B871–B875.
- 64** Picht, O., Müller, S., Alber, I., Rauber, M., Lensch-Falk, J., Medlin, D.L., Neumann, R., and Toimil-Molares, M.E. (2012) Tuning the geometrical and crystallographic characteristics of  $\text{Bi}_2\text{Te}_3$  nanowires by electrodeposition in ion-track membranes. *J. Phys. Chem. C*, **116**, 5367–5375.
- 65** Peranio, N., Leister, E., Töllner, W., Eibl, O., and Nielsch, K. (2012) Stoichiometry controlled, single-crystalline  $\text{Bi}_2\text{Te}_3$  nanowires for transport in the basal plane. *Adv. Funct. Mater.*, **22**, 151–156.
- 66** Frantz, C., Stein, N., Zhang, Y., Bouzy, E., Picht, O., Toimil-Molares, M.E., and Boulanger, C. (2012) Electrodeposition of bismuth telluride nanowires with controlled composition in polycarbonate membranes. *Electrochim. Acta*, **2012** (69), 30–37.
- 67** Wagner, S. and Ellis, W.C. (1964) *Appl. Phys. Lett.*, **4**, 89.
- 68** Wang, G., Lok, S.K., Wong, G.K.L., and Sou, I.K. (2009) Molecular beam epitaxy-grown  $\text{Bi}_4\text{Te}_3$  nanowires. *Appl. Phys. Lett.*, **95** (26), 263102.
- 69** Wei, Q., Su, Y., Yang, C.J., Liu, Z.G., Xu, H.N., Xia, Y.D., and Yin, J. (2011) The synthesis of  $\text{Bi}_2\text{Te}_3$  nanobelts by vapor–liquid–solid method and their electrical transport properties. *J. Mater. Sci.*, **46** (7), 2267–2272.

- 70** Wei, Q., Mukaida, M., Kirihara, K., Naitoh, Y., and Ishida, T. (2014) Polymer thermoelectric modules screen-printed on paper. *RSC Adv.*, **4**, 28802–28806.
- 71** Franciosi, L., De Pascali, C., Siciliano, P., De Risi, A., Bartali, R., Morganti, E., and Lorenzelli, L. (2013d) Structural Reliability and Thermal Insulation Performance of Flexible Thermoelectric Generator for Wearable Sensors. *IEEE Sensors 2013 – Proceedings 2013*, 6688438.
- 72** Sato, N. and Masatoshi, T. (2005) Fabrication and Evaluation of a Flexible Thermoelectric Device Using Metal Thin Films. *ICT 2005, 24th International Conference on Thermoelectrics*, pp. 160–163.
- 73** Du, Y., Cai, K., Chen, S., Wang, H., Shen, S.Z., Donelson, R., and Lin, T. (2015) Thermoelectric fabrics: toward power generating clothing. *Sci. Rep.*, **5**, 6411. doi: 10.1038/srep06411
- 74** Leonov, V., Gyselinckx, B., Van Hoof, C., Torfs, T., Yazicioglu, R.F., Vullers, R.J.M., Fiorini, and P. (2008) Wearable Self-powered Wireless Devices with Thermoelectric Energy Scavengers. *Proceedings of the Smart Systems Integration*, Barcelona, April 9–10, pp. 217–224.
- 75** Leonov, V., Torfs, T., Van Hoof, C., and Vullers, R.J.M. (2009) Smart wireless sensors integrated in clothing: an electrocardiography system in a shirt powered using human body heat. *Sens. Transducers J.*, **107**, 165–176.
- 76** Leonov, V., Vullers, R.J.M., and Van Hoof, C. (2012) Thermoelectric Generator Hidden in a Shirt with a Fabric Radiator. *9th European Conference on Thermoelectrics*, AIP Conference Proceedings 1449, pp. 556–559.
- 77** Franciosi, L., De Pascali, C., Farella, I., Martucci, C., Cretì, P., Siciliano, P., and Perrone, A. (2010) Flexible Thermoelectric Generator for Wearable Biometric Sensors. *Proceedings of the IEEE Conference on Sensors*, IEEE, Kona, HI, USA, pp. 747–750.
- 78** Franciosi, L., De Pascali, C., Farella, I., Martucci, C., Cretì, P., and Siciliano, P. (2011b) Polyimide/PDMS flexible thermoelectric generator for ambient assisted living applications. *Proc. SPIE – Int. Soc. Opt. Eng.*, **8066**, 80662H.
- 79** Veri, C., Franciosi, L., Pasca, M., De Pascali, C., Siciliano, P., and D'Amico, S. (2016) An 80 mV startup voltage fully electrical DC–DC converter for flexible thermoelectric generators. *IEEE Sens. J.*, **16**, 2735–2745, 7184928.
- 80** Veri, C., Pasca, M., D'Amico, S., and Franciosi, L. (2014) A 40 mV Start Up Voltage DC–DC Converter for Thermoelectric Energy Harvesting Applications. *10th Conference on Ph.D. Research in Microelectronics and Electronics*, PRIME 2014, 06872740.
- 81** Veri, C., Pasca, M., D'Amico, S., Franciosi, L., De Pascali, C., and Siciliano, P. (2015a) A Flexible Thermoelectric Generator with a Fully Electrical, Low Startup Voltage and High Efficiency DC–DC Converter. *Proceedings – 2015 6th IEEE International Workshop on Advances in Sensors and Interfaces*, IWASI 2015, 7184928, pp. 141–145.
- 82** Veri, C., Pasca, M., D'Amico, S., Franciosi, L., De Pascali, C., and Siciliano, P. (2015b) A thin film flexible thermoelectric generator with a fully electrical, low startup voltage and high efficiency DC–DC converter. *IEEE Sens. Proc.* 7370285, pp. 1–4.

- 83 Kim, S.J., We, J.H., and Cho, B.J. (2014) A wearable thermoelectric generator fabricated on a glass fabric. *Energy Environ. Sci.*, **7**, 1959–1965.
- 84 Hicks, L.D. and Dresselhaus, M.S. (1993) Thermoelectric figure of merit of a one-dimensional conductor. *Phys. Rev. B*, **47**, 16631(R).
- 85 Friedel, J. (1956) On some electrical and magnetic properties of metallic solid solutions. *Can. J. Phys.*, **34** (12A), 1190–1211. doi: 10.1139/p56-134
- 86 Heremans, J.P., Wiendlocha, B., and Chamoire, A.M. (2012) Resonant levels in bulk thermoelectric semiconductors. *Energy Environ. Sci.*, **5**, 5510–5530.
- 87 Garg, J. and Chen, G. (2013) Minimum thermal conductivity in superlattices: a first-principles formalism. *Phys. Rev. B*, **87**, 140302.
- 88 Biswas, K., He, J., Blum, I.D., Wu, C.-I., Hogan, T.P., Seidman, D.N., Dravid, V.P., and Kanatzidis, M.G. (2012) High-performance bulk thermoelectrics with all-scale hierarchical architectures. *Nature*, **489**, 414–418.
- 89 Jaworski, C.M., Kulbachinskii, V., and Heremans, J.P. (2009) Resonant level formed by tin in  $\text{Bi}_2\text{Te}_3$  and the enhancement of room-temperature thermoelectric power. *Phys. Rev. B: Condens. Mat. Mater. Phys.*, **80**, 233201.
- 90 Curtin, B.M., Codecido, E., Krämer, S., and Bowers, J.E. (2013) Field-effect modulation of thermoelectric properties in multigated silicon nanowires. *Nano Lett.*, **13**, 5503–5508.
- 91 Hou, Q., Gu, B.F., Chen, Y.B., He, Y.J., and Sun, J.L. (2014) Enhancement of the thermoelectric power factor of MnSi 1.7 MnSi 1.7 film by modulation doping of Al and Cu. *Appl. Phys. A*, **114**, 943–949.
- 92 Pei, Y.-L., Wu, H., Wu, D., Zheng, F., and He, J. (2014) High thermoelectric performance realized in a BiCuSeO system by improving carrier mobility through 3D modulation doping. *J. Am. Chem. Soc.*, **136**, 13902.
- 93 Neophytou, N. and Kosina, H. (2014) Gated Si nanowires for large thermoelectric power factors. *Appl. Phys. Lett.*, **105**, 073119.
- 94 Narducci, D., Selezneva, E., Cerofolini, G., Frabboni, S., and Ottaviani, G. (2012) Impact of energy filtering and carrier localization on the thermoelectric properties of granular semiconductors. *J. Solid State Chem.*, **193**, 19–25.
- 95 Neophytou, N. and Mischa, T. (2016) Modulation doping and energy filtering as effective ways to improve the thermoelectric power factor. *J. Comput. Electron.*, **15** (1), 16–26.
- 96 Neophytou, N., Zianni, X., Kosina, H., Frabboni, S., Lorenzi, B., and Narducci, D. (2013) Simultaneous increase in electrical conductivity and Seebeck coefficient in highly boron-doped nanocrystalline Si. *Nanotechnology*, **24**, 205402.
- 97 Zhang, Q., Sun, Y., Xu, W., and Zhu, D. (2014) Organic thermoelectric materials: emerging green energy materials converting heat to electricity directly and efficiently. *Adv. Mater.*, **26**, 6829–6851.
- 98 Kim, G.H., Shao, L., Zhang, K., and Pipe, K.P. (2013) Engineered doping of organic semiconductors for enhanced thermoelectric efficiency. *Nat. Mater.*, **12**, 719.
- 99 Sun, Y.M., Sheng, P., Di, C.A., Jiao, F., Xu, W., Qiu, D., and Zhu, D.B. (2012) Organic thermoelectric materials and devices based on p- and n-type poly(metal 1,1,2,2-ethenetetrathiolate)s. *Adv. Mater.*, **24** (14), 1781.

- 100 Wang, X.J., Ho, V., Segalman, R.A., and Cahill, D.G. (2013) Thermal conductivity of high-modulus polymer fibers. *Macromolecules*, **46** (12), 4937–4943.
- 101 Bubnova, O., Khan, Z.U., Wang, H., Braun, S., Evans, D.R., Fabretto, M., Hojati-Talemi, P., Dagnelund, D., Arlin, J.B., Geerts, Y.H., Desbief, S., Breiby, D.W., Andreasen, J.W., Lazzaroni, R., Chen, W.M., Zozoulenko, I., Fahlman, M., Murphy, P.J., Berggren, M., and Crispin, X. (2014) Semi-metallic polymers. *Nat. Mater.*, **13**, 190–194.

# 11

## Thermoelectric Modules as Efficient Heat Flux Sensors

Gennadi Gromov

*PromLegion Ltd., 46 Warshavskoeshosse, 115230, Moscow, Russia*

### 11.1 Introduction

*Heat flux* is the quantity of heat transmitted through an isothermal surface per unit time. Heat flux per unit of an isothermal surface is *heat flux density*. Heat flux is a vector and each component of it is numerically equal to the amount of heat transmitted per unit time through unit area taken perpendicular to the direction of the component.

Heat fluxes accompany most physical processes, natural and technological phenomena, and are a result of human activity.

Measurement of heat fluxes, as well as of temperature, allows controlling these processes to obtain necessary information for a variety of control and optimization tasks. Heat flux and temperature sensors find a significant niche in the market of modern sensors. Many existing and new applications require accurate measurement of heat fluxes.

#### 11.1.1 Applications of Heat Flux Sensors

Measurement of heat fluxes is necessary in various fields of science, technology, industry, ecology security, and so on. Here a list of the application fields is presented, which is, of course, not complete.

- Research
- Agriculture
- Climatology
- Building engineering
- Solar energy
- Industrial applications
- Safety and security

### 11.1.2 Units of Heat Flux and Characteristics of Sensors

The heat flux  $Q_s$  is measured in watts per unit of surface area  $s$  perpendicular to its direction –  $\text{W/m}^2$ .

$$Q_s = \frac{Q_a}{s} \quad (11.1)$$

If the area is known, it can be measured in terms of total heat flux –  $Q_a$ .

$$Q_a = Q_s \times s \quad (11.2)$$

Heat flux sensors have sensitivity to the heat flux. The sensitivity can also have two types of units.

*The sensitivity*  $S_e$  to the measured heat flux is the ratio of the electrical signal of the sensor (typically microvolts) to the heat flux density  $Q_s$ . The units are  $\mu\text{V}/(\text{W/m}^2)$ .

$$S_e = \frac{U}{Q_s} \quad (11.3)$$

*The integral (absolute) sensitivity*  $S_a$  is the ratio of the electrical signal of the sensor to the total heat flux  $Q_a$ . The units are  $\text{V/W}$ .

$$S_a = \frac{U}{Q_a} \quad (11.4)$$

$$S_a = \frac{U}{s \times P_e} = \frac{S_e}{s} \quad (11.5)$$

The term integral sensitivity makes heat flux sensors similar to photodetectors, since radiation is also an energy flux. Heat flux sensors are often used to measure thermal radiation. Thus, they are called *thermal radiation detectors*, to distinguish them from quantum photodetectors.

For thermal radiation (heat flux) sensors the usual parameters of photodetectors are applied: noise  $U_t^2$ , sensitivity threshold  $F_{th}$ , NEP (noise-equivalent power), detectivity  $D^*$ .

The spectral density of RMS of thermal noise voltage  $U_t^2$  is equal to

$$U_t^2 = 4kTR\Delta f \quad (11.6)$$

where  $k$  is the Boltzmann constant ( $=1.38 \times 10^{-23} \text{ J/K}$ );  $T$  is the sensor temperature;  $R$  is the sensor electric resistance; and  $\Delta f$  is the frequency band in which the measurements are done.

The sensitivity threshold  $F_{th}$  is the value of the heat flux, causing the sensor output voltage equal to the voltage noise RMS, with reference to the unit bandwidth and unit area of the sensor. The units are  $\text{W}/(\text{cmHz})^{1/2}$ .

$$F_{th} = \frac{\sqrt{U_t^2}}{S_a \sqrt{s\Delta f}} \quad (11.7)$$

where  $S_a$  is the integral volt–watt sensitivity and  $s$  is the sensor working area in  $\text{cm}^2$ .

The inverse value of  $F_{th}$  is called the *detectivity*  $D^*$ .

$$D^* = \frac{S_a \sqrt{s\Delta f}}{\sqrt{4kTR\Delta f}} \quad (11.8)$$

### 11.1.3 Modern Heat Flux Sensors

The principle of operation of most heat flux sensors is based on the method of “additional wall,” which was formulated by Schmidt at the beginning of the last century [1]. The “additional wall” with a known thermal conductivity  $K$  is located in the path of the heat flux  $Q$  to be measured. The temperature gradient  $\Delta T$  between the wall sides is proportional to the amount of heat flux. The thermal resistance  $R_T$  of the wall is the reciprocal value of the thermal conductance  $K$ :

$$\Delta T = R_T \times Q \quad (11.9)$$

Thus, it is necessary to measure the sensor temperature difference created by the heat flux. At a known thermal resistance of the sensor the measured temperature difference allows obtaining the heat flux value [2].

Most state-of-art heat flux sensors [3] are made on the basis of differential thermocouples connected in series (Figure 11.1).

The temperature difference  $\Delta T$  between two junctions of a thermocouple, separated by a layer of the medium with a given thermal resistance, induces the electric voltage difference  $E$ , which is proportional to the temperature difference and depends on the material properties of the thermocouple. It is the Seebeck effect.

$$E = \alpha \times \Delta T \quad (11.10)$$

where  $\alpha$  is the Seebeck coefficient.

Most differential thermocouples involve the Seebeck effect in metals.

Values of the Seebeck coefficient (thermo-EMF – thermal electromotive force – at temperature difference of 1 °C) for various metals and alloys are well known. However, for metals the Seebeck coefficient is relatively low – maximum of tens of  $\mu\text{V}/^\circ\text{C}$ .

Table 11.1 gives the Seebeck coefficient for different materials paired with platinum [4].

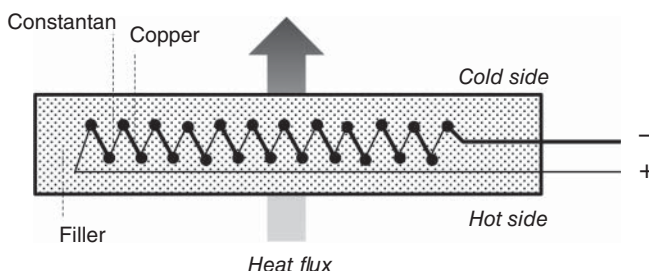


**Figure 11.1** Schematic view of a state-of-the-art heat flux sensor.

**Table 11.1** Seebeck coefficient of different materials.

Metals	Seebeck coefficient ( $\mu\text{V}$ )	Semiconductors	Seebeck coefficient ( $\mu\text{V}$ )
Antimony	+47	Se	+900
Nichrome	+25	Te	+500
Molybdenum	+10	Si	+440
Cadmium	+7.5	Ge	+300
Tungsten	+7.5	n-type $\text{Bi}_2\text{Te}_3$	-230
Gold	+6.5	p-type $\text{Bi}_{2-x}\text{Sb}_x\text{Te}_3$	+300
Silver	+6.5	p-type $\text{Sb}_2\text{Te}_3$	+185
Copper	+6.5	PbTe	-180
Rhodium	+6.0	$\text{Pb}_{03}\text{Ge}_{39}\text{Se}_{58}$	+1670
Tantalum	+4.5	$\text{Pb}_{06}\text{Ge}_{36}\text{Se}_{58}$	+1410
Lead	+4.0	$\text{Pb}_{09}\text{Ge}_{33}\text{Se}_{58}$	-1360
Aluminum	+3.5	$\text{Pb}_{13}\text{Ge}_{29}\text{Se}_{58}$	-1710
Carbon	+3.0	$\text{Pb}_{15}\text{Ge}_{37}\text{Se}_{58}$	-1990
Mercury	+0.6	$\text{SnSb}_4\text{Te}_7$	+25
Platinum	+0.0	$\text{SnBi}_4\text{Te}_7$	+120
Sodium	-2.0	$\text{SnBi}_3\text{SbTe}_7$	+151
Potassium	-9.0	$\text{SnBi}_{2.5}\text{Sb}_2\text{Te}_7$	+110
Nickel	-15	$\text{SnBi}_2\text{Sb}_2\text{Te}_7$	+90
Constantan	-35	$\text{PbBi}_4\text{Te}_7$	-53
Bismuth	-72		

Serial connection of many thermocouples (Figure 11.1) is used to increase the sensitivity. The lateral density of the thermocouples in state-of-the-art heat flux sensors can reach up to 1000–2000 thermocouples per centimeter square. This allows a multiple increase (by number  $N$  of thermocouples in series) of the thermoelectric output voltage and, as a result, of the sensor sensitivity.

$$E = N \times \alpha \times \Delta T \quad (11.11)$$

Modern sensors measure heat flux from  $10^{-3} \text{ W/m}^2$ . The upper limit of the measured heat flux density reaches values of the order  $10^7 \text{ W/m}^2$ . Thus, heat flux sensors are able to cover a considerable range,  $10^{-3}$ – $10^7 \text{ W/m}^2$ .

#### 11.1.4 Thermoelectric Heat Flux Sensors

Recently, interest in the use of thermoelectric modules as heat flux sensors has grown [5–7]. Thermoelectric modules are widely used for cooling (Peltier effect) or generation of energy (Peltier and Seebeck effects). In heat flux sensors the

thermoelectric effect – the Seebeck effect – is also used, which is the physical basis for the differential thermocouple sensors too.

The construction of thermoelectric modules is similar to that of the matrix of thermocouples. It is a sequential connection of thermoelements (pellets) of different n- and p-type semiconductors. Only, here the “couple” is a pair of semiconductor thermoelements with different conductivity (n- and p-types). The Seebeck effect in semiconductors is many times higher than that in metals. For example, in copper–constantan thermocouple the Seebeck coefficient of a couple is about  $38 \mu\text{V}/^\circ\text{C}$ . In a thermoelectric module – for one p–n thermoelement pair – it is more than  $400 \mu\text{V}/^\circ\text{C}$ .

This advantage makes the use of semiconductor thermoelectric modules as heat flux sensors, along with thermoelectric coolers and generators, very promising.

While thermoelectric modules have long been used as generators and coolers, this advantage for the sensors applications has not been realized for a long time. The key reason is a low degree of integration of thermoelements. For a long time, it was at the level of 100–150 pellets per centimeter squared. With such a low elements density, the thermoelectric modules used as heat flux sensors lose out to matrices of differential thermocouples.

At a given temperature difference the serial connection gives a sum of signals of individual junctions, pairs of thermocouples. In metal thermocouples the specific signal is much less than in semiconductor junctions, but due to the high degree of integration this shortcoming is offset.

However, the modern trend of miniaturization of thermoelectric modules (Figure 11.2), mainly because of the needs of optoelectronics, where thermoelectric cooling is widely used, has led to significant progress in the construction of thermoelectric micromodules – extremely miniature design and dense packing of pellets. This allows effectively using them as heat flux sensors [8].

Advanced thermoelectric micromodules are comparable with the sensors based on differential thermocouples in dimensions and dense integration,

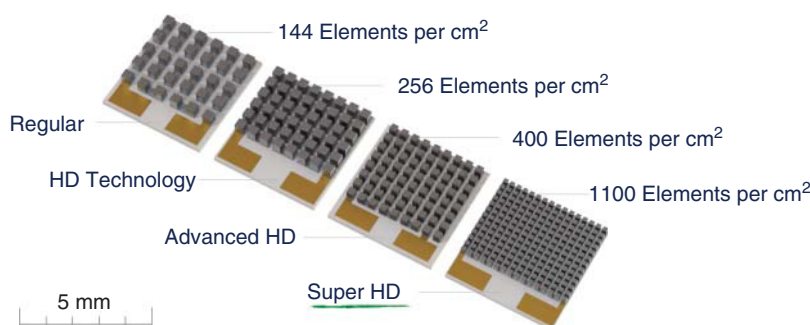


**Figure 11.2** Advances in miniaturization of thermoelectric modules – example of micromodules technology development.

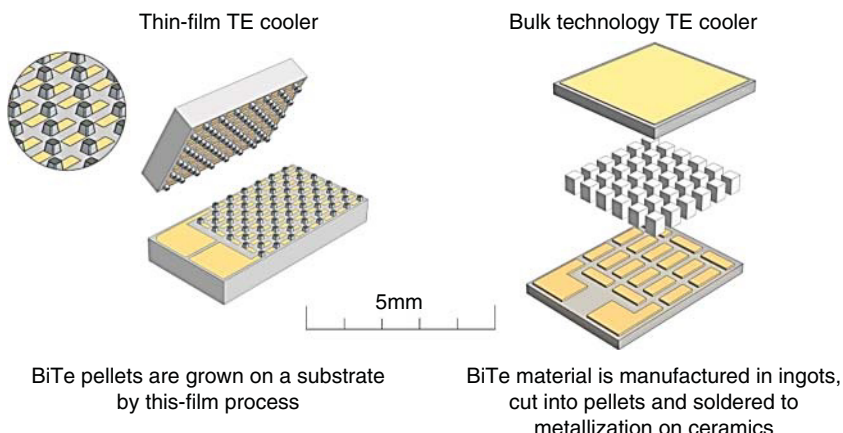


**Figure 11.3** Comparison of the designs of thermoelectric modules: thin-film and bulk.

which allows us to use them as heat flux sensors. Miniature and high-density packaged modules are manufactured by two technologies: thin film (new) and bulk (mature) technology (Figure 11.3). Each technology has its advantages and limits of use, but both provide the ability to produce fascinatingly miniature modules (down to the level of  $1 \text{ mm}^2$  and less), very small thermoelement sizes, and high density of packing.

One of the disadvantages of semiconductor modules in comparison with thermocouples may be the comparatively high temperature sensitivity of the parameters. This is the other side of the coin. However, in modern applications, heat flux sensors are most often used with temperature sensors. So, advanced electronics makes it easy to realize the mathematical processing of the results with necessary corrections taking into account temperature dependences known in advance. Moreover, such temperature sensors can be directly integrated into a miniature thermoelectric module.

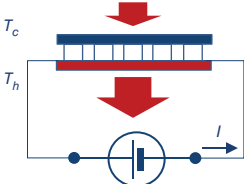
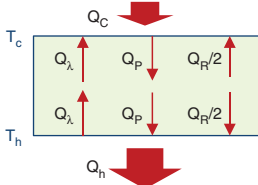
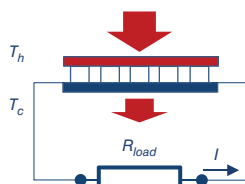
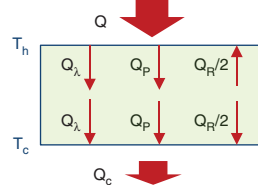
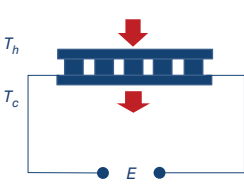
## 11.2 Applications of Thermoelectric Modules

Heat flux sensors complement the two already existing niches of thermoelectric modules (coolers and generators) [9] with a very promising new one (Table 11.2).

Thus, thermoelectric coolers and heat flux sensors are “extreme” ways of using thermoelectric effects. In the first case it is the Peltier effect, and in the second it is the Seebeck effect.

Thermoelectric generation is based on the two opposite thermoelectric effects – the third case.

**Table 11.2** Three applications of thermoelectric modules.

Thermoelectric cooling	Thermoelectric generation	Thermoelectric heat flux sensor
 	 	
<p>Figure a Peltier effect</p> $Q_C = 2N\alpha T_c I - \frac{I \times ACR}{2} - K\Delta T$ $Q_{\max} = \frac{(2N\alpha)^2 \times T_c}{2 \times ACR}, T_{\max} = 0$ $\Delta T_{\max} = \frac{1}{2} ZT_c^2, Q_{\max} = 0$	<p>Figure b Seebeck effect – Peltier effect</p> $E = \alpha \times 2N \times \Delta T$ $I = \frac{E}{R_{load} + ACR}$ $P = E^2 \times \frac{R_{load}}{(R_{load} + ACR)^2}$ $\eta_{\max} = \frac{Z \times \Delta T}{4}$	<p>Figure c Seebeck effect</p> $\Delta T = Q \times R_T$ $E = \alpha \times 2N \times (T_h - T_c)$ $S_a = \frac{1}{f} \times \frac{\alpha}{k}$ $S_a = \frac{1}{\alpha \times 2N} Z \times ACR$

The current in a thermoelectric module causes heat transfer from the cold to the hot side due to the Peltier effect, thereby creating a temperature difference

The temperature difference induces the opposite flow of heat by thermal conduction. The Joule heat is emitted in thermoelectric elements

Cooling parameters depend on the properties of the thermoelectric material and the number of elements

In the presence of a heat flux or a temperature difference module, a thermo-EMF is generated in a module due to the Seebeck effect

When the circuit is closed, there is a non-zero electric current

The current in the module causes a Peltier heat transfer from the hot to the cold side Generator parameters depend on the properties of the thermoelectric material, number of elements, and resistance of external load

In the presence of a heat flux a temperature difference appears on the module. The temperature difference generates a thermo-EMF due to the Seebeck effect

The thermo-EMF is proportional to the temperature difference and the heat flux

The sensitivity to heat flux depends on the properties of the thermoelectric material

## 11.3 Parameters of Thermoelectric Heat Flux Sensors

### 11.3.1 Integral Sensitivity $S_a$

The heat flux  $Q_a$  through the sensor is expressed by its total thermal resistance  $R_T$  and the temperature difference  $\Delta T$ :

$$Q_a = \frac{(T_h - T_c)}{R_T} \quad (11.12)$$

where  $T_h$  and  $T_c$  are the temperature on the hot and cold sides of the sensor, respectively.

The electrical signal  $E$  of the thermoelectric heat flux sensor is the following:

$$E = \alpha \times 2N \times (T_h - T_c) \quad (11.13)$$

where  $\alpha$  is the Seebeck coefficient of a thermoelement (averaged value in a pair of n- and p-type of elements) and  $2N$  is the number of thermoelements.

Therefore,

$$E = \alpha \times 2N \times Q_a \times R_T \quad (11.14)$$

Then the integral (absolute) sensitivity  $S_a$  is given by:

$$S_a = \frac{E}{Q_a} = \alpha \times 2N \times R_T \quad (11.15)$$

In the ideal case (heat flows only through the thermoelements)

$$R_T = \frac{1}{K_T} = \frac{1}{2N \times k \times \frac{\alpha \times b}{h}} \quad (11.16)$$

where  $K_T$  is the thermal conductance of the sensor;  $k$  is the average thermal conductivity for the thermoelement, and  $\frac{\alpha \times b}{h}$  is the ratio of the cross-section ( $\alpha \times b$ ) of the element to its height ( $h$ ), which is the form-factor ( $f$ ) of a thermoelement.

$$f = \frac{\alpha \times b}{h} \quad (11.17)$$

Thus, the sensor sensitivity is obtained as

$$S_a = \frac{1}{f} \times \frac{\alpha}{k} \quad (11.18)$$

The thermoelectric heat flux sensor sensitivity is determined by the ratio of the Seebeck coefficient  $\alpha$  to the thermal conductivity of the thermoelement  $k$  and is inversely proportional to the form-factor  $f$  of the thermoelement (pellet).

The important consequence of expression (11.18) is that the sensitivity does not depend on the number of the thermoelements in the sensor. The inverse proportionality to the thermoelement form-factor works instead. The sensitivity can be increased by smaller cross sections  $\alpha \times b$  of thermoelements at a relatively larger height  $h$ .

### 11.3.2 Sensitivity $S_e$

The sensitivity  $S_e$  to the density of heat flux is derived from the integral sensitivity  $S_a$ , if you multiply it by the area of the sensitive surface of the sensor  $s$ :

$$S_e = S_a \times s \quad (11.19)$$

### 11.3.3 Thermal Resistance $R_T$

The value of the thermal resistance  $R_T$  of the thermoelectric heat flux sensor is crucial for its application.

$$R_T = \frac{1}{2N \times k \times f} \quad (11.20)$$

First of all, it is the thermal resistance  $R_T$  that provides a temperature difference  $\Delta T$  (11.9), which causes the signal. Higher the thermal resistance  $R_T$ , higher the sensitivity of the sensor.

On the other hand, the effect of the presence of the measuring sensor (the "additional wall"), that is, its thermal resistance should be preferably minimized. Therefore, for a correct measurement the thermal resistance of the sensor should be significantly lower than the thermal resistance of the environment in which the heat flux is measured.

Table 11.3 shows thermal resistance values of a number of popular media for the thickness of the order of heat flux sensors often applied.

According to this table, the thermal resistance of a heat flux sensor in most practical applications should be no greater than  $10^{-2}$ – $10^{-3}$  K/(W/m<sup>2</sup>). Then it will not cause distortion in the heat fluxes to be measured reliably.

### 11.3.4 Noise Level

The spectral density of voltage RMS of thermal noise  $U_t^2$  can be written as

$$U_t^2 = 4k_B T \times ACR \times \Delta f \quad (11.21)$$

where  $k_B$ , the Boltzmann constant, equals  $1.38 \times 10^{-23}$  J/K;  $T$  is the sensor average temperature;  $ACR$  is the sensor resistance; and  $\Delta f$  is the frequency band in which the measurements are done.

### 11.3.5 Sensitivity Threshold

Sensitivity threshold is the value of the heat flux causing the sensor output voltage equal to the RMS noise voltage.

Sensitivity threshold with reference to the unit pass band and unit area of the sensor [W/cm Hz<sup>1/2</sup>]:

$$F_{th} = \frac{\sqrt{U_t^2}}{S_a \sqrt{s \times \Delta f}} \quad (11.22)$$

where  $S_a$  is the volt–watt sensitivity [V/W];  $s$  is the sensor working area in cm<sup>2</sup>.

**Table 11.3** Thermal resistances of some materials.

Material	Thermal conductivity (W/mK)	Average thermal resistance of a layer (K/(W/m <sup>2</sup> ))			
		1 mm	2 mm	3 mm	4 mm
Fresh snow	0.10–0.15	8.0E-03	1.6E-02	2.4E-02	3.2E-02
Water	0.6	1.7E-03	3.3E-03	5.0E-03	6.7E-03
Petroleum oils	0.12	8.3E-03	1.7E-02	2.5E-02	3.3E-02
Sand and clay	0.84–1.26	1.0E-03	2.0E-03	3.0E-03	4.0E-03
Peat	0.84	1.2E-03	2.4E-03	3.6E-03	4.8E-03
Foam concrete	0.05–0.3	5.7E-03	1.1E-02	1.7E-02	2.3E-02
Building brick	0.2–0.7	2.2E-02	4.4E-02	6.7E-02	8.9E-02
Wood	0.15	6.7E-03	1.3E-02	2.0E-02	2.7E-02
Granite	2.4	4.2E-04	8.3E-04	1.3E-03	1.7E-03
Wadding	0.055	1.8E-02	3.6E-02	5.5E-02	7.3E-02
Basalt	1.3	7.7E-04	1.5E-03	2.3E-03	3.1E-03
Stone wool	0.035–0.039	2.7E-02	5.4E-02	8.1E-02	1.1E-01
Quartz	8	1.3E-04	2.5E-04	3.8E-04	5.0E-04
Iron	92	1.1E-05	2.2E-05	3.3E-05	4.3E-05
Aluminum	202–236	4.5E-06	9.1E-06	1.4E-05	1.8E-05
Copper	401	2.5E-06	5.0E-06	7.5E-06	1.0E-05
Brass	97–111	9.4E-06	1.9E-05	2.8E-05	3.8E-05
Silicon	150	6.7E-06	1.3E-05	2.0E-05	2.7E-05
Convection heat exchange, air, normal conditions	0.026	1.67E-01			

### 11.3.6 Noise-Equivalent Power NEP

Noise-equivalent power (*NEP*) is the sensor parameter characterizing the minimum detectable radiation power in a 1 Hz bandwidth causing the sensor signal to equal RMS noise. The unit of the same is W/Hz<sup>1/2</sup>.

$$\text{NEP} = \frac{\sqrt{U_t^2}}{S_a} \quad (11.23)$$

$$\text{NEP} = \frac{k}{\alpha} \sqrt{4k_B T \times \frac{2N \times f}{\sigma}} \quad (11.24)$$

where  $\sigma$  is the electrical conductivity of the thermoelement (averaged value in a pair of n- and p-types of the elements).

### 11.3.7 Detectivity $D^*$

The reciprocal value of the sensitivity threshold  $F_{th}$  is detectivity  $D^*$ . The unit of detectivity is cm Hz<sup>1/2</sup>/W.

$$D^* = \frac{1}{F_{th}} \quad (11.25)$$

Or

$$D^* = \frac{\sqrt{s}}{NEP} \quad (11.26)$$

Specific detectivity is the reciprocal value of the radiation power, which at band  $\Delta f = 1$  Hz and sensor working area  $s = 1 \text{ cm}^2$  causes the sensor output signal to equal the noise.

$$D^* = \frac{S_a \sqrt{s}}{\sqrt{4k_B T \times ACR}} \quad (11.27)$$

$$D^* = \frac{1}{\sqrt{4k_B T}} \times \frac{\alpha \times \sqrt{\sigma}}{k} \times \sqrt{\frac{s}{2N \times f}} \quad (11.28)$$

### 11.3.8 Time Constant $\tau$

In the classic case the thermal time constant is calculated by thermal diffusivity ( $x$ ). It characterizes the velocity of the heat wave in a homogeneous medium after a single impulse.

$$x = \frac{k}{\rho \times C_p} \quad (11.29)$$

$$\tau = \frac{4}{\pi^2} \frac{h^2}{x} \quad (11.30)$$

where  $k$  is the thermal conductivity;  $\rho$  is the density of the media;  $C_p$  is the specific heat capacity; and  $h$  is the height of the thermoelement – sample thickness.

For heat flux sensors the expression of the time constant of thermoelectric microcoolers is applicable:

$$\tau = \frac{C_c}{f \times k \times 2N} \quad (11.31)$$

where  $C_c$  is the total heat capacity of the thermoelectric module ceramic substrate or sensor plate.

$$\tau = \frac{1}{f \times k \times 2N} \times C_p \times \rho \times h_c \times s_c \quad (11.32)$$

where  $\rho$  is the ceramics density,  $C_p$  is its specific heat capacity;  $h_c, s_c$  are the thickness and area of ceramics, respectively.

## 11.4 Self-Calibration Method of Thermoelectric Heat Flux Sensors

### 11.4.1 Sensitivity

#### 11.4.1.1 Method

As the sensors are measuring devices, their calibration is required to ensure high accuracy for applications. Calibration allows getting the coefficient of the output signal proportionality to the heat flux.

For calibration, two methods are known.

One method is the use of an external heat flux reference source [10–12]. With a known heat flux reference source and a corresponding response of the sensor to be calibrated the sensitivity is determined.

This calibration is carried out with the use of special equipment and in the laboratory. It is available only during periodical maintenance of the sensor and requires removal of the sensor from the measured object. So it is time consuming, expensive and limited in application.

Another method is to embed a reference heat source into the sensor [13, 14]. When electric power is applied to the embedded heater, it produces heat of a known value. It results in a signal of the sensor.

For example, it is a vacuum deposition of a resistive heater to one of the sensor sides [14].

With this calibration method the sensor is named self-calibrating. It is possible to calibrate it at any time without external hardware.

A disadvantage of this method is the assumption that a share of the thermal power of the reference source that passes through the sensor is known in advance. Ideally, it is equal to half of the electric power, but in practice this ratio could differ. And this causes mistakes in calibration.

Another downside is that the reference heat source should be integrated in the sensor. This complicates the design and production costs.

At the same time, thermoelectric modules have long been widely used for cooling and power generation. In these applications a number of measurement parameters of the modules are used to determine their quality and performance properties.

Such parameters are the thermoelectric figure of merit  $Z$ , the internal electrical resistance  $ACR$ , and, less commonly, the time constant  $\tau$  [15, 16].

The use of these parameters to specify the basic properties of thermoelectric heat flux sensors is also attractive.

The formula for the sensitivity shows its dependence on the ratio:

$$S_a = 2N \times \alpha \times R_T \quad (11.33)$$

It is possible to express this formula (11.33) by the parameters  $Z$  and  $ACR$  of a thermoelectric module.

The figure of merit  $Z$  of the thermoelectric module can be written as

$$Z = \frac{(2N \times \alpha)^2}{K_T \times ACR} = \frac{(2N \times \alpha)^2 \times R_T}{ACR} \quad (11.34)$$

Therefore,

$$\alpha \times R_T = \frac{1}{(2N)^2 \times \alpha} Z \times ACR \quad (11.35)$$

Then,

$$S_a = \frac{1}{\alpha \times 2N} Z \times ACR \quad (11.36)$$

This is a key formula of the new method of calibrating the thermoelectric heat flux sensors by measuring the figure of merit  $Z$  and AC resistance  $ACR$  of the sensor [17].

The design of a thermoelectric module (the number of pellets  $2N$ ) is known in advance. The Seebeck coefficient  $\alpha$  of the thermoelectric material used for manufacturing of sensors can be controlled. At a given area of the sensitive surface  $s$ , the number of the thermoelements in the sensors  $2N$  and known Seebeck coefficient of the thermoelectric material  $\alpha$ , it is easy to determine the sensitivity ( $S_a$  and  $S_e$ ) by Eqs. (11.36) and (11.5) respectively, by measuring the thermoelectric figure of merit  $Z$  and the resistance  $ACR$  of the sensor.

The calibration by the new method does not require applying reference thermal sources, does not need maintenances of sensors, and the calibration procedure can be performed with any periodicity. The method is characterized by high accuracy.

#### 11.4.1.2 Examples

Four samples of different types of thermoelectric heat flux sensors are produced. The design and geometrical parameters of the sensors are shown in Table 11.4.

Two types of calibration of the samples were done: using precision external heat source and by the proposed method. Both measurements were carried out in the temperature range of  $-20$  to  $+80$  °C. The results of calibration and temperature dependence of the sensitivity were compared.

**Table 11.4** Samples of heat flux sensors manufactured to verify the calibration method.

Parameter	Units	Sample 1	Sample 2	Sample 3	Sample 4
Size (diameter)	mm	20	20	27	27
Thickness	mm	3.2	3.2	3.7	3.7
Number of thermocouples		97	97	126	126
Filler	No	Silicon resin	No	Silicon resin	
Thermo-EMF at 27 °C	µV/°C	205	205	207	207
Thermo-EMF temperature dependence	µV/°C	$\alpha = 3.22E-5*T^3 - 3.26E-08*T^2 + 11.37e^T - 938.7$			

**Table 11.5** Results of calibration using precision external heat source and by the method proposed for Samples 1 and 2.

$T, (\text{°C})$	With external heat source		Method proposed by thermoelectric parameters						Comparison	
			$S_e \mu\text{V}/(\text{W}/\text{m}^2)$		$Z \times 1000 (\text{K}^{-1})$		$ACR (\text{Ohm})$		$S_e(Z) (\mu\text{V}/(\text{W}/\text{m}^2))$	
	#1	#2	#1	#2	#1	#2	#1	#2	#1	#2
-20	111.93	75.48	2.617	1.804	5.020	4.920	113.39	76.61	1.3	1.5
0	121.83	79.96	2.671	1.796	5.610	5.510	123.23	81.38	1.1	1.8
20	130.63	84.16	2.678	1.768	6.220	6.100	132.39	85.72	1.3	1.9
40	138.16	87.77	2.586	1.717	6.840	6.700	137.13	89.19	-0.7	1.6
60	137.40	89.22	2.433	1.616	7.480	7.360	138.30	90.38	-1.2	-0.6
80	138.23	90.59	2.184	1.668	4.650	4.660	106.25	81.32	-0.2	-0.4

**Table 11.6** Results of calibration using precision external heat source and by the method proposed for samples 3 and 4.

$T$ (°C)	With external heat source		Method proposed by thermoelectric parameters				Comparison			
	$S_e$ ( $\mu\text{V}/(\text{W/m}^2)$ )		$Z \times 1000$ ( $\text{K}^{-1}$ )		ACR (Ohm)		$S_e(Z)$ ( $\mu\text{V}/(\text{W/m}^2)$ )		$\Delta S_e$ (%)	
	#3	#4	#3	#4	#3	#4	#3	#4	#3	#4
-20	83.70	66.53	2.395	1.892	2.910	2.920	84.40	66.91	0.8	0.6
0	92.19	71.23	2.429	1.907	3.230	3.250	90.52	71.51	-1.8	0.4
20	99.14	76.56	2.449	1.894	3.570	3.590	97.49	75.82	-1.7	-1.0
40	104.02	79.89	2.411	1.885	3.920	3.950	102.80	80.99	-1.2	1.4
60	106.56	81.14	2.308	1.763	4.280	4.290	105.32	80.64	-1.2	-0.6
80	106.44	81.67	2.184	1.668	4.650	4.660	106.25	81.32	-0.2	-0.4

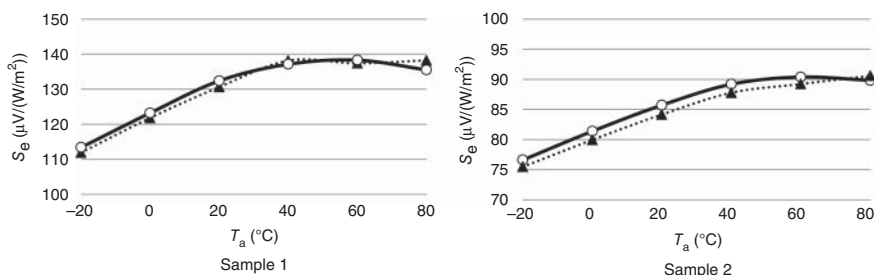


**Figure 11.4** Samples 1 and 2, comparison of calibration using precise external heat source (dashed) and by the method proposed (solid).

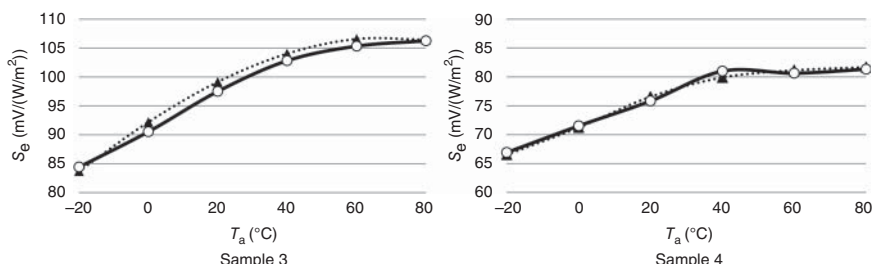


**Figure 11.5** Samples 3 and 4, comparison of calibration using precise external heat source (dashed) and by the method proposed (solid).

The required parameters of the sensors figure of merit  $Z$  and its own resistance  $ACR$  were measured by Z-metering method [15].

Tables 11.5 and 11.6 as well as Figures 11.4 and 11.5 show the comparison of the results of the two calibration methods.

The results of measurements by the two methods are very close.

Calibration by the new method is no more than 2% different from the results of the calibration with a reference source.

This is a good result for the practical use of the new method.

#### 11.4.2 Values of NEP and $D^*$

The new method also allows us to obtain the values of the parameters  $NEP$  and  $D^*$  for heat flux sensors by measuring the values  $Z$ ,  $ACR$ , and average temperature  $T$ :

$$NEP = \sqrt{4k_B} \times a \times 2N \times \frac{\sqrt{T}}{Z \times \sqrt{ACR}} \quad (11.37)$$

$$D^* = \frac{1}{\sqrt{4k_B}} \times \frac{\sqrt{s}}{a \times 2N} \times \frac{Z \times \sqrt{ACR}}{\sqrt{T}} \quad (11.38)$$

## 11.5 Sensor Performance and Thermoelectric Module Design

In the previous section, the main parameters of heat flux sensors and formulas that determine their dependence on physical properties and design features were discussed.

Table 11.7 presents these parameters of the sensors together with the key factors influencing them.

**Table 11.7** Main parameters of thermoelectric heat flux sensors.

#	Parameter	Symbol	Units	Formula	Optimal	Physical properties	Design parameters		
1	Absolute sensitivity	$S_a$	V/W	$S_a = \frac{1}{f} \times \frac{\alpha}{k}$	↑	$\alpha$	$\frac{1}{k}$	—	$\frac{1}{ab}$
2	Sensitivity	$S_e$	$\mu\text{V}/(\text{W}/\text{m}^2)$	$S_e = S_a \times s$	↑	$\alpha$	$\frac{1}{k}$	—	$\frac{1}{ab}$
3	Thermal resistance	$R_T$	K/W	$R_T = \frac{1}{2Nkf}$	↓	—	$\frac{1}{k}$	—	$\frac{1}{ab}$
4	Time constant	$\tau$	s	$\tau = \frac{C}{f \times k \times 2N}$	↓	—	$\frac{1}{k}$	—	$\frac{1}{2N}$
5	Detectivity	$D^*$	$\text{cm Hz}^{1/2}/\text{W}$	$D^* = \frac{1}{\sqrt{4k_B T}}$ $\frac{\alpha\sqrt{\sigma}}{k} \sqrt{\frac{s}{2Nf}}$	↑	$\alpha$	$\frac{1}{k}$	$\sqrt{\sigma}$	$\frac{1}{\sqrt{ab}}$
						$\sqrt{h}$	$\sqrt{s}$	$\frac{1}{\sqrt{2N}}$	

### 11.5.1 Dependence on Physical Properties

As follows from Table 11.7 thermoelectric heat flux sensors should be optimized by the physical properties ( $\alpha$ ,  $k$ ,  $\sigma$ ).

For sensitivity, the Seebeck coefficient  $\alpha$  should be higher with a lower thermal conductivity  $k$ .

On the contrary, a fast response ( $\tau$ ) and lower thermal resistance  $R_T$  require high thermal conductivity  $k$ .

Table 11.7 shows that a number of parameters affect the efficiency of thermoelectric heat flux sensors in different directions. Only one parameter in all cases should be as large as possible – it is the Seebeck coefficient.

### 11.5.2 Design Parameters

The dependence of the properties of the sensors on the design parameters is also different (Table 11.8).

- High sensitivity is achieved by reducing the cross-section  $ab$  and increasing the height  $h$  of thermocouples, and by growth of the sensitive area  $s$  of the sensor.
- At the same time, lower thermal resistance  $R_T$  and dynamic parameters ( $\tau$ ) require a greater cross-section  $ab$  and lower height  $h$  of a thermoelement.
- Only the thermal resistance and detectivity depend on thermocouples number. The dependence is multidirectional.

**Table 11.8** Dependence of sensor properties on design parameters.

Cross-section $a \times b$ , (mm <sup>2</sup> )	Height $h$ (mm)	$f$ , (mm)	Sensor parameters <sup>a)</sup>			
			$S_a$	$R_T$	$\tau$ ,	$D^*$ <sup>b)</sup>
0.2 × 0.2	0.3	0.133	1.00	1.00	1.00	1.00
	0.4	0.100	1.33	1.33	1.78	1.15
	0.5	0.080	1.66	1.66	2.78	1.29
0.3 × 0.3	0.4	0.225	0.59	0.59	1.78	1.28
	0.5	0.180	0.74	0.74	2.78	1.43
	0.8	0.113	1.19	1.19	7.11	1.81
0.4 × 0.4	0.5	0.320	0.42	0.42	2.78	1.29
	0.8	0.200	0.67	0.67	7.11	1.63
	1.0	0.160	0.83	0.83	11.11	1.83
	1.5	0.107	1.25	1.25	25.00	2.24

a) The parameters of sensors with pellets cross section  $0.2 \times 0.2$  mm<sup>2</sup> and height 0.3 mm are taken as reference (100%).

b) For these comparisons a constant (the same) number of thermocouples is taken for the different sensors.

## 11.6 Features of Thermoelectric Heat Flux Sensor Design

The above parameters of thermoelectric heat flux sensors do not take into account practical design features of the sensor.

Let us consider these features. Figure 11.6 shows a cross section of a thermoelectric heat flux sensor.

The special features of its design, in contrast to that of a thermoelectric module, are the following.

- External heat-conducting substrates
- Ceramic plates of module (not taken into account in some calculations)
- Sealing that fills the entire interior of the sensor

These features should be allowed for in the accurate simulation of a heat flux sensor.

First of all, it concerns a thermal “circuit” of the sensor. Figure 11.7 shows the equivalent diagram of the heat flux sensor with all the essential elements of design.

The equivalent circuit of the sensor makes it possible to introduce certain corrections to the basic formulae.

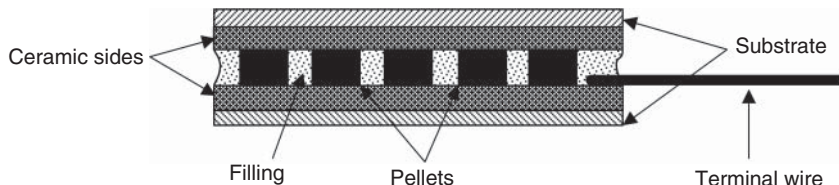
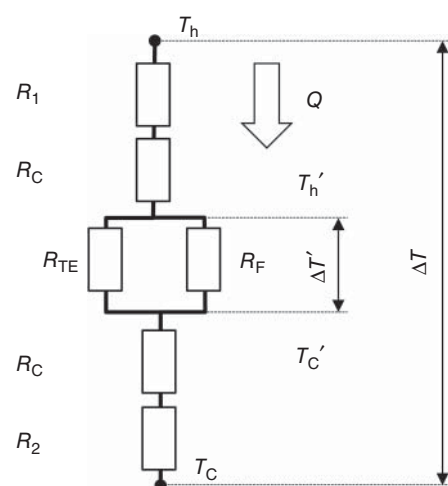


**Figure 11.6** Outlines of thermoelectric heat flux sensor.

**Figure 11.7** Equivalent diagram of heat flux sensor:  $R_1$ ,  $R_2$  – thermal resistance of upper and lower substrates;  $R_c$  – thermal resistance of upper and lower ceramic sides;  $R_F$  – thermal resistance of filling;  $R_{TE}$  – thermal resistance of thermocouples (pellets);  $T'_c$ ,  $T'_h$  – temperature of the hot and cold sides directly on pellets;  $\Delta T'$  – temperature difference directly on thermocouples.



Obviously, the thermo-EMF of the sensor results from the temperature difference on the sides of the thermocouples  $\Delta T'$ .

$$E = \alpha \times 2N \times \Delta T' \quad (11.39)$$

$$\Delta T' = \Delta T \times \frac{R_T}{\sum R_i} \quad (11.40)$$

The thermo-EMF depends on the ratio of the thermal resistance of the internal part of the sensor (thermocouples and filler)  $R_T$  to the full thermal resistance  $\sum R_i$  including the remaining external parts of the system –  $(R_1, R_2, R_c)$  for a given total temperature difference ( $\Delta T$ ).

However, the sensitivity to the heat flux according to formula (11.18) does not depend on the thermal resistance of the external elements and is only dependent on the internal thermal resistance (thermocouples and filler). The thermal resistance of the module with the filler is calculated taking into account the parallel thermal resistance of the thermocouples and the filler:

$$\frac{1}{R_T} = \frac{1}{R_{TE}} + \frac{1}{R_p} \quad (11.41)$$

With respect to the thermal conductance of the internal part of the sensor, the sum of thermal conductance values of the thermocouples and the filler is given by

$$K_T = K_{TEG} + K_p \quad (11.42)$$

$$K_T = 2N \times k_{TE} \times f + 2N \times k_p \times f \times (1 - y) = 2N \times f \times [k_{TE} + k_p(1 - y)] \quad (11.43)$$

where  $y$  is the filling factor of thermoelements ( $y = \frac{2Nab}{s}$ ).

Then the expression for sensitivity takes the form

$$S_a = \frac{1}{f} \times \frac{\alpha}{k_{TE} + k_p(1 - y)} \quad (11.44)$$

The sensor sensitivity is reduced due to the filler.

However, additional thermal conductance of the filler plays a positive role because it reduces the thermal resistance of the sensor as a whole, which is important for practical applications – the “additional wall.”

This more complex thermal equivalent circuit of the sensor influences its dynamic characteristics.

## 11.7 Optimization of Sensors Design

Properties of thermoelectric heat flux sensors depend on the design parameters. The technology of thermoelectric micromodules allows manufacturing such modules in a wide range of dimensions, degree of miniaturization, packing factors, thermocouples size, and so on.

So, it is possible to develop both individual and series heat flux sensors optimized for different applications.

The company TEC Microsystems uses this practice in the development and manufacturing of thermoelectric micromodules for cooling and generation. The same well-tested approaches are applicable to sensor optimization.

The key parameters of thermoelectric heat flux sensors are interrelated:

$$S_a = \frac{1}{f} \times \frac{\alpha}{k} \quad (11.45)$$

$$S_e = \frac{1}{f} \times \frac{\alpha}{k} \times s \quad (11.46)$$

$$D^* = \frac{1}{\sqrt{4k_B T}} \times \frac{\alpha \sqrt{\sigma}}{k} \times \sqrt{\frac{h}{y}} \quad (11.47)$$

$$\tau = \frac{C_c}{f \times k \times 2N} \quad (11.48)$$

As seen, the efficiency of thermoelectric heat flux sensors depends on

- 1) properties of the thermoelectric material –  $\alpha, k, \sigma, Z$ ;
- 2) design parameters of the thermoelectric module and its thermoelements –  $f, h, 2N, y$ ;
- 3) sensitive surface area  $s$ ; it can be the size of the thermoelectric module and larger.

### 11.7.1 Properties of Thermoelectric Material

The properties of thermoelectric material are specified by its manufacturing technology. These parameters can hardly be varied significantly for sensor optimizing. The only important thing is to select a material with a maximum Seebeck coefficient  $\alpha$ , typically at the level of the average values of 200  $\mu\text{V/K}$ .

In Table 11.9, the parameters of the typical thermoelectric material are given.

### 11.7.2 Parameters of Thermoelectric Module

The parameters of the thermoelectric module can be controlled over a wide range. Modern technologies allow producing modules of pellets in wide ranges of cross sections and heights, package densities, and element numbers.

Therefore, a detailed analysis of the dependence of sensor parameters on these design features is of primary interest for optimization problems.

#### 11.7.2.1 Pellets Form-Factor

The dependence of the sensitivity  $S_a$  of thermoelectric heat flux sensors on the form-factor  $f$  of pellets is shown in Figure 11.8.

**Table 11.9** Typical parameters of thermoelectric material of p- and n-type at 300 K.

Conductivity type	$\alpha$ ( $\mu\text{V/K}$ )	$\sigma$ , ( $\text{Ohm}^{-1} \times \text{cm}^{-1}$ )	$k$ ( $\text{W}/(\text{m} \times \text{K})$ )	$Z \times 10^3$ (1/K)
p	$\geq 190$	900–1100	1.30–1.45	2.9–3.2
n	$\geq 190$	900–1100	1.35–1.55	2.7–3.0

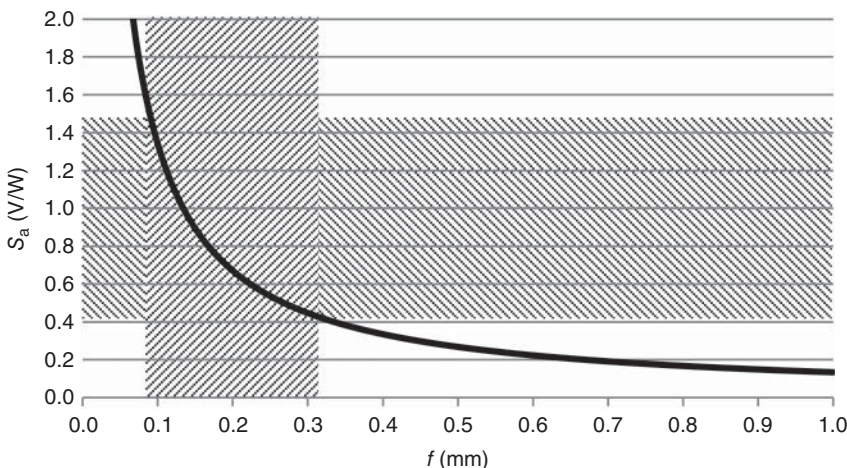


**Figure 11.8** Dependence of thermoelectric heat flux sensor sensitivity on the pellet form-factor.

**Table 11.10** Values of form-factors of the thermoelectric pellets.

Pellet height $h$ (mm)	$f$ (mm)		
	$a \times b = 0.2 \times 0.2$ (mm <sup>2</sup> )	$a \times b = 0.3 \times 0.3$ (mm <sup>2</sup> )	$a \times b = 0.4 \times 0.4$ (mm <sup>2</sup> )
	0.133	—	—
0.3	0.100	0.225	—
0.4	0.080	0.180	0.320
0.5	—	0.113	0.200
0.8	—	—	0.160
1.0	—	—	0.133
1.2	—	—	0.107
1.5	—	—	—

Table 11.10 shows the values of the form-factor of pellets.

Correspondingly, in Figure 11.8 the available range of sensitivities of heat flux sensors is marked.

### 11.7.2.2 Thermoelement Height

According to expression (11.45), at a given value of thermoelement cross-section  $a \times b$ , it follows that the sensitivity increases with the increasing of the height of the thermoelement  $h$ .

However, with the increasing of the height of the sensor its time constant grows too, according to formula (11.48). Therefore, obtaining a highly sensitive sensor together with high-speed performance is the optimization task for a particular application.

In Figure 11.9, the dependences of sensitivity and time constant on the thermoelement height for their various cross sections are given.

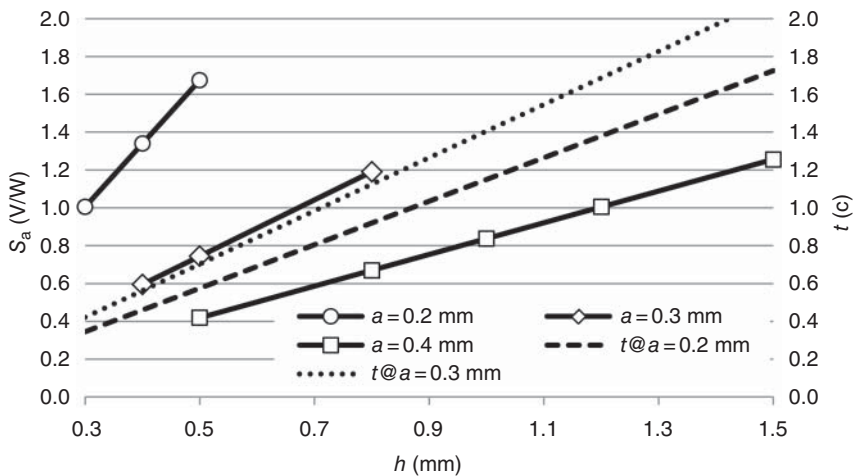


**Figure 11.9** Estimated dependences of the sensitivity  $S_a$  and the time constant  $\tau$  of the sensor on thermoelements height  $h$  for their different widths: 0.2; 0.3; and 0.4 mm.

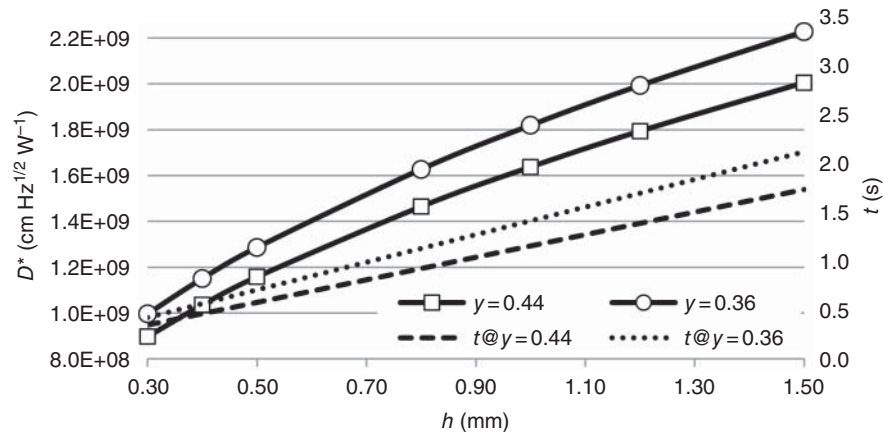


**Figure 11.10** Calculated dependence of the detectability  $D^*$  and time constant  $\tau$  of the height of thermocouples at their different packing density  $y$ .

The fastest and most sensitive sensors are possible using thermocouples of minimum cross section of 0.2 mm. High sensitivity is attainable for large element cross sections, but this reduces performance owing to the larger thermoelement height of such sensors.

Figure 11.10 depicts the calculated dependence of the detectability of the sensor on the height and packing density of the thermocouples.

The reduced dependence of  $D^*$  is similar to that of sensitivity. The value  $D^*$  increases with increasing height of thermoelements. At the same time, a less dense packing of thermocouples,  $y = 0.36$ , has an advantage compared to  $y = 0.44$ . But it has a simple explanation as a less dense packing implies a larger sensor, and correspondingly, more signal is collected by the sensor. However, a smaller packing density results in a larger time constant.

### 11.7.2.3 Dimensions of Sensors

The sensitivity to heat flux density  $S_e$  depends on the dimensions of the heat absorption side of the sensor. In a thermoelectric module, it is its hot side.

The size of a thermoelectric module side is determined by the number of elements, their cross section, and density of packing.

Figure 11.11 shows the calculated relative sensitivity for thermoelectric sensors from different series of modules (thermocouples of different sections and height).

### 11.7.2.4 Pellets Number

A larger size of the sensors means a larger number of thermoelements in them. This dependence is shown in Figure 11.12.

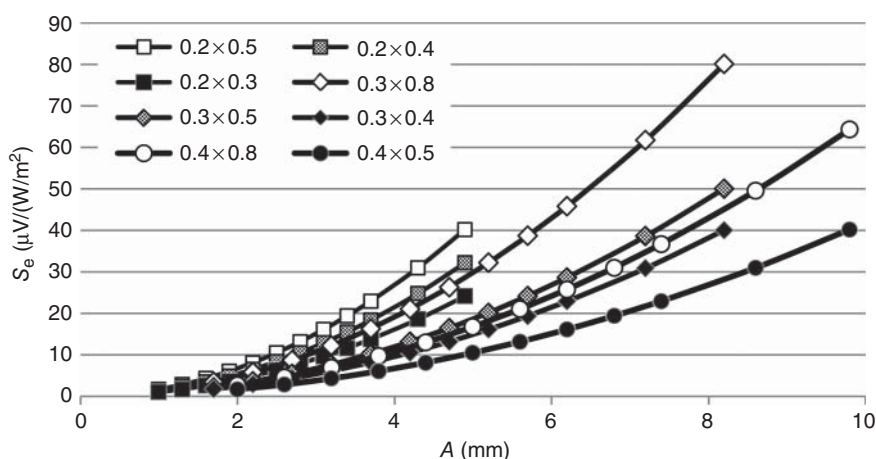


Figure 11.11 Dependence of sensitivity of thermoelectric sensors  $S_e$  on their size  $A$ .

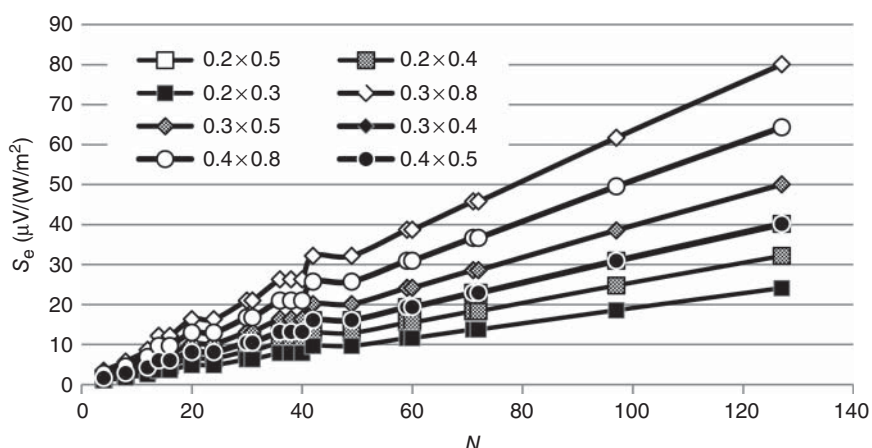


Figure 11.12 The relative sensitivity of thermoelectric sensors depending on the number of thermocouples in the sensor.

However, a greater number of thermoelements involves higher manufacturing complexity and, accordingly, a higher price of the sensor.

It should be noted that it is not the number of thermocouples that determines sensitivity. This dependence does not exist. It is the size of the module's receiving side that increases with the number of thermoelements.

### 11.7.3 Features of Real Design

The above dependences of the basic parameters of heat flux sensors on the main structural elements of the thermoelectric module give an idea of the order of magnitude. However, more accurate estimations of the main parameters require consideration of the real design of the sensor (Figure 11.13).

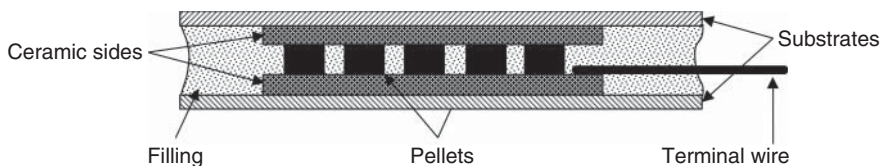


Figure 11.13 Outlines of a thermoelectric heat flux sensor.

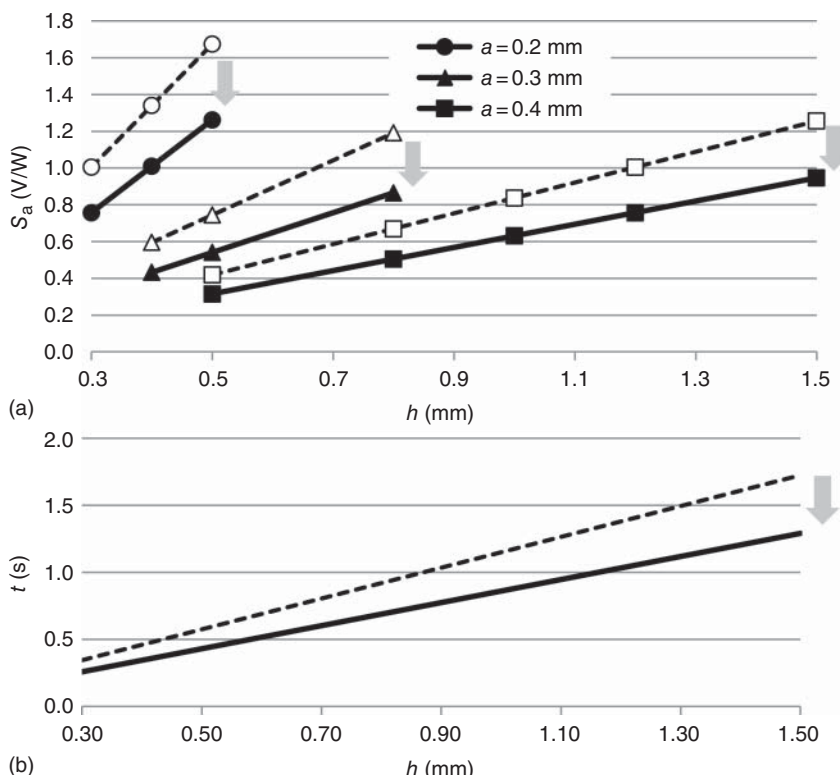
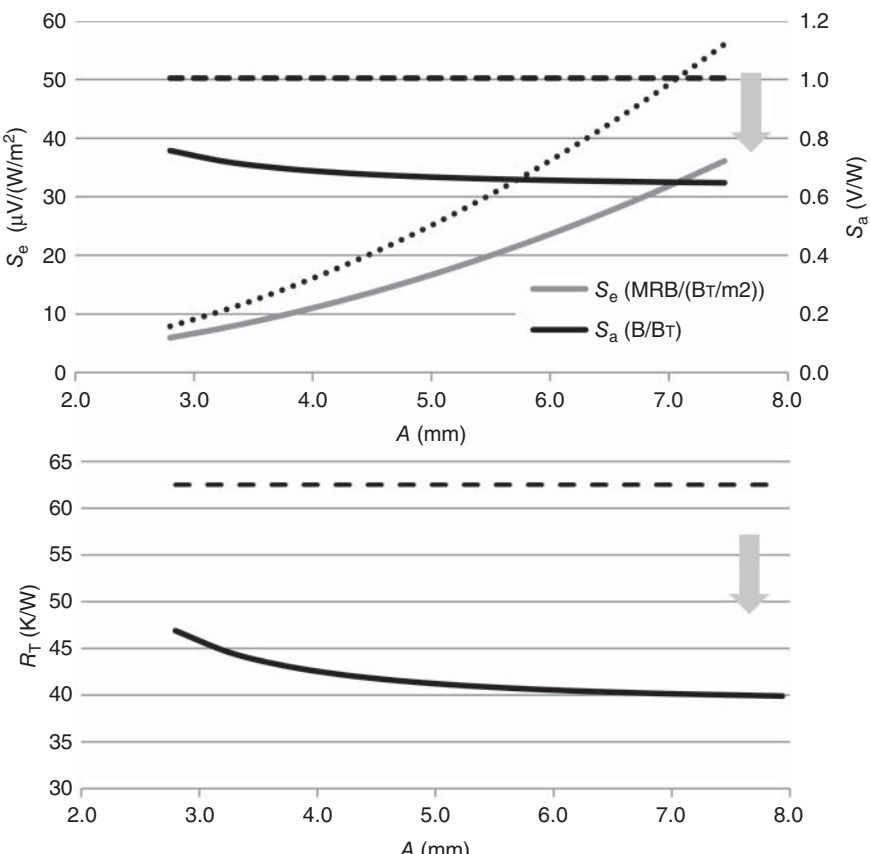


Figure 11.14 Effect of filler on sensitivity (a) and time constant (b) of sensors of various sections  $a$  and height  $h$  of thermocouples: with silicone filler and no fill (dotted line).

The actual sensor design must take into account the following (Figure 11.14):

- 1) A filler/sealant almost always fills the interior of the sensor. First of all, it ensures protection from moisture and other environmental factors. Secondly, the correct operation of the sensor by the method of “additional wall” depends on the sensor thermal resistance. The lower the thermal resistance, the less distortion of the measured heat flux. However, the thermal resistance of the filler contributes to the thermal resistance of the module. Thus, the total thermal resistance increases and the temperature drops are reduced. The filler effect should be optimized.
- 2) To increase the relative sensitivity of the sensors, its sensitive side may have an increased size in comparison with that of the thermoelectric module. On the one hand, it increases the sensitivity; on the other hand, it results in some inhomogeneity on the receiving surface. It also increases the sensor time constant.

Figure 11.15 demonstrates the above dependences with the example of a particular heat flux sensor.



**Figure 11.15** An example of the calculated parameters of the heat flux sensor based on a 40-pair thermoelectric module 1MD02-040-03 of thermocouples  $0.2 \times 0.2 \times 0.3 \text{ mm}^3$  depending on the size of the sensor surface  $A$ . The dotted line – no filler.

## 11.8 Experimental Family of Heat Flux Sensors

Based on the above analysis the experimental family of heat flux sensors consisting of three subseries was developed [18].

### 11.8.1 HTX – Heat Flux and Temperature Sensors (HT – Heat Flux and Temperature)

The sensors (Table 11.11) contain a thermoelectric heat flux sensor and embedded Pt1000 thermistor. They have a round shape and external aluminum sides with black finish. The sensors are potted by a silicone resin.

### 11.8.2 HFX – Heat Flux Sensors without Temperature (HF – Heat Flux)

The sensors (Table 11.12) have a square shape and external sides of AlN ceramics with black paint finish. The sensors are potted by a silicone resin.

### 11.8.3 HRX-IR Radiation Heat Flux Sensors (HR – Heat Flux Radiation)

These are miniature thermoelectric heat flux sensors (Table 11.13). They are made suitable for flip-chip mounting. They have a square shape and external sides of AlN ceramics. The downside has gold-plated electrical contacts, and the

**Table 11.11** Performance parameters of heat flux sensors series HTX.

Sensor	Sensitivity		$\tau$ (s)	$R_T$	ACR (Ohm)	$dS/dT^a$ (%/°C)	
	$S_a$ (V/W)	$S_e$ ( $\mu$ V/(W/m <sup>2</sup> ))					
HTD04-059-08D12	0.45	50	3.2	18.6	2.1E-03	5.91	0.20
HTD04-127-05D16	0.35	70	3.1	6.77	1.4E-03	8.03	0.20
HTD04-126-05D20	0.32	100	6.8	6.21	2.0E-03	7.96	0.20
HTD06-126-08D25	0.23	110	6.6	4.40	2.1E-03	5.55	0.20
HTD06-126-08D30	0.18	130	7.2	3.54	2.5E-03	5.55	0.20
HTD06-284-08D40	0.21	265	6.8	1.81	2.3E-03	12.5	0.20

Name	Dimensions	Range	Temperature (°C)	Temperature sensor							
				Dia.	Height	± W/m <sup>2</sup>	W (mm)	Type	$R_0$ (Ohm)	$\delta R$ (Ohm)	$dR/dT$ (%/°C)
HTD04-059-08D12	12	2.4	4500	0.5	–40 ... +80	Pt1000	1000	1	0.375	±0.1	
HTD04-127-05D16	16	2.1	7500	1.5	–40 ... +80	Pt1000	1000	1	0.375	±0.1	
HTD04-126-05D20	20	3.1	5000	1.6	–40 ... +80	Pt1000	1000	1	0.375	±0.1	
HTD06-126-08D25	25	3.4	4500	2.3	–40 ... +80	Pt1000	1000	1	0.375	±0.1	
HTD06-126-08D30	30	3.4	4000	2.8	–40 ... +80	Pt1000	1000	1	0.375	±0.1	
HTD06-284-08D40	40	3.4	4500	5.5	–40 ... +80	Pt1000	1000	1	0.375	±0.1	

a) The average operating range temperature dependence is given.

**Table 11.12** Performance parameters of heat flux sensors series HFX.

Sensor	Sensitivity		$\tau$ (s)	$R_T$		ACR (Ohm)	$dS/dT^a)$ (%/°C)
	$S_a$ (V/W)	$S_e$ ( $\mu$ V/(W/m <sup>2</sup> ))		K/W	K/(W/m <sup>2</sup> )		
HFD02-040-04L04	1.32	21	1.4	80.1	1.3E-03	7.95	0.25
HFD03-060-04L06	0.72	26	1.5	29.2	1.1E-03	5.36	0.25
HFD04-059-05L08	0.47	30	1.6	19.3	1.2E-03	3.73	0.25
HFD04-097-05L10	0.48	48	1.6	12.0	1.2E-03	6.08	0.25
HFD06-127-05L12	0.28	40	1.0	5.29	7.6E-04	8.03	0.25
HFC06-126-05L14	0.24	47	1.3	4.65	9.1E-04	7.96	0.25

Name	Dimensions (mm)			Range of measured values		Temperature range (°C)
	A	B	H	$\pm$ W/m <sup>2</sup>	W	
HFD02-040-04L04	4	4	1.10	8 000	0.15	-40 ... +80
HFD03-060-04L06	6	6	1.10	10 000	0.35	-40 ... +80
HFD04-059-05L08	8	8	1.60	8 500	0.55	-40 ... +80
HFD04-097-05L10	10	10	1.60	8 500	0.85	-40 ... +80
HFD06-127-05L12	12	12	1.60	13 500	1.90	-40 ... +80
HFC06-126-05L14	14	14	1.60	11 000	2.15	-40 ... +80

a) The average operating range temperature dependence is given.

**Table 11.13** Performance parameters of heat flux sensors series HRX.

Name	Sensitivity		$\tau$ (s) $D^*$ (cm Hz <sup>1/2</sup> /W)	Emissivity	$R_T$ K/W	ACR (Ohm)	$dS/dT$ (%/°C) <sup>a)</sup>
	$S_a$ (V/W)	$S_e$ ( $\mu$ V/(W/m <sup>2</sup> ))					
HRD02-040-03L04	0.68	11	0.43 1.3E+09	0.95	42.4 6.8E-04	6.0	0.25
HRD02-040-05L04	1.14	18	0.71 1.7E+09	0.95	70.5 1.3E-03	10.0	0.25
HRD03-040-05L06	0.51	18	0.71 1.7E+09	0.95	31.3 1.3E-03	4.4	0.25

Name	Dimensions (mm)			Measurement range		Temperature range (°C)
	A	B	H	$\pm$ W/m <sup>2</sup>	W	
HRD02-040-03L04	4	4	0.8	14 500	0.24	-40 ... +80
HRD02-040-05L04	4	4	1.0	9 000	0.14	-40 ... +80
HRD03-040-05L06	6	6	1.0	9 000	0.32	-40 ... +80

a) The average operating range temperature dependence is given.

radiation absorption surface has a black coating with high emissivity (95%). The sensors are potted by a silicone resin.

## 11.9 Investigation of Sensors Performance

### 11.9.1 General Provisions

The purpose of the investigation is to study the characteristics of the developed sensors.

The sensor electrical resistance ACR and figure of merit  $Z$  were measured at different temperatures in the thermostat by the Z-meter.

The purpose of the measurements in the thermostat is to find the most convenient method for the sensors' calibration in a temperature range.

Two sensors of each type were measured.

The temperature dependences of the following parameters of the sensors were studied:

- Figure of merit (Z-metering)
- Electrical resistance
- Thermo-EMF versus sensor heat load
- Sensor temperature difference at various heat loads
- Sensor thermal resistance

*Note:*

The figure of merit (Z-metering) and electrical resistance of the sensors were also measured in the thermostat by the Z-meter with a massive thermal screen in the area of the sensors, thus avoiding a temperature gradient in this area.

### 11.9.2 Calibration of Sensor Sensitivity

Two methods were used for calibration of the sensors' sensitivity and the results were compared.

First – calibration with precise reference heat source mounted to sensor samples. Temperature dependence and all measurements were done with use of the machine DX8020 [19].

The sensors' sensitivity (11.36) by a new method [17] in the same temperature range was measured with samples placed into the thermostat DX2100 and with use of Z-meter DX4190 [20].

For this new method (11.36) the standard temperature dependence of the Seebeck coefficient for the material of micromodules was applied.

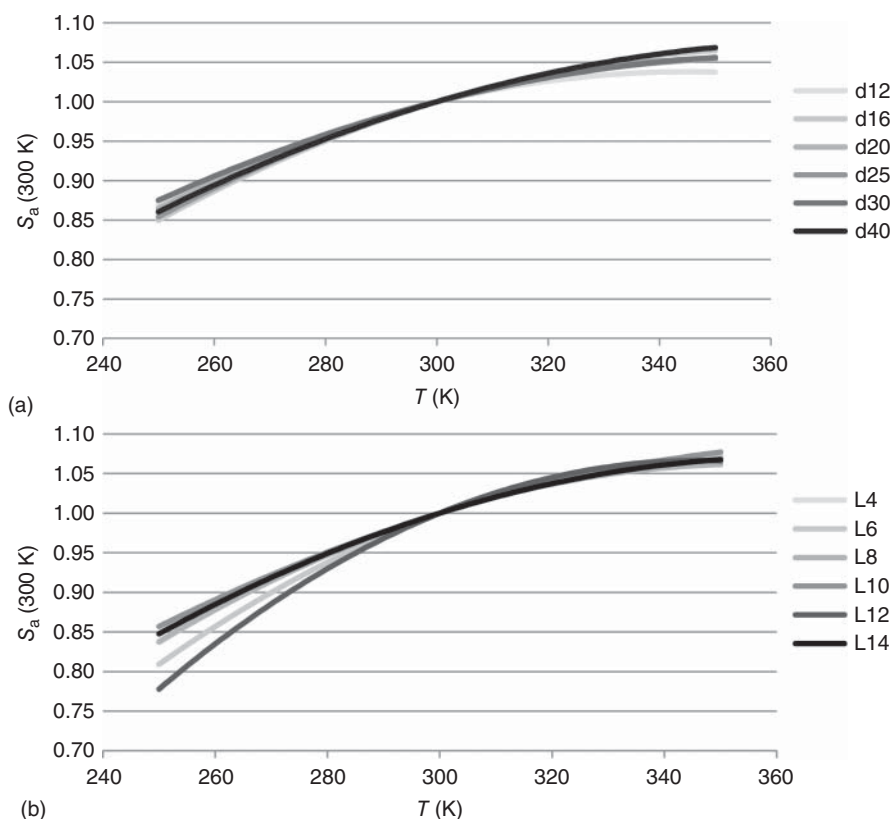
$$\alpha = 3,224788 \times 10^{-11} \times T^3 - 3,25788 \times 10^{-8} \times T^2 + 1,137103 \times 10^{-5} \\ \times T - 9,387217 \times 10^{-4} \quad (11.49)$$

The resulting temperature dependences of sensitivity for the examined sensors measured by the two methods are given in Table 11.14. On the basis of this table the averaged polynomial dependence of sensor sensitivity on temperature is built (temperature in Kelvin).

The results obtained by the two methods are in good agreement (Figure 11.16).

**Table 11.14** Experimental temperature dependences of sensitivity.

Sensor type	Polynomial by data of DX8020	Polynomial by Z-meter DX4190
HFD02-040-04L04	$S_e = -2.20E-04*T^2 + 1.60E-01*T - 1.49E+01$	$S_e = -2.93E-04*T^2 + 2.08E-01*T - 2.17E+01$
HFD03-060-04L06	$S_e = -2.20E-04*T^2 + 1.60E-01*T - 1.49E+01$	$S_e = -3.55E-04*T^2 + 2.52E-01*T - 2.88E+01$
HFD04-059-05L08	$S_e = -3.44E-04*T^2 + 2.61E-01*T - 2.64E+01$	$S_e = -4.34E-04*T^2 + 3.09E-01*T - 3.20E+01$
HFD04-097-05L10	$S_e = -3.83E-04*T^2 + 2.86E-01*T - 1.83E+01$	$S_e = -4.37E-04*T^2 + 3.35E-01*T - 2.81E+01$
HFD04-127-05L12	$S_e = -1.33E-03*T^2 + 9.25E-01*T - 1.10E+02$	$S_e = -1.51E-03*T^2 + 1.04E+00*T - 1.29E+02$
HFC04-126-05L14	$S_e = -1.14E-03*T^2 + 7.90E-01*T - 7.53E+01$	$S_e = -1.01E-03*T^2 + 7.41E-01*T - 7.10E+01$
HTD04-059-08D12	$S_e = -9.98E-04*T^2 + 6.874E-01*T - 6.53E+01$	$S_e = -9.57E-04*T^2 + 6.61E-01*T - 6.06E+01$
HTD04-127-05D16	$S_e = -1.08E-03*T^2 + 7.68E-01*T - 7.27E+01$	$S_e = -1.01E-03*T^2 + 7.35E-01*T - 7.01E+01$
HTC04-126-05D20	$S_e = -1.53E-03*T^2 + 1.07E+00*T - 1.02E+02$	$S_e = -1.34E-03*T^2 + 9.61E-01*T - 8.50E+01$
HTC06-126-08D25	$S_e = -2.14E-03*T^2 + 1.52E+00*T - 1.51E+02$	$S_e = -2.02E-03*T^2 + 1.44E+00*T - 1.38E+02$
HTC06-126-08D30	$S_e = -1.99E-03*T^2 + 1.42E+00*T - 1.10E+02$	$S_e = -1.87E-03*T^2 + 1.37E+00*T - 1.07E+02$
HTC06-284-08D40	$S_e = -4.46E-03*T^2 + 3.18E+00*T - 2.75E+02$	$S_e = -3.92E-03*T^2 + 2.93E+00*T - 2.49E+02$

**Figure 11.16** Temperature dependences of sensitivity of the sensor series HTX (a) and HFX (b).

### 11.9.3 Sensitivity Temperature Dependence

We are to obtain the average sensitivity temperature dependence (Figure 11.17) of the following polynomial form:

$$S_a = S_{a0} \times [(A_2 \times (T - T_0)^2 + A_1 \times (T - T_0) + A_0)] \quad (11.50)$$

The coefficients of the polynomial of the  $S_a$  temperature dependence of the sensitivity  $S_a$  of the above series in the range of  $-50$  to  $+80$  °C and temperature coefficient in the calibration point (300 K) are shown in Table 11.15.

The difference in the temperature dependences (temperature coefficients) is associated with additional thermal conductance of the sensors' filler.

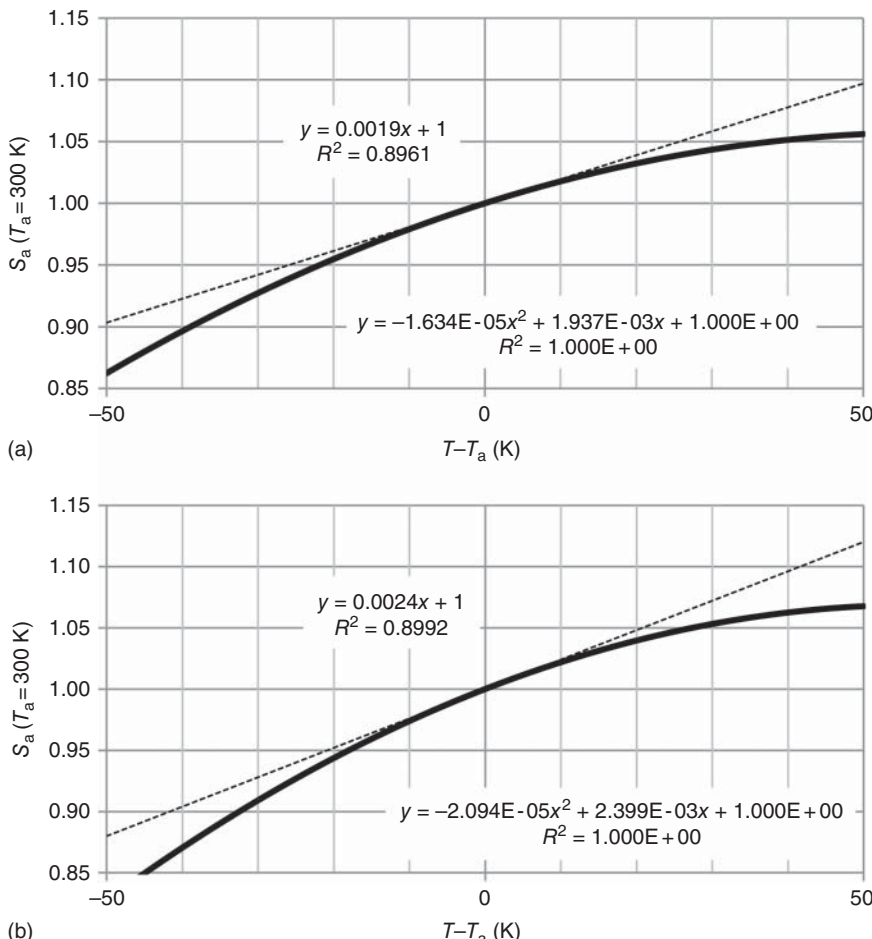


**Figure 11.17** Average calibration temperature dependence of sensitivity for the sensors of the series HTX (a) and HFX (b).

**Table 11.15** Coefficients of the polynomial of the sensitivity temperature dependence of sensors.

Sensor series	A0	A1	A2	dS/dT (%)	T <sub>a</sub> (K)
HTX	1	1.937E-05	-1.634E-03	0.19	300
HFX	1	2.299E-05	-2.094 E-03	0.24	300
HRX	1	2.299E-05	-2.094 E-03	0.24	300

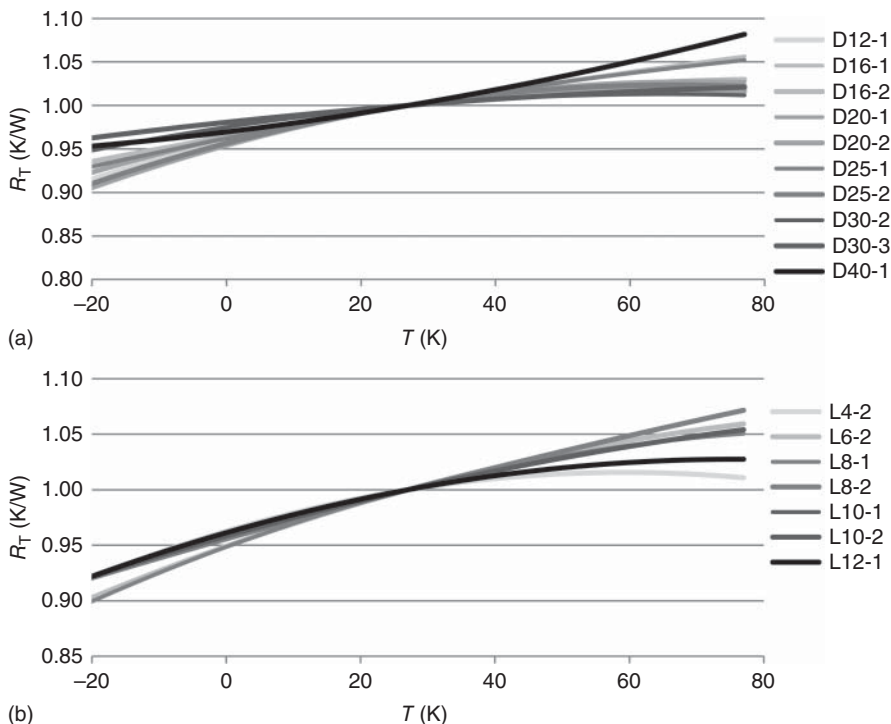


**Figure 11.18** Temperature dependences of thermal resistance of sensors series HTX (a) and HFX (b).

In the sensors of the series HTX the filler occupies a larger volume, and therefore the temperature dependence of their properties is less pronounced than in the series HFX.

Similar tests of temperature dependences for the HRX sensor series are complex, but the design of the sensors of this series is similar to that of the series HFX, so the temperature dependences for the series HRX are taken to be the same as for the series HFX.

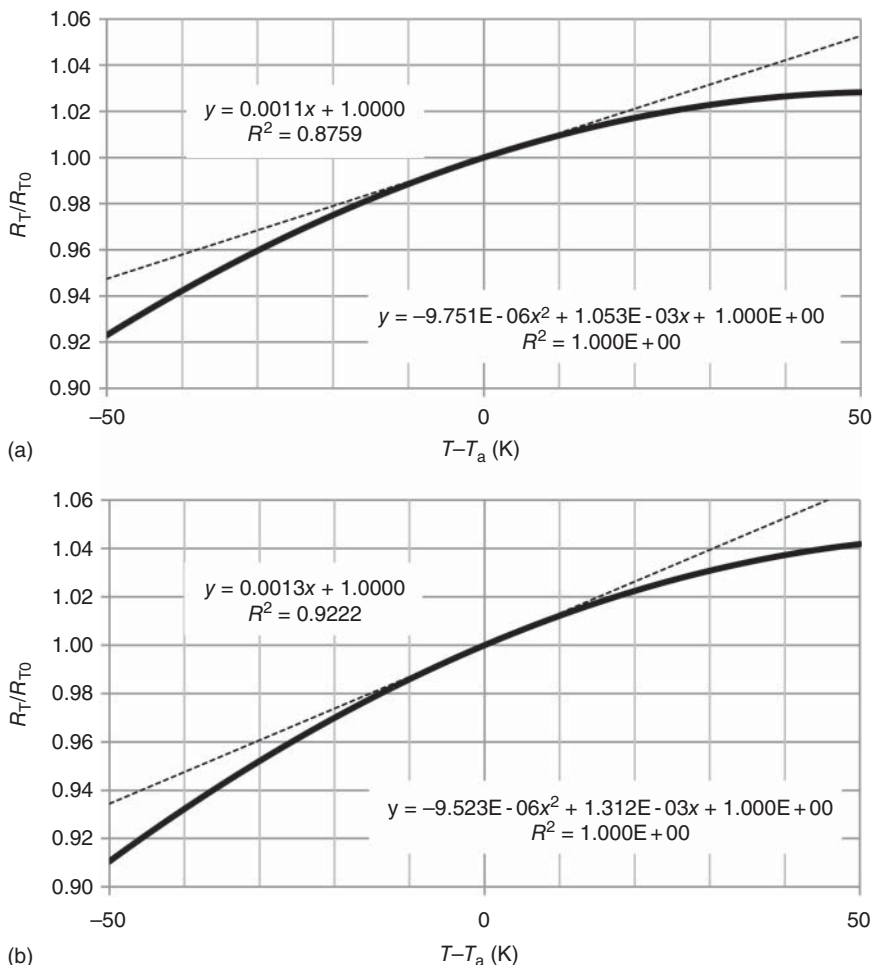


**Figure 11.19** Average calibration temperature dependences of thermal resistance of sensors series HTX (a) and HFX (b).

#### 11.9.4 Thermal Resistance

The experimental temperature dependences of thermal resistance of sensors are shown in Figure 11.18. The thermal resistance change in the temperature range of  $-20$  to  $+80$  °C is about 11%.

We are to obtain the temperature dependence of the average thermal resistance (Figure 11.19) of the following polynomial form:

$$R_T = R_{T_0} \times [(A_2 \times (T - T_0)^2 + A_1 \times (T - T_0) + A_0)] \quad (11.51)$$

The coefficients of the temperature dependence polynomials of the thermal resistance of the sensors in the range of  $-50$  to  $+80$  °C and the temperature coefficient in the calibration point (300 K) are given in Table 11.16.

**Table 11.16** Coefficients of the temperature dependence polynomials of the thermal resistance  $R_T$ .

Sensors series	A0	A1	A2	$dR_T/dT$ (%)	$T_a$ (K)
HTX	1	-9.751E-05	+1.053E-03	0.11	300
HFX	1	-9.523E-05	+1.312E-03	0.13	300
HRX	1	-9.523E-05	+1.312E-03	0.13	300

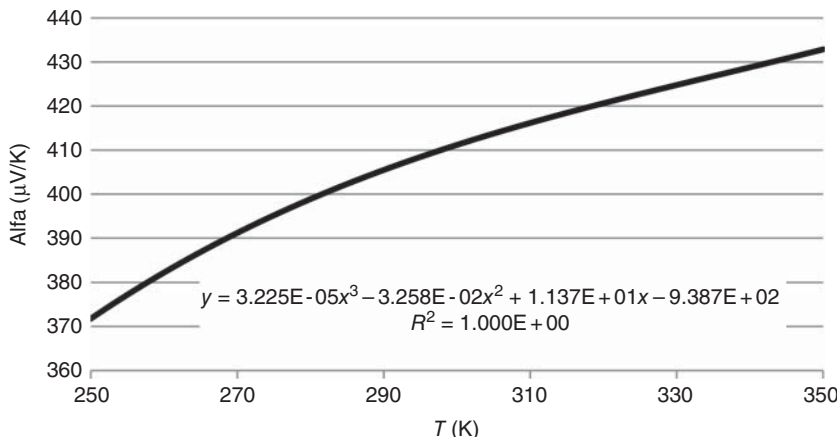


Figure 11.20 Typical temperature dependence of Seebeck coefficient.

### 11.9.5 Typical Temperature Dependence of the Seebeck Coefficient

Since the heat flux sensor self-calibration method involves the thermoelectric material parameter – the Seebeck coefficient, it should be also given in the specifications. It is the value at the standard temperature 300 K and the temperature dependence is similar to the polynomials for sensitivity and thermal resistance.

The typical temperature dependence of the Seebeck coefficient is shown in Figure 11.20. In the coordinates  $(T - T_a)$  this dependence is as shown in Figure 11.21. The coefficients of the polynomials in the range  $-50 \dots +80^\circ\text{C}$  are given in Table 11.17.

### 11.9.6 Conclusions

The methods of self-calibration of sensor sensitivity – direct measurements with use of precise thermal reference source with the machine DX8020 [19] and the new method [17] in the thermostat DX2100 by the Z-meter DX4190 [20] – showed approximately equal results.

For the self-calibration the value of the Seebeck coefficient and its temperature dependence are specified.

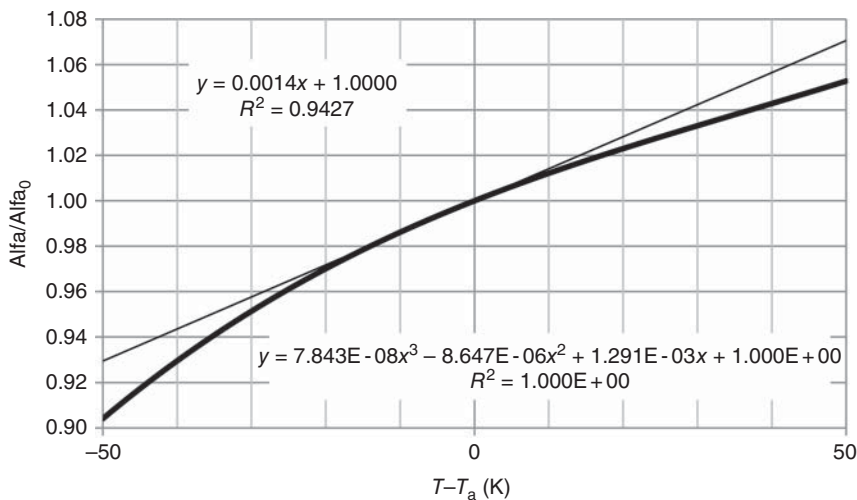


**Figure 11.21** Calibration temperature dependence of Seebeck coefficient.

**Table 11.17** Coefficients of the polynomial of Seebeck coefficient.

Typical value $a_0$ ( $\mu\text{V/K}$ )	A0	A1	A2	A3	$T_a$ (K)
410	1	+1.291E-03	-8.647E-06	+7.843E-08	300

The following parameters are also found in the specifications (all referred to  $T_a = 300$  K):

- Sensitivity  $S_e$  ( $\mu\text{V}/(\text{W/m}^2)$ )
- Thermal resistance  $R_T$  ( $\text{K}/(\text{W/m}^2)$ )
- AC resistance ACR (Ohm)

Typical (average) temperature dependences of these parameters are also given. The sensor thermal resistance is a reference parameter, and this value can be given as an estimated value.

Average thermal conductivity of the thermoelectric material W/(mK):

$$k = 3.3564 \times 10^{-7} \times T^3 - 2.7982 \times 10^{-4} \times T^2 + 7.3939 \times 10^{-2} \times T - 4.4958 \quad (11.52)$$

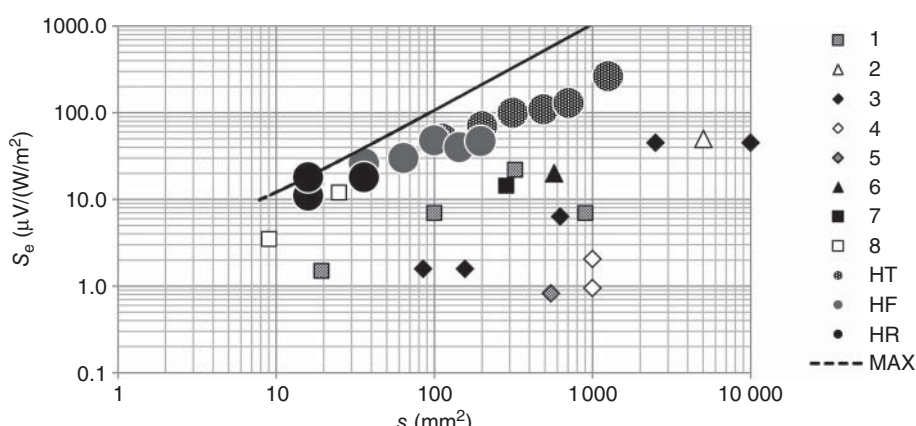
## 11.10 Heat Flux Sensors at the Market

Owing to innovative solutions to designing thermoelectric micromodules, such thermoelectric heat flux sensors have significant advantages over the heat flux sensors of manufacturers known in the market (Table 11.18).

- 1) High absolute sensitivity 10–50 times higher than in sensors based on differential thermocouples.
- 2) Miniature design, due to a high degree of integration of thermal elements in micromodules.
- 3) Controlled thermal resistance due to the flexibility in the design of micromodules – height of pellets. This allows obtaining quite low thermal resistance for heat flux sensors used in soil, for example. A sensor used in microcalorimetry and so on can have high thermal resistance, thus significantly increasing sensor sensitivity.
- 4) Fast response.

**Table 11.18** Manufacturers of state-of-art heat flux sensors.

#	Company	Country	Contact information
1	greenTEG AG	Switzerland	<a href="http://shop.greenteg.com/">http://shop.greenteg.com/</a>
2	Hukseflux Thermal Sensors B.V.	Netherlands	<a href="http://www.hukseflux.com/">http://www.hukseflux.com/</a>
3	ITI Thermal Instrument Company	USA	<a href="http://www.thermalinstrumentcompany.com/">http://www.thermalinstrumentcompany.com/</a>
4	Omega Engineering, Inc.	USA	<a href="http://www.omega.com/">http://www.omega.com/</a>
5	RdF Corporation	USA	<a href="http://www.rdfcorp.com/index.html">http://www.rdfcorp.com/index.html</a>
6	NPP "Etalon" Llc	Russia	<a href="http://www.omsketalon.ru/">http://www.omsketalon.ru/</a>
7	WUNTRONIC GmbH	Germany	<a href="http://www.wuntronic.com/">http://www.wuntronic.com/</a>
8	JonDeTech Sensors AB	Sweden	<a href="http://jondetech.com/">http://jondetech.com/</a>

**Figure 11.22** The sensitivity  $S_e$  of heat flux sensors of various manufacturers (1–8) and experimental series of TEC Microsystems (HT, HF, HR) depending on size. The dashed line is the line of the maximum attainable parameters of the technology.

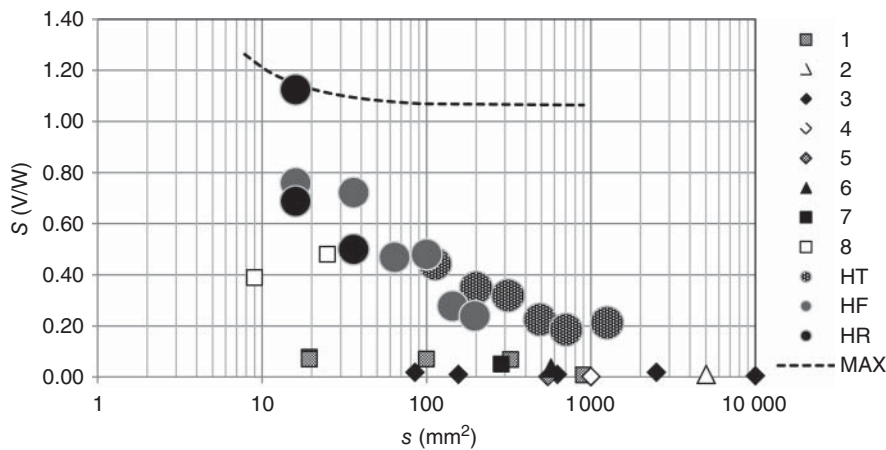


**Figure 11.23** Absolute sensitivity  $S_a$  of heat flux sensors of various manufacturers (1–8) and experimental series (HT, HF, HR) depending on size. The dashed line is the line of the maximum attainable parameters of the technology.

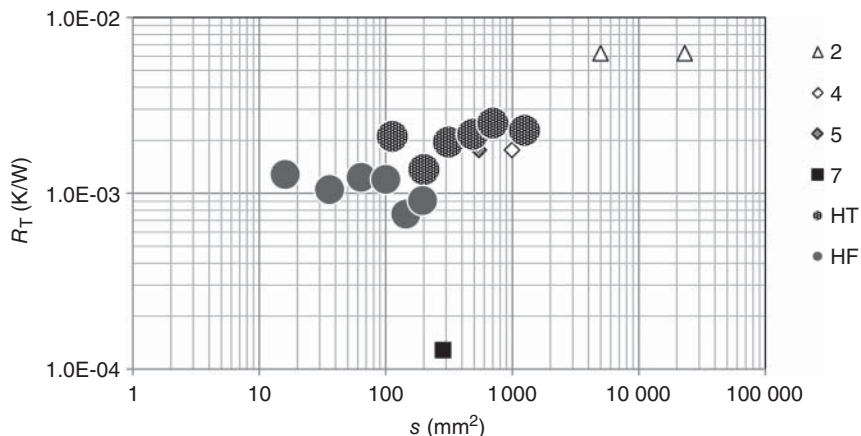


**Figure 11.24** Thermal resistance  $R_T$  of heat flux sensors of various manufacturers (2, 4, 5, 7) and experimental series (HT, HF) depending on size.

Figures 11.22–11.24 graphically depict a comparison of the main parameters of the developed series of TEC Microsystems heat flux sensors with those of well-known manufacturers. The manufacturers are represented by numbers 1–8 (Table 11.18).

As follows from the data on sensitivity, the heat flux sensors of the experimental series are significantly superior to most sensors currently in use. Moreover, the technology allows manufacturing sensors of more high performance (the dashed curve on the graphs).

The heat flux sensors based on the principle of additional wall should have low thermal resistance so as not to distort the measured heat flux.

The sensors have thermal resistance at the level of values used in practice (other manufacturers).

## 11.11 Examples of Applications

### 11.11.1 Microcalorimetry: Evaporation of Water Drop

A classic example of the use of a heat flux sensor is the study of water evaporation.

In Figure 11.25, the experimental setup is illustrated.

A drop of water is placed directly on the sensitive surface of the heat flux sensor – model HTD04-126-05D20 (Table 11.11).

When water evaporates, there is a process of heat absorption. The evaporation heat is 2256 J/g. Heat is absorbed both from the base surface and the environment. We can assume the relationship between the heat fluxes from the base and from the environment as 50 : 50.

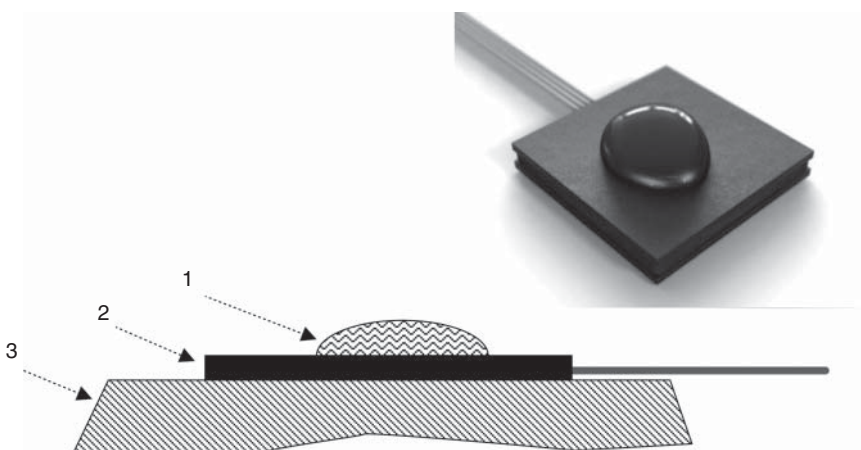


**Figure 11.25** Experimental scheme of microcalorimetry of water evaporation: 1 – water drop; 2 – heat flux sensor; 3 – massive base.

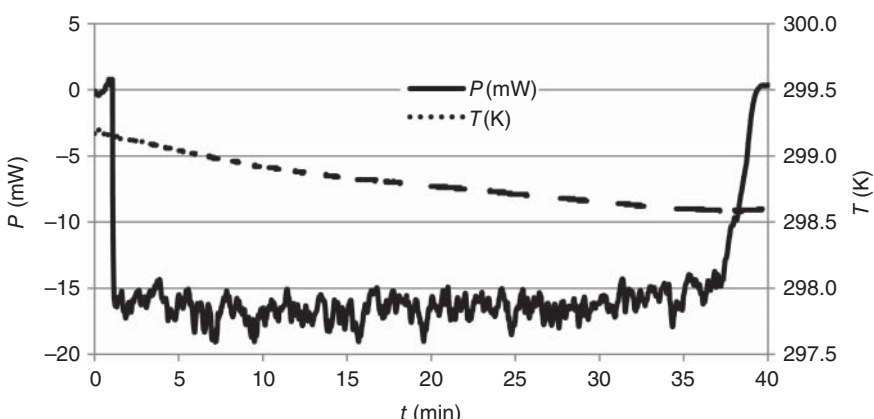


**Figure 11.26** Experiment of water drop evaporation. The dynamics of heat flux from the base absorbed and the average base temperature for the period considered.

The sensor can measure the heat flux absorbed from the base and the average temperature by the integrated thermistor.

Figure 11.26 shows the results of the experiment.

Since the heat of evaporation of water is known, from the heat flux (the total absorbed energy) and the assumption of 50:50 we can obtain the dynamics of the evaporation of the drop mass and its total weight. Figure 11.27 shows the corresponding experimental data.

It is interesting that the evaporation rate is approximately constant throughout the cycle.

The experimental results give an estimate of the drop volume of about 0.032 ml, which is consistent with the known data. These results indirectly confirm a good calibration of the heat flux sensor.

### 11.11.2 Measurement of Heat Fluxes in Soil

Figure 11.28 depicts a model of the measurement of heat flux in the soil. Two heat flux sensors are placed in the soil at different depths. The heat source is an incandescent lamp – imitates sunlight. The intensity of the heat flux is varied by changing the amount of radiation from the heat source.

Figure 11.29 shows the corresponding experimental data.

This application of thermoelectric heat flux sensors is very helpful for purposes of agricultural working, particularly during periods of season transformations.

### 11.11.3 Thermoelectric Ice Sensor

Ice sensor is an important type of sensor. It has various applications [21–24]. Ice sensors are intended for definition of characteristics of freezing (formation of ice) for the purpose of timely notification, effective use of anti-icing systems, safety on transport, in industrial applications, and in life.

The main objectives of the ice sensor are measurement of temperature of freezing; determination of intensity of ice formation; definition of proximity of conditions for formation of ice.

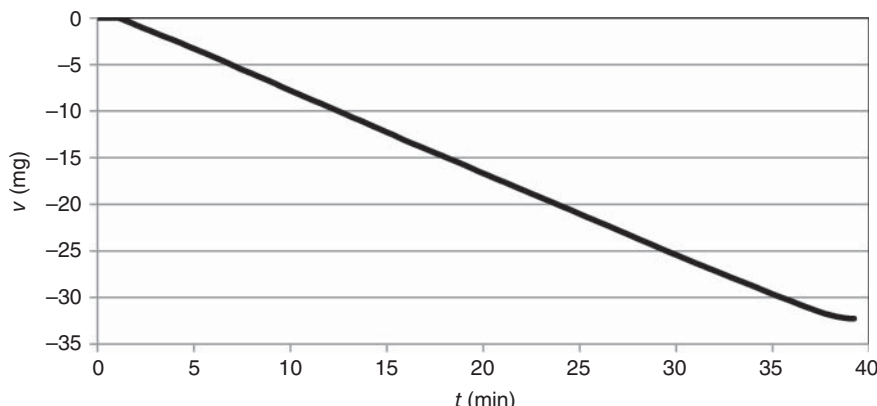
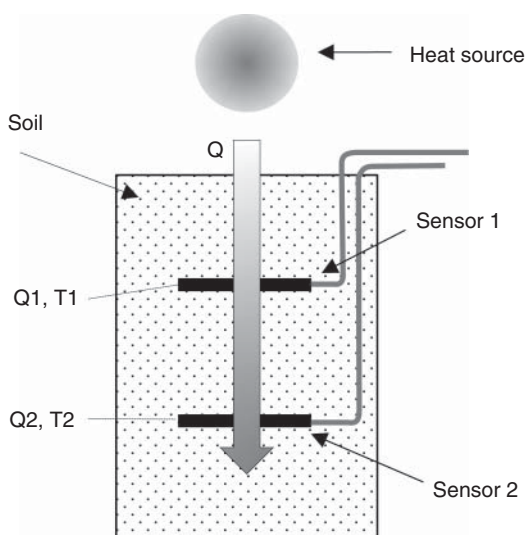
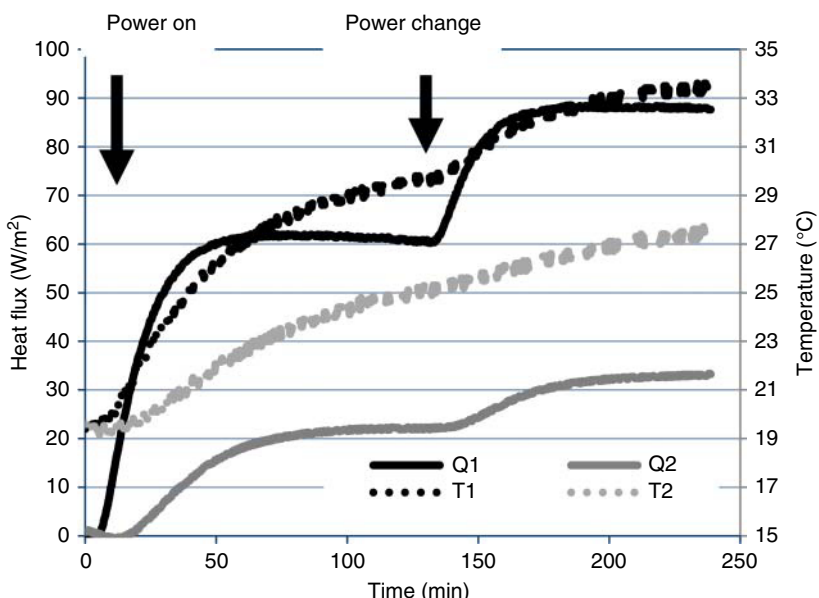


Figure 11.27 Dynamics of water evaporation (mass loss).



**Figure 11.28** Model experiment of heat fluxes in the soil.



**Figure 11.29** Results of experiment of heat fluxes in the soil.

Important consumer parameters of ice sensors include accuracy of determination of the measured parameters, speed of response, overall dimensions, and energy consumption.

Various physical principles in modern ice sensors [24], however in most cases that is indirect measurement of ice formation, with an insufficient accuracy. It is quite often sensing of the presence of a noticeable layer of the formed ice.

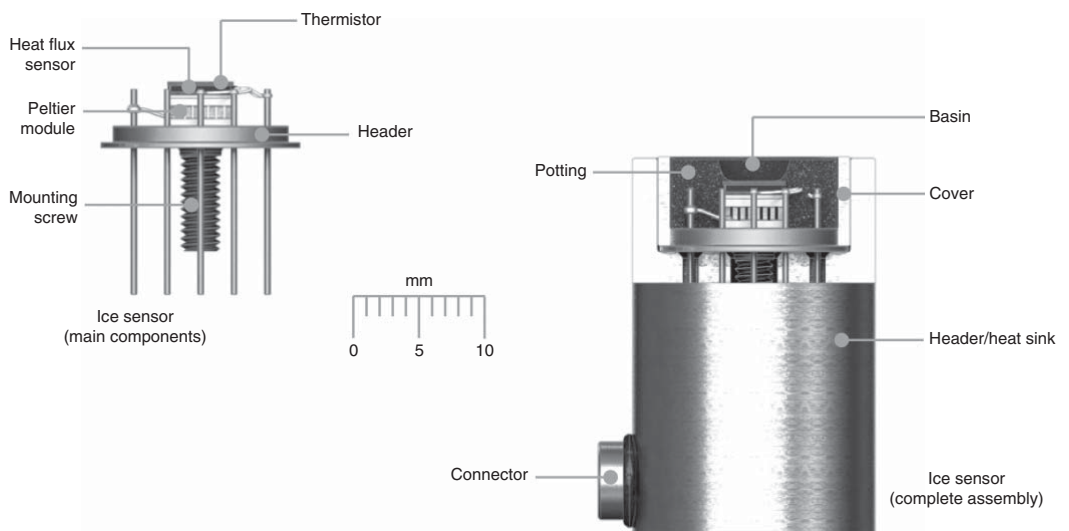


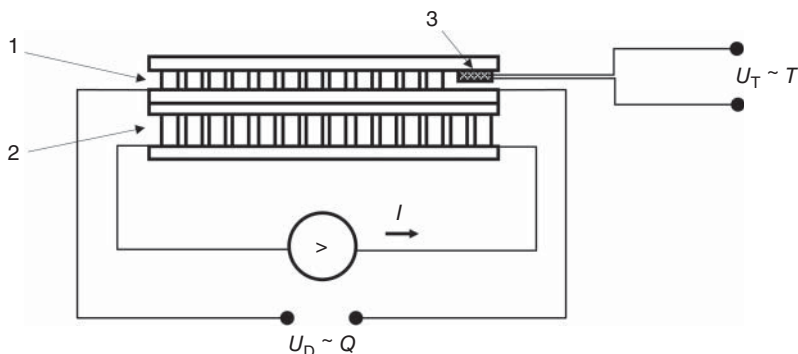
Figure 11.30 Thermoelectric ice sensor.

The advantage of use of heat flux sensors in this application is the principle of direct measurements – namely, definition of freezing by enthalpy of the ice crystallization that is released or absorbed during the water-to-ice phase transformation.

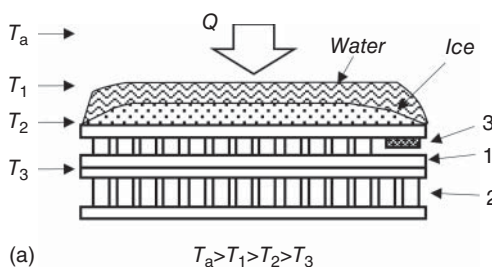
It allows defining freezing parameters with high precision, to predict ice formation conditions.

One of the models of such ice sensors is given in Figure 11.30 and in Figure 11.31 – schematic of the ice sensor. The ice sensor consists of Peltier module and the thermoelectric heat flux sensor. The thermistor is mounted on a sensitive surface of the heat flux sensor for exact determination of temperature.

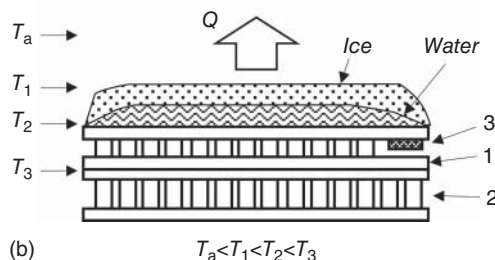
The principle of operation of such an ice sensor is shown in Figures 11.32–11.34.



**Figure 11.31** Ice sensor design: 1 – heat flux sensor; 2 – Peltier module; 3 – thermistor.  
 $U_T$  – signal of thermistor;  $U_D$  – signal of heat flux sensor;  $I$  – electric current;  $T$  – temperature;  
 $Q$  – heat flux.



**Figure 11.32** Thermoelectric ice sensor operating modes: (a) cooling;  
(b) heating.  $Q$  – heat flux; 1 – heat flux sensor; 2 – Peltier module;  
3 – thermistor.  $T_a, T_1, T_2, T_3$  – temperatures, correspondingly:  
ambient; surface of water or ice;  
surface of heat flux sensor; surface of  
Peltier module.



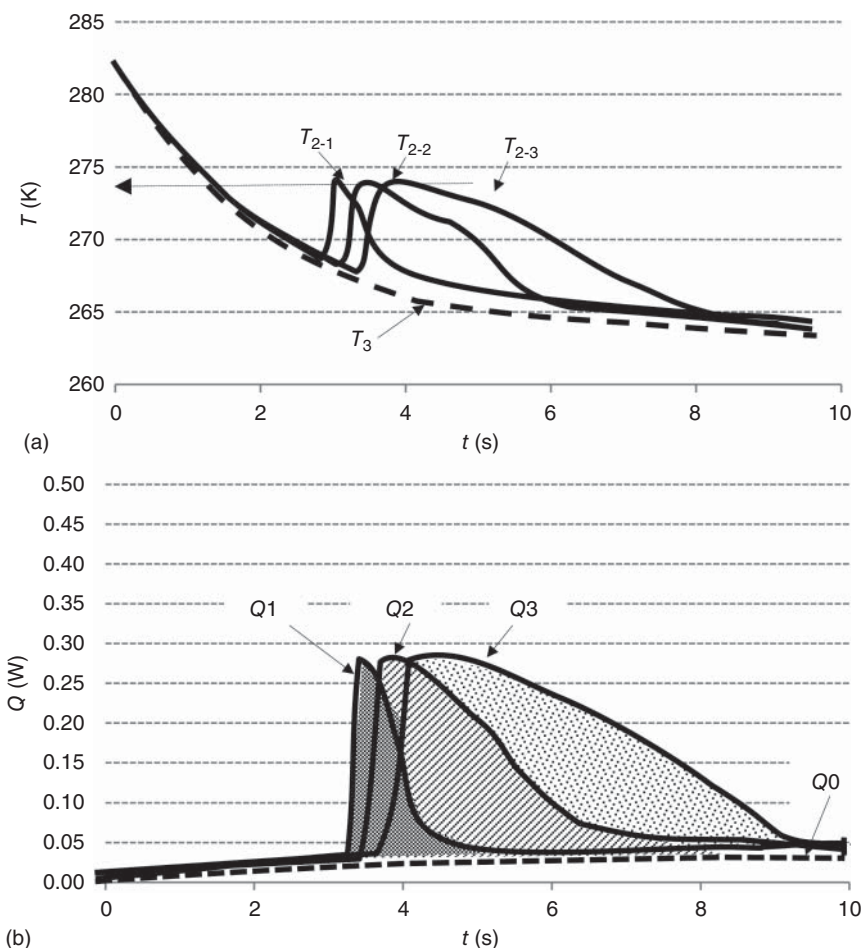


**Figure 11.33** Cooling mode: (a) thermistor signal; (b) heat flux sensor signal.

The cycle of cooling or heating is provided by the Peltier module.

If on the outer surface of the heat flux sensor the water is presented, then when crossing the temperature of formation of ice, the heat flux sensor will record the heat of water crystallization released or absorbed during water-to-ice phase transition. The integrated thermistor will define the freezing temperature.

The size of a signal measured by the heat flux sensor and the corresponding integrated heat measured by it allow to measure the amount of ice or water directly.

Experimental data are presented in Figure 11.35. It is a cycle of cooling/heating of the experimental thermoelectric ice sensor. Using the freezing temperature of the ice sensor, the amount of the released or absorbed heat is measured. This amount of heat signals about the intensity of ice formation, and allows calculating quantitatively the ice formation.

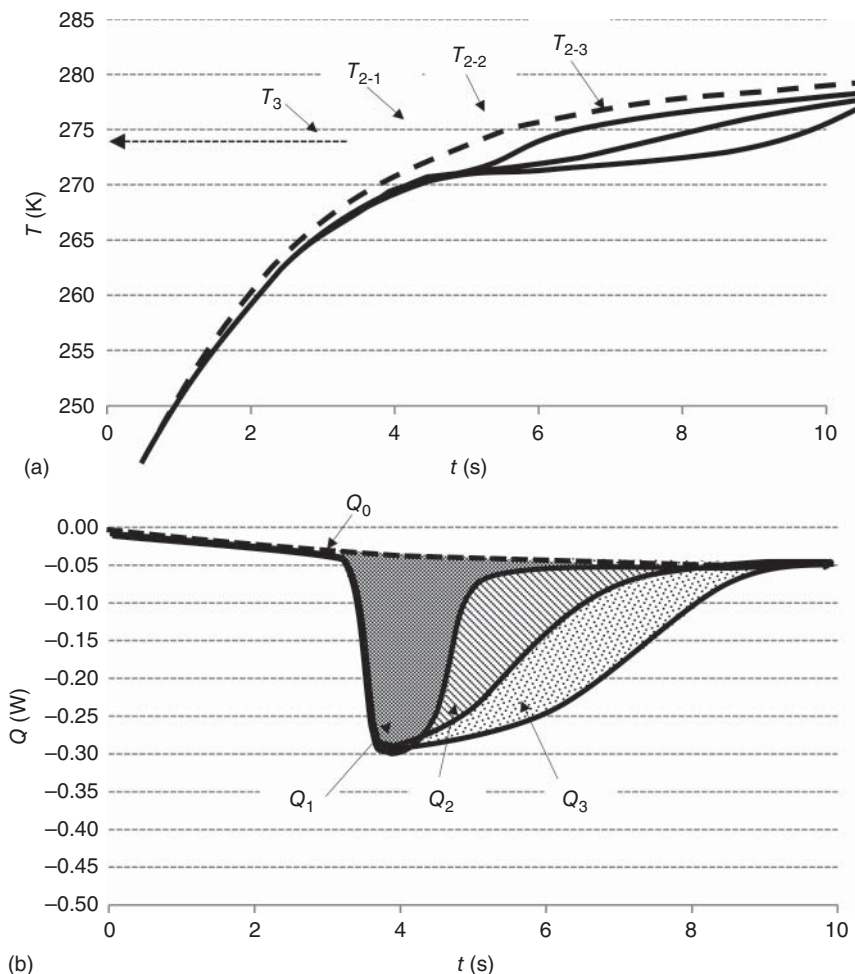


**Figure 11.34** Heating mode: (a) thermistor signal; (b) heat flux sensor signal.

Such thermoelectric ice sensor possesses unique informational content in a tiny design, high precision of definition. Owing to the simple miniature design it can be mass produced, providing a range of applications at reasonable prices.

As a final comment on such ice sensors it should be noted that such a sensor is a unique device. All its components work on the principles of thermoelectricity: the Peltier module – effect of Peltier; the thermoelectric heat flux sensor, and even a thermistor – Seebeck effect (look at the Table 11.2).

#### 11.11.4 Laser Power Meters

Modern life is not imaginable without the universal use of lasers any more. Lasers transfer optical energy and power. Measurement of these parameters is of priority in all areas of applications: optical communication and data recording; industrial applications, in materials processing; in scientific researches, and so on.

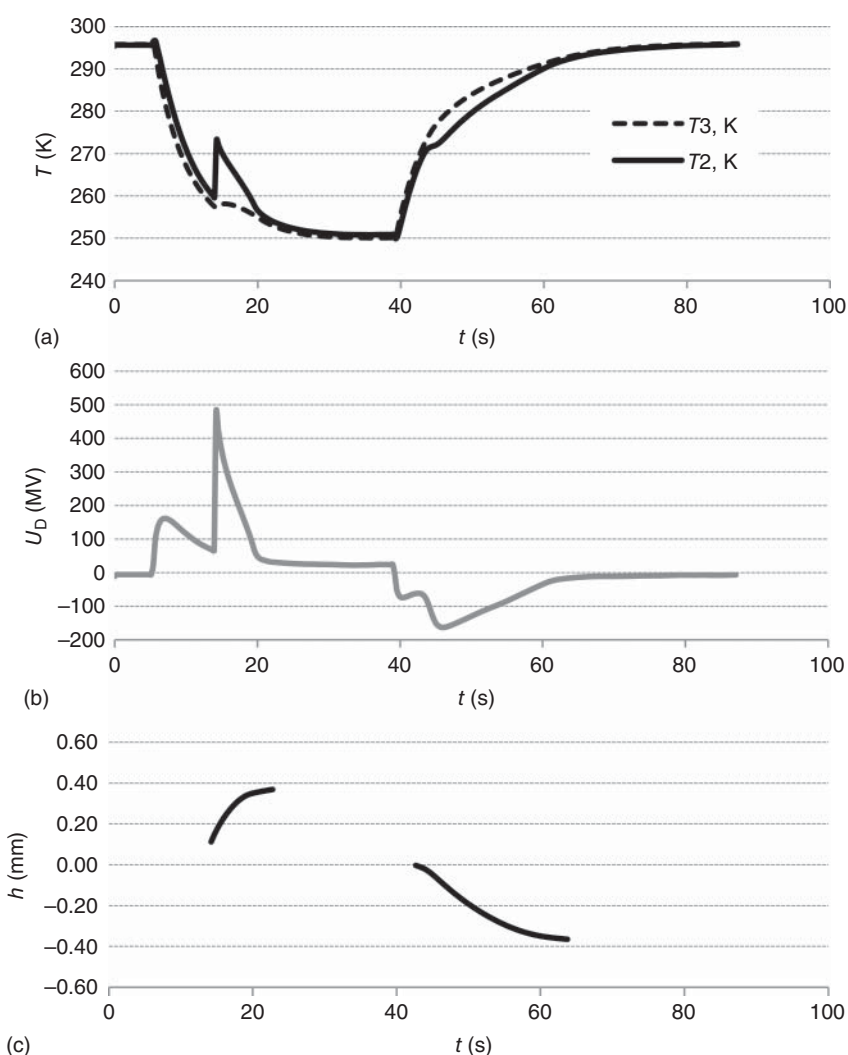


**Figure 11.35** Experimental cooling–heating cycle: (a) thermistor signal; (b) heat flux sensor signal; (c) thickness of ice or water layer, correspondingly.  $T_2$  – temperature at the surface of ice sensor;  $T_3$  – temperature at the surface of Peltier module.

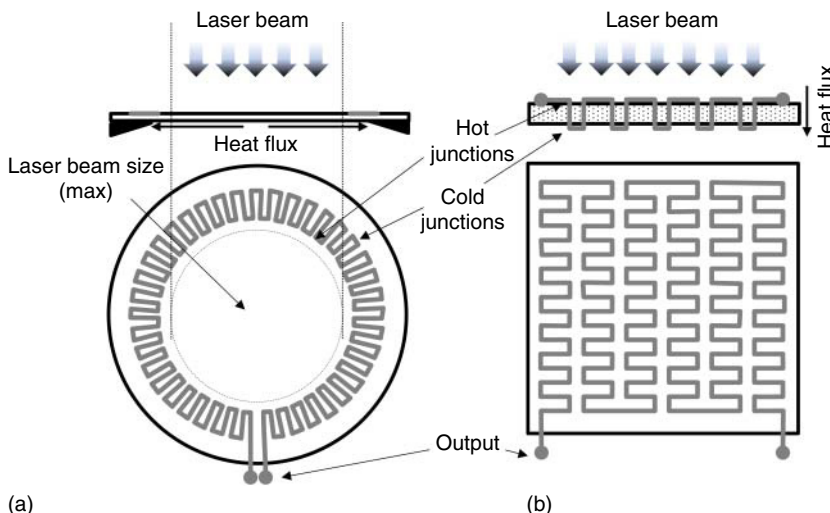
Laser power meter is a device for the measurement of power or energy of the laser beam. Different technologies are applied in the state-of-the-art power meters (Table 11.19):

Every technology has advantages but for a limited range of applications.

Thermopile sensors – power meters are based on the principle that the optical (laser) power is converted to heat, and the resulting temperature rise (the temperature difference between the absorber and the heat sink) is measured by a thermopile. Thermopile power meters are also called thermal power meters. Thermoelectric heat flux sensors can be also related to the class.

**Table 11.19** Types of laser power meters [25].

Technology	Measurement type
Pyroelectric sensors	Measures the energy of pulsed lasers and can only work with pulsed lasers Average power is calculated by measuring laser repetition rate and multiplying by the pulse energy
Thermopile sensors	Measures CW lasers and integrates energy of pulsed lasers to produce an average power measurement Can also be used to integrate the energy of a single pulse – most common for measuring energy of millisecond and longer pulse width medical and industrial lasers
Semiconductor photodiode/optical	Most often used for measuring low CW laser power Also used in some sensors for measuring low pulse energy; however, may not respond to CW lasers when used in this way

**Figure 11.36** Design of thermopile laser power meters: (a) “disk” type; (b) “wafer” type.

Moreover, there are two kinds of thermopiles used in laser power measurement. One is the so-called “disk” type thermopile power meter, and the other is the “wafer” type thermopile sensor (Figure 11.36).

The disk-type is made of two sets of junctions laid out radially (Figure 11.36a). One set of junctions is arrayed under the aperture while the alternate set is near the edge of the disk, which is attached to a massive heat sink. The laser power heats the absorber in the center and creates a temperature difference between the center and the edge.

In the wafer-type sensor thermopiles hot and cold junctions are located in the same direction with laser power beam (Figure 11.36b). The top side of the media with hot side junctions is heated by laser power. The bottom side with

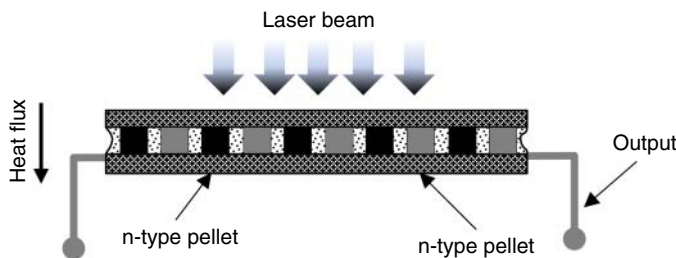


Figure 11.37 Thermoelectric laser power meters.

cold junctions is connected with a massive heat sink. The temperature difference measured by differential thermopiles is proportional to the power.

When a lot of average power is absorbed and has to flow through the small gap containing the thermocouples, the temperature becomes hot enough to damage the thermocouple junctions.

The thermoelectric heat flux sensor as laser power meter must be exactly classified as “wafer” type thermal laser power meter (Figure 11.37).

Thermoelectric heat flux sensors have a set of advantages when both types of thermopile power meters are compared.

- 1) First of all, it has considerably bigger sensitivity because the pairs of p- and n-semiconductor pellets have at least 10 times ( $>10\times$ ) bigger Seebeck coefficient (means sensitivity) than metal thermocouples (Table 11.1).

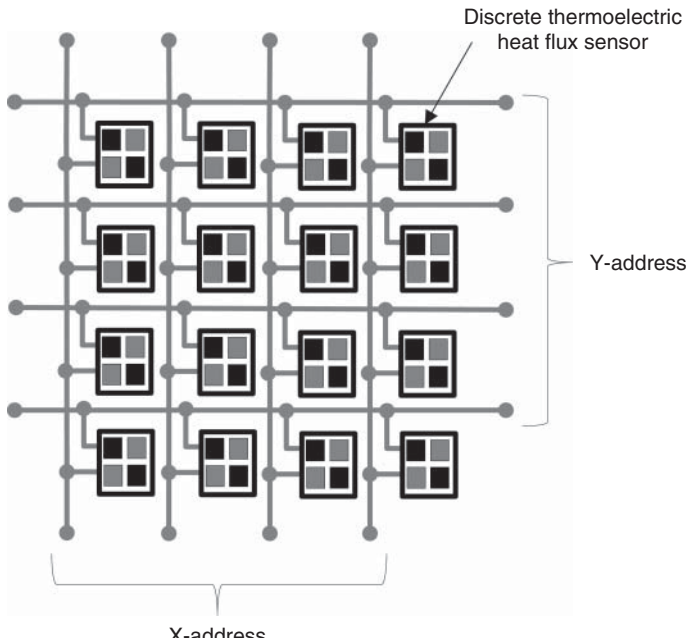


Figure 11.38 Design of matrix thermoelectric laser power meter (16-element matrix example).

- 2) As known, because of the small gap in the medium in the path of heat flux generated by laser power, the speed of response of the “wafer” type sensors is faster than that of disk type sensors with radial placement of the couples. In the case of thermoelectric heat flux sensors the medium is the thermoelectric material of the pellets itself. The height of the pellets can be very small and so such sensors will be quite fast.
- 3) It was shown above that thermoelectric heat flux sensors have unique performance advantage. The integral sensitivity  $S_a$  does not depend on the number of pellets (pellet pairs) in the sensor (11.18). In other words, in the sensor, even one pair (or even one pellet) has the same sensitivity  $S_a$  as a complete sensor.
- 4) The conclusion of the above is that on the basis of thermoelectric heat flux sensor technology it is possible to create matrix power meters where a pixel could be one pair of n- and p-pellets, or even every pellet to build special electric connection for such a matrix (Figure 11.38).

## References

- 1 Schmidt, E. (1925) Device for the Measurement of Heat. US Patent 1,528,383, filled June 11, 1923 and issued Mar. 3, 1925.
- 2 Barnes, A. (1999) Heat flux sensors. Part 1: theory. *Sens. Mag.*, **16** (1). <http://archives.sensorsmag.com/articles/0199/flu0199/index.htm> (accessed 8 May, 2017).
- 3 Diller, T.E. (2013) Ch. 18, Heat flux measurement, in *Handbook of Measurement in Science and Engineering* (ed. M. Kutz), John Wiley & Sons, New York, pp. 629–659.
- 4 Lasance, C. J. M., (2006) The Seebeck Coefficient. Electronic Cooling, Nov. 1, 2006. <http://www.electronics-cooling.com/2006/11/the-seebeck-coefficient/> (accessed 24 April 2016).
- 5 Leephakpreeda, T. (2012) Application of thermoelectric modules on heat flow detection. *ISA Trans.*, **51** (2), 345–350.
- 6 Sippawit, N. and Leephakpreeda, T. (2015) Study of sensing heat flow through thermal wall by using thermoelectric module. *Therm. Sci.*, **19** (5), 1497–1505.
- 7 McKinnon, C., Bernardini, R.R., Thresher, W., Ruis, S.L. and Yarbrough, D.W. Commercial Bismuth Telluride-Based Peltier Plates for Use as Heat Flux Transducers (A Concept), [http://www.airah.org.au/imis15\\_prod/Content\\_Files/EcoLibrium/2010/May/2010-05-01.pdf](http://www.airah.org.au/imis15_prod/Content_Files/EcoLibrium/2010/May/2010-05-01.pdf) (accessed 24 April 2016).
- 8 Gromov, G.G., Glyazer, S.A., and Zakhartsev, Y.V. (2015) Thermoelectric Heat Flux Sensors. *J. of Thermoelectricity*, **6** (2016), 88–98.
- 9 Rowe, D.M. (2006) Ch. 1, General Principles and Basic Considerations, in *Thermoelectric Handbook: Macro to Nano* (ed. D.M. Rowe), CRC Press, Boca Raton, pp. 1.1–1.14.
- 10 Tsai, B.K., Gibson, C.E., Murthy, A.V., Early, E.A., Dewitt, D.P., and Saunders, R.D. (2006) Heat-flux sensor calibration. *NIST Spec. Publ.*, 250–265, 1–37 <http://www.nist.gov/calibrations/upload/sp250-65.pdf> (24 April 2016).

- 11 Murthy, A.V., Tsai, B.K., and Saunder, R.D. (1998) High-heat-flux sensor calibration using blackbody radiation. *Metrologia*, **25**, 501–504.
- 12 Ballestrin, J., Estrada, C.A., Rodriguez-Alonso, M., Perez-Rabago, C., Langley, L.W., and Barnes, A. (2004) High-heat-flux sensor calibration using calorimetry. *Metrologia*, **41**, 314–318.
- 13 Brown, R.E. and Garfinkle, D.R. (1969) Self-Calibrating Heat Flux Transducer. US Patent 3,599,474, filled Jul. 25, 1969 and issued Aug. 17, 1971.
- 14 HFP01SC(2016) Self-Calibrating Heat Flux Sensor. [http://www.hukseflux.com/product/hfp01sc?referrer=/product\\_group/heat-flux-sensors](http://www.hukseflux.com/product/hfp01sc?referrer=/product_group/heat-flux-sensors) (accessed 24 April 2016).
- 15 Gromov, G., Kondratiev, D., Rogov, A. and Yershova, L. (2001) *Z-meter: Easy-to-use Application and Theory*. Proceedings of European Conference on Thermoelectrics, June 2001, Freiberg, Germany.
- 16 Yershova, L.B., Gromov, G.G. and Drabkin, I.A. (2003) Complex Express TEC Testing. Proceedings of The 22nd International Conference on Thermoelectrics, August 2003, La Grande-Motte, Herault – France.
- 17 Gromov, G.G. (2015) Method of Calibration of Thermoelectric Heat Flux Sensors. Russian Patent RU 2,577,389 C1, filled Jan. 21, 2015 and issued Mar. 20, 2016.
- 18 Thermoelectric heat flux sensor technologies (2016) <http://www.tec-microsystems.com/products/te-heat-flux-sensor-technologies.html> (accessed 8 May 2017).
- 19 DX8020 TEC Expert. (2017) <http://www.tec-microsystems.com/products/equipment-and-instruments/dx8020-tec-expert.html> (accessed 8 May 2017).
- 20 Z-Meters for TEC Express Quality Control (2016). <http://www.tec-microsystems.com/EN/Z-Meters.html> (accessed 24 April 2016).
- 21 Elman, U. (2008) Novel Cost-Effective Remote Ice Detection System Allows Extensive Deployment. Proceedings Transport Research Arena (TRA) Conference 2008, Ljubljana, Slovenia.
- 22 Le Bot C. (2004) SIGMA: System of Icing Geographic Identification in Meteorology for Aviation. *11th Conf. on Aviation, Range, and aerospace*, Hyannis, Mass., 4–8 Oct 2004, Amer. Meteorol. Soc. (Boston).
- 23 Jasinski, W.J., Noe, S.C., Selig, M.S., and Bragg, M.B. (1998) Wind turbine performance under icing conditions//Transactions of the ASME. *J. Sol. Energy Eng.*, **120**, 60–65.
- 24 Vavilov, V.D. and Sukonkin, A.N. (2013) Review of Domestic and Foreign Ice Detectors. Electro-mechanical systems. Proceedings of Nizhniy Novgorod state university, 4, 297–310.
- 25 Coherent. Laser Measurement and Control 2016/2017 Product Catalog (2016). [https://cohrcdn.azureedge.net/assets/pdf/COHERENT\\_LMC\\_2016-2017\\_Catalog\\_.pdf](https://cohrcdn.azureedge.net/assets/pdf/COHERENT_LMC_2016-2017_Catalog_.pdf) (accessed 8 May 2017).
- 26 Westgate, A.J., McLellan, W.A., Wells, R.S., Scott, M.D., Meagher, E.M., and Pabst, D.A. (2007) A new device to remotely measure heat flux and skin temperature from free-swimming dolphins. *J. Exp. Mar. Biol. Ecol.*, **346**, 45–59.

## Further Reading

- 27 Pullins, C.A. and Diller, T.E. (2012) Direct measurement of hot-wall heat flux. *J. Thermophys. Heat Transfer*, **26**, 430–438.
- 28 Pullins, C.A. and Diller, T.E. (2011) Adaptation of the in-cavity calibration method for high temperature heat flux sensors. *Int. J. Heat Mass Transfer*, **54**, 3369–3380.
- 29 Westgate, A.J., McLellan, W.A., Wells, R.S., Scott, M.D., Meagher, M., and Pabst, D.A. (2007) A new device to remotely measure heat flux and skin temperature from free-swimming dolphins. *J. Exp. Mar. Biol. Ecol.*, **346**, 45–59.
- 30 Chun, J., et al, (1999) Design and Fabrication of Micro Heat Flux Sensor, Proceedings, IEEE/RSJ International, Conference on Intelligent Robots and Systems, Kyongju, Korea, 2, 1045–1048.
- 31 Gridchin, V.A. and Lobach, O.V. (2009) Heat Flux Sensor Modeling, Proceedings International School and Seminar on Internano, Novosibirsk, Russia, 87–90.
- 32 ASTM C518-04 (2008) Standard test method for steady-state thermal transmission properties by means of the heat flow meter apparatus. *Annu. Book ASTM Stand.*, **04** (06), 155–169.
- 33 ASTM C177-13 (2013) *Standard Test Method for Steady-State Heat Flux Measurements and Thermal Transmission Properties by Means of the Guarded-Hot-Plate Apparatus*, ASTM International, West Conshohocken, PA.
- 34 General Purpose Heat Flux sensors. ETO Denki Co. Tokyo Japan. Preliminary Edition (2011). [http://www.etodenki.co.jp/web\\_pdf/hf-doc-e-d.pdf](http://www.etodenki.co.jp/web_pdf/hf-doc-e-d.pdf) (accessed 24 April 2016).
- 35 Diller, T.E. (1993) Advances in heat flux measurements, in *Advances in Heat Transfer*, vol. 23, Academic Press, Edited by James P. Hartnett and Thomas F. Irvine, pp. 279–368.
- 36 Schmidt, F.W. et al. (1984) *Introduction to Thermal Sciences—Thermodynamics, Fluid Dynamics, Heat Transfer*, John Wiley & Sons.
- 37 Wesley, D.A. (1979) Thin disk on a convectively cooled plate—application to heat flux measurement errors. *J. Heat Transfer*, **82**, 341–348.
- 38 Lartz, D.J. et al. (1994) Heat Flux Measurement Used for Feedforward Temperature Control, Proceedings 10th International Heat Transfer Conference, Vol. 2, Brighton, UK.
- 39 Barnes, A. (1999) Heat flux sensors Part 2: applications. *Sens. Mag.*, **16** (2). <http://archives.sensorsmag.com/articles/0299/flu0299/index.htm> (accessed 8 May, 2017).
- 40 Elman, U. (2008) Novel Cost-Effective Remote Ice Detection System Allows Extensive Deployment. Proceedings Transport Research Arena (TRA) Conference 2008, Ljubljana, Slovenia.
- 41 Heat Flux Sensors (2016), <http://www.tec-microsystems.com/products/te-heat-flux-sensor-technologies.html> (accessed 8 May, 2017).

- 42** ISO 9060:1990 (1990) *Solar Energy-Specification and Classification of Instruments for Measuring Hemispherical Solar and Direct Solar Radiation*, International Standards Organization.
- 43** ASTM C1155-95 (2013) *Standard Practice for Determining Thermal Resistance of Building Envelope Components from the In-Situ Data*, American Society for Testing and Materials.
- 44** Murthy, A.V., Tsai, B.K., and Saunder, R.D. (1998) High-heat-flux sensor calibration using blackbody radiation. *Metrologia*, **25**, 501–504.
- 45** Filtz, J.R., Valin, T., Hameury, J., and Dubard, J. (2009) New vacuum blackbody cavity for heat flux meter calibration. *Int. J. Thermophys.*, **30** (1), 236–248.
- 46** Ballestrin, J., Estrada, C.A., Rodriguez-Alonso, M., Perez-Rabago, C., Langley, L.W., and Barnes, A. (2004) High-heat-flux sensor calibration using calorimetry. *Metrologia*, **41**, 314–318.
- 47** Martins, N., Carvalho, M.G., Afgan, N.H., and Leontiev, A.I. (1998) Experimental verification and calibration of the blow-off heat flux sensor. *Appl. Therm. Eng.*, **18** (6), 481–489.
- 48** Carslaw, H.S. and Jaeger, J.C. (1959) *Conduction of Heat in Solids*, Oxford University Press, London.
- 49** Ballestrin, J., Estrada, C.A., Rodriguez-Alonso, M., Perez-Rabago, C., Langley, L.W., and Barnes, A. (2006) Heat flux sensor: calorimeters or radiometers. *Sol. Energy*, **80** (10), 1314–1320.
- 50** Martins, N., Carvalho, M.G., Afgan, N.H., and Leontiev, A.I. (1995) A new instrument for radiation heat flux measurement: analysis and parameter selection. *Heat Recovery Syst. CHP*, **15** (8), 787–796.
- 51** Neal, S.B.H.C. and Northover, E.W. (1980) The measurement of radiant heat flux in large boiler furnaces-I. Problems of ash depositions relating to heat flux. *Int. J Heat Mass Transfer*, **23** (1980), 1015–1021.
- 52** Neal, S.B.H.C., Northover, E.W., and Preece, R.J. (1980) The measurement of radiant heat flux in large boiler furnaces-II. development of flux measuring instruments. *Int. J Heat Mass Transfer*, **23**, 1023–1031.
- 53** Diller, T.E. (1999) Heat Flux, Ch. 34, in *The Measurement, Instrumentation and Sensors Handbook* (ed. J.G. Webster), CRC Press, Boca Raton, FL, pp. 34.1–34.15.
- 54** Incropera, F.P. and DeWitt, D.P. (2002) *Fundamentals of Heat and Mass Transfer*, John Wiely & Sons, Inc.
- 55** Venkatasubramanian, R., Siivola, E., Colpitts, T., and O'Quinn, B. (2001) Thin-film thermoelectric devices with high room-temperature figures of merit. *Nature*, **413**, 597–602.
- 56** Rowe, D.M. (1994) *CRC Handbook of Thermoelectrics*, CRC Press, Boca Raton.
- 57** Bernstein, B.C., McDonough, F., Politovich, M.K., Brown, B.G., Ratvasky, T.P., Miller, D.R., Wolff, C.A., and Cunning, G. (2005) Current icing potential: algorithm description and comparison with aircraft observations. *J. Appl. Meteorol.*, **44**, 969–986.
- 58** Minnis P., Smith W.L., Young D.F., Nguyen L., Rapp A.D., Heck P.W., Sun-Mack S., Trepte Q. and Chen Y. (2001) A Near Real-Time Method for

- Deriving Cloud and Radiation Properties from Satellites for Weather and Climate Studies. Proc. AMS 11th Conf. Satellite Meteorology and Oceanography, Madison, WI, 15–18 Oct, pp. 477–480.
- 59 Ganander H. and Ronsten G. (2003) Design Load Aspects Due to Ice Loading on Wind Turbine Blades, Proceedings of the 2003 BOREAS VI Conference, 2003. pp. 49–55.
  - 60 Model HFP01 Soil Heat Flux Plate. Instruction Manual (2016).  
<https://s.campbellsci.com/documents/us/manuals/hfp01.pdf> (accessed 8 May, 2017).
  - 61 GreenTEG's Heat Flux Sensor for the Assessment of Thermal Behavior of Buildings. AZoSensors.com (2014), <http://www.azosensors.com/Article.aspx?ArticleID=464> (accessed 24 April, 2016).
  - 62 gSKIN Application Note. U-Value Measurement Case Study, [http://shop.greenteg.com/wp-content/uploads/gSKIN\\_Application-note\\_U-Value-measurement-case-study.pdf](http://shop.greenteg.com/wp-content/uploads/gSKIN_Application-note_U-Value-measurement-case-study.pdf) (accessed 24 April, 2016).
  - 63 Hukseflux Heat Flux Sensors for Industrial Use. V1402 [http://www.hukseflux.com/sites/default/files/product\\_group\\_bi\\_file/hukseflux\\_industrial\\_heat\\_flux\\_sensors\\_v1402.pdf](http://www.hukseflux.com/sites/default/files/product_group_bi_file/hukseflux_industrial_heat_flux_sensors_v1402.pdf) (accessed 24 April, 2016).
  - 64 Hukseflux Surface Energy Flux Sensors. V1403 [http://www.hukseflux.com/sites/default/files/product\\_group\\_bi\\_file/hukseflux\\_surface\\_energy\\_flux\\_sensors\\_v1403.pdf](http://www.hukseflux.com/sites/default/files/product_group_bi_file/hukseflux_surface_energy_flux_sensors_v1403.pdf) (accessed 24 April, 2016).

# 12

## Photovoltaic–Thermoelectric Hybrid Energy Conversion

*Ning Wang*

*University of Electronic Science and Technology of China, Department of Microelectronics and Solid-state Electronics, Jianshe North Road, Section 2 No.4, Chengdu 610054, China*

### 12.1 Background and Theory

#### 12.1.1 Introduction

The average global electricity production in 2014 was estimated at more than 24 000 TWh, of which only a small fraction of 7% was produced from solar and wind energy. Increasing the fraction by 1% means a reduction of CO<sub>2</sub> emission by roughly  $1.32 \times 10^8$  tons. There is an abundant energy input from the solar radiation received on earth, estimated at 162 000 TW, which means a vanishingly small fraction of it can meet all the energy demand on earth for all human activities. Photovoltaic (PV) technology converts solar energy directly into electricity. The conversion efficiency  $\eta_{\text{PV}}$  is expressed as  $\eta_{\text{PV}} = P_{\text{out}}/P_{\text{in}}$ , where  $P_{\text{out}}$  is the electricity output and  $P_{\text{in}}$  is the solar energy input [1, 2]. However, the solar energy input cannot be fully utilized because of the limitations in solar spectrum absorption and the quantum efficiency (QE). The solar energy that cannot be converted into electricity is converted into waste heat. Therefore, improvement of  $\eta_{\text{PV}}$  can be achieved by utilizing the waste heat.

Thermoelectrics is a promising energy conversion technology that converts heat directly into electricity [3–5]. The design of a thermoelectrics module (TEG) follows the principle that the p–n junctions are electrically connected in series and thermally connected in parallel [6]. Such a flat device is capable of being combined with PV panels for energy conversion. Therefore a photovoltaic–thermoelectric (PVTE) hybrid device becomes a promising solution for improving the overall solar to electrical conversion efficiency [7–11]. Figure 12.1 shows a schematic setup of a typical PVTE device. The hot side of the TEG is thermally connected to the back electrode of the PV panel, harvesting waste heat from it. When a temperature gradient is built vertically in the TEG, the TEG power output will be added to the PV power output by electrically connecting them in series.

The concept of the solar spectrum energy utilization by a PVTE module is represented in Figure 12.2. For the specific example of the AM1.5G spectrum, 69.32% of the solar radiation is converted by the solar cell. The short wavelength

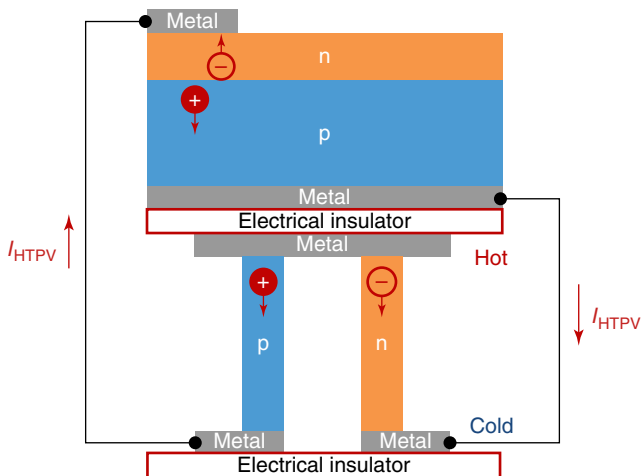


**Figure 12.1** A typical schematic diagram of the PVTE device, in which a TEG device is connected thermally and electrically in series with the PV cell. (Lorenzi *et al.* 2015 [12]. Reproduced with permission of Springer.)

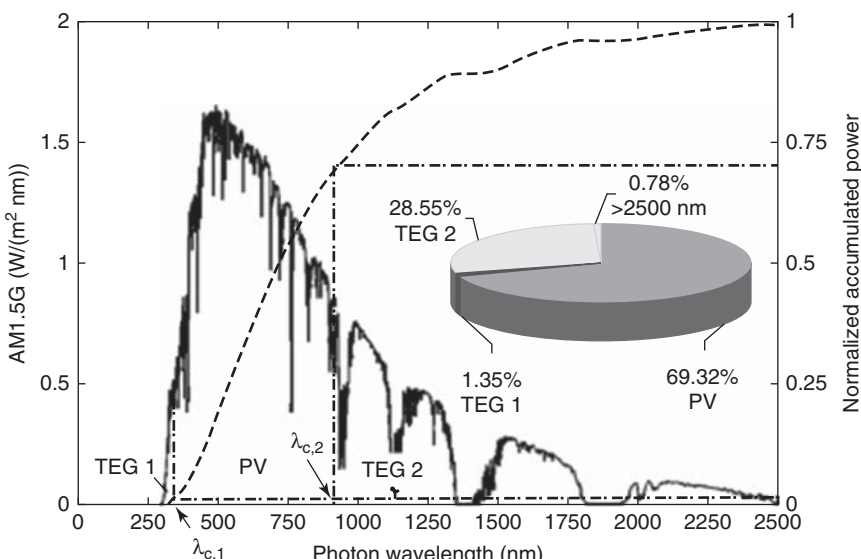


**Figure 12.2** Segmentation of AM1.5G spectrum in three regions for an mc-Si:H solar cell and solar TEG with 4% efficiency. Normalized accumulated radiation power. Pie chart: converted power fraction of each module. (Kraemer *et al.* 2008 [9]. Reproduced with permission of American Institute of Physics.)

region of the power spectrum that can be used for TEG only accounts for 1.35% of the total incident radiation power. The main contribution of the TEG comes along with the conversion of the long wavelength fraction of 28.55%. It gives the principles for the combination of PV and TEG modules in the most efficient way [9].

### 12.1.2 PV Efficiency

The efficiency of a generic PV system is simply the ratio of output power to input power; that is,

$$\eta_{\text{PV}} = \frac{P_{\text{out}}}{P_{\text{in}}} = \frac{V_{\text{oc}} I_{\text{sc}} \text{FF}}{\varphi_{\text{Sun}} S_{\text{cell}}}$$

where  $V_{\text{oc}}$ ,  $I_{\text{sc}}$ ,  $\text{FF}$ ,  $\varphi_{\text{Sun}}$ , and  $S_{\text{cell}}$  are the open circuit voltage, the short-circuit current, the filling factor, the solar radiation intensity, and the device area, respectively. And the fill factor FF follows the relation  $\text{FF} = (V_{\text{max}} \times I_{\text{max}}) / (V_{\text{oc}} \times I_{\text{sc}})$ , where  $V_{\text{max}}$  and  $I_{\text{max}}$  are the maximum voltage and maximum current achievable.

### 12.1.3 TEG Efficiency

The efficiency of a TEG depends on the materials used. The most important material properties can be described by a dimensionless figure of merit ( $ZT$ ),  $ZT = TS^2\sigma/\kappa$ , where  $T$ ,  $S$ ,  $\sigma$ , and  $\kappa$  are the absolute temperature, the Seebeck coefficient, electrical conductivity, and thermal conductivity, respectively [6, 13]. The maximum efficiency of an ideal thermoelectric device,  $\eta_{\text{TEG}}$ , can be written as a function of the temperatures and the device figure of merit, as follows:

$$\eta_{\text{TEG}} = \frac{\Delta T}{T_h} \frac{\sqrt{1 + ZT} - 1}{\sqrt{1 + ZT} + T_c/T_h}$$

where  $T_h$ ,  $T_c$ , and  $\Delta T$  correspond to the hot-side temperature, cold side temperature, and the temperature difference, respectively.  $\Delta T/T_h$  corresponds to the Carnot efficiency, the maximum efficiency of a heat engine operating between two temperatures. The term  $ZT$  is the dimensionless figure of merit, one of the most important and popular terms in thermoelectrics.  $ZT$  is a pure material property, regardless of the engineering design of the modules. The  $ZT$  value is directly related to the maximum possible conversion efficiency  $\eta_{\text{max}}$  [6]. Given the different values for  $T_h$  and  $T_c$ ,  $\eta_{\text{max}}$  monotonically increases with increasing  $ZT$  and  $\Delta T$ .

### 12.1.4 PVTE Module Generated Power and Efficiency

Incident solar irradiation is converted by the PV module with efficiency  $\eta_{\text{PV}}$ . The remaining heat flux is assumed to be available to the TEG module, and is converted with efficiency  $\eta_{\text{TEG}}$ . Thus, the heat flux lost at the module sides and front cover as well as the radiation loss is not taken into account. The total amount of generated power then is

$$P_{\text{PVTE}} = P_{\text{PV}} + P_{\text{TEG}} = \eta_{\text{PV}} G + (1 - \eta_{\text{PV}}) G \eta_{\text{PV}}$$

and the efficiency of the hybrid PVTE system is written as

$$\eta_{\text{PVTE}} = \eta_{\text{PV}} + (1 - \eta_{\text{PV}}) \eta_{\text{TEG}}$$

### 12.1.5 Energy Loss

The equations described above allow for the calculation of the maximum enhancement of efficiency as a result of adding a TEG. However, several losses

are not considered, according to Sark *et al.* [10], such as reflection losses, heat flux, and radiation losses from the side and front cover. Further, it is assumed that the back side temperature of the TE converter always equals the ambient temperature. This is a critical assumption, and may not be realized in practice. Clearly, a higher back side temperature lowers the TEG efficiency.

Lorenzi *et al.* had a detailed investigation on the energy losses in single-junction devices [12]. According to their analysis, the maximum efficiency  $\eta_c$  achievable by a solar cell is equal to the Carnot efficiency, that is,  $\eta_c = 1 - T_{\text{cell}}/T_{\text{sun}}$ , where  $T_{\text{cell}}$  is the device (cold side) temperature and  $T_{\text{Sun}}$  is the Sun temperature. According to Landsberg, this formula should be modified taking into account the non-zero radiation emitted by the absorber:

$$\eta_{\max} = \frac{P_{\max}}{P_{\text{in}}} = 1 - \frac{3}{4} \left( \frac{T_{\text{cell}}}{T_{\text{sun}}} \right) + \frac{1}{3} \left( \frac{T_{\text{cell}}}{T_{\text{sun}}} \right)^4$$

Taking  $T_{\text{cell}} = 300$  K and  $T_{\text{Sun}} = 6000$  K one obtains an efficiency of 93.33%. However, Shockley and Queisser showed how, in a single-junction device, the actual achievable efficiency is bound to be much lower, because of several types of energy loss, as shown in Table 12.1.

Sark pointed out that the largest contribution to the overall loss comes from the  $L_2$  term, which corresponds to  $\approx 60\%$  of the overall incoming power, and the other three terms total less than 20%. The detailed expressions of  $L_2$ , containing loss as a result of non-absorbed photons  $L_{2a}$ , thermalization of hot carriers  $L_{2b}$ , and degradation as a result of cell heating  $L_{2c}$ , were shown in his paper [12]. Figure 12.3 shows the histograms of the contribution of  $L_2$  for different PV technology.

### 12.1.6 Cost

The high cost of TEG is a major concern for limiting widespread use of PVTE modules. According to an estimation [12], the price for generating electricity using a TEG is dependent on the size of the modules, for example, 5 to 10 \$/W for  $50 \times 50$  mm<sup>2</sup> modules of 0.3–0.5 W/cm<sup>2</sup>. For a 15% efficiency PV module, if

**Table 12.1** Energy loss in a single-junction device powered by solar energy.

---

1. Optical losses ( $L_1$ ):	(a) Contact grid shadow ( $L_{1a}$ ) (b) Radiation reflection ( $L_{1b}$ ) (c) Spurious absorption ( $L_{1c}$ )
2. Source-absorber decoupling losses ( $L_2$ ):	a) Non-absorbed photons with $E < E_g$ b) Thermalization of hot carriers (photons with $E > E_g$ ) c) Efficiency degradation because of cell heating
3. Thermal losses ( $L_3$ )	The Joule effect
4. Electrical and recombination losses ( $L_4$ ):	(a) Non-unitary quantum efficiency (b) $qV_{\text{oc}} < E_g$

---

Source: Lorenzi *et al.* 2015 [12]. Reproduced with permission of Springer.

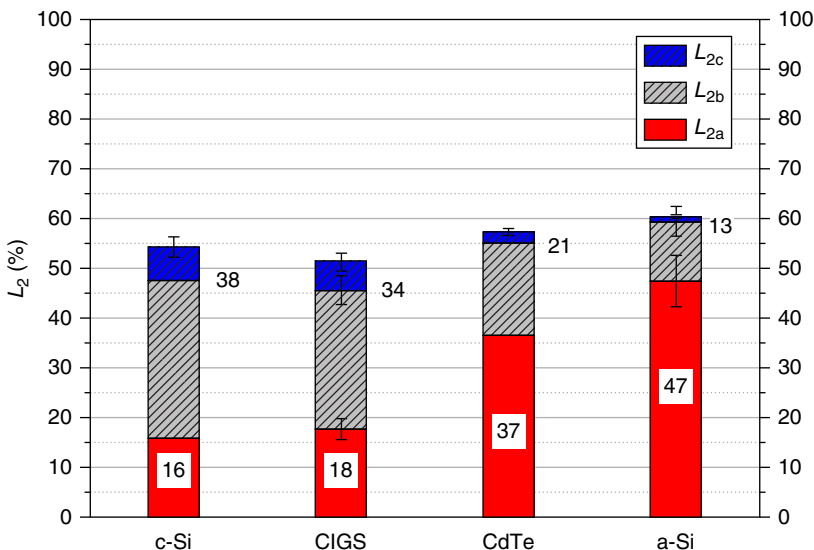


**Figure 12.3** Histograms showing the contribution of  $L_2$  for different technologies. The numbers on the bars are  $L_{2a}$  and  $L_{2b} + L_{2c}$  values. Error bars show the range of minimum and maximum values for each  $L_2$  component. Bars on  $L_{2a}$  result from the variability of the energy gaps of CIGS and a-Si. (Lorenzi *et al.* 2015 [12]. Reproduced with permission of Springer.)

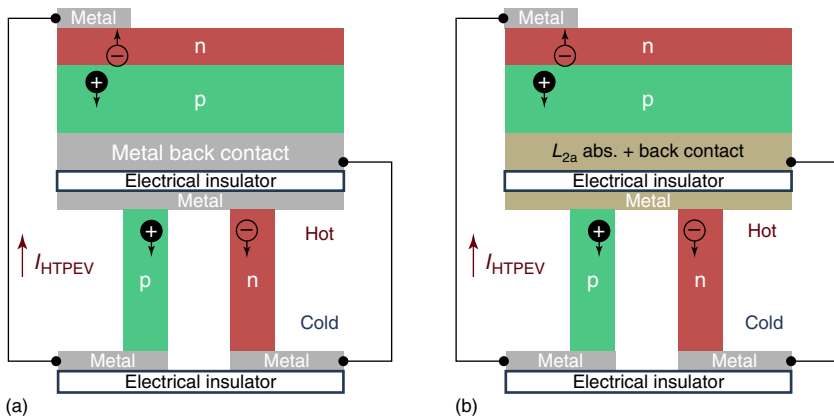


**Figure 12.4** Schematics of the device structures discussed in this work. (a) CASE 1, in which the TEG is just placed underneath the solar cell and is electrically connected to it; (b) CASE 2, where also the low frequency portion of the spectrum is recovered by introducing an additional absorbing layer. (Lorenzi *et al.* 2015 [15]. Reproduced with permission of Cambridge University Press.)

adding a TEG leads to 10% increase in power, thus a  $165 \text{ W/m}^2$  PVTE module, the extra cost can be as high as 150 \$. However, for large size and large quantities prices may easily be halved. As higher efficiency TEGs are developed, the present high prices should come down with increased amounts of units produced, following experience curve theory, for example, [14].

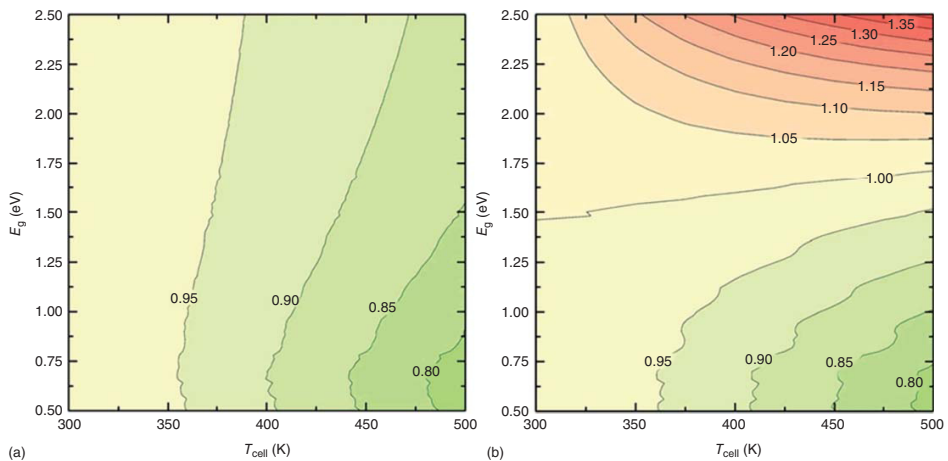


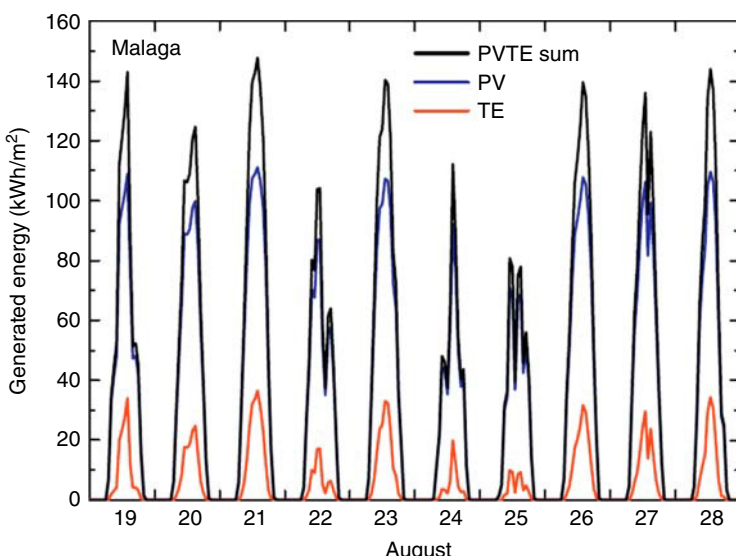
**Figure 12.5** PVTE efficiency (%) versus  $E_g$  and  $T_{cell}$ , normalized to the PV efficiency for  $T_{cell} = 300$  K: (a) Case 1, without absorbing layer (b) Case 2, with absorbing layer. (Lorenzi *et al.* 2015 [15]. Reproduced with permission of Cambridge University Press.)

### 12.1.7 Overall Feasibility

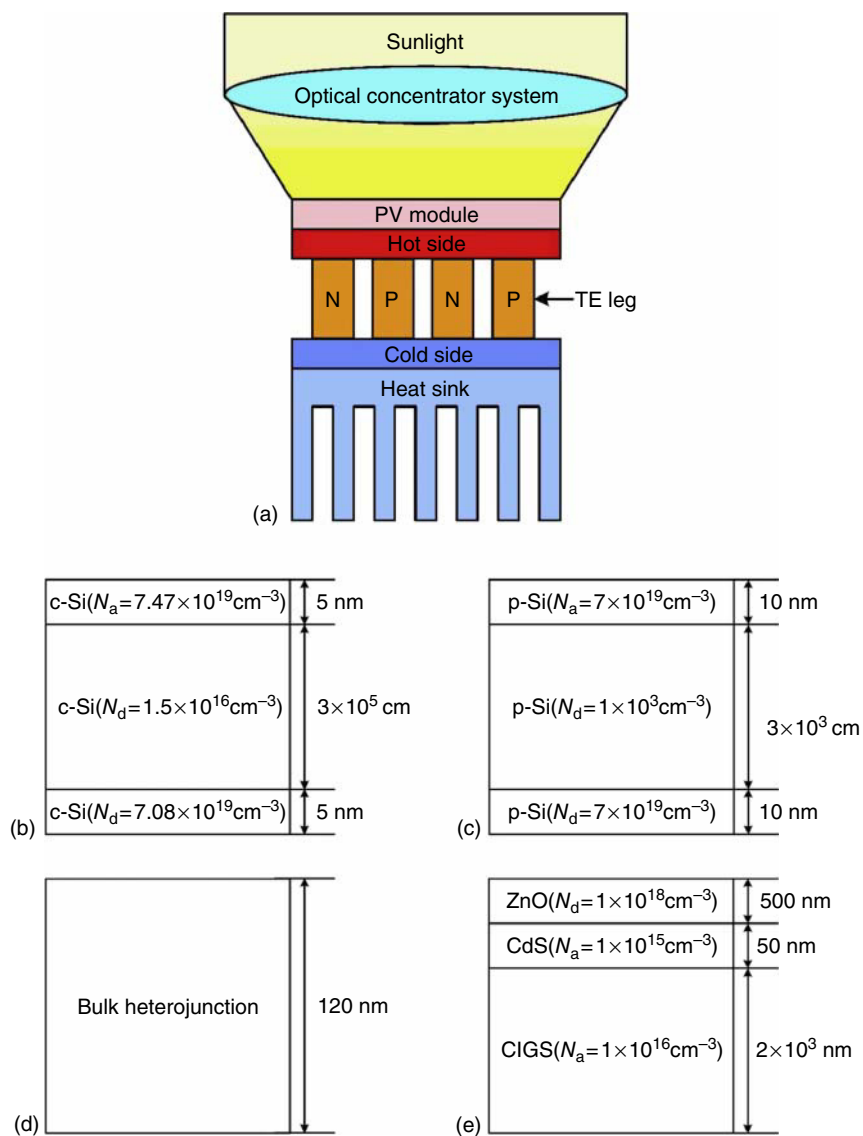
Lorenzi *et al.* investigated the conditions for beneficial coupling of TEG and PV devices [15]. Their quantitative model correlated the efficiency of the PVTE with the energy gap and the working temperature of the solar cell. The results showed that one should not only recover the heat released by relaxation of hot electron–hole pairs but also capture the low-energy part of the solar spectrum. Figure 12.4 shows two schematics of the device structures discussed in this work. The PVTE efficiency of the two PVTE devices are shown in Figure 12.5 as a function of energy band gap  $E_g$  and cell temperature  $T_{cell}$ . A detailed calculation process was described in the paper [15].

The feasibility of the PVTE hybrid module was also investigated by Sark *et al.* [10]. He proposed to use the thermal waste from PV by attaching TEG to the back of the PV modules to form a PVTE hybrid module. Because of the temperature difference over the TEG, additional electricity can be generated. According to his calculation, employing present day thermoelectric materials with a typical figure of merit ( $ZT$ ) of 1.2 at 300 K may lead to an efficiency enhancement of up to 23% for roof integrated PVTE modules. The annual energy yield would increase by 14.7–11%, for two annual irradiance and temperature profiles studied, that is, for Malaga, Spain, and Utrecht, the Netherlands, respectively. The generated energy for a 10-day period in August for the city of Malaga, Spain, is shown in Figure 12.6 [10].

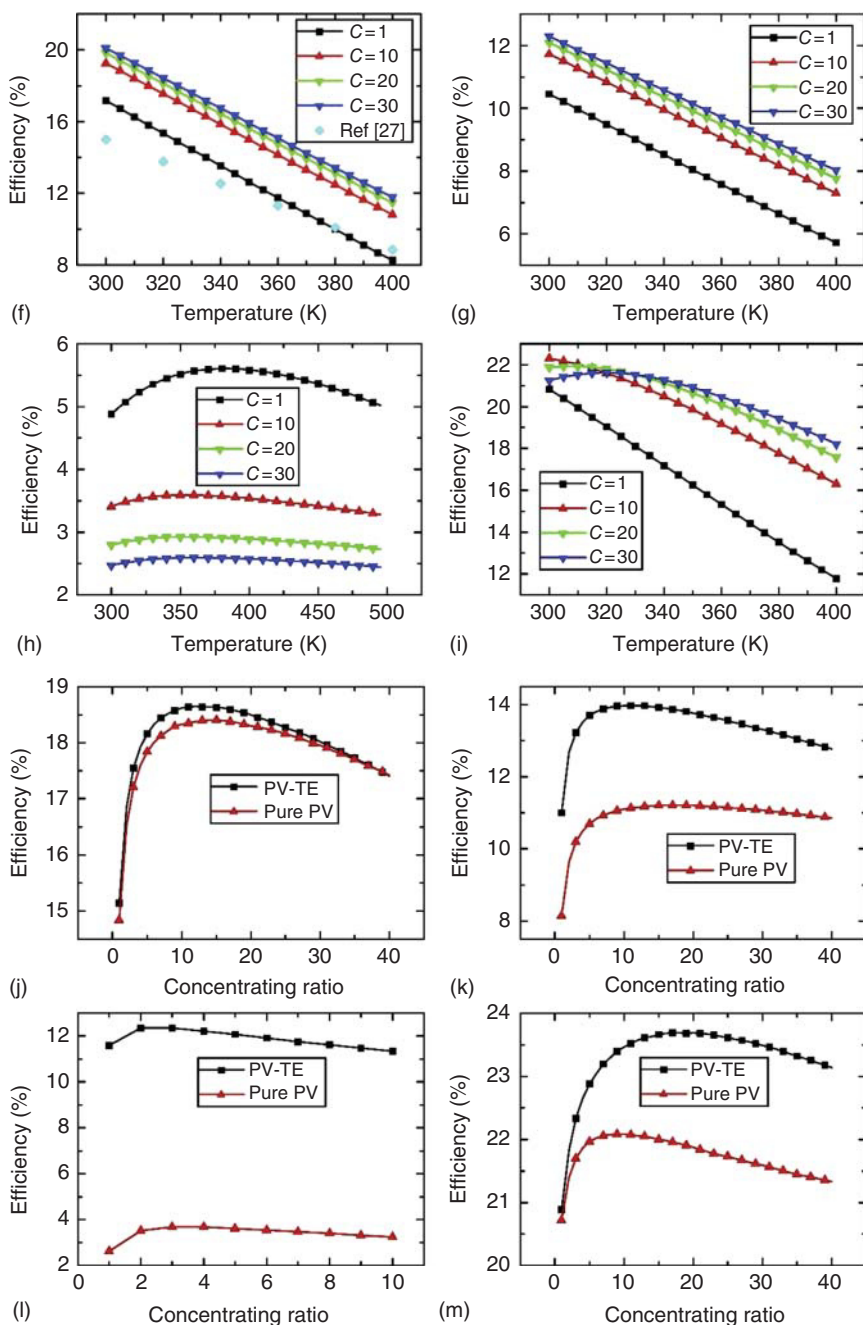
In order to estimate the performances of different PVTE modules, Zhang *et al.* [16] developed a theoretical model for evaluating the efficiency of concentrating PVTE hybrid systems, as shown in Figure 12.7a. The total efficiency can be calculated as  $\eta_{PVTE} = \eta_{PV} + (1 - \eta_{PV})\eta_{TE} - P_{cs}/P_s$ , in which  $P_s$  is the PVTE



**Figure 12.6** Generated PV, TE, and total energy for a 10-day period in August for the city of Malaga, Spain. (van Sark 2011 [10]. Reproduced with permission of Elsevier.)



**Figure 12.7** (a) Schematic diagram of the PVTE hybrid system; the simulation structure of PV: (b) c-Si PV, (c) p-Si TFPV, (d) polymer PV, (e) CIGS PV; influence of temperature on efficiency of PV: (f) c-Si PV, (g) p-Si TFPV, (h) polymer PV, (i) CIGS PV; efficiency of PVTE as a function of concentrating ratio: (j) c-Si PV, (k) p-Si TFPV, (l) polymer PV, (m) CIGS. (Zhang et al. 2014 [16]. Reproduced with permission of Elsevier.)

**Figure 12.7 (Continued)**

system power output and  $P_{cs}$  is the cooling system power consumption. Different PVs including crystalline silicon PV cell, silicon thin-film PV cell, polymer PV cell, and copper indium gallium selenide PV cell were considered as the PV part of the hybrid device, and their configurations used in the simulations are shown in Figure 12.7b–e. According to their calculated results, it was shown that the influence of temperature on the efficiency of PV cells was a crucial factor. In Figure 12.7f–i, the influence of temperature on the efficiency of different PV cells – (f) c-Si PV, (g) p-Si Thin-Film Photovoltaic (TFPV), (h) polymer PV, and (i) Copper Indium Gallium Selenide (CIGS) PV cell is presented. Among them, polymer PV has the best temperature stability at an elevated temperature compared to other PV technologies. It was also demonstrated by their simulations that the polycrystalline silicon thin-film PV cell is suitable for concentrating PVTE hybrid systems, whereas the polymer PV cell was more suitable for non-concentrating PVTE hybrid systems, as shown in their results in Figure 12.7j–m.

## 12.2 Different Forms of PVTE Hybrid Systems: The State of the Art

### 12.2.1 PVTE Hybrid Systems Based on Dye-Sensitized Solar Cell (DSSC)

Wang *et al.* first proposed a PVTE hybrid system based on dye-sensitized solar cell (DSSC) and the micro TEG based on bismuth telluride [7]. Figure 12.8 presents a schematic illustration and photograph of the novel PVTE hybrid device. A DSSC and a TE generator are the top cell and “bottom cell,” respectively, while an solar selective absorber (SSA) is placed in between the DSSC and the TE generator. The electric connection of the DSSC and TE generator are in series, and the cathode and anode of the hybrid device are the cathode of the DSSC and the anode of the TE generator, respectively. According to the transmittance spectrum of the glass sheet coated with fluorine-doped tin oxide (FTO) and the DSSC cell shown in Figure 12.9a, the DSSC absorbs part of the sunlight, which is converted into electricity.

A relatively high transmittance from a wavelength of 600–1600 nm can be observed from the spectrum, which suggests that this part of the illumination energy is not utilized by the DSSC cell. On the other hand, it is shown in Figure 12.9b that the SSA has a markedly low reflectance in the wavelength range from 600 to 1600 nm. This means the transmitted sunlight through a DSSC can be well absorbed by the SSA. Then the SSA converts the residual sunlight transmitted through a DSSC into heat energy. This heat is further converted into electricity by the TE generator using the Seebeck effect. The hybrid device as a whole can absorb a wide wavelength range of incident sunlight, and hence, should lead to higher energy conversion efficiency. The overall conversion efficiency of 13.8% was achieved using such a system. The power density generated from the PVTE system was about 12.8 mW/cm<sup>2</sup> when the temperature difference was around 6 °C. However, it was expected that the device performance might increase with further optimization [7].

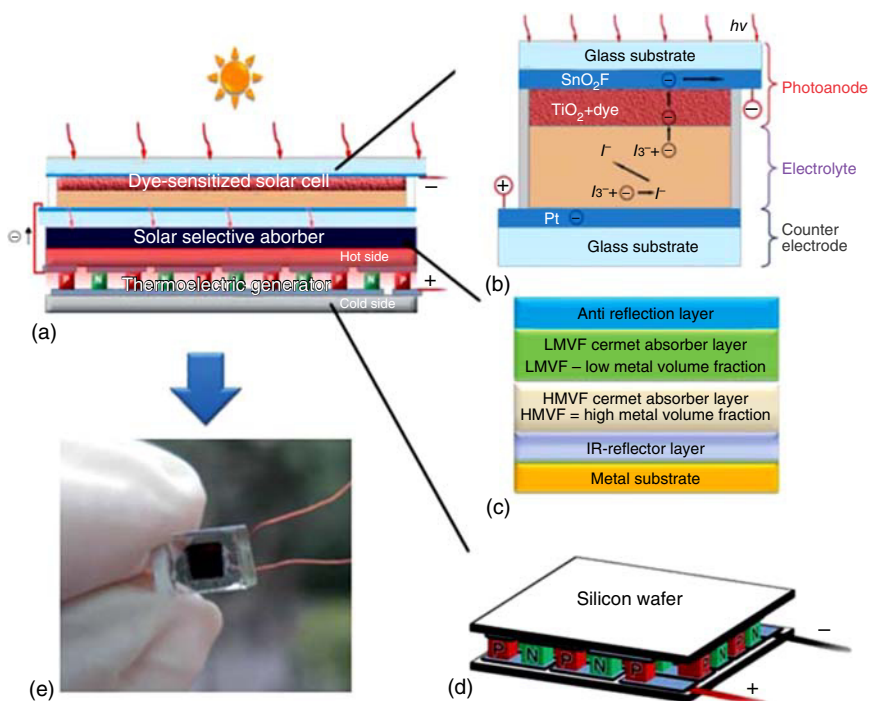


**Figure 12.8** Schematic illustration and photograph of the novel PVTE hybrid device using DSSC and SSA-pasted TE generator as the top cell and the “bottom cell”: (a) hybrid device; (b) DSSC; (c) SSA; (d) TE; and (e) photograph of the hybrid device. (Wang *et al.* 2011 [7]. Reproduced with permission of Royal Society of Chemistry.)

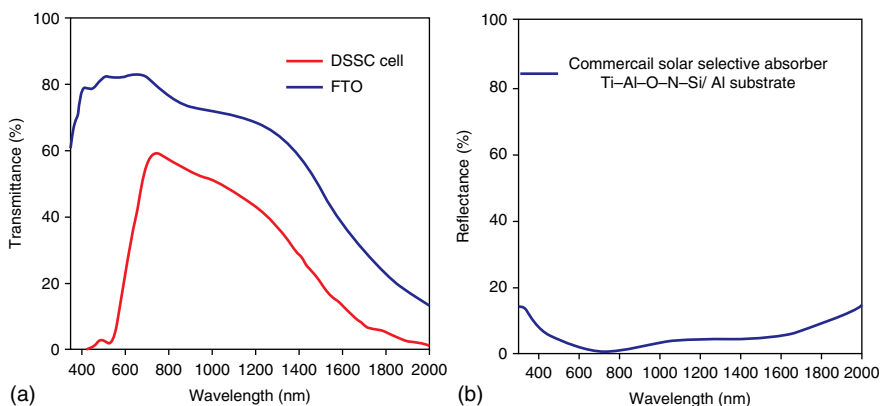


**Figure 12.9** (a) Transmittance spectra of the FTO and DSSC; (b) reflectance spectrum of the commercial SSA. (Wang *et al.* 2011 [7]. Reproduced with permission of Royal Society of Chemistry.)

### 12.2.2 Dye-Sensitized Solar Cell with Built-in Nanoscale $\text{Bi}_2\text{Te}_3$ TEG

Chen *et al.* proposed a new DSSC based on a thermoelectric  $\text{Bi}_2\text{Te}_3/\text{TiO}_2$  composite anode, in which the incorporated  $\text{Bi}_2\text{Te}_3$  nanoplates functioned as built-in nanoscale electron generators to convert “waste heat” into electricity and as a good photoreaction catalyst to enhance the charge transfer rate, resulting in 28% improvement of the overall power conversion efficiency [17]. The structure and mechanism for the built-in PVTE cell was demonstrated in Figure 12.10.

### 12.2.3 PVTE Using Solar Concentrator

PVTEs using concentrated solar energy are also of much interest because of the higher conversion efficiency and potentially lower cost. Da *et al.* proposed a comprehensive photon and thermal management approach to increase the full-spectrum solar energy utilization in PVTE hybrid systems [18]. According to their unique design, the spectrum control strategy is considered to suppress the reflection of full solar spectrum photons and enhance the transmission of photons with energy below the band gap of the PV cell from the top-located cell to the TE module in a PVTE hybrid system in order to realize reasonable utilization of the solar spectrum energy. The bioinspired moth-eye nanostructured surface and enhanced transmission film have been incorporated together to achieve such photon management in their study. The results have revealed that

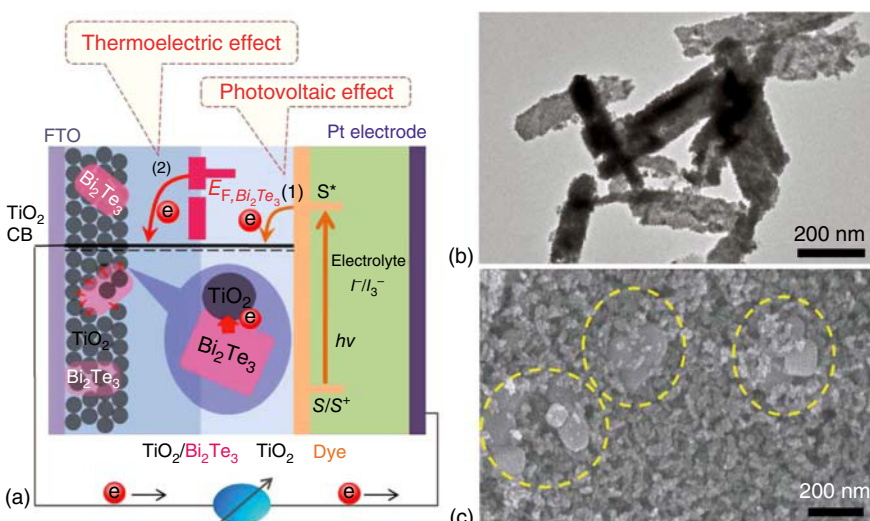


**Figure 12.10** Structure and electron generation/transfer of the composite anode-based DSSC. (a) Schematic illustration of the structure and electron generation/transfer process of the DSSC. There are two routes for energy conversion. Route (1) is the photovoltaic effect: from the excited dye to the conduction band (CB) of  $\text{TiO}_2$ ; route (2) is the thermoelectric effect: charge transport from the Fermi level of  $\text{Bi}_2\text{Te}_3$  nanoplate to  $\text{TiO}_2$  upon heating by sunlight irradiation. (b) TEM image of the as-synthesized  $\text{Bi}_2\text{Te}_3$  nanoplates. (c) SEM image of the composite anode film, in which  $\text{Bi}_2\text{Te}_3$  nanoplates are embedded in the mesoporous  $\text{TiO}_2$  network;  $\text{Bi}_2\text{Te}_3$  nanoplates are highlighted with dashed circles. (Source: Chen *et al.* 2012 [17]. Reproduced with permission of Royal Society of Chemistry.)

the reflection loss decreases significantly because of the moth-eye structured surface while the transmission is improved with enhanced transmission film. The performance of the PVTE hybrid systems was evaluated under both AM1.5 and AM0 illumination conditions for both terrestrial and space applications. Water cooling and radiative cooling were selected as thermal management methods for terrestrial and space applications, respectively. According to their results, it was found that the conversion efficiency of the PVTE hybrid system is higher than that of a single PV cell under the same conditions without any optical concentration. If a solar concentrator was used, although the overall efficiency of the PVTE hybrid system may decrease with the increment in the optical concentration ratio, the system could produce more total power output for both terrestrial and space applications (Figure 12.11). This work has provided instructive guides for designing PVTE hybrid systems working in both terrestrial and space environments [18].

Another hybrid PVTE system for concentrated solar energy conversion was proposed by Beeri *et al.* [19]. In their work, a hybrid PVTE demonstrator based on CMJ architecture was experimentally and theoretically investigated. Using commercially available MJ PV cell and TEG, their hybrid system's efficiency reached  $\sim 32\%$ . The direct electrical contribution of the TEG to the hybrid system's efficiency was enhanced by increasing the sun's concentration and temperature, reaching a maximal value of almost 20% for a sun concentration of  $\sim 300$ . According to their estimations, even higher efficiency and power values were expected when using more advanced PV cells and TE materials, with a real potential to exceed 50% total efficiency. They also evaluated the contribution of the Peltier cooling effect to the hybrid system's efficiency using finite element simulation of the TEG. Including this cooling effect, the total contribution of the TEG to the hybrid system's efficiency reached a value of almost 40% at a sun concentration level of 200. In their cooling effect analysis, a simple procedure was proposed for combining FEM and experimental approaches for estimation of the system's heat losses ( $\sim 33\%$  in the currently investigated conditions) by

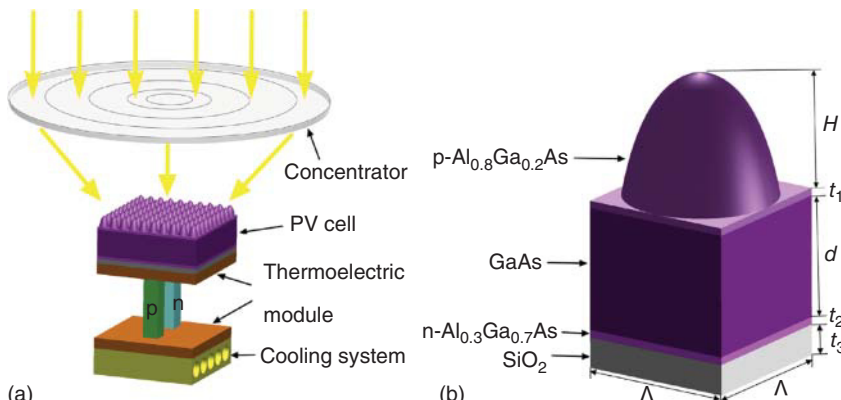


**Figure 12.11** (a) Schematic diagram of the PVTE hybrid system with an optical concentrator; (b) the structure of the PV cell within one period. (Da *et al.* 2016 [18]. Reproduced with permission of Elsevier.)

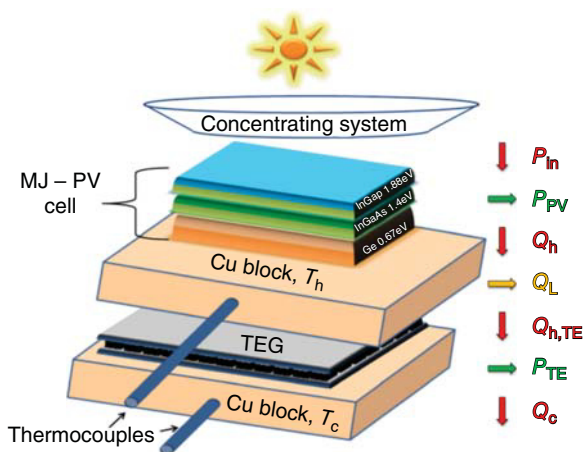


**Figure 12.12** Schematic description of the PVTE hybrid system. Light from the sun is concentrated and illuminates the MJ PV cell ( $P_{in}$ ), generating electrical power ( $P_{PV}$ ). The cell's input energy that is not converted into electrical power ( $Q_h$ ) heats a copper block that flattens the temperature and conducts some of the heat,  $Q_h$ , TE, toward the TEG's hot side, while some of the heat is lost to the environment,  $Q_L$ .  $Q_h$ , TE is conducted through the TEG, converting a part of it to an additional electrical power ( $P_{TE}$ ) while the rest of the heat ( $Q_c$ ) is removed from the system through a copper heat sink attached to the cold side of the TEG. The hot and cold copper blocks' temperatures,  $T_h$  and  $T_c$ , respectively, are measured by thermocouples. The materials and energy gap of each layer in the MJ PV cell are also illustrated. (Beeri *et al.* 2015 [19]. Reproduced with permission of American Institute of Physics.)

simple temperature measurements, rather than by complicated calorimetric heat flow measurements [19] (Figure 12.12).

#### 12.2.4 Solar-Thermoelectric Device Based on $\text{Bi}_2\text{Te}_3$ and Carbon Nanotube Composites

Another concept of utilizing solar energy is to first convert solar energy to heat and then use TE to convert such heat into electricity. Xia *et al.* proposed a solar–thermoelectric device based on this method. They utilized CNTs as solar energy absorber and heat convertor [20]. Figure 12.13c shows the schematics of their device. They investigated the solar thermoelectric properties of  $\text{B}_2\text{T}_3/\text{CNT}$  composites, which combined the solar–heat conversion advantage of CNT sheets and the thermoelectric power generation advantage of bismuth telluride. The higher light absorption up to 95% was attributed to the crossover-lapped structure feature of the CNT sheets in their study. The solar–thermoelectric conversion efficiency of the composite reaches up to 1% in natural sunlight without the aid of any kind of optical concentrator or thermal concentrator. According to their estimations, if an optical concentrator or thermal concentrator were applied, a much higher solar energy conversion efficiency of above 10% could be expected by further optimization. The scanning electron microscopy (aSEM) image CNT films, the SEM image of the CNT films coated with  $\text{Bi}_2\text{Te}_3$  at a thickness of 5  $\mu\text{m}$ , and an illustration of the device are shown in Figure 12.13.

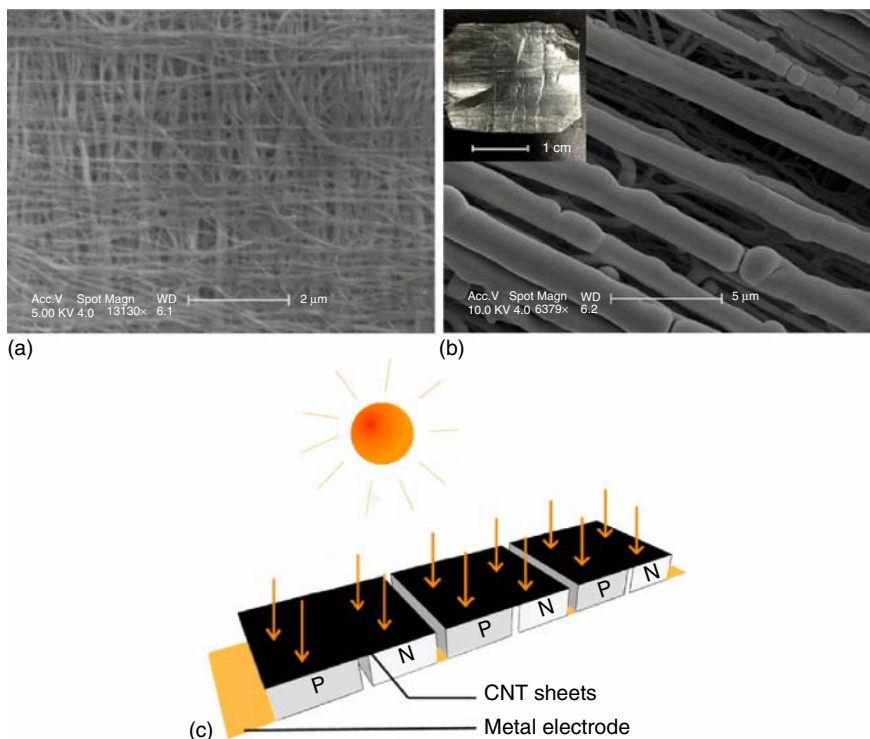


**Figure 12.13** (a) The scanning electron microscopy (SEM) image of 0.16 g/m<sup>2</sup> CNT films composed of crosswise overlapped multilayers. (b) The SEM image of the CNT films (areal density of 0.16 g/m<sup>2</sup>) coated with Bi<sub>2</sub>Te<sub>3</sub> at a thickness of 5 μm. Inset: photograph of the corresponding sample. (c) Illustration of the series connection of the devices for solar energy conversion. (Xia *et al.* 2014 [20]. Reproduced with permission of American Chemical Society.)

## 12.3 Optimizations of PVTE Hybrid Systems

### 12.3.1 Geometry Optimization of Thermoelectric Devices in a Hybrid PVTE System

Finding an optimized geometry for PVTE hybrid systems is a meaningful engineering work because it could result in the best efficiency out of the lowest possible cost. Hashim *et al.* investigated the optimal geometry for obtaining maximum power output and conversion efficiency of a thermoelectric generator (TEG) of hybrid PVTE system using a model developed in his work [2]. The overall power output  $P_{\text{out}}$  and conversion efficiency  $\eta_c$  of a hybrid PVTE system were estimated in their work. The results of their simulation showed that an increase in both the overall power output and the conversion efficiency may be achieved by incorporating a TEG to harvest waste heat from a PV cell. Their results also demonstrated that in practice an optimized geometry had to be a “trade-off” between achieving a large power output and using minimal

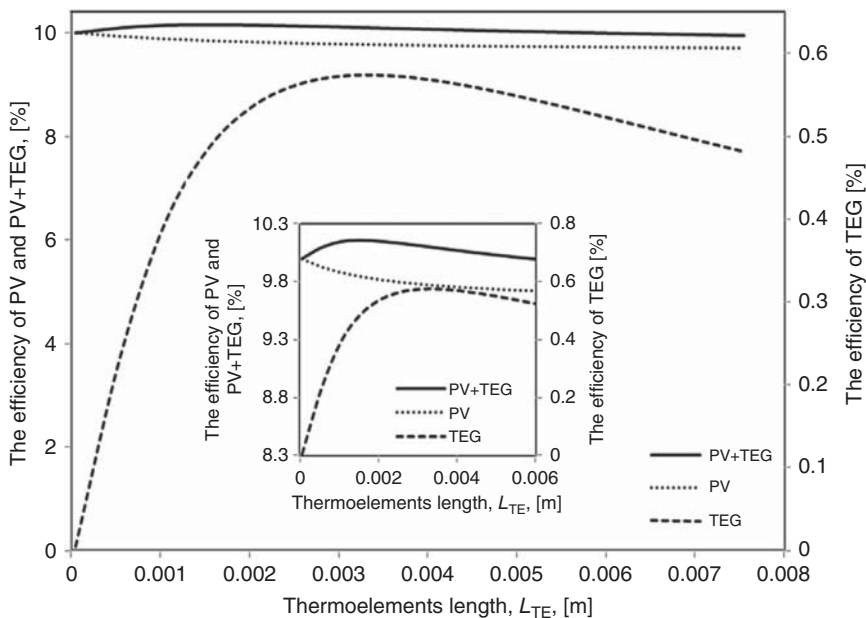
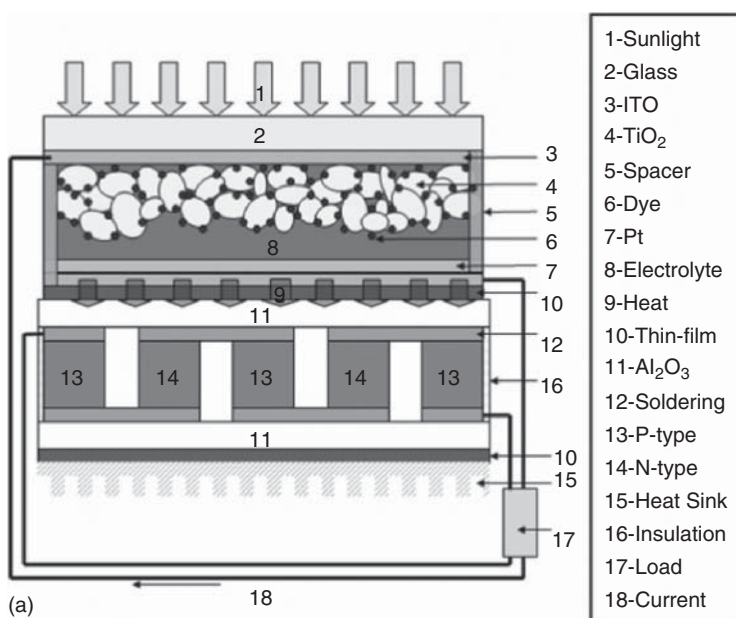


**Figure 12.14** The conversion efficiency of TEG, PV, and PV+TEG type versus thermoelement length in ambient atmosphere. (Hashim *et al.* 2016 [2]. Reproduced with permission of Elsevier.)

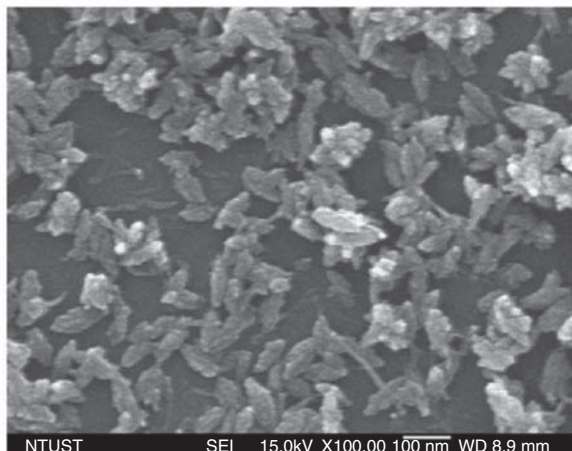
thermoelectric material, which means that a thermoelectric module (TEM) that has a smaller cross-sectional area than that of the PV cell can generate more electrical power than those having a larger cross-sectional area. Another finding in their study is that a significant increase in the power output could be obtained if the system operates in vacuum. In an ideal case where the convective heat losses are completely eliminated, the power output could be almost doubled. Some of their calculation results are shown in Figure 12.14.

### 12.3.2 Enhancing the Overall Heat Conduction and Light Absorption

Another strategy of increasing the overall conversion efficiency of a PVTE system is to enhance the heat conduction between PV and TE parts, as well as increasing the light absorption for PVTEs. Chang *et al.* proposed a method that increased the PVTE conversion efficiency by adding a CuO layer between the PV and TE parts [21]. They used electrophoresis deposition and self-prepared CuO nanofluid to deposit a CuO thin-film coating onto a Cu plate and then adhered it to the surface of a TEG. Experimental results showed that the CuO thin film coating on the TEG surface could enhance the overall heat conduction and elevate the temperature by around 2 °C and therefore increase the voltage by around 14.8%, thus enhancing the thermoelectric conversion efficiency of the TEG by 10% and increasing the overall power output by 2.35%. It was found that this solar-TEM could generate about 4.95 mW/cm<sup>2</sup> under a solar radiation intensity of about 100 mW/cm<sup>2</sup> according to their results (Figure 12.15).



(a)



(b)

**Figure 12.15** (a) Schematic diagram of a solar-thermoelectric module. (b) SEM image of the CuO nanoparticles produced by the proposed process. (Chang *et al.* 2011 [21]. Reproduced with permission of Elsevier.)

### 12.3.3 Fishnet Meta-Structure for IR Band Trapping for Enhancement of PVTE Hybrid Systems

Since the TE part of the hybrid system mainly utilizes the IR band of the solar energy, finding a way to improve the IR band trapping can therefore enhance the overall conversion efficiency for PVTE hybrid systems. Oh *et al.* proposed the

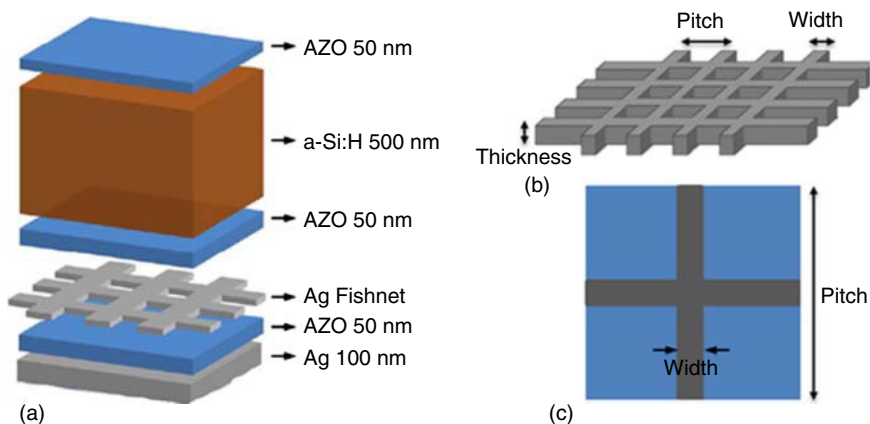


**Figure 12.16** (a) Schematic of the thin-film solar cell of the hybrid system with the fishnet embedded in the back passivation layer. (a) 3D schematic of the solar cell; (b) design parameters of the fishnet structure; (c) top view of the schematic. (Oh et al. 2015 [22]. Reproduced with permission of Elsevier.)

embedding of a Ag fishnet meta-structure for a PVTE hybrid system to produce more electrical power of a TEG by absorbing more solar thermal energy [22]. The schematics of the thin-film solar cell of the hybrid system with the fishnet embedded in the back passivation layer are shown in Figure 12.16. The hybrid system consists of a hydrogenated amorphous silicon (a-Si:H) thin-film solar cell as a top cell and a TEG as a bottom cell. As shown in Figure 12.16, the planar fishnet structure is embedded in a back passivation layer of the solar cell to enhance solar thermal absorption near the infrared band of the solar spectrum. The main concept of this design was to conduct the absorbed thermal energy by the fishnet to the TEG, which could increase the temperature difference between the hot and cold sides of the TE generator. In their work, the fishnet structure was optimized through parametric simulation in terms of pitch, width, and thickness. The solar power spectrum was modeled by using the power spectral density of blackbody radiation to calculate the total solar thermal energy of the hybrid system. Their results showed that the hybrid system with the optimized fishnet structure could absorb more solar thermal energy than the system without fishnet by around 12 folds [22].

#### 12.3.4 Full-Spectrum Photon Management of Solar Cell Structures for PVTE Hybrid Systems

Xu *et al.* proposed an ultra-broadband photon management structure for crystalline silicon thin-film solar cells used in the PVTE hybrid system [23]. The significance of this structure was the ability to absorb 300–1100 nm solar spectrum and transmit 1100–2500 nm inferred energy, and this was realized by the nanostructures designed by them. According to their explanation, the smooth graded effective refractive index of the composite surface structure of moth-eye and inverted-parabolic can improve absorption in the shorter wavelength (300–700 nm), while absorption enhancement in the longer wavelength

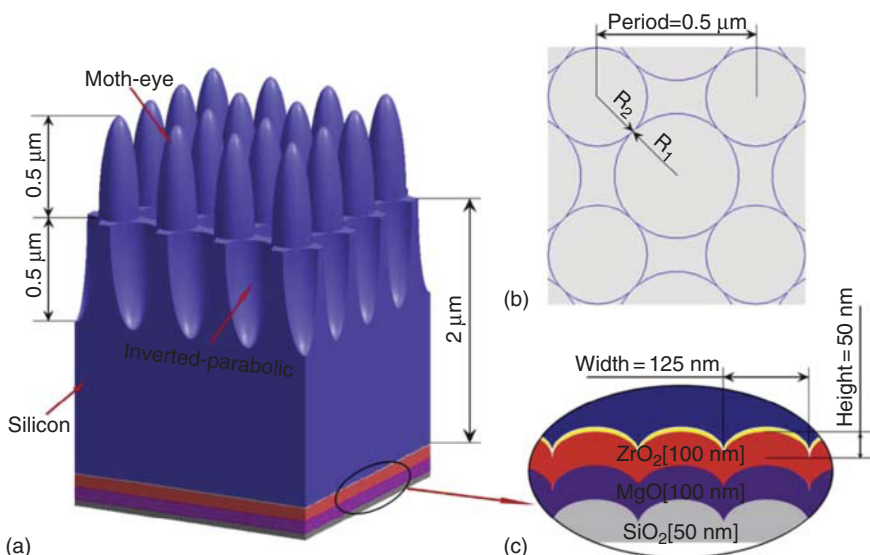


**Figure 12.17** (a) Structure of the designed c-Si thin-film solar cell. (b) Top view of the structure. (c) Cross- view of bottom patterned ITO- $ZrO_2$ - $MgO$ - $SiO_2$  antireflection coating. (Zhang *et al.* 2011 [24]. Reproduced with permission of Elsevier.)

(700–1100 nm) could be achieved by employing plasmonic back reflector and metallic gratings on the back side, which resulted in efficient light-trapping via broad angular scattering and microcavity mode, respectively. They were optimistic that this method of photon management in full spectrum could also be a guidance for many other types of thin-film PV devices used in the hybrid system (Figure 12.17).

### 12.3.5 An Automotive PVTE Hybrid Energy System Using Maximum Power Point Tracking

As one of the most important power management technologies for solar cells systems, the maximum power point tracking (MPPT) plays an equally important role in PVTE hybrid systems. Zhang *et al.* proposed a new automotive TEPV hybrid energy system. Based on the proposed MPPT, both the TEG and PV branches could achieve maximum power transfer independently [24]. In their work, a 100 W prototype was built and tested. Their results successfully verified the validity of the proposed system. By scaling up the power ratings proportionally up to 1 kW, the proposed system showed promise for different types of automobiles. Figure 12.18 gives a comparison of the advances in using the MPPT control by comparing the power output to the fixed duty cycle system. According to their result, the power improvement is from 7.5% to 9.4% due to the use of the MPPT when varying the hot-side temperature of the TE part of the hybrid system. Secondly, when the irradiance varied, as shown in Figure 12.18b, the power improvement was from 4.8% to 17.9% resulting from the use of the MPPT. Thus, their MPPT system successfully improved the overall output power of the hybrid energy system.

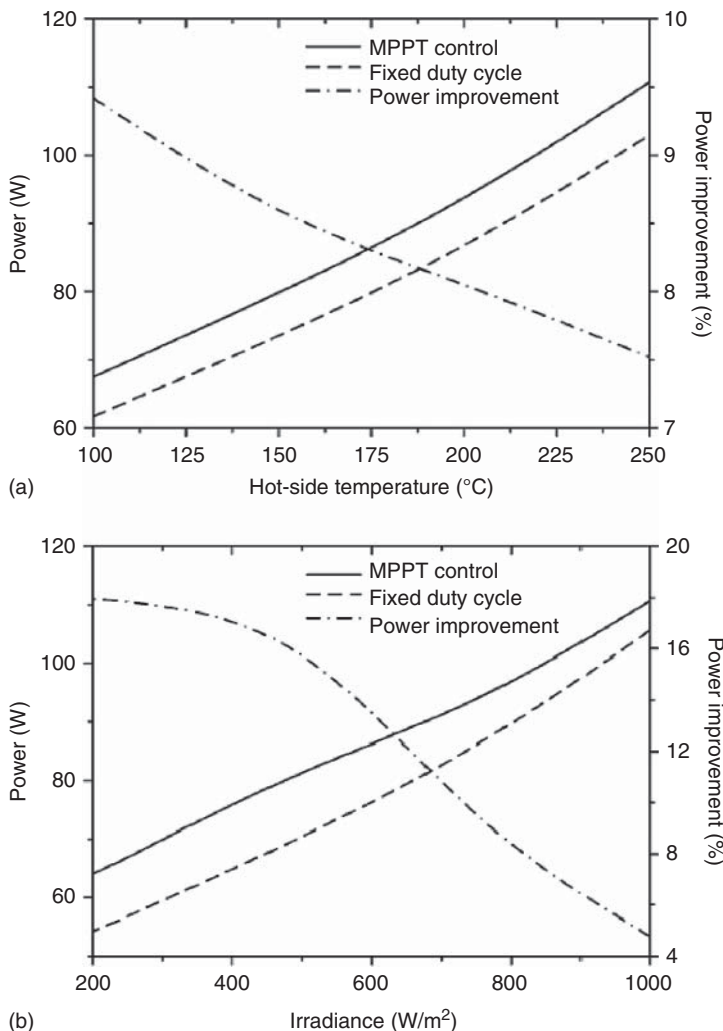


**Figure 12.18** Output power and power improvement. (a) With varying TEG output power. (b) With varying PV output power. (Xu 2015 [23]. Reproduced with permission of Elsevier.)

## 12.4 Application of PVTE Hybrid Systems

PVTE hybrid systems are based on the conventional solar cells and TEMs, where both light and heat are utilized, thereby increasing the total energy efficiency. As a result, the PVTE hybrid systems can be used in household roof panels, district heating by solar energy, and so on. Since the TEM can also be used as a Peltier cooler, the hybrid systems can also be used as solar-driven cooling modules, or by cooling the PV panel itself, which can result in the increase of photon electron conversion efficiencies in hot sites.

#### 12.4.1 Novel Hybrid Solar System for Photovoltaic, Thermoelectric, and Heat Utilization

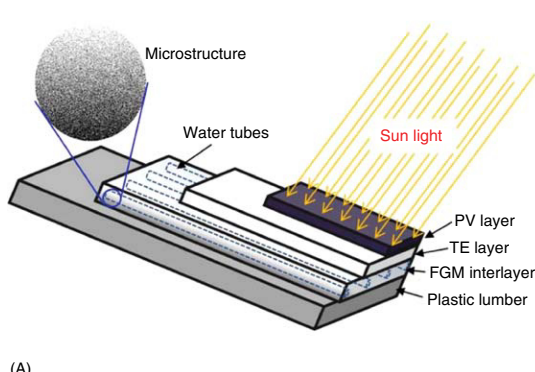
A novel hybrid solar system was designed by Yang *et al.* to utilize PV cells, thermoelectric (TE) modules, and hot water (HW) through a multilayered building envelope [8]. A schematic illustration of the hybrid solar panel was shown in Figure 12.19. According to their design, hybrid solar panels integrated with Si solar cells, TE materials, and FGM water tube systems were demonstrated; water pipelines were cast within a functionally graded material layer to serve as a heat sink, allowing heat to be easily transferred into flowing water through an aluminum-rich surface, while remaining insulated by a polymer-rich bottom. Their results showed that compared to the traditional solar panel, this design could achieve better overall efficiencies with higher electrical power output and thermal energy utilization. Based on theoretical conversion efficiency limits, the PV/TE/HW system was superior to PV/HW and traditional PV systems with 30% higher output electrical power according to their results. However, the advantages of the PV/TE/HW system were not significant from experimental data because of the low efficiency of the bulk TE material. This design was general and open to new PV and TE materials with emerging nanotechnology for higher efficiencies.

#### 12.4.2 Development of an Energy-Saving Module via Combination of PV Cells and TE Coolers for Green Building Applications

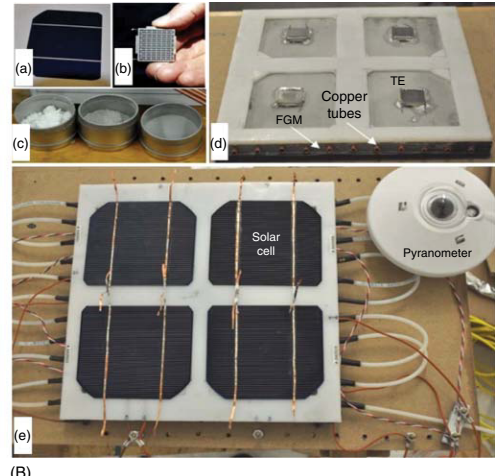
A solar-driven thermoelectric cooling module with a waste heat regeneration unit designed for green building applications was investigated by Cheng *et al.* [25]. In their work, the waste heat regeneration unit consisting of two parallel copper plates and a water channel with staggered fins was installed between the solar cells and the thermoelectric cooler. The useless solar energy from the solar cells and the heat dissipated from the thermoelectric cooler could both be removed by the cooling water such that the performance of the cooling module is elevated. Moreover, it made engineering sense to take advantage of the hot water produced by the waste heat regeneration unit during the daytime. Experiments were conducted by them to investigate the cooling efficiency of the module. Their results showed that the performance of the combined module was increased by increasing the flow rate of the cooling water flowing into the heat regeneration water channel due to the reductions of the solar cell temperature and the hot-side temperature of the thermoelectric coolers. The combined module was tested in the applications in a model house. It was found that the present approach is able to produce a 16.2 °C temperature difference between the ambient temperature and the air temperature in the model house. Figure 12.20 shows the schematic diagram of their designed experimental system.

#### 12.4.3 Performance of Solar Cells Using TE Module in Hot Sites

It was found that the efficiency of solar cell decreases with increase in its temperature. The efficiency of solar cells drops by 0.5% per degree celsius rise in



(A)



(B)

**Figure 12.19** (A) Schematic illustration of novel hybrid solar panel; (B) photos of (a) single-crystalline Si solar cell, (b) TE module, (c) HDPE and Al powder, (d) solar panel before attachment of solar cell, and (e) prototype of hybrid solar panel with water tube connections. (Yang and Yin 2011 [8]. Reproduced with permission of IEEE.)

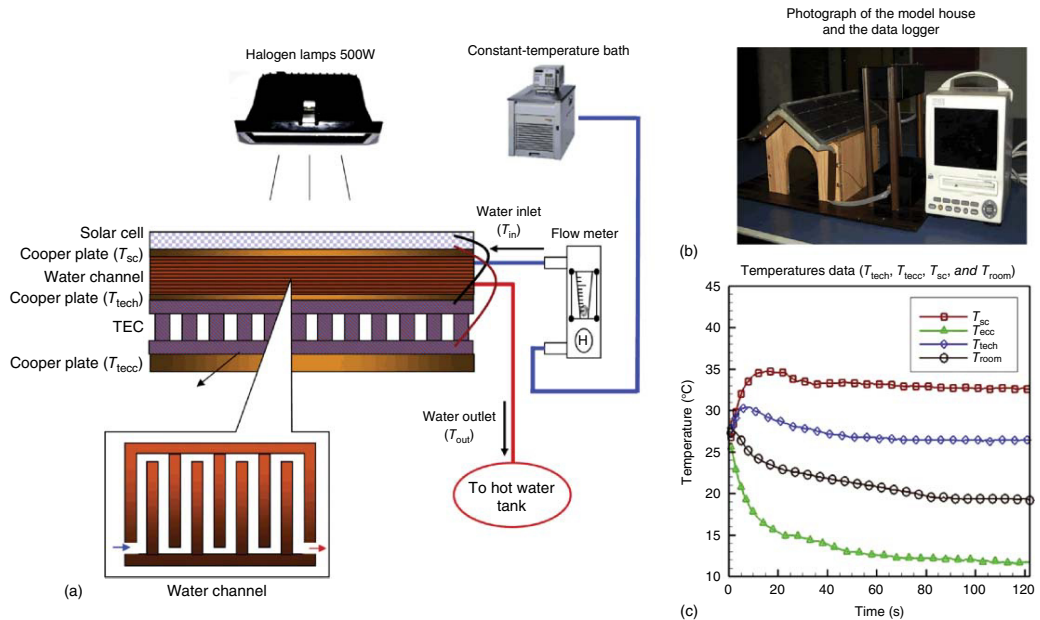


**Figure 12.20** (a) Schematic diagram of the experimental system, (b and c) performance test of the combined modules used in model house, with 2000 ml/min cooling flow rate. (Cheng *et al.* 2011 [25]. Reproduced with permission of Elsevier.)

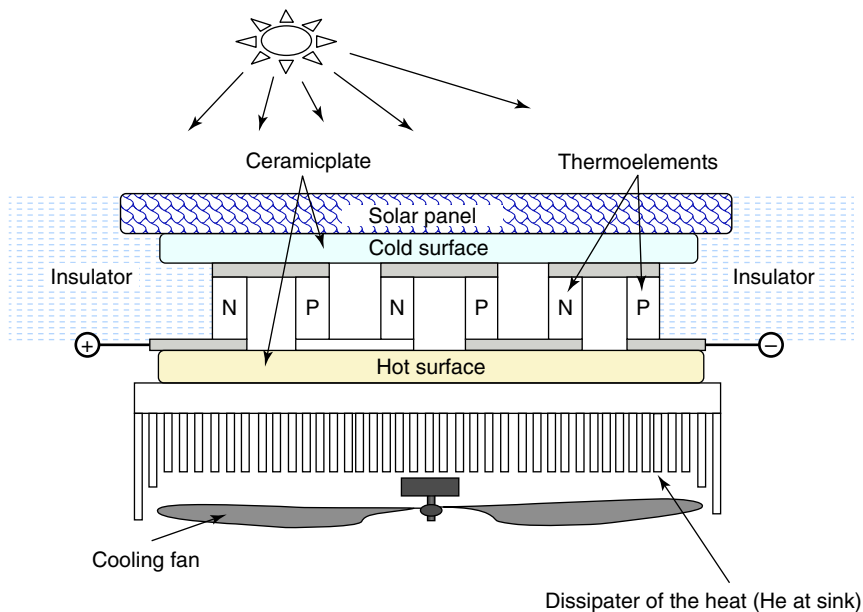


**Figure 12.21** Solar cell cooling system using a TE cell. (Benghanem *et al.* 2016 [26]. Reproduced with permission of Elsevier.)

temperature. For hot sites such as Madinah, the day time temperature is between 40 °C and 50 °C during the summer months. The cell temperature can reach a temperature as high as 83 °C. This affects the behavior of solar cells (SC) and decreases their efficiency. So cooling the solar cells is needed for its optimum performance. In order to address this issue, a hybrid PVTE system was proposed for PV applications in hot sites by Benghanem *et al.* [26]. The performance of solar cells was presented in this work using a TEM as cooling system. According to their study, the maximum cell temperature without cooling was 83 °C, and the cell temperature can be cooled down by 18 °C, therefore the system can be operated at 65 °C for solar cell temperature without loss of PV output. By operating the solar cell at lower temperature, more power can be drawn from it for the same solar irradiance, and longer life of solar cell is expected. On the other hand, the hybrid PVTE system proposed for PV applications in hot sites gives good performance while the additional cost is about 6% of the total cost of classical PV systems. Figure 12.21 shows the schematics of the solar cell cooling system using a TE cell.

## 12.5 Summary

The current PVTE hybrid systems are mostly based on the DSSC, a-Si solar cells for the PV part and BiTe modules for the TE part. Such combinations

are based on the absorption spectrums of the solar cells and the optimized working temperature of the TE module. At present, BiTe modules show the best conversion efficiency at near room temperature region. As for concentrated PVTE applications, TE materials with higher working temperature must be used, such as PbTe.

The optimization methods of PVTE hybrid systems include optimization of geometry of the device, improving the thermal contact between the PV and TE parts, improving the IR absorption, and the full-spectrum management of the incoming solar energy. Nevertheless, improving the individual efficiencies of the PV and TE modules is as well beneficial to the hybrid system.

PVTE hybrid systems have various applications just like its precedent solar panels. Because the hybrid systems not only utilize the light but also utilize the heat, such a system can be used in household roof panels, district heating by solar energy, energy supply for buildings, and so on. At the same time, the TEM can be used as a Peltier cooler; therefore the hybrid systems can also be used as solar-driven cooling modules, or by cooling the PV panel itself, which can result in the increase of photon electron conversion efficiencies in hot sites.

## References

- 1 Bjørk, R. and Nielsen, K. (2015) The performance of a combined solar photovoltaic (PV) and thermoelectric generator (TEG) system. *Solar Energy*, **120**, 187–194. doi: 10.1016/j.solener.2015.07.035
- 2 Hashim, H., Bomphrey, J.J., and Min, G. (2016) Model for geometry optimisation of thermoelectric devices in a hybrid PV/TE system. *Renewable Energy*, **87**, 458–463. doi: 10.1016/j.renene.2015.10.029
- 3 Rowe, D.M. (1995) *CRC Handbook of Thermoelectrics*, vol. **16**, CRC Press, New York, pp. 1251–1256. doi: 10.1016/S0960-1481(98)00512-6
- 4 TEG for Energy Efficiency in Heavy Vehicles n.d.:1–33.
- 5 Lan, Y., Minnich, A.J., Chen, G., and Ren, Z. (2010) Enhancement of thermoelectric figure-of-merit by a bulk nanostructuring approach. *Adv. Funct. Mater.*, **20**, 357–376. doi: 10.1002/adfm.200901512
- 6 Snyder, G.J. and Toberer, E.S. (2008) Complex thermoelectric materials. *Nat. Mater.*, **7**, 105–114. doi: 10.1038/nmat2090
- 7 Wang, N., Han, L., and He, H. (2011) A novel high-performance photovoltaic–thermoelectric hybrid device. *Energy Environ.*, **4**, 3676–3679. doi: 10.1039/c1ee01646f
- 8 Yang, D. and Yin, H. (2011) Energy conversion efficiency of a novel hybrid solar system for photovoltaic, thermoelectric, and heat utilization. *IEEE Trans. Energy Convers.*, **26**, 662–670. doi: 10.1109/TEC.2011.2112363
- 9 Kraemer, D., Hu, L., Muto, A., Chen, X., Chen, G., and Chiesa, M. (2008) Photovoltaic–thermoelectric hybrid systems: a general optimization methodology. *Appl. Phys. Lett.*, **92**, 6–9. doi: 10.1063/1.2947591
- 10 van Sark, W.G.J.H.M. (2011) Feasibility of photovoltaic: thermoelectric hybrid modules. *Appl. Energy*, **88**, 2785–2790. doi: 10.1016/j.apenergy.2011.02.008

- 11 Dallan, B.S., Schumann, J., and Lesage, F.J. (2015) Performance evaluation of a photoelectric-thermoelectric cogeneration hybrid system. *Sol. Energy*, **118**, 276–285. doi: 10.1016/j.solener.2015.05.034
- 12 Lorenzi, B., Acciarri, M., and Narducci, D. (2015) Analysis of thermal losses for a variety of single-junction photovoltaic cells: an interesting means of thermoelectric heat recovery. *J. Electron. Mater.*, **44**, 1809–1813. doi: 10.1007/s11664-014-3562-y
- 13 Han, L., Van Nong, N., Zhang, W., Hung, L.T., Holgate, T., Tashiro, K. et al. (2014) Effects of morphology on the thermoelectric properties of Al-doped ZnO. *RSC Adv.*, **4**, 12353. doi: 10.1039/c3ra47617k
- 14 Van Sark, W.G.J.H.M., Alsema, E.A., Junginger, H.M., De Moor, H.H.C., and Schaeffer, G.J. (2008) Accuracy of progress ratios determined from experience curves: the case of crystalline silicon photovoltaic module technology development. *Prog. Photovoltaics Res. Appl.*, **16**, 441–453. doi: 10.1002/pip.806
- 15 Lorenzi, B. and Narducci, D. (2015) Conditions for beneficial coupling of thermoelectric and photovoltaic devices. *J. Mater. Res.*, **30**, 2663–2669. doi: 10.1557/jmr.2015.174
- 16 Zhang, J., Xuan, Y., and Yang, L. (2014) Performance estimation of photovoltaic-thermoelectric hybrid systems. *Energy*, **78**, 895–903. doi: 10.1016/j.energy.2014.10.087
- 17 Chen, T., Guai, G.H., Gong, C., Hu, W., Zhu, J., Yang, H. et al. (2012) Thermoelectric Bi<sub>2</sub>Te<sub>3</sub>-improved charge collection for high-performance dye-sensitized solar cells. *Energy Environ. Sci.*, **5**, 6294. doi: 10.1039/c1ee02385c
- 18 Da, Y., Xuan, Y., and Li, Q. (2016) From light trapping to solar energy utilization: a novel photovoltaic-thermoelectric hybrid system to fully utilize solar spectrum. *Energy*, **95**, 200–210. doi: 10.1016/j.energy.2015.12.024
- 19 Beeri, O., Rotem, O., Hazan, E., Katz, E.A., Braun, A., and Gelbstein, Y. (2015) Hybrid photovoltaic-thermoelectric system for concentrated solar energy conversion: experimental realization and modeling. *J. Appl. Phys.*, **118**, 115104. doi: 10.1063/1.4931428
- 20 Xia, D., Liu, C., and Fan, S. (2014) A solar thermoelectric conversion material based on Bi<sub>2</sub>Te<sub>3</sub> and carbon nanotube composites. *J. Phys. Chem. C*, **118**, 20826–20831.
- 21 Chang, H., Kao, M.J., Cho, K.C., Chen, S.L., Chu, K.H., and Chen, C.C. (2011) Integration of CuO thin films and dye-sensitized solar cells for thermoelectric generators. *Curr. Appl. Phys.*, **11**, S19–S22. doi: 10.1016/j.cap.2010.12.039
- 22 Oh, S., Rai, P., Ramasamy, M., and Varadan, V.K. (2015) Fishnet metastructure for IR band trapping for enhancement of photovoltaic-thermoelectric hybrid systems. *Microelectron. Eng.*, **148**, 117–121. doi: 10.1016/j.mee.2015.10.016
- 23 Xu, Y., Xuan, Y., and Yang, L. (2015) Full-spectrum photon management of solar cell structures for photovoltaic-thermoelectric hybrid systems. *Energy Convers. Manag.*, **103**, 533–541. doi: 10.1016/j.enconman.2015.07.007

- 24 Zhang, X. and Chau, K.T. (2011) An automotive thermoelectric–photovoltaic hybrid energy system using maximum power point tracking. *Energy Convers. Manag.*, **52**, 641–647. doi: 10.1016/j.enconman.2010.07.041
- 25 Cheng, T.C., Cheng, C.H., Huang, Z.Z., and Liao, G.C. (2011) Development of an energy-saving module via combination of solar cells and thermo-electric coolers for green building applications. *Energy*, **36**, 133–140. doi: 10.1016/j.energy.2010.10.061
- 26 Benghanem, M., Al-Mashraqi, A.A., and Daffallah, K.O. (2016) Performance of solar cells using thermoelectric module in hot sites. *Renewable Energy*, **89**, 51–59. doi: 10.1016/j.renene.2015.12.011

## Index

### **a**

amorphous limit 222

### **b**

Boltzmann transport equation (BTE) 63  
boron-doped nanocrystalline silicon 223  
boost converter 182  
buck converter 180–182

### **c**

capacitively-coupled (CC) etching systems 73  
chemical vapor deposition (CVD) 67–68  
cold finger effect 102  
continuity equations 130–132  
cooling technologies 154–156  
 $\text{CuO}$  thin film 298

### **d**

deposition methods  
  electrochemical deposition (ECD) 216  
  inkjet printing 213  
  lithography 214  
  molding technique 213–214  
  screen-printing technique 213  
  vacuum depositions techniques  
    MBE technique 215  
    MOCVD 216  
    sputtering deposition 215  
    thermal evaporation 214–215  
  vapor–liquid–solid (VLS) growth 216–217

dye-sensitized solar cell (DSSC) 292–294

### **e**

elastic thermoelectric polymers 48  
electrical contact resistance 117–121  
electrical insulator plates 127  
electrical power output 128  
electrochemical deposition (ECD) 216  
electroencephalography (EEG) system 218  
electron beam lithography (EBL) 72  
*Electronic Resonance States* approach 221  
energy absorption/release processes 133  
*Energy filtering* technique 223

### **f**

flyback converter 184–185  
focused high-energy ion beam (FIB) 72  
fractional open circuit voltage 189–191  
functionally graded materials (FGM)  
  concept 3

### **h**

half-Heusler (HH) alloys 22–23  
heat equation 132  
heat exchangers  
  cold side heat exchanger 150–154  
  conductive heat transport 96  
  constant input heat flux 136  
  constant power 136  
  in TEG systems 148–150

- heat flux sensors  
 design parameters 248  
 detectivity D 242–243  
 features 249  
 ice sensor 269–274  
 integral sensitivity  $S_a$  240  
 laser power meter 274–278  
 microcalorimetry 268  
 modern sensors 235  
 noise-equivalent power (NEP) 242  
 noise level 241  
 physical properties 248  
 radiation heat flux sensors 257  
 real design, features of 255  
 self-calibration method 243–247  
 sensitivity  $S_e$  241  
 sensitivity threshold 241  
 sensors performance  
   Seebeck coefficient typical  
     temperature dependence 264  
   sensitivity temperature dependence 261–263  
   sensors sensitivity, calibration of 259  
   thermal resistance 263–264  
 thermal resistance  $R_T$  241  
 thermal time constant 243  
 thermoelectric material, properties of 251  
 thermoelectric modules  
   application 238  
   dimensions of sensor 254  
   miniaturization 237  
   pellets form-factor 251  
   pellets number 254  
   Seebeck effect 237  
   thermoelement height 252  
 units and characteristics 234–235  
 high-resolution transmission electron microscopy (HRTEM)  
   image 27
- i*  
 ice sensor 269–274  
 incremental conductance (IC)  
   method 189  
 infrared thermography 207
- inkjet printing 213
- I*  
 laser ablation 68  
 laser flash analyze/laser flash method 103  
 laser power meter 274–278  
 lead chalcogenides 2  
 lithography 214
- m*  
 macroscopic composites 62  
 maximum conversion efficiency 152  
 maximum power generation 152  
 maximum power point tracking (MPPT) 301  
 metal organic chemical vapor deposition (MOCVD) 216  
 microcalorimetry 268  
 microchannel heat exchangers 156  
 modulation doping 223  
 molding technique 213–214  
 molecular beam epitaxy (MBE)  
   technique 68, 215  
 Mott's formula 41  
 MPPT-methods  
   fractional open circuit voltage 189–191  
   incremental conductance (IC)  
     method 189  
   perturb and observe (P&O)  
     method 187–188
- n*  
 nanoprecipitates (NPs) 59  
 nanostructured materials  
   bulk nanostructured materials  
      $\text{Bi}_2\text{Te}_3$ -based nanocomposites 20–21  
   interfacial contact resistances 29  
   mechanical properties 29  
   PbTe-based nanostructured materials 21–22  
   stability, temperature gradients 28–29  
 nanostructured oxide materials  
   n-type oxides 28

- p-type oxides 26–28  
 ZT improvement  
   band bending concept 17  
   decouple thermopower and electrical conductivity 17  
   low thermal conductivity 16  
   nanocomposite system 17  
   PbS-Ag nanocomposite 18  
   PGEC concept 17  
   phonon scattering 17  
   Seebeck coefficient 16
- nanostructured silicon  
   electrical transport 63–66  
   nanometric defects 63  
   phonon transport 66  
   power factor 63
- nanowire geometry 73  
 nanowires 15  
 noise-equivalent power (NEP) 242  
 n-type polybenzimidazobenzophen-anthroline (BBL) 47
- o**  
 3 Omega method 105  
 organic thermoelectric materials 223–225
- p**  
 parasitic resistance 127  
 Peltier effect 135  
 perturb and observe (P&O) method 187–188  
 phase separation effects, IV-VI alloys 1–6  
 photoresists 216  
 plasma enhanced vapor deposition (PECVD) 68  
 photovoltaic-thermoelectric hybrid energy conversion  
   cost of TEG 286  
   dye-sensitized solar cell (DSSC) 292–294  
   energy loss 285–286  
   feasibility 289  
   fishnet meta-structure, IR band trapping 299–300
- full-spectrum photon management 300–301  
 generated power and efficiency 285  
 geometry optimization 297–298  
 green building applications 303  
 novel hybrid solar system 303  
 overall heat conductions and light absorptions 298–299  
 photovoltaic-thermoelectric hybrid energy conversion (*contd.*)  
   PV efficiency 285  
   solar cells (SC) performance 303–306  
   solar concentrator 294–296  
   solar spectrum energy utilization 283  
   TEG efficiency 285  
 polycrystalline silicon 57–60  
 polycrystalline silicon nanowires 76  
 poly-methyl methacrylate (PMMA) 72  
 power electronic converter  
   boost converter 182  
   buck converter 180–182  
   electric isolations 180  
   flyback converter 184–185  
   inductor voltage and capacitor currents 181  
   magnetic coupling 178  
   MPPT-methods  
     fractional open circuit voltage 189–191  
     incremental conductance (IC) method 189  
     perturb and observe (P&O) method 187–188  
     requirements 193  
     specification 192–193  
     transfer functions 194–196  
     transformer 178  
 power factor (PF) 60, 62, 63, 222  
 power output 130, 137–139
- r**  
 radiation heat flux sensors 257  
 radioisotope thermoelectric generators (RTGs) 77  
 reactive ion etching (RIE) 73

**s**

screen-printing technique 213  
 Seebeck coefficient 37, 60, 101–103,  
     152, 223, 235, 245  
     and charge carrier mobility 44–45  
     and electronic structure 41–43  
 Seebeck effect 37, 237  
 self-calibration method 243–247  
 semi-crystalline bipolaronic polymers  
     43  
 sensitivity threshold 241  
 SiGe alloys 77–79  
 silicon  
     bottom-up nanowires  
     catalyst deposition methods  
         70–71  
     catalyst materials 69–70  
     chemical vapor deposition  
         technique 67–68  
     laser ablation 68–69  
     material properties and  
         thermoelectric efficiency 71  
     molecular beam epitaxy (MBE)  
         68  
     solution based techniques 69  
 bulk and thin-film silicon and SiGe  
     alloys 77–79  
 degenerate and phase-segregated  
     silicon 60–63  
 nanocrystallinity and second-phase  
     formation 56  
 nanostructured silicon  
     electrical transport 63–66  
     energy harvesting 79–83  
     nanometric defects 63  
     phonon transport 66  
     power factor 63  
 nanowires and nanolayers 55  
 polycrystalline silicon 57–60  
 single-crystalline silicon (scSi)  
     57–60  
 thermoelectric generators (TEGs)  
     57–60  
 thermoelectric sensors 57  
 top-down silicon nanowires

material properties and  
 thermoelectric efficiency  
 75–76

preparation strategies 71–75  
 single-crystalline silicon (scSi) 57–60  
 single-junction device 286  
 skutterudites materials 24–26  
 solar concentrator 294–296  
 solar energy 286  
 solar power spectrum 300  
 soldering process 128  
 solution-liquid-solid (SLS)  
     process 69  
 spark plasma sintering (SPS) 23, 61,  
     115  
 supercritical-fluid-liquid-solid (SFLS)  
     processes 69  
 super-lattice systems 15

**t**

TDTR measurement 104  
 TEG system  
     channel hydraulic diameter, effect of  
         167–168  
     cold side heat exchanger 150–154  
     conversion efficiency 148  
     flat-plate heat exchanger *vs.* cross-cut  
         heat exchanger 164–167  
     governing equations 157  
     heat exchanger inlet/outlet plenums  
         158–162  
     heat exchanger performance 150  
     heat recovery 148  
     heat transfer coefficient 150  
     isothermal boundary conditions 148  
     micro- and nano-thermoelectric  
         materials 148  
     modified channel configuration  
         162–163  
     power-efficiency map 168  
     power generation 150  
     section design optimization 169  
     and thermoelectric power system  
         design 148  
     waste heat recovery systems 148

- tetrakis(dimethylamino)ethylene (TDAE) 45
- tetra-methyl-ammonium hydroxide (TMAH) 74
- thermal conduction 224
- thermal contacts 142
- thermal evaporation 214
- thermal resistances 242
- thermal time constant 243
- thermal transport
- conductive heat transport 96
  - via* convection 94–96
  - via* radiation 94
- thermoelectric generators (TEGs)
- CMOS circuit 57
  - cost of 286–287
  - deposition methods
    - electrochemical deposition (ECD) 216
    - inkjet printing 213
    - lithography 214
    - molding technique 213–214
    - screen-printing technique 213
    - vacuum depositions techniques 214  - vapor–liquid–solid (VLS) growth 216–217
- efficiency of 38
- elastic thermoelectric polymers 48
- human body heat source
- conduction heat transfer 205
  - infrared thermography 207
  - Seebeck effect 206
  - theoretical and experimental methods 206
- n-type organic conductors 47
- PV devices 289
- Seebeck effect 37
- thermal and electrical considerations 208–212
- thermal flow design approach 217
- wearable devices 218–220
- thermoelectric interfaces/junctions
- bismuth telluride based systems 115
- conventional thermoelectric module 111
- electrical and thermal contact resistances
- power output 114
  - Seebeck coefficient 113
  - Seebeck voltage 113
  - $ZT$  reduction 113
- electrical contact resistance 117–121
- infrared microscope 121–123
- soldering/brazing processes 115
- spark plasma sintering (SPS) 115
- thermoelectric module fabrication 111
- thermoelectric materials 5
- bismuth chalcogenides 39
  - bulk nanostructured materials
    - $\text{Bi}_2\text{Te}_3$ -based nanocomposites 20–21  - half-Heusler (HH) alloys 22–23
  - interfacial contact resistances 29
  - mechanical properties 29
  - PbTe-based nanostructured materials 21–22
  - skutterudites materials 24–26
  - stability, temperature gradients 28–29
  - CNT 40
  - conducting polymers 38
  - efficiency of 18
  - electrochemical transistor 45
  - nanostructured oxide materials
    - n-type oxides 28
    - p-type oxides 26–28
    - neutral/undoped conjugated polymers 39  - n-type thermoelectric materials 18
  - Onsager–Callen-relation 93
  - organic and inorganic semiconductors 38
  - organic conductors 38
  - physical properties 221
  - p-type materials 18

- radioisotope thermoelectric generators 39
- Seebeck coefficient  
and charge carrier mobility 44–45  
and electronic structure 41–43
- thermal transport 94–96
- thermoelectric power factor 40
- ZT*-value  
electrical conductivity 98–101  
Seebeck coefficient 101–103  
thermal conductivity 103–107
- thermoelectric micro-generator 79
- thermoelectric modules 114, 191, 192, 283  
characterization 128  
constant heat input and constant  $\Delta T$  144–145  
constant power 136  
cooling technologies and design  
challenges 154–156
- coupled and comprehensive simulation 157–168
- efficiency 139–142
- electrical and thermal contact  
resistance 112
- electrode/leg junction 128
- energy fluxes and heat equation 132
- heat exchangers design, in TEG systems 148–150
- microchannel heat exchangers 156
- miniaturization 237
- particle fluxes and continuity  
equation 130–132
- power output 137–139
- Seebeck effect 237
- soldering process 128
- thermal contacts 142
- thermocouples 144
- thermopiles 276
- thin film solar cell 300
- Thomson effect 135
- transfer functions 194–196
- transformer 178
- transmission electron microscopy (TEM) 62
- V**
- vacuum depositions techniques  
MBE technique 215  
MOCVD 216  
sputtering deposition 215  
thermal evaporation 214
- van- der- Pauw method 100
- vapor–liquid–solid (VLS) growth 216–217
- Z**
- ZT*-value 1, 15, 38, 53, 97, 106, 112, 113, 141, 148, 208, 221, 285  
electrical conductivity 98–101  
Seebeck coefficient 101–103